

An International
Forum For
The AE Science
and Technology

JOURNAL OF ACOUSTIC EMISSION

Vol.20/January-December 2002



EWGAE 2002 at Prague, Czech Republic

Endorsed by
AEWG
and
EWGAE

Published by
Acoustic Emission Group
Encino, CA USA

JOURNAL OF ACOUSTIC EMISSION

VOLUME 20, 2002

VIEWING AN ARTICLE

You need a software that can read a pdf-file. Two folders are provided for Windows 95/98/ME/2000 and for Macintosh. Each contains **Adobe Acrobat Reader®** Installer (ACRD5ENU.EXE or Reader Installer). Install one first before going further. Use of Adobe Acrobat ® (not provided) allows one to utilize the Search function. This gives the power to search for a name or a word in the entire volume.

PDF Files: Contents are listed below. Individual papers have file names of **20-xxx.pdf**, with xxx as their first page number.

ISSN 0730-0050

Copyright©2002 Acoustic Emission Group

Coden JACEDO

Contents

20-001	DAMAGE ESTIMATION OF CONCRETE BY AE RATE PROCESS ANALYSIS Masayasu Ohtsu, Makoto Ichinose and Hiroshi Watanabe	1
20-016	EXTRACTION OF HISTORIES OF DAMAGE MICRO-MECHANISMS IN UNIDIRECTIONAL COMPOSITES BY TRANSIENT-PARAMETRIC ANALYSIS Jie Qian and Yuris Dzenis	16
20-025	ACOUSTIC EMISSION SOURCES BY ATOMISTIC SIMULATIONS M. Landa, J. Cerv, A. Machová and Z. Rosecky	25
20-039	A WAVELET TRANSFORM APPLIED TO ACOUSTIC EMISSION SIGNALS: PART 1: SOURCE IDENTIFICATION M. A. Hamstad, A. O’Gallagher and J. Gary	39
20-062	A WAVELET TRANSFORM APPLIED TO ACOUSTIC EMISSION SIGNALS: PART 2: SOURCE LOCATION M. A. Hamstad, A. O’Gallagher and J. Gary	62
20-083	DIAGNOSTICS OF REINFORCED CONCRETE BRIDGES BY ACOUSTIC EMISSION Leszek Golaski, Pawel GebSKI and Kanji Ono	83
20-099	ANALYSIS AND IDENTIFICATION OF ACOUSTIC EMISSION FROM DAMAGE AND INTERNAL FRETTING IN ADVANCED COMPOSITES UNDER FATIGUE Yuris Dzenis and Jie Qian	99
20-108	ACOUSTIC EMISSION FROM MAGNESIUM-BASED ALLOYS AND METAL MATRIX COMPOSITES	

	Frantisek Chmelík, Florian Moll, Jens Kiehn, Kristian Mathis, Pavel Lukác, Karl-Ulrich Kainer and Terence G. Langdon	108
20-129	TRAINING AND CERTIFICATION ON THE FIELD OF ACOUSTIC EMISSION TESTING (AT) IN ACCORDANCE WITH THE EUROPEAN STANDARDISATION (EN 473) P. Tscheliesnig	129
20-134	THRESHOLD COUNTING IN WAVELET DOMAIN Milan Chlada and Zdenek Prevorovsky	134
20-145	DAMAGE DIAGNOSIS TECHNIQUE FOR BRICK STRUCTURES USING ACOUSTIC EMISSION Takuo Shinomiya, Yasuhiro Nakanishi, Hiroyuki Morishima and Tomoki Shiotani	145
20-153	EVALUATION OF DRYING SHRINKAGE MICROCRACKING IN CEMENTITIOUS MATERIALS USING ACOUSTIC EMISSION Tomoki Shiotani, Jan Bisschop and J. G. M. Van Mier	153
20-163	TRANSFORMATION PROCESSES IN SHAPE MEMORY ALLOYS BASED ON MONITORING ACOUSTIC EMISSION ACTIVITY Michal Landa, Václav Novák, Michal Blaháček and Petr Sittner	163
20-172	CHARACTERIZATION OF STRESS CORROSION CRACKING OF CuZn-ALLOYS BY ACOUSTIC EMISSION TESTING U.-D. Hünicke, M. Schulz, R. Budzier and J. Eberlein	172
20-179	ACOUSTIC EMISSION TESTING ON FLAT-BOTTOMED STORAGE TANKS: HOW TO CONDENSE ACQUIRED DATA TO A RELIABLE STATEMENT REGARDING FLOOR CONDITION G. Lackner and P. Tscheliesnig	179
20-188	ACOUSTIC EMISSION MEASUREMENTS ON SHELL STRUCTURES WITH DIRECTLY ATTACHED PIEZO-CERAMIC Franz Rauscher and Mulu Bayray	188
20-194	AE MONITORING OF CRYOGENIC PROPELLANT TANK Yoshihiro Mizutani, Takayuki Shimoda, Jianmei He, Yoshiki Morino and Souichi Mizutani	194
20-206	NON-DESTRUCTIVE TESTING FOR CORROSION MONITORING IN CHEMICAL PLANTS M. Winkelmanns and M. Wevers	206
20-218	AE TECHNOLOGY AS A KEY ELEMENT OF THE OPERATION SAFETY SYSTEM AT REFINERY B. S. Kabanov, V. P. Gomera, V. L. Sokolov, A. A. Okhotnikov and V. P. Fedorov	218
20-229	STRUCTURAL INTEGRITY EVALUATION OF WIND TURBINE BLADES USING PATTERN RECOGNITION ANALYSIS ON ACOUSTIC EMISSION DATA	

	A. A. Anastassopoulos, D. A. Kouroussis, V. N. Nikolaidis, A. Proust, A. G. Dutton, M. J. Blanch, L. E. Jones, P. Vionis, D. J. Lekou, D. R. V. Van Delft, P. A. Joosse, T. P. Philippidis, T. Kossivas and G. Fernando	229
20-238	LOW ALLOY STEEL METAL DUSTING: DETAILED ANALYSIS BY MEANS OF ACOUSTIC EMISSION P. J. Van De Loo, A. Wolfert, R. Schelling, H. J. Schoorlemmer and T. M. Kooistra	238
20-248	RECONSTRUCTION METHOD OF DYNAMIC FRACTURE PROCESS INSIDE THE MATERIAL WITH THE AID OF ACOUSTIC EMISSION Yasuhiko Mori, Yoshihiko Obata and Takateru Umeda	248
20-257	NON-DESTRUCTIVE EVALUATION OF BRAZED JOINTS BY MEANS OF ACOUSTIC EMISSION H. Traxler, W. Arnold, W. Knabl and P. Rödhammer	257
20-265	DAMAGE MODE IDENTIFICATION AND ANALYSIS OF COATED GAS TURBINE MATERIALS USING A NON-DESTRUCTIVE EVALUATION TECHNIQUE Y. Vougiouklakis, P. Hähner, V. Kostopoulos and S. Peteves	265
20-274	ACOUSTIC EMISSION DURING STRUCTURE CHANGES IN SEMI-CRYSTALLINE POLYMERS J. Krofta, Z. Prevorovsky, M. Blaháček and M. Raab	274
20-285	ACOUSTIC EMISSION CHARACTERISTICS OF SURFACE FRICTION IN BIO-MEDICAL APPLICATION D. Prevorovsky, Z. Prevorovsky, J. Asserin, and D. Varchon	285
20-292	ACOUSTIC EMISSION DURING MONOTONIC AND CYCLIC DEFORMATION OF A BRITTLE LIMESTONE A. Lavrov, M. Wevers and A. Vervoort	292
20-300	LEAK DETECTION BY ACOUSTIC EMISSION USING SUBSPACE METHODS Amani Raad, Fan Zhang and Ménad Sidahmed	300

Contents20.pdf	Contents of Volume 20 (2002)	I-1 - I-3
AuIndex20.pdf	Authors Index of Volume 20	I-4
AusNotes.pdf	Policy/Author's Notes/Announcement/Subscription Information	I-5 - I-7
Ewgae02.pdf	EWGAE 2002, 25-th European Acoustic Emission Conference	10 p.

APPENDICES (Available on CD-ROM only)

Prosser.ppt	Presentation at AEWG45 by W. Prosser (NASA Langley)
PAC Folder	Presentation at AEWG45 by T. Tamutas (Physical Acoustics Corp.)
Vallen Folder	Presentation at AEWG45 by H. Vallen (Vallen Systeme)
AGU-Vallen	Wavelet Transform Freeware and Introduction by M. Hamstad

Authors Index of Volume 20 (2002)

A. A. Anastassopoulos,	229	Yasuhiko Mori	248
W. Arnold	257	Yoshiki Morino	194
J. Asserin	285	Hiroyuki Morishima	145
Mulu Bayray	188	Yasuhiro Nakanishi	145
Jan Bisschop	153	V. N. Nikolaidis,	229
Michal Blaháček	163, 274	Václav Novák	163
M. J. Blanch	229	Yoshihiko Obata	248
R. Budzier	172	A. O'Gallagher	39, 62
J. Cerv	25	Masayasu Ohtsu,	1
Milan Chlada	134	A.A. Okhotnikov	218
Frantisek Chmelík	108	Kanji Ono	83
A. G. Dutton	229	S. Peteves	265
Yuris Dzenis	16, 99	T. P. Philippidis	229
J. Eberlein	172	D. Prevorovsky	285
V. P. Fedorov	218	Zdenek Prevorovsky	134, 274, 285
G. Fernando	229	A. Proust	229
L. E. Jones	229	Jie Qian	16, 99
D. J. Lekou	229	M. Raab	274
P. A. Joosse,	229	Amani Raad	300
T. Kossivas	229	Franz Rauscher	188
T. M. Kooistra	238	P. Rödhammer	257
J. Gary	39, 62	Z. Rosecky	25
Pawel GebSKI	83	R. Schelling	238
Leszek Golaski	83	H. J. Schoorlemmer	238
V. P. Gomera	218	M. Schulz	172
P. Hähner	265	Takayuki Shimoda	194
M. A. Hamstad	39, 62	Takuo Shinomiya	145
Jianmei He	194	Tomoki Shiotani	145, 153
U.-D. Hünicke	172	Ménad Sidahmed	300
Makoto Ichinose	1	Petr Sittner	163
B. S. Kabanov	218	V. L. Sokolov	218
Karl-Ulrich Kainer	108	H. Traxler	257
Jens Kiehn	108	P. Tscheliesnig	129, 179
W. Knabl	257	Takateru Umeda	248
D. A. Kouroussis,	229	P. J. Van De Loo	238
V. Kostopoulos	265	D. R. V. Van Delft	229
J. Krofta	274	J. G. M. Van Mier	153
G. Lackner	179	D. Varchon	285
M. Landa	25, 163	A. Vervoort	292
Terence G. Langdon	108	P. Vionis	229
A. Lavrov	292	Y. Vougiouklakis	265
Pavel Lukác	108	Hiroshi Watanabe	1
A. Machová	25	M. Wevers	206, 292
Kristian Mathis	108	M. Winkelmanns	206
Souichi Mizutani	194	A. Wolfert	238
Yoshihiro Mizutani,	194	Fan Zhang	300
Florian Moll	108		

JOURNAL OF ACOUSTIC EMISSION

Editor: Kanji Ono

Associate Editors: A. G. Beattie, T. F. Drouillard, M. Ohtsu and W. H. Prosser

1. Aims and Scope of the Journal

Journal of Acoustic Emission is an international journal designed to be of broad interest and use to both researcher and practitioner of acoustic emission. It will publish original contributions of all aspects of research and significant engineering advances in the sciences and applications of acoustic emission. The journal will also publish reviews, the abstracts of papers presented at meetings, technical notes, communications and summaries of reports. Current news of interest to the acoustic emission communities, announcements of future conferences and working group meetings and new products will also be included.

Journal of Acoustic Emission includes the following classes of subject matters;

A. Research Articles: Manuscripts should represent completed original work embodying the results of extensive investigation. These will be judged for scientific and technical merit.

B. Applications: Articles must present significant advances in the engineering applications of acoustic emission. Material will be subject to reviews for adequate description of procedures, substantial database and objective interpretation.

C. Technical Notes and Communications: These allow publications of short items of current interest, new or improved experimental techniques and procedures, discussion of published articles and relevant applications.

D. AE Literature section will collect the titles and abstracts of papers published elsewhere and those presented at meetings and conferences. Reports and programs of conferences and symposia will also be presented.

E. AE Program and Data Files: Original program files and data files that can be read by others and analyzed will be distributed in CD-ROM.

Reviews, Tutorial Articles and Special Contributions will address the subjects of general interest. Non-technical part will cover book reviews, significant personal and technical accomplishments, current news and new products.

2. Endorsement

Acoustic Emission Working Group (AEWG), European Working Group on Acoustic Emission (EWGAE), and Committee on Acoustic Emission from Reinforced Composites (CARP) have endorsed the publication of Journal of Acoustic Emission.

3. Governing Body

The Editor and Associate Editors will implement the editorial policies described above. The Editorial Board will advise the editors on any major change. The Editor, Professor Kanji Ono, has the general responsibility for all the matters. Associate Editors assist the review processes as lead reviewers. Mr. Thomas F.

Drouillard is responsible for the AE Literature section. The members of the Editorial Board are selected for their knowledge and experience on AE and will advise and assist the editors on the publication policies and other aspects. The Board presently includes the following members:

P. Cole	(UK)
L. Golaski	(Poland)
M.A. Hamstad	(USA)
H.R. Hardy, Jr.	(USA)
T. Kishi	(Japan)
O.Y. Kwon	(Korea)
J.C. Lenain	(France)
P. Mazal	(Czech Republic)
S.L. McBride	(Canada)
C.R.L. Murthy	(India)
A.A. Pollock	(USA)
F. Rauscher	(Austria)
I. Roman	(Israel)
C. Scala	(Australia)
C. Scruby	(UK)
P. Tscheliesnig	(Austria)
H. Vallen	(Germany)
P. J. Van de Loo	(Netherlands)
M. Wevers	(Belgium)
B.R.A. Wood	(Australia)

4. Publication

Journal of Acoustic Emission is published annually in CD-ROM by Acoustic Emission Group, PMB 409, 4924 Balboa Blvd, Encino, CA 91316. It may also be reached at 6531 Boelter Hall, University of California, Los Angeles, California 90095-1595 (USA). tel. 310-825-5233. FAX 818-990-1686. e-mail: ono@ucla.edu

5. Subscription

Subscription should be sent to Acoustic Emission Group. Annual rate for 2003 and 2004 is US \$111.00 including CD-ROM delivery, by priority mail in the U.S. and by air for Canada and elsewhere. For additional print copy, add \$40. Print only +shipping is \$140. Overseas orders must be paid in US currencies with a check drawn on a US bank. VISA/MC accepted. Inquire for individual (with institutional order) and bookseller discounts.

6. Advertisement

No advertisement will be accepted, but announcements for books, training courses and future meetings on AE will be included without charge.

Notes for Contributors

1. General

The Journal will publish contributions from all parts of the world and manuscripts for publication should be submitted to the Editor. Send to:

Professor Kanji Ono, Editor - JAE
6531 Boelter Hall, MSE Dept.
University of California
Los Angeles, California 90095-1595 USA
FAX (1) 818-990-1686
e-mail: ono@ucla.edu

Authors of any AE related publications are encouraged to send a copy for inclusion in the AE Literature section to:

Mr. T.F. Drouillard, Associate Editor - JAE
11791 Spruce Canyon Circle
Golden, Colorado 80403 USA

Only papers not previously published will be accepted. Authors must agree to transfer the copyright to the Journal and not to publish elsewhere, the same paper submitted to and accepted by the Journal. A paper is acceptable if it is a revision of a governmental or organizational report, or if it is based on a paper published with limited distribution.

Compilation of annotated data files will be accepted for inclusion in CD-ROM distribution, so that others can share in their analysis for research as well as training. ASCII or widely accepted data formats will be required.

The language of the Journal is English. All papers should be written concisely and clearly.

2. Page Charges

No page charge is levied. One copy of CD-ROM will be supplied to the authors free of charge.

3. Manuscript for Review

Manuscripts for review need only to be typed legibly; preferably, double-spaced on only one side of the page with wide margins. The title should be brief. An abstract of 100-200 words is needed for Research and Applications articles. Except for short communications, descriptive heading should be used to divide the paper into its component parts. Use the International System of Units (SI).

References to published literature should be quoted in the text citing authors and the year of publication. These are to

be grouped together at the end of the paper in alphabetical and chronological order. Journal references should be arranged as below. Titles for journal or book articles are helpful for readers, but may be omitted.

H.L. Dunegan, D.O. Harris and C.A. Tatro (1968), Eng. Fract. Mech., 1, 105-122.

Y. Krampfner, A. Kawamoto, K. Ono and A.T. Green (1975), "Acoustic Emission Characteristics of Cu Alloys under Low-Cycle Fatigue Conditions," NASA CR-134766, University of California, Los Angeles and Acoustic Emission Tech. Corp., Sacramento, April.

A.E. Lord, Jr. (1975), Physical Acoustics: Principles and Methods, vol. 11, eds. W. P. Mason and R. N. Thurston, Academic Press, New York, pp. 289-353.

Abbreviations of journal titles should follow those used in the ASM Metals Abstracts. In every case, authors' initials, appropriate volume and page numbers should be included. The title of the cited journal reference is optional.

Illustrations and tables should be planned to fit a single page width (6.5"). For the reviewing processes, these need not be of high quality, but submit glossy prints or equivalent electronic files with the final manuscript. Lines and letters should be legible.

4. Review

All manuscripts will be judged by qualified reviewer(s). Each paper is reviewed by one of the editors and may be sent for review by members of the Editorial Board. The Board member may seek another independent review. In case of disputes, the author may request other reviewers.

5. Electronic Media

This Journal will be primarily distributed electronically by CD-ROM. In order to expedite processing and minimize errors, the authors are requested to submit electronic files or floppy disk copy of the paper. We can read Macintosh and IBM PC formats. On the INTERNET, you can send an MS Word file or the text portion to "ono@ucla.edu".

6. Color Illustration

We can process color illustration needed to enhance the technical content of an article. With the new format, authors are encouraged to use them.

e-MAIL ADDRESSES OF SELECTED AUTHORS

Athanasio Anastasopoulos <nassos@envirocoustics.gr >
Mulu Bayray <mbayray@iaa1.iaa.tuwien.ac.at>
Michal Blaháček <blahacek@it.cas.cz>
Franticek Chmelík <chmelik@met.mff.cuni.cz>
Yuris Dzenis <ydzenis@unl.edu>
Leszek Golaski <bmtlg@tu.kielce.pl>
Gerald Lackner <lag@tuev.or.at>
Michal Landa <ml@it.cas.cz>
Pavel Mazal <mazal@uk.fme.vutbr.cz>
Yoshihiro Mizutani <mizutani.yoshihiro@nasda.go.jp>
Yasuhiko Mori <mori@me.cit.nihon-u.ac.jp>
Masayasu Ohtsu <ohtsu@gpo.kumamoto-u.ac.jp>
Kanji Ono <ono@ucla.edu>
Zdenek Prevorovsky <zp@it.cas.cz>
Amani Raad <amani.raad@utc.fr>
Franz Rauscher <f.rauscher+e329@tuwien.ac.at>
Takuo Shinomiya <shinomiya@jreast.co.jp>
Tomoki, Shiotani <shiotani@mx1.alpha-web.ne.jp>, tomoki_shiotani@tobishima.co.jp
Michaela Schulz <Michaela.schulz@mbst.uni-rostock.de>
Hannes Traxler <hannes.traxler@plansee.at>
Peter Tscheliesnig <tsc@tuev.or.at>
Peter Van de Loo <peter.vandeloo@shell.com>
Yannis Vougiouklakis <vougiouklakis@jrc.nl>
Martine Wevers <martine.wevers@mtm.kuleuven.ac.be>
Mark Winkelmans <mark.winkelmans@notes.basant.be>

MEETING CALENDAR: The 46-th Meeting of AEWG

The next meeting of AEWG will be at Portland State University on Aug 5 and 6, 2003. The primer will be held on Aug 4, 2003. Send inquiry to "Richard Nordstrom" <nordsr@cecs.pdx.edu>.

Registration forms, as well as other information regarding this conference, can be found at:
<http://www.cecs.pdx.edu/~nordsr/AEWG46/aewg46.htm>

2003/2004 SUBSCRIPTION RATE

Base rate (CD-ROM) for one year	\$ 103.00
Add Postage of U.S. - Priority rate	\$ 8.00
All others - Air mail rate	\$ 8.00
CD-ROM + printed copy, surface mail: add	\$ 40.00
Print copy only with priority/air shipping	\$140.00

Payment must be in U.S. dollars drawn on a U.S. bank. Bank transfer accepted at
California Bank and Trust, San Fernando Valley Office (Account No. 080-03416470)
16140 Ventura Blvd, Encino, CA 91436 USA

Back issues available; Inquiry and all orders should be sent to (or Fax 1-818-990-1686):
Acoustic Emission Group
PMB 409, 4924 Balboa Blvd. Encino, CA 91316 USA

For inquiry through Internet, use the following address: ono@ucla.edu
Editor-Publisher Kanji Ono Tel. (310) 825-5233
Publication Date of This Issue (Volume 20): 31 March 2003.

DAMAGE ESTIMATION OF CONCRETE BY AE RATE PROCESS ANALYSIS

MASAYASU OHTSU, MAKOTO ICHINOSE and HIROSHI WATANABE

Graduate School of Science & Technology, Kumamoto University, Kumamoto 860-8555, Japan

Abstract

Damage estimation of structural concrete from concrete-core samples is developed, applying acoustic emission (AE) activity and damage mechanics. Generating behavior of AE events from a concrete sample in a uniaxial compression test is quantitatively analyzed, based on the rate process theory, because notable discrepancy of AE activity is observed between damaged and undamaged concrete. It is confirmed that the rate is substantially associated with pore volume responsible for the damage in concrete. The damage is quantitatively defined by a scalar-damage parameter in damage mechanics. Correlating the rate with the damage parameter, quantitative estimation of the damage is proposed in terms of the relative modulus of elasticity. An applicability of the procedure is confirmed in concrete samples of controlled damage due to freezing and thawing and of various cured ages. Further, concrete-core samples taken from reinforced concrete columns of an existing bridge are tested. The results suggest that the damage of concrete at the current state could be quantitatively estimated from AE rate process analysis without knowing the original state of the concrete at construction.

1. Introduction

Lately it is widely realized that concrete structures are no longer maintenance-free. As a result, evaluation techniques for diagnostic inspection are in great demand in concrete engineering. As a detailed inspection of a concrete structure in service, core samples are usually drilled out and then both chemical and physical properties are measured. Concerning mechanical property of the physical property, the compressive strength and the modulus of elasticity (Young's modulus) are normally determined by conducting a uniaxial compression test. These values are then compared, if possible, with those of the specification. Otherwise, there is no qualified procedure to estimate mechanical properties responsible for the durability and the deterioration of concrete. In most cases, only the strength is evaluated whether the obtained value is good enough against designed stress.

One example is shown in Fig. 1. These are results of tests on deteriorated concrete samples due to freezing-thawing cycles. The decrease of Young's modulus is reasonably observed with the increase in freezing-thawing cycles, whereas the decrease of the strength is unconfirmed. Because the tested concrete contained high percentage of entrained air (over 5%), the damages due to freezing and thawing cycles were minor up to 300 cycles. Ordinary concrete is a composite material of cement paste and aggregate. Even though cementation in the intergranular layer is deteriorated, the decrease of the strength might be not yet dominant due to load-bearing capacity of aggregate. Poor cementation, however, could lead to the decrease of the modulus and readily to loss of the durability. Not relying only on the strength, therefore, it is desirable to estimate the decrease of the modulus of elasticity in the existing concrete structures.

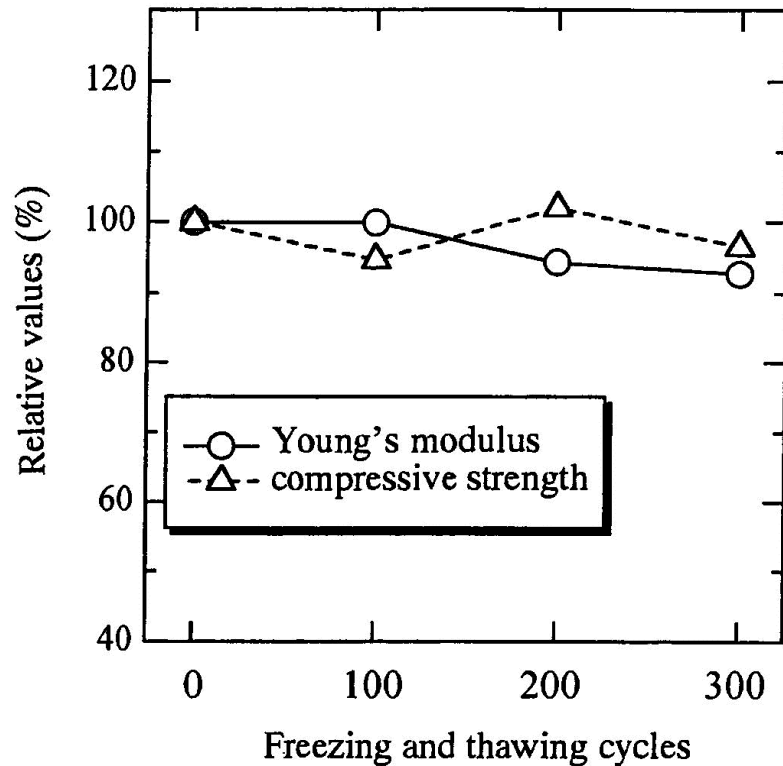


Fig. 1 Variations of the modulus of elasticity and the compressive strength during the process of freezing and thawing.

To inspect existing structures for maintenance, acoustic emission (AE) techniques deserve to draw a careful attention. This is because crack nucleation and extension are readily detected and monitored. In this respect, measurement of AE activity in the uniaxial compression test of core samples was proposed (Ohtsu et al., 1988; Ohtsu, 1992; Farahat and Ohtsu, 1994).

In order to formulate AE generating behavior under compression, the rate process analysis was introduced. It is demonstrated that the result of AE rate process analysis is closely associated with the presence of micro-cracks in concrete (Ishibashi et al., 1995). In concrete, the damage of defects and cracks are primarily nucleated due to chemical reaction and fatigue. It is also confirmed that the procedure based on the rate process analysis is applicable to these types of the damage in concrete (Yuno et al., 1995).

In the present paper, damage mechanics is introduced and the damage parameter is correlated with AE rate process analysis to estimate the decrease of the modulus in concrete. An applicability of the procedure is investigated by employing concrete samples of controlled damage, and then is applied to a field measurement.

2. Rate Process Analysis

When concrete contains a considerable amount of critical micro-cracks, AE activity is observed from low stress level in the compression test. In contrast, AE activity in intact or sound concrete is mostly observed right after dilatancy occurs due to micro-cracking prior to final failure. Thus, the presence and the nucleation of critical micro-cracks in concrete are closely associated with AE generating behavior under compression.

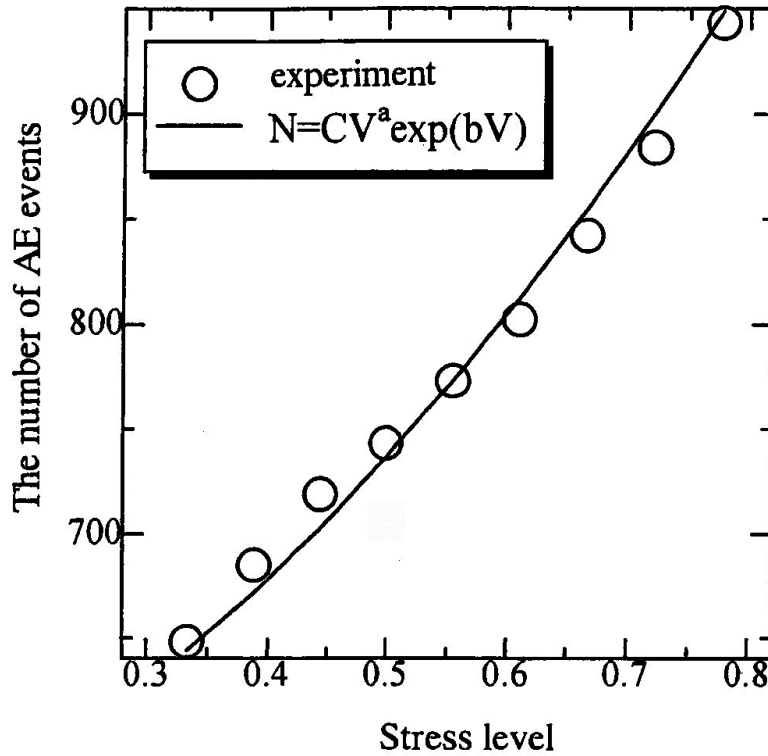


Fig. 2 Probability functions $f(V)$ in the rate process analysis of AE activity.

To formulate AE activity under compression, the rate process theory was introduced (Ohtsu, 1992). Probability function $f(V)$ of AE occurrence from stress level $V(\%)$ to $V+dV$ (%) is represented as a function of the incremental number of AE counts or hits, dN ,

$$f(V) dV = dN/N, \quad (1)$$

where N is the accumulated number of AE counts (hits) up to stress level $V(\%)$, which is normalized by the compressive strength. Equation 1 is known as the governing equation of the rate process, because the gradient dN/dV is not only a function of the probability $f(v)$, but also of the accumulated number N . To discriminate AE activities at low stress level, the function $f(V)$ is approximated as a hyperbolic function,

$$f(V) = (a/V) + b, \quad (2)$$

where a and b are empirical constants. In Fig. 2, typical results obtained in uniaxial compression tests are shown. Histograms on the values $f(V)$ were directly determined as $dN/(N dV)$ at each stress increment dV . In order to eliminate the noise due to fretting between the sample and loading plates in early stage as well as AE activity at final failure, only the stress range from 30% to 80% is taken into consideration. Applying Eq. 2, the distribution was approximated by the hyperbolic function with the least-square-error estimation. In Case A of which concrete sample was damaged due to freezing–thawing action, AE activity is observed to be high at low stress level. Thus, the probability function is modeled such that the coefficient ‘ a ’ is positive. Hereinafter, this coefficient is called the rate. In Case B of newly-cast concrete sample, the function is modeled as the negative rate ($a < 0$), presenting low AE activity at low stress level. These results show that AE activity at low stress level could be discriminated from the rate ‘ a ’.

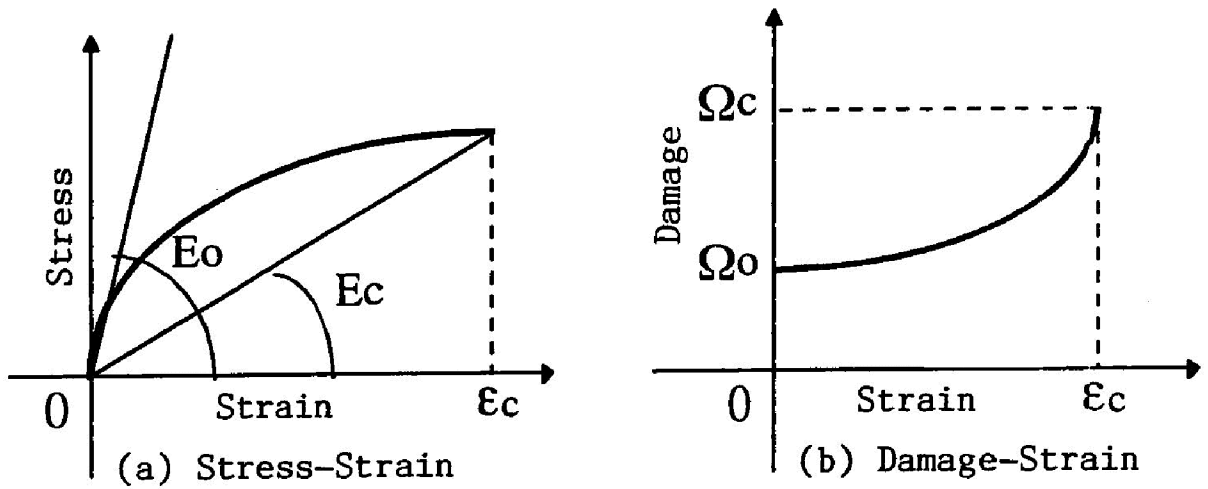


Fig. 3 Relation between total number of AE events and stress level, analyzed by the rate process analysis.

Substituting Eq. 2 into Eq. 1 and integrating it, a relationship between the total number of AE counts N and stress level $V(\%)$ is derived as,

$$N = C V^a \exp(bV). \quad (3)$$

Here, C is the integration constant. One example of the rate process analysis in the uniaxial compression tests is shown in Fig. 3. AE activity under compressive stress is approximated in reasonable agreement by Eq. 3, as confirmed in the previous research (Ohtsu, et al., 1988; Ohtsu, 1992; Farahat and Ohtsu, 1994).

3. Damage Parameter and the Rate ‘a’

From the continuum damage mechanics (Kachanov, 1980), the state of damage is represented by the scalar damage parameter Ω . In a simple model, modulus of elasticity (Young's modulus) E of a damaged material is expressed as,

$$E = E^*(1 - \Omega), \quad (4)$$

where modulus E^* is that of an intact material. In the uniaxial compression test of a concrete sample, a relation between stress and strain is obtained as shown in Fig. 4(a). Taking into account an initial or current damage when the core is drilled out, modulus E_o is defined as a tangential modulus and is associated with the degree of initial damage Ω_o as,

$$E_o = E^*(1 - \Omega_o). \quad (5)$$

During the uniaxial compression test, the damage increases from Ω_o to Ω_c as shown in Fig. 4(b), where Ω_c is the damage at the ultimate strain ϵ_c . In order to define the stress (σ) – strain (ϵ) relation as $\sigma = E\epsilon$, modulus E_c is defined as a secant modulus as shown in Fig. 4(a) and is presented,

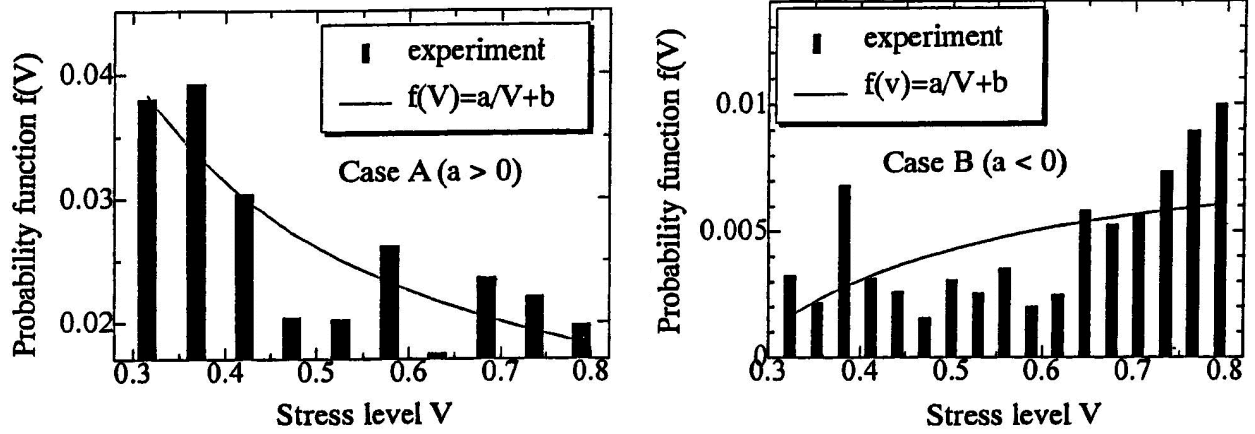


Fig. 4 (a) Stress-strain relation and elastic moduli: E_o and E_c . (b) Relation between damage and strain.

$$E_c = E^* (1 - \Omega_c). \quad (6)$$

In order to relate damage evolution $\Omega_c - \Omega_o$ with AE activity in the compression test, the relationship on amplitude distribution is introduced (Mogi, 1962),

$$n(A) = k A^{-m}. \quad (7)$$

Here $n(A)$ is the number of AE events of the amplitude from A to $A+dA$. k and m are empirical constants. Assuming that the crack volume is proportional to the amplitude of AE event, the evolution is formulated as

$$\Omega_c - \Omega_o = \int n(A) A dA. \quad (8)$$

Substituting Eqs. 3 and 7 into Eq. 8, the damage evolution is eventually represented as

$$\Omega_c - \Omega_o = (1 - m) A_o C (100)^a \exp(100b) / (2 - m), \quad (9)$$

where A_o is the threshold amplitude of the measuring system. This implies that the damage evolution is closely correlated with parameters m , a , and b . The correlation of these parameters with the damage evolution was previously studied in concrete samples of various damage levels (Iida et al., 2000). It is found that the evolution is highly correlated with the rate 'a', and that the parameter m is primarily associated with failure mechanisms (Ohtsu, 1987). Because failure mode of only uniaxial compression is generated in the test, the parameter m does not vary much during the evolution process. The parameter b is normally small and to be less correlated than others. Thus, it is concluded that the damage evolution $\Omega_c - \Omega_o$ is predominantly associated with the variation of the rate 'a'.

In concrete core samples taken from harbor structures, uniaxial compression tests were conducted (Ishibashi et al., 1998). After determining the pore distribution by the mercury intrusion method from the same core samples, the ratio of pore volume over $0.1 \mu\text{m}$ radius was compared with the rate 'a'. Results are given in Fig. 5. Strong correlation between the rate 'a' and the ratio of pore volume is observed. Because it is considered that the volume of large pores is closely associated with the deterioration of concrete (Matsuyama and Ohtsu, 1992), this result

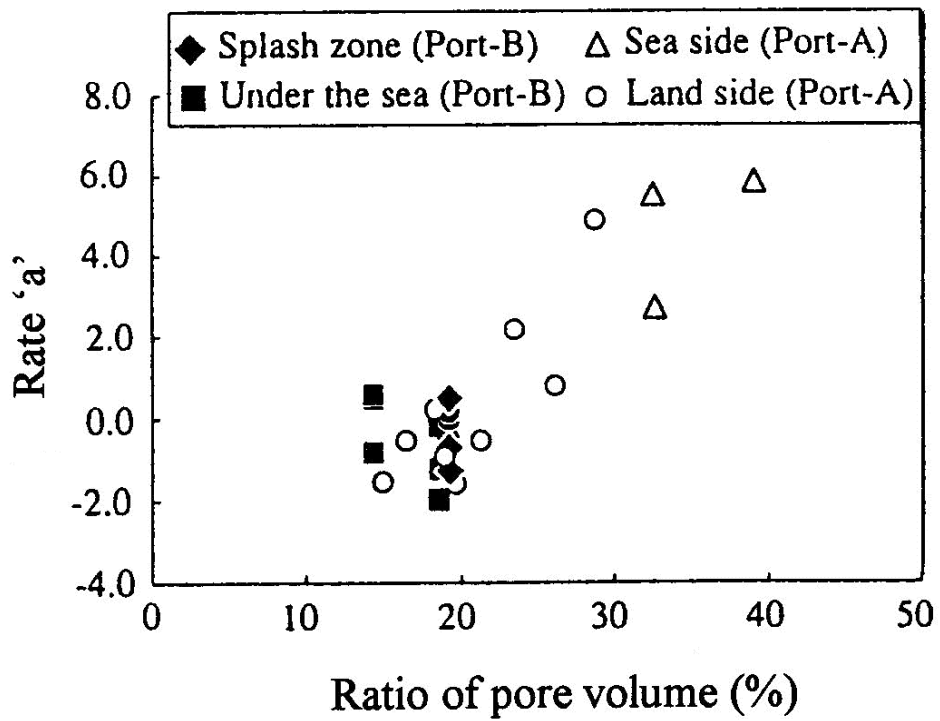


Fig. 5 Relation between the rate 'a' and pore volume.

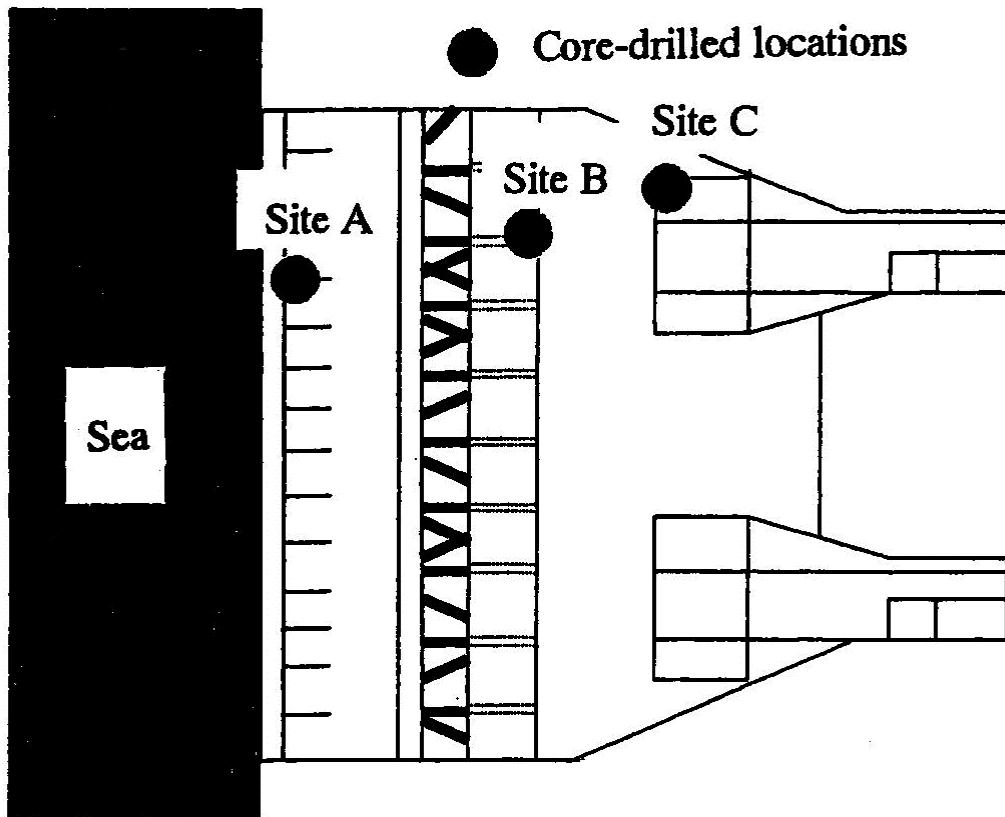


Fig. 6 Locations of core samples core-drilled in a nuclear power plant.

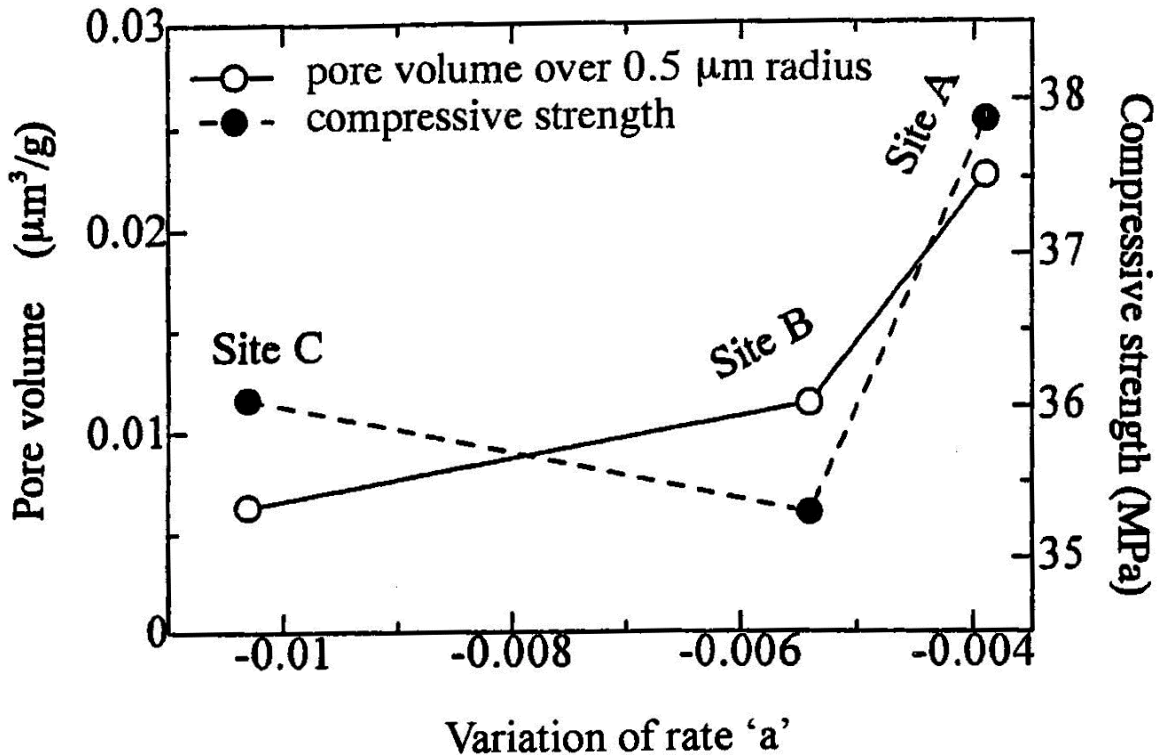


Fig. 7 Relations among the pore volume, the compressive strength, and the rate 'a' of the core samples.

confirms the feasibility of the relation in Eq. 9 and the rate 'a' is to be a key factor of the damage in concrete.

In order to confirm the relationship in Eq. 9, core samples were taken from an aqueduct of a nuclear power plant shown in Fig. 6. To drill core samples out, three sites were selected: at the gate (Site A), 20 m inland (Site B), and 30 m inland from the gate (Site C). Three core samples at each site were mold-cut of dimensions 7.4 cm diameter and 14.5 cm height. The uniaxial compression tests of the samples were conducted. AE events generated under compression were counted up to final failure by AE processor (LOCAN; PAC). An AE sensor of 1 MHz resonance was attached at the middle of the sample, where the surface was ground flat. For event-counting, the threshold level was set to 150 mV and the dead-time for event-counting was 1 ms. The filter frequency range was from 10 kHz to 300 kHz, and total amplification was 60 dB.

The compressive strength and the rate 'a' were determined as the averaged value of the three. Distribution of pore radii was also measured by the mercury intrusion method from concrete fragments at the three sites. After determining the pore distribution, the total volume of pore with the radii over 0.5 μm was determined, because the pore volume from 0.1 μm to 0.5 μm was negligible. Results of the pore volumes, the rate 'a', and the compressive strength are summarized in Fig. 7. From Site A to Site C, the pore volume decreases monotonously with the increase in the distance from the sea. This implies that the heaviest damage was introduced in concrete at the gate (Site A), where concrete was frequently deteriorated by seawater. Leaving from the seaside, the damage of concrete decreases. In accordance with the increase in the pore volume, the rate 'a' increases from Site C to Site A. Thus, the increase of the pore volume (over 0.5 μm radius) corresponds remarkably to the increase in the rate 'a'. It confirms that with the

increase in the rate 'a', the volume of the micro-voids responsible for damage increases. Because the rate 'a' is still negative, the degree of damage is supposed to be minor in these concrete samples. This is a reason why compressive strengths did not correlate with the rate 'a' or with the pore volume. It is again observed that the strengths are not explicitly associated with the damages defined by the pore volumes, as is the case of freezing-thawing damages. Even though the damage is minor, the durability of concrete definitely decreases. These results suggest that the strength may not be a key factor for the durability, but the rate 'a' is sensitive to it.

4. Estimation of Damage

(1) Samples of controlled damage

To prepare concrete samples of controlled damage, cylindrical specimens of 10 cm diameter and 20 cm height were made. Mixture proportion of concrete was water: cement : sand : gravel = 0.55 : 1.0 : 2.5 : 3.2 and the maximum size of gravel was 20 mm. The compressive strength after 28 day moisture-cure was 45.4 MPa. Controlled damage was induced in the concrete samples, by the freezing and thawing test. After 28 day moisture-cure, freezing and thawing cycles from -16° C to 3° C in three hours interval were applied. The damaged samples were prepared and tested after 100 cycles, 200 cycles and 300 cycles.

Since initial modulus E_0 should be determined as the tangential modulus: $d\sigma/d\varepsilon$ at $\varepsilon = 0$, the stress versus strain (σ - ε) relation was approximated by a parabolic equation which is adopted in the Standard Specification for Concrete Structures of JSCE and the CEB-FIP Model Code 1990. Consequently, it is represented as,

$$\sigma = a_0 + a_1\varepsilon + a_2\varepsilon^2. \quad (10)$$

One example is shown in Fig. 8 as the stress-strain relation is approximated by Eq. 10 and the initial modulus E_0 is determined as the coefficient a_1 . It is confirmed that the stress-strain curve is approximated by the parabolic equation with high correlation (0.9998).

In the damage-mechanics model of a pore-cracked material, a relation between the modulus of elasticity and the strength is mathematically derived (Nielsen, 1998),

$$\sigma_c/\sigma_c^* = \exp[-0.75 (E^*/E_0 - 1)], \quad (11)$$

where σ_c is the compressive strength of a cracked material and σ_c^* is the strength of the intact (zero porosity) material. In an ordinary cracked material, as the limiting case for which voids are squeezed out, and Eq. 11 is simplified to

$$\sigma_c/\sigma_c^* = 0.25 + 0.75E_0/E^*. \quad (12)$$

Taking the average of three specimens tested, the modulus of elasticity E_0^n and the compressive strength σ_c^n were determined after n freezing-thawing cycles. To estimate the damage introduced, the ratios σ_c^n/σ_c^0 were compared with σ_c/σ_c^* in Eqs. 11 and 12. Relative moduli were also estimated from E_0^n/E_0^0 , where E_0^0 is the modulus of elasticity of concrete after 28 day moisture-cure (but prior to the freezing-thawing cycles) and E_0^n is that after n freezing-thawing cycles. Results are plotted in Fig. 9. The relation given by Eq. 11 is indicated by a broken curve and that of Eq. 12 is shown by a solid line. The damages introduced are

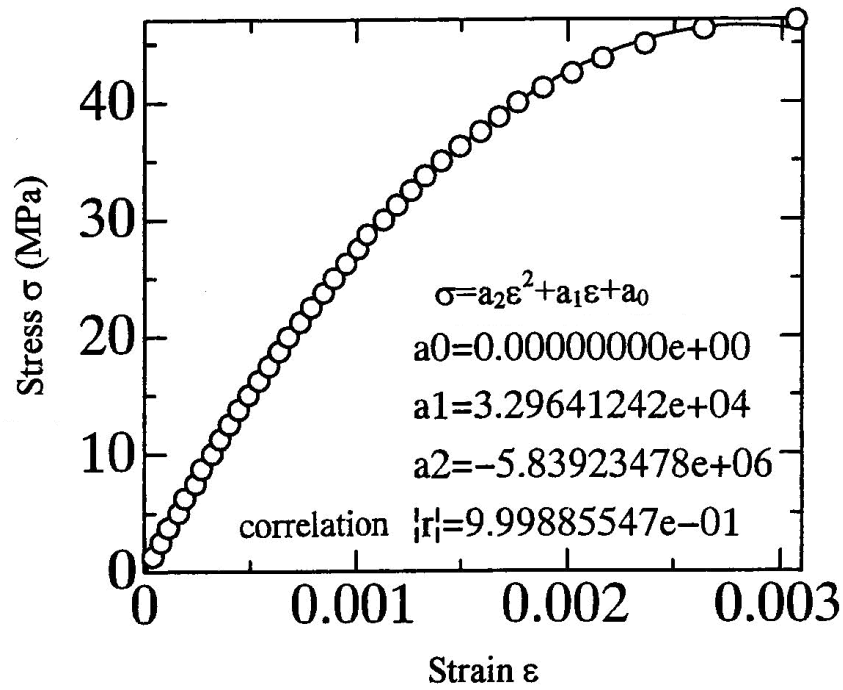


Fig. 8 Stress-strain relation approximated by a parabolic equation.

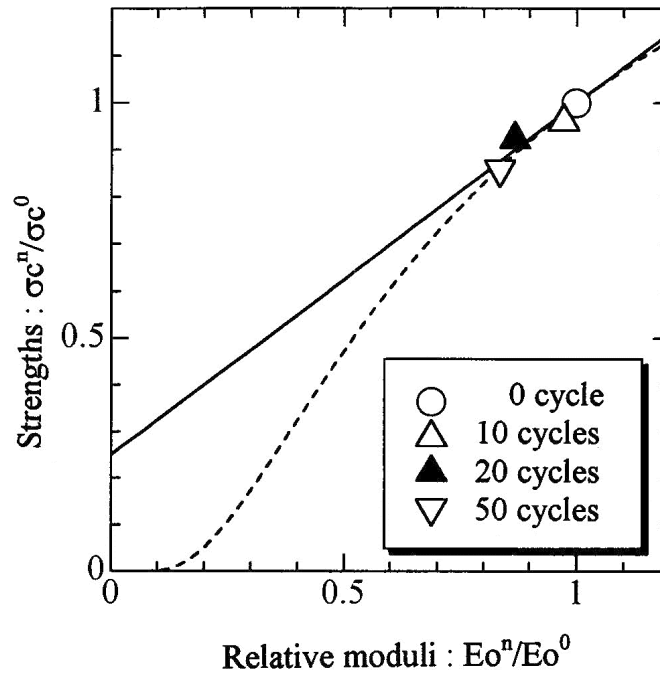


Fig. 9 Relative moduli E_o^n / E_o^0 and ratios of the strength σ_c^n / σ_c^0 in the freezing and thawing test.

reasonably approximated by the relations of damage mechanics. The strengths decrease even lower than the relative moduli in Eq. 11, while the relative moduli are lower than the strengths in Eq. 12. It is observed that the damages introduced are moderate so that results are plotted on the both curves with reasonable agreement

From Eqs. 5 and 6, the damage evolution is expressed as,

$$\Omega_c - \Omega_0 = (E_o - E_c) / E^* \quad (13)$$

As mentioned in Sec. 3, it is found that the damage evolution is closely associated with the rate 'a'. Since modulus E^* of an intact concrete is unknown in an actual case, a relationship between the difference $E_0 - E_c$ and the rate 'a' of the samples is studied and plotted as shown in Fig. 10. For the sake of simplicity, a linear correlation is approximated as shown in the figure, where the difference $E_0 - E_c$ is represented as,

$$E_0 - E_c = E^*(\Omega_c - \Omega_0) = X a + Y. \quad (14)$$

Because the rate 'a' varies depending on the degree of the damage, it is assumed that the initial modulus E_0 is identical to intact modulus E^* in the case where the rate 'a' is equal to 0. From the figure, intact modulus E^* is determined by

$$E^* = E_c + Y. \quad (15)$$

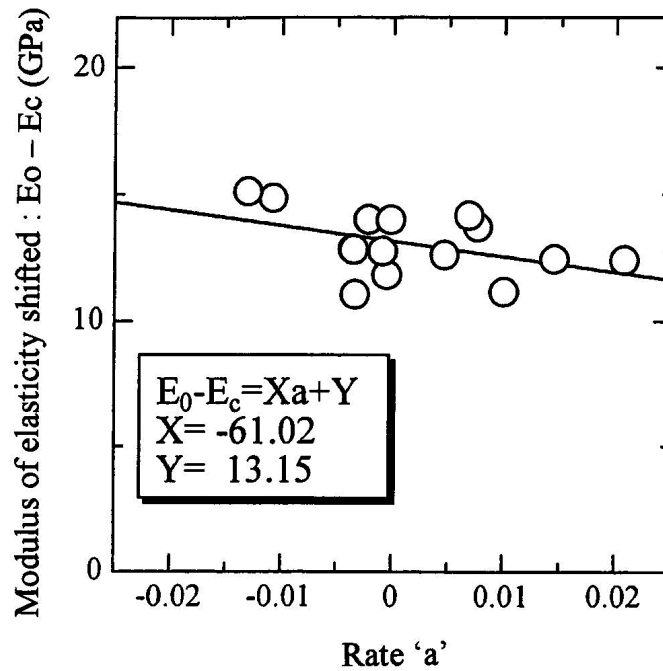


Fig. 10 Correlation between the rate 'a' and the difference between the tangential modulus E_0 and the secant modulus E_c in the concrete samples of controlled damage.

Through this procedure, relative modulus E_0/E^* was estimated at each freezing-thawing cycle as an average value of three samples. In Fig. 11, results of relative moduli E_0/E^* are compared with ratios E_0^n/E_0^0 , which were determined as the ratios of the tangential moduli E_0 after n cycles to that of 0 cycle in the experiment. It appears that the ratios E_0/E^* obtained from the above procedure slightly overestimate the actual ratios E_0^n/E_0^0 , while the trend of the decrease due to deterioration is in reasonable agreement. This result implies that the damage of concrete can be practically estimated without knowing the modulus of elasticity at the initial construction stage. Because the mechanical properties of concrete at the time of construction are mostly missing when inspection is conducted years later, the procedure is promising to estimate the degree of damage using the relative modulus E_0/E^* determined via the AE rate process analysis described here.

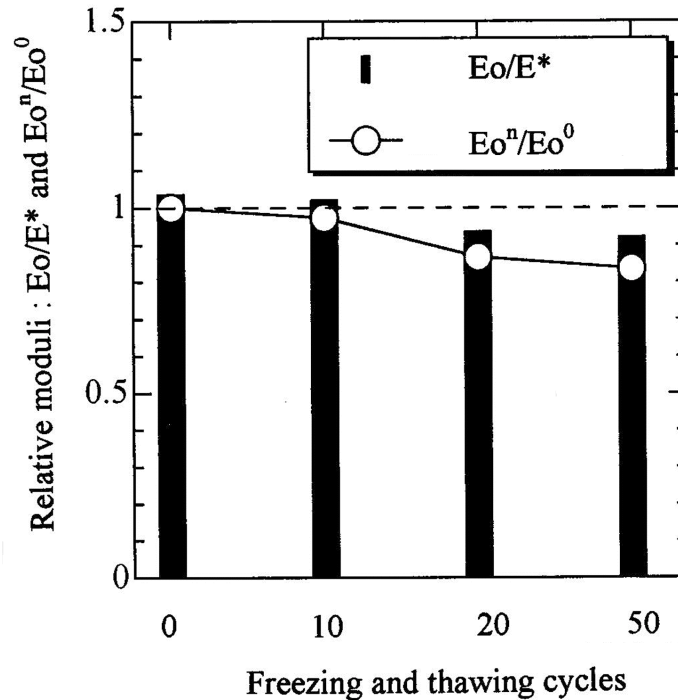


Fig. 11 Relative moduli E_o/E^* and E_o^n/E_o^0 in the freezing and thawing test.

(2) Concrete of various ages

Casting concrete samples of the same mixture as in (1), the effect of cementation due to age is studied. First, in the early age after 7, 14, 21, and 28 days, uniaxial compression tests were conducted. It is noted that the designed strength of concrete is estimated at the age of 28 days. All samples were moisture-cured in the standard room (20°C), and were taken from a reservoir one day before the test. In Fig. 12, E_o^n/E_o^{28} represents the relative moduli actually measured in the experiment as the modulus of elasticity E_o^n at n days elapsed. E_o/E^* represents the relative modulus of elasticity, which is estimated from AE rate process analysis. It is found that relative moduli measured and those estimated from the rate process analysis agree after 21 days. Thus, it is confirmed that the damage due to weak cementation or inadequate hydration could be estimated by this method.

Although the rate process analysis is originally investigated to estimate the deterioration of hardened concrete, the degree of soundness is also studied in the ages after 28 days. In Fig. 13, results of moisture-cured samples after 7, 9, 11, 13, 15, and 17 months are summarized. It is well known that hydration process of concrete still continues even after 50 years. Accordingly, the ratios E_o^n/E_o^{28} becomes over 1.0 after 7 months. In this case, the ratios E_o/E^* underestimate the actual ratios E_o^n/E_o^{28} , although the trend of the relative moduli in hardening process is similar to the actual ratios. Thus, the procedure is not quite effective to estimate the more sound concrete due to hardening.

(3) Field Survey

The procedure was applied to concrete-core samples taken from concrete columns of an existing bridge. A sketch of pier and anchor of the bridge is given in Fig. 14. From each portion, three cores were taken and tested. Results of relative moduli E_o/E^* estimated are

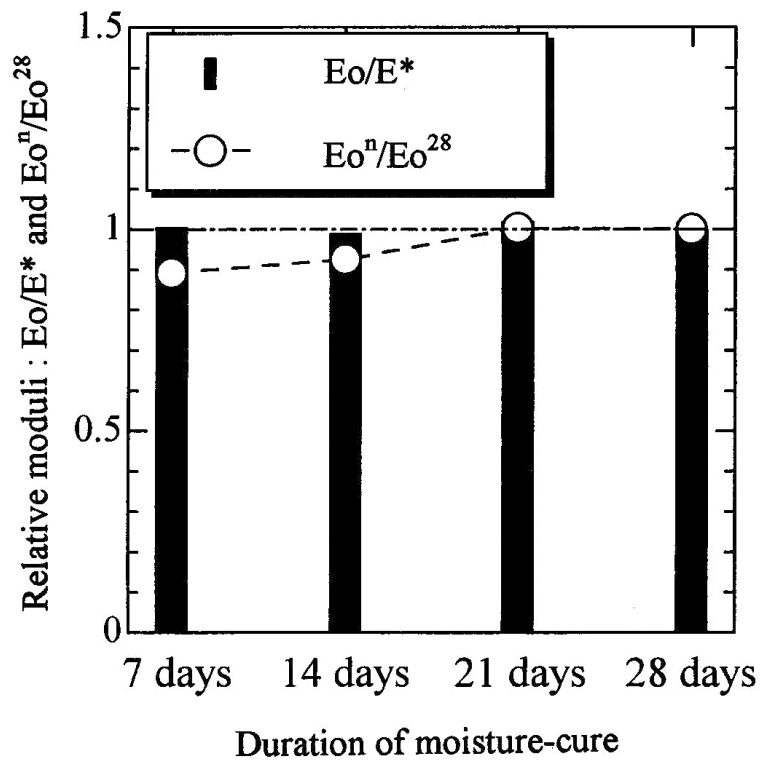


Fig. 12 Relative moduli E_o/E^* and E_o^n/E_o^{28} in early-age concrete.

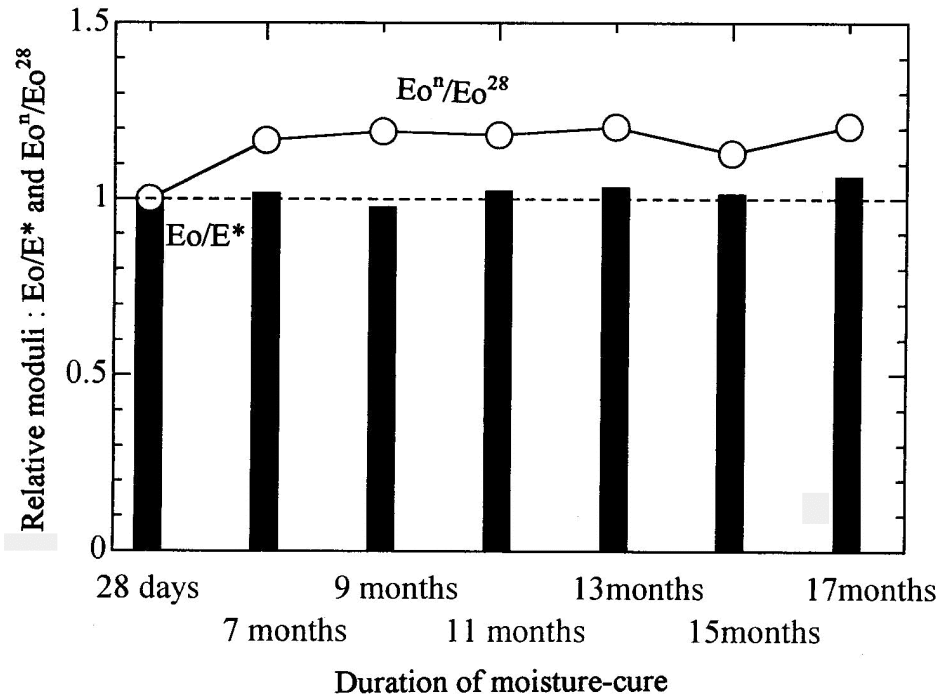


Fig. 13 Relative moduli E_o/E^* and E_o^n/E_o^{28} in long-age cured concrete

summarized in Fig. 15. It is observed that the relative moduli of cores in the anchor A2 are larger than 1.0, while the relative moduli of cores in the piers P1 and P2 are slightly smaller than 1.0. From Eq. 5, it is derived that

$$\Omega_o = 1 - E_o/E^* \tag{16}$$

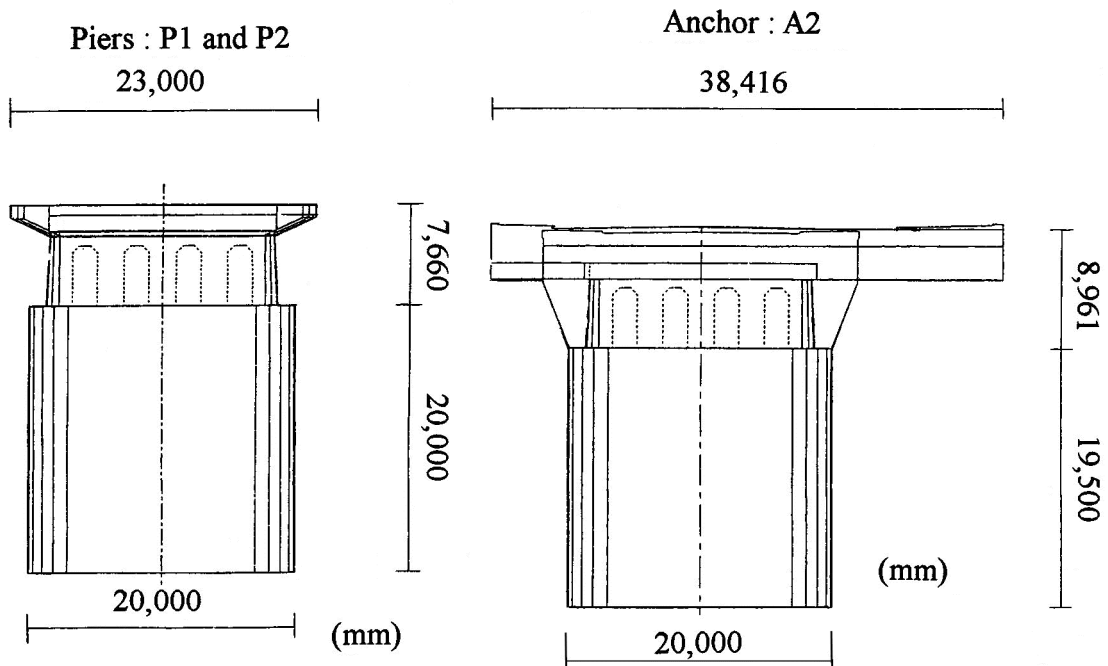


Fig. 14 Sketch of piers and an anchor of a concrete bridge.

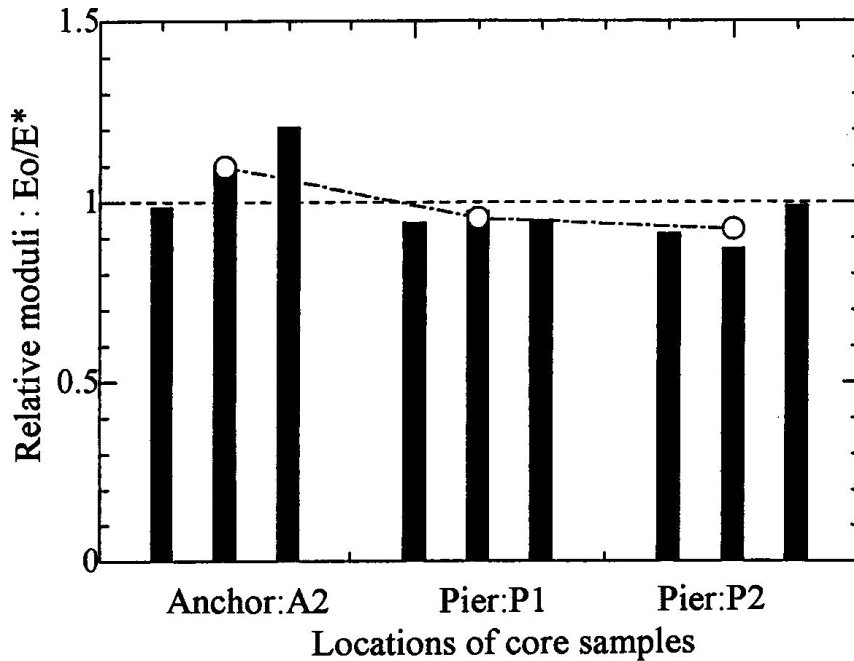


Fig. 15 Relative moduli E_o/E^* estimated from core samples.

Consequently, the degree of current damage Ω_o was estimated from the average values E_o/E^* at three locations, although a negative value is set to zero in Eq. 16. Results are summarized in Fig. 16. This suggests that the concrete in the anchor A2 is undamaged, while the concrete of the piers P1 and P2 is a little deteriorated. The trend of these results is found to be in good agreement with a numerical study on fatigue damage of the bridge columns. It was also confirmed that the strengths of these core samples were similar and higher than the designed strength. Based on these results, it was decided to retrofit this bridge with slightly repairing the two piers.

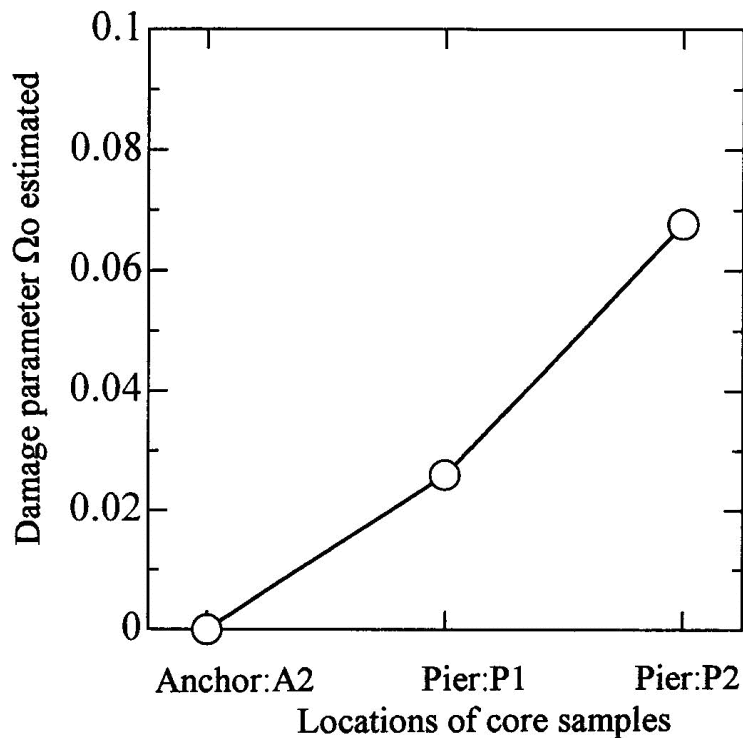


Fig. 16 The damage parameter estimated from the core samples.

5. Conclusion

For quantitative estimation of the damage in structural concrete, AE measurement is applied to the uniaxial compression test of concrete samples. AE generating behavior, which is closely associated with the damage inside concrete, is quantitatively formulated by the rate process theory. Then, the damage is defined from the damage mechanics. Correlating the rate process analysis and damage mechanics, the procedure is developed to quantitatively estimate the damage of the concrete sample taken out of the structure. From the results, it is demonstrated that the damage of concrete at the current state could be estimated from AE rate process analysis without knowing the original state at construction. All results obtained are summarized, as follows:

- 1) From the results of core samples taken out of a nuclear power plant, it is confirmed that with the increase in the rate 'a', the pore volume of the micro-voids responsible for the damage increases. This demonstrates that the rate 'a' could give a quantitative reference on damage level of concrete.
- 2) A procedure to estimate the damage of the current state is studied, introducing damage mechanics and correlating the rate 'a' with the scalar-damage parameter. From the correlation between the damage evolution and the rate 'a', the modulus of elasticity in the intact state is estimated.
- 3) By using concrete samples of controlled damage and of various ages, it is confirmed that relative moduli estimated by the proposed procedure are in reasonable agreement with actual moduli in the tests for damaged concrete.

4) In order to check the feasibility, the procedure was applied to concrete-core samples taken from an existing bridge. It is suggested that concrete of the anchor is not deteriorated, but concrete of the piers is slightly deteriorated. Because the trend of these results is found to be in good agreement with analytical study, the retrofit plans of the bridge were decided, based on the result of AE rate process analysis.

References

Farahat, A. M. and Ohtsu, M. (1994), "Assessment of Concrete Deterioration using Plastic Analysis and Acoustic Emission Technique," *Journal of AE*, **11**(4), 37-46.

Iida, T., Watanabe, H., Tomoda, Y. and Ohtsu, M. (2000), "Damage Estimation of Concrete Core by AE Rate Process Analysis," *Proc. Japan Concrete Institute*, **22**(1), 271-276 (in Japanese).

Ishibashi, A, Hidaka, E., Farahat, A. M. and Ohtsu, M. (1995), "Deterioration Evaluation by AE in Concrete Samples," *Proc. Sixth Int. Conf. Structural Faults and Repair*, **2**, 69-74.

Ishibashi, A., Matsuyama, K., Ohta, S. and Ohtsu, M. (1998), "Acoustic Emission Application for Diagnosis of Deteriorated Concrete of Harbor Structures," *Proc. Sixth Int. Sym. on AE from Composite Materials*, AECM-6, ASNT, 145-152.

Kachanov, M. (1980), "A Continuum Model for Medium with Cracks," *J. Engineering Mechanics*, ASCE, **106**(5), 1039-1051.

Matsuyama, K. and Ohtsu, M. (1992), "Rate Process Analysis of AE Activity to Evaluate the Deterioration of Concrete by Core Tests," *Proc. 4th Int. Sym. on AE from Composite Materials*, AECM-4, ASNT, 132-138.

Mogi, K. (1962), "Magnitude Frequency Relation for Elastic Shocks accompanying Fracture of Various Materials and Some related Problems in Earthquakes," *Bull. Earthq. Res. Inst.*, **40**, 831-853.

Nielsen, L. F. (1998), "On Strength of Porous Material: Simple Systems and Densified Systems," *Materials and Structures*, **31**, 651-661.

Ohtsu, M. (1987), "Acoustic Emission Characteristics in Concrete and Diagnostic Applications," *Journal of AE*, **6**(2), 99-108.

Ohtsu, M., Sakimoto, T., Kawai, Y. and Yuji, S. (1988), "Evaluation of Concrete Structure Deterioration via AE Observation of Core Test," *Journal of AE*, **7**(4), 167-172.

Ohtsu, M. (1992), "Rate Process Analysis of Acoustic Emission Activity in Core Test of Concrete," *Concrete Library of JSCE*, No. 20, 143-153.

Yuno, K., Inoue, Y. and Ohtsu, M. (1995), "Evaluation of Deterioration in Concrete by Stochastic Analysis of AE Activity under Uniaxial Compression," *J. Materials, Concrete Structures and Pavement*, JSCE, No. 520/V-28, 13-24.

EXTRACTION OF HISTORIES OF DAMAGE MICRO-MECHANISMS IN UNIDIRECTIONAL COMPOSITES BY TRANSIENT-PARAMETRIC ANALYSIS

JIE QIAN and YURIS DZENIS

Department of Engineering Mechanics, University of Nebraska, Lincoln,
Lincoln, NE 68588-0526, USA

Abstract

The problem of micro-damage evolution to failure in advanced composites is addressed. A combination of transient waveform classification and multi-parametric filtering was used to extract the histories of damage evolution in a unidirectional graphite/epoxy composite loaded in the fiber and transverse directions. Three characteristic AE waveforms with different amplitudes, durations, and frequency spectra were identified based on the transient analysis. The waveforms were associated with matrix cracks, fiber breaks, and longitudinal splitting in the composite. Parametric regions for the characteristic waveforms were identified in the amplitude-rise time parametric space. Multi-parametric filtering was applied to extract the micro-damage evolution histories. The method is expected to be advantageous for the real-time damage and fracture monitoring of composite structures.

1. Introduction

Advanced composite materials under loading gradually accumulate several types of damage. These include matrix cracks, fiber breaks, fiber-matrix debonding, longitudinal splitting, and delamination. Studies of damage evolution are needed for better understanding of mechanisms of the ultimate failure and life of composites and structures. Acoustic emission has been used to analyze overall damage accumulation in composites by many authors (Bakuckas et al., 1994; Ely and Hill, 1995; Luo et al., 1995). Different damage mechanisms have been reported to produce AE signals with different parameters. However, attempts to apply single-parameter filters to separate damage mechanisms have been largely unsuccessful due to the overlap of the parametric ranges for different damage micro-mechanisms (Kouvarakos and Hill, 1996). This overlap is due to high unpredictability of AE signals caused by the variability and complexity of both damage and wave propagation phenomena in composites (Chang and Sun, 1988; Gorman, 1992). In this paper, a hybrid transient-parametric method was applied to separate the overall AE histories from unidirectional composites into the histories for different damage mechanisms. The method is based on a combination of transient AE classification and multi-parametric filtering.

2. Technical Approach

Recently, Ono and Huang (1994), Prosser et al. (1995), and de Groot et al. (1995) have applied transient AE analysis for AE source recognition. Methods of pattern recognition and neural networks have been used for signal classification. These methods can be used to extract histories of AE signals with different waveforms based on the transient AE data. However, the bulk of the AE evaluations at present are performed by a parametric analysis that requires simpler and cheaper hardware and may be especially advantageous for long-term AE monitoring

when the accumulation and analysis of huge amounts of transient data is impossible or impractical.

The following hybrid approach for the AE analysis of damage evolution histories in composites was applied in this work. AE transient waveforms were acquired along with the parametric AE data. The waveforms were screened and the characteristic waveforms were identified. AE parametric spaces were then analyzed and parametric regions occupied by signals of different types were identified. Evolution histories for different waveforms were then extracted by multi-parameter filtering. Finally, damage mechanisms associated with different waveforms were identified based on the expected and observed damage in composites.

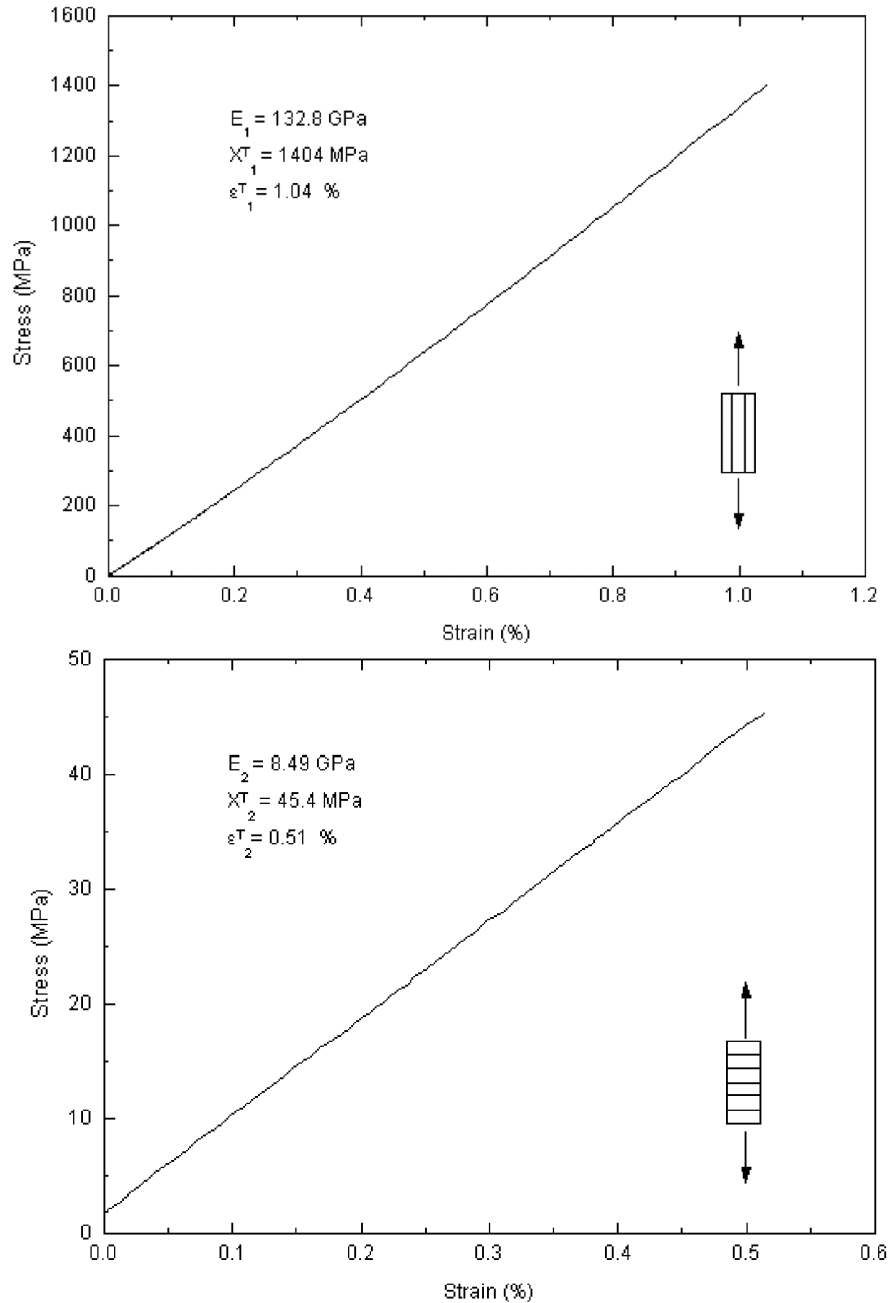


Fig. 1. Mechanical response. Above: $[0]_8$ and below: $[90]_{16}$.

3. Experimental

Damage evolution in unidirectional composites subjected to tensile loading was analyzed. Two composite panels, $[0]_8$ and $[90]_{16}$, were manufactured from Hexcel T2G190/F263 graphite/epoxy prepreg following the manufacturer-recommended curing cycle. The panels were tabbed and rectangular 250mm x 15 mm ($[0]_8$) and 175mm x 25 mm ($[90]_{16}$) specimens were machined by a high-speed diamond saw. Tensile testing was performed by a *MTS* testing machine retrofitted with a digital Instron test control and data acquisition system. The constant displacement rate of 0.5 mm/min was applied. The AE was acquired and analyzed by a two-channel Vallen AMS3 acoustic emission system equipped with a transient recorder. Two wideband, high fidelity B1025 AE sensors by Digital Wave were used. The AE gage zone (the distance between the AE sensors) was 80 mm for the $[0]_8$ composite and 60 mm for the $[90]_{16}$ composite. The AE source location analysis was performed on the incoming signals and the signals originating outside the acoustic gage zone were eliminated from the analysis. A 34.5 dB system gain and a 40.5 dB threshold were used in the AE data acquisition. The load and strain data were fed from the testing machine and recorded as parameters. Several specimens of each type were tested.

4. Results and Analysis

The typical mechanical response of the unidirectional composites is shown in Fig. 1. The overall, unfiltered AE histories are shown in Fig. 2a and b. The AE signal location distributions were rather uniform (within the acoustic gage zone) for all tests. It is seen that the overall AE histories for the $[0]_8$ and $[90]_{16}$ composites were qualitatively different. Loading in the fiber direction produced very little emission at the load levels below 50% of the ultimate load. At higher loads, the accumulation rate was non-uniform with considerable jumps observed at 65% and 90% of the ultimate load. Loading in the transverse direction produced the highest accumulation rate at the low load levels, from 10 - 20% of the ultimate load. As the load increased, the AE accumulation rate decreased and stayed almost constant to failure.

Analysis of the transient AE data for both composites revealed three characteristic waveforms with different amplitudes, durations, and frequency spectra. Examples of these waveforms are shown in Fig. 3. The A-type signals had peak frequency in the range from 100-220 kHz. The B-type signals had higher amplitude and peak frequency between 300-700 kHz. The C-type signals had high amplitude, extremely long duration ($>1000 \mu\text{s}$), and a wide frequency spectrum. These three types of signals accounted for 65% to 90% of the overall AE, depending on the specimen. The balance contained signals with random or mixed waveforms and frequency spectra that could not be easily classified.

The C-type signals were extracted from the overall parametric AE data by a simple duration filter. Several parametric spaces were then analyzed in an attempt to separate the signals of the types A and B. The best separation was achieved in the amplitude-rise time space. The parametric regions for the A-type and B-type signals in this space for the two specimens are shown in Fig. 4. The multi-parameter filtering technique was then applied to separate the accumulation histories for these AE signals. Extracted histories of the AE with different waveforms for the two composites are shown in Fig. 5. The failed composite specimens are shown in Fig. 6.

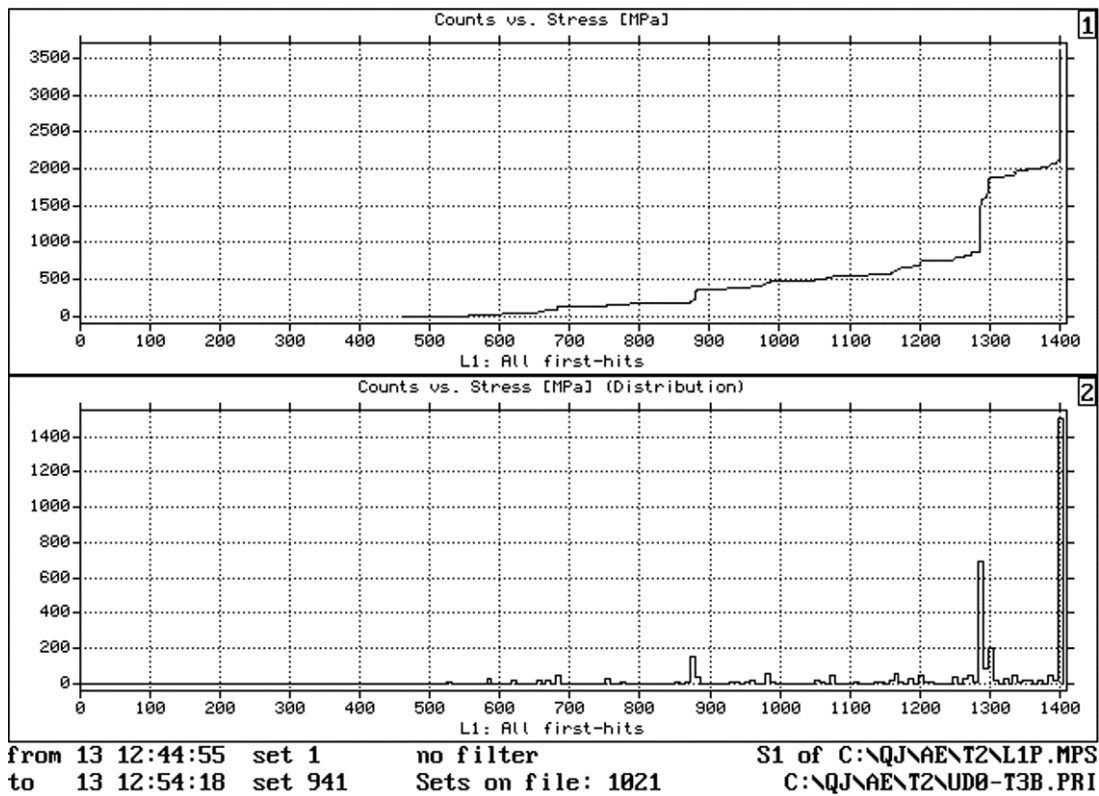


Fig. 2a Overall AE count histories for [0]_s.

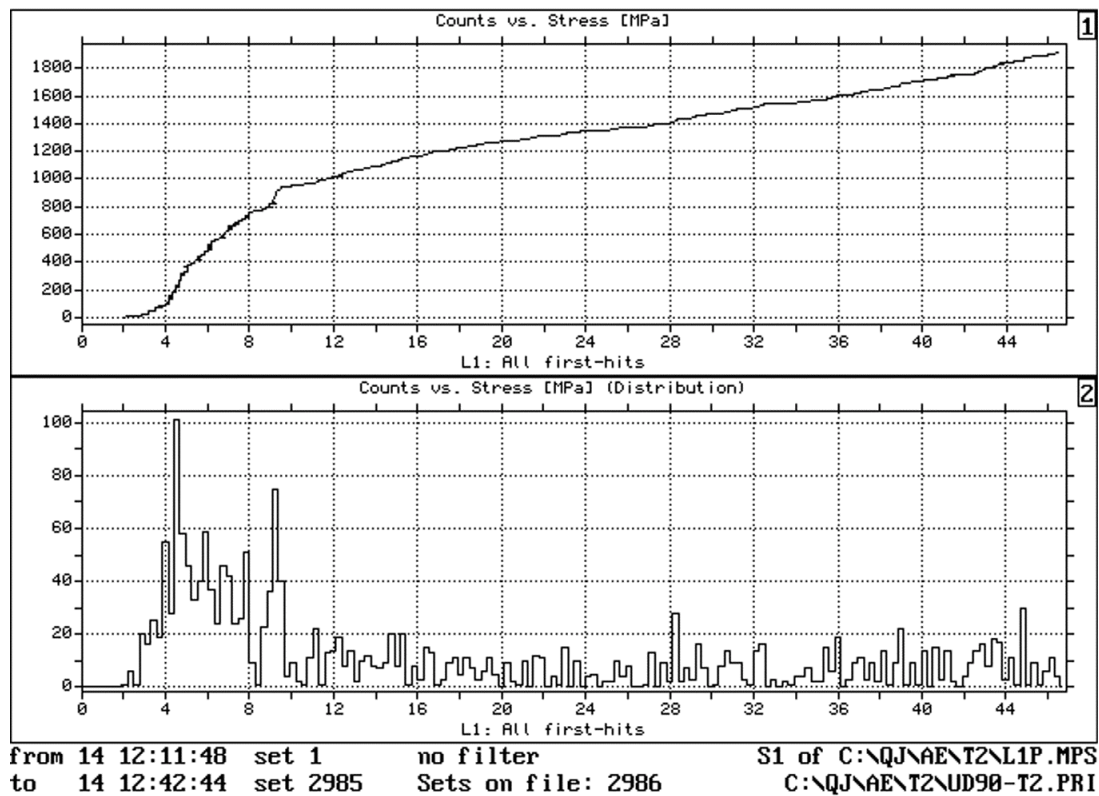


Fig. 2b Overall AE count histories for [90]₁₆.

The comparison of the classified AE histories with the damage mechanisms identified by both on-line observations and fractographic analysis of the broken specimens allowed the

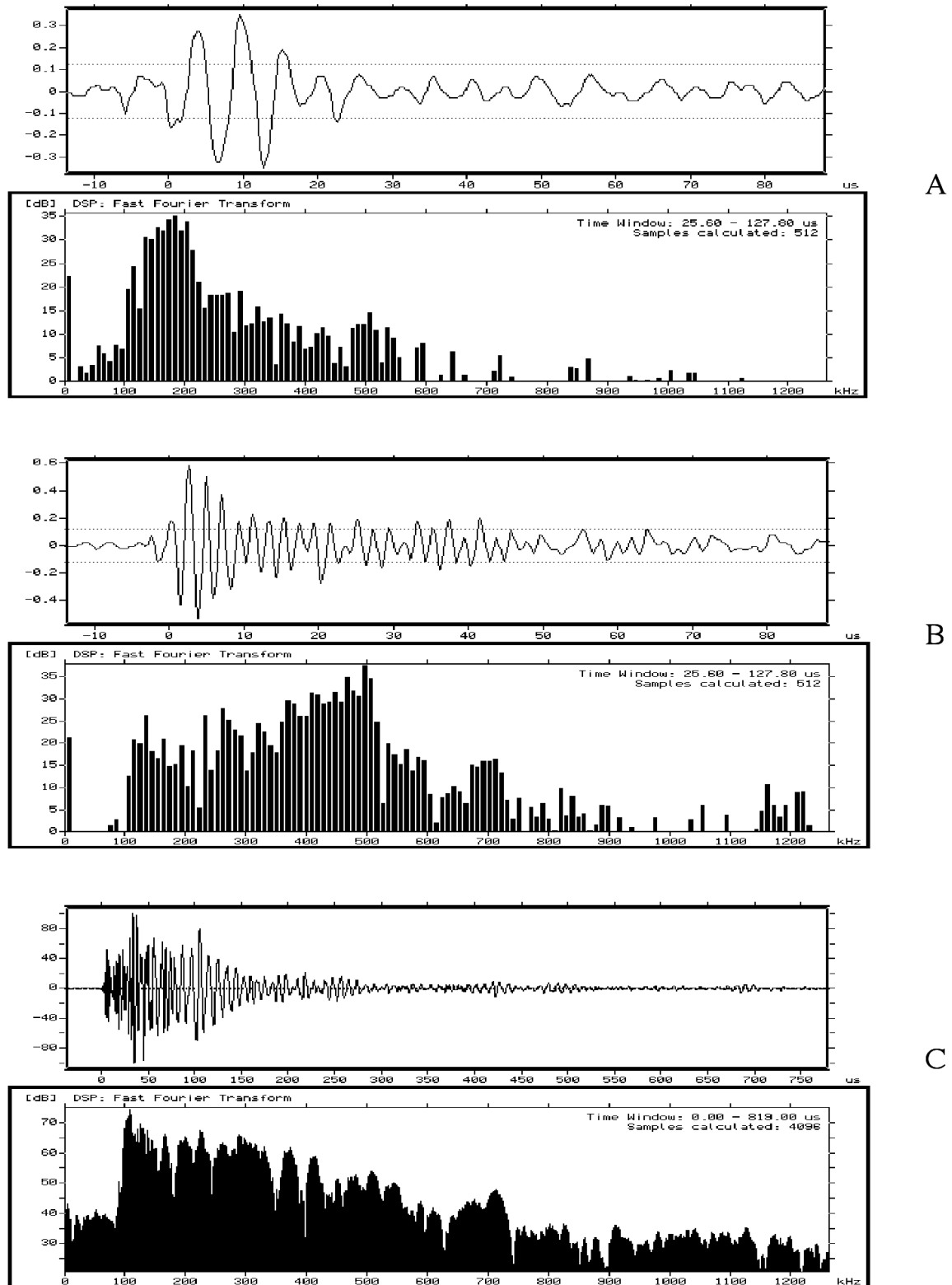


Fig. 3 Characteristic waveforms for Types A, B and C.

correlation of the damage mechanisms with the characteristic AE signals. The A-type signals were associated with the matrix damage, the B-type signals with the fiber breaks, and the C-type signals with the macroscopic longitudinal splitting. The analysis of the classified AE histories for

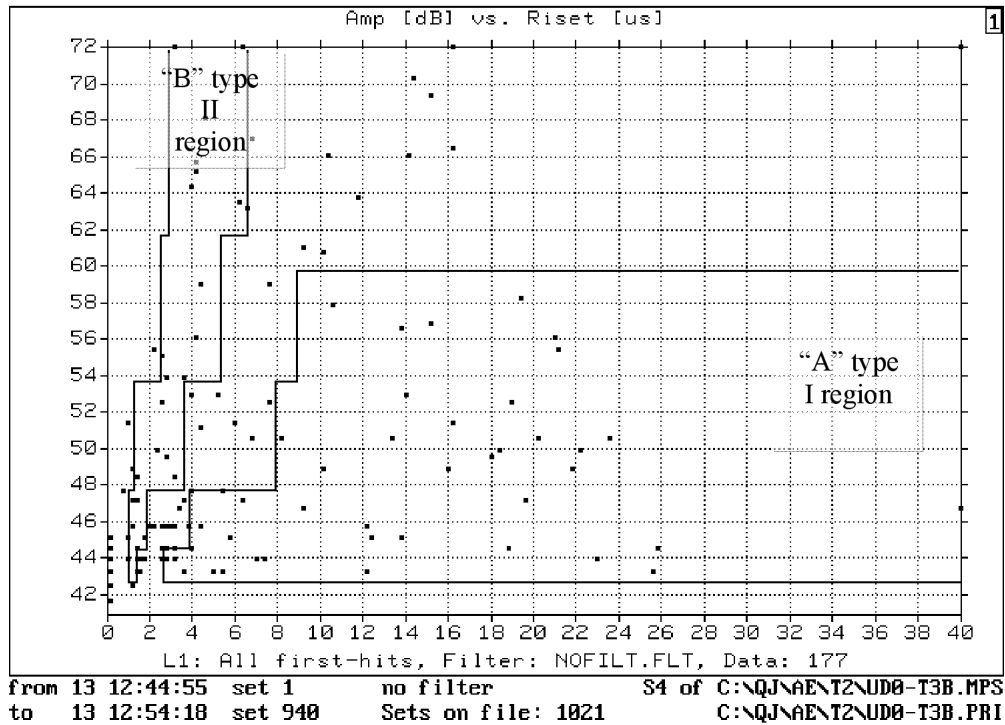
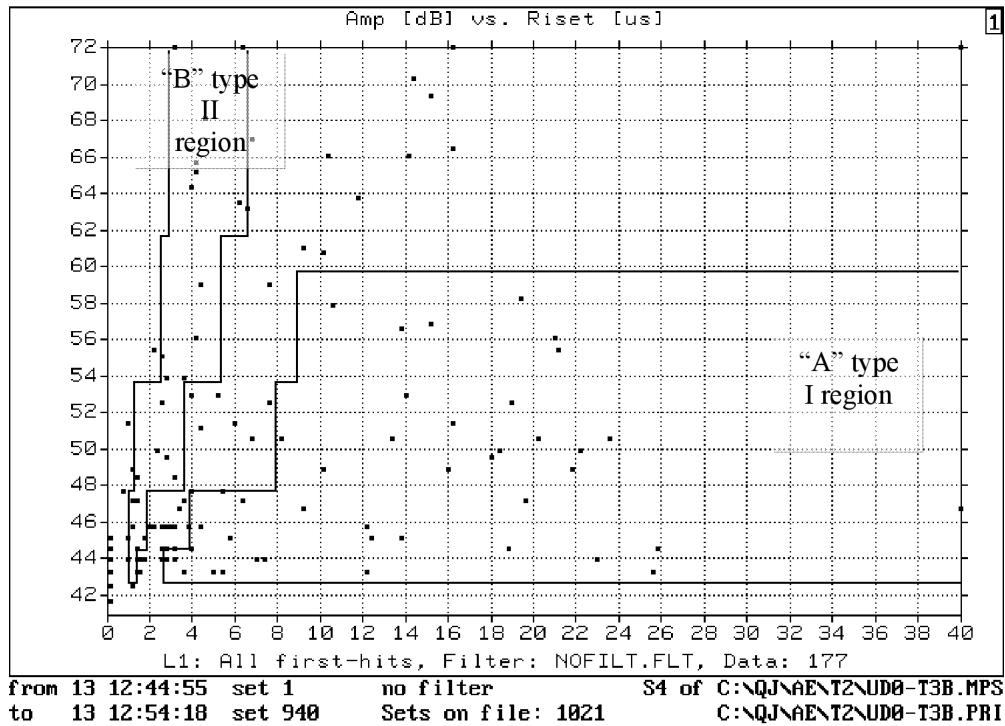


Fig. 4. Parametric regions for the A-type and B-type AE signals in the amplitude-rise time space. Above: $[0]_8$ and below: $[90]_{16}$.

the $[0]_8$ composite (Fig. 5a) showed that the two jumps on the overall AE history plot (Fig. 2) were due to longitudinal splitting. The fiber breaks and matrix cracks in this composite accumulated rather smoothly, except for the jump in the fiber damage caused by the second splitting event at 90% of the ultimate load. The early start of the fiber break accumulation in the graphite/epoxy composite (at around 40-50% of the ultimate load) was consistent with the

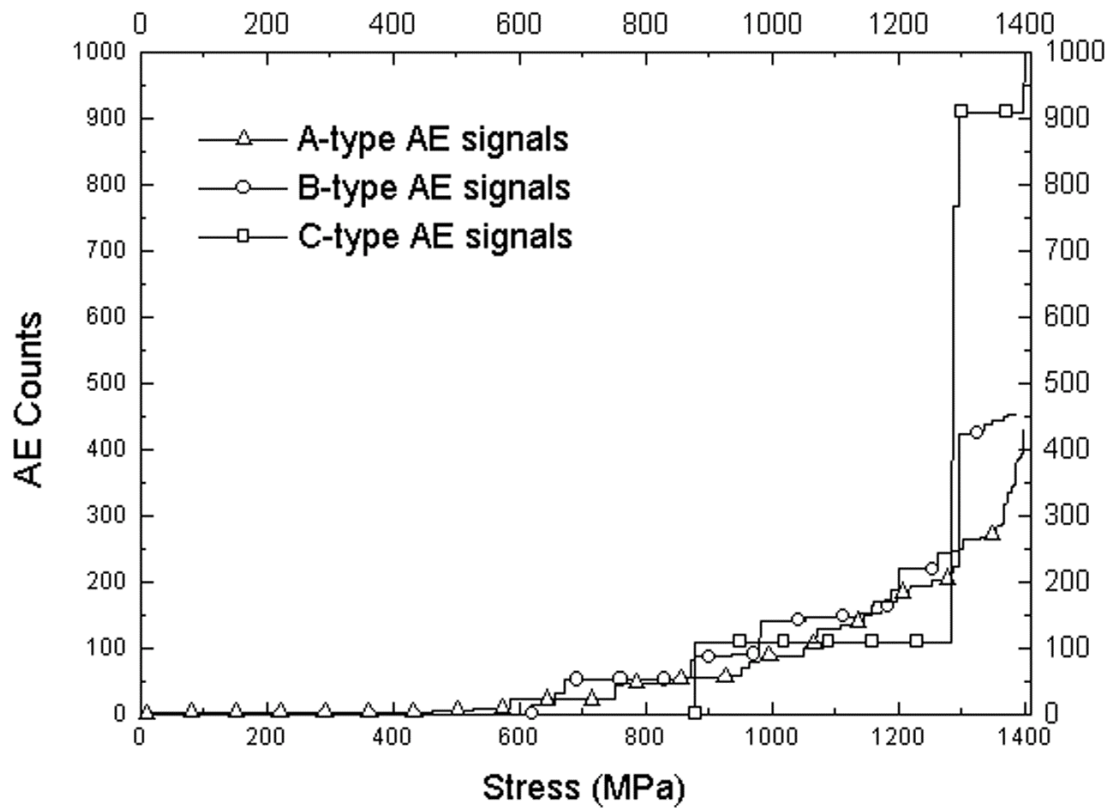


Fig. 5a. Classified histories for various AE signals for $[0]_8$ composite.

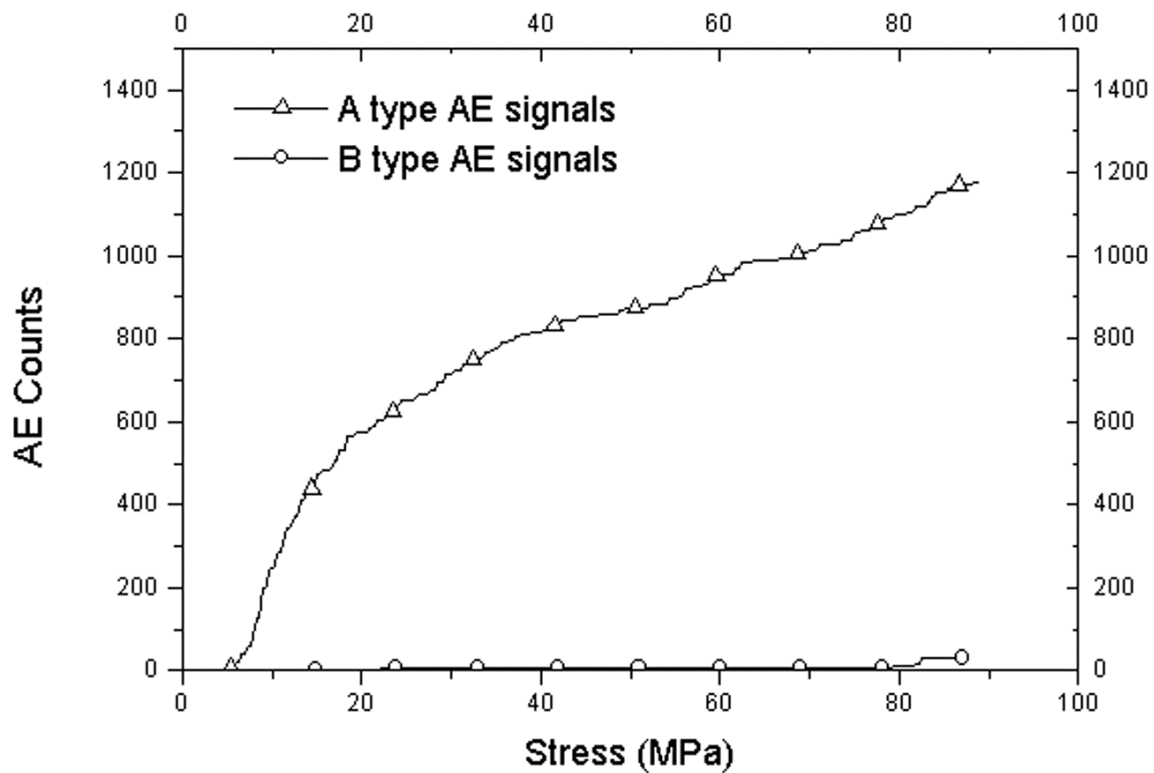


Fig. 5b. Classified histories for various AE signals for $[90]_{16}$ composite.

observations made earlier by other authors (Ono and Huang, 1994). It is different from the situation with glass fiber reinforced composites where fiber breaks were sometimes observed to start accumulating at the loads as high as 90% of the ultimate. The damage in the $[90]_{16}$ composite (see Fig. 5b) consisted almost entirely of matrix cracks with a small amount of fiber breaks developed near the final failure. The differences in the observed AE behavior are readily reflected in the failed composite specimens, shown in Fig. 6. Fractured fibers and numerous fiber-matrix failures along the 0° -direction are found in the 0° -sample failure, while clean fiber-matrix fracture characterizes the 90° -sample failure.

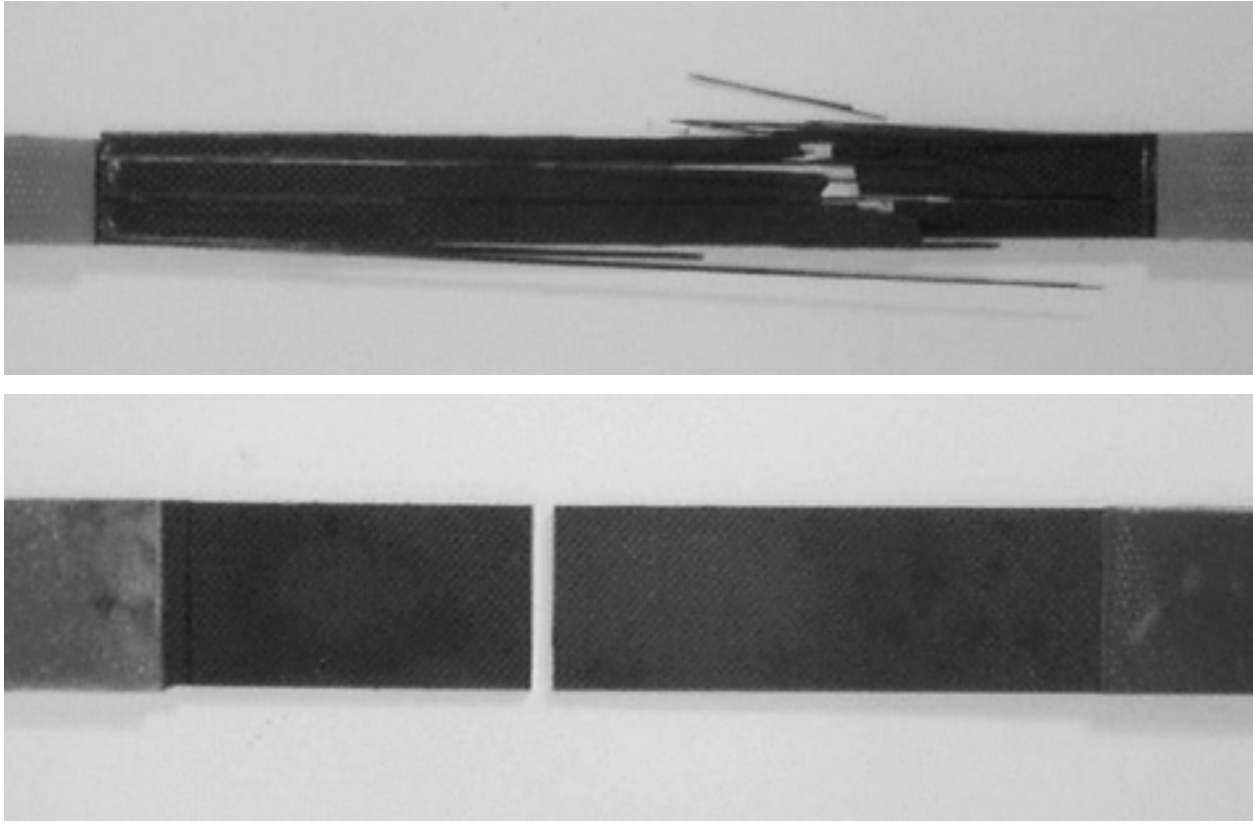


Fig. 6 Failed composite specimens. Above: $[0]_8$ and below: $[90]_{16}$.

5. Conclusions

A new approach for the AE damage evolution analysis of composites is proposed. The approach combines the advantages of the transient and parametric AE methods. Capabilities of the new method are illustrated on extraction of the histories of damage micro-mechanisms in the unidirectional graphite/epoxy composites. Applications of the new method to static and fatigue damage evolution studies in advanced laminated composites are in progress. The method is expected to be advantageous for real-time monitoring of damage and fracture in composites subjected to long-term loadings when massive transient AE data analysis is impractical.

Acknowledgment

The support of this work by the Air Force Office of Scientific Research is gratefully acknowledged. The graphite/epoxy prepreg for the experiments conducted was provided by Hexcel Corporation.

References

- Bakuckas, J.G., Jr., Prosser, W.H., and Johnson, W.S., "Monitoring damage growth in titanium matrix composites using acoustic emission", *J. Composite Materials*, **28**(4), 305-328 (1994).
- Chang, C. and Sun, C.T., "Acoustic emission and transient elastic waves in an orthotropic laminate", *Composites Science and Technology*, **22**, 213-236 (1988).
- de Groot, P.J., Wijnen, P.A.M., and Janssen, R.B.F., "Real-time frequency determination of acoustic emission for different mechanisms in carbon/epoxy composites", *Composite Science and Technology*, **55**, 405-412 (1995).
- Ely, T.M. and Hill, E.v.K., "Longitudinal splitting and fiber breakage characterization in graphite epoxy using acoustic emission data", *Materials Evaluation*, **53**, Feb, 288-294 (1995).
- Gorman, M.R., "Plate wave acoustic emission; Composite materials", *Proc. 4th Int. Symp on AE from Composites*, Seattle: ASNT, Columbus, OH, pp. 395-400 (1992).
- Kouvarakos, M. and Hill, E.v.K., "Isolating tensile failure mechanisms in fiberglass epoxy from acoustic emission signal parameters", *Materials Evaluation*, **54**, Sept, 1025-1031 (1996).
- Luo, J.J., Wooh, S.C., and Daniel, I.M., "Acoustic emission study of failure mechanisms in ceramic matrix composite under longitudinal tensile loading", *J. Composite Materials*, **29**(15), 1946-1961 (1995).
- Ono, K. and Huang, Q., "Pattern Recognition Analysis of Acoustic Emission Signals", *Progress in Acoustic Emission VII*, eds. Kishi, T. et al., Japan Soc. NonDestructive Inspection, Tokyo, 1994, pp. 69-78.
- Prosser, W.H., Jackson, K.E., Kellas, S., Smith, B.T., McKeon, J., and Friedman, A., "Advanced waveform-based acoustic emission detection of matrix cracking in composites", *Materials Evaluation*, **53**, Sept, 1052-1058 (1995).

ACOUSTIC EMISSION SOURCES BY ATOMISTIC SIMULATIONS

M. LANDA, J. CERV, A. MACHOVÁ and Z. ROSECKY

Institute of Thermomechanics AS CR, Dolejskova 5, 182 00 Prague 8, Czech Republic

Abstract

We present acoustic emission (AE) sources at the crack tip obtained from atomistic simulations by molecular dynamic technique in bcc iron under plane strain conditions. We show that the character of acoustic emission is different when different processes operate at the crack tip. Wave processes during brittle fracture, twin extension and dislocation emission from the crack tip are visualized and analyzed. For better understanding of the basic feature of the atomistic results, we also include a simplified reconstruction of the most important wave patterns in anisotropic elastic continuum.

1. Introduction

Stress wave radiation caused by crack extension (Freund and Rosakis, 1991; Prakash et al., 1992), by motion of dislocations (Trochidis and Polyzos, 1995) and at twin extension (Rosakis and Tsai, 1995) have been analyzed recently in the framework of isotropic continuum. Unlike isotropic continuum, where only two different velocities of longitudinal and shear wave exist, such an analysis in anisotropic crystals has not been performed due to a very complex character of wave phenomena in the crystals. Pure longitudinal and transverse modes exist here only in some special crystallographic directions; in other directions, quasi-longitudinal or quasi-transverse waves transfer the energy. Their velocity is different in dependence on the orientation of wave vectors. Atomistic simulations by molecular dynamic technique offer an opportunity to visualize the radiation of stress waves in anisotropic crystals with defects in a relatively simple way (Holian and Ravelo, 1995; Gumbsch and Gao 1999a, b). Moreover, such simulations may also bring information in the framework of the non-linear dynamic approach, since the interatomic forces are of a non-linear character.

In molecular dynamic (MD) simulations, Newtonian equations of motion are solved for the set of atoms using an explicit time integration scheme and a very fine time integration step. The equations for individual atoms have generally a form:

$$\begin{aligned} (d^2m/dt^2) u_\alpha(l) + R_\alpha(l) &= 0 \text{ at interior atoms, or} \\ &= F_\alpha^{\text{ext}}(l) \text{ at surface atoms, respectively, } \alpha = 1, 2, 3. \end{aligned}$$

The resulting force $R_\alpha(l)$, acting at an atom l in the direction x_α , is calculated as a sum of the non-linear interatomic forces between individual atoms l and k . The interatomic forces are derived from the potential energy with limited range of interaction. The forces and potentials have to secure at least: the mechanical stability, the basic energetics of the lattice and to describe well the elastic constants in anisotropic crystals. The other quantities denote: u_α the displacement, F^{ext} the external force and m the mass of the atom. MD-technique enables the simultaneous mapping of the displacement field and the local potential and kinetic energies of individual atoms during defect growth in a loaded crystal. The displacement field describes well

the type of defect (Machová et al., 1999), while the local kinetic energies of individual atoms describe well the wave processes during defect growth (Landa, et al., 1998; Machová and Ackland, 1998; Cerv et al., 2000), it means AE on the atomic level.

In our MD simulations, relatively large bcc iron crystals are oriented along the coordination axes $x_1 = [-110]$, $x_2 = [001]$ and $x_3 = [110]$. We use short-ranged interatomic potentials and forces (Landa et al., 1998; Machová and Ackland, 1998) with the so-called cut-off radius r_c lying between the second and the third nearest neighbors in the bcc lattice. If the distance r between individual atoms is smaller than the r_c the interaction exists, if $r \geq r_c$ the interatomic force is zero. Beside the elastic constants and basic energetics, our interatomic potentials and forces also describe well the phonon frequency spectra (lattice vibrations), in agreement with the experimental data for bcc iron (Machová and Ackland, 1998). It secures a correct propagation of the stress waves in the model, in agreement with the expectation according to the elastic anisotropic continuum. The bcc lattice is projected onto a (110) plane. Plane strain conditions are considered along x_3 , therefore in this direction the atomic motion is not allowed and periodic (translational) boundary conditions are imposed. The atoms are free to move in x_1 and x_2 . Each projected atom represents a chain of atoms in the perpendicular $[110]$ direction, moving simultaneously with the projected atom. The initial temperature corresponds to 0 K and further atomic thermal motion is not controlled. Central difference scheme and time integration step $h = 1 \times 10^{-14}$ s have been used for time integration of Newtonian equations of motion in all the simulations. The magnitude of the time step is sufficient to secure numerical stability in the system and also a reliable transfer of the elementary AE events during defect growth studied. We consider a pre-existing crack loaded in mode I. The crack front is oriented along the direction $x_3 = [110]$. The crack plane lies either on (001) or on (-110) planes. In dependence on the type of loading, this crystal orientation enables the observation of both a brittle fracture and important shear processes in the slip systems $\langle 111 \rangle \{112\}$. Before loading, surface relaxation of the crystals is performed to avoid its influence on the kinetics of the microscopic processes studied.

The wave patterns obtained from MD simulations are discussed in the light of existing predictions following from isotropic continuum (Freund and Rosakis, 1991; Prakash et al., 1992; Trochidis and Polyzos, 1995; Rosakis and Tsai, 1995). To understand the basic feature of the anisotropic atomistic results, we also include a simplified reconstruction of the most important wave patterns by means of the expected wave processes in anisotropic elastic continuum under plane strain.

2. Brittle Crack Extension

Brittle (Machová et al., 1999) or quasi-brittle (Machová and Ackland, 1998) fracture is observed in atomistic simulations when a crack is loaded in elastic regime. We present here brittle crack extension in a relatively long sample of the SEN-type with an edge pre-existing crack. The sample is loaded linearly by external forces (PE) acting in the x_2 direction with a loading rate $dPE/dt \approx 2.5$ kN/s. It simulated a fracture tension test on a single crystal of bcc iron presented in (Landa et al., 1998). The atomic sample has 200 atomic planes in x_2 and 50 atomic planes in x_1 . The initial crack is atomically sharp, the crack plane is (001) and the initial crack length is $l_0 = 15 d_{110}$, where $d_{110} = a_0/\sqrt{2}$ is the interplanar distance in a $\langle 110 \rangle$ direction and a_0 is the lattice parameter. The edge crack (001)/[110] (crack plane/crack front) propagates in the direction $x_1 = [-110]$. Crack initiation has been monitored at the applied stress intensity $K_{IC} = 1.23 \text{ MPa m}^{1/2}$ (Landa et al., 1998).

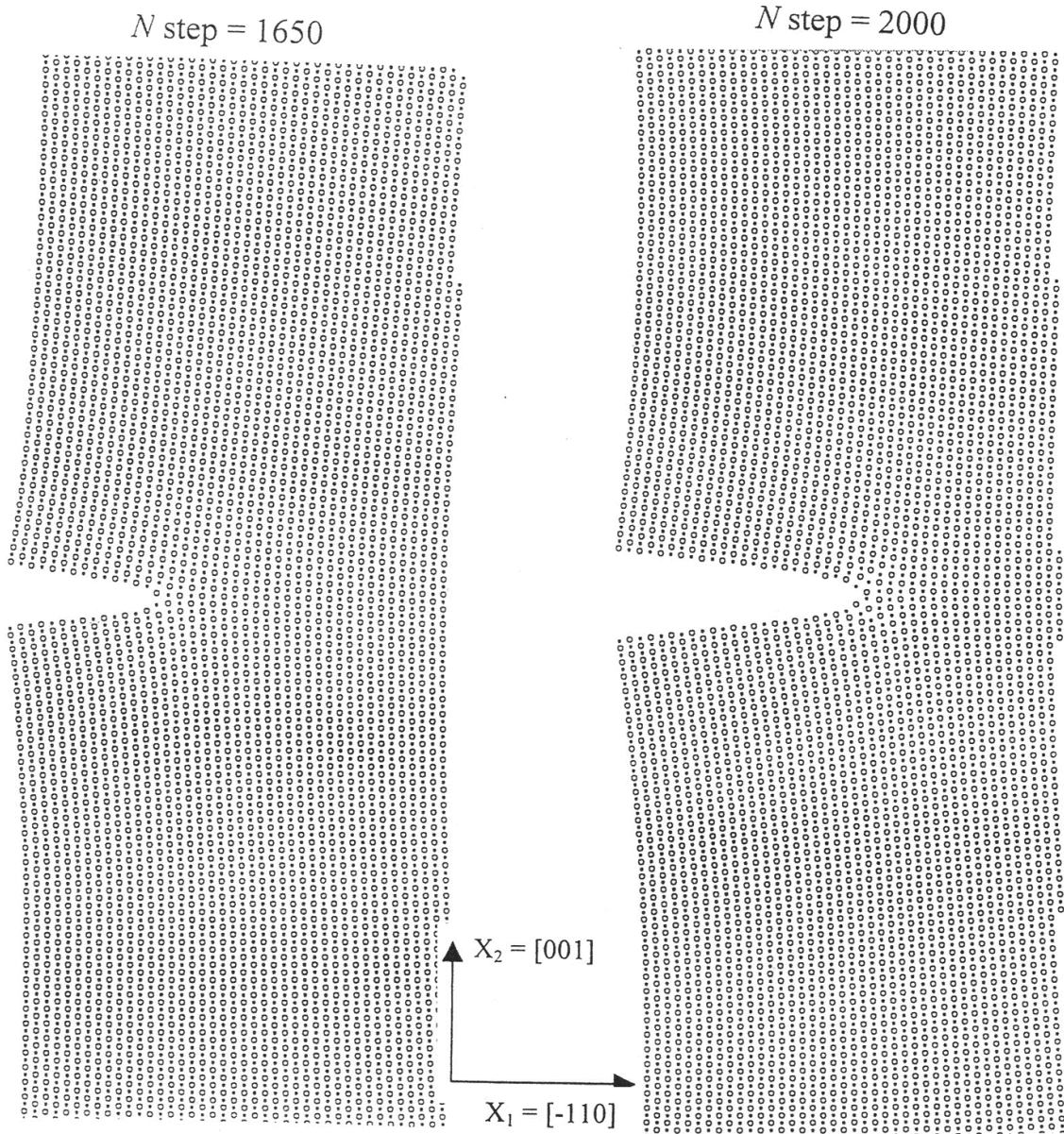


Fig. 1 Brittle initiation of an edge crack (001)/[110] in tension mode I from MD simulations. Detail of atomic configuration at the crack tip at time step Nstep =1650 (stationary crack) and at Nstep = 2000 (brittle crack extension).

The details of atomic configuration at the crack tip before crack initiation (time step 1650) and during crack extension (time step 2000) are shown in Fig. 1. According to Fig. 1, the crack extension corresponds to 8 elementary displacements d_{110} in the atomic lattice, i.e. when 8 elementary AE events have been realized.

Figure 2 presents a relief of the kinetic energy distribution inside the whole atomic sample, created from the mapping of local kinetic energies at individual atoms (i) and scaled as $(E_{kin}(i)/10^{-22})^{1/2}$. The black horizontal line denotes the actual crack length. The configuration at time step 1650 illustrates the situation before crack growth, where wave patterns arise only due to the loading and scattering of loading waves at the free crack faces (Machová and Ackland, 1998) (including the crack tip). The loading waves arrive to the crack faces continuously after each increment of loading at external sample borders. The situation at time step 2000 is already

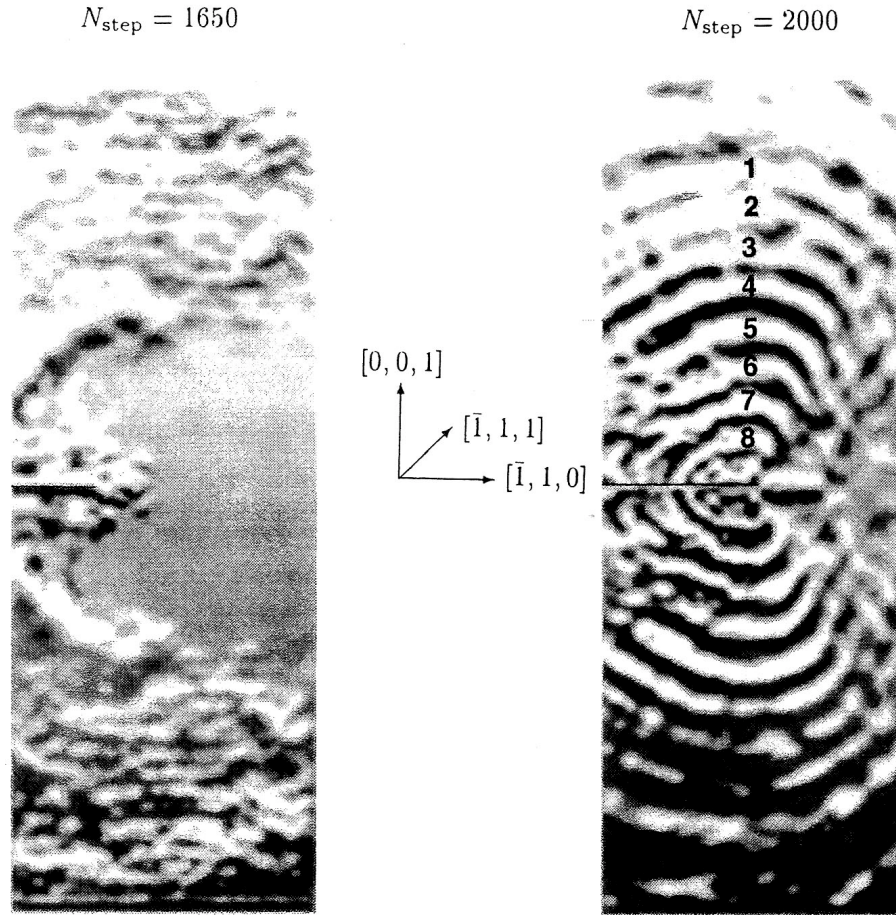


Fig. 2 A relief of the local kinetic energies at individual atoms obtained from MD for the stationary crack ($N_{\text{step}} = 1650$ – scattering of loading waves at the crack) and after brittle crack extension in mode I ($N_{\text{step}} = 2000$ – stress wave radiation from the moving crack, quasi-longitudinal waves).

influenced by the crack extension. The 8 partial AE events may be recognized in the [001] direction, where the 8 wave fronts propagate to the upper and lower sample border being under load. Acoustic emission from the crack tip in the [001] directions is well visible at the time step 2000, since the first reflection of the wave front in the [001] directions appears at the [001] borders later, nearly at time step 2100. The character of the acoustic emission is given mainly by the relaxation of the tension stress components in front of the crack tip and by bond breakage during crack extension. The position of the individual wave fronts well corresponds to the velocity of longitudinal waves $C_{L\langle 001 \rangle}$. The distances between the individual wave fronts well correspond to average crack velocity $V_{\text{crack}} = d_{110}/\Delta t = 1013$ m/s, where $\Delta t \approx 0.2$ ps means the average time needed for the change of the crack front position in the lattice. Figure 2 shows that the AE-source during brittle fracture can be characterized as a sequence of high frequency pulses, emitted after each elementary crack tip hop, with a repetition frequency $\nu = 1 / 0.2$ ps = 5 THz.

The patterns in the $\langle 110 \rangle$ and $\langle 111 \rangle$ directions in Fig. 2 at $N_{\text{step}} = 2000$ are already influenced by the reflections of the acoustic waves from the left and right sample borders. They

have a more complicated character due to the interaction of the emitted waves from the crack tip with the reflected waves. A similar situation arises also in experimental fracture tension tests but at different times.

Acoustic emission during crack extension, unimpeded by back wave reflections from sample borders, may be found also in the atomistic simulation (Holian and Ravelo, 1995) and (Machová and Ackland, 1998). The character of acoustic emission during crack extension presented here and in (Holian and Ravelo, 1995; Machová and Ackland, 1998) is in a qualitative agreement with the expectation by continuum model, presented in (Freund and Rosakis, 1991). The wave patterns in (Machová and Ackland, 1998) are somewhat influenced by transient local twinning at the crack tip.

3. Transonic twinning from the crack tip

In agreement with experimental observations in bcc iron (Hertzberg, 1983; Smida and Bosansky 2000), twinning in atomistic simulations occurs at some stress concentrators either under high strain rates (Machová and Ackland, 1998) or at sufficiently large applied stress at low temperatures in a quasi-static (Machová et al., 1999; Hu et al., 1998) or static case (Cerv et al., 2000).

We present here unpublished results on the character of acoustic emission during fast twinning from the crack tip under a gradual quasi-static loading from Machová et al. (1999). A central pre-existing crack (001)/[110] is considered in an initially rectangular sample. Due to the symmetry of the problem, only one half of the sample is treated in the simulations. The initial half crack length is $l_0 = 20 d_{110}$. The simulation box consists of 200 atomic planes (-110) in the x_1 direction and 400 planes (001) in the x_2 direction, parallel to loading. The sample was loaded gradually (during 4000 time steps) by external forces distributed at the upper and lower (001) sample borders up to the level corresponding to Griffith stress σ_G .

Twin formation at the crack tip in the slip systems $\langle 111 \rangle \{112\}$ (Fig. 3) and a fast twin extension into bulk crystal is already observed during the linear phase of loading between time steps 3000 and 3360. As follows from Machová et al. (1999), the unstable three layers stacking fault (3SF) at the crack tip has been transformed to a thin twin at time step 3000. At this moment, the relative shear displacements between interior neighboring planes k and l in the $\langle 111 \rangle \{112\}$ shear systems near the crack tip reach the expected value for ideal twinning $u_{kl} = b/3$, where $b = a_0/2 \langle 111 \rangle$ is the Burgers vector of the magnitude $a_0\sqrt{3}/2$. As mentioned in Cerv et al. (2000), the length of the initial twins in the $\langle 111 \rangle$ direction corresponds to about $10b$ at time step 3000. The twins extended up to $30b$ at time step 3100, at time step 3200 the corresponding length of a twin lamella is $50b$, at 3300 it is $70b$ and at final step 3360 (see Fig. 1 in Cerv et al., 2000) the twins are extended in the $\langle 111 \rangle$ directions up to the distance $82(\pm 1)b$ from the crack tip. (Note that 100 time steps represent 1 ps). The twins extend from the crack tip toward the crystal with a constant velocity $V_{\text{twin}} = 1.65 C_T$, where $C_T = 3007$ m/s is the velocity of the shear waves in the $\langle 111 \rangle \{112\}$ slip systems. The slip system is inclined with respect to the $[-110]$ direction at the angle $\theta \approx 35^\circ$. Note that Burgers vector b corresponds to an elementary distance between atoms in the $\langle 111 \rangle$ direction.

Figure 4 shows a local map of kinetic energies of individual atoms, normalized by $1J$. The individual figures correspond to the situation at time steps 3100, 3200, 3300 and 3360. The wave patterns at the upper and lower sample borders come from the gradual (step by step) external

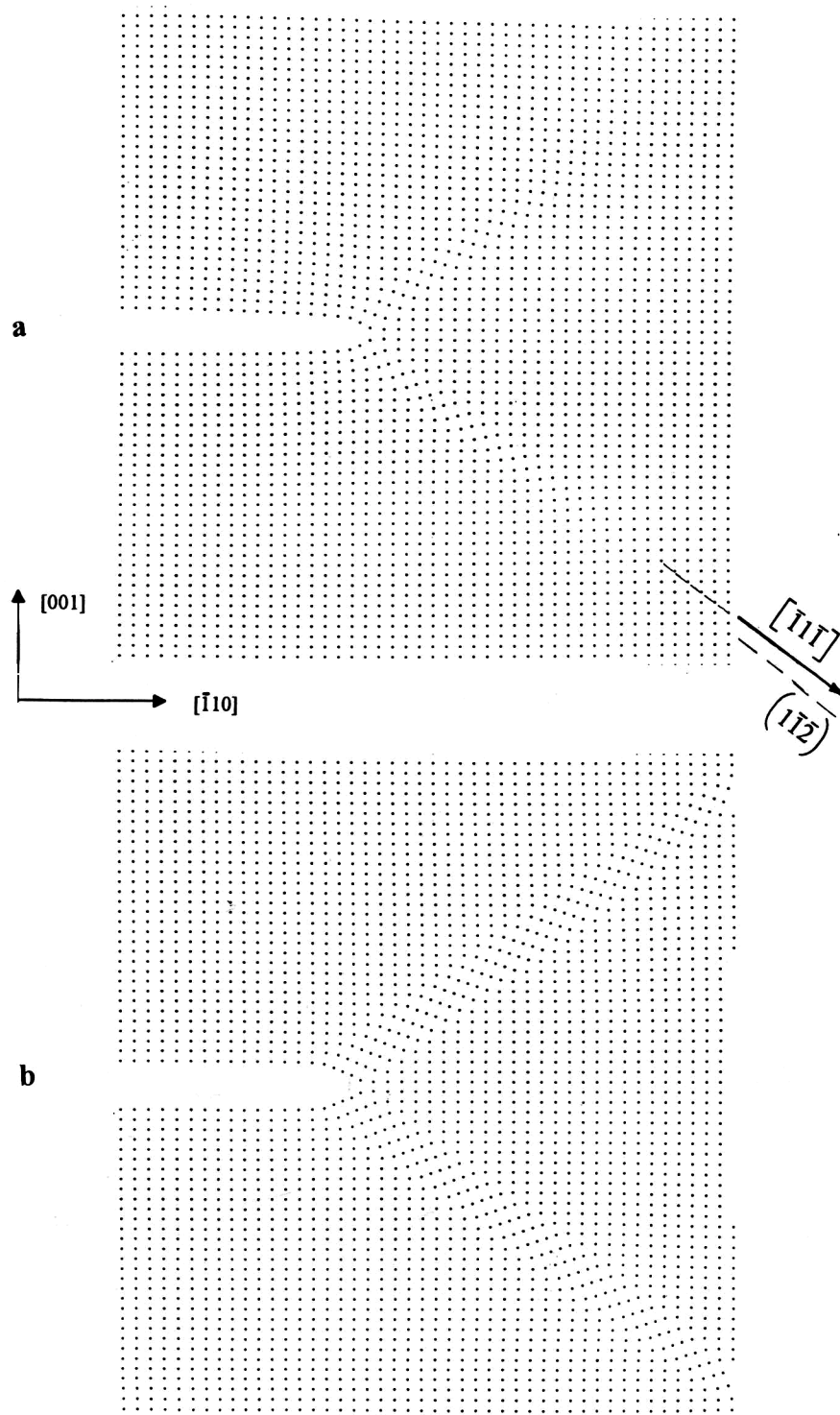


Fig. 3 Atomic configuration at the crack tip during twin generation (a) and fast twin extension (b) at a crack $(001)/[110]$ loaded in mode I.

loading. These patterns do not occur in Cerv et al. (2000), where transonic twinning under static loading is presented. Exchange of interactions occurs during twinning, i.e. some bonds are broken and new created in the $\langle 111 \rangle \{112\}$ slip systems. The bond breakage and relaxation of the shear stresses contribute to acoustic emission during twin extension. Our results are not influenced by the back wave reflections from external sample borders, caused by the shear bond

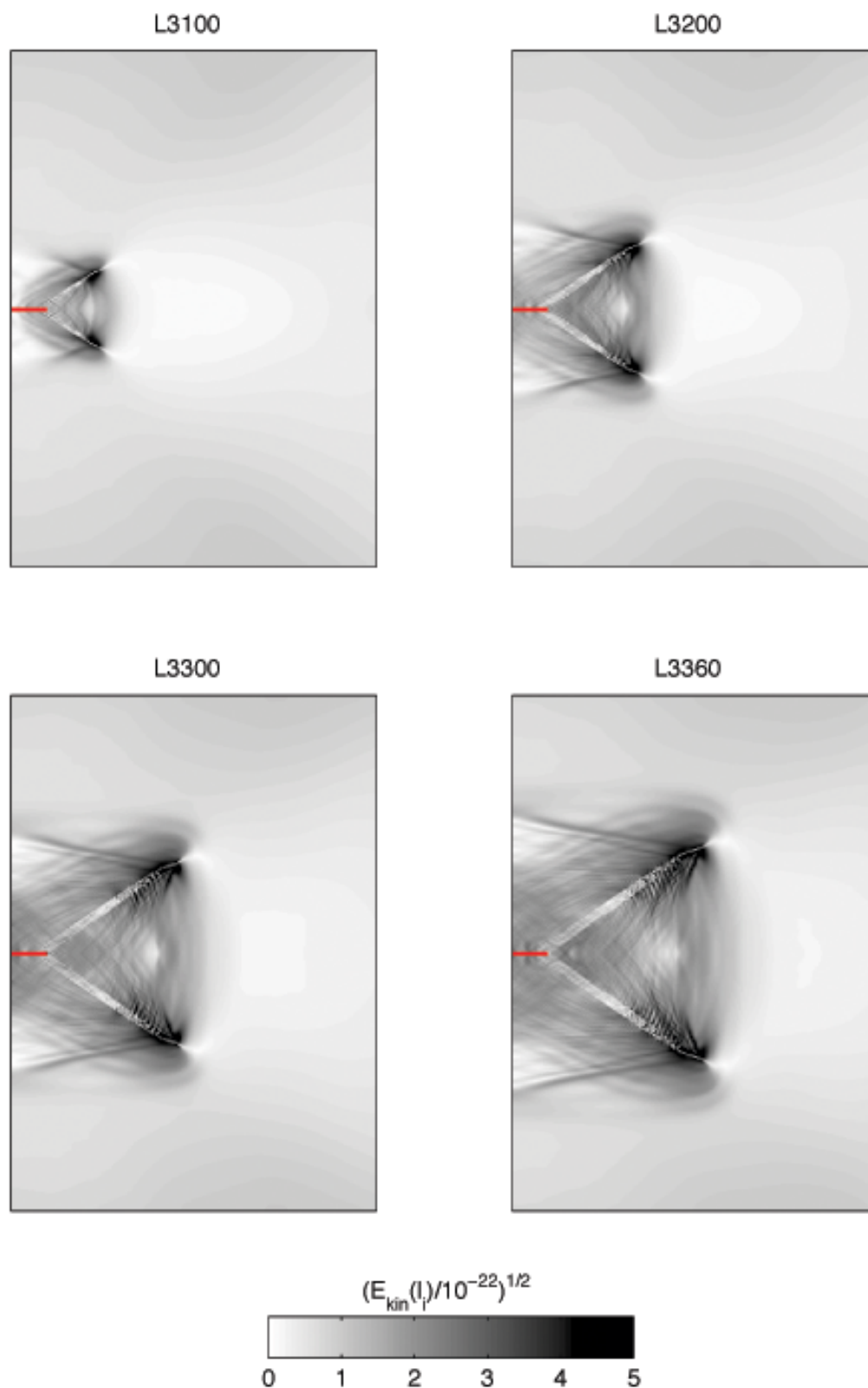


Fig. 4 Local map of kinetic energies of individual atoms from MD in the simulated sample loaded gradually in mode I at time steps 3100, 3200, 3300 and 3360. The pre-existing crack (001)/[110] is shown as the horizontal black line. The oblique lines emanating from the black twin tips are shock waves generated by transonic twinning.

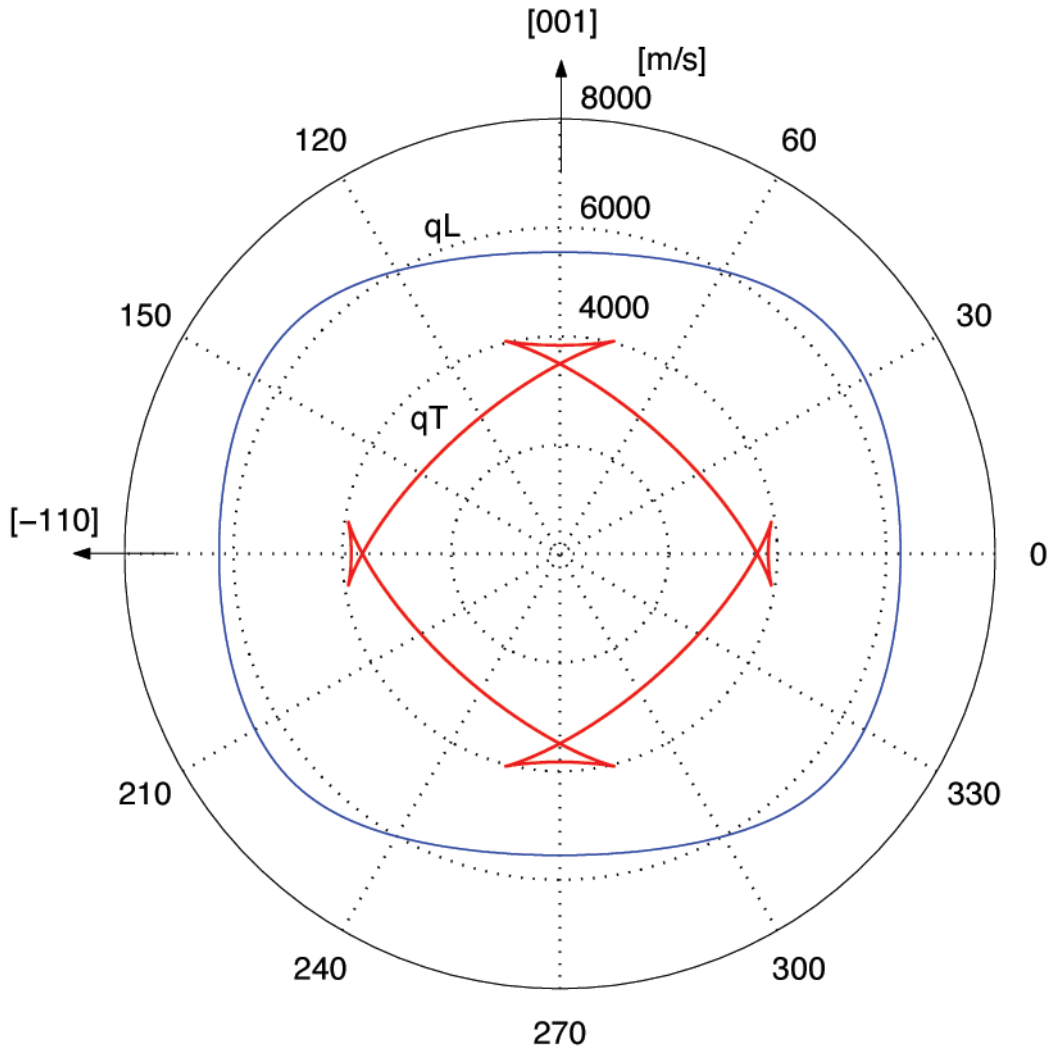


Fig. 5 Sections of the ray (wave) surfaces (quasi-longitudinal (qL) and quasi-transverse (qT)) in the (110) plane in bcc iron under plane strain.

breakage. When twins expand with a velocity higher than the velocity of shear waves, shock waves are expected, both in continuum model (Rosakis and Tsai, 1995) and in our atomistic model. Although the situation in Fig. 4 is influenced by gradual loading, bond breakage and stress relaxation mentioned above, the shock waves arising during transonic twin extension are clearly visible as oblique lines at twin tips. The oblique lines represent the envelopes of elementary shear waves, generated by the twin tips and by the twin corners (Rosakis and Tsai, 1995) when they propagate with a speed higher than the velocity of shear waves in the shear direction $\langle 111 \rangle$. Contrary to isotropic medium, the elementary waves have slightly complicated wave fronts due to the anisotropic cubic symmetry (Fig. 5). The oblique lines in Fig. 4 make with twin boundaries so called Mach angles of about 46° . It is in a reasonable agreement with angles 47° - 55° coming from a reconstruction (Fig. 6) of the fast moving ray (wave) surfaces, generated by the upper moving twin tip in the $\langle 111 \rangle$ direction in elastic anisotropic continuum of the same orientation as in our case. The results for a static loading presented in (Cerv et al., 2000) show that the character of acoustic emission at twin boundaries is similar, i.e. in our case transonic twinning is not significantly influenced by the non-zero loading rate. The hot (black) fine structure at the twin tips is probably caused by fast structural changes at the twin tips and also by

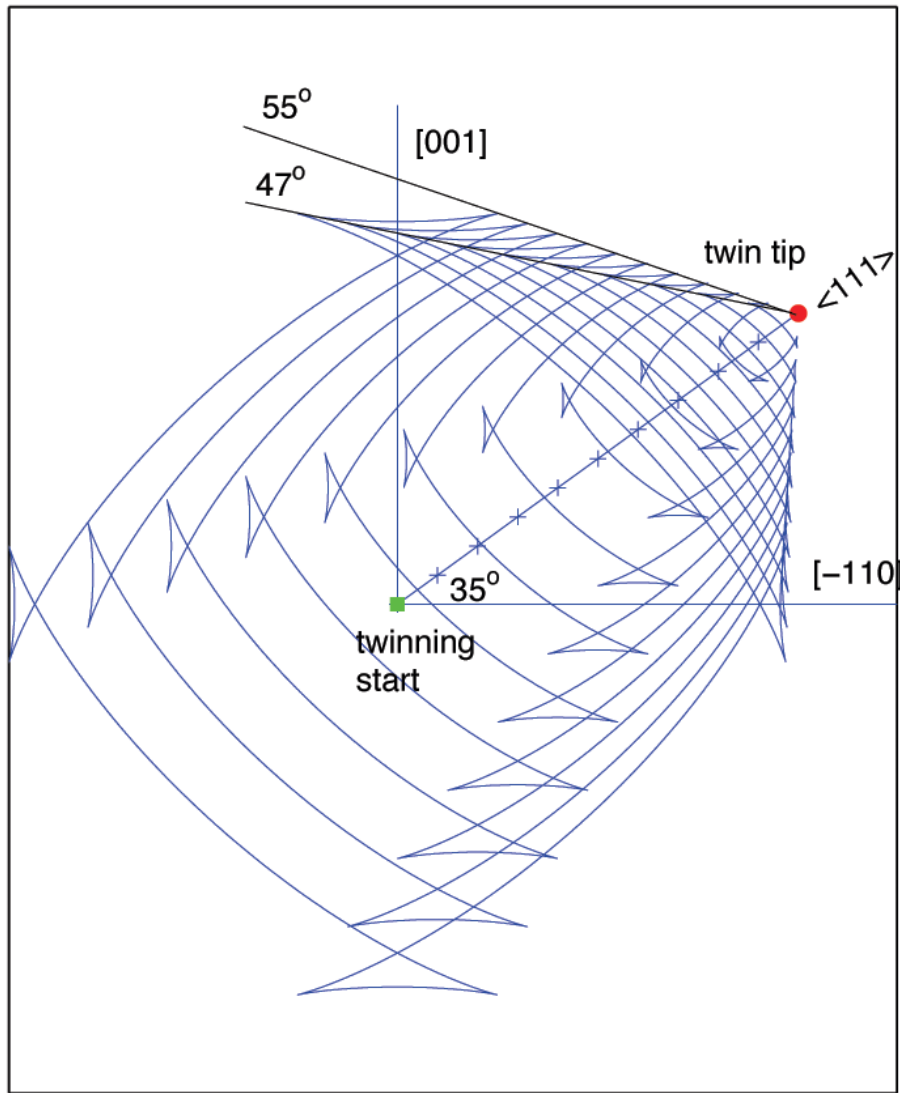


Fig. 6 Reconstruction of the shear wave patterns for fast twinning in anisotropic continuum of the same orientation as in Fig. 5. The crosses denote the position of the moving twin tip (at the upper twin in Fig. 4) with a constant transonic velocity $V_{\text{twin}} = 1.65 C_T$. The distance between crosses corresponds to Burgers vector $b = a_0/2 \langle 111 \rangle$ and the time corresponds to 0.5 ps after the beginning (start) of the fast twin extension. The oblique lines under the angles 47° and 55° denote the envelopes of the individual shear waves fronts and they represent the shock waves arising after transonic motion of a local source of the shear stress waves.

partial twinning dislocations that operate at interfaces with transonic velocities. Note that in this case twinning occurs in the easy twinning direction, described e.g. in Hertzberg (1983).

4. Dislocation emission from the crack tip

Emission of complete edge dislocations with Burgers vector $b = a_0/2 \langle 111 \rangle$ in the slip systems $\langle 111 \rangle \{112\}$ has been observed recently (Rosecky et al., 2001) in atomistic simulations with a different crack orientation $(-110) / [110]$ – see Fig. 7. In this section we present new results on the character of acoustic emission during subsonic motion of dislocations away from the crack tip.

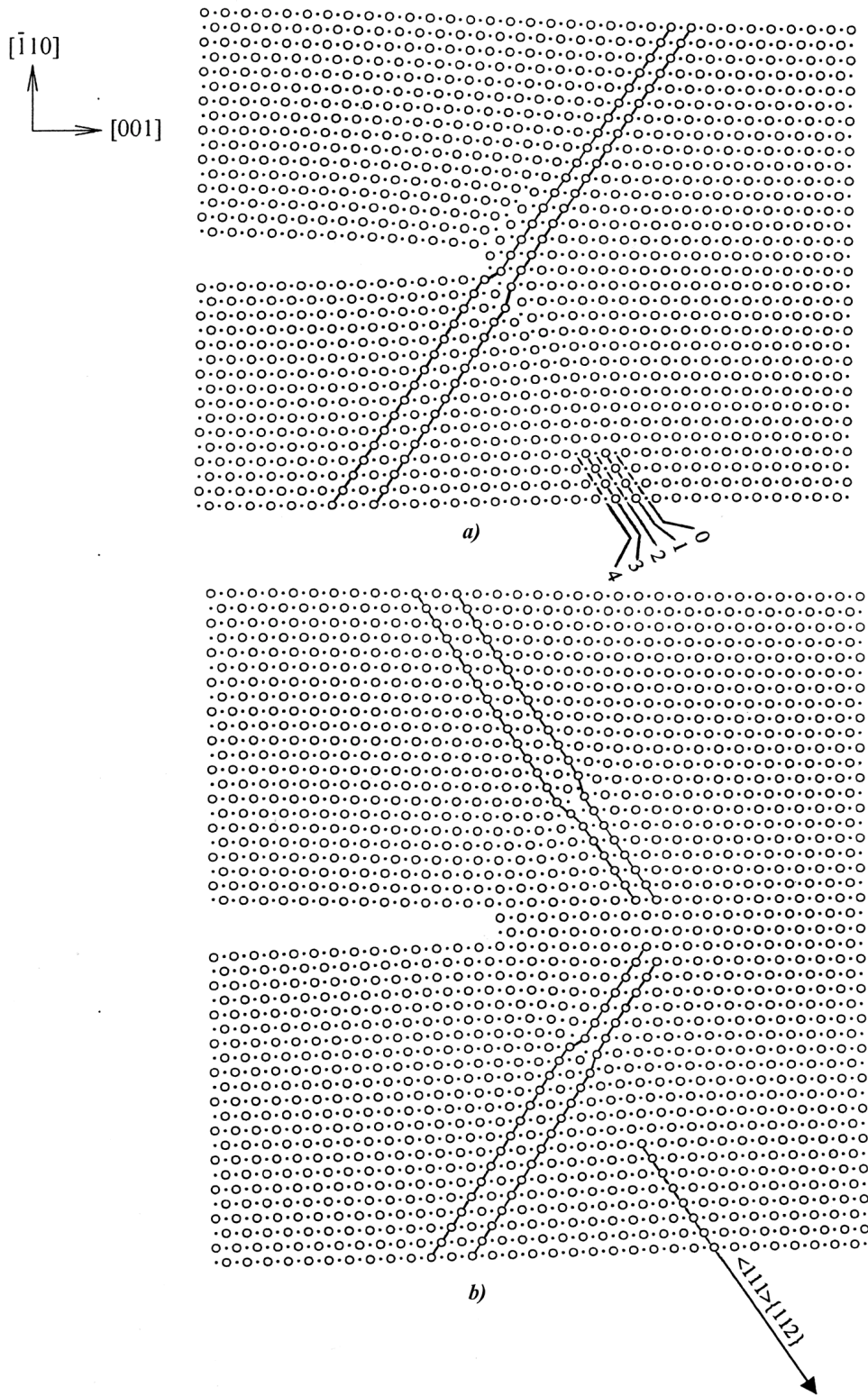


Fig. 7 Detail of atomic configuration at the crack tip: (a) during dislocation generation at a pre-existing crack $(-110)/[110]$, (b) at pair emission of complete edge dislocations in the slip systems $\langle 111 \rangle \{112\}$. The crack is loaded in tension mode I.

A central pre-existing crack $(-110) / [110]$ is embedded in a rectangular sample. Due to the symmetry, only one half of the sample is treated in the simulations. The initial half-crack length is $l_0 = 30 a_0/2$. The simulated crystal consists of 300 planes in the $x_1 = [-110]$ direction (parallel to loading) and 300 planes in the $x_2 = [001]$ direction. The sample is loaded gradually (during 6000 time steps) by external forces up to the level corresponding to Griffith stress σ_G . After that the external forces are kept at the constant level.

Dislocation generation at the crack tip (Fig. 7a) has been observed at time step 6500. In this case, the slip system $\langle 111 \rangle \{112\}$ is inclined with respect to the $[001]$ direction at an angle $\theta \approx 55^\circ$ and dislocation motion away from the crack tip is realized in the anti-twinning direction (Hertzberg, 1983). During the dislocation generation, the relative shear displacements U_{01} , U_{12} , U_{23} and U_{34} at the crack tip have been monitored between the planes 0,1,2,3,4 respectively (see Fig.7a). The most significant component is the U_{01} , the other relative shear displacements were negligible (small) during the process. The relative shear displacement U_{01} reached the expected value $U_{01} = b$ at time step 6549, when the generation process finished and the two complete edge dislocations in Fig.7b were emitted from the crack tip. The emission is realized as a fast block like shear of the lower crystal parts lying below the slip planes, which enlarges crack opening displacements and causes crack tip blunting and crack stability. At this moment (time step 6549), the position of the dislocation nucleus in the $\langle 111 \rangle$ direction corresponds to a distance $8b$ from the crack tip and the dislocations start to move in the $\langle 111 \rangle \{112\}$ slip systems away from the crack tip. At time step 6700, the position of the dislocation nucleus already corresponds to $23b$. At time step 7000, the dislocations occur at a distance $53b$ from the crack tip. The average dislocation velocity is $V_{\text{disl}} = (53 - 8) b / (7000 - 6549) h = 2476 \text{ m/s}$; i.e. it is subsonic, smaller than the velocity of the shear waves in the slip system $\langle 111 \rangle \{112\}$.

Shear bond breakage and exchange of interactions exist in the slip systems also during dislocation emission and dislocation motion. The presented results are not influenced by the back wave reflections from the external sample borders.

The local kinetic energies of individual atoms in the whole crystal are visualized at the mentioned time steps 6500, 6549, 6700 and 7000 in Fig. 8. Unlike Fig. 4, the loading waves are not visible in Fig. 8 since the external forces are kept at a constant level after the time step 6000. The higher kinetic energy, the darker color in Fig. 8 occurs, similar to Fig. 4. The crack length in Fig. 8 is shown as a vertical short line. The oblique dark patterns in figures R6500 and R6549 denote the “hot” slip systems $\langle 111 \rangle \{112\}$ where dislocation generation is realized and the local kinetic energies of the participating atoms are very high. Small shock patterns are visible at dislocation positions in figure R6549, since the emission process is very fast, as already mentioned in (Holian and Ravelo, 1995). The fast crack opening after the emission significantly contributes also to the generation of longitudinal waves. The wave front of the longitudinal waves emanating from the crack is well visible in figure R6700 as a light half ring around the crack, located in front of the dark patterns. The dark oblique line patterns represent the slip systems. The darkest place at the end of each slip system is the moving dislocation nucleus. The wave fronts of the shear waves generated during subsonic motion of the dislocations are visible almost perpendicularly to the slip systems. While the analysis (Trochidis and Polyzos, 1995) brings information on transverse elastic displacements caused by motion of a dislocation in isotropic continuum, we are concerned with the field of atomic velocities in anisotropic medium. The reconstruction of the shear wave processes arising in anisotropic continuum due to a moving source with the speed $V_{\text{disl}} = 0.82 C_T$ is shown in Fig. 9. This figure shows that the darker region at the end of the lower slip system in Fig. 8 is created as a diffusive wave front of the shear

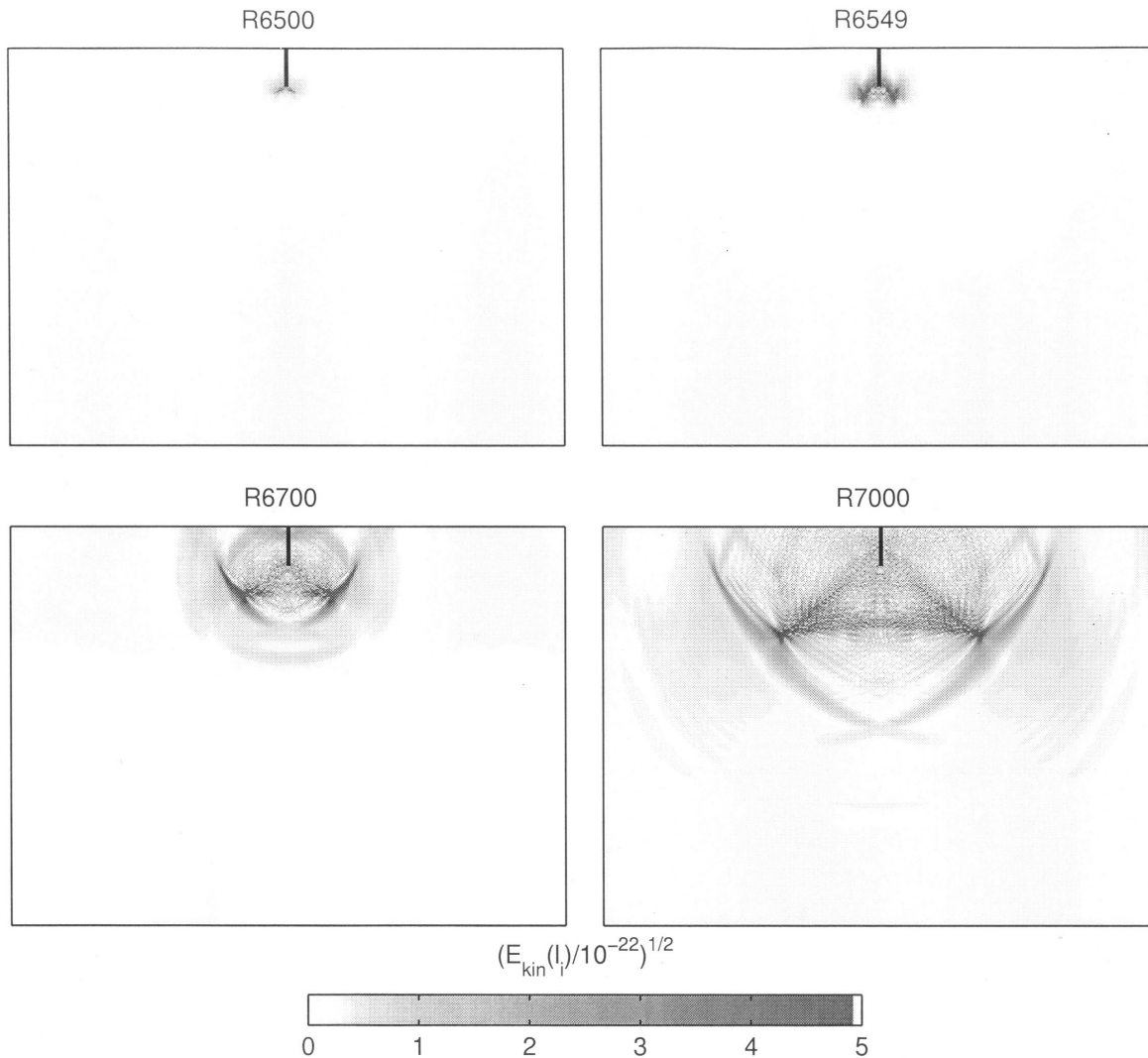


Fig. 8 Local kinetic energies of individual atoms from MD in the simulated cracked crystal: R6500 - dislocation generation at the crack tip at time step 6500; R6549 - emission of the complete edge dislocations in the slip systems $\langle 111 \rangle \{112\}$ at time step 6549; R6700 and R7000 - subsonic motion of the two dislocations with a velocity $V_{disl} = 0.82 C_T$ away from the crack tip. The crack $(-110)/[110]$ is shown by vertical short lines, the slip systems are visible as the thin oblique patterns starting from the crack tip.

waves emitted by the moving dislocation. A larger level of the kinetic energy and of atomic velocities is expected in the region of the shear wave front and so, this region in Fig. 8 is dark. The shear waves are generated during the shear bond breakage and relaxation of the shear stress in the $\langle 111 \rangle \{112\}$ slip systems. They represent the most intensive processes in the system. The relaxation of the normal stress components (dilatation above and compression below the dislocation slip plane) does not seem to contribute significantly to acoustic emission from the moving dislocations. It indicates figure R7000, where the wave front of the longitudinal waves is almost already invisible.

The results on transonic twinning and subsonic motion of dislocations in the equivalent slip systems $\langle 111 \rangle \{112\}$ illustrate how different shear wave patterns arise during transonic and subsonic motion of a local AE source.

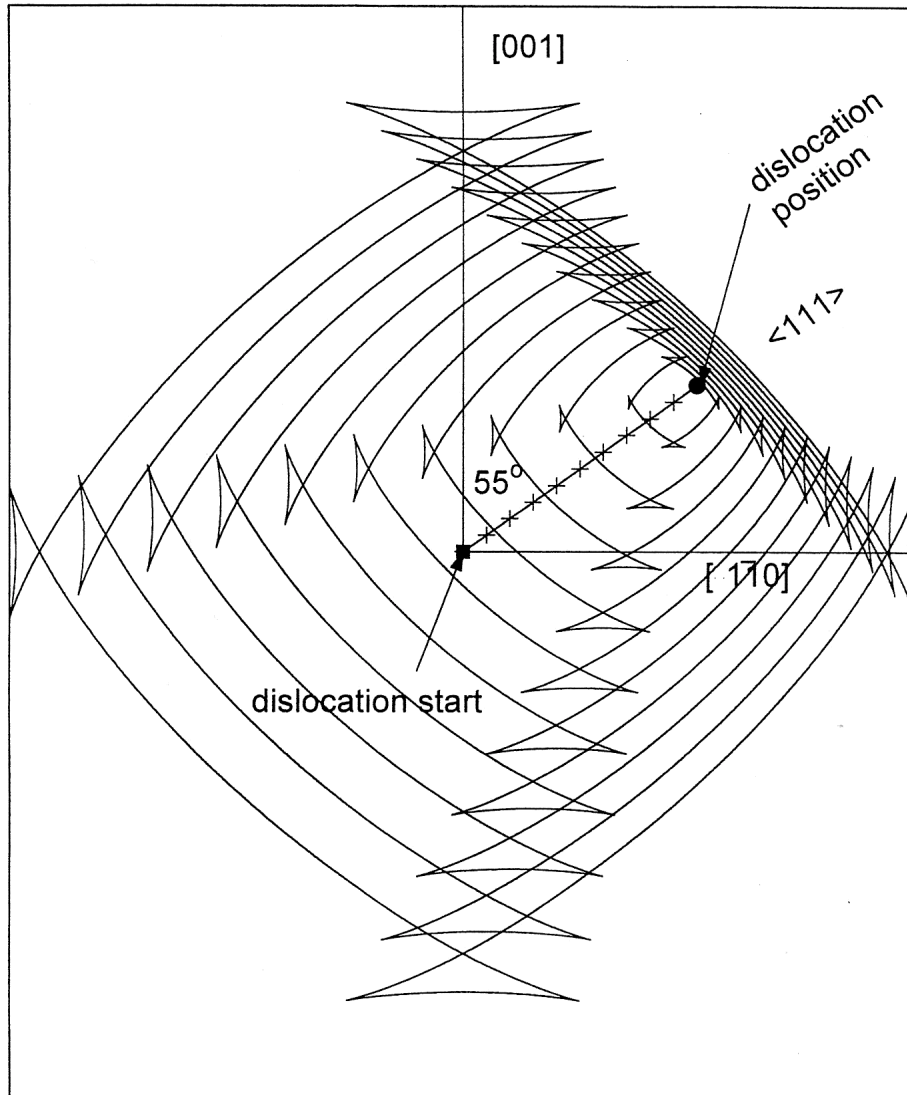


Fig. 9 Reconstruction of the shear wave patterns in anisotropic elastic continuum for subsonic dislocation motion. The crosses in the direction $\langle 111 \rangle$ denote the position of the dislocation (the lower dislocation in Fig. 8) moving with the velocity $V_{\text{disl}} = 0.82 C_T$. The distance between crosses corresponds again to Burgers vector. This figure shows that the darker region at the end of the lower slip system in Fig. 8 represents a diffusive wave front of the shear waves emitted by the moving dislocation.

MD simulations offer an opportunity to study acoustic emission during a defect growth on atomic scale level, where very high frequencies in THz region may occur. It is not yet directly accessible experimentally, where to at most GHz frequency of AE can be detected. However, the emitted pulses still contain low-frequency components, which have low intensity, but may be detectable.

Acknowledgements

The work was supported by the grant agencies of the Czech Republic under a contract GA106/00/D106 and of the Academy of Sciences CR under contracts A2076001 and A2076201.

References

- J. Cerv, M. Landa and A. Machová (2000), “Transonic twinning from the crack tip”, *Scripta mater.*, **43**, 423-428.
- L. B. Freund and A. J. Rosakis (1991), “The structure of the near tip field during transient elastodynamic crack growth”, research report R.I.02912, Brown University, Division of Engineering, April 1991, pp. 1-23.
- P. Gumbsch and H. Gao (1999a), “Dislocations faster than the speed of sound”, *Science*, **283**, 965-968.
- P. Gumbsch and H. Gao (1999b), “Driving force and nucleation of supersonic dislocations”, *J. Computer-Aided Materials Design*, **6**, 137-144.
- R. W. Hertzberg (1983), *Deformation and fracture mechanics of engineering materials*, John Wiley, New York, p. 119.
- B. L. Holian and R. Ravelo (1995), “Fracture simulations using large-scale molecular dynamics”, *Phys. Rev.*, **B 51**, 11 275-11 289.
- S. Y. Hu, M. Ludwig, P. Kizler and S. Schmauder (1998), “Atomistic simulations of deformation and fracture of α -Fe”, *Modelling Simul. Mater. Sci. Eng.*, **6**, 567-586.
- M. Landa, A. Machová, Z. Prevorovsky, J. Cerv and J. Adánek (1998), “Crack growth in single crystals of α -iron (3 wt% Si)”, *Czech. J. Phys.*, **B 48**, 1589-1606.
- A. Machová and G. J. Ackland (1998), “Dynamic overshoot in α -iron by atomistic simulations”, *Modelling Simul. Mater. Sci. Eng.*, **6**, 521-542.
- A. Machová, G. E. Beltz and M. Chang (1999), “Atomistic simulations of stacking fault formation in bcc iron”, *Modelling Simul. Mater. Sci. Eng.*, **7**, 949-974.
- V. Prakash, L. B. Freund and R. J. Clifton (1992), “Stress wave radiation from a crack tip during dynamic initiation”, *J. Appl. Mech.*, **59**, 356-365.
- P. Rosakis and H. Tsai (1995), “Dynamic twinning processes in crystals”, *Int. J. Solids Structure*, **32**, 2711-2723.
- Z. Rosecky, A. Machová and J. Cejp (2001), “Dislocation emission from the crack tip in bcc iron”, *CD-ROM Proceedings of the 3rd International Conference on Materials Structure & Micromechanics of Fracture*, Brno, Czech Republic, June 27-29, 2001.
- T. Smida and J. Bosansky (2000), “Deformation twinning and its possible influence on the ductile brittle transition temperature of ferritic steels”, *Mater. Sci. Eng.*, **A287**, 107-115.
- A. Trochidis and P. Polyzos (1995), “Dislocation dynamics and acoustic emission during plastic deformation of crystals”, *Wave motion*, **21**, 343-355.

A WAVELET TRANSFORM APPLIED TO ACOUSTIC EMISSION SIGNALS: PART 1: SOURCE IDENTIFICATION #

M. A. HAMSTAD⁺, A. O'GALLAGHER and J. GARY

National Institute of Standards and Technology, Materials Reliability Division (853), Boulder, CO 80305-3328;

⁺Also Department of Engineering, University of Denver, Denver, CO 80208.

Abstract

A database of wideband acoustic emission (AE) modeled signals was used in Part 1 to examine the application of a wavelet transform (WT) to identify AE sources. The AE signals in the database were created by use of a validated three-dimensional finite element code. These signals represented the out-of-plane displacements from buried dipole sources in aluminum plates 4.7 mm thick and of small and large lateral dimensions. The surface displacement signals at three far-field distances were filtered with a 40 kHz high-pass filter prior to applying the WT. The WTs were calculated with AGU-Vallen Wavelet, a freeware software program. The effects of propagation distance, AE source type, and the depth of the AE source below the plate surface were examined. Specifically, a ratio of the WT magnitude (WT coefficient) from the fundamental anti-symmetric mode to that from the fundamental symmetric mode was studied for correlation with the AE source type. The WT magnitudes were those corresponding to a particular group velocity and signal frequency for each mode. For sources in the large plate located at the same depth, the ratios were able to distinguish different source types and exhibited only small changes with increasing propagation distance. But, when the variable of depth of the source was introduced, the ratios did not uniquely classify the AE source type. In the case of the small coupon plate specimen, reflections from the specimen edges distorted and complicated the WTs. Since the current coupon database excludes (except for one case) the parameter of changes in the distance of the source from the coupon sides, a full examination of these complications was not possible.

1. Introduction

Since early in the history of AE, a goal of AE practitioners has been to use AE signals as the means to identify the type of source that generated the signals (Mehan and Mullin, 1971). Papers have been published indicating the successful identification of AE sources, and commercial AE companies offer software for the purpose of identifying AE sources. These efforts are often controversial because they lack an analytical justification (based on the theory of AE) of the signal features used to sort the experimental signals into different types of sources. Alternatively, some AE source-identification experiments have been carried out with specimen geometries and sensor locations such that signals are obtained from the direct longitudinal bulk waves in several directions of radiation (Buttle and Scruby, 1990a). The analysis that is used to sort these signals into different source types (or combinations of source types) is based on analytical calculations (forward modeling) that determine the relative amplitudes of the first bulk longitudinal signals in different radiation directions. By comparing relative experimental bulk wave amplitudes in different directions with the calculated results for a series of possible sources, the experimental

Contribution of the U.S. National Institute of Standards and Technology; not subject to copyright in the US.

sources were identified in a more satisfying fashion. However, in many AE applications Lamb waves are present due to plate-like test specimens and observation of the AE signals in the far-field. In this case, this more satisfying approach is not directly applicable. Some AE researchers (Weaver and Pao, 1982a, b; Guo et al., 1998) have presented analytical results (forward modeling) for Lamb waves in infinite plates, but to date they have not published an extensive database that could lead to source identification of experimental signals by appropriate comparisons.

The AE source-identification research presented here uses an extensive database of modeled Lamb-wave AE signals. These signals were obtained by use of a validated finite-element modeling code (Hamstad et al., 1999). Since the exact source type and all its characteristics are known for each signal, the features of the AE signals can be unequivocally associated with particular source types. In the case of experimental signals, this is not the case. In this paper we examine the possibilities of extracting meaningful source identification features by the use of a wavelet transform (WT). To retain the possibility of a direct method of source identification (rather than an artificial-intelligence method), this paper examines the extraction of limited data sets from the WT results. In addition, if the direct method is not completely successful, these results could provide insight into the most relevant WT results to input into an artificial-intelligence approach.

2. Description of AE Database

The AE signals that comprised the analyzed database were all calculated by the NIST- Boulder finite-element modeling (FEM) code. This code has been validated (Hamstad et al., 1999; Prosser et al., 1999) for buried dipole-type point sources operating in plate specimens with infinite lateral dimensions and for surface and edge monopole sources on plates with small and large lateral dimensions. The specimen domains in the database were aluminum plates 4.7 mm thick. These plates had lateral dimensions of either 1000 mm by 1000 mm (representing the infinite-plate case) or 480 mm by 25.4 mm (representing a small coupon specimen). Figure 1 shows a drawing of the small specimen superimposed on the large specimen. The lateral position of the AE source and the positions where the plate top surface out-of-plane displacement was determined as a function of time are shown. These displacement signals provide the AE signals that would be obtained in a single direction of radiation (toward sensors 1, 2 and 3) or the opposite direction (toward sensors 5, 6, and 7). All the sensor positions were 60 mm apart.

The calculated signals provided a unique and ideal database that was far superior to experimental AE signals for the study of AE source identification. The reasons for this superiority are due to exact knowledge of key information not always available in experimental data: point-source location in three dimensions; source rise time; magnitude and orientation of source dipoles; absolute out-of-plane displacement of a perfect wideband point sensor at an exact location; known filtering of the AE signal; signals both with specimen edge reflections and without such reflections; and signals that are largely free of noise.

For this study of AE source identification, the analyzed database included three types of buried point-sources: (1) in-plane dipole, aligned with the propagation direction to the sensors, (2) out-of-plane dipole, and (3) crack initiation (three dipoles) with the largest dipole aligned with the propagation direction to the sensors. The dipole forces (body forces) were all 1 N except for the two smaller dipoles in the microcrack case, which were 0.52 N (based on the elastic constants of aluminum). Each dipole was made up of a “central” cell having no body force, along with single cells on each side of the “central” cell having body forces. All the

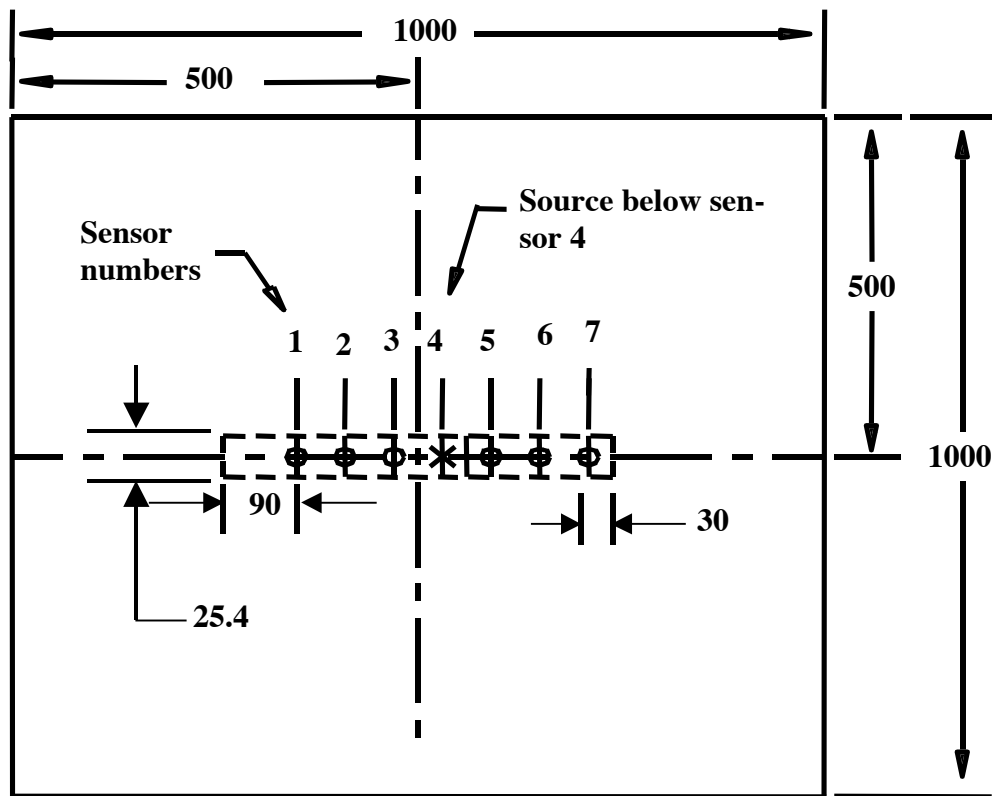


Fig. 1 Large specimen with superimposed small coupon specimen. Sensor positions, spaced 60 mm apart, show points where out-of-plane displacement was determined versus time. All dimensions in mm.

calculations were based on a uniform three-dimensional cell size of 0.313 mm, which was chosen to conform to the requirements for convergence (Hamstad et al., 1999). For the examination of propagation distance, the database included three propagation distances (60, 120, and 180 mm). The three distances were all in the far-field for the 4.7 mm thick plate. In addition, the database included the very important (as will be seen below) variable of depth of the point source below the top surface of the plate. All the sources had a rise time (of the dipole) of 1.5 μs with a “cosine bell” temporal dependence (Hamstad et al., 1999). This rise time resulted in AE signals with frequencies up to about 1 MHz (as determined from spectra calculated by a Fast Fourier Transform (FFT)). To provide a realistic database, all the AE signals were filtered with a 40 kHz high-pass four-pole Butterworth filter prior to analysis. Also, to represent experimental practice, all the calculated digital signals were resampled to a time step of 0.1 μs from the original calculation time step of 0.045 μs . Comparisons demonstrated that this resampling had no apparent effect on the waveforms or their FFTs. The calculated total signal length in each case was 200 μs beginning from the start of operation of the AE source.

3. General Examination of WT Results

Figure 2 shows an example of an AE signal without edge reflections and its calculated WT magnitude (WT coefficients) as a function of frequency versus time. The source for this signal was an in-plane dipole centered at a depth of 1.723 mm (the center of the “central” cell) below the plate top surface. The signal represents the top-surface out-of-plane displacement at 180 mm from the epicenter of the source. All the WTs were calculated with AGU-Vallen Wavelet, a freeware software program (Vallen-Systeme GmbH, 2001; H. Suzuki et al., 1996). AGU-Vallen

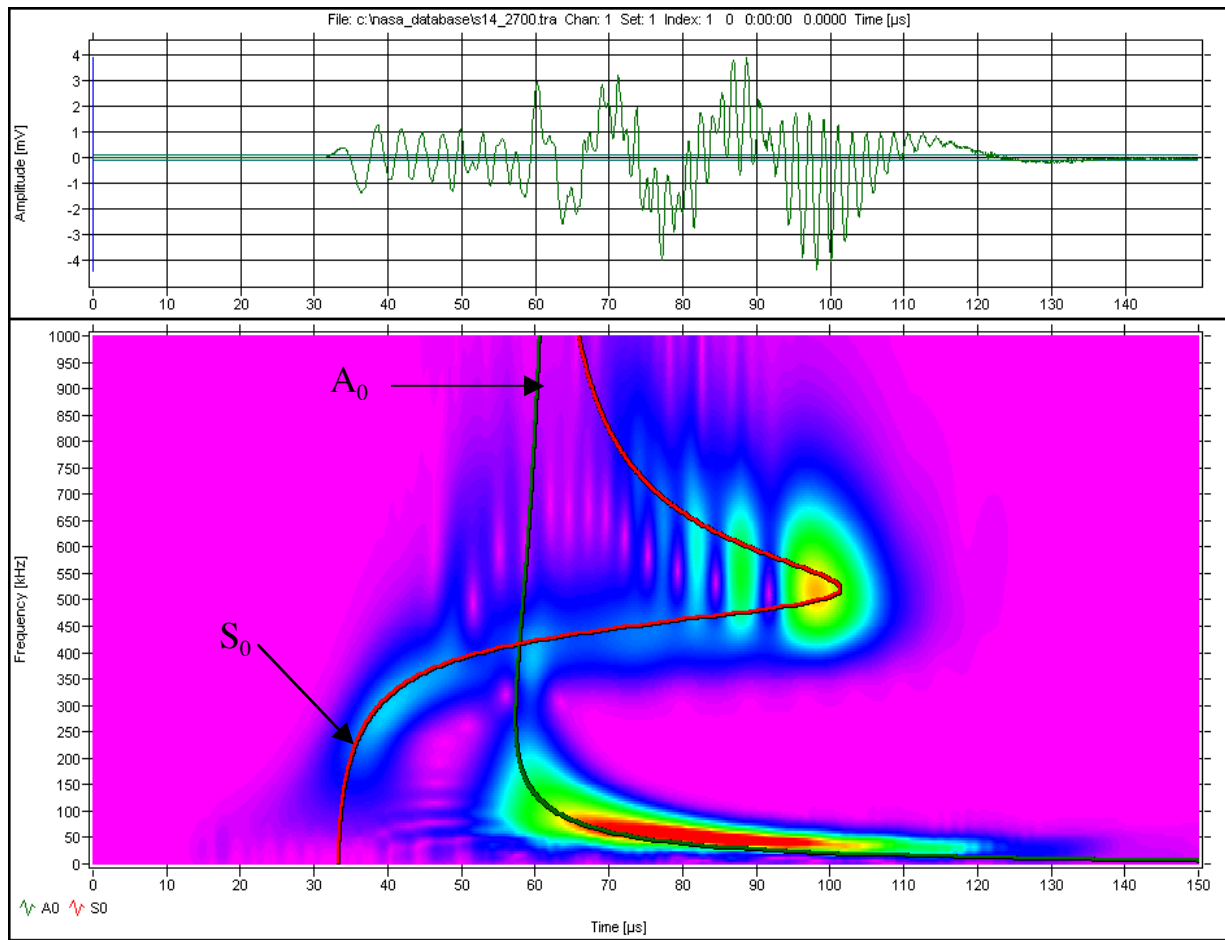


Fig. 2 Typical calculated AE signal from an in-plane dipole source with corresponding WT. Superimposed fundamental symmetric, S_0 , and anti-symmetric, A_0 , modes after converting group velocity to time based on 180 mm propagation distance. Red color corresponds to highest magnitude of the WT. Source depth is 1.723 mm in large specimen. (WT scale: 1 MHz: 150 μ s)

Wavelet has been developed in collaboration between Vallen-Systeme GmbH and Aoyama Gakuin University (AGU), Tokyo, Japan. The AGU group has pioneered in the research of wavelet analysis in the field of acoustic emission (Suzuki et al., 1996; Takemoto et al., 2000; Yamada et al., 2000). This program has a Gabor function as the “mother” wavelet with a central frequency of 7 MHz. The software program also includes a program to calculate the relevant group-velocity curves for the lowest ten modes of the infinite number of Lamb modes that govern the far-field wave propagation in a plate. Figure 2 shows the two lowest modes (fundamental symmetric, S_0 , and anti-symmetric, A_0) superimposed on the WT. This superposition is facilitated by an option that converts the group velocity scale to a time scale using the known exact propagation distance. The group-velocity curves were calculated by use of the same bulk velocities that were used in the finite-element computations (6,320 m/s bulk longitudinal velocity and 3,100 m/s bulk shear velocity). The FEM calculation also uses the material density of 2700 kg/m³. The color scale in Fig. 2 is a linear scale with red representing the highest-magnitude region of the WT and pink the smallest or zero-magnitude region. The display includes an option to change the color scale (called the color factor) so as to include a greater or lesser portion of the maximum magnitudes in the “red” region. The WT in Fig. 2 has a color-factor (CF) value of 0.8. A color factor of less than 1 (the default value) means that a wider range of the WT peak magnitudes are displayed in red. The converse applies for color factors greater than 1.

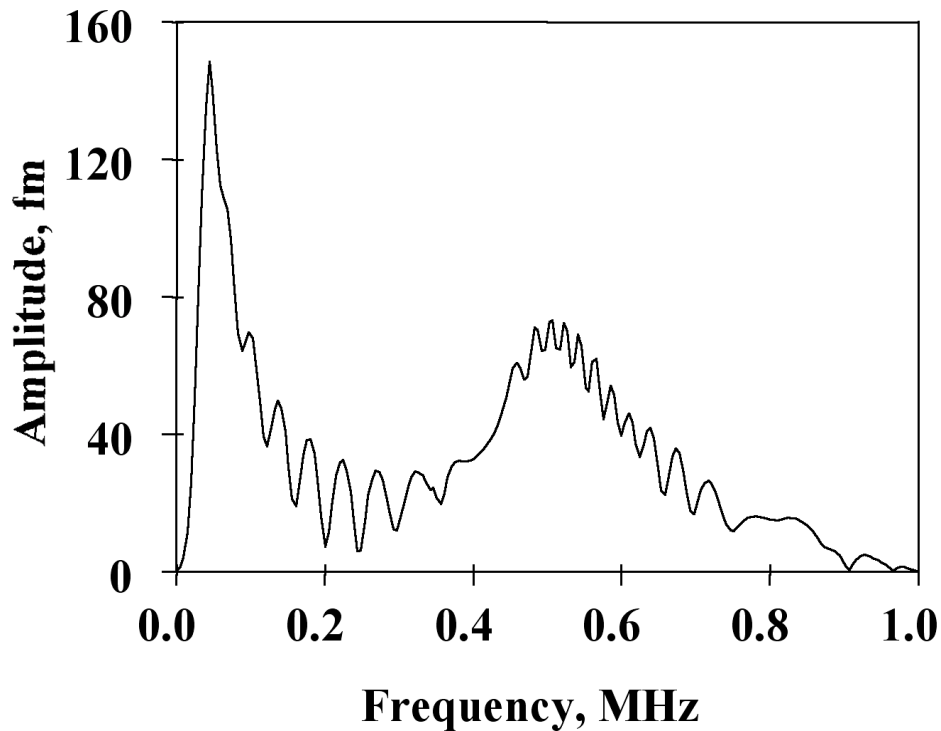


Fig. 3 FFT of the waveform shown in Fig. 2.

Clearly, Fig. 2 shows the presence of AE signal energy in portions of both the fundamental symmetric and anti-symmetric modes. The WT also demonstrates that the AE signal energy is not uniformly distributed between the modes that are present, nor is it uniformly distributed as a function of frequency along each of the dominant modes. These aspects demonstrate a key advantage of the WT as compared to an FFT. The WT shows how the signal energy is distributed as a function of frequency, time (or group velocity), and mode. In contrast, as is well known and illustrated in Fig. 3, the FFT of the same AE signal provides only the frequency content of the whole signal and does not allow one to easily see the modal division or how the intensity of the energy in particular frequency ranges and modes varies as a function of time (or group velocity). Thus, Fig. 2 shows that this AE source has the greatest concentration (most red color) of energy in the anti-symmetric fundamental mode in a frequency range of about 40 to 80 kHz over a range of group velocities from 1.8 to 2.7 mm/ μ s. Another large amplitude region of the WT is the part of the fundamental symmetric mode in a frequency range from about 500 to 540 kHz, which is centered about a group velocity of about 1.9 mm/ μ s. With regard to these frequency ranges and group velocities, we point out that the WT algorithm allows the user to select both the frequency resolution and the wavelet size. The effects on the WT results of different choices for these parameters are discussed next.

4. Parameter Selection to Enhance the Resolution/Smoothness of WT Results

The wavelet transform program, AGU-Vallen Wavelet, used in this research is that freely distributed on the World Wide Web (see web site www.vallen.de). There are several parameters that need to be selected prior to the wavelet calculation. Figure 4 shows the setup screen for this wavelet transform. Two parameters must be chosen properly to obtain sufficient resolution of the WT. These parameters are the “Frequency Resolution” and the “Wavelet size”. The “Freq. Resolution” gives the frequency interval for the WT calculation, and has a default value of 10

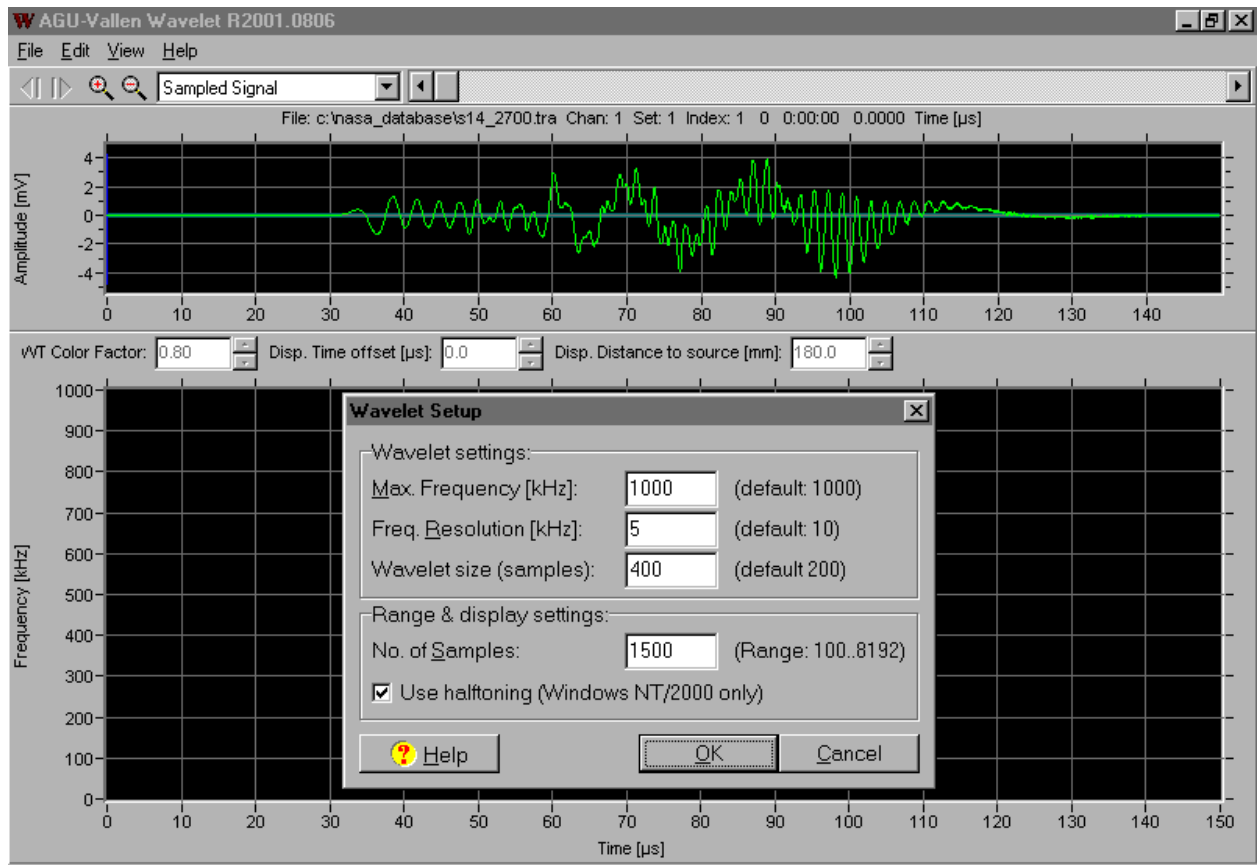


Fig. 4 “Wavelet Setup” screen for AGU-Vallen Wavelet.

kHz. This value is not necessarily the best, as is shown in Fig. 5. In this case the WT was calculated for an in-plane dipole centered at a depth of 0.47 mm in the large plate with a source-to-sensor propagation distance of 180 mm. Figure 5 (a) shows the WT result (CF = 1) with the default value of “Freq. Resolution” of 10 kHz and a “Wavelet size” of 800 samples, and Fig. 5 (b) shows the WT result (CF = 1) using a “Freq. Resolution” of 2 kHz and the same “Wavelet size”. Clearly the 10 kHz frequency steps can be seen in Fig. 5 (a). These steps are not present in Fig. 5 (b), which shows a much smoother result. The disadvantage of using the smaller value for the frequency resolution is that the calculation takes longer. For example, on a personal computer with a CPU speed of 0.7 GHz, the WT shown in Fig. 5(a) took about 5 s and that shown in Fig. 5(b) took about 18 s.

The “Wavelet size” has a default value of 200 samples. Figure 6 shows the WT results of the same AE signal used for Fig. 5 with the default value (a) and a size value of 800 samples (b). For this figure the “Freq. Resolution” of 2 kHz was used along with a color factor of 1. It can be seen that the larger “Wavelet size” gives a smoother result. With a larger “Wavelet size” value, the calculation requires more time. To date, our observation has been that an increase in the “Wavelet size” is advisable when the larger amplitudes in the WT are at frequencies below about 100 kHz. Thus, we conclude that it is worthwhile to enhance the resolution and smoothness of the WT results at the cost of slightly longer computational times. For example, on a modern personal computer, the WT shown in Fig. 6 (a) took about 6 s and that shown in Fig. 6 (b) took about 18 s. When WT results were used to extract quantitative results, the parameters were selected to provide better resolution. In other cases lower resolution was used for more qualitative results.

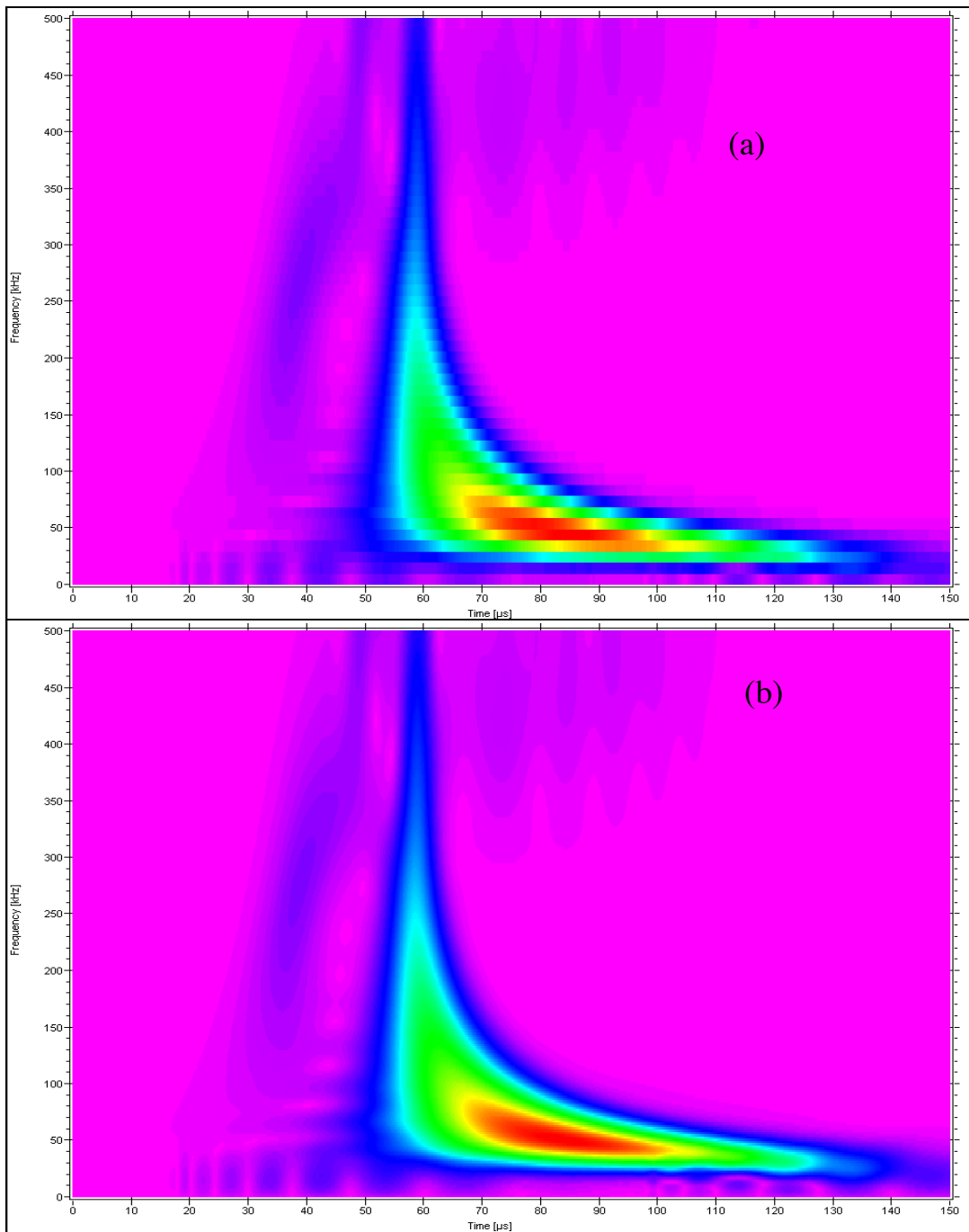


Fig. 5 WT results with low “Frequency resolution” (default) of 10 kHz (a) and high “Frequency resolution” of 2 kHz (b). Both results with a “Wavelet size” of 800 samples. Figures show frequency (0 to 500 kHz) versus time (0 to 150 μ s).

5. Correlation of WTs with Source Type (Large Plate)

To begin to study source identification using the FEM database, we first focus on WT results of calculated AE signals at three different propagation distances from a single source. Figure 7 shows the WT results (“Freq. Resolution” of 2 kHz, “Wavelet size” of 600 samples and $CF = 1$) at the three available distances for an in-plane dipole source (dipole forces are aligned with the direction of propagation to the sensors) at a depth of 1.723 mm in a large plate. This figure

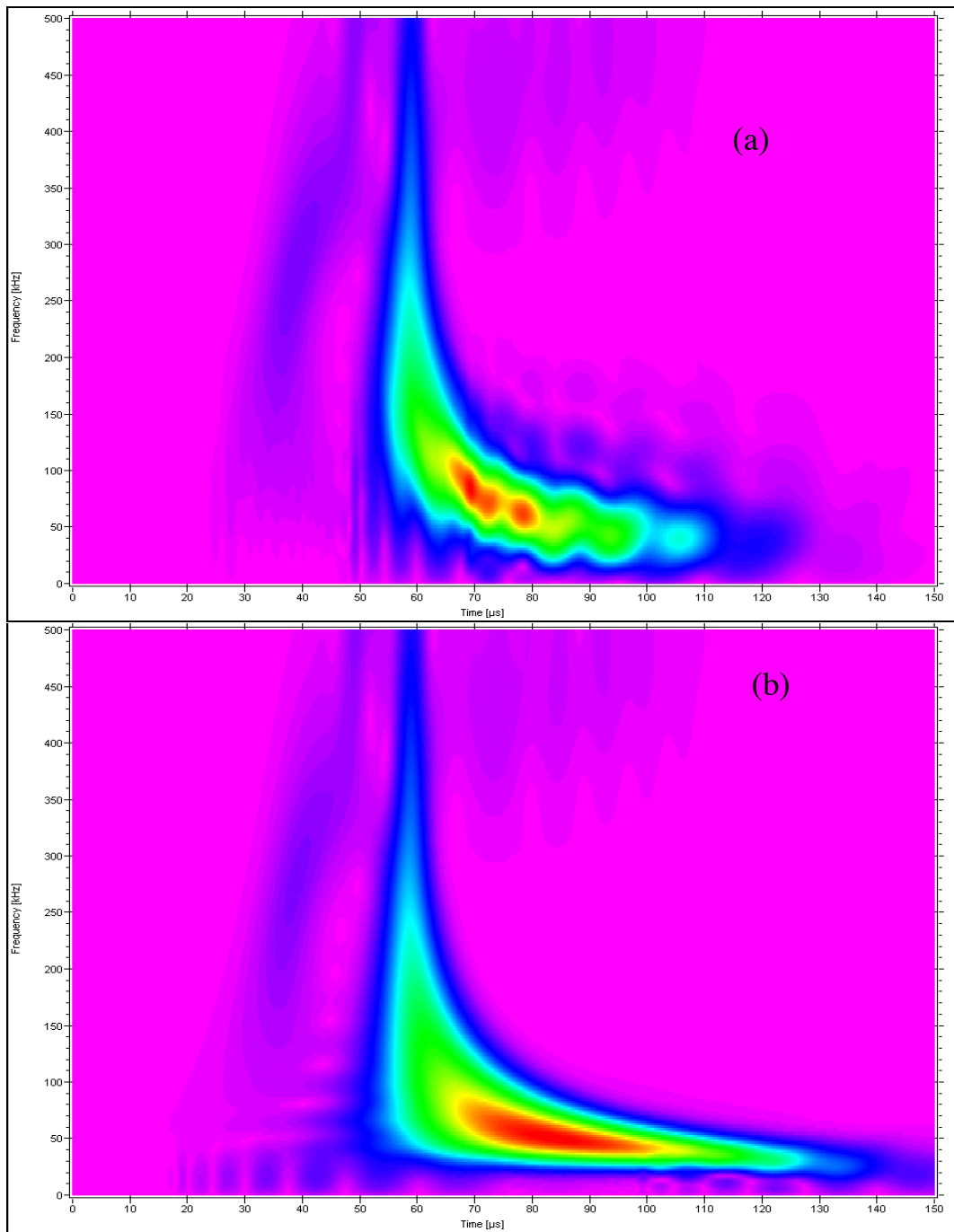


Fig. 6 WT results with small (default) “Wavelet size” of 200 samples (a) and large “Wavelet size” of 800 samples (b). Scales are the same as Fig. 5.

demonstrates that the WT results look very similar at different propagation distances when the time axis has been adjusted for the different distances. Due to this similarity with propagation distance, a limited data set could be extracted from the WT results that potentially shows that these three signals are from the same source. This potential was examined by extracting the WT peak magnitudes at two pairs of frequency and approximate group velocity. The frequencies and approximate group velocities were selected, one from each of the dominant WT magnitude regions of the fundamental modes. The circles in Fig. 7 show the two modal regions where the WT peak magnitudes and associated arrival times were extracted. The selected pairs of fre-

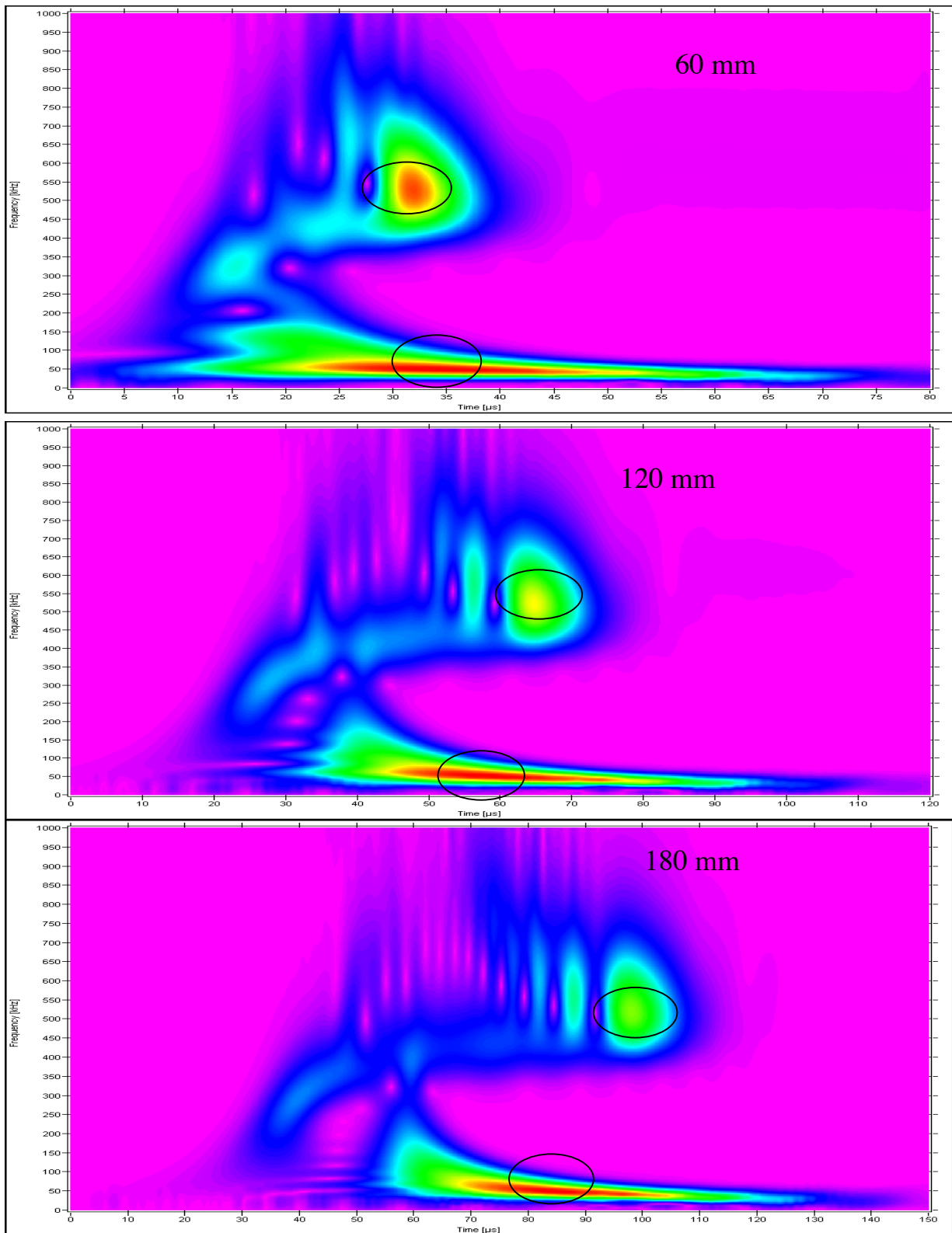


Fig. 7 WT results at three propagation distances 60 mm, 120 mm, and 180 mm for an in-plane dipole source at a depth of 1.723 mm. Circles show approximate regions from which the maximum WT magnitudes and group velocities were extracted at 50 kHz (A_0) and 522 kHz (S_0). Figures show frequency (0 to 1 MHz) versus time (0 to 80, 120, and 150 μs for the three propagation distances).

Table 1. WT magnitudes (peak value) for specified mode and frequency at indicated group velocity for in-plane dipole source at a depth of 1.723 mm.

Propagation distance, mm	Ao mode at 50 kHz		So mode at 522 kHz		Magnitude ratio, Ao/So
	Indicated group velocity, mm/ μ s	WT Magnitude	Indicated group velocity, mm/ μ s	WT Magnitude	
60	1.76	83,454	1.88	77,724	1.1
120	2.02	58,265	1.86	45,904	1.3
180	2.17	46,415	1.84	33,225	1.4

Table 2. WT magnitudes (peak value) for specified mode and frequency at indicated group velocity with sources at a depth of 1.723 mm and a propagation distance of 180 mm.

Source Type	Ao mode at 50 kHz		So mode at 522 kHz		Magnitude ratio, Ao/So
	Indicated group velocity, mm/ μ s	WT Magnitude	Indicated group velocity, mm/ μ s	WT Magnitude	
Out-of-plane	2.18	22,819	1.84	35,924	0.64
In-plane	2.17	46,415	1.84	33,225	1.4
Crack initiation	2.14	34,603	1.83	14,546	2.4

quency and group velocity were 50 kHz and about 2.16 mm/ μ s for the flexural mode (Ao) and 522 kHz and about 1.84 mm/ μ s for the extensional mode (So). The extraction of the peak WT magnitudes and their arrival times (in the approximate group-velocity region) was facilitated by an option that allows exporting the WT results into spreadsheets. Table 1 shows the extracted results. The indicated group velocity was obtained by dividing the extracted arrival time into the propagation distance from the source epicenter to the sensor location. Table 1 also shows the ratios of the Ao/So peak WT magnitudes at the selected frequencies and group velocities. The use of such a ratio provides a measure that is independent of the original source strength.

Although the Ao/So ratio experiences an increase with increasing propagation distance, this change could be corrected for by developing approximate rates of travel-distance attenuation of the WT magnitudes for the different modes and frequencies being used. Thus, it seems a limited set of data can be extracted (from WT results) that indicates the same source was observed at different propagation distances. However, it should be pointed out that the current dataset studies only the effect of propagation distance in one source-radiation direction (and the direction 180 degrees opposed; a symmetrical direction). Since a source in a plate emits different amounts of energy of the bulk modes in different radiation directions, future research should check the above conclusions (for source identification) when the propagation distance varies along with the two-dimensional radiation direction in the plane of the plate. Due to the typical symmetries of radiation patterns of sources aligned with the plate coordinate axes, this check will need to be done for only one quadrant rather than for a full 360 degrees.

To extend the study of extraction of a limited database for AE source identification from WT results, the next focus was on three different source types and their signals at a fixed propagation distance of 180 mm. Figure 8 shows (CF = 1) the WTs for an in-plane dipole (a), out-of-plane dipole (b), and a microcrack initiation (c) with all the sources centered at 1.723 mm below the top surface. These WTs were calculated with a “Frequency Resolution” (FR) of 2 kHz and a “Wavelet size” (WS) of 600 samples. Following the same procedure that was used with Fig. 7 to obtain the data in Table 1, the data shown in Table 2 were obtained from the WTs in Fig. 8. Again circles have been drawn in Fig. 8 about the regions from which the modes, approximate group velocities and frequencies were selected. Examination of Table 2 indicates that the sig-

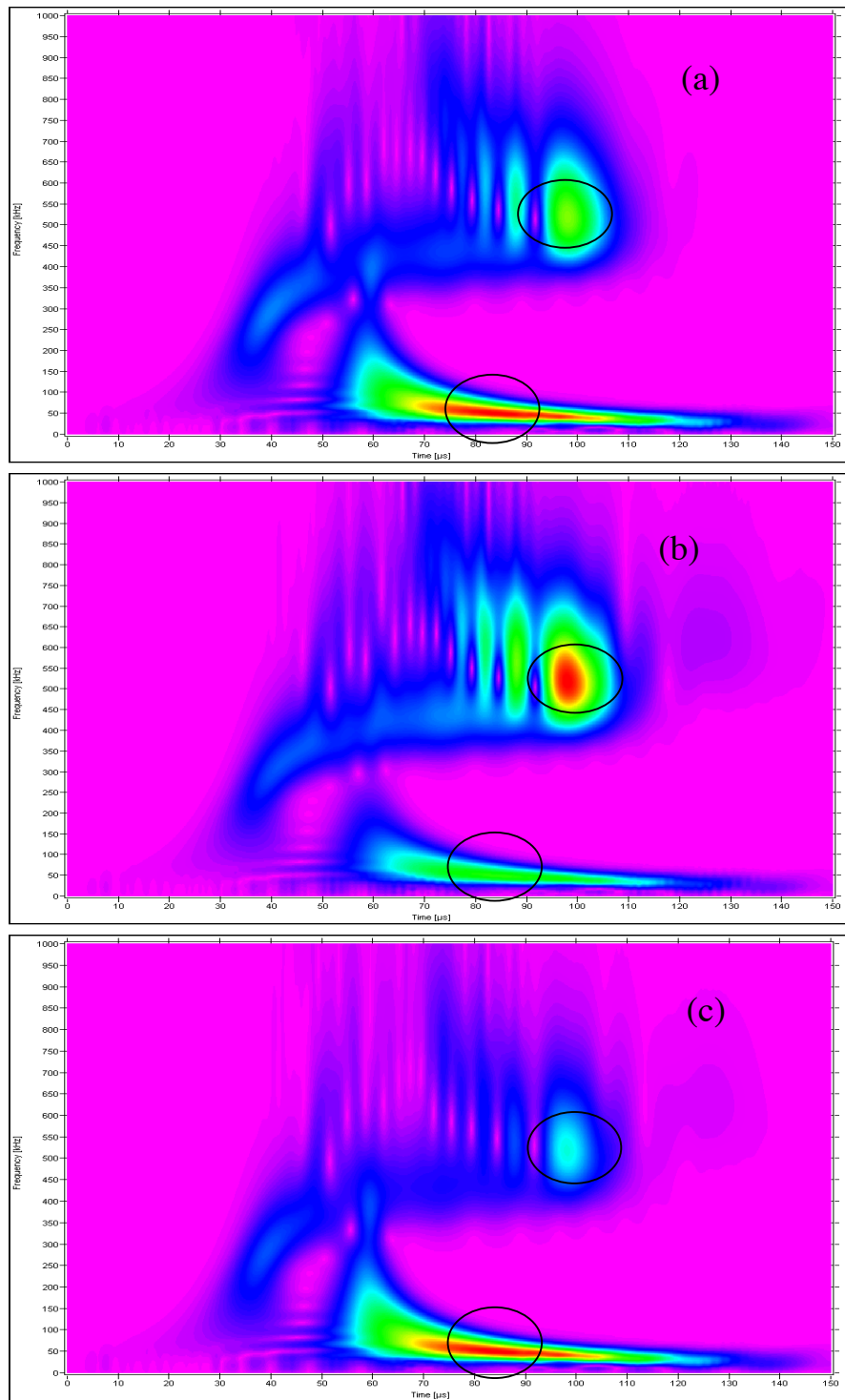


Fig. 8. WT results from out-of-plane displacement signals for three different source types: (a) in-plane dipole, (b) out-of-plane dipole and (c) crack initiation. Sources are all at a depth of 1.723 mm. Circles show approximate regions from which the maximum WT magnitudes and group velocities were extracted at 50 kHz (A_o) and 522 kHz (S_o). Figures show frequency (0 to 1 MHz) versus time (0 to 150 μ s) for the signals at 180 mm propagation distance.

nificant changes of the simple A_o/S_o ratio potentially could be used for source identification. The out-of-plane dipole source had the smallest ratio, and the crack-initiation source had the largest ratio.

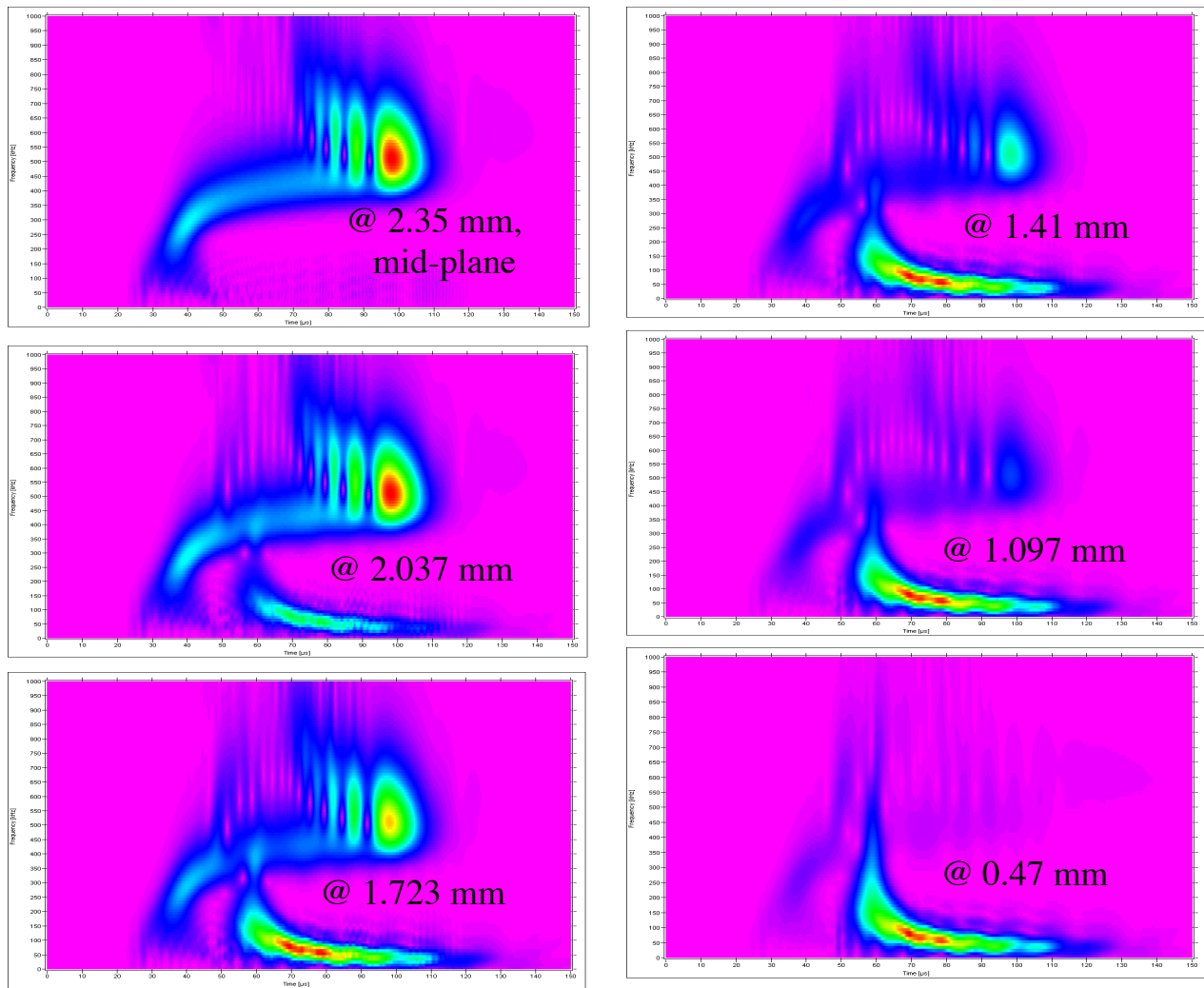


Fig. 9. WT plots as a function of the indicated source depths below the plate top surface. The source was an in-plane dipole with a 180 mm propagation distance. Figures show frequency (0 to 1 MHz) versus time (0 to 150 μ s).

Examination of WT results for a single source type as a function of source depth reveals some potential difficulties in the approach suggested above. Figure 9 demonstrates the changes in WTs (with default values and $CF = 1$ for the AE signals at 180 mm) for an in-plane dipole as a function of the depth of the source below the top surface of the plate. Even a casual examination of the results in this figure shows that the WT result varies substantially as the depth of the source changes. For the source located at the mid-plane (at 2.35 mm) the fundamental symmetric (extensional) mode dominates. As the source is moved closer to the surface, it is clear that the energy carried in the extensional mode decreases and most of the energy is carried in the fundamental anti-symmetric (flexural) mode. This dependence of the dominant Lamb modes and associated frequencies can also be seen in the signal waveforms and their FFTs. These results are shown in Fig. 10 as a function of source depth for the same series of depths. The dependence of the WT results on source depth also is apparent for the out-of-plane dipole source and the more complicated microcrack initiation source. These WT results (default parameters and $CF = 1$) for the AE signals at 180 mm are shown in Fig. 11 for two different depths (0.783 and 1.723 mm).

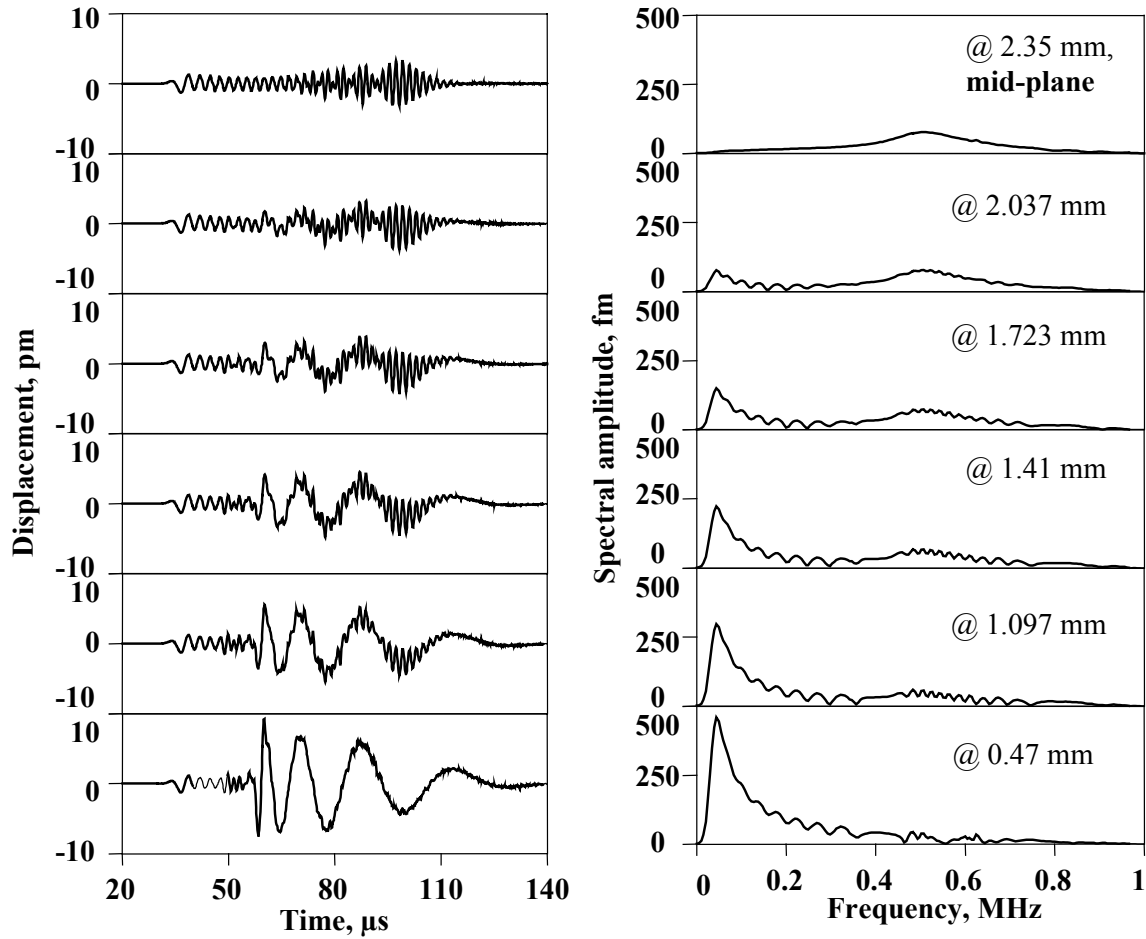


Fig. 10. Calculated AE signals with corresponding FFTs (in the same sequence top to bottom) for same cases shown in Fig. 9.

The possibility of extracting from WTs (of the out-of-plane displacement signals) a more limited data set to uniquely identify the different AE sources certainly exists. However, it is complicated by the dependence of the AE signals and their WTs on the depth of the sources. There are two primary reasons for this complication. First, the Ao/So ratio changes not just with source type but with source depth. The primary change (for the three source types considered) that takes place when the depth of a source changes is a transfer of more energy to either the extensional mode or the flexural mode from the alternate mode. Thus, it does not seem possible to extract simple Ao/So ratio information, such as in Tables 1 and 2, from the WTs that is unique to a particular source type. Second, since at a fixed depth there are clear differences between source types (see Fig. 8 and Table 2), it is likely, as a consequence of the transfer of energy between modes, that two different sources at two different source depths could have very similar WTs. This is in fact the case, as Figs. 12 and 13 show (calculated using default WT parameters) for signals at 180 mm from the sources. Figure 12 shows ($CF = 1$) that a microcrack initiation source (a) at a depth of 0.783 mm has nearly the same WT as an in-plane dipole source (b) at a depth of 0.47 mm. Figure 13 demonstrates ($CF = 1$) the close WT similarities between an out-of-plane dipole source (a) at a depth of 1.723 mm and an in-plane dipole source (b) at a depth of 2.037 mm.

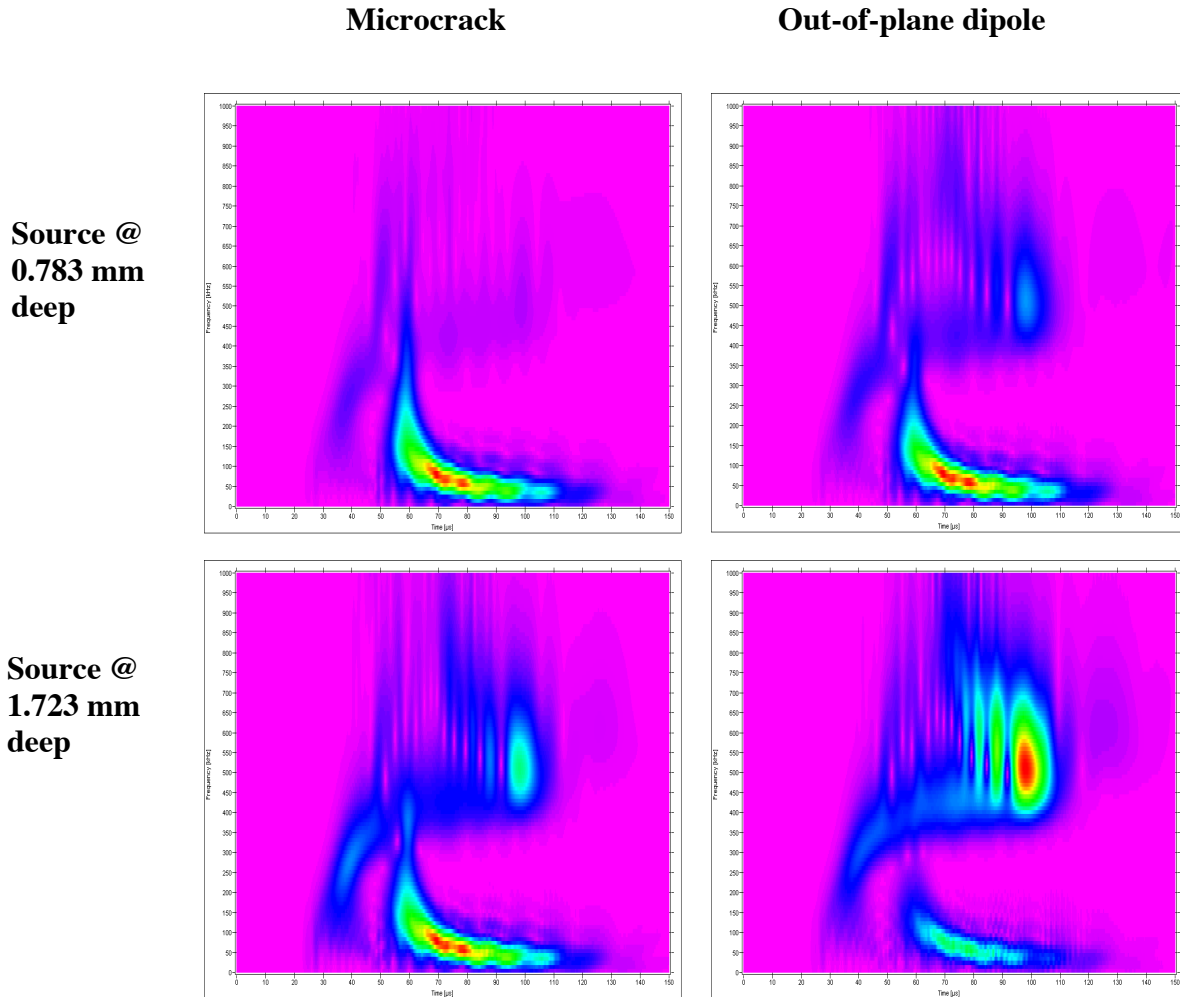


Fig. 11. WT plots showing the distinctions between a microcrack initiation source and an out-of-plane dipole compared at the same two different source depths and at 180 mm propagation distance. Plots show frequency (0 to 1 MHz) versus time (0 to 150 μ s).

One might consider whether the lower-magnitude regions of the WTs in Figs. 12 and 13 might provide suitable simple features that would distinguish these sources. This might be the case as shown in Fig. 14, which shows WTs for the same signals used for Fig. 13 calculated with $WS = 600$ samples and $FR = 2$ kHz. Also in Fig. 14, the CF was set at 0.8 to provide a wider-magnitude range for the red color region. This setting of the CF effectively shows more features of the lower-magnitude parts of the WTs. The arrows in Fig. 14 point to regions where the WT of the in-plane dipole (b) has a larger magnitude than the WT of the out-of-plane dipole (a). But, this aspect that shows up very well in the FEM modeled data may not be nearly as clear when the typical signal-to-noise ratios of real AE signals are considered. In the modeled case, data has little or no apparent noise. Thus, examining differences in regions of lower WT magnitude may not be a practical solution for real AE signals.

To examine the depth effects more systematically and quantitatively, high-resolution WTs were calculated from signals at a propagation distance of 180 mm for the different source types and depths in the available database. The WT peak magnitudes at two pairs of frequency and approximate group velocity were then extracted for each case. The frequencies and approximate

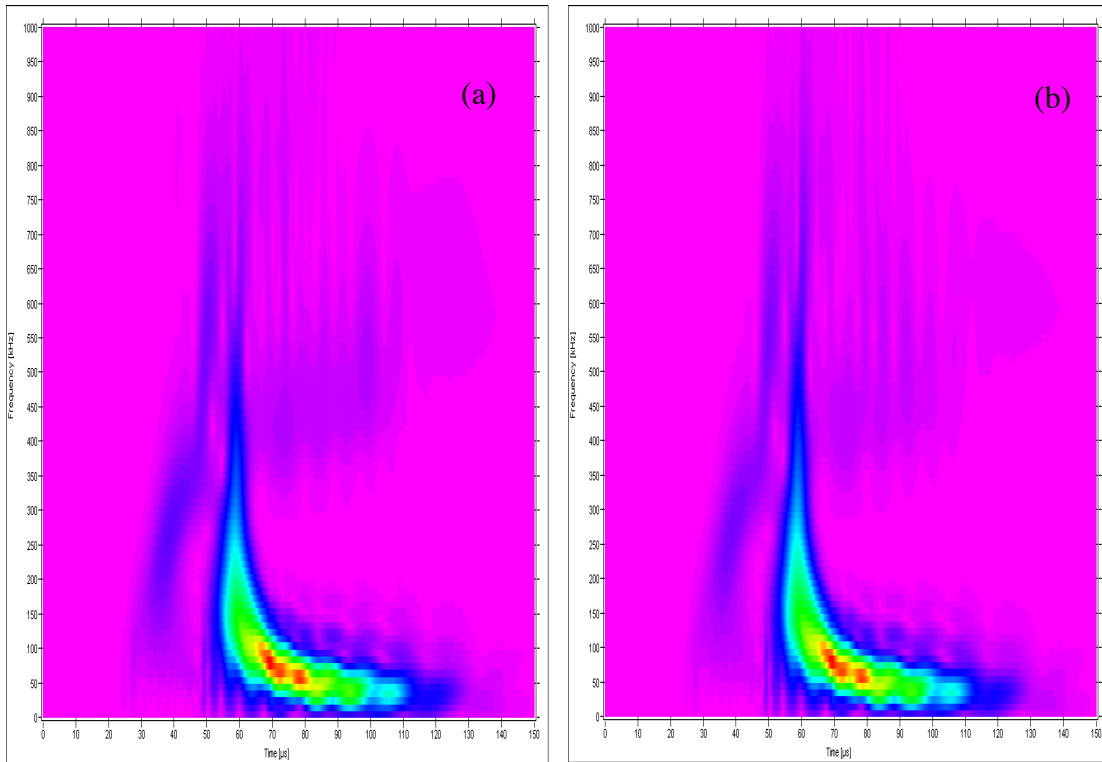


Fig. 12. WT plots showing the similarities for two different source types at different depths. At 180 mm propagation distance. Microcrack initiation (a) at 0.783 mm depth and in-plane dipole (b) at 0.470 mm depth. Plots show frequency (0 to 1 MHz) versus time (0 to 150 μ s).

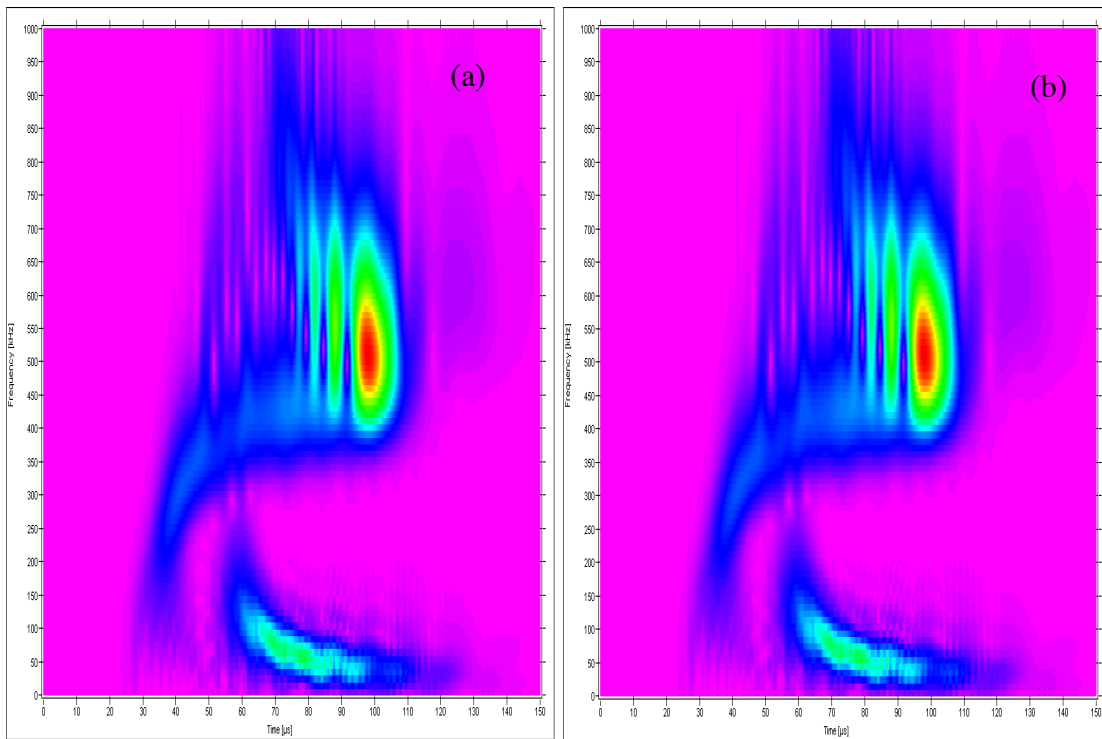


Fig. 13. WT plots show the similarities for two different source types at different depths. At 180 mm propagation distance. Out-of-plane dipole (a) at 1.723 mm depth and in-plane dipole (b) at 2.037 mm depth. Plots show frequency (0 to 1 MHz) versus time (0 to 150 μ s).

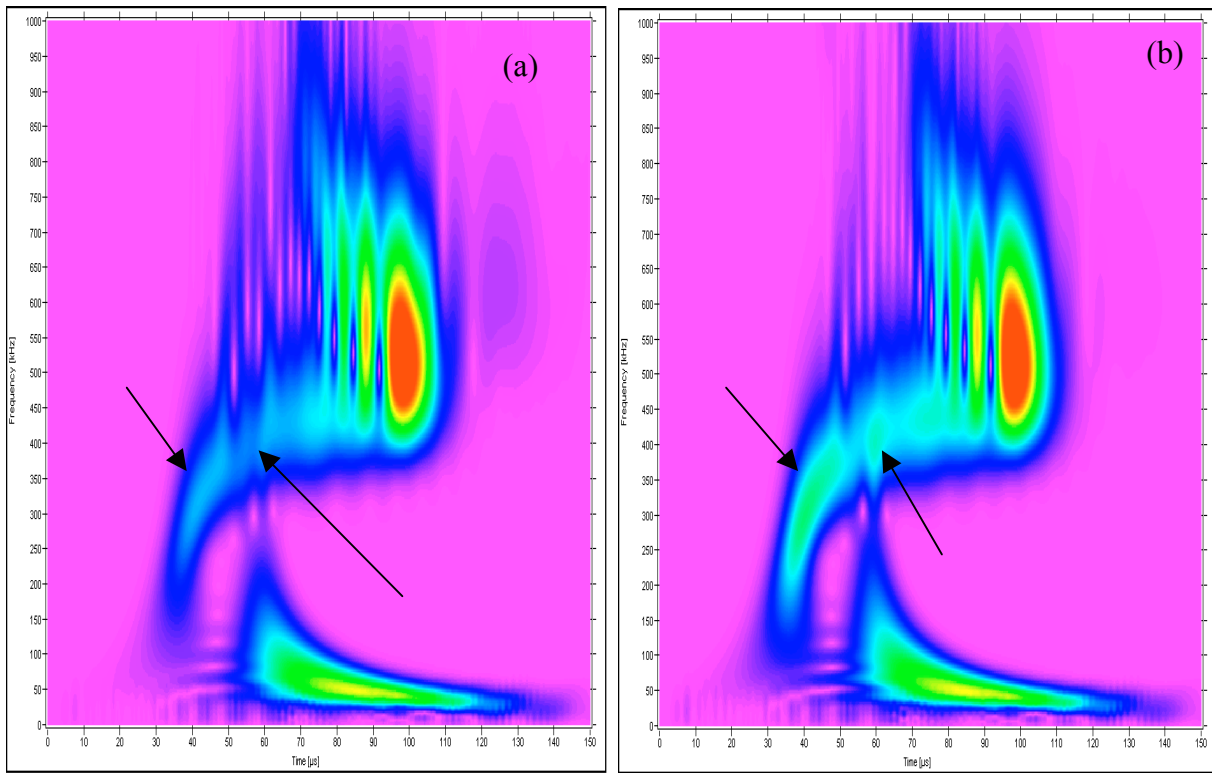


Fig. 14. Same cases and scales as Fig. 13 with color factor changed to 0.8 to examine differences in WTs in their lower magnitude regions. Arrows point to higher magnitude regions in the in-plane dipole (b) versus the out-of-plane dipole (a).

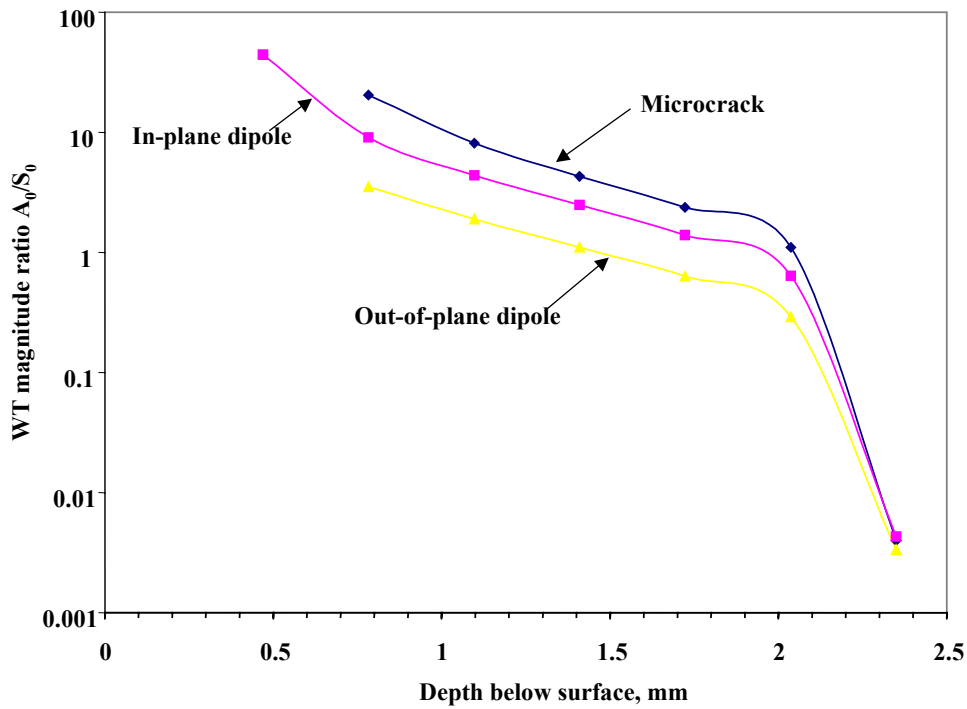


Fig. 15. A_0/S_0 ratio of peak WT magnitudes versus AE source depth for the microcrack initiation, in-plane dipole and out-of-plane dipole sources at 180 mm propagation distance. Peak magnitudes at 50 kHz and approximate group velocity of 2.16 mm/ μ s for A_0 and at 522 kHz and approximate group velocity of 1.84 mm/ μ s for S_0 .

Table 3a. WT magnitudes (peak value) for specified mode and frequency at indicated group velocity for in-plane dipole source at 180 mm. (Note * indicates a peak was not present)

Source depth, mm	Ao mode at 50 kHz		So mode at 522 kHz		Magnitude ratio, Ao/So
	Indicated group velocity, mm/ μ s	WT Magnitude	Indicated group velocity, mm/ μ s	WT Magnitude	
2.35	2.18	160*	1.84	37,124	0.0043
2.037	2.18	23,104	1.84	36,138	0.64
1.723	2.17	46,415	1.84	33,225	1.4
1.41	2.14	70,427	1.84	28,398	2.5
1.097	2.14	95,209	1.83	21,738	4.4
0.783	2.14	121,144	1.83	13,331	9.1
0.47	2.15	148,578	1.82	3,357	44

Table 3b. WT magnitudes (peak value) for specified mode and frequency at indicated group velocity for microcrack initiation at 180 mm. (Note * indicates a peak was not present)

Source depth, mm	Ao mode at 50 kHz		So mode at 522 kHz		Magnitude ratio, Ao/So
	Indicated group velocity, mm/ μ s	WT Magnitude	Indicated group velocity, mm/ μ s	WT Magnitude	
2.35	2.14	166*	1.84	16,535	0.004
2.037	2.14	17,248	1.84	16,035	1.1
1.723	2.14	34,603	1.83	14,546	2.4
1.41	2.18	52,296	1.83	12,084	4.3
1.097	2.14	70,490	1.83	8,669	8.1

Table 3c. WT magnitudes (peak value) for specified mode and frequency at indicated group velocity for out-of-plane dipole at 180 mm.

Source depth, mm	Ao mode at 50 kHz		So mode at 522 kHz		Magnitude ratio, Ao/So
	Indicated group velocity, mm/ μ s	WT Magnitude	Indicated group velocity, mm/ μ s	WT Magnitude	
2.35	2.16	132.7	1.84	39,605	0.0034
2.037	2.14	11,343	1.84	38,676	0.29
1.723	2.18	22,819	1.84	35,924	0.64
1.41	2.14	34,843	1.84	31,402	1.1
1.097	2.14	47,510	1.84	25,177	1.9
0.783	2.14	61,099	1.84	17,365	3.5

group velocities selected were those from the dominant WT magnitude regions of both fundamental modes. The selected values for the flexural mode (Ao) were 50 kHz and about 2.16 mm/ μ s. For the extensional mode (So), the values were 522 kHz and about 1.84 mm/ μ s. Then, as before, at each frequency the maximum WT magnitude and its arrival time were determined near the selected approximate group velocities. For certain cases the magnitudes of the WT are relatively small at the selected frequency and approximate group velocity, and in some cases the WT did not have a clear maximum in the approximate group-velocity region. In these latter cases, the WT magnitude at the selected frequency was selected at the same arrival time that the peak magnitude occurred when the same source type was at the nearest depth where the WT as a function of time had a true maximum in that region. The values determined are shown in Tables 3a, b and c for the three different source types. Also, these tables include the calculated magnitude ratio Ao/So for the range of source depths and source types. Figure 15 shows a plot of Ao/So versus source depth with the source type as a parameter. It is reasonable to conclude that there is a definite ordering of the Ao/So ratio as function of source depth. The microcrack initia-

tion source results in the highest values and the out-of-plane dipole has the lowest values, with the in-plane dipole source in between. The relative differences between the ratios at a fixed depth are not small, since the ratio scale in the figure is logarithmic. At the mid-plane depth (2.35 mm), the ratio values are likely not reliable due to the very small WT magnitudes for the Ao mode. Also, these Ao values were in most cases arbitrarily selected as described above since the Ao mode did not have a peak value for the approximate group velocity region of the mode.

It is clear in the case of experimental data when the source depth is unknown that the Ao/So ratio alone will not uniquely define a source type. But, if one considers the data in Fig. 15 to be that for a radiation direction of zero degrees, then it may be possible that results of Ao/So ratios from other radiation directions could provide sufficient additional information to uniquely identify the source type. This expectation, not unlike the approach of Buttle and Scruby (1990a), uses the fact that the radiation pattern is different for different source types. Since in experimental situations typically three or four sensors are hit when two-dimensional source location is determined (a prerequisite for the above approach, since the selected approximate group velocity needs to be converted to an approximate arrival time), signals are typically available in several two-dimensional radiation directions. For these different radiation directions, the Ao/So ratio could be extracted from WTs of the signals. These ratios could then be compared as a function of the radiation angle with modeled results of the Ao/So ratio versus radiation angle determined for different source types and depths. This method could possibly add sufficient information to uniquely identify the source type and source depth. Based upon these observations in future research we expect to examine the above approach with a FEM database that includes other radiation directions.

The application to experimental AE data of the Ao/So ratio approach will likely experience difficulties when the source is located very near the plate surfaces or very near the plate's mid-plane. As the first and last rows of Tables 3a, b and c show, in these cases either the Ao or So WT-based magnitude is small, and they do not always have a local maximum (at a given frequency and associated approximate group velocity). Thus, for experimental data from sources near the mid-plane, effects of low signal-to-noise ratios will likely eliminate the possibility of calculating meaningful Ao/So ratios. A possible solution to this problem might be to focus on the single dominant mode for these source-depth cases. For example, for a source located near or at the mid-plane of the plate two or more frequencies and associated approximate group velocities could be selected from the So mode. At these frequencies and velocities the maximum magnitudes of the WT could be determined within the So mode. Then ratios such as So (at 522 kHz) to So (at say 325 kHz) could be calculated. It is possible that this ratio or other appropriate ones might result in distinguishing different source types located near the plate mid-plane. And for a source located near the plate surfaces, a ratio from two frequencies of the Ao mode could be used. Hence, in future research we expect to examine such an approach using the current FEM database extended to include other source types, such as a shear source, and various radiation angles.

6. WT Data Subsets for Source Identification in Specimens with Nearby Edges

When the lateral size of the test specimen is decreased so that nearby edges are present, the AE signals and their WTs become much more complicated. This result is clearly seen in Fig. 16, which compares WTs of the AE signals (40 kHz high-pass) at 180 mm from in-plane and out-of-plane dipole sources in the small coupon specimen (Fig. 16(a)) and the large specimen (Fig. 16(b)) both at a depth of 1.723 mm. Figure 17(a) also shows as a function of propagation dis-

In-plane dipole

Out-of-plane dipole

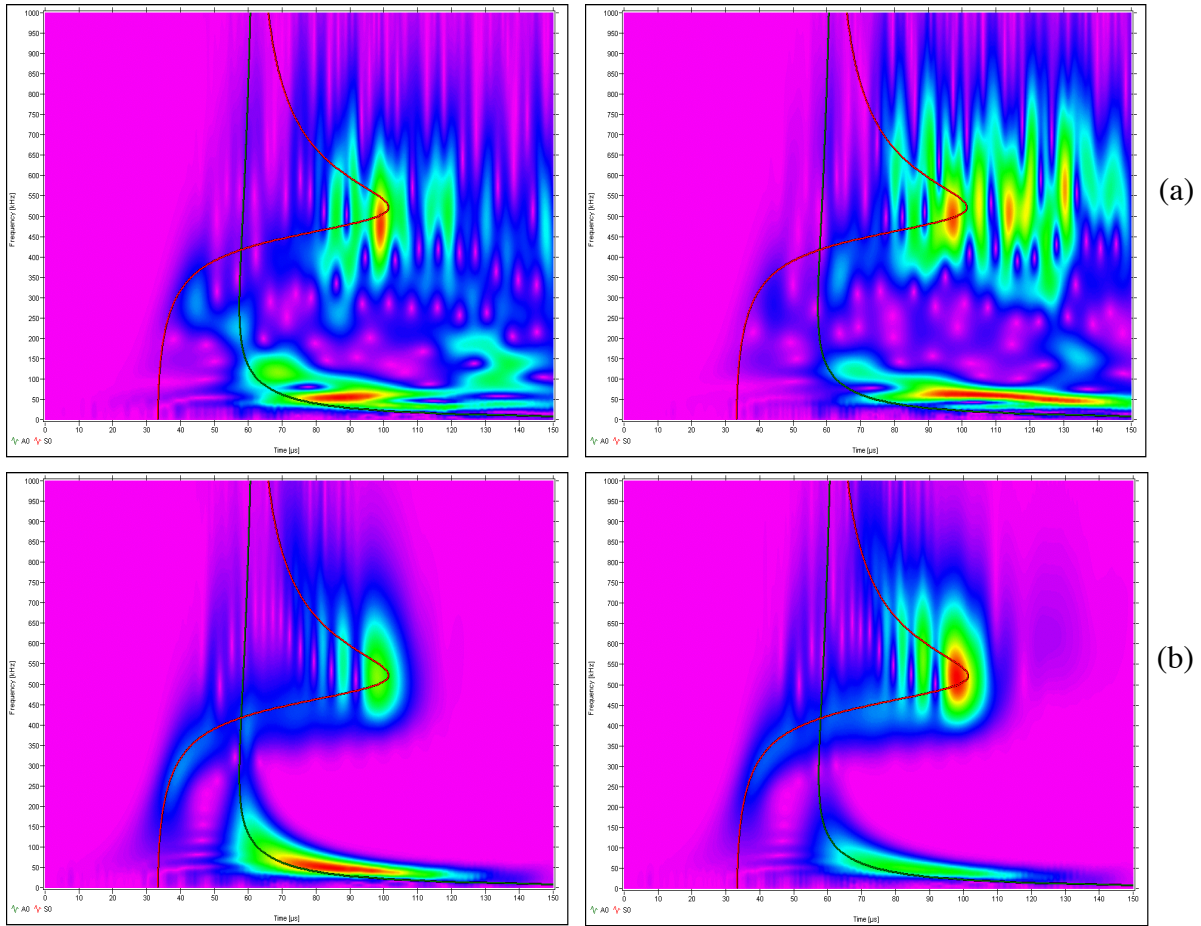


Fig. 16. WT results (40 kHz high-pass AE signals) for coupon specimen (a) with multiple edge reflections compared to large specimen (b) without edge reflections. Results shown for an in-plane dipole source and an out-of-plane dipole source with a propagation distance of 180 mm. Sources centered at 1.723 mm below the top surface of the plate. Frequency (0 to 1 MHz) versus time (0 to 150 μ s). Superimposed fundamental modes shown.

tance the significant distortion in the WT results (of AE signals from an in-plane dipole) for the coupon specimen compared to the large specimen (Fig. 17(b)) with sources at a depth of 1.723 mm. The distribution of signal energy in the coupon as shown in Figs. 16(a) and 17(a) does not clearly follow the shapes of the superimposed fundamental Lamb-mode curves from the dispersion relations. Thus the extension of the possible extraction approaches proposed for source identification in the large plate is not straightforward for the coupon specimen. Further, since the distortion of the WT results is due to edge reflections (sides and at later times the specimen ends), moving the source from side-to-side across the 25.4 mm dimension of the coupon specimen will change the reflections in the AE signals. These source-position changes will also change the associated WTs as shown in Fig. 18 with superimposed fundamental modes. This figure compares the WTs for in-plane dipole sources as a function of the transverse position of the AE source. In Fig. 18(a), the source was located half-way across the specimen at 12.7 mm from the coupon side edge. In Figs. 18(b) and 18(c), the source was successively at 6.13 mm and 3.31 mm from the coupon side edge. The WTs (CF = 1, WS = 600) in these figures were calculated from the AE signals at 180 mm from the sources. The source depth was 2.35 mm. The

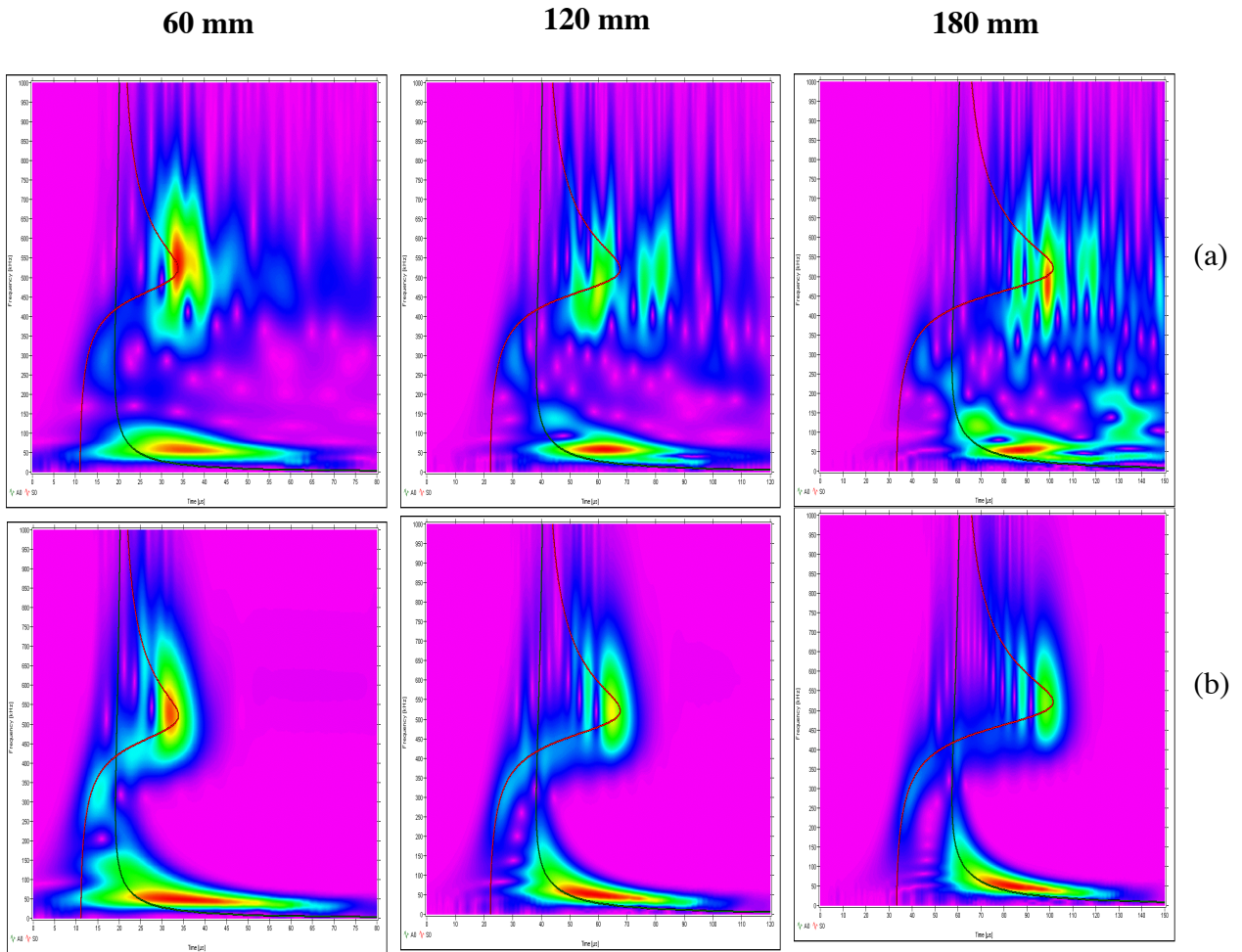


Fig. 17. WT results (40 kHz high-pass AE signals) for coupon specimen (a) with multiple edge reflections contrasted to large specimen (b) without edge reflections at three propagation distances: 60 mm, 120 mm, and 180 mm. Source in-plane dipole centered at a depth of 1.723 mm below the top surface of the plate. Frequency (0 to 1 MHz) versus time (0 to 80, 120, and 150 μ s with increasing propagation distance). Superimposed fundamental modes shown

current coupon database, except for the case illustrated in Fig. 18, does not include the side-to-side variation of the source position.

We believe the possible use of a WT for source identification in small specimens needs study because researchers use such specimens. Thus the necessary FEM database should be developed. But, it is prudent in the case of source identification that such studies be done after the potential difficulty of the dependence of the AE signals on the depth of the source is resolved. If the resolution of source depth difficulties requires the use of AE signals in several directions of radiation, then source identification in the small coupon specimen will likely require an alternate approach. This conclusion follows from the fact that in the coupon specimen far-field signals will not be available for different radiation directions. Researchers might be forced to use the bulk wave approach mentioned earlier (Buttle and Scruby, 1990a) if information from different propagation directions is required. This approach has been used in a 8-mm-thick coupon by placing the sensors in very close proximity to known crack tips (Buttle and Scruby, 1990b). Reducing the coupon thickness will eventually result in a sample that is too thin to allow one to

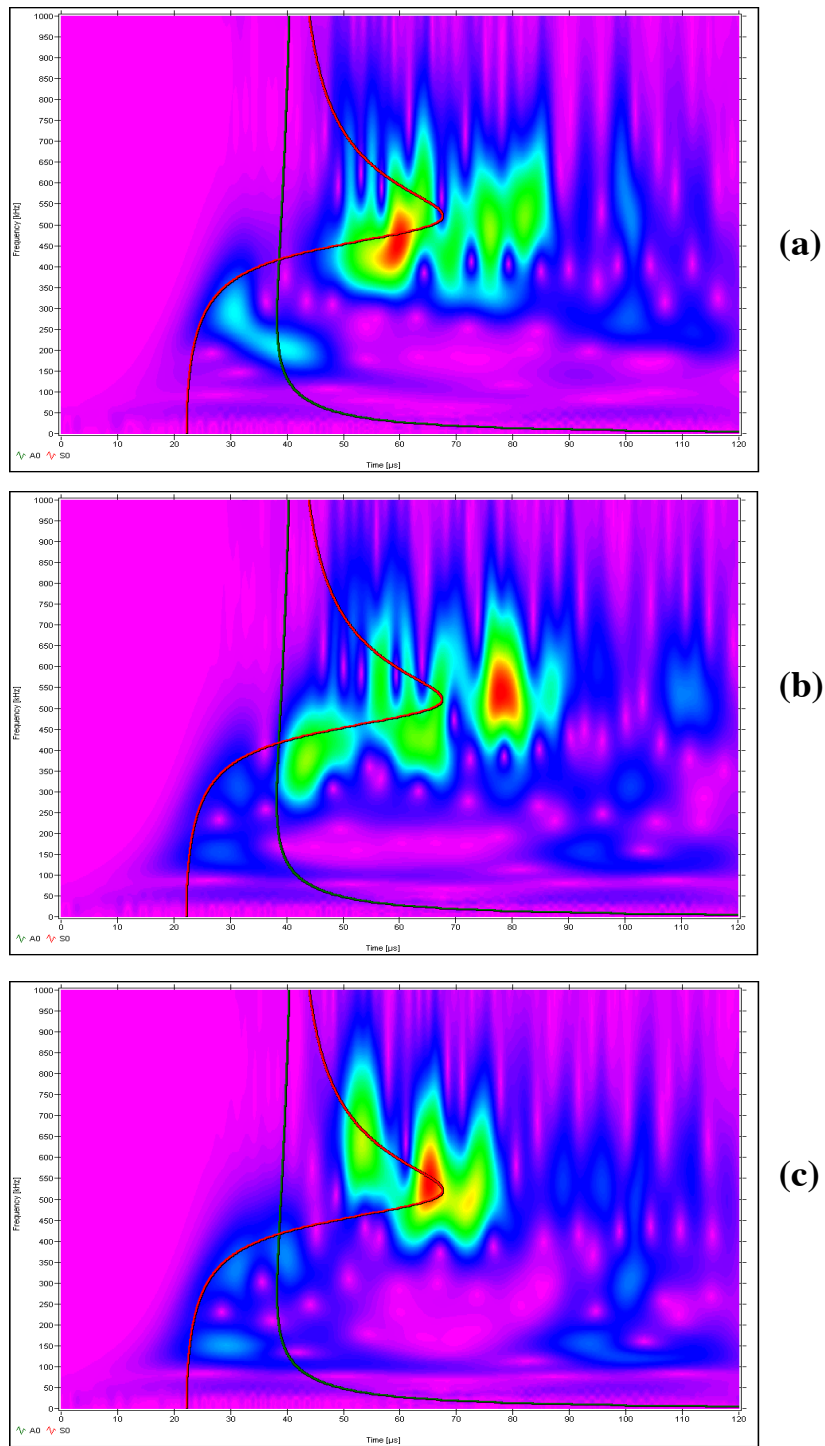


Fig. 18. Comparison of WT results (40 kHz high-pass AE signals) as a function of transverse position of the in-plane dipole source in the coupon specimen. The WTs with superimposed fundamental modes were calculated from the displacement signals at 120 mm for the mid-plane depth source. The sources were located half-way across the specimen (a) at 12.7 mm from the edge, (b) at 6.13 mm from the edge, and (c) at 3.31 mm from the edge. Plots show frequency (0 to 1 MHz) versus time (0 to 120 μ s).

distinguish the bulk-wave arrivals from sample surface reflections. Also, to practice the bulk-wave approach, the AE sources of interest must be located in a small known region.

7. Conclusions

A. Source Identification–Large Plates

- For the 4.7 mm aluminum plate thickness of the current FEM database, a potentially useful parameter for source identification has been found. Using a separate selected frequency and approximate group velocity for each fundamental mode, the WT coefficients (usually local maxima for the frequency and group velocity) can be combined to form an Ao/So magnitude ratio. This ratio was found to distinguish different source types when the sources were all centered at the same depth below the plate surface and with the same propagation distance.
- But, since the values of this ratio overlap for different source types at different depths, it is not possible to uniquely identify the source type with this small set of WT-based data.
- The current database indicates that the value ranking of the Ao/So magnitude ratio for different source types remains in the same order as a function of source depth. Since this result is for a single radiation direction, it is to be expected that obtaining this ratio for other radiation directions will supplement the WT-based data with possibly sufficient information to uniquely classify the AE source type even with changing source depth. This expectation is based upon the fact that different source types have different AE-energy radiation patterns. Thus a series of WT-based magnitude ratios from a total number, n , of different radiation angles (e.g., $(Ao/So)_1, (Ao/So)_2, \dots, (Ao/So)_n$) could form an input vector to an artificial intelligence (AI) software program that would determine the AE source type. The AI program could be initially trained using a FEM-generated database.

B. Source Identification–Small Coupon Specimens

- The inherent multiple edge reflections present in small coupon specimens complicate the use of WT coefficients for source identification. Since the current small coupon FEM database does not include (except for one case) the important parameter (relative to edge reflection effects) of changes in specimen side-to-side position of the source, the current database did not allow a full examination of these complications.

Acknowledgement

This work was partially supported by NASA Langley. We wish to express our gratitude to Prof. Takemoto, who released the source code of the wavelet transform software his group had developed and made AGU-Vallen Wavelet available. We also thank Dr. Y. Mizutani and Mr. Jochen Vallen for making the program into a highly usable form. Their contributions have significantly advanced the field of AE.

References

D. J. Buttle and C. B. Scruby, “Characterization of Fatigue of Aluminum Alloys by Acoustic Emission, Part 1-Identification of Source Mechanism”, *Journal of Acoustic Emission*, **9**, No. 4, 1990a, 243-254.

D. J. Buttle and C. B. Scruby, “Characterization of Fatigue of Aluminum Alloys by Acoustic Emission, Part II – Discrimination Between Primary and Secondary Emissions”, *Journal of Acoustic Emission*, **9**, No. 4, 1990b, 255-269.

Dawei Guo, Ajit K. Mal and Marvin A. Hamstad, "AE Wavefield Calculations in a Plate", in *Progress in Acoustic Emission IX*, Acoustic Emission Working Group and Acoustic Emission Group, 1998, pp. IV-19 to IV-29.

M. A. Hamstad, A. O'Gallagher and J. Gary, "Modeling of Buried Acoustic Emission Monopole and Dipole Sources With a Finite Element Technique", *Journal of Acoustic Emission*, **17**, No. 3-4, 1999, 97-110.

R. L. Mehan and J.V. Mullin, "Analysis of Composite Failure Mechanisms Using Acoustic Emissions", *Journal of Composite Materials*, **5**, April 1971, 266-269.

W. H. Prosser, M. A. Hamstad, J. Gary and A. O'Gallagher, "Reflections of AE Waves in Finite Plates: Finite Element Modeling and Experimental Measurements", *Journal of Acoustic Emission*, **17**, No. 1-2, 1999, 37-47.

H. Suzuki, T. Kinjo, Y. Hayashi, M. Takemoto and K. Ono, "Wavelet Transform of Acoustic Emission Signals", *Journal of Acoustic Emission*, **14**, No. 2, 1996, 69-84.

M. Takemoto, H. Nishino and K. Ono, "Wavelet Transform - Applications to AE Signal Analysis", *Acoustic Emission - Beyond the Millennium*, Elsevier (2000), pp. 35-56.

Vallen-Systeme GmbH, München, Germany, <http://www.vallen.de/wavelet/index.html>, 2001.

R. Weaver and Y. H. Pao, "Axisymmetrical Waves Excited by a Point Source in a Plate", *Journal of Applied Mechanics*, **49**, 1982a, 821-836.

R. Weaver and Y. H. Pao, "Spectra of Transient Waves in Elastic Plates", *Journal of the Acoustical Society of America*, **72**, 1982b, 1933-1941.

H. Yamada, Y. Mizutani, H. Nishino, M. Takemoto and K. Ono, "Lamb Wave Source Location of Impact on Anisotropic Plates", *Journal of Acoustic Emission*, **18**, (2000, December), 51-60.

A WAVELET TRANSFORM APPLIED TO ACOUSTIC EMISSION SIGNALS: PART 2: SOURCE LOCATION[#]

M. A. HAMSTAD⁺, A. O'GALLAGHER and J. GARY

National Institute of Standards and Technology, Materials Reliability Division (853),
Boulder, CO 80305-3328;

⁺Also Department of Engineering, University of Denver, Denver, CO 80208.

Abstract

In Part 2, the same finite-element-generated database of acoustic emission (AE) signals was used, as in Part 1: Source Identification, to examine the application of a wavelet transform (WT) to improve the accuracy of AE source location. These signals represented the top surface out-of-plane displacement versus time from buried dipole sources in aluminum plates 4.7 mm thick. The method utilizes a WT result to select AE signal-arrival times for a single group velocity from energetic modes. The cases of both the large plate without edge reflections and the small plate (coupon) with multiple edge reflections were examined. The arrival time of a specific frequency of an energetic fundamental mode of the far-field signals was determined from the WT. Using these arrival times at three propagation distances, a group velocity was determined for comparison with the appropriate group velocity based on dispersion curves. Both filtered narrow-band (100 to 300 kHz) and wideband (40 kHz high-pass) signals were examined. In addition, in the large-plate case, experimental sensor/preamplifier electronic noise was added to the AE signals to examine the effect of noise on the determination of accurate arrival times as a function of signal-to-noise (S/N) ratios. Results for the large plate indicate that very accurate arrival times can be determined that correspond to a particular group velocity. In the coupon case, the results indicate significant distortions in the arrival times due to the multiple edge reflections. The perturbation due to the presence of electronic noise was relatively small for the case of the wideband signals in the large plate until signal-to-noise ratios reached levels where an AE hit would likely not be recorded.

1. Introduction

One of the important aspects of acoustic emission (AE) technology is the ability to use the arrival times of the signals (from a single event) at three or more sensors to calculate the location of the source in the test object. Often the two-dimensional location in a plate is determined. The standard technique combines the measured arrival times with an appropriate single propagation velocity to calculate the source location. In most AE applications, the arrival times of the signals are obtained from the time that the signals first penetrate a fixed voltage threshold. As has been documented (Hamstad, 1986; Gorman, 1990; Hamstad and Downs, 1995), this approach leads to location errors. In particular, the arrival times at the different sensors often are determined from different unknown velocities. This situation is a direct result of both the AE source characteristics (for example the source strength) and effects of the propagation of dispersive Lamb waves along with geometry-based attenuation. The net result is that source location may be calculated on the basis of inconsistent data. Specifically, the arrival times are not all obtained at the same

[#] Contribution of the U.S. National Institute of Standards and Technology; not subject to copyright in the US.

velocity, and the velocity used in the location calculation is not the correct one for each sensor hit.

Some previous research has demonstrated an approach to decrease the location errors (Ziola and Gorman, 1992). In this approach, cross-correlation techniques were used to determine the arrival times for a particular mode (typically the flexural mode) and frequency. The AE signals analyzed were obtained from sensors responding to out-of-plane surface displacements. These arrival times were combined with a corresponding theoretical group velocity to calculate a more accurate source location. The resulting improvement in location accuracy was demonstrated by out-of-plane pencil-lead breaks on the surface of a plate test specimen. This validation approach is potentially incomplete. First, out-of-plane lead breaks create relatively large flexural mode (anti-symmetric) components of the AE signals as compared to real AE sources, which can be dominated by in-plane dipoles with smaller flexural-mode signals. Second, the surface lead breaks do not account for the substantial differences in the dominate mode in AE signals as a function of the depth of a real AE source through the plate thickness, as was shown in Part 1 (Hamstad et al., 2002).

In the research reported here, we examine the use of a wavelet transform (WT) to accurately obtain arrival times at known group velocities from realistic modeled AE signals. We utilized AGU-Vallen Wavelet program for obtaining WTs as in Part 1 (Hamstad et al., 2002). The AGU group first used WT for determining the group velocity dispersion of the Lamb waves (Cho et al., 1996; Hayashi et al., 1999) and for AE source location on anisotropic CFRP plates (Yamada et al., 2000; Takemoto et al., 2000). Yamada et al. (2000) determined the group velocity of flexural Lamb waves (generated by pencil-lead breaks or ball drops) from the maxima of WT coefficients of a certain frequency. A few other research works used a WT for AE source location (Yamada et al., 2000; Takemoto et al., 2000; Kwon and Joo, 2000; Jeong and Jang, 2000). The validation approach used in these experimental studies is incomplete due to the reliance on monopole sources from out-of-plane pencil-lead breaks or ball drops on the plate surface. In this work, we obtained the AE signals in plate samples by finite-element modeling (FEM), and the sources of these signals include realistic dipoles as well as the important variable of source depth. The modeled signals also have the advantage that the exact three-dimensional source location is known. Thus, WT-based signal-arrival times at different propagation distances can be quantitatively evaluated for their correspondence to a single group velocity.

2. Signal Database and Wavelet Transform

An AE signal database of plate top surface out-of-plane displacement as a function of time at three propagation distances was used. The AE signal database, specimen geometry and the relevant WT information were described in detail in Part 1 (Hamstad et al., 2002) of this two-part paper. Hence, we have not repeated that description here.

3. WT-Based Source Location (Large Plates)

The extraction of arrival times from the WTs of AE signals was successively examined by several approaches. The first approach was based on the results of a WT of the simulated wide-band AE signals that had been filtered with a 40 kHz high-pass filter. In this case, the information extracted from the WT result consisted of data pairs of arrival time and frequency based upon absolute peaks of the WT's magnitude (WT coefficient). When sets of such data pairs were compared for three different propagation distances from a given AE source, it was deter-

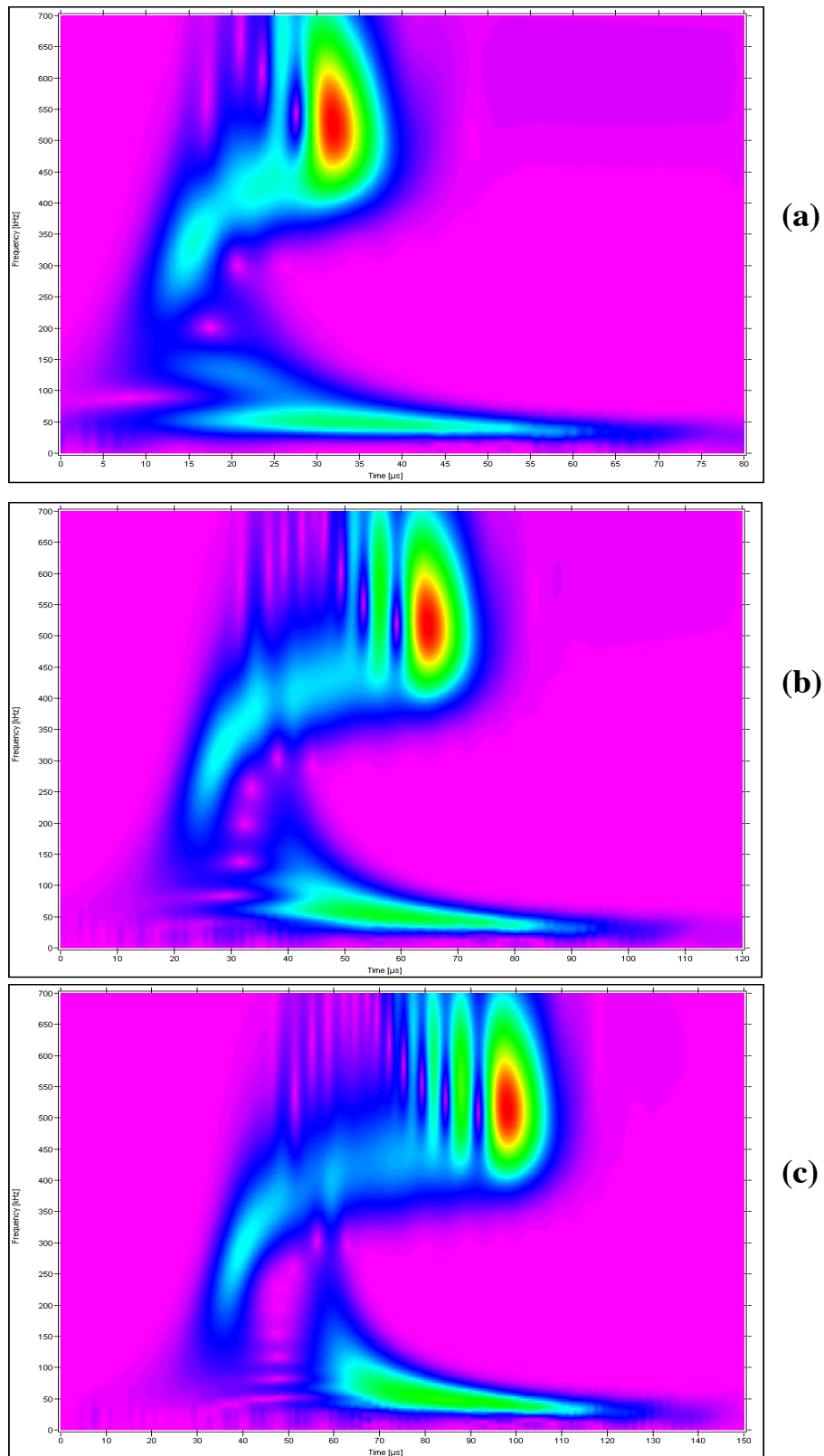


Fig. 1 WT plots used to determine AE signal arrival times from the peak WT magnitudes of the So mode at 522 kHz. The AE source was an in-plane dipole at a depth of 2.037 mm with propagation distances of (a) 60 mm, (b) 120 mm, and (c) 180 mm. AE signals filtered with 40 kHz high pass filter prior to WT. Frequency (0 to 1 MHz) versus time (a: 0 to 80 μ s, b: 0 to 120 μ s, and c: 0 to 150 μ s from top to bottom).

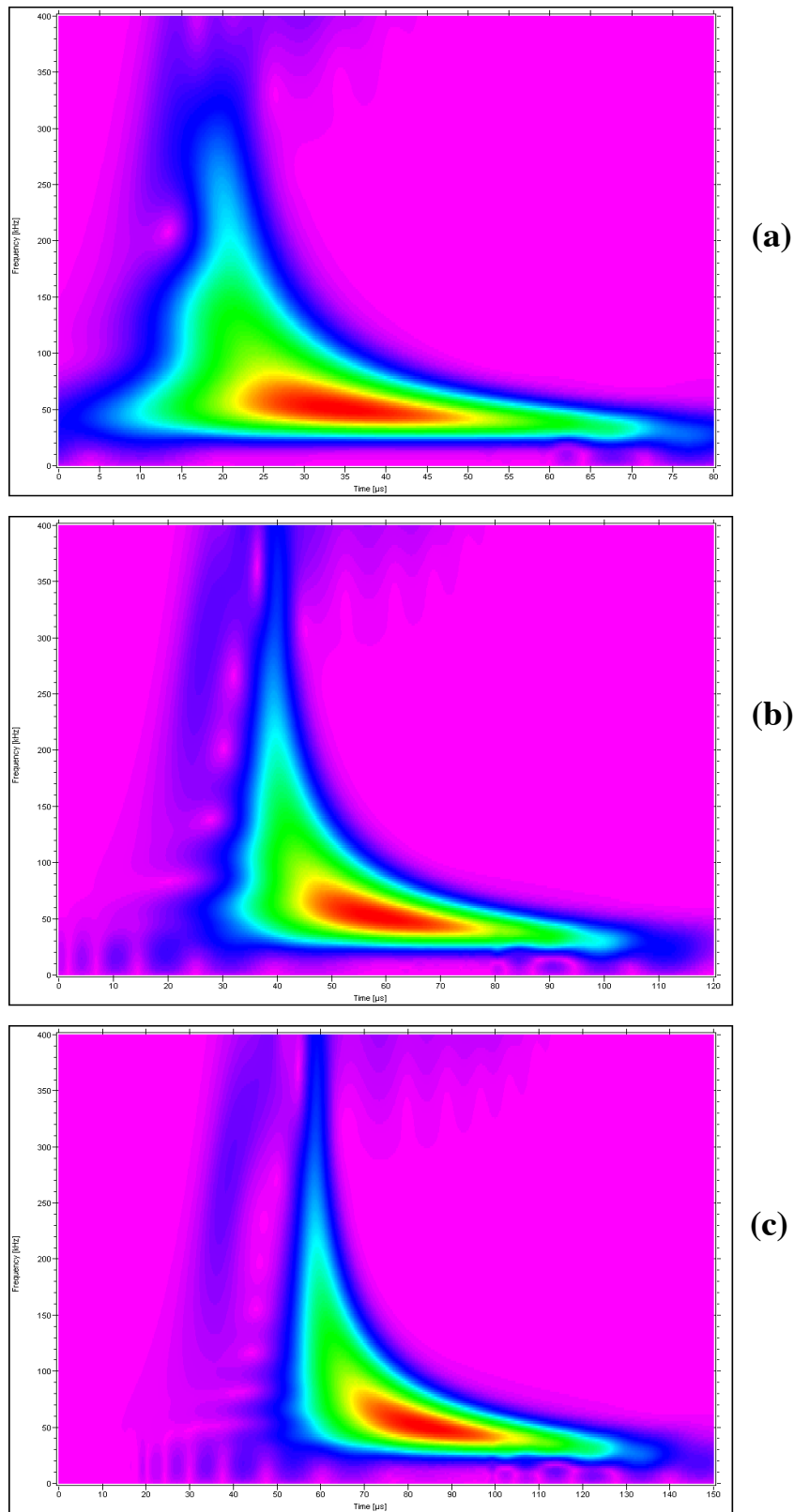


Fig. 2 WT plots used to determine AE signal arrival times from the peak WT magnitudes the Ao mode at 66 kHz. The AE source was an in-plane dipole at a depth of 0.783 mm. The propagation distances and filter were the same as for Fig. 1(a), (b), and (c). Frequency (0 to 400 kHz) versus time (same scales as Fig. 1; 1 MHz vs. a: 80 μ s, b: 120 μ s, and c: 150 μ s top to bottom).

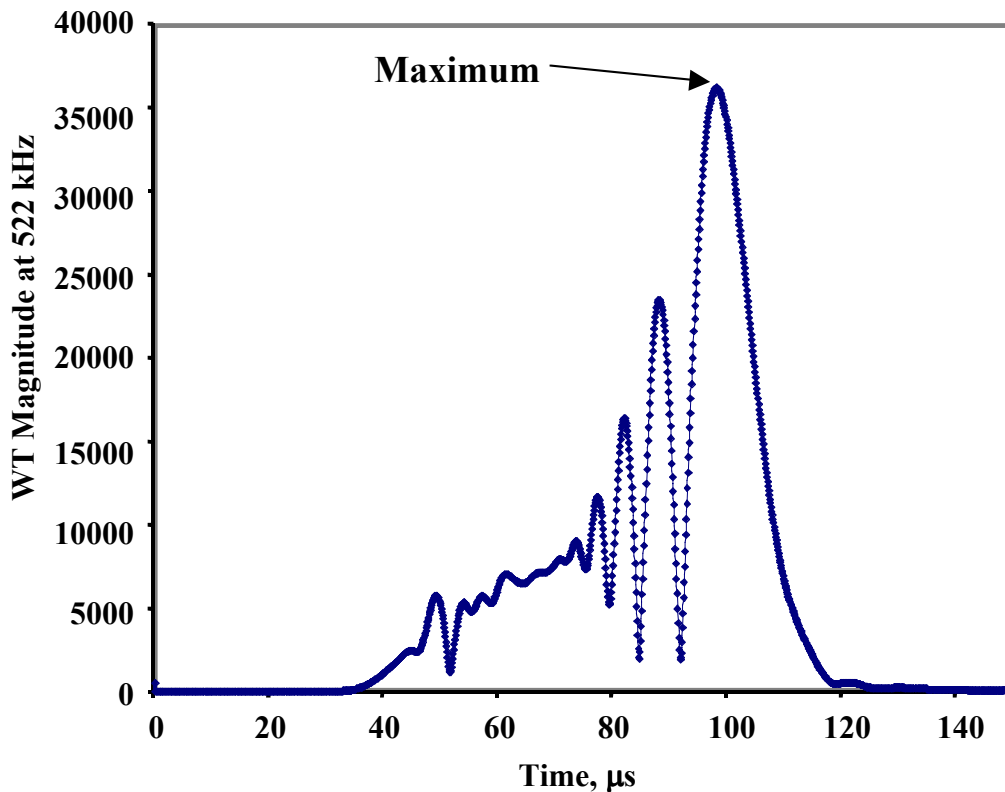


Fig. 3 Example of the WT magnitude versus time for the S_o mode at 522 kHz from the WT result shown in Fig. 1(c). Plot illustrates the determination of the arrival time of the peak magnitude near the selected group velocity of the mode.

mined that there were differences in the frequency values of the maximum magnitude as a function of propagation distance. Since determining arrival times at different frequencies and thus different group velocities at each sensor would complicate the process of source location, it seemed best to examine alternative approaches so that the simplest use of WT data to extract arrival times could be developed.

The second approach that was examined was based upon choosing a single frequency for a particular fundamental Lamb symmetric (S_o) or anti-symmetric (A_o) mode. Based upon the modal region of the WT that had a large magnitude, a single frequency was chosen in the same fashion as the source-identification approach in Part 1 (Hamstad et al., 2002). Then, using this frequency, the arrival time of the maximum magnitude of the WT at that frequency (and associated mode) was determined, as was done by Yamada et al. (2000). It was found that choosing the parameters of the WT to enhance the resolution and smoothness (as discussed in Part 1: Hamstad et al., 2002) of the WT result was important to facilitate the determination of the maximum at the selected frequency and mode. To initially examine this approach in more depth, two different in-plane dipole source cases were chosen. In one case the source depth was chosen such that the maximum magnitudes of the WT were in the lower-frequency regime of the fundamental anti-symmetric mode. In the other source-depth case, the maximum magnitudes of the WT were in the higher-frequency regime of the fundamental symmetrical mode. Table 1 shows the arrival times obtained at the indicated frequencies and modes (A_o , 66 kHz and S_o , 522 kHz) for the three available propagation distances (60, 120, 180 mm). In contrast to Part 1, a higher frequency was used for A_o to be more certain that the arrival times would not be altered by the 40 kHz high-pass filter. Figures 1 and 2 show the high-resolution WT results, which were used in the two cases. The WT-parameters used were Wavelet size (WS) = 600 samples, Maximum Fre-

Table 1. Arrival times (μs) of the peak WT magnitude for in-plane dipole source signals filtered with a 40 kHz high-pass filter in the large plate.

Source depth, mm	So mode at 522 kHz					Ao mode at 66 kHz				
	Distance, mm			Velocity, mm/ μs		Distance, mm			Velocity, mm/ μs	
	60	120	180	Slope	Theoretical	60	120	180	Slope	Theoretical
2.037	31.9	64.6	98	1.82	1.78	-	-	-	-	-
0.783	-	-	-	-	-	29.1	51.9	75.1	2.61	2.61

quency (MF) = 700 kHz, Frequency Resolution (FR) = 3 kHz for the signal dominated by the So mode and WS = 600 samples, MF = 400 kHz, FR = 2 kHz for the signal dominated by the Ao mode. The sources were at depths of 2.037 mm (Fig. 1 for the dominant symmetric mode) and 0.783 mm (Fig. 2 for the dominant anti-symmetric mode). Figure 3 shows a plot of the WT magnitude as a function of time at a single frequency of 522 kHz for the 180 mm distance case of Fig. 1. The time of arrival of the maximum WT magnitude for the selected mode and frequency was obtained from the available spreadsheet that gives the WT magnitude (WT coefficient) as a function of time and frequency. The time resolution of the spreadsheet was 0.1 μs , which is the same resolution as the re-sampled simulated AE signal. Since the exact locations of the source and sensors are known, the information in Table 1 can be plotted to form distance-versus-time plots. The slopes of these plots provide group velocities as well as coefficients of determination (R^2) for the straight line fits. Table 1 shows these slope-based group velocities as well as the group velocity (for the mode and frequency) available from the relevant theoretical dispersion curves. Figure 4 shows an example of one of the plots (for the Fig. 1 case, 2.037 mm source depth) of distance versus arrival time along with the equation that describes the straight-line fit. The plot (not shown) of the other case (0.783 mm depth) gave a similar straight-line fit. The excellent straight-line fits imply that the arrival times correspond very closely to a single group velocity that is quite near the theoretical group velocity.

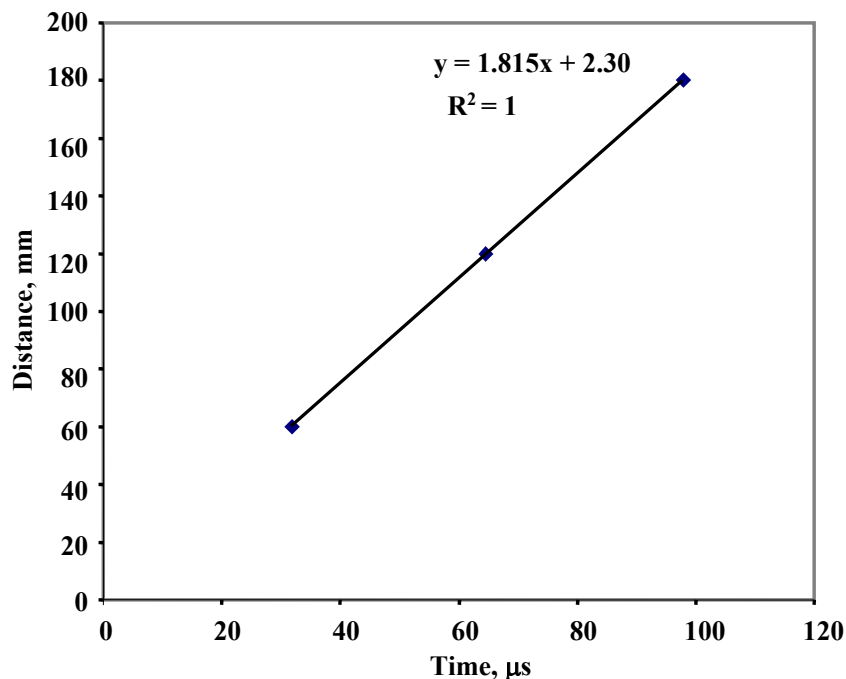


Fig. 4. Plot of propagation distances versus arrival time of peak magnitude of the So mode at 522 kHz for the WTs in Fig. 1. Equation of straight-line fit with slope of 1.815 mm/ μs representing the slope-based group velocity. $R^2 = 1$, correlation coefficient.

Table 2. Arrival times (μs) of the peak WT magnitude for in-plane dipole source signals filtered with a 100 to 300 kHz bandpass in the large plate.

Source depth, mm	Distance, mm			Velocity, mm/ μs		Distance, mm			Velocity, mm/ μs	
	60	120	180	Slope	Theoretical	60	120	180	Slope	Theoretical
2.037	15.9	28.2	40.5	4.88	4.88	-	-	-	-	-
0.783	-	-	-	-	-	25.2	45.7	65.7	2.96	3.00

It is worthwhile to point out that the straight-line fit has an intercept that does not pass through the source origin (even with an excellent fit, $R^2 = 1$, of the data to a straight line). The reason for this behavior is likely due to the fact that the wave propagation needs to progress over some number of plate thicknesses in order to fully develop the Lamb modes at their propagation velocity. We also note that the group velocities determined from the WTs of the finite element data did not always correspond exactly to those determined from the theoretical group velocity (dispersion) curves. For example, when the arrival times used to calculate the indicated velocity in Table 1 of Part 1 (Hamstad et al., 2002) were used along with the propagation distances to obtain a plot of distance versus time the slope-based group velocity was 2.45 mm/ μs . This value is 1.2 % faster than the dispersion curve velocity of 2.42 mm/ μs for the Ao mode at 50 kHz. As will be seen later in the description of a proposed source location procedure, we suggest the group velocities determined from WT results might be expected to provide more accurate results. But the correctness of this assumption will need to be determined through additional research.

A third approach was also examined. This approach was really just a deviation of the second one. In this case the modification was to filter the FEM-based signals with a 100 to 300 kHz bandpass filter before calculating the WTs. This frequency range was chosen since it has often been used in experimental AE applications. Figure 5 (Fig. 1 case) and Figure 6 (Fig. 2 case) show the resulting high-resolution WT results for the same two sources. These WT results were calculated for the filtered signals, which are also shown in Figs. 5 and 6. The WT-parameters used were $WS = 600$ samples, $FR = 2$ kHz, and $MF = 400$ kHz. In this case the maximum magnitudes of the WTs are in a different frequency range. Table 2 shows the selected frequencies and modes (Ao, 134 kHz and So, 262 kHz) for each case as well as the arrival times determined from the WTs; also shown are the group velocities from the plots of distance versus time and the group velocities from the dispersive group-velocity curves at the selected frequencies and modes. The slope-based group velocities shown in Table 2, again, were quite close to those obtained from dispersion curves. As before, the plots of distance versus arrival time had excellent fits but again did not pass through the origin, presumably due to the need to propagate several plate thicknesses to develop the Lamb modes and their group velocities. Thus, in this range of bandpass frequency, the arrival times correspond very closely to a single group velocity very near the theoretical velocity.

4. Proposed Method of WT-Based Source Location for Experimental Data (Large Plate)

The results above indicate that the approach of using a fixed frequency of an energetic mode to determine an arrival time at the maximum magnitude of a WT (Yamada et al., 2000) could result in accurate arrival times that are associated with a particular wave mode and corresponding group velocity. But, since the calculated group velocities from the finite-element data did not always correspond exactly to the dispersion-curve values, it may be useful to account for this aspect. By providing for this aspect, it may be possible to obtain the best possible experimental location accuracy with a WT-based technique. The approach we suggest would use the group

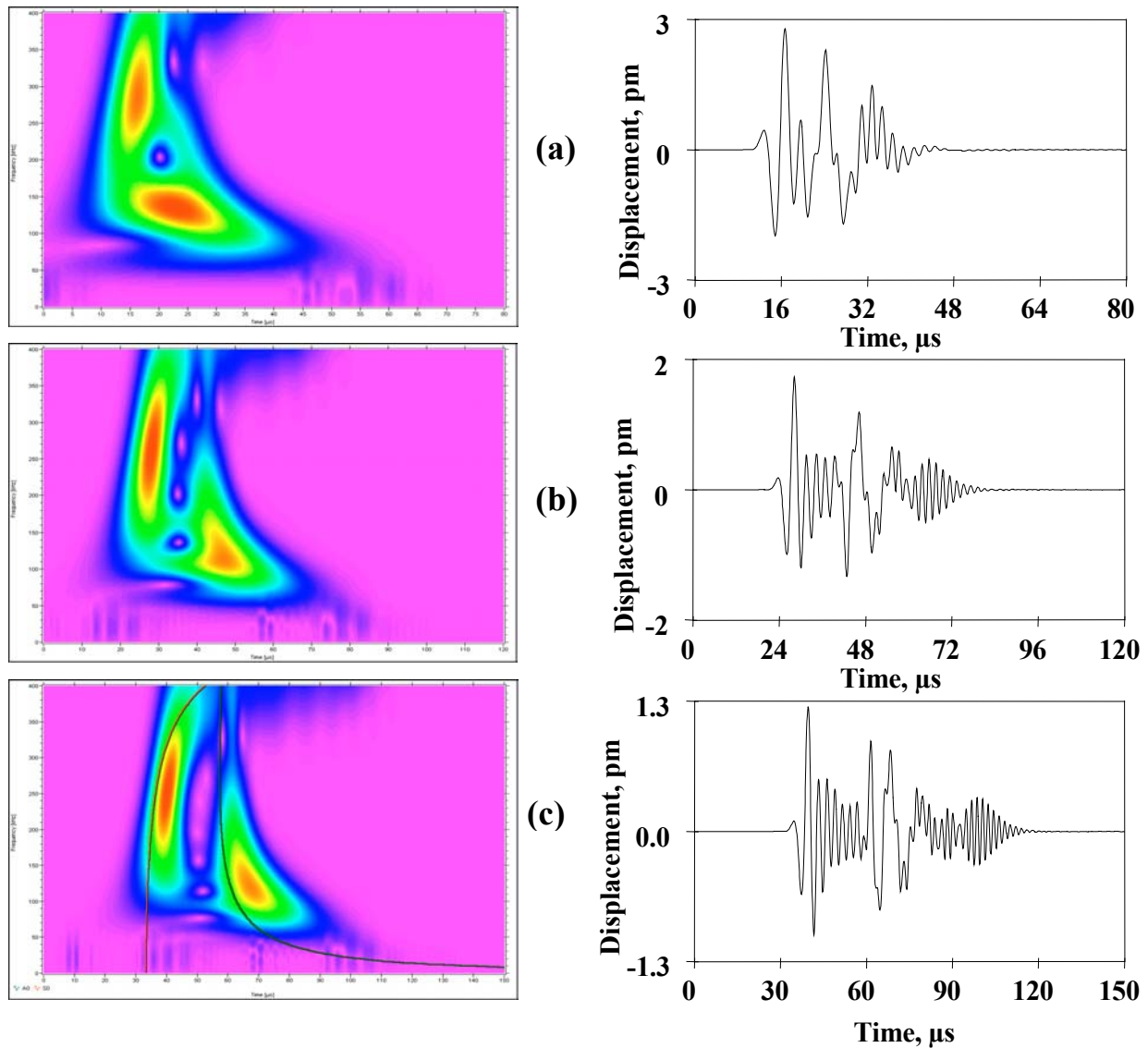


Fig. 5 WT results (frequency 0 to 400 kHz versus time (0 to 80, 0 to 120, and 0 to 150 μ s)) for the same cases shown in Fig. 1 but with a 100 to 300 kHz bandpass filter prior to calculating the WT. Fig. 5(c) also shows superimposed A_0 and S_0 group-velocity-based dispersion curves after conversion to arrival times based on the propagation distance of 180 mm. Also shown are the corresponding filtered AE signals.

velocity from the dispersion-based curves as an initial group-velocity estimate. Possibly a better group-velocity value could be determined as described below by pre-experiments. The pre-experiment approach would replace that illustrated in Fig. 4 since the propagation distances used to construct that figure are available only for the FEM data. We point out that the “calibrated” group velocity extracted from Fig. 4 could be viewed as compensating for small differences in group velocity (compared to dispersion-based values) induced by the WT algorithm. Presumably these algorithm-induced differences would be a part of each WT calculation with a particular algorithm. Also, the pre-experiments would be necessary when accurate group velocities cannot be calculated.

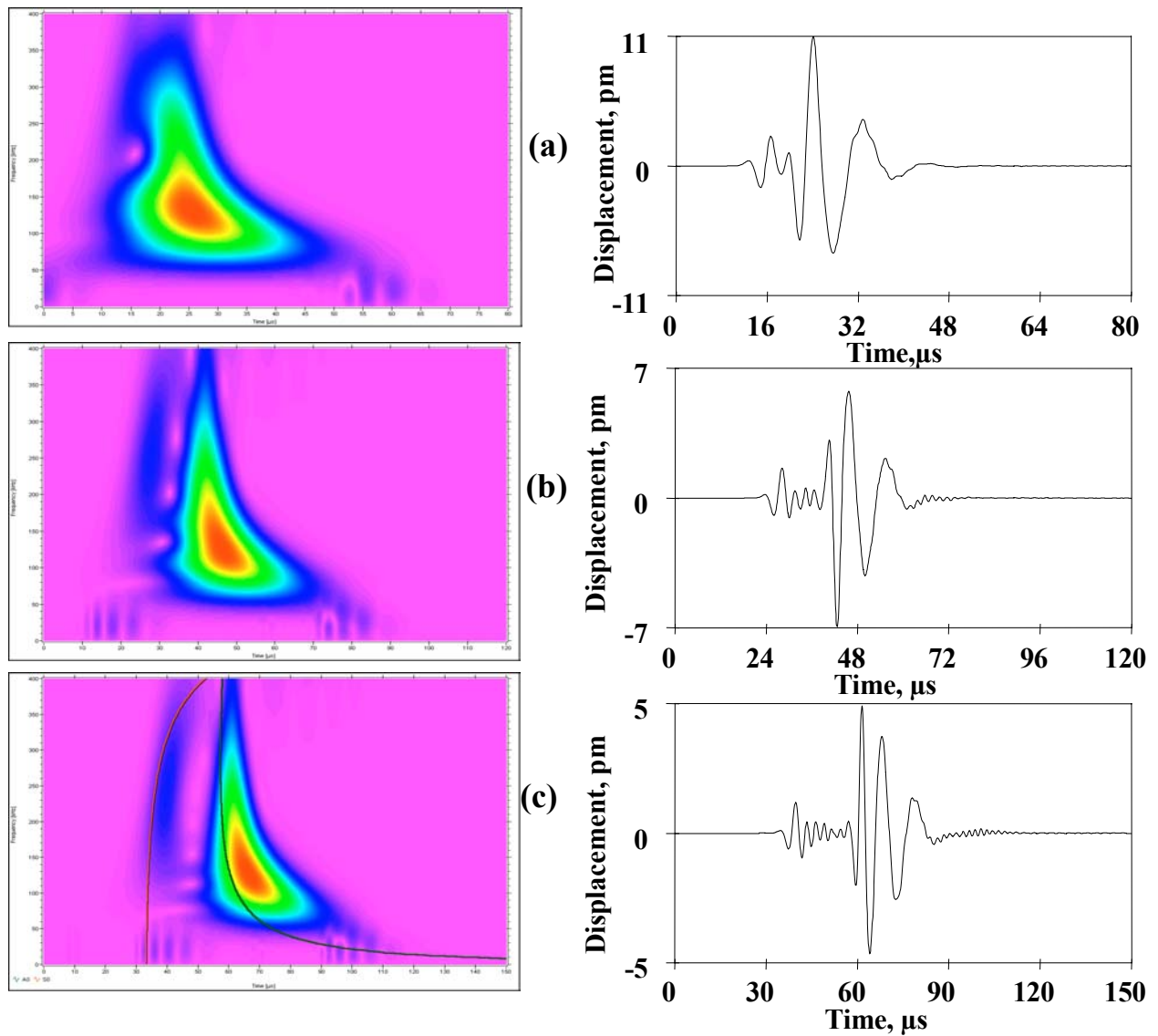


Fig. 6 WT results (same scales as Fig. 5) for the same cases shown in Fig. 2 but with a 100 to 300 kHz bandpass filter prior to calculating the WT. Fig. 6(c) shows the superimposed A_0 and S_0 group-velocity-based dispersion curves after conversion to arrival times based on the propagation distance of 180 mm. Also shown are the corresponding filtered AE signals.

5. Comments Relative to the Location Approach for Real AE Signals

With actual AE data, in particular narrow-band data, the preliminary task of selecting the wave mode to associate with the WT maximum magnitude region may require some pre-experiments. The purpose of conducting pre-experiments with pencil lead breaks and the real sensors would be to identify the mode(s) associated with the peak magnitude frequency range(s) of the WT and to determine corresponding WT-based group velocities. A large plate of the same thickness and material could be used for these pre-experiments. Good control of the position and force direction of the lead break is necessary. But in principle, an in-plane pencil break on the plate edge close to the top or bottom surfaces would allow identification of the dominant-energy WT frequencies for the anti-symmetric modes (typically for thin plates this will be the fundamental anti-symmetric mode). And an in-plane lead break located almost exactly at the mid-

plane could allow (with careful filtering) the determination of the dominant frequencies of the peak-magnitude region of the WT for the symmetric modes (typically for thin plates this is expected to be the fundamental symmetric mode). These frequencies and modes could then be used with dispersion-based group-velocity curves to provide the initial estimates of the group velocities to be used to calculate the source location. In addition WTs from sensors at several accurately known distances from these experimental sources could be used to obtain “calibrated” group velocities (as referred to above).

In contrast to the source-identification task with a subset of WT data, the dependence of the WT results on source depth does not cause significant problems in determining source location. It is necessary only to add a step in the calculation of source location that determines which mode is dominant in an AE signal by calculating appropriate Ao/So ratios as described in Part 1 (Hamstad et al., 2002). Based on the ratio determined, the most energetic mode and associated frequency can be used to extract the WT-based arrival times. Also, the correct group velocity for the dominant mode and frequency for each AE signal can be selected for the calculation of the source location.

6. Effects of Electronic Noise

In experimental cases, the AE signal is a combination of signal (from the AE source) and noise (from the electronics). Thus, to be useful, the above method of WT-based source location must retain its determination of accurate arrival times for a single group velocity in the case of experimental signals that combine signal and noise. To examine this issue we added electronic noise to the calculated FEM signals and studied the WT-based determination of arrival times. The study was carried out as a function of the signal-to-noise (S/N) ratio.

The noise signals were taken from two different wideband sensor/preamplifier combinations. These experimental signals were obtained with the wideband sensors coupled only to air. In addition, the sensors were protected from any possible laboratory airborne signals. Prior to being added to the FEM calculated signals, the noise signals were filtered with a six-pole digital Butterworth filter from 40 kHz to 1.2 MHz. As Fig. 7 shows, the typical spectra of the noise signals were considerably different from each other. In one case the electronic noise increases significantly with decreasing frequency. In the other case, the electronic noise amplitude is distributed more uniformly with frequency, with a peak region near the middle of the frequency range. By using noise signals with these two different spectrums, we attempted to broaden the results of the study.

Also to broaden the results of the study, two distinctly different FEM calculated signals were selected. In one case, a higher-frequency region of the fundamental symmetric mode dominated the AE signal energy. In the second case, a lower-frequency region of the fundamental anti-symmetric mode dominated the AE signal energy. The source for both signals was an in-plane dipole located at 180 mm from the sensor. In the case of the dominant symmetric mode the source was at a depth of 2.35 mm (mid-plane). The dominant anti-symmetric-mode source was at a depth of 0.47 mm below the top surface of the large plate.

In order to quantitatively characterize the S/N ratio, the peak amplitudes of the noise and the calculated AE signals (40 kHz high-pass) were determined over the 150 μ s portion of each signal used in the WTs. Then the noise signals were multiplied by appropriate factors to obtain the desired range of S/N ratios, based on the peak amplitudes.

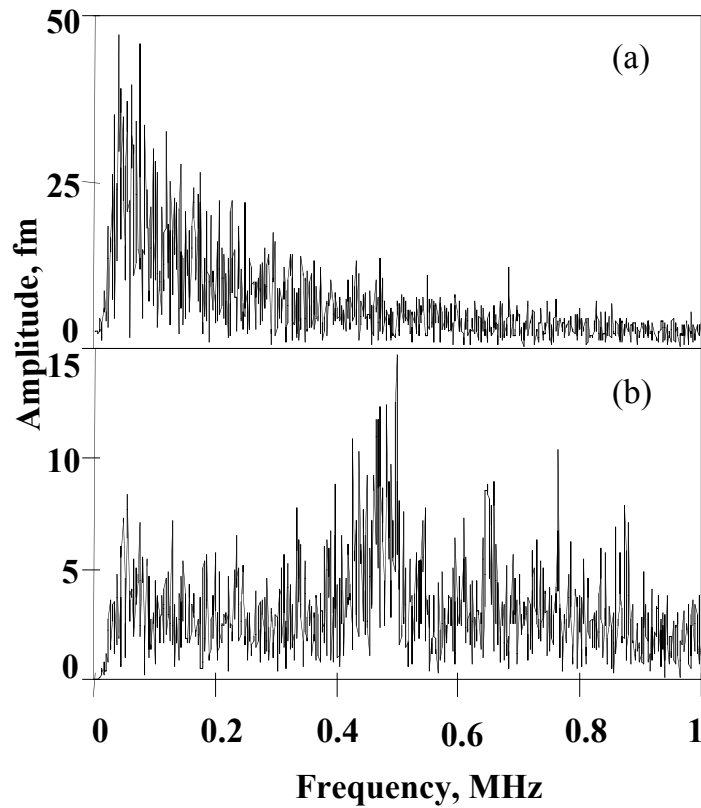


Fig. 7 Typical frequency spectra for the two experimental noise signals calculated from an 819.2 μs signal length. Low-frequency emphasis (a) and distributed frequencies (b).

Figure 8 shows the WTs of the two calculated AE signals ((a) and (b) without added noise) and the two noise signals ((c) and (d)). These WTs were calculated with the following high-resolution parameters (WS = 600, FR = 3 kHz [0-600 kHz case] and 2 kHz [0-400 kHz case]). Following the approach used earlier in this paper, the arrival times of the peak magnitudes of the WTs were determined at 522 kHz (AE signals dominated by the symmetric mode) and at 66 kHz (AE signals dominated by the anti-symmetric mode). Table 3 shows the determined arrival times at 522 kHz for the two different noise types at the selected S/N ratios. Table 4 shows the arrival times at 66 kHz for the two noise cases. No arrival times are shown in the tables when the peak magnitude of the WTs was not obvious. In all cases the WTs were calculated with the high-resolution parameters used to produce Fig. 8.

Table 3. Arrival times (μs) determined from the peak WT magnitude at 522 kHz for the original AE signal dominated by a higher-frequency region of the fundamental symmetric mode.

S/N ratio	Noise dominated by low frequencies	Noise with distributed frequencies
no noise	97.9	97.9
10:1	97.9	97.9
5:1	97.9	97.9
2:1	97.9	97.9
1:1	97.9	97.8
1:2	97.9	87.8
1:5	101.8	117.2
1:10	101.8	—
Noise signal	33.1, 101.5	115.9, 15.5

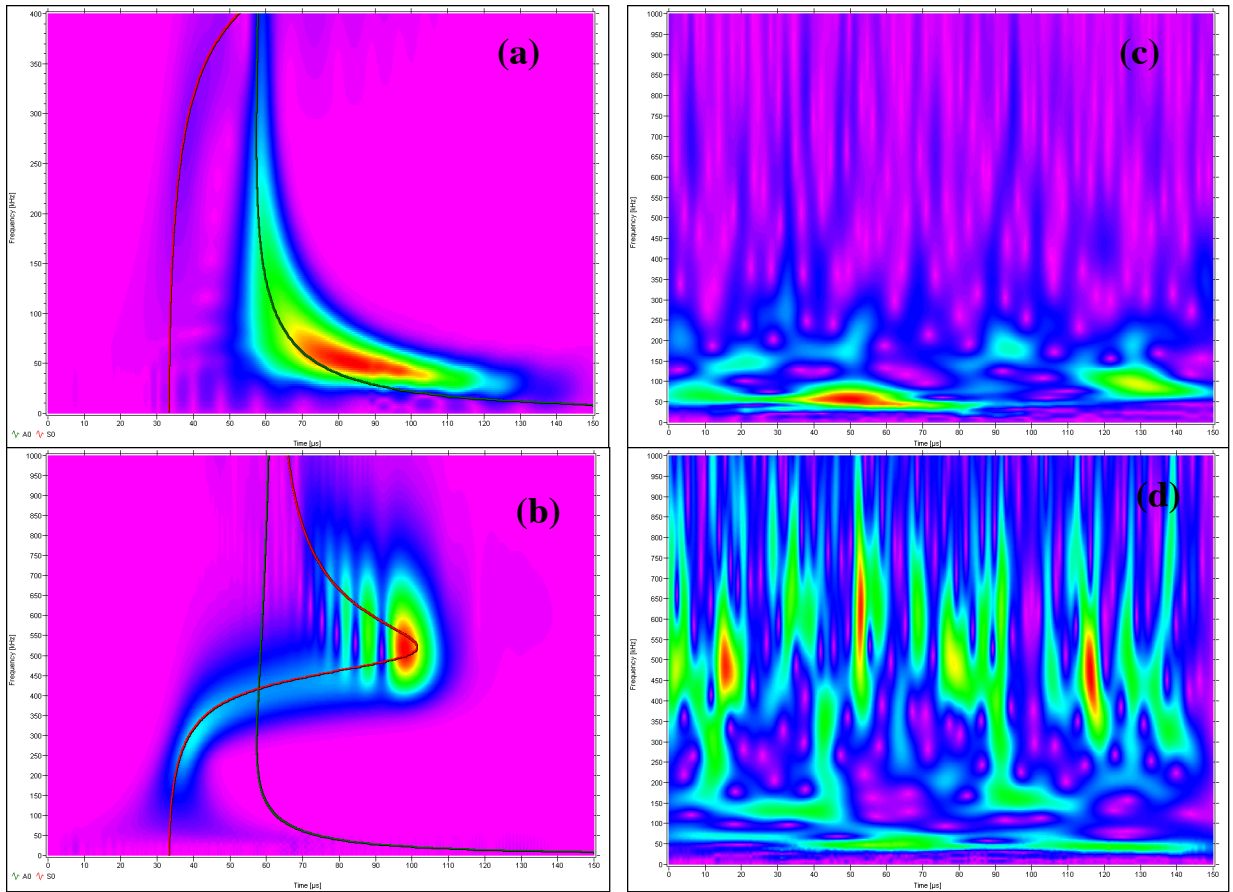


Fig. 8 WTs of the calculated AE signals and the experimental electronic noise for 150 μs length signals: (a) for AE signal at 180 mm propagation distance with dominant fundamental anti-symmetric mode; (b) for AE signal at 180 mm propagation distance with dominant fundamental symmetric mode; (c) for electronic noise with low-frequency emphasis; and (d) for electronic noise with distributed-frequency emphasis.

Table 4. Arrival times (μs) determined from the peak WT magnitude at 66 kHz for the original AE signal dominated by a lower frequency region of the fundamental antisymmetric mode.

S/N ratio	Noise dominated by low frequencies	Noise with distributed frequencies
no noise	75.1	75.1
10:1	75.6	75.2
5:1	76.1	75.3
2:1	77.1	75.6
1:1	80.3	76.1
1:2	47.7	76.2
1:5	—	74.6
1:10	—	26.7
Noise signal	49.2	66.6, 24.4

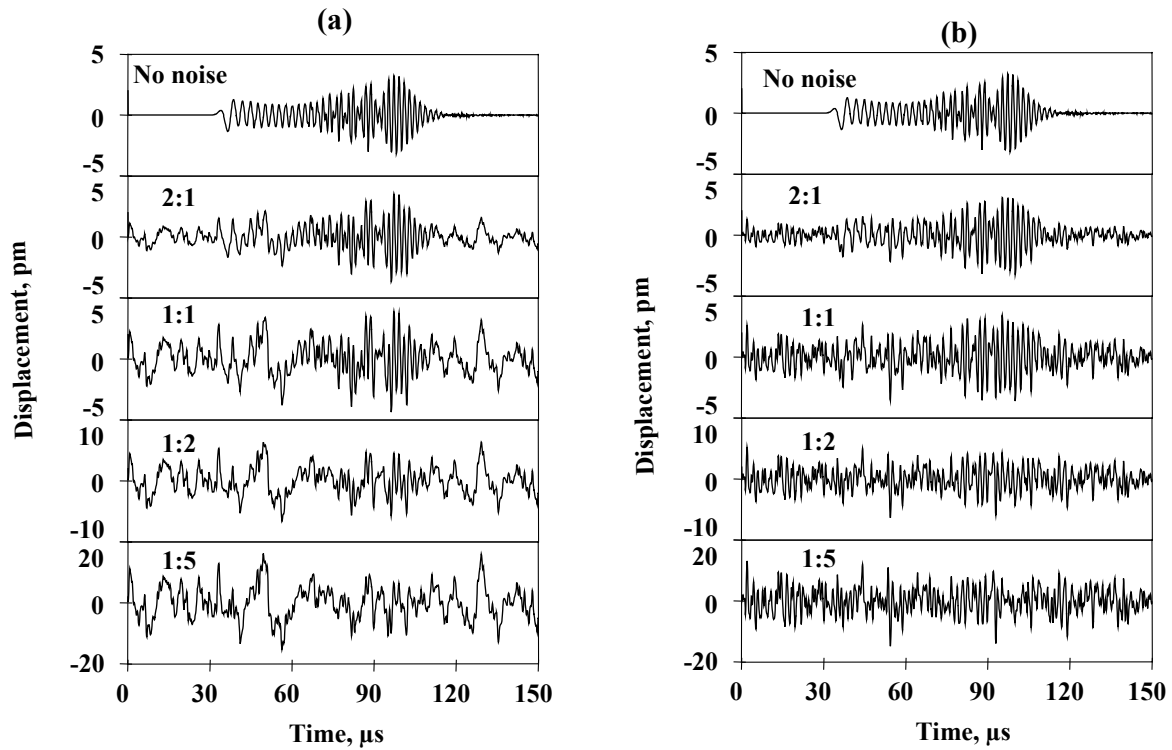


Fig. 9 Waveforms of signal-plus-noise at the indicated S/N ratios for the AE signal at 180 mm propagation distance dominated by the fundamental symmetric mode: (a) noise with low-frequency emphasis; (b) noise with distributed-frequency emphasis.

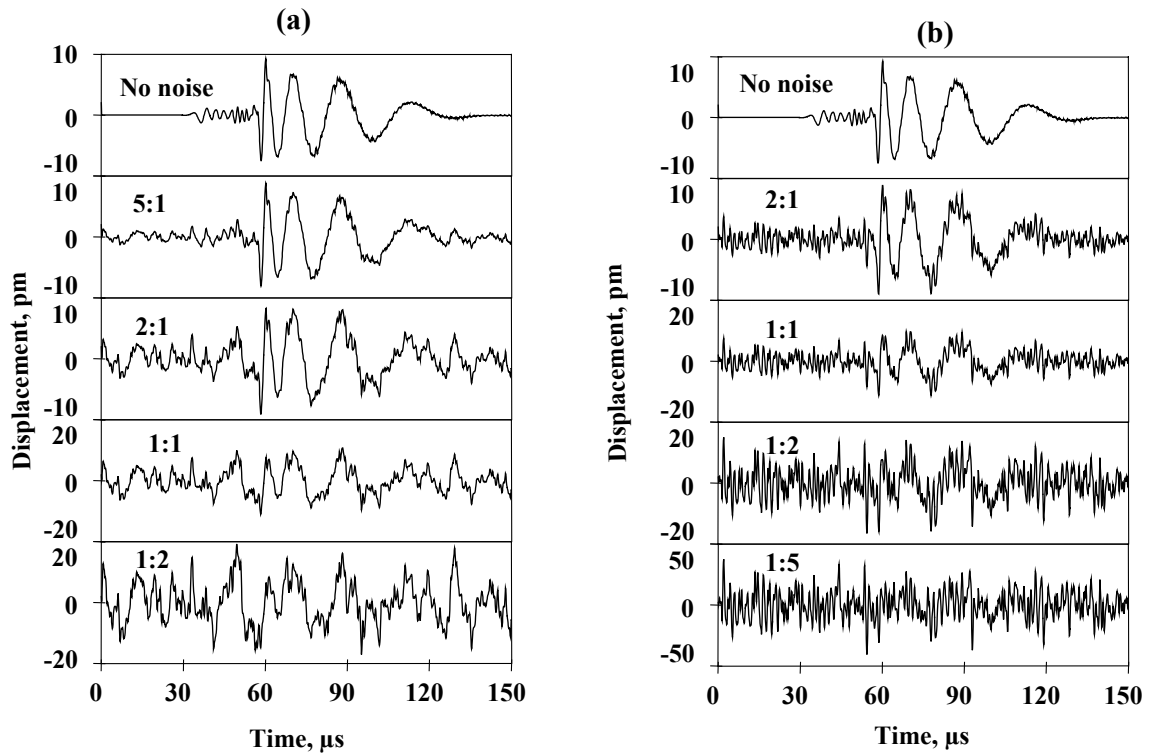


Fig. 10 Same types of waveforms as Fig. 9 for the AE signal at 180 mm propagation distance dominated by the fundamental anti-symmetric mode.

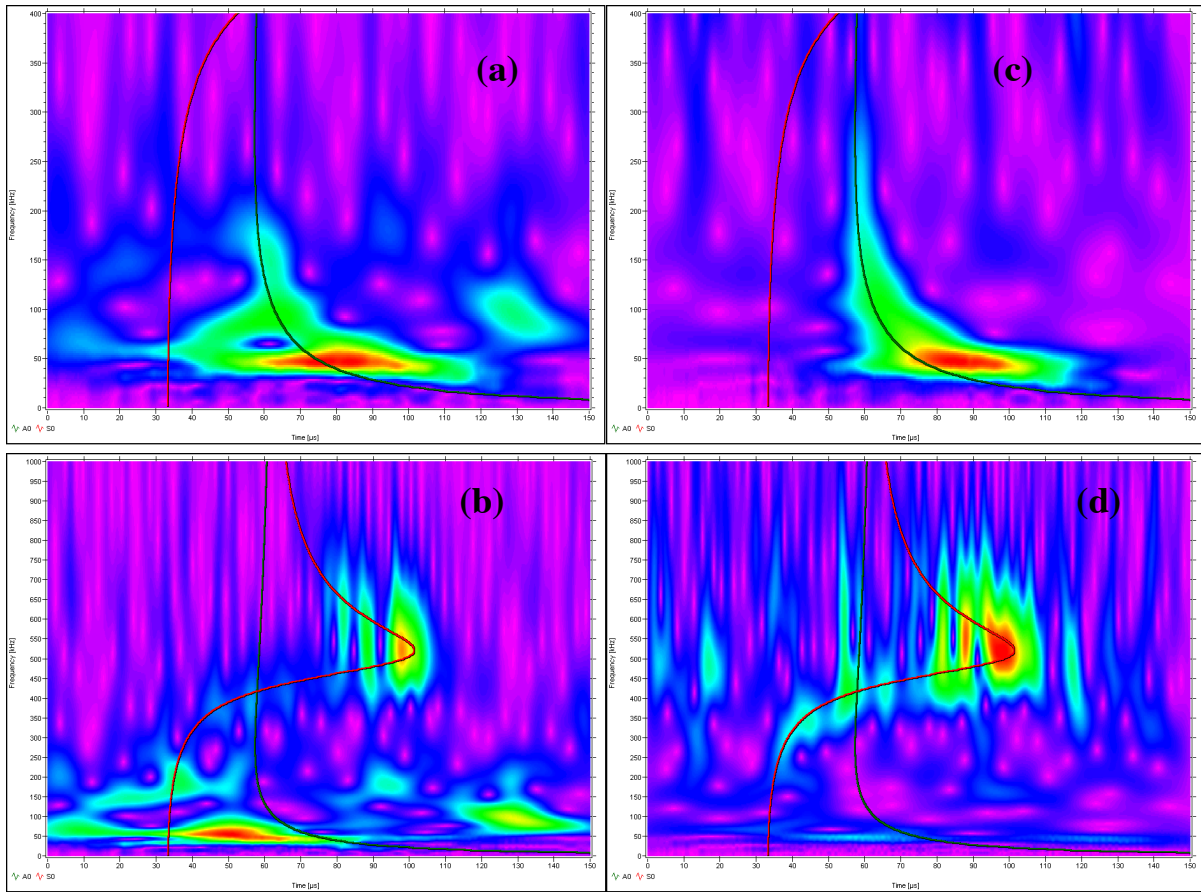


Fig. 11 WTs of waveforms of signal plus noise. Signals at 180 mm from the in-plane dipole source. The noise in (a) and (b) was dominated by low frequencies and in (c) and (d) by distributed frequencies. The signal in (a) and (c) was dominated by the fundamental anti-symmetric mode from the source at a depth of 0.47 mm. In (b) and (d) the signal was dominated by the fundamental symmetric mode from the source at a depth of 2.35 mm. The signal-to-noise ratio in each case was 1:1.

To provide a clearer understanding of the results in Tables 3 and 4, Fig. 9 shows selected waveforms of signal-plus-noise for the two noise cases when the original AE signal was dominated by a higher-frequency region of the symmetric mode. Figure 10 shows the same type of selected results when a lower-frequency region of the anti-symmetric mode dominated the original AE signal. Examination of the above figures and tables reveals several key aspects about the effects of electronic noise on the WT-determination of arrival times from a particular mode and frequency. First, when the S/N ratio becomes too small, the arrival time of the WT magnitude peak typically moves toward the WT peak magnitude of the noise signal (at the selected frequency). Second, even with a relatively poor S/N ratio of 1:1 as shown in Figs. 9 and 10, the WT-based arrival time is still reasonably accurate. As Figs. 9 and 10 show for these cases, it is becoming difficult to extract by eye the AE signal. And clearly, a threshold-based technique would lead to inaccurate arrival times (or no hit detected) not associated with a known group velocity. The worst result at this 1:1 ratio is the case of the signal dominated by the low-frequency anti-symmetric mode and the noise dominated by low frequencies. Since WTs result in better time resolution at higher frequencies, it is possible that the slightly poorer accuracy at 66 kHz is due to the characteristics of the WT. More likely, the result is due to the frequency peaks of the original AE signal and the noise being in the same frequency range. This conclusion

is based on the observation (see Tables 3 and 4) that errors in the arrival times appear at higher S/N ratios when the noise and original signals have peaks in the same frequency region.

The reason why reasonably accurate arrival times can be extracted from the WT results at S/N ratios of 1:1 or less seems to be due to the fact that the WT spreads out the noise over the bandpass frequency range while preserving the spread of the noise in time. Determinations of arrival times by penetration of a fixed threshold have the noise spread out only in time. Thus, such approaches typically cannot even detect an AE hit at S/N ratios as low as 1:1. Figure 11 demonstrates at a S/N ratio of 1:1 that the WT of the AE signal plus noise is dominated in all four cases by the same WT region that dominated when only the AE signal was present (compare Fig. 11 with Figs. 8(a) and 8(b)). In Fig. 11 the four cases of AE signal plus noise are: (a) low-frequency noise and low-frequency AE signal; (b) low-frequency noise and high-frequency AE signal; (c) distributed noise and low-frequency AE signal; (d) distributed noise and high-frequency AE signal.

We did not investigate the narrow-band S/N ratio case, since we did not have available the digital displacement calibration of a typical 150 kHz resonant commercial AE sensor. Thus, we could not properly alter the calculated sensor signal for the AE source to correspond to the sensor resonance. We expect that the above WT-based method of detection of arrival times would not be as robust at low S/N ratios, since both the AE signal and the noise would be concentrated in the same relatively narrow frequency range.

An additional positive of the WT-based method, in the case of wideband waveform-based AE measurement systems, may be that fewer AE events would have only one useable hit. If the measurement system were configured so that all the waveforms from a group of sensors were recorded when one sensor was hit (i.e. a signal above the threshold), then WT-based processing could extract relevant arrival times from the sensor channels where threshold-penetration hits would not occur. Thus, signal arrival times corresponding to a single group velocity could be extracted from the channels where the AE signal had attenuated into the background electronic noise. And potentially a source location could be calculated for an event where it could not be calculated with a threshold-based AE system.

7. WT for Source Location in Samples with Nearby Edges

When the lateral size of the test specimen is decreased so that nearby edges are present, the AE signals and their WTs become much more complicated. This result was illustrated in Part 1 (Hamstad et al., 2002) in Figs. 16 and 17. Since the distribution of WT-illustrated signal energy in these figures does not clearly follow the shapes of the superimposed fundamental Lamb-mode curves from the dispersion relations, the use of the approaches developed for source location in the large plate might be expected to experience difficulties for the coupon specimen. Further, since the distortion of the WT results is due to edge reflections, moving the source from side-to-side across the 25.4 mm width of the coupon specimen will change the reflections and WTs as was illustrated in Fig. 18 of Part 1 (Hamstad et al., 2002). The current coupon database, except for the case illustrated in Fig. 18 of Part 1 (Hamstad et al., 2002), does not include the side-to-side variation of the source position.

In spite of the limited database (side-to-side source position), we examined for the coupon specimen the application of the techniques applied to the large-plate signals. The results of this examination in the coupon (using 40 kHz high-pass signals) for the same source cases used in the

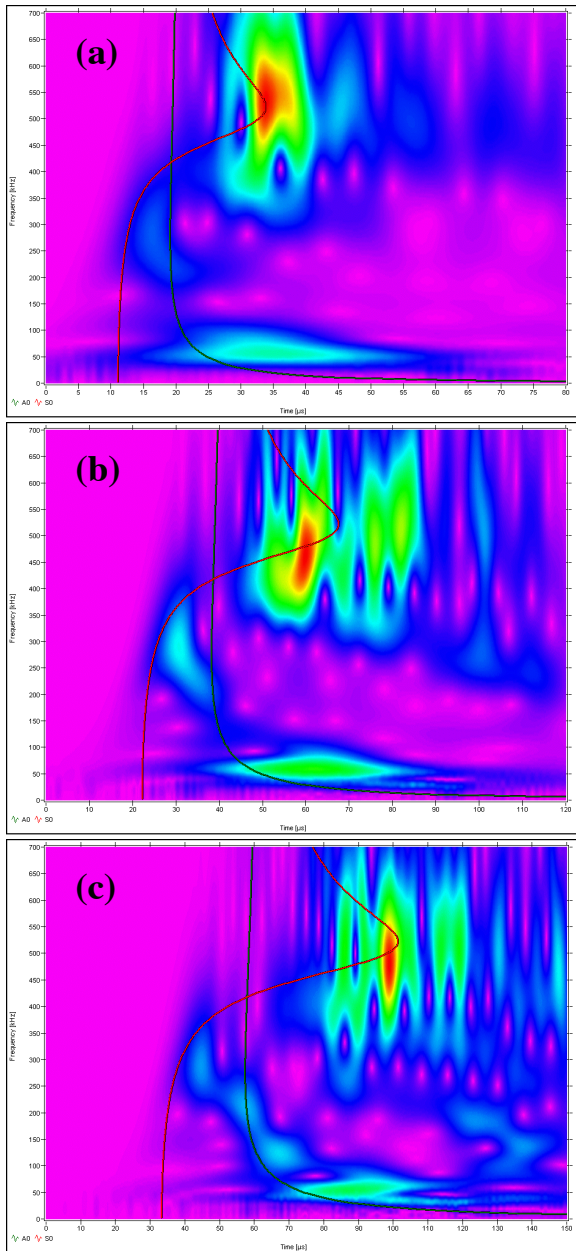


Fig. 12 WT plots used to determine AE signal arrival times from the peak magnitudes of the So mode at 522 kHz for the coupon specimen. The AE source was an in-plane dipole at a depth of 2.037 mm with propagation distances of (a) 60 mm, (b) 120 mm, and (c) 180 mm. AE signals filtered with 40 kHz high-pass filter prior to WT. Frequency (0 to 700 kHz) vs. time (0 to 80, 0 to 120, 0 to 180 μ s from top to bottom). Superimposed group velocity curves of fundamental modes.

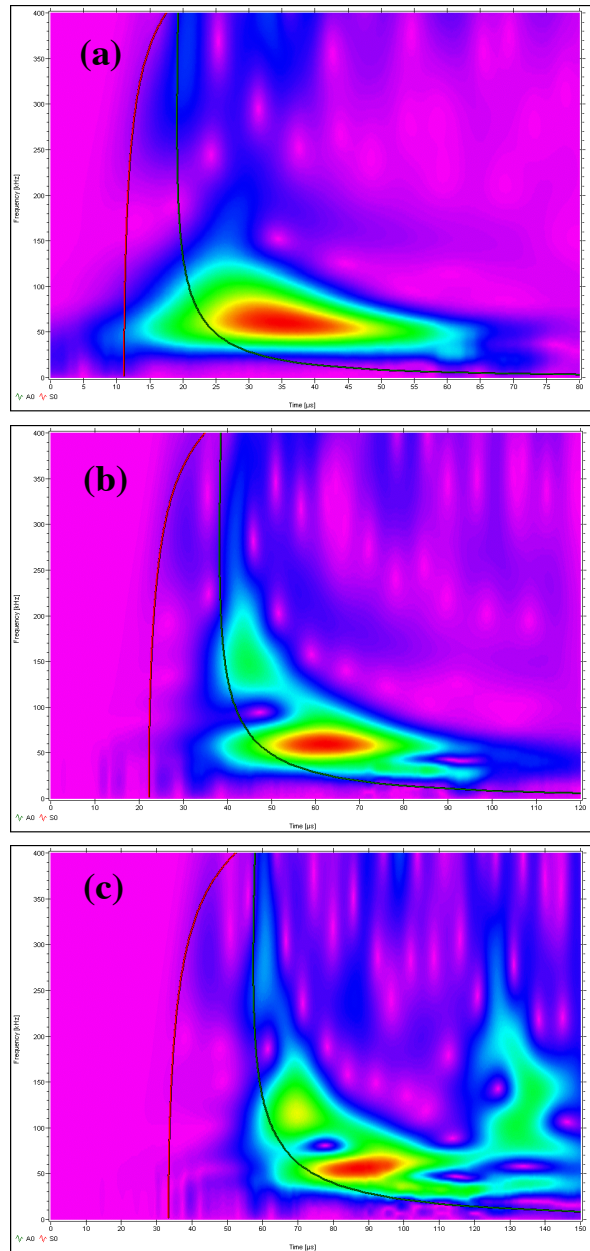


Fig. 13 WT plots used to determine AE signal arrival times from the peak magnitudes of the Ao mode at 66 kHz for the coupon specimen. The AE source was an in-plane dipole at a depth of 0.783 mm. The propagation distances and filter were the same as for Fig. 12 (a), (b), and (c). Frequency (0 to 400 kHz) versus time (same scales as Fig. 12, top to bottom).

Table 5. Arrival times (μs) of the peak WT magnitude for in-plane dipole source signals filtered with a 40 kHz high-pass filter in the coupon specimen.

Source depth, mm	So mode at 522 kHz					Ao mode at 66 kHz				
	Distance, mm			Velocity, mm/ μs		Distance, mm			Velocity, mm/ μs	
	60	120	180	Slope	Theoretical	60	120	180	Slope	Theoretical
2.037	33.8	60	99	1.82	1.78	-	-	-	-	-
0.783	-	-	-	-	-	33.8	61.9	91.2	2.09	2.62

large plate (those that lead to Figs. 1 and 2 and Table 1) are shown in Figs. 12 and 13 and Table 5 for the coupon. For the WT calculations the WS = 600 samples was used for both modes; and the FR and MF values used were 2 kHz and 400 kHz for the Ao mode and 3 kHz and 700 kHz for the So mode. The maximum WT magnitude arrival times were selected while ignoring reflections from the ends of the coupon specimen. Figure 12 shows the WTs for the coupon for the in-plane dipole at a depth of 2.037 mm. Figure 13 shows the coupon WTs for a depth of 0.783 mm. The source position for the results shown in Figs. 12 and 13, as well as Table 5, was located half-way across the coupon (12.7 mm from the side). Table 5 indicates the results were mixed. For the 2.037 mm depth and the So mode at 522 kHz, the slope-determined velocity of 1.82 mm/ μs was the same as the large plate velocity of 1.82 mm/ μs , but in the plot of distance versus arrival time the data did not fit the straight-line slope very well. For the 0.783 mm depth and the Ao mode at 66 kHz the slope-determined velocity in the coupon was 2.09 mm/ μs (again data with a poor fit) which was 20 % lower than the value of 2.61 mm/ μs in the large plate.

Table 6. Arrival times (μs) of the peak WT magnitude for in-plane dipole source at 2.35 mm depth and different distances from the coupon side. So mode at 522 kHz.

Case	Distance, mm			Velocity, mm/ μs	
	60	120	180	Slope	Theoretical
Coupon, 3.31 mm	32.4	65.1	87.8	2.13	1.78
Coupon, 6.13 mm	36.4	77.7	103.8	1.75	1.78
Coupon, 12.7 mm	33.9	60	98.7	1.82	1.78
Large plate	31.9	64.6	97.9	1.82	1.78

To study the effect of side-to-side variation of the source position, we applied the same approach (522 kHz WT-peak arrival time) to the cases for the in-plane dipole at the mid-plane depth of 2.35 mm. Table 6 (same WT-parameters as for Table 5) shows the results (40 kHz high-pass data) for the coupon with the source at three different distances (12.7, 6.13, and 3.31 mm) from the coupon side compared to the equivalent large plate case. For convenience, the propagation distances are reported as 60, 120, 180 mm, but in determining the slope-based group velocities the actual straight-line distances from the source to the sensors were used. Table 6 clearly shows significant differences in the slope-determined group velocity (of the fundamental symmetric mode at a frequency of 522 kHz) as a function of transverse source position. Compared to the velocity determined from the large-plate signals (for the same case) the group velocity changes range from 0.6 % to 17 %. It is also clear from Table 6 that the arrival times at the different sensors vary over a considerable range compared to the large plate values, which were not influenced by the side-edge reflections. Figure 14 compares the differences in the WT magnitude versus time at 522 kHz for the large plate compared to the coupon specimen with the source at 3.31 mm from the coupon side. This figure is for the sensor located at the nominal propagation distance of 180 mm. The alteration of the peak arrival time in the coupon specimen is clearly visible along with the generally significantly larger magnitudes of the WT in that case.

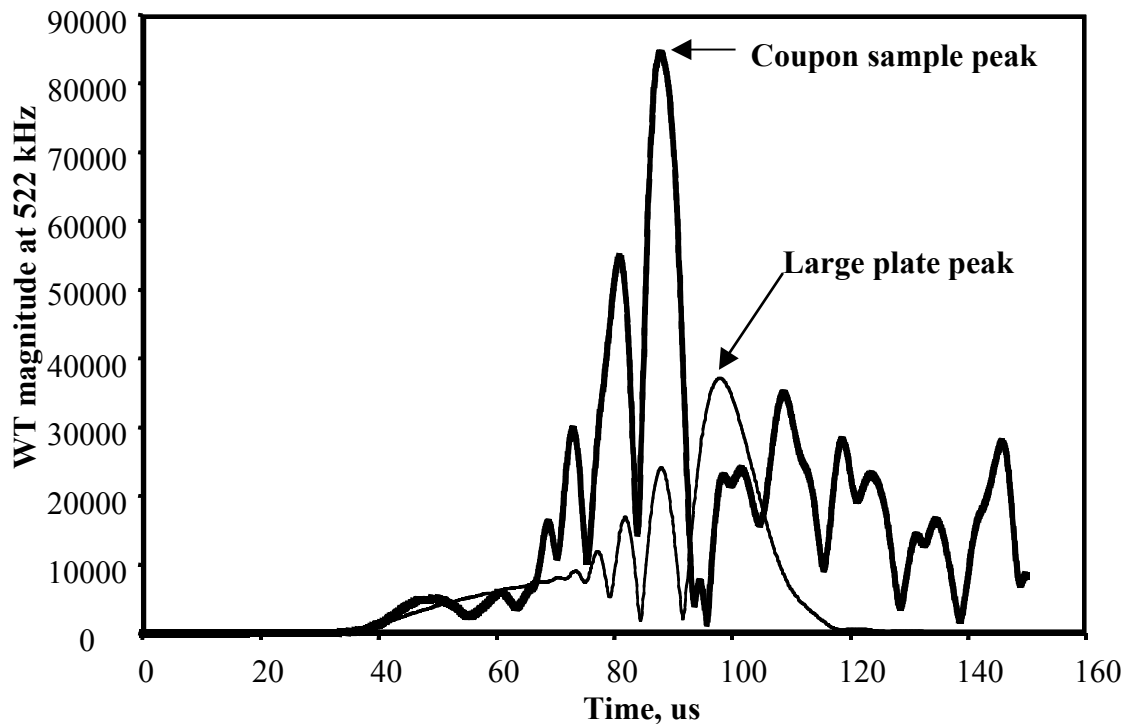


Fig. 14 WT magnitude at 522 kHz versus time for a large plate and coupon specimen. In both cases the source was an in-plane dipole at a depth of 2.35 mm and a propagation distance of 180 mm. The coupon source was located at 3.31 mm from the coupon side.

We conclude that significant and variable errors can be present in the arrival times for the coupon specimens when they are determined by the WT approach examined here. The errors in coupon-determined group velocities could be overcome by appropriate pencil lead-break data from a large-plate specimen of the same material and plate thickness as the coupon specimen, but arrival-time errors would remain. These errors would result in poor accuracy for source location calculations.

The effect of the side-to-side transverse source position was also examined using signals that had been filtered from 100 to 300 kHz. The WTs were calculated with high-resolution parameters ($WS = 600$ samples, $MF = 400$ kHz and $FR = 2$ kHz) for the in-plane dipole at a depth of 2.35 mm. Table 7 compares the three small coupon cases with the equivalent large-specimen results and the dispersion-curves-based group velocity at 262 kHz. As was the case above, the arrival time at maximum WT magnitude was selected by ignoring a magnitude maximum caused by reflections from the coupon-specimen's ends. The propagation distance versus the arrival times was plotted to determine the group velocity for each case of transverse source position. Compared to the large-plate data, the straight-line fits to the data for distance versus time were poor. The best fit was for the symmetrical center-line source position. But, even in that case, the group velocity was reduced by 13 % compared to the large-plate velocity. The group velocity determined when the source was located 6.13 mm from the coupon edge was very close to the result determined for the large plate. However, this was happenstance as the straight-line fit was very poor. Figure 15 shows the excellent fit and equation for the large plate as well as the significant error and typical scatter (relative to a straight line) of the three small-coupon cases. Thus, again, we conclude that side-edge reflections distort the determination of accurate arrival times. Obviously, inaccurate arrival times would lead to significant errors in source location.

Table 7. Arrival times (μs) of the peak WT magnitude for in-plane dipole sources at 2.35 mm depth and different distances from the coupon side. Signals were filtered from 100-300 kHz and the So mode at 262 kHz was used.

Case	Distance, mm			Velocity, mm/ μs	
	60	120	180	Slope	Theoretical
Coupon, 3.31 mm	15.3	34.8	46.8	3.74	4.89
Coupon, 6.13 mm	26.4	44.5	47	4.89	4.89
Coupon, 12.7 mm	19.4	34.4	47.6	4.25	4.89
Large plate	15.8	28.3	40.5	4.86	4.89

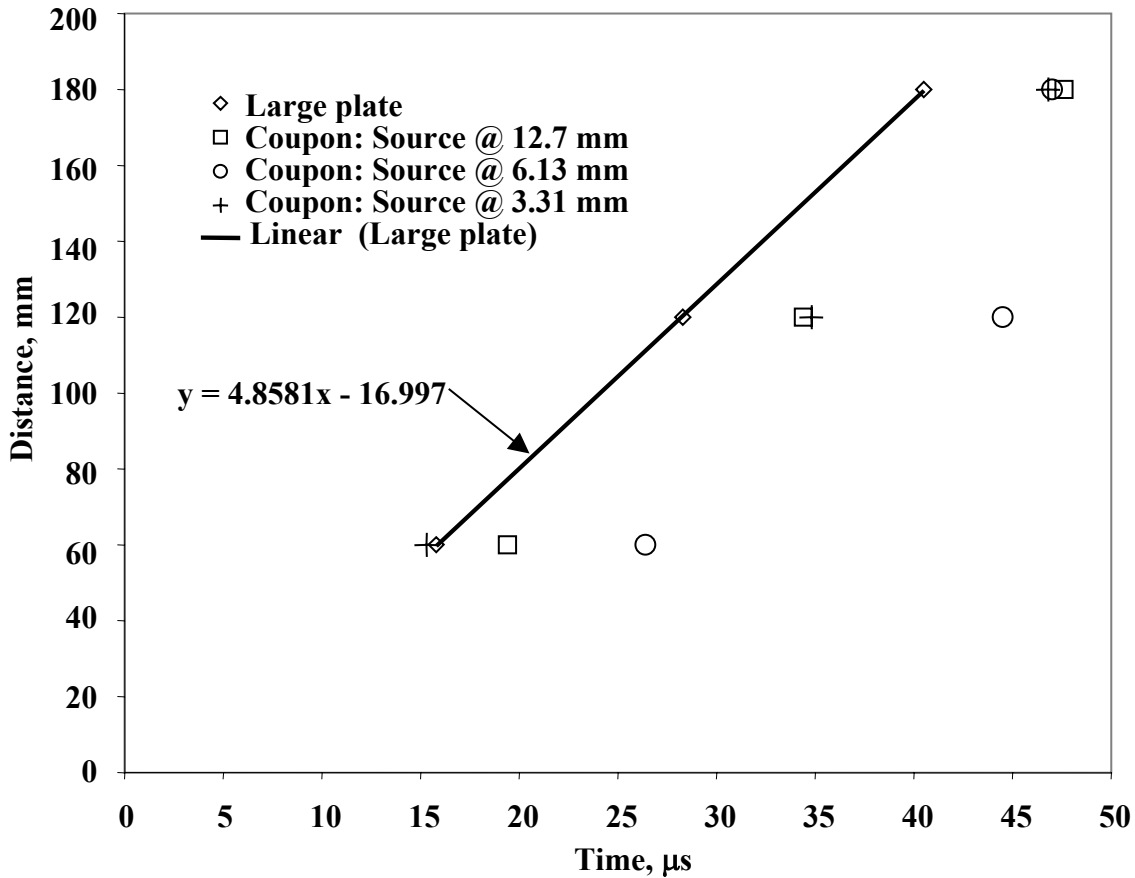


Fig. 15 Excellent fit of distance versus arrival time from WT peak magnitude at 262 kHz for large plate as compared to scatter and consequent lack of straight line fit for coupon specimen cases with variation in source distance from specimen side. AE signals were filtered from 100 to 300 kHz prior to the WT. Source was an in-plane dipole at a depth of 2.35 mm below the plate surface.

8. Conclusions

A. Source Location–Large Plates

- Excellent straight-line correlations of propagation distance versus the WT-based arrival times of the fundamental modes at fixed frequencies indicate that source location in large plates

can be significantly enhanced by use of WT results compared to that possible with fixed thresholds and an assumed constant group velocity.

- Since the amount of energy in a particular mode depends on the source depth, it will be necessary to first select the mode with the dominant energy in each AE signal. Then WT-based arrival times of the maximum WT magnitude of the experimental AE signals can be obtained from that mode at a selected frequency.
- In experimental situations, carefully applied pencil-lead breaks can be used to determine the key frequency to use for each dominant mode. Then only the WT-based arrival times and peak magnitudes at these frequencies need to be extracted. The source location can then be directly calculated from the arrival times for the mode with the dominant peak magnitude. The group velocity for the calculation could be taken from dispersion curves for the selected mode and frequency or from a WT-based group velocity obtained during pre-experiments with careful pencil lead breaks.
- The technique for extraction of WT-based arrival times corresponding to a single group velocity was found to be applicable for both wideband and narrow-band signals.
- In the wideband case, the extraction of single-velocity arrival times was found to be robust in the presence of electronic noise even for signal-to-noise ratios as low as 1:1.

B. Source Location–Small Coupon Specimens

- The inherent multiple side-edge reflections present in small-coupon specimens complicate the use of the WT for the purpose of obtaining accurate source locations.

Acknowledgement

This work was partially supported by NASA Langley.

References

H. Cho, S. Ogawa and M. Takemoto, "Non-contact Laser Ultrasonics for Detecting Subsurface Lateral Defects", *NDT and E International*, **29**-5, 1996, 301-306.

Hayashi et al., 1999

M. R. Gorman, "Plate Wave Acoustic Emission", *Journal of the Acoustic Society of America*, **90** (1), 1990, 358-364.

M. A. Hamstad, "On Determination of Arrival Times for Acoustic Emission Source Location in Composites", *Proceedings AECM-2*, Society of the Plastics Industry, New York, New York, 1986, pp. 202-208.

M. A. Hamstad, A. O’Gallagher and J. Gary, "Examination of the Application of a Wavelet Transform to Acoustic Emission Signals: Part 1. Source Identification", *Journal of Acoustic Emission*, **20**, 2002, 39-61. (preceding paper)

M. A. Hamstad and K. S. Downs, "On Characterization and Location of Acoustic Emission Sources in Real Size Composite Structures – A Waveform Study", *Journal of Acoustic Emission*, **13**, No. 1–2, 1995, 31-41.

Yasuhisa Hayashi, Shingo Ogawa, Hideo Cho and Mikio Takemoto, "Non-contact estimation of thickness and elastic properties of metallic foils by the wavelet transform of laser-generated Lamb waves", *NDT and E International*, **32-1**, 1999, 21-27.

Hyunjo Jeong and Young-Su Jang, "Fracture Source Location in Thin Plates Using the Wavelet Transform of Dispersive Waves", *IEEE Transactions on Ultrasonics, Ferroelectrics and Frequency Control*, **47-3**, 2000, 612-619.

O.Y. Kwon and Y.C. Joo, "Source Location in Plates by Using Wavelet Transform of AE Signals", *Journal of Acoustic Emission*, **18**, 2000, S212-221.

M. Takemoto, H. Nishino and K. Ono, "Wavelet Transform - Applications to AE Signal Analysis", *Acoustic Emission - Beyond the Millennium*, Elsevier, 2000, pp. 35-56.

H. Yamada, Y. Mizutani, H. Nishino, M. Takemoto and K. Ono, "Lamb Wave Source Location of Impact on Anisotropic Plates", *Journal of Acoustic Emission*, **18**, 2000, 51-60.

Steven M. Ziola and Michael R. Gorman, "Acoustic Emission Source Location in Thin Plates Using Crosscorrelation", *Proceedings AECM-4*, The American Society for Nondestructive Testing Inc., Columbus, OH, 1992, pp. 411-417.

DIAGNOSTICS OF REINFORCED CONCRETE BRIDGES BY ACOUSTIC EMISSION

LESZEK GOLASKI¹, PAWEŁ GEBSKI¹ and KANJI ONO²

¹ Kielce University of Technology, Kielce, Poland

² University of California, Los Angeles, California 90095-1595 USA

Keywords: acoustic emission, concrete structures, damage monitoring

Abstract

Our work on concrete bridges will be reported. We found that AE is the most suitable method for the purpose of old bridge inspection and further development effort was conducted. This culminated in a draft document, "Recommended Practice for Testing Reinforced and Pre-stressed Concrete Structures by Acoustic Emission" (RP), following the lead of documents of a similar nature in Japan and in Texas. We will report here selectively the test results of five full-scale bridges following the procedures we have proposed. These bridges were of different types of construction: reinforced concrete, pre-stressed concrete (post-tensioned and pre-tensioned) and combined concrete-steel construction. These justified the basic principles of RP, but also demonstrated needs of individual modification fitting the structures and testing conditions.

Introduction

Extensive acoustic emission (AE) studies of concrete structures have been reported [1-5]. However, most concrete bridges and other structures are still inspected using traditional methods. In Poland, there are about 30,000 concrete bridges, many of which were built over 30 years ago. These structures have sustained various degrees of damage and their continued usage requires maintenance and renovation. We need a method to select the bridges that must be renovated urgently, but conventional testing methods for concrete structures do not provide the full information about the severity of defects. With the support of the Polish construction industry and the administrators of highways and bridges, we have embarked on developing a procedure that can be applied for testing a large number of bridges.

"Recommended Practice" documents for concrete structures have appeared in Japan [6] and from Texas Department of Transportation [7]. We have prepared a similar document for use in Poland and conducted some tests according to the procedures proposed. These bridges tested were of different types of construction: reinforced concrete, pre-stressed concrete (post- and pre-tensioned) and combined concrete-steel construction. Selected results will be given here.

Philosophy of Testing Concrete Bridges By Acoustic Emission

Before any reliable tests on bridges could be done, it was necessary to perform a series of measurements on model elements and full-scale structures under controlled loading condition. Testing elements in a laboratory enable us to learn more about the features of the observed phenomenon. It also gives important information concerning the setup of the testing equipment. The research was performed following the scheme shown in Fig. 1. We have utilized a standard 12-channel PAC MISTRAS system for AE data acquisition and analysis.

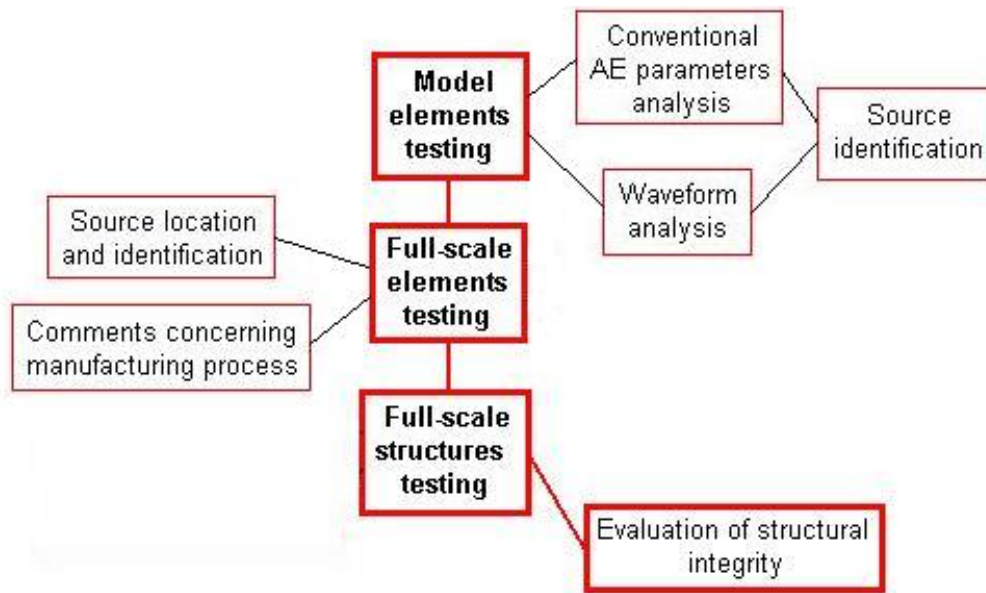


Fig. 1. Philosophy of testing concrete bridges by AE.

Model structural element testing by AE is well recognized (especially for reinforced concrete beams). Test results have been published in a number of papers [e.g., 5] and results of our tests are in general agreement. However, the results obtained during model testing cannot be directly moved to *in situ* monitoring.

The model tests generated useful information about the wave propagation and attenuation in concrete, which was helpful for setting up the measuring equipment. The attenuation has a critical influence on the values of AE signal parameters: amplitude, duration and energy (or MARSE¹), which are the most important in evaluating the damage severity of structure [6, 7]. The attenuation depends on tested concrete structures. For example, in pre-stressed concrete elements, the attenuation of AE signals is relatively low (2~3 dB/m at 55 kHz), while in old concrete or concrete containing numerous tiny cracks or porosity, severe attenuation (greater than 10 dB/m) essentially limits AE wave propagation. Therefore, the sensor placement scheme must be designed individually for each of the tested structures or elements. For most structures, we selected zonal location and zonal analysis of AE signals. The tested element (beam, slab, etc.) shall be divided in zones and AE signals from each zone are recorded by one sensor. In the RP, it is specified that the attenuation within each zone must be precisely determined and must not exceed 10 dB in amplitude. This assures adequate coverage of the structure under test in evaluating the integrity of the monitored structure. It also enables us to compare results obtained from different tests. In addition, planar or volume locations are recommended when AE sources are located in the vicinity of a known damage.

In the present RP, the following four AE parameters, the number of AE events, energy of AE signals, duration and amplitude, are taken into consideration in damage evaluation of concrete structures. If any of those parameters significantly exceeds the threshold value, more careful inspection is required. Furthermore, in this procedure, multi-parameter analysis of these AE features is performed. It is also recommended to compare the results for the test structure with results from previously performed tests on similar objects and other information, such as damage

¹ MARSE – Measured Area of the Rectified Signal Envelope

identified post-test. This analysis procedure depends on the tested structure and testing conditions. Thus, it is important to accumulate the database of differently constructed bridges or structures in properly assessing the integrity of the tested structure.

Another important problem in the RP is the AE sensor selection for RC testing. For this purpose, we have selected two types of DECI AE sensors for these tests: resonant sensors with the center frequency of 55 and 150 kHz. However, it has been noticed that AE signals acquired from different structures vary significantly, and depend as well on type of cracking, type of reinforcement and parameters of concrete. Wide-band sensors are currently used rarely due to the low sensitivity (and additional background noise recorded, which are not caused by damage propagation), but using resonant sensors of a particular frequency may result in losing some important signals. In such cases, a solution is to perform an initial AE measurement on similar concrete beams or bridge monitoring during service using wideband sensors, choosing the suitable resonant frequency of test sensors.

Care should be taken when new pre-stressed prefabricated beams or structures are examined. These beams exhibit significantly higher AE activity, which diminish over time. During the period of high AE activities, which typically last about 1 month, these should not be included in AE tests of structures. In addition it is recommended to compare the AE signals during bridge testing with those generated during destructive tests of full-scale beams of similar construction. Starting at the beginning of year 2003 the AE characteristics of selected pre-stressed beams (one beam taken from each series) will be provided.

We decided to give special emphasis to the full-scale element testing, namely (12 and 18-meters-long) pre-stressed concrete beams loaded on stands up to fracture under smooth and repeated loading. Pictures of these tests are shown in Fig. 2. During loading the parameters of AE signals were analyzed and compared with other parameters such as: crack appearance, deflection and strain, in order to obtain the full range of failure processes that occur in the tested beams.



Fig. 2. Left: Pre-stressed beam (type KUJAN), Right: AE sensor attached to the bottom surface.

As expected, the features of conventional parameters of AE signals depend on the load applied (as a consequence of changes in integrity of tested element). Hits rate, values of amplitude, energy and duration increased while load was raised. However, because of the large scale of the element, it was impossible to assign each acquired signal to the particular crack occurred. Due to this difficulty, a different method of data analysis had to be developed; namely,

a zonal location was used. Each of the tested pre-stressed beams was divided in 10 measuring areas (10 sensors were used). The structural integrity together with the intensity of AE was analyzed separately for each area. The tested beams were loaded in 4-point-bending. This scheme of loading means that in the middle part (1/3 of the beam's length) the tensile stress had the highest value. Those measuring areas were inspected more carefully (both by AE and visually). The analysis of only conventional AE parameters could provide qualitative results. To evaluate the load capacity or the level of deterioration more precisely, the quantitative analysis is necessary. We suggest examining the intensity (based on historic index and severity) as a measure of deterioration. In order to calculate the intensity of an emission source, the historic index and severity must be calculated on data taken during the loading. To determinate the intensity, the maximum historic index (HI) and severity values are plotted on a chart.

Historic index is a measure of the changes in Signal Strength throughout the test, defined by

$$H(t) = \frac{N}{N - K} \frac{\sum_{i=K+1}^N S_{O_i}}{\sum_{i=1}^N S_{O_i}}$$

where $H(t)$ is the historic index at time t , N is the number of hits up to and including time t , S_{O_i} is the signal strength of the i -th event, and K is an empirically derived factor that varies with the number of hits. For $N < 50$, $K = 0$; for $50 \leq N < 200$, $K = N - 30$; for $201 \leq N < 500$, $K = 0.85N$; and for $501 \leq N \leq 2000$, $K = N - 35$ [8]. The second parameter used for this analysis is known as severity (S_r) and is defined as the average signal strength for the 50 events having the largest numerical value of signal strength and is defined by the following equation:

$$S_r = \frac{1}{50} \sum_{i=1}^{i=50} S_{O_i}$$

where S_r is severity and S_{O_i} is the signal strength of the i -th event as above. CARP first introduced this procedure for damage evaluation in large laminated structures such as FRP tanks and pipelines [8].

Intensity for different level of loading was analyzed. Although all the intensity parameters and curves were experimentally derived for composite materials, our experiments show that they may be applied for concrete structures as well. Surely, the more accurate evaluation based on those criteria requires performing much more research. The intensity curves must be corrected in order to provide absolutely reliable results. In Fig. 3 intensity for selected channels is shown (historic index on horizontal axis and severity on vertical axis) for different levels of loading.

The applied gradation scale and the boundary values of severity and historic index were the same as given by Fowler [8]. The general descriptions of the plotted zones are as follows:

- A – minor emission, not for further reference,
- B – “small” defect,
- C – significant defect, further evaluation required,
- D, E – major defect, immediate shutdown and follow-up nondestructive examination needed.

Each dot plotted in Fig. 3 represents a group of measuring zones producing AE signals characterized by the similar features. As shown in these graphs, at the early stages of loading, signals recorded by all sensors are graded as A (up to 40% of the failure load), which means no

serious deterioration within monitored zones. For this loading, no cracks were observed. The analysis shows that as the load exceeds 60% of the beam loading capacity, intensity plots are placed in area B, that means that small scale cracking took place and indeed a number of tiny cracks were observed. The last graph shows the intensity at failure, which took place in compres-

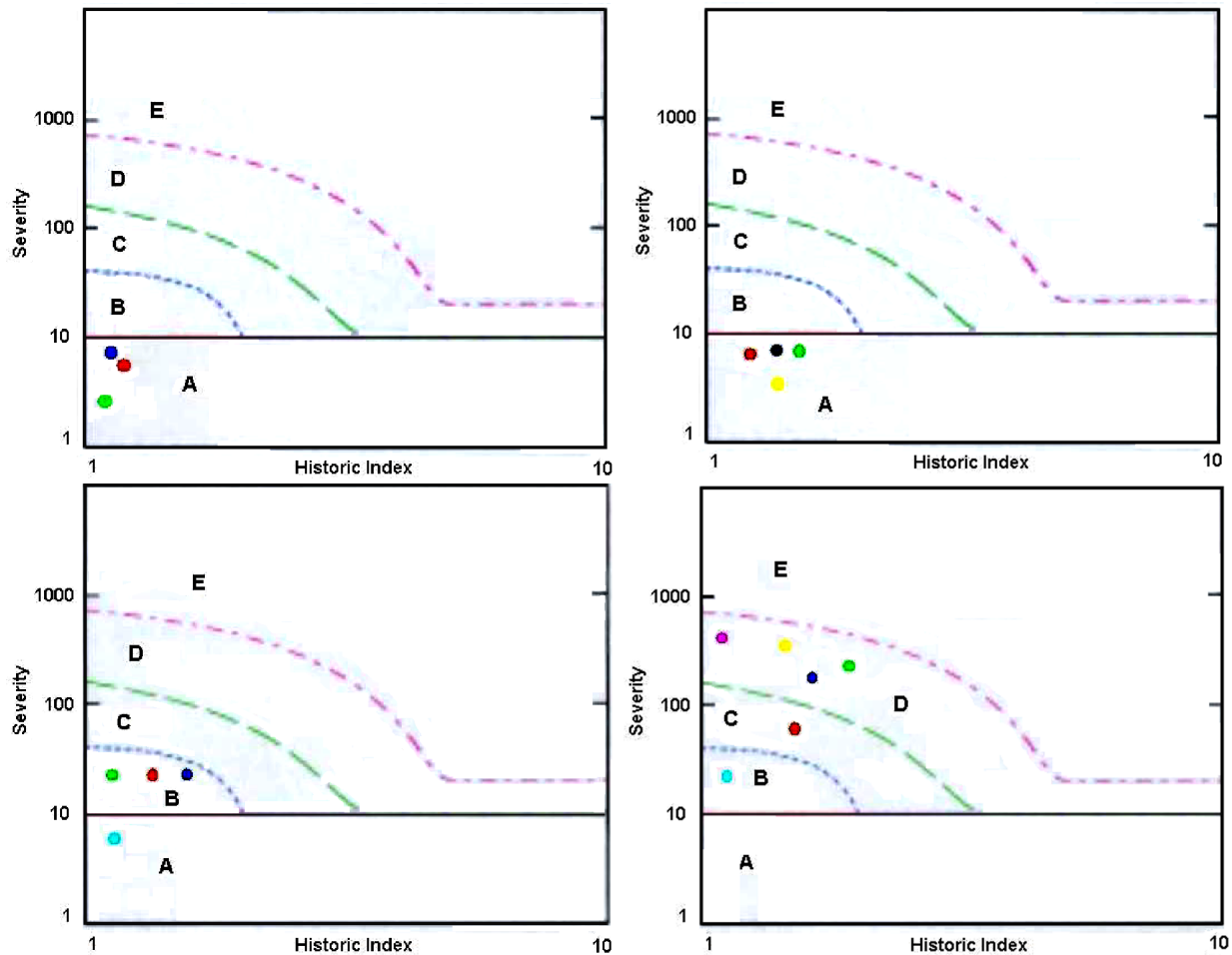


Fig. 3. Intensity plots for different stages of loading: 25% of failure load (upper left), 40% of failure load (upper right), 60% of failure load (lower left), failure load (lower right). Different colored dots indicate different measuring zones or sensor positions.

sion zone, where no reinforcement was situated. However, at the side surfaces, the tensile crack could be seen. No fracture of reinforcing wires was observed.

The method of data analysis, which was described above, is a new way in the field of full-scale concrete elements or structures evaluating by AE [7]. The zonal analysis and calculating of historic index together with severity is the only method that provides results based on quantitative criteria. It was used for evaluating the integrity of five bridges in Poland.

Examples of Reinforced Concrete Bridges Tested by AE

Acoustic emission method enables the testing of the structural integrity of concrete bridges in following cases:

- under regular traffic,
- under nominal moving load (dynamic),
- under nominal stationary load (static),
- special cases (during overloading).

The basic tests are performed during regular traffic. This approach does not require closing the bridges and does not cause any traffic problems. If the bridge is graded as A or B class (using Fowler's scale), no further examination is needed. In other cases the bridges are monitored under nominal loading (static and dynamic). A different procedure is required in special cases, for example during overloading. Such type of AE monitoring is also described below. While testing new bridges (before regular traffic is applied), the examination under nominal loading only is performed.

A. New bridge built of pre-stressed beams.

One of the first bridges in Poland that was tested by AE was a new pre-stressed bridge shown in figure 4. This was a 2 span structure built of 30 pre-stressed beams – type KUJAN. Beams of the same type were examined by acoustic emission in a laboratory up to fracture. The bridge was loaded in two modes (dynamic and static) by two heavy trucks (the load was equal to the nominal capacity of this structure). As expected, the new bridge did not show any signs of damage. During this AE monitoring, the bridge was loaded for the first time and this was the reason of some initial friction, which produced AE signals at the supports typical for new structures. This emission diminished during the following stages of loading.



Fig. 4. New pre-stressed bridge tested by AE.

The main purpose of these AE measurements was to get the initial AE features of the structure. In the future the periodical tests will be performed. The results of all those tests will be compared and in this way the deterioration of the bridge will be evaluated.

The results obtained from the bridge are similar to those acquired during the early stages of loading of the pre-stressed beams. Both the conventional AE parameters and intensity (Fig. 5) (based on severity and historic index) were determined. Again, the zonal location was applied and each dot plotted in Fig. 5 represents a group of zones producing AE signals characterized by the similar features. As shown, AE signals recorded by all sensors were graded as A, which means no damage or a minor one.

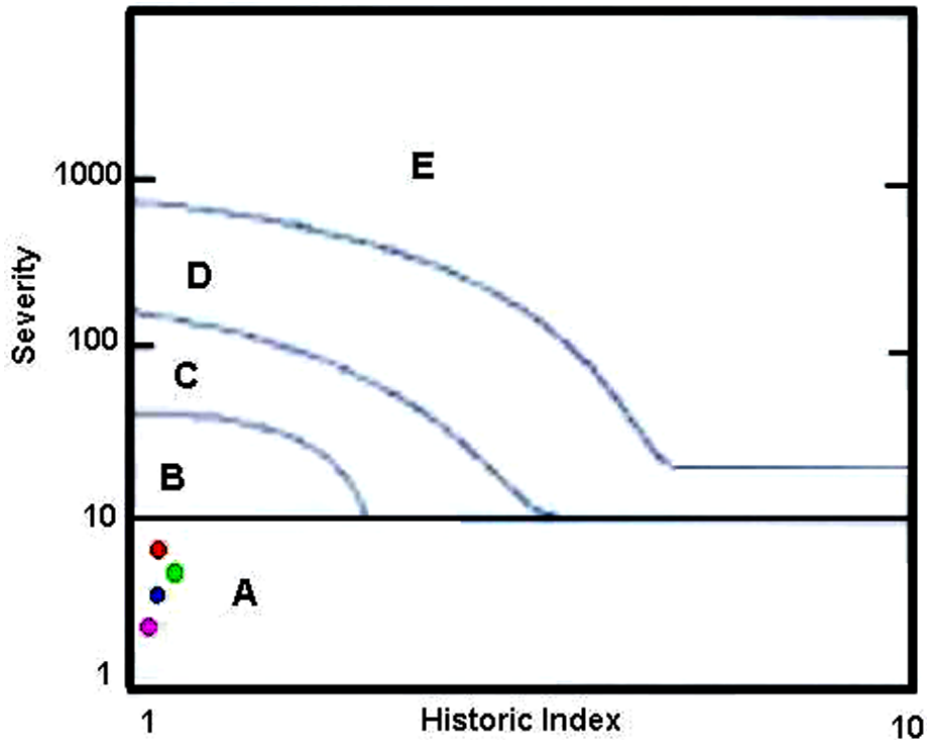


Fig. 5. Intensity parameter for tested bridge.

The testing of a new object became surprisingly one of the most often performed *in situ* tests in Poland. Many investors and supervisors see a great need for evaluation of the quality of engineering structures and the initial damage level of the structure. For a bridge that was graded as A-intensity, a so-called “AE Certificate” is provided.

B. Severely Damaged Bridge Built of Post-tensioned Beams.

This AE measurement was intended to evaluate the damage of a bridge before repairing (shown in Fig. 6) during loading. This bridge deteriorated severely and was selected for repair. The visual inspection revealed: a) uncovered reinforcement, b) corrosion of the reinforcing cables, c) corrosion of concrete, d) cracks in concrete. Those damages are shown in Fig. 7.

During field AE examination, the bridge was loaded by two heavy trucks placed closely to each other (15 tons each – 30 t was the nominal loading capacity for this bridge). The structure was subjected to two loading modes: dynamic and static. During the dynamic loading, the trucks passed the bridge with the speed of 0.5 km/h, while during static loading the trucks were placed at the center of the span in order to cause the highest stress in tested beams. To record AE activities, 12 resonant (55 kHz) AE sensors were attached to the bottom surface of one of the beams and zonal location was applied. The length of the beams was equal to 14.85 m. The sensor spacing was 1.25 m.



Fig. 6. Monitored bridge built of post-tensioned beams.



Fig. 7. Existing damages of the tested bridge.

Because of numerous visible damages, a large number of AE hits was expected during the bridge loading. The purpose of this AE test was to identify the active damage (propagating throughout the test) and their location of the most damaged zones. Using zonal location mode does not require determining precisely the velocity of stress wave propagating in the tested element. Direct source location would be very difficult especially in old fractured concrete elements.

Results of AE activity recorded only for one of tested beams will be presented. AE from the second beam did not indicate any active damage that would be detrimental for the structural integrity of the beam. Due to this the description of those results has been omitted.

Results of AE activity during dynamic loading.

In Table 1, the number of hits and the maximum values of AE signal parameters that were recorded by the channels during a dynamic loading are given. The other channels recorded no hits.

Table 1. Number of hits and maximum values of AE signal parameters during dynamic loading.

AE sensor number	Number of Hits	Amplitude [dB]	Energy	Duration [μ s]	Rise Time [μ s]	Counts
3	79	55	20	1300	346	24
9	1	42	1	32	10	2
11	38	55	7	828	141	20
12	1	50	27	1958	369	56

Relatively weak AE activity indicates that there is no danger for the structural integrity of this beam under applied loading conditions. No AE signals were produced in the middle part of the beam, although that part received the highest stress. All the acquired signals are characterized by low amplitude (not greater than 55 dB), low energy, and relatively short duration.

The graphs of AE parameters (number of hits rate, amplitude, energy and duration) vs. time, given in Fig. 8a and Fig. 8b, indicate that AE activity took place when the trucks were passing through the middle part of the beam. However, during the following passes the level of AE did not increase. The surface of beam in zones 3 and 11, where most of AE events were recorded, were visually examined in detail and no cracks were observed. This suggests the friction between concrete and uncovered reinforcing cables under the heavy loading was the main sources of recorded emission.

Results of AE measurements under static loading.

The second stage of this AE examination consisted in measuring AE produced within the beam under static loading. Two heavy trucks were positioned over the tested beam, and then AE processor was switched on. After two minutes, it started to record AE activities. Almost all AE signals were recorded on channel 4, meaning that these were produced within the zone about 4 m from the supported end of the beam. A very intensive AE activity was observed at the beginning of the third minute of the test and it has been clearly shown in Energy vs. Time and Duration vs. Time plots in Fig. 9. Duration of some of the recorded signals amounted to 500 ms. Although strong AE observation clearly indicates the development of active damage, the loading has not been stopped because the signals' amplitude did not exceed 80 dB at first. In later part of the test, such high amplitude signals were observed. The loading was removed when the number of strong AE hits (>80 dB) exceeding a critical value (derived experimentally). Channels 3, 9, 11 and 12 recorded only one or two AE hits throughout the test. In Table 2, the number of hits and maximum values of their parameters are given. The other channels recorded no hits.

Table 2. Number of hits and maximum values of AE signal parameters during dynamic loading.

AE sensor's number	Number of Hits	Amplitude [dB]	Energy	Duration [μ s]	Rise Time [μ s]	Counts
3	1	45	1	30	4	1
4	70950	85	11250	500000	1600	17200
9	2	45	10	1310	80	11
11	2	73	200	3200	290	100
12	1	45	9	1090	700	200

The increase of the AE hits at sensor 4 recorded under the constant loading indicated the serious damages were taking place in the vicinity of sensor 4. Visual examination of beam surface in zone 4 did not reveal new cracks. Therefore, it was suggested that this emission must have been caused by sources located in concrete-reinforcement interface. It was concluded that the bridge has to be repaired (by constructing a continuous slab for all three spans) or reinforced.

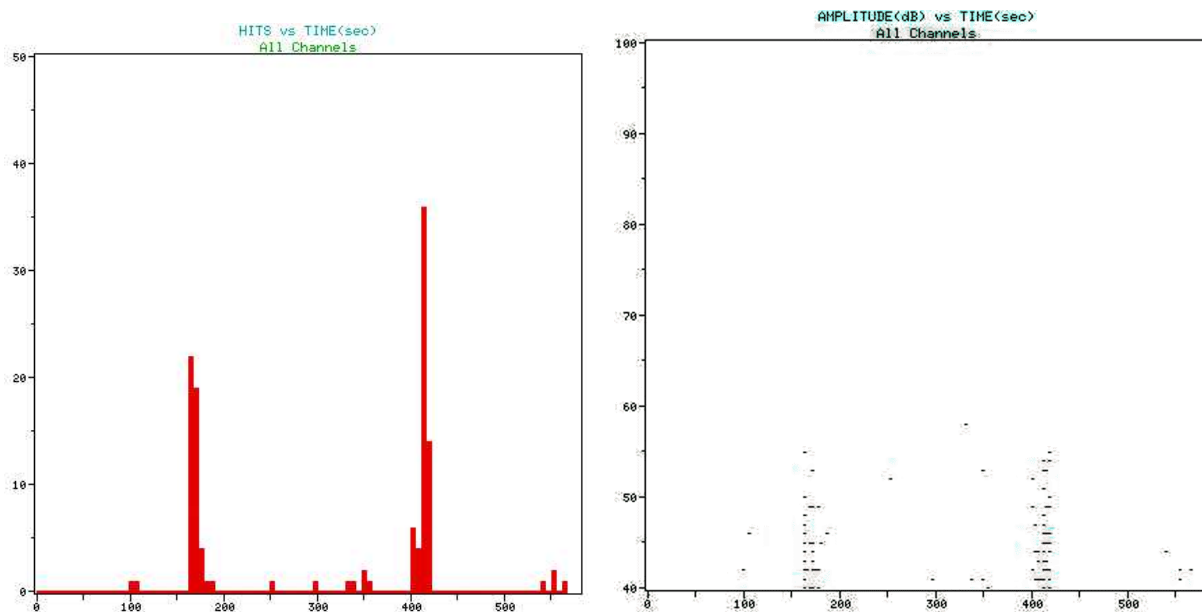


Fig. 8a. AE parameters (hits rate, amplitude) vs. time during dynamic loading.

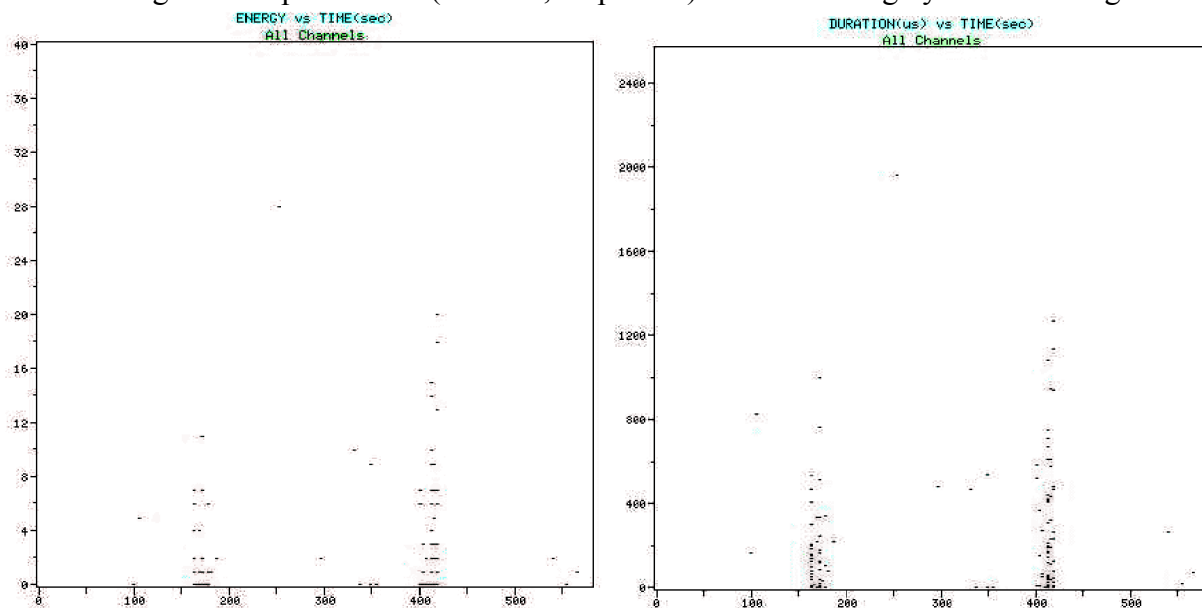


Fig. 8b. AE parameters (energy, duration) vs. time during dynamic loading.

In rare cases, it is relatively easy to evaluate the structural integrity of the examined structure. In this particular case, the real-time analysis of AE parameters described here clearly indicated a serious damage in one girder. However, more often, only a multi-parameter analysis enables the final reliable evaluation. The important conclusion to note from this test is that the dynamic loading did not reveal any serious defects that were detected under static loading.

The same bridge was tested after it was repaired. The design of repair was prepared following our suggestions. Next, selected beams were tested by AE (the same beams as previously). The purpose of this action was to compare the parameters of AE signals obtained from a damaged bridge and a renovated one. As expected, the multi-parameter analysis of acquired data did not indicate any active damage. This example shows the potential of using AE as a method for testing the quality of repair. This advantage of AE will be developed in cooperation with Polish Management of Highways and Bridges.

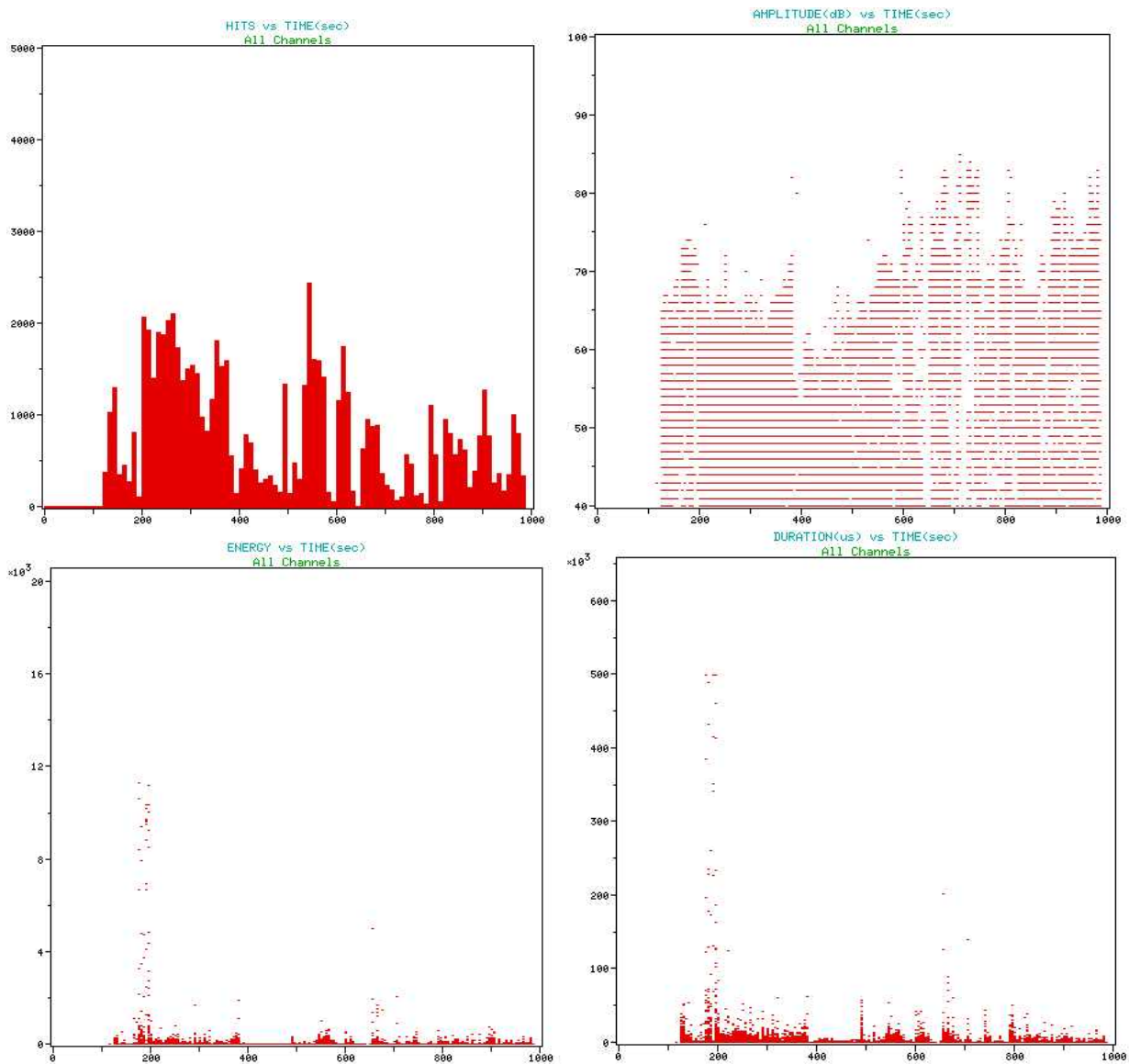


Fig. 9. AE parameters (Hits rate, Amplitude, Energy, Duration) vs. time during static loading.

C. An old viaduct built of pre-stressed concrete beams.

Some results obtained during the monitoring of a pre-stressed concrete viaduct together with the evaluation criteria are given. On this viaduct, several pre-stressed concrete beams (17.5-meters-long) were chosen for testing by AE technique. The examination was performed under the loading from regular traffic. Resonant sensors (frequency = 55 kHz) were used. After preliminary measurements (concerning the attenuation of produced stress waves), it was decided that the sensors should be placed at the bottom surface of a tested beam. The distance between the neighboring sensors was equal to 145 cm. Zonal location was performed.

The main goals of these measurements was to select beams that need to be removed (if there are any) and to indicate seriously damaged zones of the beams. To achieve these goals, each beam was divided in 12 measuring zones (145 cm long) according to the scheme of sensors' placement. The conventional AE parameters (Amplitude, Duration and Energy) together with Signal Strength were recorded. In Fig. 10, Amplitude vs. Time point plot is shown for 12 sensors (for one beam only). It can be seen that only channel-2 signals exceeded the value of 70 dB.

Other conventional AE parameters were higher in this zone as well. However, the number of hits and the values of its parameters were higher on channels 4, 7, 8 and 10 than on others. It was decided that the best solution for evaluating the structural integrity is to use a “comparative criterion”. This method is based on comparing values of AE parameters acquired on individual independent channel with the mean values of those parameters form all channels. Based on those criteria, the measuring areas were divided in three types described as:

- low (or zero) AE intensity,
- medium AE intensity (comparable with the medium value),
- high AE intensity (greater than double mean value).

In Fig. 11, these areas for one of the tested beams are shown. These areas correspond with the plots shown in Fig. 10. The final evaluation of the tested structure proved the usefulness of the criteria described in the RP. This shows that preparing and using the RP was a successful attempt of applying AE results obtained in laboratory to practical cases. In addition, for selected channels, Historic Index (HI) was analyzed. It was assumed [7] that HI value exceeding 1.85 indicates the presence of active damage in pre-stressed concrete beams. However, the analysis of this HI parameter does not always provide proper and reliable results in our tests and much work remains to be done to derive the universal coefficients that allow the use of Historic Index for reinforced concrete girders. Such experiments are currently performed at Kielce University of Technology. For the examined structure, the value of HI did not exceed 1.85 for any zone.

It was noticed, that for some structures (especially the seriously deteriorated ones) the stress-wave’s velocity and attenuation might be good and reliable criteria for evaluating the level of damage of concrete. It is well recognized that the higher the level of deterioration is, the stronger attenuation of AE signals is observed. It is also known that, in new concrete structures or elements, the velocity of AE signals is much higher that in seriously damaged ones. The aspects listed above are very helpful during the initial *in-situ* selection of the most damaged zones.

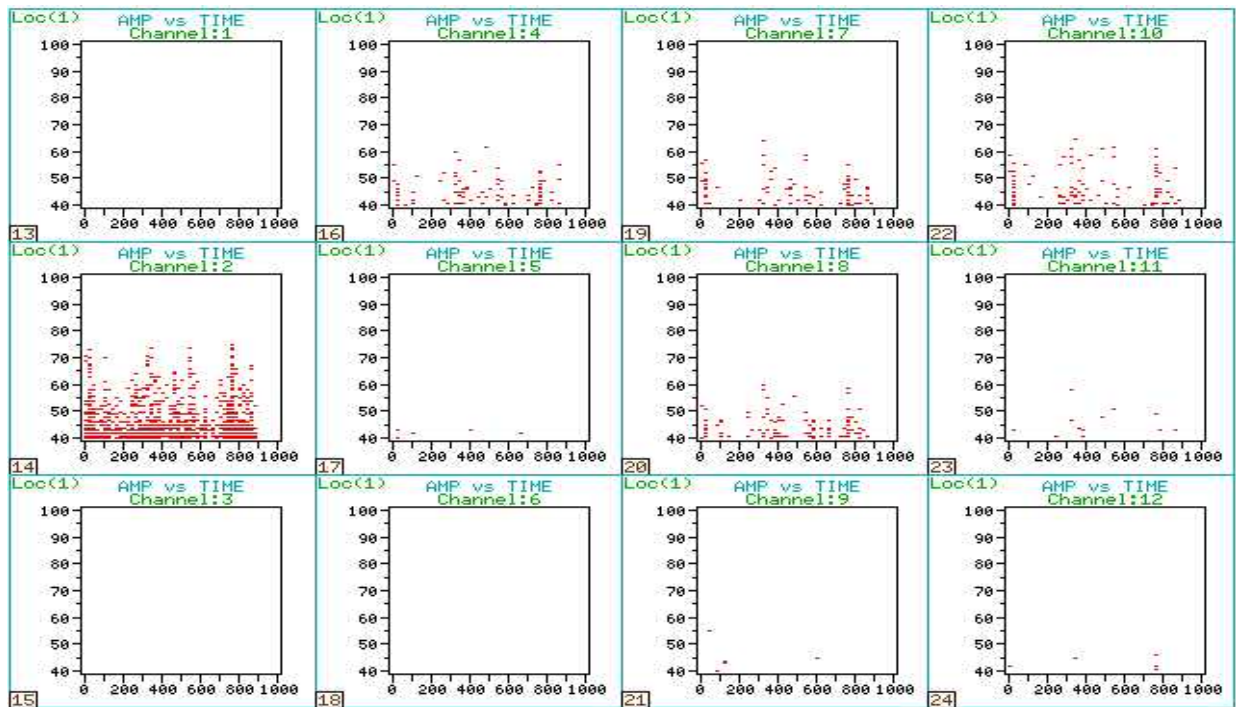


Fig. 10. Amplitude vs. Time point plot.

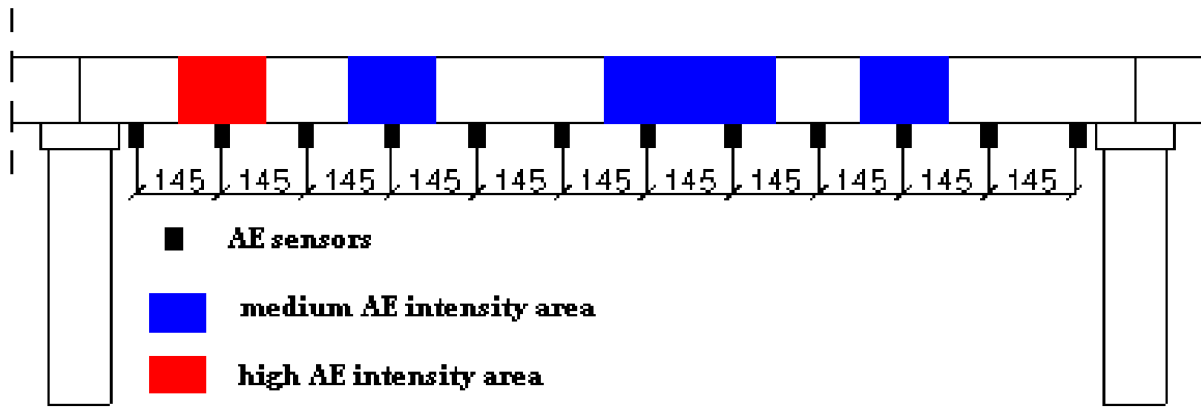


Fig. 11. Measuring areas with different level of AE intensity.

As mentioned above, AE parameters strongly depend on the type of structure and the loading mode. Using “comparative criteria” of evaluation gives very good results and is probably the most reliable method of evaluation. For this particular structure, based on the selected criteria, the monitoring of selected zones under nominal loading was suggested in order to provide the final evaluation.

D. Monitoring of a reinforced concrete bridge during overloading.

A small reinforced concrete bridge was monitored during overloading. The pictures taken during this measurement are shown in Fig. 12.

The purpose of this test was to monitor the behavior of the bridge during transportation of a heavy electrical transformer (470 tons) transported on two trailers. The monitoring was divided in two stages: passing of the truck together with the first trailer and passing of the second trailer. The number of hits and hits rate obtained during this transportation is shown in Fig. 13. It can be seen that during both stages, the intensity of AE was similar. It means that there was no damage caused by the heavy load.

It should be mentioned that AE was also recorded before and after the transportation under regular traffic. The comparison of the results obtained during those measurements also did not suggest any new damage. The evaluation based on AE was then confirmed by analyzing another parameter: deflection.

The promising results of the first AE real-time monitoring had strong effects in the development of this method. In the near future the Polish Management of Highways and Bridges is going to use AE as a mandatory method for monitoring overloaded transports and selecting routes for them.

E. A New Steel-Concrete Bridge.

The main purpose of this test was to obtain the initial AE level of a new combined steel-concrete structure (shown in Fig. 14) in order to provide the “AE Certificate”. Selected areas of the reinforced concrete slab were tested under nominal loading equal to 30 tons. As expected, no damage was indicated. During the loading of the bridge, some emissions were recorded close to the supports and steel girders, but these were of low levels and in Grade A.



Fig. 12. Reinforced concrete bridge monitored during overloading.

During post-test analysis, intensity for each sensor was calculated. All measuring areas were classified with grade A, which means low emission and no damage.

Conclusion

Acoustic emission method is useful for the evaluation of the integrity of reinforced concrete structures. It can be successfully used for selecting bridges or their elements that need to be renovated or scrapped. However, for each type of structures, individual evaluation criteria must be selected. This requires performing model tests of reinforced and pre-stressed concrete beams in different loading modes. In laboratory, it is possible to compare AE parameters with other physical parameters such as: width of cracks, deflection and strain. The combined analysis of these values gives a comprehensive view of processes occurring in tested elements and allows the use of AE method for *in situ* structure testing. We strongly believe that, in the near future, the owners of bridges and bridge industry in Poland will accept the „Recommended Practice for Testing Reinforced and Pre-stressed Concrete Structures by Acoustic Emission”.

In many reports, the Felicity Ratio (FR) is recommended as a useful criterion. Although it gives good results in laboratory tests, it cannot be used for evaluating *in situ* structures. The main disadvantage of using FR for evaluating full-scale structures is the requirement of an accurate

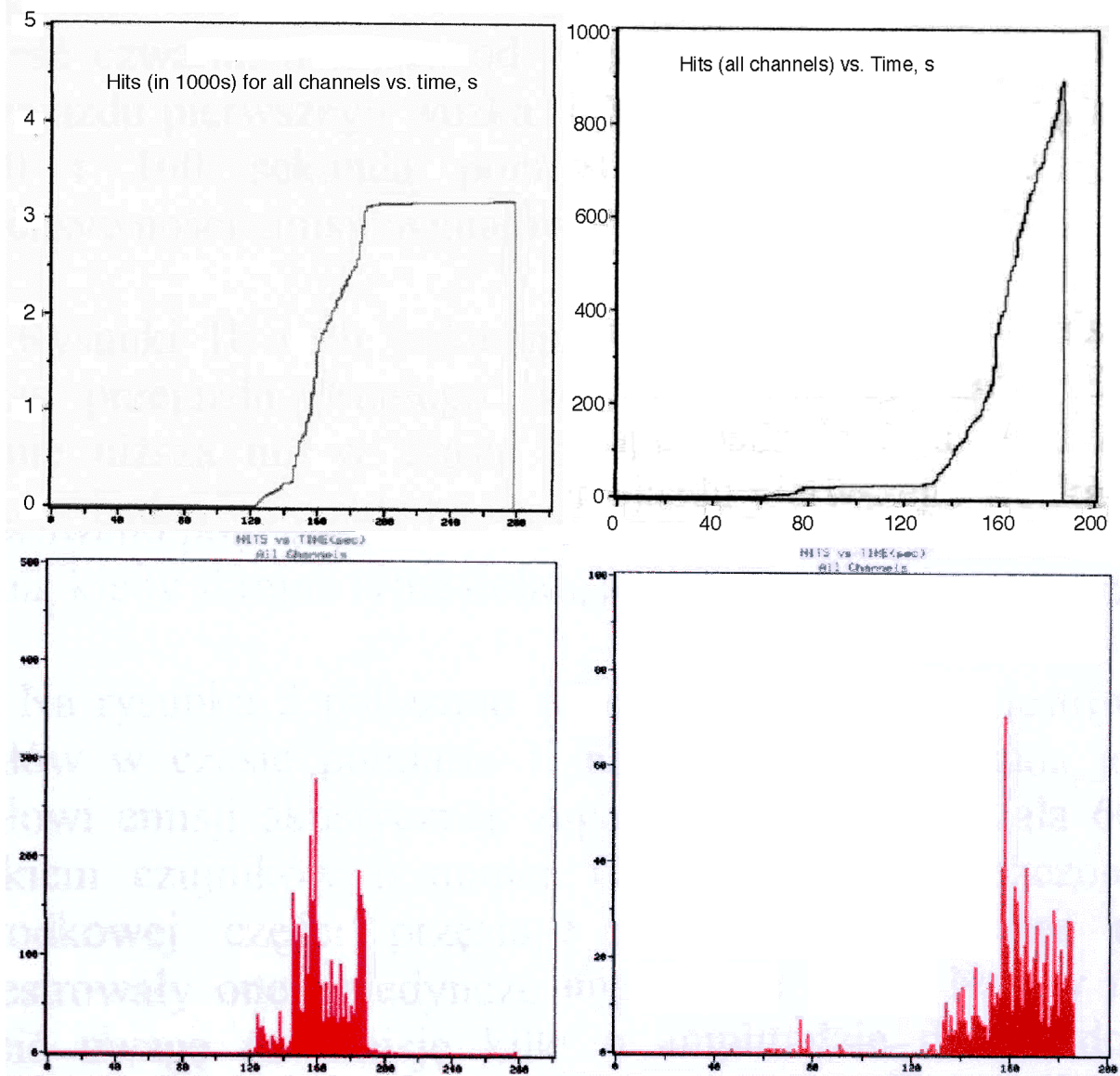


Fig. 13. AE hits and hit rates: First stage of transportation – on the left,
Second stage of transportation – on the right.

control of loading. This is impossible in practice while testing existing objects in regular traffic. Possible inaccuracies that may occur make this method useless.

We need to perform AE examination for each different type of reinforced and pre-stressed beams, which are currently used in full-scale structures. Collecting their acoustic emission characteristics will be useful in evaluating AE data recorded during bridge monitoring. Such an archive for beam designs used in Poland is currently being prepared at Kielce University of Technology and will be assessable for our partners in this cooperative effort. A series of new bridges will be tested as well in order to estimate their level of damage during subsequent periodic monitoring.



Fig. 14. New steel-concrete bridge tested by AE.

References

1. M. Ohtsu, "Acoustic Emission Characteristics in Concrete and Diagnostic Applications", *J. of Acoustic Emission* **6**, 99, 1987.
2. C. U. Grosse, B. Weiler and H. W. Reinhardt, "Relative Moment Tensor Inversion Applied to Concrete Fracture Tests", *J. of Acoustic Emission*, **14**, S74-S87, 1996,
3. K. Matsuyama, T. Fujiwara, A. Ishibashi and M. Ohtsu, "Field Application of Acoustic Emission for the Diagnosis of Structural Deterioration of Concrete", *J. of Acoustic Emission*, **11**, S65-S73, 1993.
4. T. Bradshaw, K. Holford, P. Cole and A. Davies, "Ball bearing calibration of concrete structures using AE", *Proc. 25th European Conference on AE Testing*, Prague, Czech Republic, 2002, I/91.
5. S. Colombo, I. G. Main, M.C. Forde and J. Halliday "AE on bridges: experiments on concrete beams", *Proc. 25th European Conference on AE Testing*, Prague, Czech Republic, 2002. I/127.
6. S. Yuyama, T. Okamoto, M. Shigeishi, M. Ohtsu and T. Kishi, "A Proposed Standard for Evaluating Structural Integrity of Reinforced Concrete Beams by AE", ASTM-STP 1353, ASTM, West Conshohocken, PA, 1999; pp. 25-40.
7. Texas Department of Transportation "Procedure for Acoustic Emission Monitoring of Prestressed Concrete Girders", 2001. (*J. of Acoustic Emission*, volume 19 CD-ROM)
8. T. J. Fowler, J. A. Blessing and P. J. Conlisk, "New Directions in Testing", *Proc. 3rd International Symposium on AE from Composite Materials*, Paris, France, 1989.

ANALYSIS AND IDENTIFICATION OF ACOUSTIC EMISSION FROM DAMAGE AND INTERNAL FRETTING IN ADVANCED COMPOSITES UNDER FATIGUE

YURIS DZENIS and JIE QIAN

Department of Engineering Mechanics, University of Nebraska-Lincoln, Lincoln, NE 68588

Abstract

Acoustic emission (AE) from advanced composites under fatigue is addressed in this paper. It is well known that composites subjected to cyclic fatigue loading exhibit gradual damage accumulation to failure. Acoustic emission analysis can be applied, in general, to characterize and quantify the damage evolution process. However, under fatigue loading, substantial AE in composites can be due to internal fretting. This emission is generated by crack face fretting and similar mechanisms and its amount can be large enough to obscure useful information on damage development in the overall AE histories. It is important to be able to recognize and eliminate this emission in order to apply the AE method to fundamental fatigue damage analysis of composites. In this paper, acoustic emission from low-cycle tension-tension fatigue of a quasi-isotropic graphite-epoxy composite laminate was analyzed. The overall AE was separated into the emission from loading and unloading. The AE count, location, and load histories, and the load range distributions were generated and analyzed. The emission from the higher and lower load levels during loading and unloading was studied. It was concluded that the AE from the higher load levels during both loading and unloading was mostly from the new damage events. In contrast, the emission from the lower load levels during unloading was attributed to internal fretting. The amount of this emission comprised 13% of the overall AE for the composite studied. The origin of the emission from the lower load levels during loading could not be positively identified, based on the available data. The amount of this emission comprised 7% of the overall AE. The results provide insights on the AE behavior of composites under fatigue and can be used for the analysis of damage micromechanisms and life and for the development of predictive models.

Introduction

It is well known that advanced composite materials subjected to loads exhibit gradual accumulation of damage of several types. These include matrix cracks, fiber breaks, fiber-matrix debonds, longitudinal splitting, and delaminations. Scattered damage development can be especially pronounced under fatigue. Experimental information on damage evolution in composites is needed for better understanding of micromechanisms of their fatigue failure and life and for the development of predictive models.

Acoustic emission has been shown to provide useful information on damage development under cyclic loading [1-9]. One problem with AE studies of fatigue damage in composites is the large amount of acoustic noise that can be generated by the testing machine and grips. In the previous studies, this noise has been reduced or eliminated by load gating [1, 8], amplitude discrimination [9], or location filtering [2, 3, 5]. The latter method, utilizing two or more AE sensors and the AE location analysis to filter out the emission originating outside of the designated acoustic gage zone (usually, part of the specimen between the sensors) is especially attractive as

it does not exclude any signals originating within the gage zone and, thus, prevents the loss of useful information on damage development.

Another, more complicated problem with the AE analysis of composites under fatigue is the emission from internal fretting [10]. It has been shown that friction or fretting between the faces of the previously developed cracks can produce substantial AE [2-5]. This emission can obscure useful information from the signals generated by the damage events. It is important to be able to recognize and separate the AE from damage and fretting in order to use the AE method for fundamental fatigue damage studies of composites.

Often, the AE signal parameters are being used to recognize the signals from different sources. It has been shown, however, that the amplitude of the fretting signals can exceed the amplitude of the signals from the new damage. It has been suggested [2, 3] that other AE parameters, such as the count number or signal duration, can be used to distinguish the signals from friction. However, the threshold values of these parameters, necessary for the parametric discrimination, are difficult to determine. Also, due to the inherent scatter of both fretting and damage events in composites, the ranges of the AE signal parameters for these two types of events can be expected to overlap.

A study of the AE from loading and unloading under fatigue can shed light on the emission from internal fretting and lead to the development of methods of its elimination. One would expect more new damage to be developed during loading and more fretting noise to be generated during unloading. The literature data on the AE from composites during fatigue loading and unloading is limited. The AE has been recorded during several cycles of the quasi-static loading-unloading with the increasing load amplitude in [10]. Eight to eleven load cycles have been applied to failure. Substantial AE observed during the unloading has been attributed to internal fretting. The absolute time scale of the acoustic and mechanical tests has been used to correlate the acoustic events with the load levels over the short time intervals (about three cycles) during the fatigue process [4]. Substantial AE has been observed in the unloading phase. Some of this emission has been attributed to the matrix cracking in compression. More detailed studies of the AE from loading and unloading are needed to produce additional information.

In this paper, such studies are conducted on an unnotched quasi-isotropic graphite-epoxy laminate subjected to low-cycle tension-tension fatigue loading. The overall AE is separated into the emission from loading and unloading by the loading phase filtering. The AE count, location, and load histories, and the load range distributions are generated and analyzed. The emission from the higher and lower load levels during loading and unloading is studied. Conclusions are drawn on the origin of the emission from different load phases and levels.

Experimental

Quasi-isotropic $[90/\pm 30]_{3S}$ laminated composite panel was manufactured from Hexcel T2G190/F263 graphite/epoxy prepreg following the manufacturer-recommended curing cycle. The panel was tabbed and the rectangular 200 x 25 mm specimens were machined by a high-speed diamond saw. Tension-tension fatigue testing was performed by an MTS testing machine retrofitted with a digital Instron test control and data acquisition system. The tests were load controlled, with the fatigue stress ratio of 0.1 and frequency of 0.5 Hz. The maximum loading was approximately 90% of the ultimate static strength for this composite.

The AE was acquired and analyzed by a two-channel Vallen AMS3 acoustic emission system. Two wide-band, high fidelity B1025 AE sensors by Digital Wave were used. The AE gage zone (the distance between the AE sensors) was 80 mm. The AE source location analysis was performed on the incoming signals and the signals originating outside of the acoustic gage zone were eliminated from the analysis. A 34.5 dB system gain and a 40.5 dB threshold (ref. 0 dB at 1 μ V) were used in the AE data acquisition. The load and strain data were fed from the testing machine and recorded as parameters.

Results and Discussion

Overall Acoustic Emission

Figure 1 shows the overall AE from a representative fatigue test. The specimen failed in the 432nd cycle of fatigue loading. Subplot 1 of Fig. 1 presents the history of the accumulated AE counts as a function of cycle number. Subplot 2 shows the distribution of the AE over the loading range. The AE location history is shown in subplot 3 and subplot 4 presents the AE load history. Each dot in the correlation-type subplots 3 and 4 corresponds to an AE event.

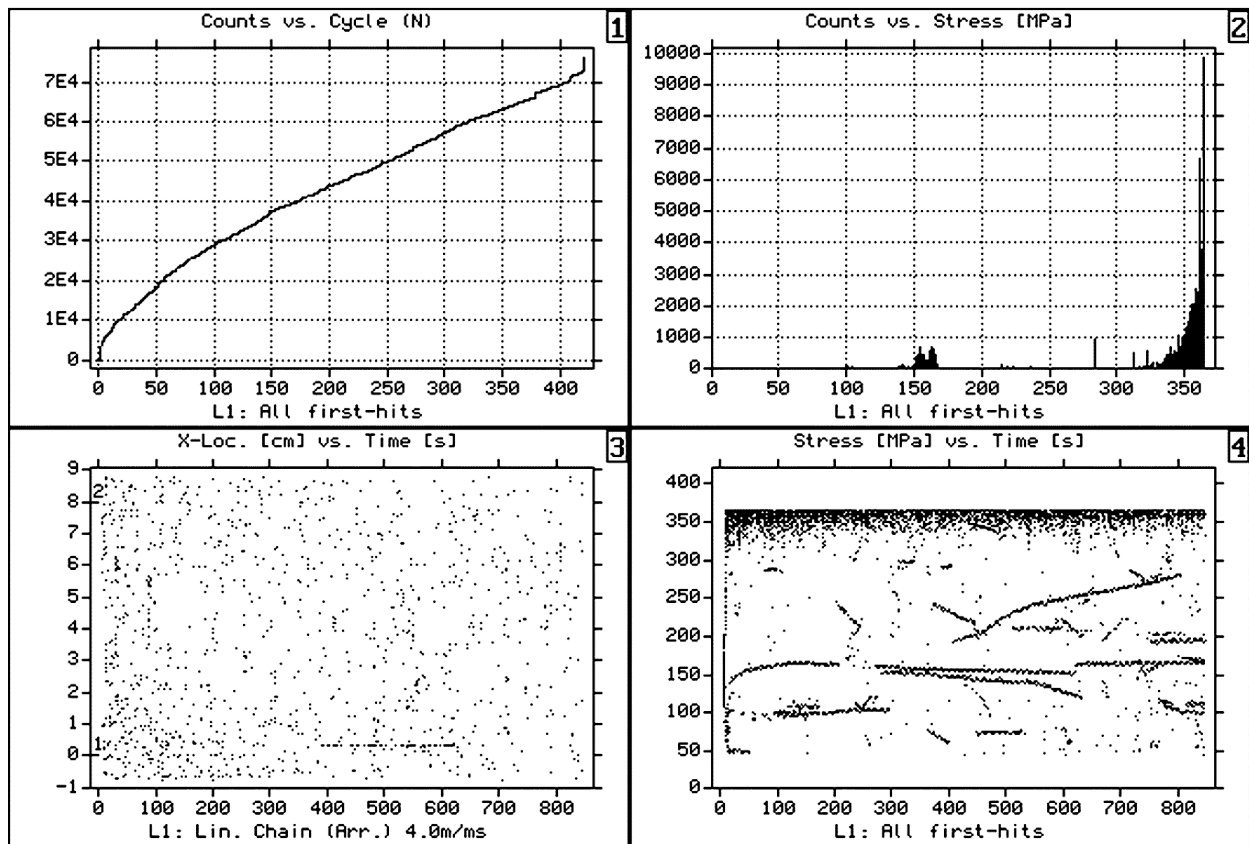


Fig. 1. Overall AE during low-cycle fatigue test.

The cumulative AE count history (subplot 1) exhibited three classical stages in the fatigue process in composites, i.e. initial fast damage development, gradual steady damage accumulation, and final failure development. The load range distribution (subplot 2) showed that most of the emission was generated at higher loads. However, some of the emission was generated at lower loads. In particular, substantial emission was generated in the range from 0.4-0.45 of the

maximum fatigue loading. It is interesting that few AE events were generated between the two peaks on the load range distribution.

The location history (subplot 3) showed that most of the AE events were scattered in respect to both location and time. A few spatial clusters of events were noticed at locations between 5 and 7 cm in the beginning of the fatigue process, but these clusters existed only through a few loading cycles. A long-lived cluster was detected near 0 cm location. This cluster lasted through about a third of the fatigue life.

The load-range history plot (subplot 4) showed that the AE events at the higher loads were generated uniformly throughout the fatigue life, with slightly higher rates in the beginning of the fatigue process. The events at the loads near the maximum load were not clustered. In contrast, most of the events at the lower loads were clustered, i.e. they occurred at the same load levels over the number of loading cycles. These AE events might be due to a well-characterized damage, such as, for example, matrix cracks in the 90° plies. They could also be due to a gradual extension of fatigue cracks or internal fretting.

Further analysis was conducted by separating AE signals from loading and unloading.

Acoustic Emission from Loading and Unloading

It can be expected that new damage is more likely to be developed during loading than during unloading. The overall AE described above was separated into the AE from loading and unloading using a unique phase filtering capability of the AMS3 system. This system can analyze an external analog signal, such as load, and determine the sign of its derivative. In the case of cyclic fatigue loading, this sign uniquely identifies the loading phase, i.e. loading or unloading. This sign can be recorded as a flag parameter, along with other AE parameters. This flag was used to separate the emission from different loading phases in the current study.

Figure 2 presents the AE from the loading phase of the cyclic loading, in the format similar to the format of the overall AE in Fig. 1. Subplot 1 of Fig. 2 showed that the emission from loading exhibited classical fatigue stages that were even more pronounced than the stages observed in the overall AE count history (Fig. 1). The load range distribution (subplot 2 of Fig. 2) showed a single maximum at the higher loads with most signal developed at loads exceeding 0.8 of the maximum fatigue load. The location history of the AE from loading (subplot 3) was well scattered while the load history (subplot 4) exhibited both dense scattered signals at the high load levels and clustered signals at the lower loads.

The results for the emission from unloading (Fig. 3) were substantially different. The accumulation rate (subplot 1) was almost uniform throughout the fatigue life, with slightly higher rates in the beginning but without a pronounced final failure development stage. The load distribution (subplot 2 of Fig. 3) exhibited two peaks at the medium and high loads. The intensity of these peaks was comparable. The location history (subplot 3) showed that the clusters observed in the overall AE were generated during unloading. The load history (subplot 4) showed fewer signals generated at the higher loads. The density of these signals was higher in the beginning of the fatigue process. This was probably responsible for the higher initial accumulation rate seen in subplot 1. Most of the signals generated at the lower loads were clustered.

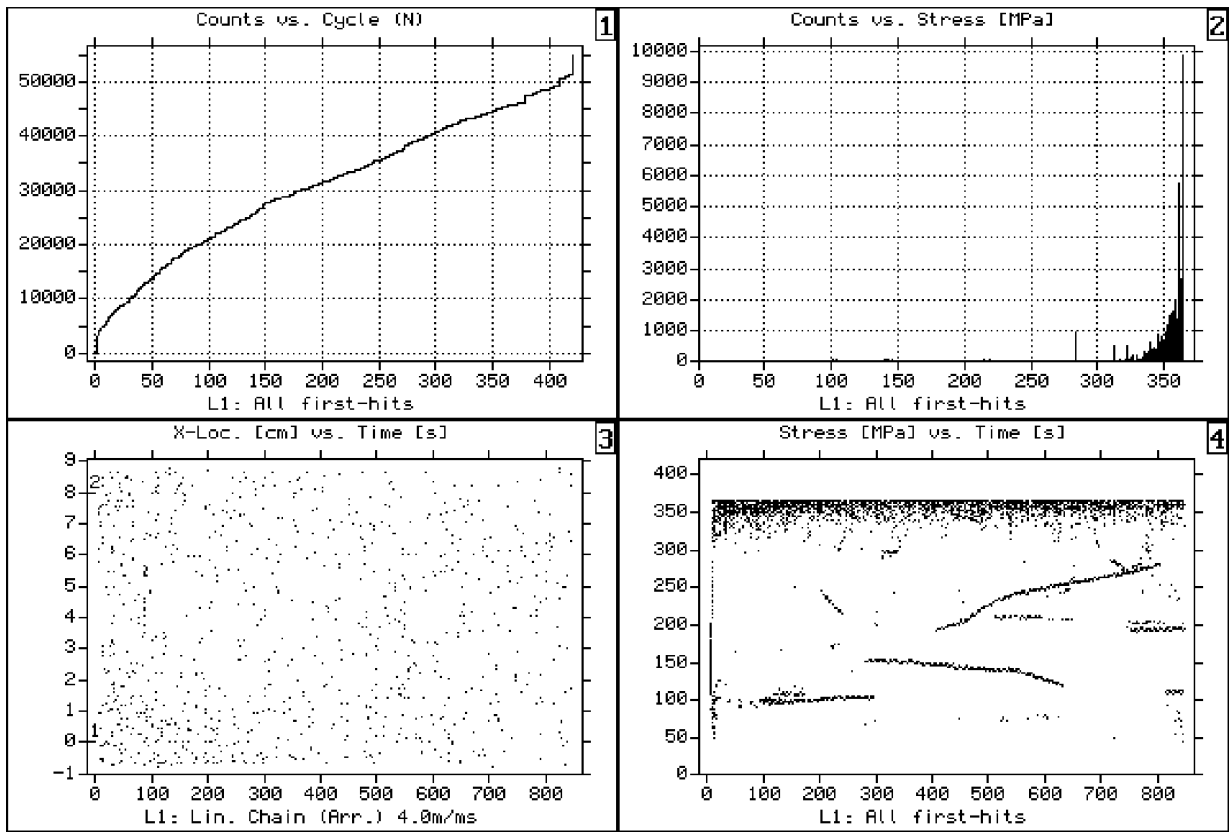


Fig. 2. AE during loading.

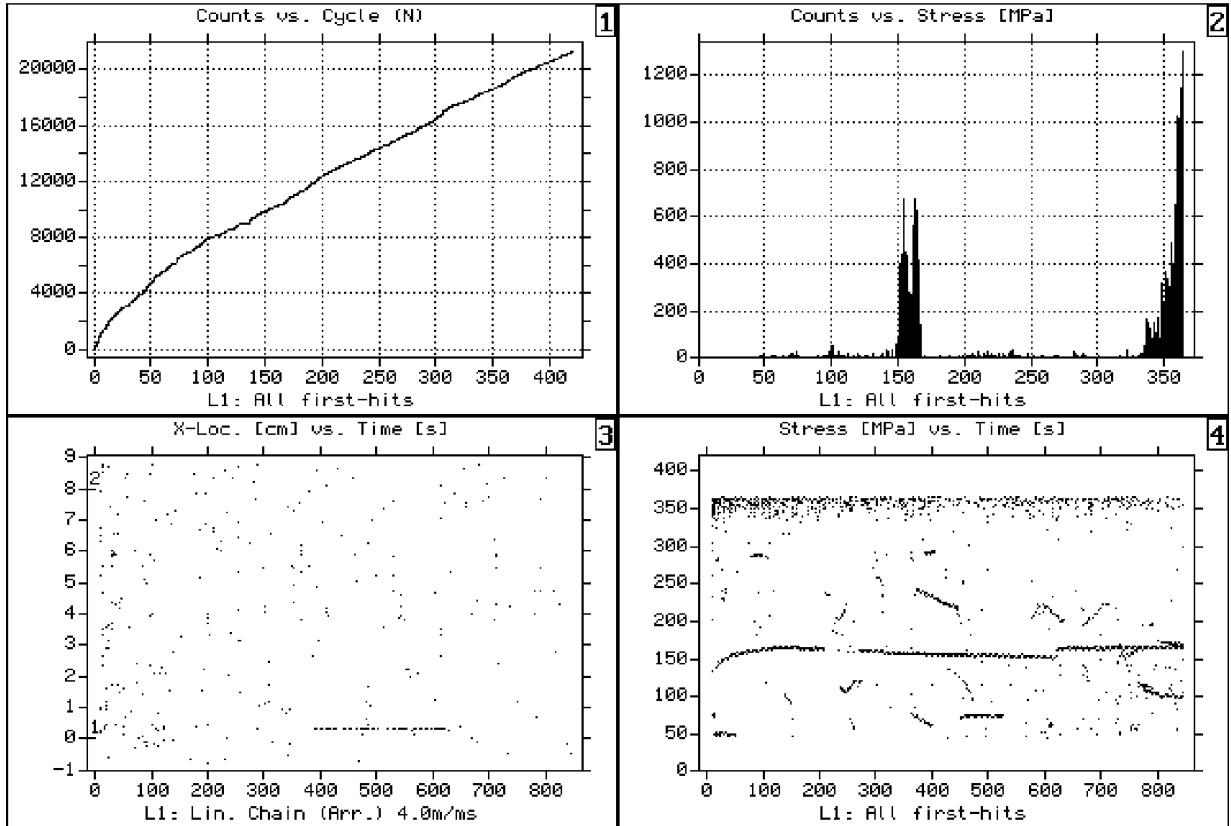


Fig. 3. AE during unloading.

The comparison of Figs. 2 and 3 with Fig. 1 showed that most of the emission at the medium load levels (a low peak in subplot 2 of Fig. 1) was generated during unloading. The signals from unloading were also more clustered. The total amount of the emission from unloading was almost half of that from loading (see maximum cumulative counts in subplots 1 of Figs. 2 and 3).

Further analysis was conducted by separating signals from higher and lower load levels under loading and unloading.

Acoustic Emission from Higher and Lower Load Levels

Figures 4 and 5 show the AE generated at higher (over 0.8 of the maximum load) and lower (under 0.8 of the maximum load) load levels during loading. The emission from the higher load levels (Fig. 4) showed pronounced fatigue staging (subplot 1) and was well scattered (subplot 3). The emission from the lower load levels (Fig. 5) was distributed over the loading range (subplot 2). It exhibited irregular accumulation history (subplot 1) with high accumulation rates in the first several cycles and much slower, varying accumulation rates afterwards. Although the AE events were clustered in respect to load (subplot 4), no spatial clusters were recorded (subplot 3). The emission from the low load levels accounted for about 10% of the total emission from the loading phase or about 7% of the overall emission in this composite.

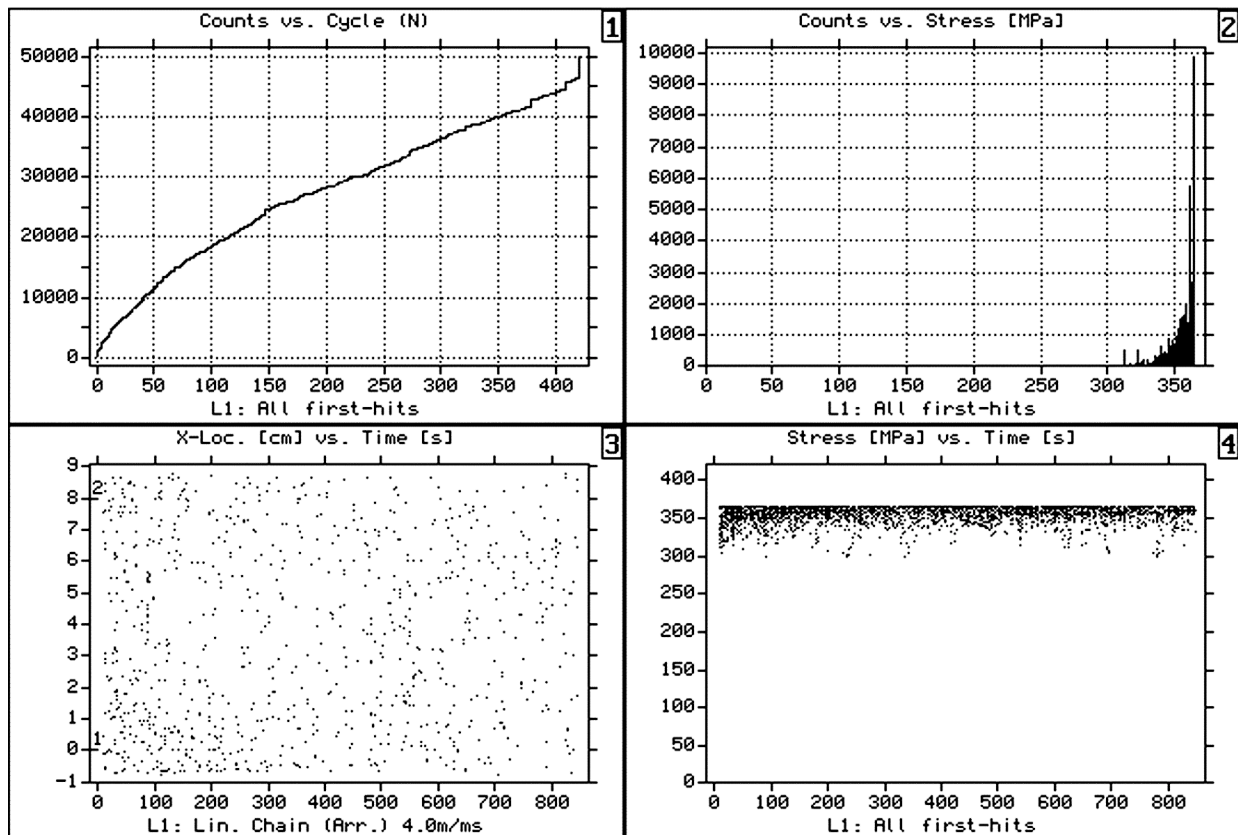


Fig. 4. AE from high load levels under loading.

Figures 6 and 7 show similar analysis of the emission generated during unloading. The emission from the higher load levels (Fig. 6) showed gradual accumulation with higher accumulation rates in the beginning of the process (subplot 1) and was well scattered (subplots 3 and 4). The emission from the lower load levels (Fig. 7) exhibited increasing accumulation rate (subplot 1).

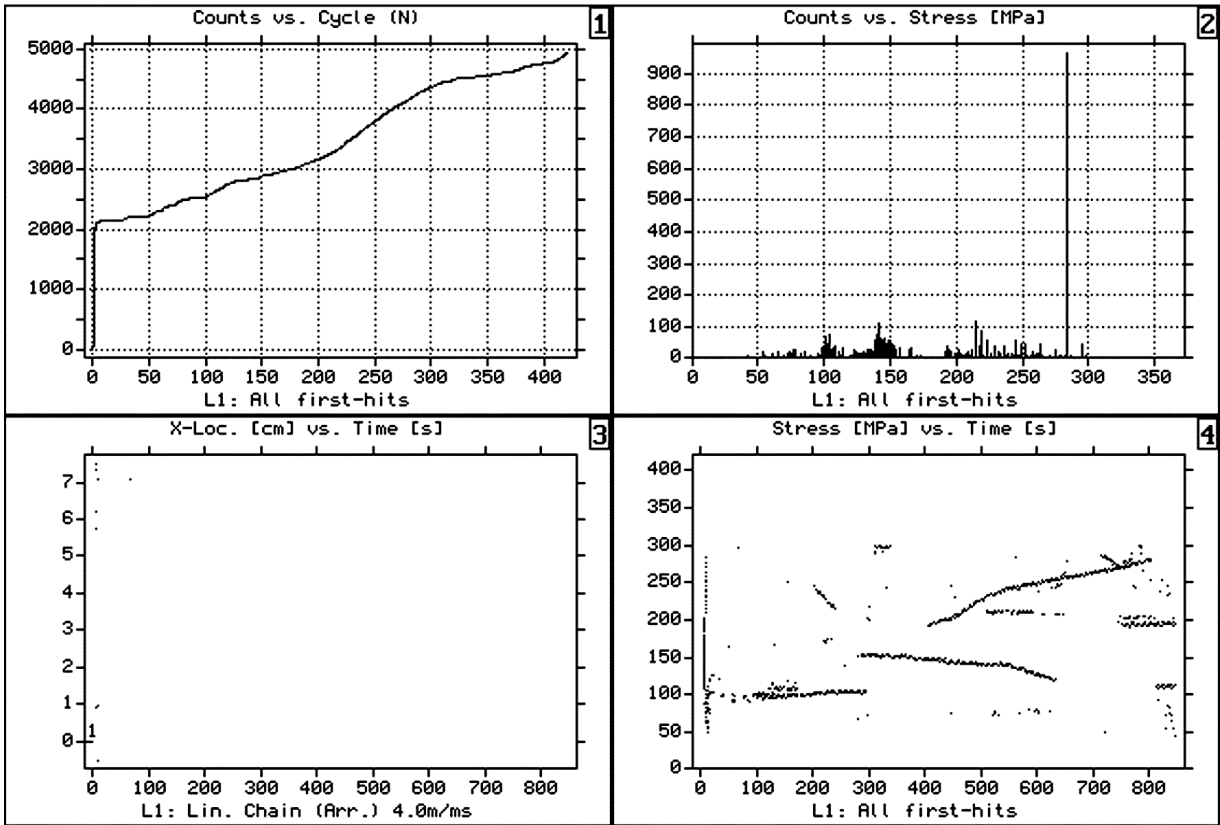


Fig. 5. AE from low load levels under loading.

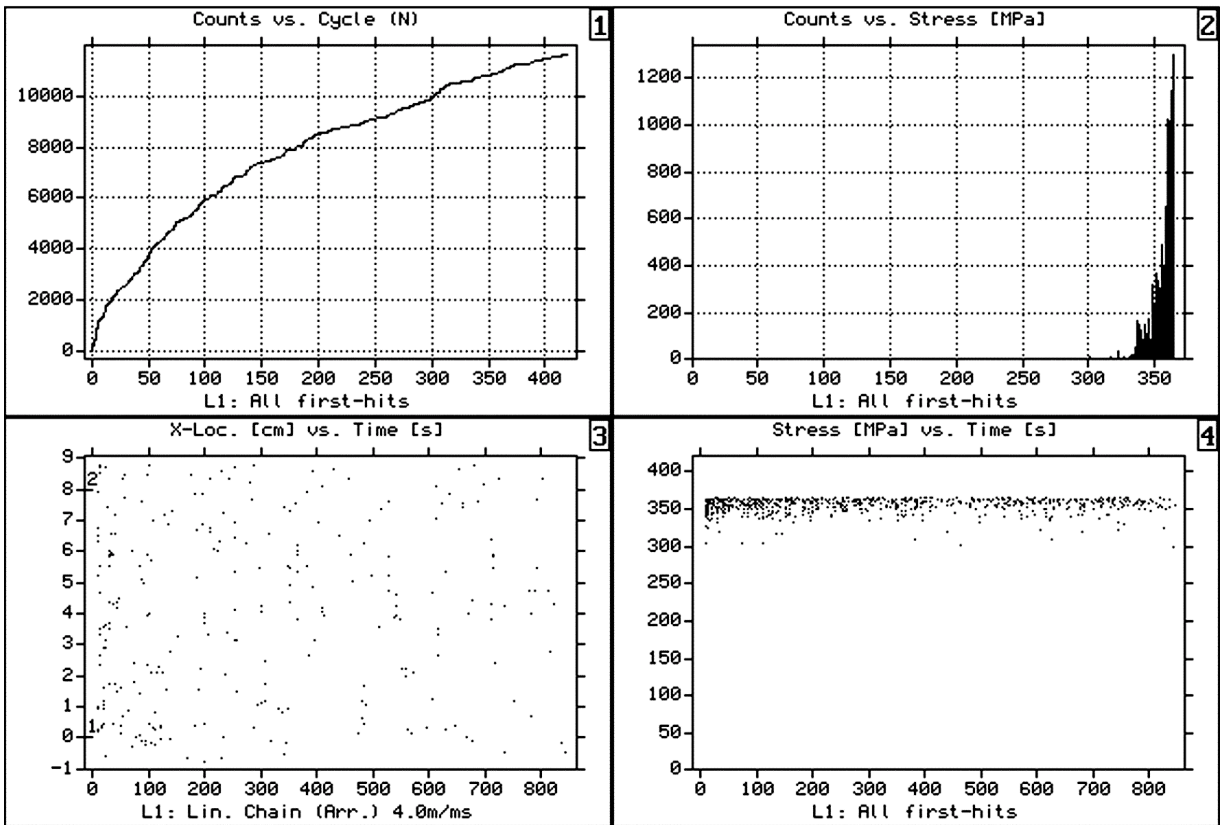


Fig. 6. AE from high load levels under unloading.

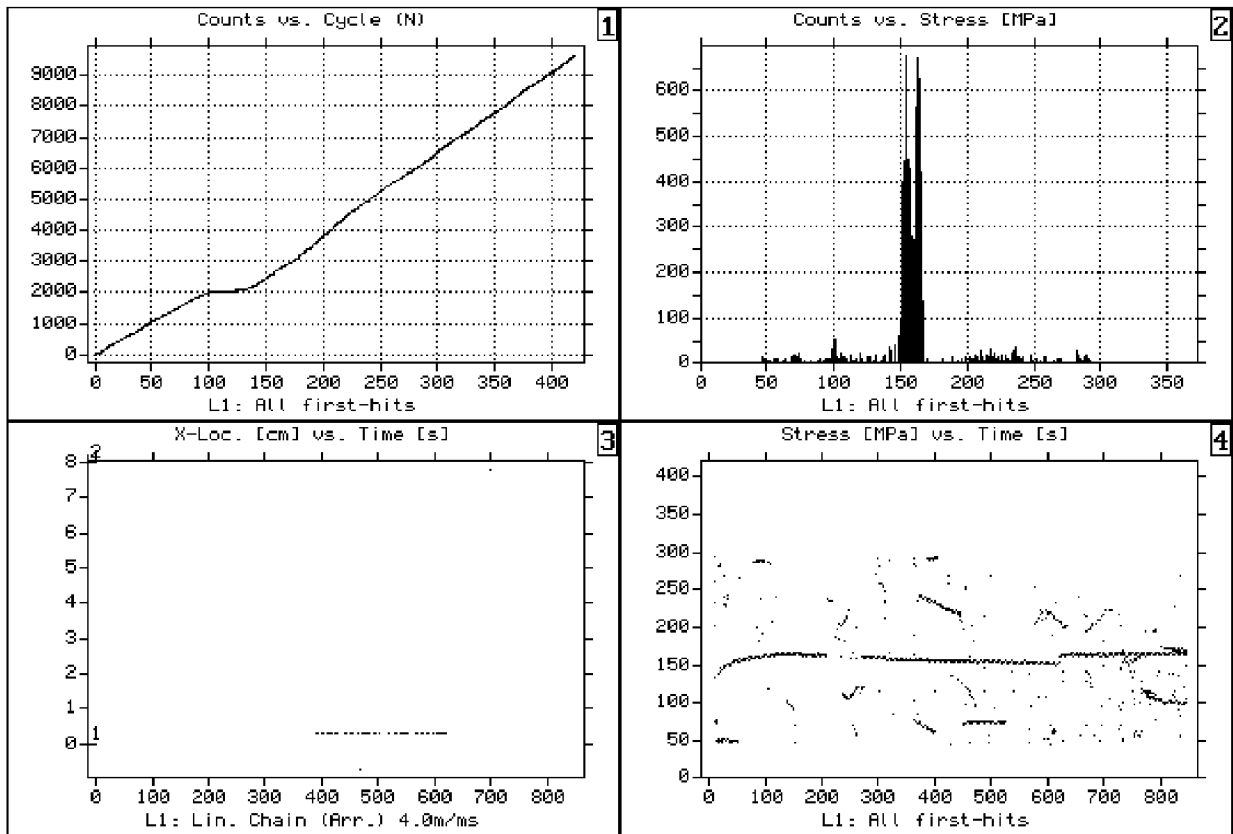


Fig. 7. AE from low load levels under unloading.

Most of this emission was generated in the narrow loading range (subplot 2) and the AE events were clustered in respect to both load (subplot 4) and location (subplot 3). The emission from the lower load levels accounted for about 46% of the total emission from unloading or about 13% of the overall AE in this composite.

Analysis and Identification of Emission from Damage and Fretting

The fatigue damage in unnotched composites is expected to exhibit scattered location and characteristic staging in the cumulative history. Also, the damage rate is expected to increase with the load level. The AE from the higher load levels (>0.8 of the maximum fatigue load) during both loading and unloading phases of the fatigue loading (Figs. 4 and 6) correlated well with these expectations. This emission was therefore attributed to the new damage development. Note that the final failure development appeared to take place mostly during the loading phase of the fatigue loading.

On the other hand, the emission from the lower load levels in the unloading phase (Fig. 7) was developed mostly in the narrow load range from 0.4-0.45 of the maximum fatigue load. In general, both new damage and fretting could be responsible for the emission at the lower load levels. However, the new damage events are expected to be distributed over the load range, with higher rates at higher loads. In contrast, the density of the fretting signals can be higher at lower loads. The accumulated cracks open and close repeatedly during cyclic loading. Their faces come into contact during unloading that can generate the emission. Depending on the type of damage, this may occur at a particular load level. The emission from friction is also expected to be less scattered and more clustered, as the fretting noise will be generated by the same cracks at

the same locations. Finally, it is also expected to exhibit the gradually increasing cumulative history, as more and more cracks will contribute to friction with the increasing fatigue damage. Based on the above, the emission from the lower load range during unloading (Fig. 7) was attributed to internal fretting.

The emission from the lower loading levels during the loading phase (Fig. 5) differed from the unloading emission. The cumulative history (subplot 1) showed elements of the classical fatigue staging. Some irregularity could be due to the overall low amount of this emission. The emission was distributed in a wide load range (subplot 2) with several peaks at both lower and higher loads within this range. Although clusters were observed in the load history (subplot 4), no spatial clusters could be identified in the location history. In general, the information above is not sufficient to make a positive identification of the emission from the lower load levels during loading. More studies are needed. It can be noted, that the cumulative content of this emission in the overall AE from the composite studied was only about 7%.

Conclusions

The conducted analysis of the AE from an advanced laminated composite subjected to fatigue loading showed that the emission from the higher load levels during both loading and unloading phases of the cyclic loading was due to new damage development. The emission from the lower load levels during unloading was from internal fretting. The emission from the lower load levels during loading could not be positively identified.

The results provide insights on the AE behavior of composites under fatigue and can be used in fundamental studies of damage micromechanisms [11] in composites under fatigue and for the development of predictive models.

Acknowledgments

This work was supported by the Air Force Office of Scientific Research. The graphite/epoxy prepreg was provided by Hexcel Corporation.

References

1. Williams, R.S. and Reifsnider, K.L., *Journal of Composite Materials*, 1974, **8**, 340.
2. Awerbuch, J. and Ghaffari, S., *Journal of Reinforced Plastics and Composites*, 1988, **7**, 245.
3. Eckles, W. and Awerbuch, J., *Journal of Reinforced Plastics and Composites*, 1988, **7**, 265.
4. Shiwa, M., Carpenter, S., and Kishi, T., *Journal of Composite Materials*, 1996, **18**, 2019.
5. Gustafson, C.-G. and Selden, R.B., *Delamination and Debonding of Materials*, ASTM STP 876 (ed. W.S. Johnson), American Society for Testing and Materials, Philadelphia, 1985, p. 448.
6. Wevers, M., Verpoest, I., De Meester, P., and Aernoudt, E., *Acoustic Emission: Current Practice and Future Directions*, ASTM STP 1077 (eds. W. Sachse, J. Roget, and K. Yamaguchi), American Society for Testing and Materials, Philadelphia, 1991, p. 416.
7. Kloua, H., Maslouhi, A., and Roy, C., *Canadian Aeronautics and Space Journal*, 1995, **41**, 21.
8. Edwards, J.H., *Composite Materials: Testing and Design*, ASTM STP 972 (ed J.D. Whitcomb), American Society for Testing and Materials, Philadelphia, 1988, p. 369.
9. Takemura, K. and Fujii, T., *JSME International Journal*, 1994, **A37**, 472.
10. Awerbuch, J., Gorman, M.R., and Madhukar, M. *Materials Evaluation*, 1985, **43**, 754.
11. Qian, J. and Dzenis, Y.A., *Journal of Acoustic Emission*, 2002, **20**, 16.

ACOUSTIC EMISSION FROM MAGNESIUM-BASED ALLOYS AND METAL MATRIX COMPOSITES

FRANTISEK CHMELÍK¹, FLORIAN MOLL², JENS KIEHN², KRISTIAN MATHIS³,
PAVEL LUKÁČ¹, KARL-ULRICH KAINER⁴ and TERENCE G. LANGDON⁵

¹ Department of Metal Physics, Charles University, CZ 121 16 Prague 2, Czech Republic

² Technical University Clausthal, D 38678 Clausthal-Zellerfeld, Germany

³ Department of General Physics, Eötvös Loránd University, Budapest, H-1117, Hungary

⁴ Institute for Materials Research, GKSS Research Center, D 21502 Geesthacht, Germany

⁵ University of Southern California, Los Angeles, CA 90089-1453, U.S.A.

Abstract

The acoustic emission (AE) technique was used to monitor structural changes and related plastic deformation in prospective Mg-based light alloys and metal matrix composites subjected to thermal loading and/or mechanical stress (tensile or creep testing). It is shown that the AE response depends significantly on the testing conditions. The deformation mechanisms and their correlation with the testing parameters are discussed. It is shown that the AE response and the residual strain after thermal cycling depend significantly on the upper temperature of cycling. The results are explained in a quantitative analysis using a model that correlates the internal thermal stresses with the changes in temperature. The AE response in deformation tests is discussed in terms of the contemporary knowledge of plastic deformation processes in metallic materials.

1. Introduction

Several magnesium-based alloys and metal matrix composites (MMCs) have been developed and manufactured over the last decade for potential use as light-weight high-performance materials in a range of applications including, for example, the automotive industry (Fritze et al., 1998). The standard operating conditions for most alloys and MMCs involve thermal and/or mechanical loading. This may induce microstructural changes and matrix plastic deformation characterized by dislocation generation and motion. In addition, for the case of MMCs thermal loading induces internal stresses owing to the often substantial mismatch between the thermal expansion coefficients of the matrix and the reinforcement. Under higher load and/or long-term exposure, structural damage (for example, interface de-cohesion, fiber fracture) may also occur.

The mechanical properties of Mg-based materials are dependent on the mechanisms of plastic deformation in hexagonal close-packed (hcp) metals. Magnesium exhibits an axial ratio of c/a equal to 1.623, which is slightly less than the ideal value of 1.633. The main deformation mechanisms are dislocation glide in the basal planes (0001) along $\langle 11\bar{2}0 \rangle$ directions and twinning in the pyramidal planes $\{10\bar{1}1\}$ (ASM Handbook, 1999). Twinning may also reorient the basal planes so that they become more favorably oriented for slip (Zhang et al., 2000). The relative importance of these various mechanisms depends strongly upon temperature. With increasing temperature, twinning becomes easier as the metal strength decreases. However, above a temperature of 250°C additional non-basal slip systems (pyramidal planes) are activated and deformation becomes much easier so that twinning is then less important. In addition,

recovery processes gain importance with increasing temperature and in polycrystalline materials there is the increasing importance of grain boundary sliding at the higher temperatures.

Acoustic emission (AE) is a non-destructive experimental technique, in which transient elastic waves are generated within a material due to sudden and irreversible structural changes. It has been established that AE is a viable procedure for monitoring the development of microstructural changes and related plastic deformation and/or structural damage in many classes of materials. Specifically, dislocation motion and microstructural damage are generally recognized to produce significant AE in most metals and alloys (Heiple and Carpenter, 1987). Hence, there is a possibility of using AE monitoring to identify and characterize the microstructural changes occurring within the Mg-based materials and to correlate these measurements with the associated temperatures or other testing parameters.

To date, there are only limited results demonstrating the use of AE in monitoring the structural response and matrix deformation of Mg-based alloys (Fisher and Lally, 1967, Siegel, 1977, Friesel and Carpenter, 1984, Kato et al., 1986). During the deformation of pure Mg, an AZ31B and various Mg-Al alloys at room temperature, there was a distinct correlation between the AE activity and the sample orientation, purity, strain rate and the mode of testing (tension, compression). In all cases, deformation twinning and dislocation glide were found to be the major sources of AE. By contrast, AE evidence for Mg-based MMCs is almost entirely lacking.

This paper provides a comprehensive review of our recent work in this area. The present experiments were conducted to investigate the use of AE as a non-destructive tool for the examination and evaluation of Mg-based materials. Special emphasis was placed on the influence of the matrix composition, the matrix reinforcement and temperature on AE, and the related microstructural evolution and plastic deformation of a variety of Mg-based alloys and MMCs. To simulate thermal and/or mechanical loading of structural parts, the specimens were subjected to thermal cycling, tensile tests at constant cross-head speeds and tensile creep tests at elevated temperatures. In addition, the potential for analyzing the experimental data using established models is evaluated.

2. Experimental Procedure

The matrix materials used in this investigation were Mg of commercial purity, magnesium alloys ZE41 alloy containing 4 wt. % Zn and 1 wt. % rare earths, an AZ91 alloy containing 9 wt. % Al and 1 wt. % Zn, a QE22 alloy containing 2 wt. % Ag and 2 wt. % rare earths and an AM60 alloy containing 6 wt. % Al-0.5 wt. % Mn, where all of these alloys have Mg as the balance. The AM60 alloy received a standard T6 thermal treatment prior to testing.

The matrix materials were reinforced with 20 vol. % of Saffil® δ -Al₂O₃ short fibers through the use of a squeeze-casting procedure, in which the molten Mg or Mg alloy is infiltrated under pressure into Saffil short fiber pre-forms having planar isotropic fiber distributions. The MMCs showed planar isotropic fiber distributions with fiber diameters of ~3-5 μ m and fiber lengths up to ~150 μ m after casting. There was a slight chemical reaction between the matrix and the reinforcement, which led to chemical bonding at the interfaces. In addition, the matrix in the vicinity of the interfaces became enriched in aluminum. The AZ91-Saffil MMC received a standard T6 thermal treatment prior to testing. A typical optical micrograph of the as-received state is shown in Fig. 1. The surfaces of selected specimens were examined after fracture using a

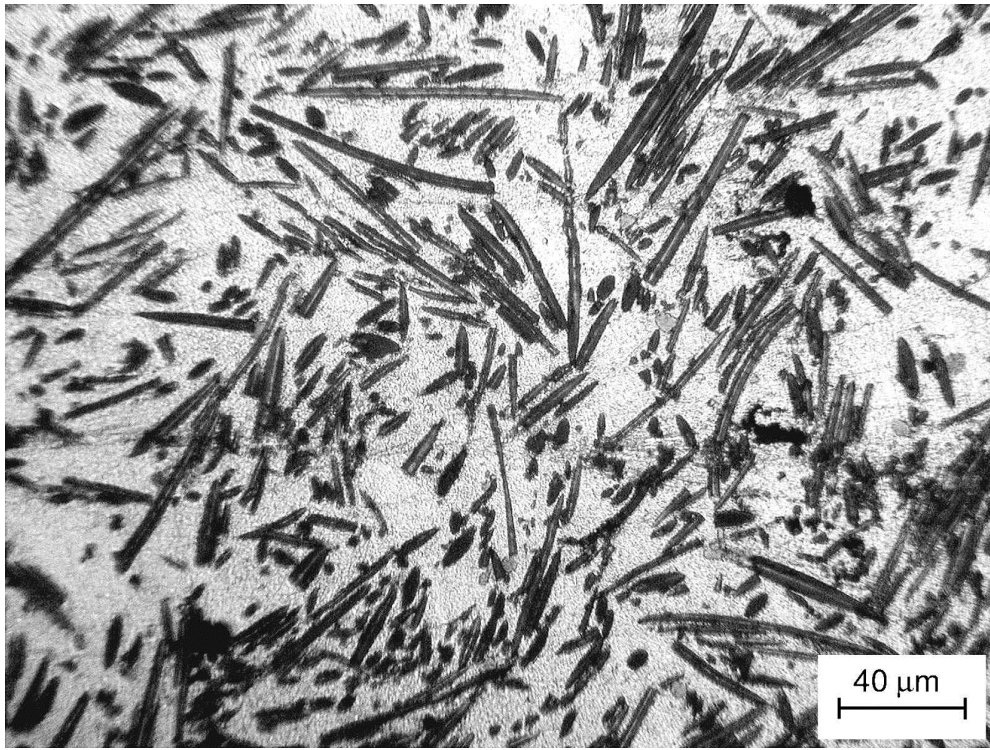


Fig. 1. Typical optical micrograph of the AZ91-Saffil in the as-received condition.

TESLA BS 343 scanning electron microscope operating at an accelerating voltage of 15 kV. Fracture surfaces were cleaned in acetone before making any observations.

An unreinforced QE22 alloy and MMCs QE22-15 vol.% SiC and AZ91-15 vol.% SiC (globular particles with a mean diameter of 30 and 10 μm , denoted as 320BL and 600BL or 600HD, respectively) were also produced by means of hot extrusion after mixing and milling of the matrix powder and particles. Almost no defects and no products of any chemical reaction were detected between the matrix and the particles at the matrix-particle interfaces. Examination revealed that the materials exhibited a wide distribution of the matrix grain sizes so that there were regions with a grain size less than 1 μm as well as regions with grain sizes up to $\sim 20 \mu\text{m}$. These materials received a standard T6 thermal treatment prior to testing.

Specimens were machined for thermal cycling in the form of rods with lengths of 50 mm and diameters of 5 mm: the reinforcement planes in these samples were parallel to the longitudinal axes. Thermal cycling was conducted *in situ* by placing the specimens within a dilatometer equipped with a radiant furnace permitting temperatures from ambient to 400°C. The residual strain was measured after each cycle and the AE signal was transmitted through a quartz rod in contact with the specimen.

Cylindrical specimens with a gauge length of 29 mm and a diameter of 4.95 mm were deformed in tension. The tensile tests were performed in furnace-equipped MTS and Instron machines in the temperature range from 20 to 300°C and at a constant crosshead speed giving an initial strain rate of $8.3 \times 10^{-5} \text{ s}^{-1}$. A steel wave-guide was used to transmit AE. One end had cylindrical envelope-shaped that fitted tightly to the round specimen surface and it was coupled to the sample surface using heat-resistant silicone paste. The other end of the wave-guide has a conical shape, to which the transducer was placed using vacuum grease and spring holders.

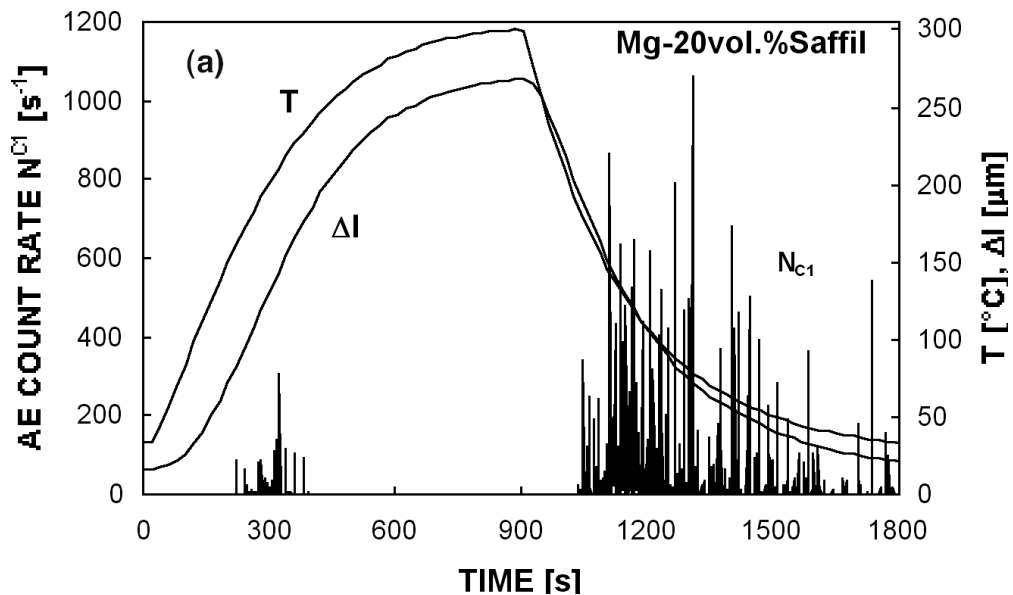
Tensile creep specimens were machined with gauge lengths of 25.4 mm and M10 screw-heads. The longitudinal specimen axes were within the plane containing the long axes of the fibers. All of the creep testing was conducted under conditions of constant stress using a creep machine equipped with a contoured lever arm. Tests were performed at stresses in the range from 35 to 95 MPa and at temperatures from 423 to 583 K (150-310°C) with the temperature controlled during each test to ± 2 K. Some tests were conducted at a single stress until failure and others used progressive loading, in which the stress was increased at selected time intervals until ultimate failure. The AE signal was monitored during each creep test using a steel wave-guide of cylindrical shape that fitted tightly to the specimen. This wave-guide was coupled to the sample surface using heat-resistant silicone paste and steel springs.

The AE was monitored directly using computer-controlled DAKEL-LMS-16 (thermal cycling and creep tests) and DAKEL-XEDO-3 (dynamic tensile tests) facilities developed by DAKEL-ZD Rpty, Czech Republic. The facilities incorporated a highly sensitive LB10A transducer (with a flat response between 100 and 500 kHz and a built-in preamplifier giving a gain of ~ 30 dB) and a miniaturized MST8S piezoelectric transducer (with a flat response between 100 and 600 kHz). As described earlier (Chmelík et al., 1998a), the AE analyzers detected the AE signals at two threshold levels, corresponding to gains of 100 and 80 dB, respectively.

3. Experimental Results and Discussion

3.1. Thermal cycling of Mg-based metal matrix composites

Figure 2 shows the variation with time of the AE count rate, N_{c1} , and the specimen deformation, Δl , with the temperature, T , for two MMCs during a single temperature cycle having upper temperatures, T_{top} , of 300°C and 400°C, respectively. It is apparent from Fig. 2a that, for the Mg-Saffil MMC, there is moderate AE during the heating within a temperature range from $\sim 140^\circ\text{C}$ to $\sim 220^\circ\text{C}$ and significant AE during the cooling of the sample at temperatures from $\sim 180^\circ\text{C}$ to room temperature. The AZ91-Saffil MMC (Fig. 2b) shows AE only during cooling at the lower temperatures from $\sim 60^\circ\text{C}$ to room temperature. Following the cycles, a residual contraction was measured in the samples.



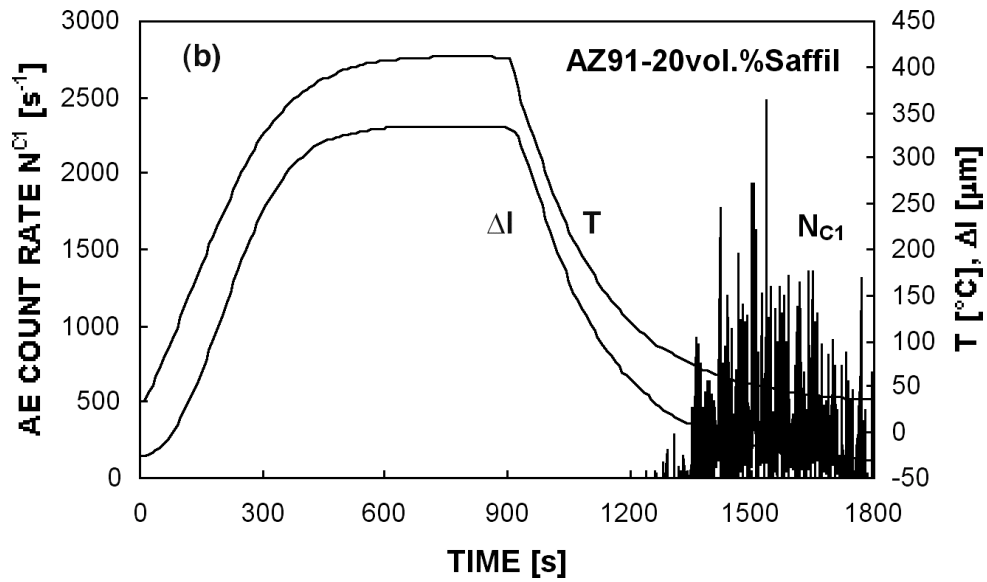


Fig. 2. Value of the AE count rate, N_{C1} , temperature, T, and sample deformation, Δl , as measured in the Mg-Saffil (a) and the AZ91-Saffil (b) during temperature cycles to upper temperatures of 300°C and 400°C, respectively.

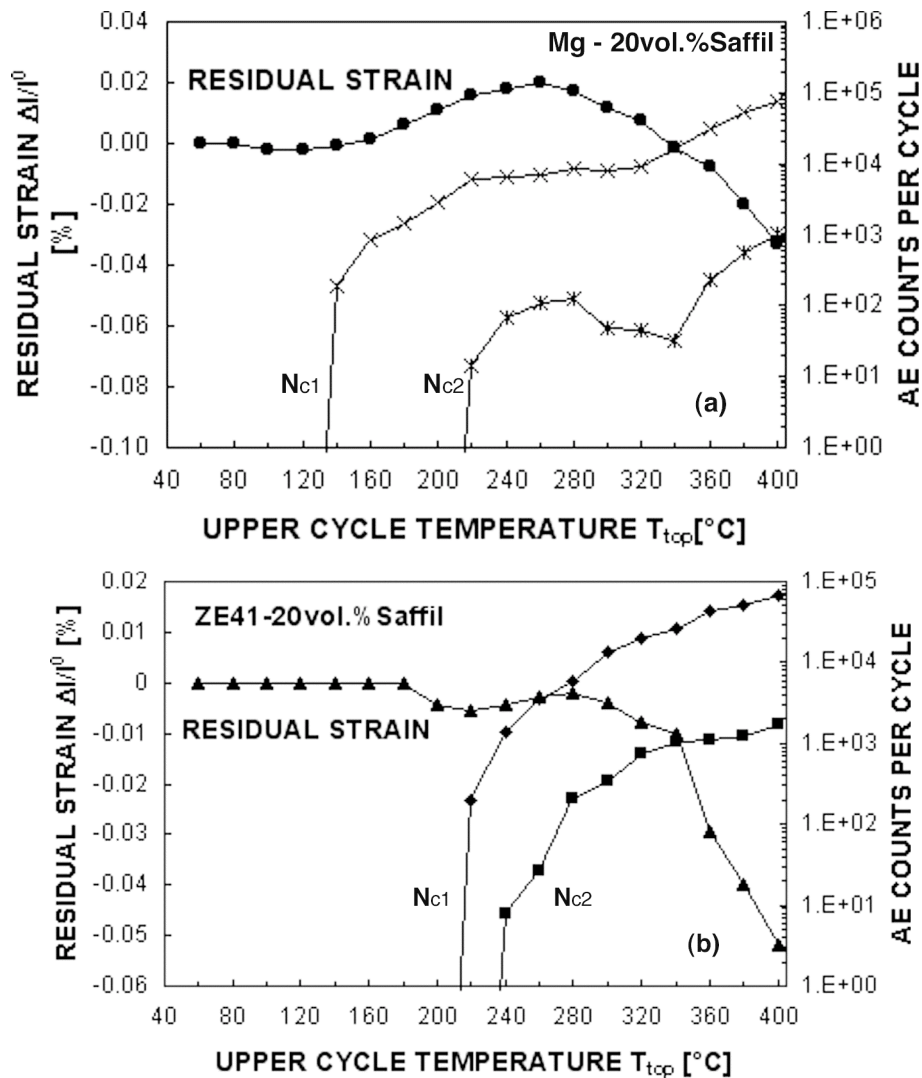


Fig. 3 (a) and (b)

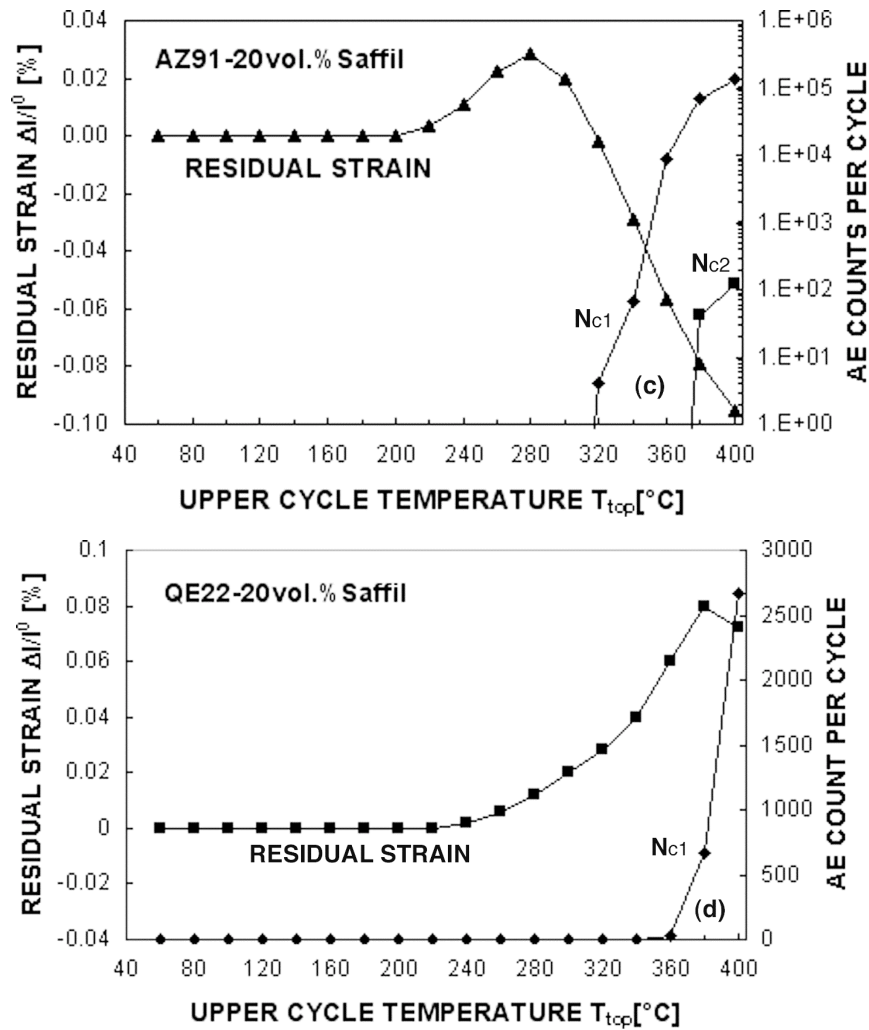


Fig. 3. Residual strain, $\Delta l/l_0$, and AE counts for two different detection levels, N_{C1} and N_{C2} , versus the upper cycling temperature, T_{top} : the residual strain was estimated with reference to a temperature of 30°C and the AE counts were evaluated for the entire cooling period of each cycle. (a) Mg-Saffil, (b) ZE41-Saffil, (c) AZ91-Saffil, (d) QE22-Saffil.

The behavior of the composites during thermal cycling was characterized in detail by using a stepped incremental temperature technique. The results are documented in Fig. 3 where the residual strain, $\Delta l/l_0$, and the AE count per cycle, N_{C1} are plotted against the upper cycle temperature, T_{top} , where l_0 is the original length of the sample and one cycle was performed for each upper temperature corresponding to each separate experimental point recorded for the residual strain. These plots demonstrate that there is no residual strain up to a certain upper temperature, followed by a slight tendency for a compressive contraction for the Mg-Saffil and the ZE41-Saffil. For all MMCs, residual elongation prevails in a certain temperature interval and for higher upper temperatures there is a residual contraction that increases in magnitude with increasing values of T_{top} . The AE response also depends on the upper temperature, increasing significantly at a critical value of T_{top} and exhibiting intense AE bursts, which appear with a further increase in T_{top} (with the exception of the QE22-Saffil MMC, which does not show bursts of AE).

It has been shown that, under conditions similar to those used in these experiments, more than 1000 thermal cycles are needed in order to produce any measurable damage in the samples

(Kiehn et al., 1994). Thus, the AE counts recorded in these experiments must be attributed to the occurrence of structural changes in the matrix and to any associated plastic deformation. Since the MMCs were fabricated by squeeze-casting at an elevated temperature, the composites contain thermal residual stresses at room temperature due to the mismatch in the thermal expansion coefficients between the matrix and the reinforcement (Arsenault and Taya, 1987; Xia and Langdon, 1994) and the magnitude of these stresses is of the order of the minimum stress required for creep in the matrix. In practice, the matrix in these MMCs experiences tensile stresses whereas the fiber reinforcements experience compressive stresses. Therefore, when the MMC is heated, the internal tensile stress acting on the matrix reduces to zero and, on further heating, there is a build up of compressive stresses; whereas on cooling, the internal stresses behave in the opposite sense. It is anticipated these stresses will be concentrated near the matrix-fiber interfaces and at the ends of the reinforcing fibers. These thermal stresses may also exceed the matrix yield stress within discrete temperature ranges and relaxation will then occur through the generation of new dislocations and plastic deformation within the matrix. This plastic deformation may appear as dislocation glide, as twinning or possibly as grain boundary sliding at the higher temperatures depending upon the precise temperature and the crystallographic structure of the matrix. In general, it is reasonable to anticipate that the compressive deformation that appears on heating will give some form of diffusion-controlled high temperature creep whereas the tensile deformation appearing on cooling will lead to dislocation glide and twinning. Thus, and in support of the experimental observations, a larger AE is expected during cooling at the lower temperatures.

It was suggested earlier that it may be possible to correlate the AE response and the internal thermal stresses produced during thermal cycling (Chmelik et al., 1998b). With respect to the dependence of the residual strain on the upper cycle temperature as plotted in Fig. 3, a quantitative analysis of internal thermal stresses has been developed for a short-fiber reinforced aluminum composite exhibiting chemical bonding at the interfaces (Urreta et al., 1996) and more recently this approach has been further developed and applied to experimental data (Carreño-Morelli et al., 1997, 2000). The analysis predicts that the thermal stresses, σ_{TS} , produced by a temperature change at the interfaces of ΔT are given by

$$\sigma_{TS} = \frac{E_f E_M}{(E_f f + E_M (1 - f))} f \Delta \alpha \Delta T \quad (1)$$

where E_f and E_M are the values of Young's modulus for the reinforcement and the matrix, respectively, f is the volume fraction of fibers and $\Delta \alpha$ is the difference between thermal expansion coefficients of the matrix and the reinforcement between the matrix and the reinforcement associated with the coefficients of thermal expansion.

For the MMCs used in these experiments, $E_f = 300$ GPa and $E_M = 45$ GPa at room temperature, $f = 0.20$, $\Delta \alpha = 20 \times 10^{-6} \text{ K}^{-1}$ and the decrease in E_M with increasing temperature is $\sim 50 \text{ MPa K}^{-1}$. Thus, eqn. (1) predicts that a temperature change by 1°C produces an increment in the thermal stress of $\sim 0.6 \text{ MPa}$ and at temperatures above $\sim 250^\circ\text{C}$ this increment decreases to $\sim 0.4 \text{ MPa K}^{-1}$.

It is shown in Fig. 3a that slight but measurable compressive deformation occurs in Mg-Saffil during cycling at upper temperatures above $\sim 100^\circ\text{C}$ and tensile deformation appears during cycling at upper temperatures above $\sim 140^\circ\text{C}$. It follows from eqn. (1) that a temperature change of 70°C produces a thermal stress of $\sim 40 \text{ MPa}$ and, by comparison with the reported compressive

acoustic yield (micro-yield) stress of ~ 20 MPa for the squeeze-cast unreinforced Mg at 100°C (Trojanová, 2002), this implies the presence of an initial internal tensile stress of ~ 20 MPa. A similar calculation may be performed for cooling of the sample from $\sim 140^\circ\text{C}$ since, on heating, a temperature change of 110°C produces a thermal stress of ~ 60 MPa so that the matrix experiences a compressive stress of ~ 40 MPa at 140°C . This stress exceeds the matrix yield stress at this temperature and is relaxed by matrix plastic deformation (cf. observed AE) to values below $\sim 15 - 20$ MPa. Cooling of the composite to room temperature produces an estimated thermal stress of ~ 70 MPa. Consequently, a tensile stress approaching ~ 40 MPa should appear at temperatures near to room temperature and this will correspond to the macroscopic yield point. This effect will lead to AE, as observed experimentally. It is noteworthy that the disappearance of AE during heating at 220°C indicates a change in the deformation mechanism towards high temperature creep. A similar calculation may be performed for the ZE41-Saffil, which exhibits a similar behavior to the Mg-Saffil (Fig. 3b).

For the AZ91-Saffil, Fig. 3c shows that reaching a T_{top} of $260-280^\circ\text{C}$ leads to the appearance of compressive deformation. The corresponding temperature change of 230°C produces a thermal stress of ~ 110 MPa. Since the compressive yield point of the squeeze-cast AZ91 alloy is ~ 75 MPa at 270°C (Trojanová, 2002), the initial internal tensile stresses of 35 MPa may be assessed. A similar calculation may be done for cooling of the specimen from T_{top} . Figure 3c shows that a measurable tensile deformation appears during cooling when T_{top} of 200°C is reached. On heating, the corresponding temperature change of 170°C produces a thermal stress of ~ 80 MPa, which demonstrates that the matrix experiences a compressive stress of ~ 45 MPa at 200°C . Cooling the composite to room temperature produces a thermal stress of ~ 90 MPa. Consequently, a tensile stress approaching ~ 45 MPa should appear close to room temperature, which corresponds to the acoustic yield point (Trojanová, 2002). Hence, it is reasonable to anticipate that a slight tensile deformation will appear, which was indeed observed. Figure 3c shows also that AE first appears after cooling from T_{top} of 320°C . On heating, a temperature change of 290°C produces a thermal stress of ~ 125 MPa so that the matrix experiences a compressive stress of ~ 90 MPa. In practice, this stress is probably relaxed by compressive deformation to below $20 \sim 30$ MPa. If the composite is cooled to 60°C where significant AE first appears, a thermal stress of ~ 160 MPa is produced. Consequently, a tensile stress approaching ~ 140 MPa should appear at 60°C and this is of the same order as the measured macroscopic tensile yield stress of the matrix alloy (Trojanová, 2002). This calculation suggests there will be an intense AE on cooling to near room temperature, as is clearly evident in Fig. 2. Similar results to those for AZ91-Saffil were also obtained for QE22-Saffil.

It follows from these calculations that there is a very good correlation between the present experimental data and the predictions of a model developed earlier to explain the characteristics of internal damping in an aluminum composite containing short fibers (Carreño-Morelli et al., 2000).

3.2 Tensile deformation at elevated temperatures

To clarify the nature of the matrix plastic deformation during thermal cycling of Mg-based MMCs, tensile tests of an aluminum-rich AM60 alloy were performed as a function of temperature. The stress-strain curves and corresponding AE count rates (\dot{N}_{C1} and \dot{N}_{C2}) for the AM60 alloy deformed at different temperatures are depicted in Fig. 4a, b, respectively. The deformation curves are smooth and indicate a substantial strain hardening at temperatures lower than 200°C . They also show a fairly large elongation to fracture of about 0.2. With increasing temperature, the flow stress decreases and softening occurs. At temperatures above 200°C , the

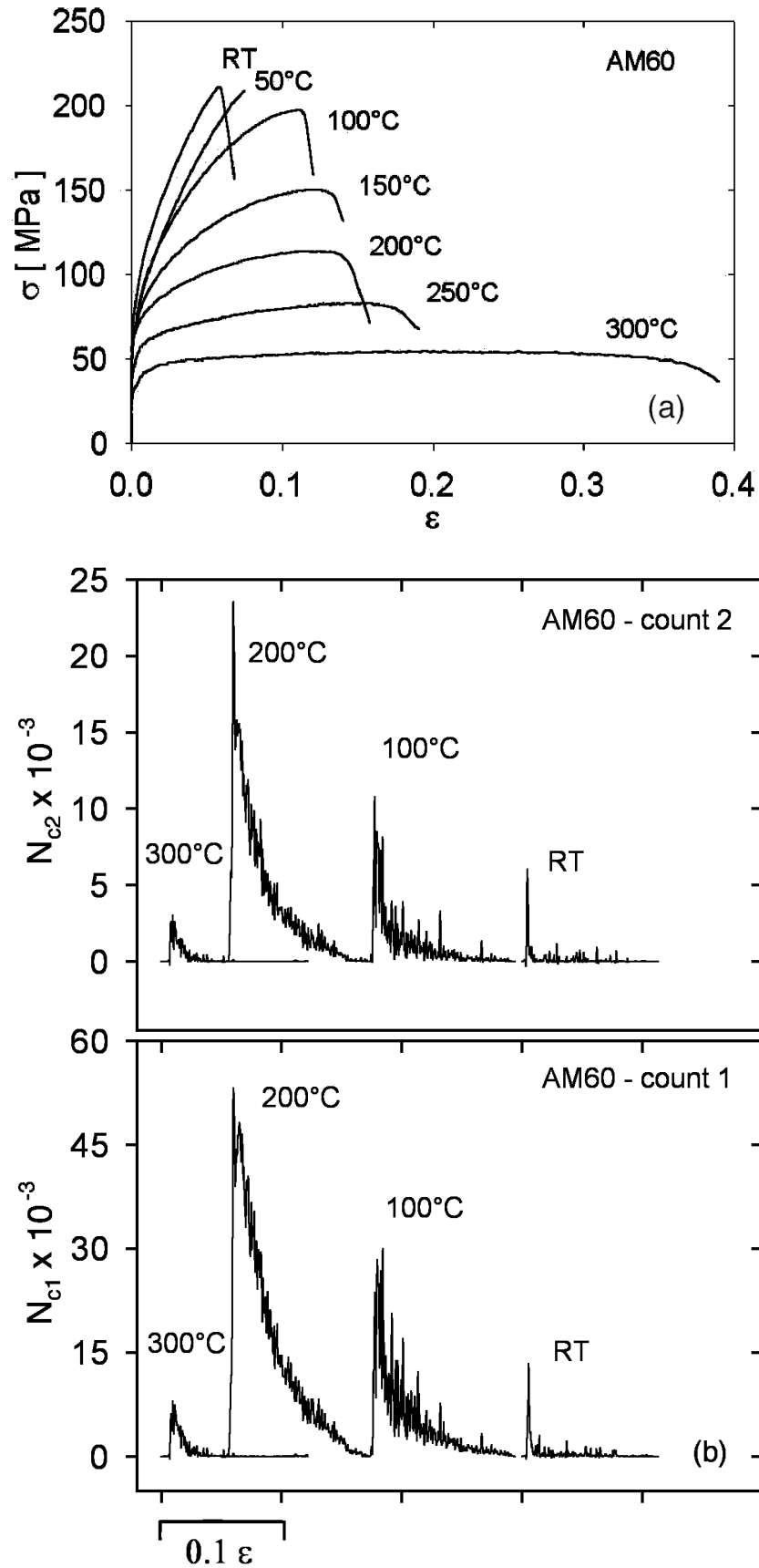


Fig. 4. (a) True stress-true strain curves for AM60 deformed at different temperatures. (b) Strain dependencies of the AE count rates N_{c1} and N_{c2} for different temperatures.

work hardening rate is close to zero and a dynamic balance occurs between hardening and softening. The strain dependencies of the AE count rates show a characteristic shape with a peak close to the yield point and a subsequent decrease in the AE activity. The AE activity vs. temperature shows a distinct maximum at 200°C. This behavior thus demonstrates clearly the temperature dependence of the plastic deformation in Mg-based alloys as discussed in Section 1. It is noteworthy that these results are consistent with the AE observations during heating of the Mg-Saffil MMC where AE vanished when the temperature exceeded 220°C (Fig. 2a).

3.3 Creep of an AZ91–Saffil composite

There are a number of reports describing the creep behavior of Mg-based MMCs reinforced with short fibers and using AZ91 (Mordike et al., 1997, 1998; Li and Langdon, 1999a and b; Li et al., 1999; Sklenicka et al., 2000; Pahutová et al., 2000), AS41 (Mordike et al., 1998) or QE22 (Mordike et al., 1997) as the matrix alloys. The present investigation was initiated to provide more information on the creep of an MMC with an AZ91 matrix alloy and especially to critically evaluate the potential for making use of AE as a monitoring tool for characterizing creep deformation and the development of creep damage during testing. Because very slow strain rates are an inherent feature of long-term creep investigations, a series of specific tests was judiciously selected and undertaken to provide information on three separate issues: (1) the ability of the fiber reinforcement to provide additional creep strengthening by comparison with the unreinforced alloy, (2) the testing conditions required to reveal a meaningful response using AE monitoring and (3) the effect on the AE response of testing at different temperatures.

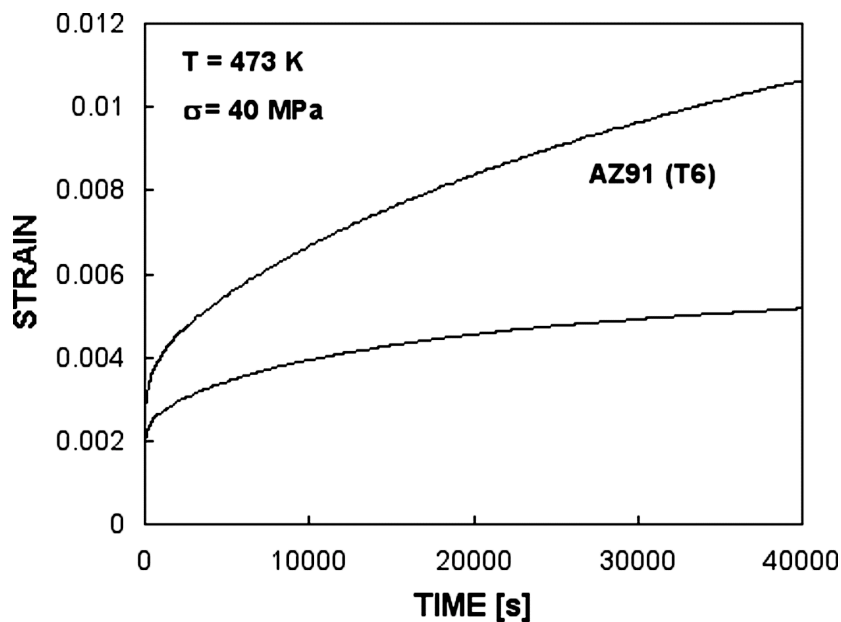


Fig. 5. Creep curves of strain versus time at 473 K with an applied stress of 40 MPa for the unreinforced AZ91 alloy and the composite: both materials were tested in a T6 condition.

When an MMC is subjected to mechanical loading, creep occurs in the matrix alloy through the generation and motion of dislocations and, in addition, there may be structural damage at the higher stress levels through debonding at the fiber-matrix interfaces or fracturing of the individual fibers. It is reasonable to anticipate that AE will provide a meaningful and measurable response to some deformation and damage mechanisms (Heiple and Carpenter, 1987) and/or flow changes. This suggests the potential for using AE measurements to characterize the flow and damage processes occurring within the material during testing.

To evaluate whether additional creep strengthening is introduced through the presence of the reinforcement, Fig. 5 shows the initial portions of the creep curves for tests conducted on the unreinforced AZ91 alloy and the composite material at a stress of 40 MPa and a temperature of 473 K: both of these materials were tested in the T6 condition. It is apparent from Fig. 5 that, when the applied stress is the same on each specimen, the creep rate is substantially slower in the composite due to an apparent strengthening effect arising from the presence of the Saffil fibers.

In practice, however, care must be taken in making a comparison of this type because there is experimental evidence for a threshold stress, σ_0 , when creep testing this MMC (Li and Langdon, 1999; Li et al., 1999; Sklenicka et al., 2000). This means in practice that the effective stress, σ_e ($= \sigma - \sigma_0$), acting on the composite may be significantly lower than in the unreinforced material where there is no threshold stress and $\sigma_0 = 0$. In the MMC used in these experiments, an earlier analysis suggested the occurrence of load transfer (Sklenicka et al., 2000) whereby part of the external load is transferred to the reinforcement. It is instructive to note that experiments on numerous Al alloys and Al-based MMCs have often revealed slower creep rates in the composites even when creep data are compared at the same values of the effective stress (Mohamed, 1998; Li and Langdon, 1999).

To elucidate the nature of the AE response in unreinforced and reinforced materials, tests were conducted on the unreinforced alloy and on the MMC at 473 K and at the same initial level of the applied stress of 40 MPa. In each test, the stress was increased progressively at selected time intervals. The results are shown in Fig. 6 for (a) the unreinforced AZ91 alloy and (b) the composite material: again, both materials were in a T6 condition. The count rate for AE is documented along the lower axes.

Inspection of Figs. 6(a) and (b) shows there is a well-defined AE response throughout the total lifetime of the unreinforced alloy whereas creep of the MMC is not accompanied by a measurable AE except only at the instances associated with the stress increases and at the very highest stress increment of 80 MPa. Several AE pulses in the MMC are observed at an applied stress of 70 MPa. It is important to note the creep lifetime of the unreinforced alloy and the MMC. There is also a large difference between the count rate associated with the stress increases during creep of the unreinforced alloy and the MMC. The AE count rate change due to the stress increase in the MMC is several times lower than for the unreinforced alloy.

The presence of a measurable AE response must be associated either with the creep deformation occurring within the material or with the advent of creep damage in the form of debonding or breaking of the fibers. However, there are no fibers in the unreinforced alloy and, since there is an AE response throughout the creep lifetime of this material, it must be associated with the flow mechanism occurring within the alloy. There are several experiments showing a stress exponent of $n = 3$ for the unreinforced AZ91 alloy (Dargusch et al., 1998, Blum et al., 1997; Pahutová et al., 2000) and this suggests that a viscous glide process is dominant whereby the movement of dislocations is impeded by the presence of aluminum solute atom atmospheres. In addition, there have been similar reports of $n = 3$ in Mg solid solution alloys containing 0.8% Al (Vagarali and Langdon, 1982) and 3% and 5% Al (Sato et al., 1993), respectively.

If viscous glide is the rate-controlling flow process in the unreinforced AZ91 alloy with $n = 3$, it is reasonable to assume there will be no AE response: but an AE response is anticipated at higher stress levels when the dislocations are able to break away from their solute atom atmospheres (Yavari and Langdon, 1982). Therefore, in order to explain the experimental results

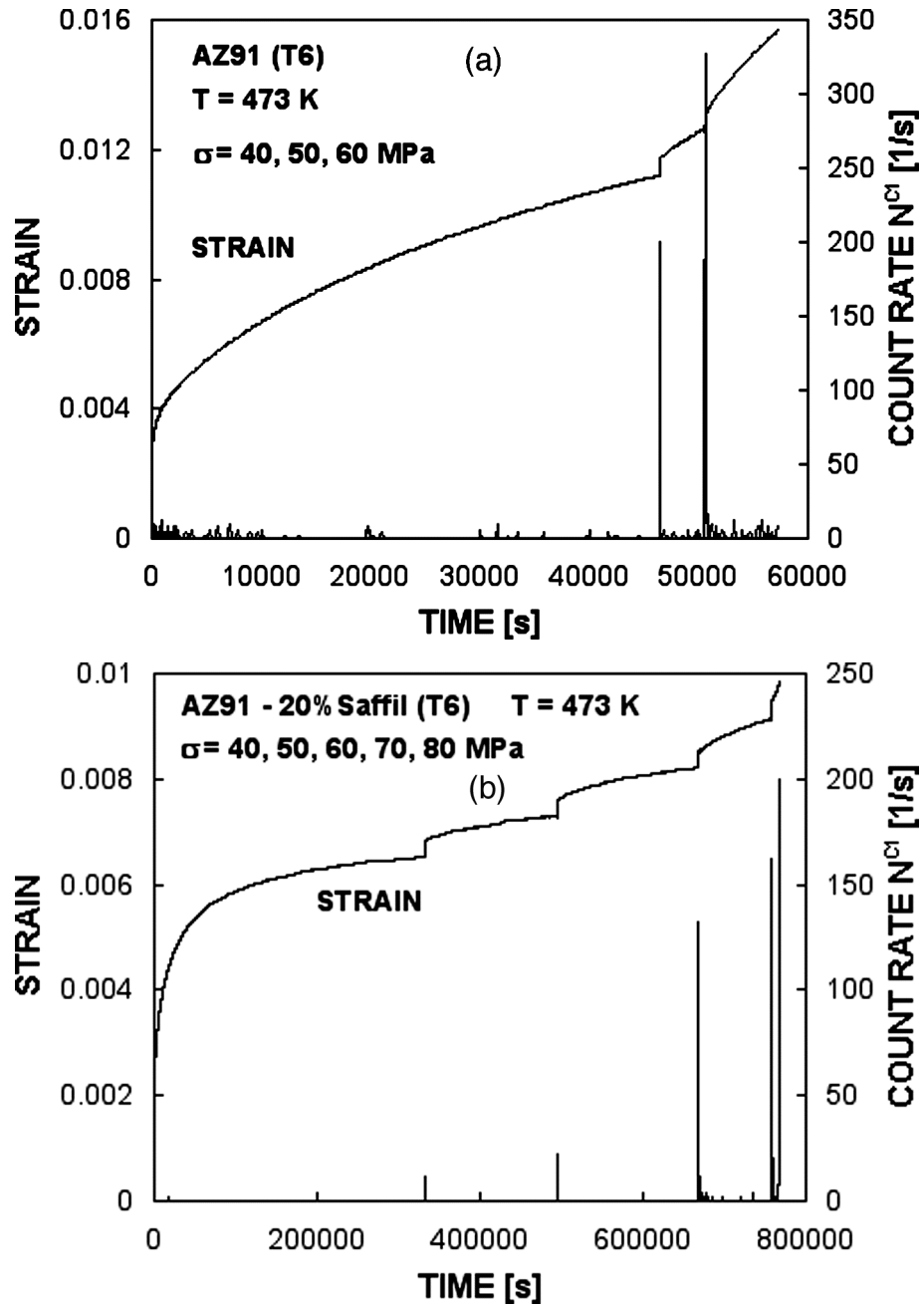


Fig. 6. Creep curves and the AE response for (a) the unreinforced alloy and (b) the composite, where both materials were tested in a T6 condition at 473 K with the same initial applied stress of 40 MPa.

documented in Fig. 6, it is necessary to demonstrate that flow occurs in the unreinforced alloy within the region of dislocation breakaway at stress levels as low as 40 MPa. The breakaway stress, σ_b , in solid solution alloys is given by an expression of the form (Friedel, 1964):

$$\sigma_b = \frac{W_m^2 c}{5b^3 kT} \quad (2)$$

where c is the concentration of the solute, b is the magnitude of the Burgers vector, k is Boltzmann's constant, T is the absolute temperature and W_m is the binding energy between the

solute atom and the dislocation, which may be written as

$$W_m = -\frac{1}{2\pi} \left(\frac{1+\mu}{1-\mu} \right) G |\Delta V_a| \quad (3)$$

where μ is Poisson's ratio, G is the shear modulus and ΔV_a is the difference in volume between the solute and the solvent atoms.

Equation (2) may be solved through the use of $\mu = 0.34$ and $\Delta V_a = 8.2 \times 10^{-30} \text{ m}^3$ (King, 1966) for aluminum atoms in magnesium and with $b = 3.2 \times 10^{-10} \text{ m}$ and $G = \{(1.92 \times 10^4) - 8.6T\} \text{ MPa}$ (Slutsky and Garland, 1957) for pure magnesium and noting that the initial concentration of aluminum in the alloy is $\sim 9 \text{ wt. \%}$, which corresponds to $\sim 8 \text{ at. \%}$ so that $c \approx 0.08$. Following this procedure, the value of the breakaway stress is estimated as $\sigma_o \approx 110 \text{ MPa}$ and this is higher than any of the applied stresses used to obtain the data in Fig. 6(a). In practice, however, it has been shown that Eq. (2) tends to overestimate the magnitude of σ_b by a factor of ~ 2 because it fails to include the variation in the interaction energy with the solute concentration and the influence of the different spacings between the solute atoms and the line of the dislocation (Endo et al., 1984). The introduction of these improvements reduces the value of σ_b to $\sim 55 \text{ MPa}$, and in practice an additional reduction is necessary because the T6 heat treatment leads to a fine dispersion of $\text{Mg}_{17}\text{Al}_{12}$ precipitates (Clark, 1968; Solberg et al. 1991), which serves to deplete the concentration of aluminum atoms remaining in solid solution within the matrix and thereby it reduces the value of c in Eq. (2). The total extent of this aluminum depletion is not known at the present time but it is reasonable to conclude that all of the stresses used in Fig. 6(a), including the lowest applied stress of 40 MPa , are within the region of dislocation breakaway and therefore the occurrence of breakaway accounts for the AE response, which is clearly visible throughout the test. This conclusion is consistent also with experimental creep data on the composite material where it was shown that breakaway occurred, and n increased above a value of 3, at an effective stress level of $\sim 14 \text{ MPa}$ at the slightly higher temperature of 573 K (Li and Langdon, 1999a and b).

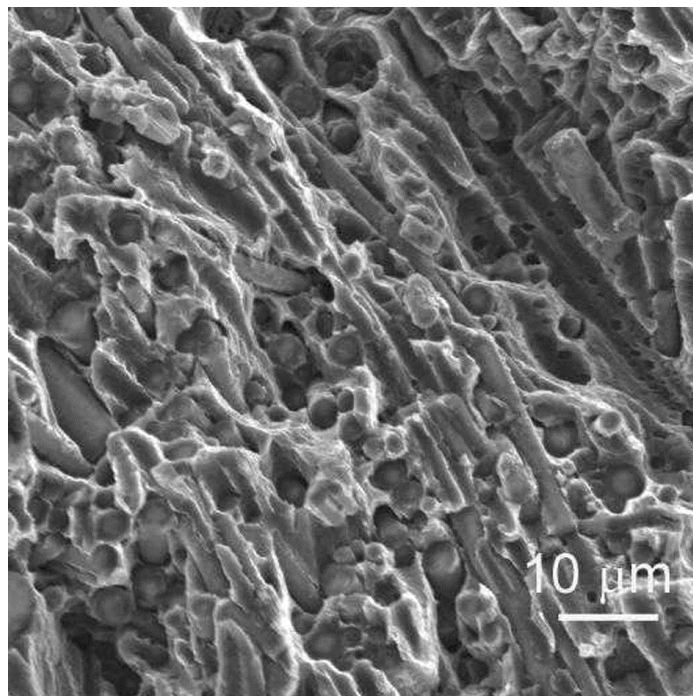


Fig. 7. Fracture surface of the composite after testing as shown in Fig. 6(b).

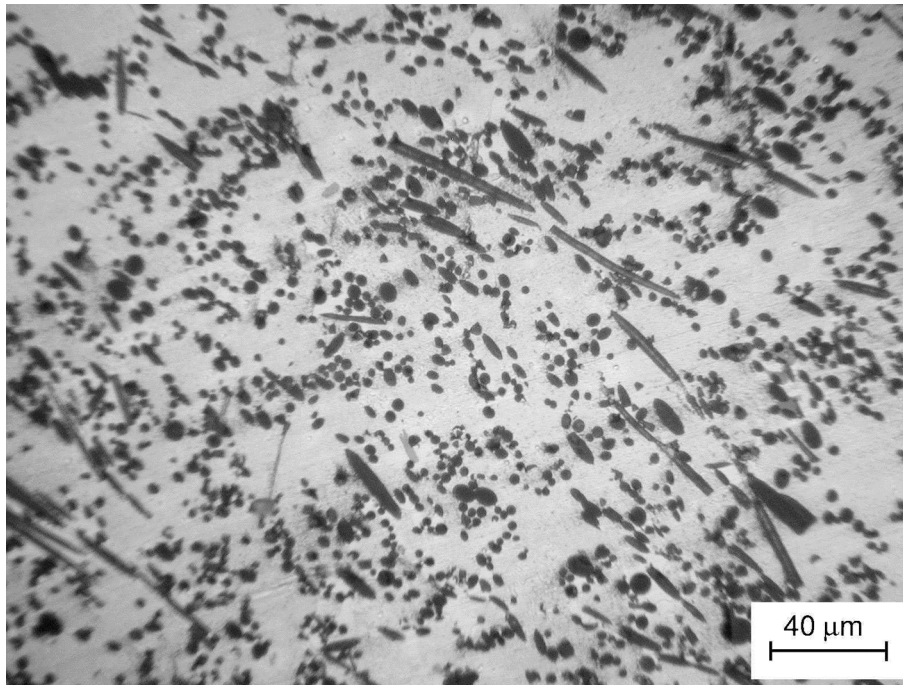


Fig. 8. Optical micrograph showing the distribution of fibers in the perpendicular plane near the crack surface shown in Fig. 7.

By contrast, no AE response is visible in the composite material shown in Fig. 6(b), at least below 70 MPa, although these tests were conducted at the same temperature of 200°C and with the same lowest applied stress of 40 MPa using material subjected to the same T6 heat treatment. This difference arises because there is a significant threshold stress in the composite and, strictly, this requires comparing the unreinforced and the reinforced materials at the same values of the effective stress acting on the dislocations. No detailed information is available on the magnitude of the threshold stress, σ_o , in the composite material at a testing temperature of 473 K but scattered results from tests conducted at this temperature under shear conditions (Li and Langdon, 1999a and b) suggest the threshold stress is of the order of $\sigma_o \approx 30$ MPa. Practically the same value of the threshold stress may be obtained from results reported in other work (Sklenicka et al., 2000a and b). If it is now assumed that the lowest applied stress level of 40 MPa used for the unreinforced alloy in Fig. 6(a) is probably close to the lowest stress for a breakaway condition in the AZ91 matrix alloy at a temperature of 473 K, it follows that breakaway in the composite will require an effective stress, σ_e , of ~ 40 MPa which is equivalent, when incorporating the threshold stress, to an applied stress of the order of $(\sigma_e + \sigma_o) \approx 70$ MPa. These calculations are therefore consistent with Fig. 6(b) and with the occurrence of a significant AE response in the composite only at the highest applied stress of 80 MPa.

Figure 7 shows the appearance of the fracture surface of the composite material after testing through the progressive loading shown in Fig. 6(b). An optical micrograph showing the distribution of fibers in the perpendicular plane near the crack surface is shown in Fig. 8. It is seen that the majority of fibers are perpendicular to this plane but some fibers lie also in the plane. It is also seen that the distribution of fibers is not homogeneous in the volume of the specimen. Thus, some areas of the volume are almost free of fibers and, by contrast, in some areas the volume content of fibers is much higher than the nominal volume of 20%. The SEM micrograph of the fracture surface (Fig. 7) shows no clear evidence for either fiber breaking or fiber pull-out. Some fibers lying in the perpendicular plane might appear to correspond to the

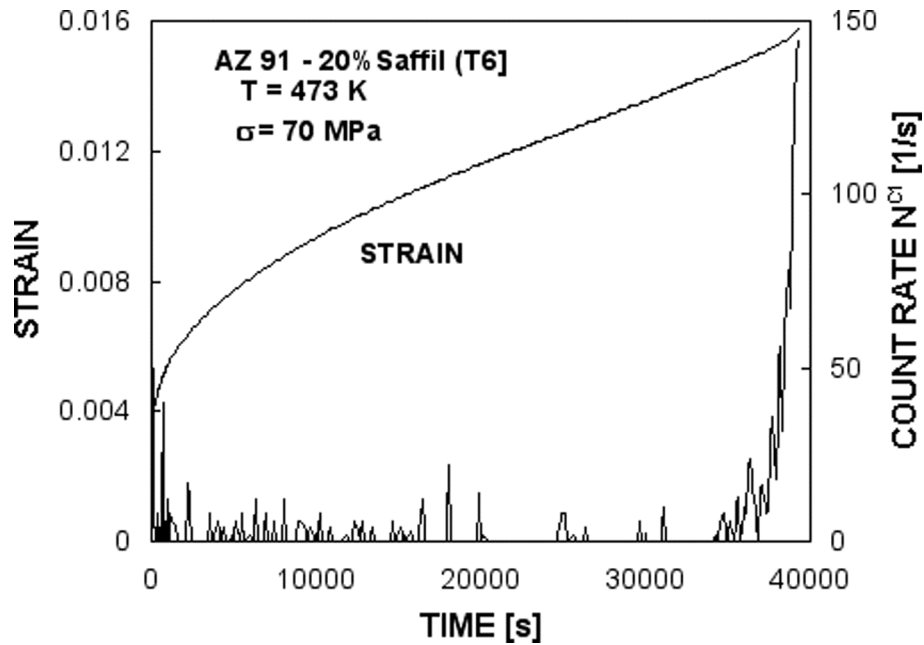


Fig. 9. Creep curve and the AE response for the composite tested at 473 K with an initial applied stress of 70 MPa after a T6 heat treatment.

occurrence of fiber fracture but these fibers broke during the squeeze-casting of the composite material. Drozd (2000) has observed similar features in a non-deformed AZ91 composite.

To evaluate the effect of increasing the applied stress and the test temperature, identical tests were conducted on the composite material using a temperature of 473 K and an applied stress of 70 MPa for samples after the T6 heat treatment. It is reasonable to expect that breakaway will occur in the composite under this applied stress and the result is shown in Fig. 9. Inspection shows the character of the AE count rate changes drastically and the AE response in Fig. 9 is significantly greater for the sample crept at 70 MPa than after creep at 40 MPa. In practice, there is a large increase in the AE activity in the later stage of tertiary creep immediately prior to fracture. The decrease in the level of the aluminum solute due to the precipitation of $Mg_{17}Al_{12}$ during the T6 heat treatment combined with the increase in the applied stress serve to increase the potential for dislocations to break away from their solute atmospheres and this gives an increase in the AE response.

An increase in the test temperature should result in a decrease of the effective stress necessary for dislocations to break away from their solute atmospheres. Tests were conducted on the composite at 583 K with an initial applied stress of 40 MPa after the T6 heat treatment. Figure 10 shows a faster creep rate and a larger AE response throughout the creep lifetime of the MMC by comparison with the results obtained at 473 K. The fracture surface is shown in Fig. 11 and there is evidence for a pull-out of the fibers corresponding to local debonding and the large AE response observed prior to failure in Fig. 10. In practice, the distribution of fibers in the perpendicular plane near the crack surface is similar to that shown in Fig. 8.

3.4 Creep of QE22 and AZ91 reinforced with SiC particles

Since no load transfer is anticipated in particle-strengthened MMCs, the creep data were analyzed using the standard relationship (Cadek, 1988):

$$\dot{\epsilon}_{ss} = A \sigma^n \exp(-Q_c/RT) \quad (4)$$

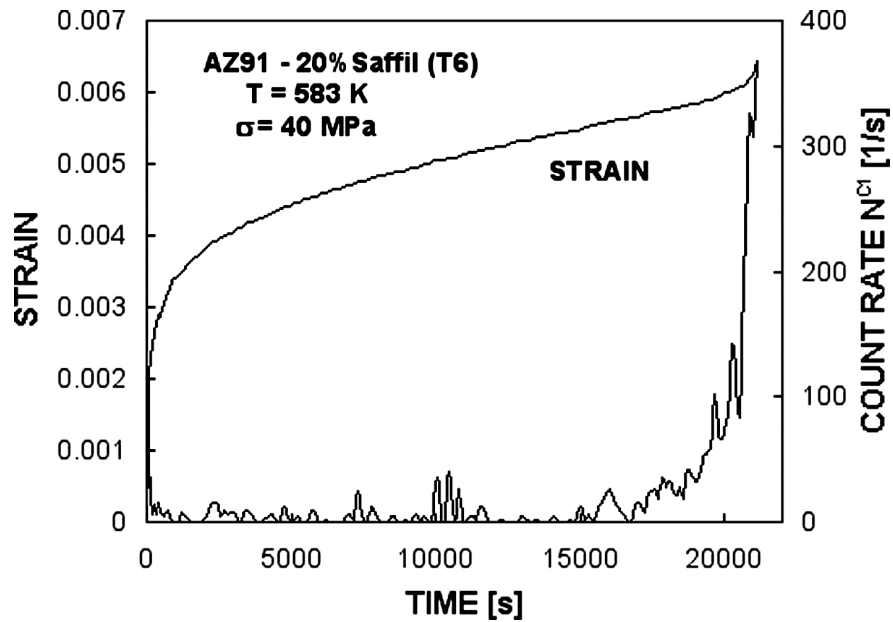


Fig. 10. Creep curve and the AE response for the composite tested at 583 K with an initial applied stress of 40 MPa after a T6 heat treatment.

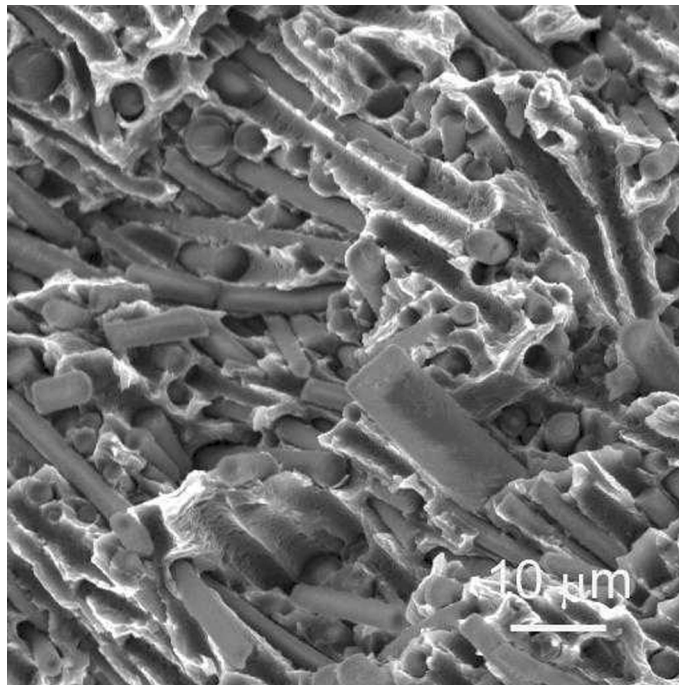


Fig. 11. Fracture surface of the composite after testing at 583 K with an initial applied stress of 40 MPa after a T6 heat treatment.

where $\dot{\epsilon}_{ss}$ is the minimum creep rate, A is a constant, σ is the applied stress, n is the stress exponent, Q_c is the activation energy for the creep process and R is the gas constant (8.314 J/Kmol).

The analysis of the creep data of the unreinforced QE22 alloy shows, for the temperature range from 423 to 473 K, an increase in the stress exponent from 2.0 to 5.8. Also, progressive

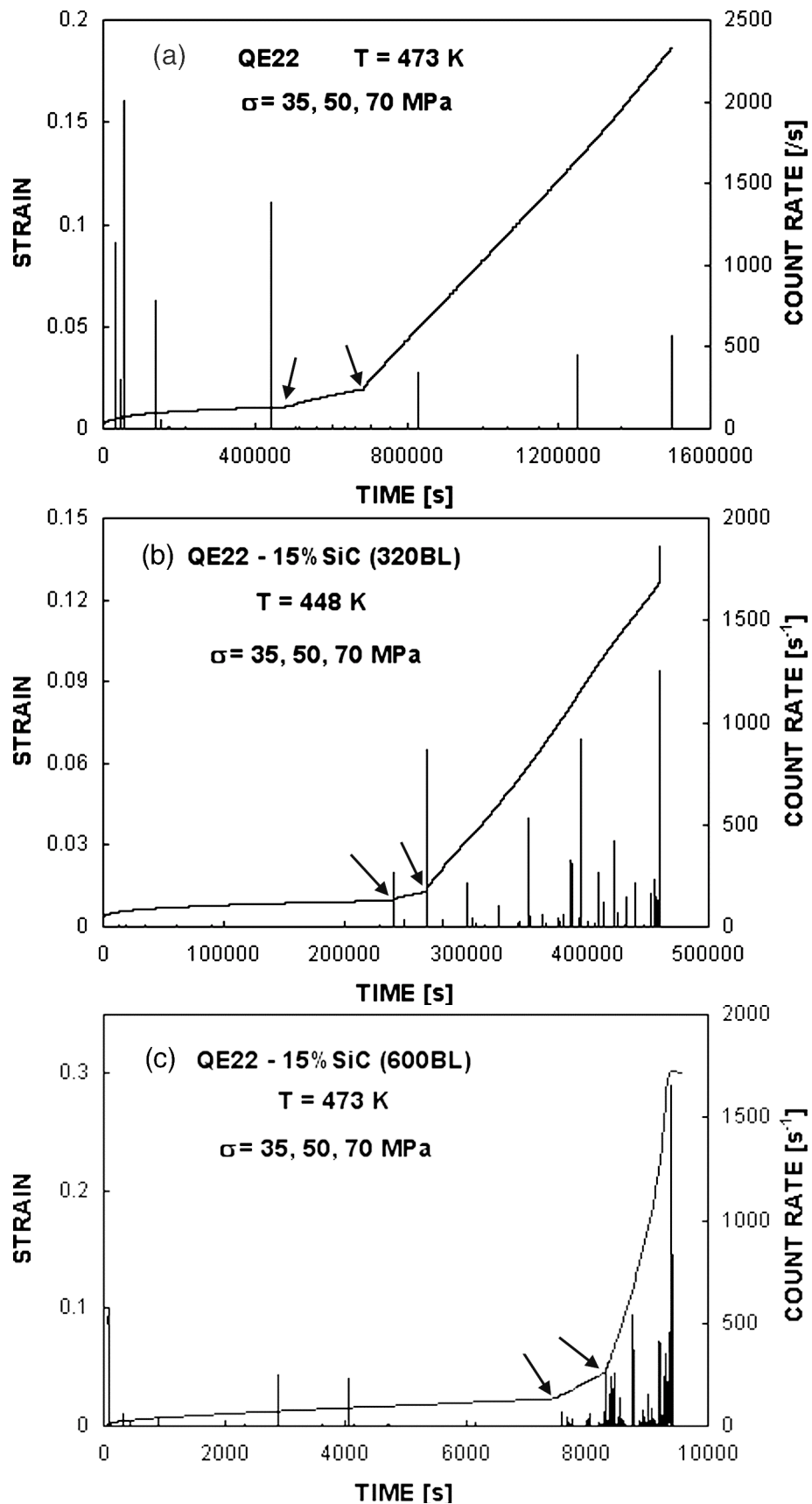


Fig. 12. The creep curve and the AE count rate tested under progressive loading: (a) the unreinforced QE22 alloy at 473 K, (b) QE22-15 vol. % SiC (320BL) tested at 448 K, (c) QE22-15 vol. % SiC (600BL) tested at 473 K. In all cases, stress changes are indicated by arrows.

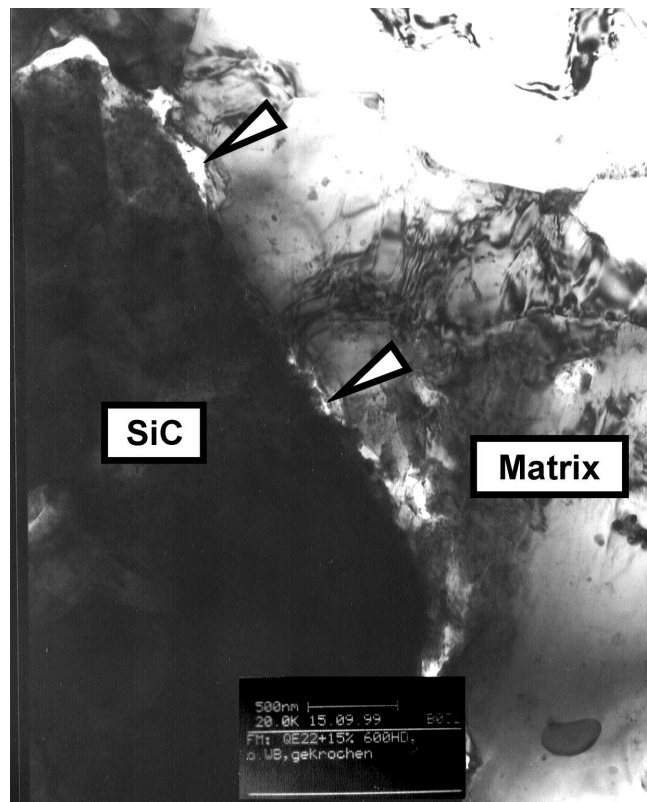


Fig. 13. Transmission electron microscopy micrograph of the QE22-SiC composite after creep deformation at 473 K showing distinct cracking (indicated by arrows) at interfaces.

loading from 35 to 70 MPa gives in an increase in the activation energy from ~ 97 to ~ 184 kJ/mol. The analysis of the creep data of the QE22-SiC reveals no clear dependence of the stress exponent and the activation energy on temperature and the applied stress. Thus, the measured values of the stress exponent are within the range from ~ 2.0 to ~ 9.4 and the measured values of the activation energy are within the range from ~ 74 to ~ 246 kJ/mol. The AZ91-SiC behaves in a very similar manner to QE22-SiC. Detailed information on the creep properties has been reported (Moll et al., 2000).

The creep rate and the AE response are shown in Fig. 12a for a test on the unreinforced QE22 alloy under progressive loading at 473 K. The test was stopped after 17 days because the limits of the AE and strain measurements were reached. Only very few AE signals appeared rather randomly during the test and these signals could not be correlated with the creep curve. Figure 12b shows the creep rate and the AE response of the QE22-SiC (320BL) MMC under progressive loading at 448 K. The creep rate is significantly higher than for the unreinforced sample deformed at 473 K. Pronounced AE activity is observed at events associated with stress increases and at the stress level of 70 MPa. In the last stage of the test, AE activity increases steadily. Figure 12c shows that a slight increase in temperature to 473 K and a reduction in the particle size to 600BL lead to a significant reduction in the creep resistance. As previously seen, intense AE is observed at a stress of 70 MPa and the AE activity is higher than shown in Fig. 12b. The AZ91-SiC MMC exhibited similar results.

The main deformation mechanism of the QE22 alloy and the QE22-SiC and AZ91-SiC MMCs is very probably diffusion-controlled dislocation motion and, possibly, also grain boundary sliding. Grain boundary sliding was not observed directly but, at a homologous

temperature of 0.5, this process tends to be unavoidable in fine-grained materials. The MMCs show a pronounced ductility and rather high creep rates in comparison with the unreinforced sample. It is reasonable to suggest, therefore, that interfacial sliding contributes significantly to the creep deformation. Since diffusion-controlled dislocation motion and grain boundary sliding are not important AE sources (Heiple and Carpenter, 1987), the observed increase of the AE activity at increasing load may indicate a growing share of interfacial sliding. Since the SiC particles are rigid, interfacial sliding is not easily accommodated sufficiently so that creep damage can take place. Indeed, many cavities and cracks were revealed at the interfaces after creep testing in examinations using transmission electron microscopy: a typical example of this cracking is shown in Fig. 13.

5. Summary

1. A number of Mg-based composites were subjected to thermal cycling and measurements were taken, using acoustic emission (AE) and dilatometry, to record the internal thermal stresses and the related structural changes and matrix plastic deformation. It is shown that the AE response and the residual strain recorded after cycling depend significantly on the upper temperature of cycling. Using a recent model developed for internal damping, it is demonstrated that the experimental data may be successfully correlated in terms of the variations of both the AE count rate with temperature and the residual strain with the upper cycling temperature.

2. The AE response during plastic deformation of the AM60 magnesium alloy is significantly dependent on the temperature. Peak AE activity is found for a deformation temperature of 200°C, which can correspond to the maximum twinning activity.

3. The introduction of short alumina fibers into an AZ91 magnesium alloy improves the creep resistance because of the introduction of a threshold stress that serves to reduce the effective stress acting on the material. The creep deformation may be monitored using AE. There is little or no AE response when deformation occurs by the viscous glide of dislocations with $n = 3$, but an AE response is visible at stress levels, which are sufficiently high such that the dislocations are able to break away from their solute-atom atmospheres. There may be also a very large AE response immediately prior to failure due to a local debonding around the fibers, which is visible as a pull-out of fibers at the fracture surface.

4. Creep behavior was investigated in a QE22 alloy in the unreinforced condition and QE22 and AZ91 alloys reinforced with 15 vol. % SiC particles. The creep of the unreinforced alloy appears to be governed by grain boundary sliding and dislocation motion. The reinforced alloy shows poor creep resistance in comparison with the unreinforced alloy at comparable stress levels and temperatures. This may be explained by taking into account interfacial sliding as an additional creep mechanism. As a consequence of this interfacial sliding, many cavities and macroscopic cracks occur at the interfaces.

Acknowledgements

This work was conducted within the framework of Research Goal No. 190-01/206054 supported by the Ministry of Education, Youth and Sports of the Czech Republic. Additional support was provided by the Grant Agency of the Czech Republic under Grant No. 103-01-1058 and the Grant Agency of the Academy of Sciences of the Czech Republic under Grant No. A2041902. Two of the authors (F.C. and P.L.) gratefully acknowledge the support of the Alexander von Humboldt Foundation (Germany). Thanks are also due to Prof. Dr. Z. Trojanová of Charles University, Prague for many stimulating discussions.

References

- R.J. Arsenault and M. Taya (1987), *Acta metall.*, **35**, 651-657.
- ASM Handbook (1999) *Magnesium and Magnesium Alloys*. ASM International, Materials Park, OH (1999).
- W. Blum, P. Weidinger, B. Watzinger, R. Sedláček, R. Rösch and H.-C. Haldenwanger (1997), *Z. Metallkd.*, **88**, 636-641.
- J. Cadek (1988), *Creep in Metallic Materials*, Elsevier, Amsterdam, the Netherlands.
- E. Carreño-Morelli, S. E. Urreta and R. Schaller (1997), *Proceedings of the International Conference on Fatigue of Composites* (S. Degallaix, C. Bathias and R. Fougères, eds.), *Société Française de Métallurgie et de Matériaux*, Paris, France, pp. 112-119.
- E. Carreño-Morelli, S. E. Urreta and R. Schaller (2000), *Acta mater.*, **48**, 4725-4733.
- J.B. Clark (1968), *Acta metall.*, **16**, 141-152.
- F. Chmelík, E. Pink, J. Król, J. Balík, J. Pesicka and P. Lukác (1998a), *Acta mater.*, **46**, 4435-4443.
- F. Chmelík, J. Kiehn, P. Lukác, K.U. Kainer and B. L. Mordike (1998b), *Scripta Mater.*, **38**, 81-87.
- M.S. Dargusch, G.L. Dunlop and K. Pettersen (1998), *Magnesium Alloys and their Applications*, (B. L. Mordike and K. U. Kainer eds.), *Werkstoff-Informationsgesellschaft*, Frankfurt, pp. 277-284.
- Z. Drozd (2000), PhD. Thesis, Charles University, Prague, Czech Republic.
- T. Endo, T. Shimada and T.G. Langdon (1984), *Acta metall.*, **32**, 1991-1999.
- R.M. Fisher and J.S. Lally (1967), *Can. J. Phys.*, **45**, 1147-1159.
- J. Friedel (1964), *Dislocations*, Pergamon Press, Oxford.
- M. Friesel, S. H. Carpenter (1984), *J. Acoustic Emission*, **3**, 11-17.
- C. Fritze, H. Berek, K.U. Kainer, S. Mielke and B. Wielage (1998), *Magnesium Alloys and their Applications* (B.L. Mordike and K.U. Kainer, eds.), *Werkstoff-Informationsgesellschaft*, Frankfurt, Germany, pp. 635-643.
- C. R. Heiple and S. H. Carpenter (1987), *J. Acoustic Emission*, **6**, 177-237.
- H. Kato, T. Tozawa and Y. Takayama (1986), *Progress in Acoustic Emission III*, (Y. Yamaguchi, K.Aoki and T. Kishi eds.), *Japanese Society for Nondestructive Inspection*, Tokyo, Japan, pp. 514-521.
- J. Kiehn, C. Köhler and K. U. Kainer (1994), *Key Engng Mater.*, **97-98**, 37-42.
- H.W. King (1966), *J. Mater. Sci.*, **1**, 79-90.
- Y. Li and T.G. Langdon (1999a), *Metall. Mater. Trans.*, **30A**, 315-324.
- Y. Li, T. G. Langdon (1999b), *Metall. Mater. Trans.*, **30A**, 2059-2066.
- Y. Li, V. Sklenicka and T. G. Langdon (1999), *Creep Behavior of Advanced Materials for the 21st Century*, (R. S. Mishra, A. K. Mukherjee and K. L. Murty eds.), *The Minerals, Metals and Materials Society*, Warrendale, PA, pp. 171-178.
- F.A. Mohamed (1998), *Mater. Sci. Eng.*, **A245**, 242-256.
- F. Moll, F. Chmelík, P.Lukác, B. L. Mordike, K. U. Kainer (2000), *Mater. Sci. Eng.*, **A291**, 246-249.
- B. L. Mordike, K. U. Kainer and B. Sommer (1997), *Proceedings of the Third International Magnesium Conference* (G. W. Lorimer, ed.), *The Institute of Materials*, London, pp. 637-645.
- B. L. Mordike, K. U. Kainer, F. Moll and B. Sommer (1998), *Magnesium 97*, (E. Aghion and D. Eliezer eds.), *Magnesium Research Institute Ltd.*, Beer-Sheva, pp. 178-185.
- M. Pahutová, V. Sklenicka, K. Kucharová, J. Brezina, M. Svoboda and T. G. Langdon (2000), *Magnesium 2000*, (E. Aghion and D. Eliezer eds.), *Magnesium Research Institute Ltd.*, Beer-Sheva, pp. 285-292.

- H. Sato, Y. Masada and H. Oikawa (1993), Aspects of High Temperature Deformation and Fracture in Crystalline Materials, (Y. Hosoi, H. Yoshinaga, H. Oikawa and K. Maruyama eds.), The Japan Institute of Metals, Sendai, pp. 107-114.
- E. Siegel (1977), *Acta metall.*, **25**, 383-394.
- V. Sklenicka, M. Pahutová, K. Kucharová, M. Svoboda and T. G. Langdon (2000a), *Key Eng. Mater.*, 171-174, 593-600.
- V. Sklenicka, M. Pahutová, K. Kucharová, M. Svoboda and T. G. Langdon (2000b), *Magnesium Alloys and their Applications*, (K. U. Kainer ed.), Wiley-VCH, Weinheim, pp. 246-251.
- L.J. Slutsky and C.W. Garland (1957), *Phys. Rev.*, **107**, 972-976.
- J.K. Solberg, J. Tørklep, Ø. Bauger and N. Gjestland (1991), *Mater. Sci. Eng.*, **A134**, 1201-1208.
- Z. Trojanová (2002), Charles University, Prague, private communication.
- S.E. Urreta, R. Schaller, E. Carreño-Morelli and L. Gabella (1996), *J. Physique*, **IV 6 C8**, 747-750.
- S.S. Vagarali and T.G. Langdon (1982), *Acta metall.*, **30**, 1157-1170.
- K. Xia and T.G. Langdon (1994), *J. Mater. Sci.*, **29**, 5219-5231.
- P. Yavari and T.G. Langdon (1982), *Acta metall.*, **30**, 2181-2196.
- P. Zhang, B. Watzinger, P.Q. Kong and W. Blum (2000), *Key Eng. Mater.*, **171-174**, 609-616.

TRAINING AND CERTIFICATION ON THE FIELD OF ACOUSTIC EMISSION TESTING (AT) IN ACCORDANCE WITH THE EUROPEAN STANDARDISATION (EN 473)

P. TSCHELIESNIG

Institute for Technical Physics, TÜV Austria, Vienna, Austria

Abstract

A brief overview of education and training of NDT personnel on acoustic emission (AE) in Europe is given. New courses prepare Levels 1 to 3 in accordance with EN 473.

Introduction and Historical Overview

The education and training of NDT personnel on acoustic emission (AE) in Europe was first given in Germany. The courses were held at the “Battelle Institut” in Frankfurt from 1975 till 1981. Through these courses, approximately 250 persons within the German speaking countries learned about the fundamentals of AE. This situation deteriorated in the following years, because of the growing refusal of AE within Germany.

Although this was a German problem, the training of AE personnel, which is one important step for the acceptance of a non-destructive testing method, was more or less absent within Europe. Also the new attempt by the German Working Group for AE failed especially due to the fact that within the EN 473/1993, “qualification and training of NDT personnel” was not accepted as a standardised NDT method, although Acoustic Emission Testing (AT) was mentioned under all NDT methods, for which the rules of EN 473 could be used. This decision was a considerable setback for the efforts to establish a common European and comparable training for AE. The efforts continue and the first European training course in acoustic emission was given at CETIM in France. This course combined the training of the Level 1 and Level 2. The new attempt in Germany to establish an “Information course about AE” led in 1999 to the first training course in AT Level 1 (AT1) in Germany, organised under the umbrella of the German Society of NDT.

Basis for the AT Training and Certification

During preparation of the training course and the examination for an AT1, the new edition of the EN 473 was under preparation. In this new standard, AT became a standardised NDT method with requirements for all three levels of certification.

Based upon the EN 473, minimum requirements for experience and training time were defined. Furthermore, beside the number of questions for the general and specific examination the minimum number and type of test specimens for Level 1 and Level 2 practical examination were standardised. Because the personnel, which shall be trained, was coming from mainly from service companies and the chemical and petrochemical industry, the examination shall be performed in the industrial sector of “Pre- and in-service testing of equipment, plant and structure.”

The content of the training courses was based on an ICNDT draft about the minimum requirement for the training of NDT personnel “Acoustic Emission”. Meanwhile the TC138 AHG8 established a training syllabus for NDT methods – minimum requirement, which shall be published as CEN Technical report in 2003. These are shown in Tables 1 - 3.

Table 1: Minimum experience requirements

NDT-method	Level 1	Level 2
AT	6 months	12 months

Table 2: Minimum training requirements

NDT-method	Level 1	Level 2
AT	40 h	64 h

Table 3: minimum number and type of test specimens for the practical examination

NDT method and level	Number and type of specimen	Declaration
AT1	1	For AT examinations the discontinuities are normally replaced by artificial sources. The level 1 candidate shall demonstrate the ability to install the equipment, verify its sensitivity and record the test data.
AT2	1 + 2datasets	The level 2 candidate shall also demonstrate the ability to interpret and evaluate previously recorded test data.

EN 473/2000 “NDT – Qualification and Certification of NDT Personnel – General Principles”

The EN 473 establishes a system for the qualification and certification of personnel, who perform industrial NDT. In this standard, levels of qualification with defined competencies will be introduced.

The Level 1 personnel may be authorised to:

- a) set up NDT equipment;
- b) perform the tests according to written instructions;
- c) record and classify the results of the tests in terms of written criteria, and
- d) report the results.

Level 1 certified personnel shall not be responsible for the choice of test method or technique to be used, nor for assessment of test results.

The Level 2 personnel may be authorised to:

- a) select the NDT technique for the test method to be used;
- b) define the limitations of application of the testing method;
- c) translate NDT standards and specifications into NDT instructions;
- d) set up and verify equipment settings;
- e) perform and supervise tests;
- f) interpret and evaluate results according to applicable standards, codes or specifications;
- g) prepare written instructions;
- h) carry out and to supervise all Level 1 duties;
- i) provide guidance for personnel at or below Level 2, and
- j) organise and report the results of non destructive tests.

An individual certified to Level 3 may

- a) assume full responsibility for a test facility and staff;
- b) establish and validate NDT instructions and procedures;
- c) interpret standards, codes, specifications and procedures;
- d) designate the particular test methods, procedures and NDT instructions to be used, and
- e) carry out and supervise all Level 1 and Level 2 duties.

This clear regulation for the distribution of the different duties sets forth that a test organisation needs all three levels of NDT personnel and also defines which competence have to be trained and examined during the required courses.

Beside the technical knowledge about AE, the Level 1 has to be trained in the equipment set up and how to use a written test instruction properly. The Level 2, which must have gained test experience during the 12-month experience time, has to learn how to write a test instruction based on the QM – NDT procedures and shall be able to perform the assessment of the test results. The Level 3, which is an absolute must for a testing organisation to retain, has to be the head of the complete organisation with the competence to evaluate and interpret results in term of existing standards, codes and specifications and a general familiarity with other NDT methods.

CEN/TC138 AHG8 “Training Syllabus”

Because the comparable applications all over Europe need for the training and certification the same minimum requirements for the education, the CEN/TC138 establish the AHG8, which became responsible for the creation of a training syllabus for all NDT methods, as mentioned in the EN 473. Table 4 shows the unified format for all NDT methods, which was created by the AHG8 during its “kick-off” meeting last year (2001) in Paris.

Table 4: Unified format

	Contents	Level 1	Level 2	Level 3
1	introduction, terminology, purpose and history of NDT ^a	X	X	X
2	physical principles and associated knowledge ^b	X	A	A
3	product knowledge and capabilities of method and its derivate techniques ^{c f}	X	A	A
4	equipment ^f	A	X	X
5	information prior of test ^{d f}	A	X	X
6	testing ^f	A	X	X
7	evaluation and reporting ^f	A	X	X
8	assessment ^f		A	X
9	quality aspects ^{e f}	X	A	A
10	environmental and safety conditions	A	A	X
11	developments		X	A

A for the considered level, it is a very important point.

- a (Brief history of NDT in general + introduction to the various NDT method, common standardised terminology)
- b (chemistry, mathematics, ...)
- c (include metallurgy)
- d (including e.g. written instruction, standards, procedures, acceptance criteria, relevant indications, performances, ...)
- e is dealing with responsibilities and guidance
- f include codes, standards and procedures

note: For Level 3 basic the contents have to be taught for at least four methods including at least one volumetric method.

Based upon this unified format the different Working Groups of CEN/TC138 started to establish minimum requirements for the content of the training courses and the examination. These minimum requirements shall be used also as a basis for an ISO standard, which shall make the comparable training applicable worldwide.

AT Training within the German-speaking Countries

As an example for the first EN473 conform training courses on the AT field, the following training courses were given under the umbrella of the German Society of NDT (DGZfP) in co-operation with the Austrian Society of NDT (ÖGfZP).

The training courses given in accordance with the EN473 before June 30th, 2002.

Level	year	location	number of candidates
1	1999	Ismaning (D)	15
2	2000	Dortmund (D)	10
3	2000	Puchberg (A)	15
1	2001	Wien (A)	12
1	2001	Dortmund (D)	10
2	2002	Dortmund (D)	11

The courses are under preparation.

Level	year	location
1	2002	Wien (A)
1 or 2	2003	Dortmund (D)
3	2003	Puchberg (A)

We shall be proud on the fact that till today no other testing was able to hold the first training courses with examinations starting from level 1 to 3, within a time period of one year, with attendees from Germany (D), Austria (A) and Switzerland (CH).

Prospects of the Future

The training and examination in conformity with the EN473/2000 is a very important step for AT to become a more accepted non-destructive testing method. Because this bring AT on

the way from the “so-called experts” to real trained and certified NDT personnel not only in the service organisations as well as in the user industry.

In the future the user industry shall have at minimum one trained AT1, 2 or 3, which is able to recognise the problem and to evaluate a possible solution in conjunction with a service organisation. He also shall be able to validate the service organisation and the proposed written procedure and supervise the testing people during their work.

A further demand for the future is, that all AT testing organisation have the responsible AT1, AT2 and AT3, because only their teamwork, with their different competence can guarantee a proper execution of the test order. This give the potential customer the opportunity to decide, which testing organisation is able to perform the job, this one, which is accredited and have certified AT testing personnel, or this, which nominates themselves as experts,

References

EN473/2000 Non-destructive testing – Qualification and certification of NDT personnel – General principles.

CEN/TC138 AHG8 training syllabus “unified format”.

“Die Ausbildung auf dem Gebiet der Schallemissionsprüfung (AT) – Historie, Inhalte und Ausblick” - P. Tscheliesnig, TÜV Österreich, Wien (A); W. Schmidt, DGZfP, Dortmund (D) presented at the annual DGZfP conference, Berlin (D) 2001.

THRESHOLD COUNTING IN WAVELET DOMAIN

MILAN CHLADA and ZDENEK PREVOROVSKY

Institute of Thermomechanics AS CR, Prague, Czech Republic

Abstract

Threshold counting of AE signal is the simplest and most frequently used type of AE signal parameterization. As the wavelet transform of AE signal appears to be useful tool for AE analysis, the threshold counting applied to the wavelet decomposition represents a logical extension of commonly used procedures. New AE signal parameters (wavelet counts) are introduced using a two-level threshold counting of wavelet coefficients. The application of wavelet counts is illustrated in three examples of both real and simulated AE data. The significance of various classical and newly introduced AE signal parameters used to AE source identification is tested using the neural network sensitivity and factor analyses. The wavelet counts, carrying the global information in both time and frequency domains, can replace ill-defined frequency spectrum parameters of AE signal in a more efficient way.

1. Threshold Counting

1.1 AE signal parameterization

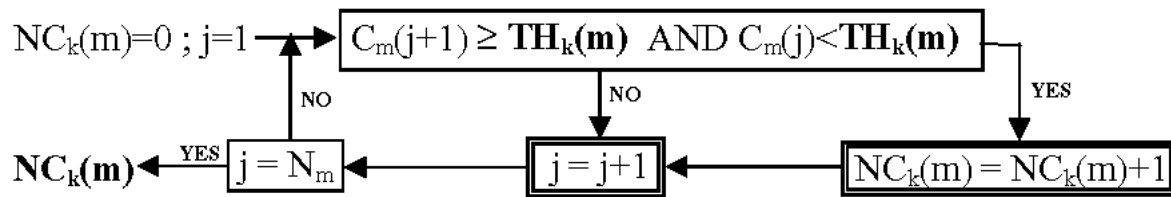
Threshold counting (TC) of AE signal crossings of predetermined voltage levels is one of the oldest and most common parameterization methods in the AE analysis. The number of threshold counts N_c or count rate, dN_c/dt , simply characterizes both the continuous and burst AE signals in time domain. TC substantially reduces information about AE signal, and saves good knowledge on the global AE activity. TC methods are very effective as simple devices and/or digital signal processing (DSP) procedures can be used for AE detection and quantitative evaluation. The most efficient seems to be the dual TC (low and high amplitude threshold level, [1]), as it allows distinguishing solitary high amplitude signal bursts in quasi-continuous AE. In the most cases, the time evolution of count rate closely correlates with, e.g. that of signal RMS value, as both quantities are related to the instantaneous signal energy. The main information differences between both signal energy measures consist in a constant noise level suppression at the TC, i.e., d.c. component of RMS curve is eliminated. Another difference deals with the signal transform linearity. Contrary to the RMS measure, TC represents a highly nonlinear signal transform, which may cause some difficulties (it is surprising that rigorous mathematical treatment of TC transform properties is still insufficient). On the other hand, due to its non-linearity, the TC allows often better recognition of some critical events (e.g. in leak detection) than linear signal treatments.

The purpose of AE signal parameterization is to reduce registered signal waveform data into the lowest possible number of signal features carrying maximum of important signal information in a simplest form. The number and type of signal features are chosen so as to conform to various criteria (diagnostic purpose, device capabilities, simple and effective DSP, etc.). Together with a number of signal parameters in time domain, parameters of frequency spectra (parameterization in frequency domain) are often used by AE source identification procedures. The time-frequency representation (windowed FFT, Wigner-Ville distribution, etc.) combines both aspects of AE signal processing [2]. The most advanced processing of AE signal in the wavelet

domain [3] may be considered as an enhancement of the time-frequency representation. The governing wavelet transform (WT) is extremely useful in analyzing time series containing non-stationary power at many different frequencies. In addition to its main destination (signal denoising and compression), the WT has shown to be very effective tool for AE signal processing (e.g. source location in plates [4], fracture mode classification in composites [5], etc.). Also from the computational point of view, the WT seems to be more effective than e.g. FFT used in real time DSP of AE signals. Nevertheless, for the purpose of AE signal classification, the WT signal representation should be parameterized to reduce the extent of input data to pattern recognition analysis (e.g. by artificial neural networks). The simplest way to extract general features from the AE signal decomposed by WT is threshold counting at various decomposition levels. This procedure may be introduced as an equivalent to the TC of AE signal in different frequency bands.

1.2. Definition of new AE parameters

Let us suppose, that we have a discrete, multi-level one-dimensional wavelet decomposition of a sampled signal $s(i)$. Let $C_m(j)$, $j=1 \dots N_m$ be the approximation coefficients ($m=1$) or detail wavelet coefficients at specific level m ($m=2, \dots, L+1$, where L is a number of decomposition levels). The three new parameters $NC_1(m)$, $NC_2(m)$ and RCG_m of each detail level and/or approximation are computed as follows:



where $TH_k(m)$ ($k=1,2$) are counting two threshold levels. They differ with each wavelet decomposition level. The value $TH_1(m)$ is usually set just under the level of noisy coefficients and $TH_2(m)$ around the first quarter between the noise magnitude and maximum coefficient of corresponding wavelet decomposition level. Parameter RCG_m is relative gravity center of wavelet coefficients in analyzed signal sample:

$$RCG_m = \frac{\sum_{j=1}^{N_m} j \cdot |C_m(j)|}{N_m \cdot \sum_{j=1}^{N_m} |C_m(j)|}$$

By the computation above, we obtain $3(L+1)$ new parameters, which are then compared with the following classical AE parameters (signal features) [6] in time and frequency (spectral) domain:

- *Time domain:* (1) Amplitude, (2) Rise time, (3) RMS, (4) Energy moment, (5) Relative center of gravity, (6) ASL, (7-9) Second-order statistical moments.
- *Frequency spectrum parameters:* parameters of power spectral density function $f(\omega)$

$$P_X = 100 \cdot \int_X f(\omega) d\omega \bigg/ \int_G f(\omega) d\omega, \quad X \in \{A, B, C, D, E, F\}$$

where arbitrarily chosen six frequency bands X are related to the Nyquist frequency, ω_N : A: $(0 - 0.12) \cdot \omega_N$; B: $(0.12 - 0.24) \cdot \omega_N$; C: $(0.24 - 0.36) \cdot \omega_N$; D: $(0.36 - 0.48) \cdot \omega_N$; E: $(0.48 - 0.6) \cdot \omega_N$; F: $(0.6 - 1) \cdot \omega_N$.

2. Analysis of AE Signal Parametrization

The main goal of any parameterization is to extract maximum of useful information on given data. On the other hand, the redundancy of computed parameters should be minimized. Two methods, the factor analysis and the neural network sensitivity analysis are helpful tools as to reduce the number of extracted parameters. Both methods show us which features support the most important information about existing problem and whether the newly developed parameters are independent with one another.

2.1 Factor analysis (FA)

FA is a method frequently used to find linear relations among parameters and to compute new, hypothetical variables (factors) explaining variance of parameters. FA is based on principal component analysis (PCA). PCA has three effects:

1. orthogonalizes components of transformed input vectors so that they become uncorrelated;
2. organizes resulting orthogonal components (principal components) so that the component with the largest variance is the first; and
3. eliminates components that contribute only little to the variance of data set.

The loss of information is minimized, and corresponds to the difference between the original and transformed data. PCA represents linear data transform (orthogonal rotation followed by scaling). It can be expressed as a matrix-multiplication $Z = AP$, where the original data are stored in matrix Z , new hypothetical variables (factors) in matrix P and the *factor scheme* A represents regression coefficients of factors to the original variables.

2.2 Sensitivity analysis of neural networks

One of the most important problems in NN-based classification systems [7] is the appropriate choice of input pattern parameters called features. The problem of optimal feature selection consists in identification of significant parameters and deletion of remaining ones from the initially large, redundant set of features. Some pattern features can be redundant for making the correct decision. When the number of features is relatively small, exhaustive or quasi-exhaustive search may be used to select the best feature subset. But increasing number of attributes results in rapid growth of the number of possible combinations. Therefore, Fidalgo [8] suggested an alternative approach to the feature subset selection, comprising of the following steps:

1. Train the BP (back propagation)-network with outputs y_j ($j = 1 \dots m$) using all possible candidate features.
2. For all training patterns, compute $\partial y_j / \partial x_i$, which is the derivative of the network outputs y_j with respect to its inputs x_i ($i = 1 \dots n$).
3. Compute the mean absolute value of the above derivatives for each input x_i to define the sensitivity coefficient s_{ij} as:

$$s_{ij} = \frac{1}{P} \sum_{p=1}^P \left| \frac{\partial y_{pj}}{\partial x_{pi}} \right|$$

where p represents the pattern index.

High values of sensitivity coefficients s_{ij} indicate “important“ features for the trained BP-networks. The differences of s_{ij} values among significant and dummy features become smaller with increasing amount of noise. If dummy features are eliminated and BP NN training is repeated using only the remaining ones, the performance error becomes lower. This confirms the advantage of eliminating dummy variables that just introduce noise. Sensitivity coefficients of the trained BP-networks can also be calculated by BP technique algorithm. These coefficients express the network sensitivity to the considered set of input patterns.

3. Comparison of Parametrized AE Data

Performance of various AE signal parameterization and classification procedures including parameterization in wavelet domain has been tested on examples of both experimental and simulated AE data obtained by different ways.

3.1 Continuous AE data

The first example is related to relatively long records of quasi-continuous AE. AE signals were recorded during the metal-sheet punching process described in [9]. Punching is usually accompanied by AE of high intensity, and AE monitoring can be used to identify occurrence of defects on cutting tools. Computer-controlled hydraulic press has been used to cutout circle and square pieces from 1-mm-thick carbon steel sheets (both the diameter of circle and side of the square were 160 mm). Punching tests were performed using intact and damaged cutting tools. The artificial damage was produced by grinding small parts of cutting tool edge (1% of circumference). Four AE transducers were placed at various positions on cutting tool (matrix). Signals from AE transducers were filtered (high-pass 100 kHz), pre-amplified (40 dB), and recorded by a transient recorder YOKOGAWA DL708 (10 MS/s at 12 bits). The length of stored AE signals was up to 0.5 s, so very large data were treated. Scheme of punching process accompanied by AE signals from four transducers (A to D) is shown in Fig. 1. Localization ANN has been trained on Pen - test data. Hundreds of AE events superimposed on continuous AE background were extracted from each record, and were localized using fuzzy neural networks.

The initial idea of these tests was to identify process changes and small cutting tool defects directly according to the changes of some typical (spectral) AE signal features. Hundreds of punching tests have been performed and analyzed by using classical AE signal parameterization mentioned above. Neither FA nor NN sensitivity analysis showed any important differences between tests with intact and damaged tools (the energy weighted probability summations of the fuzzy located events were finally used to recognize and localize cutting tool defects, which is discussed elsewhere [9]). Recently, the stored signals were re-analyzed using the TC parameterization in wavelet domain. Figure 2 illustrates the time evolution of resulting wavelet domain counts $NC_1(m)$ derived from one AE signal recorded during the test #V005. The whole record

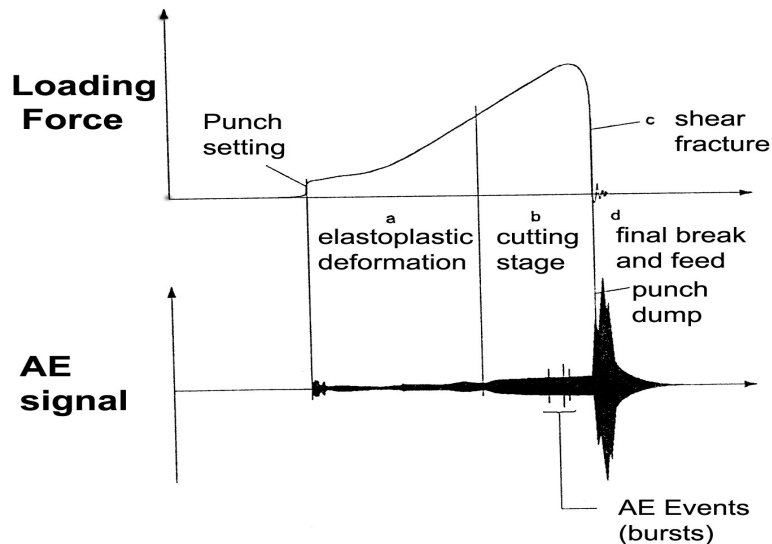


Fig. 1a. Scheme of metal punching process.

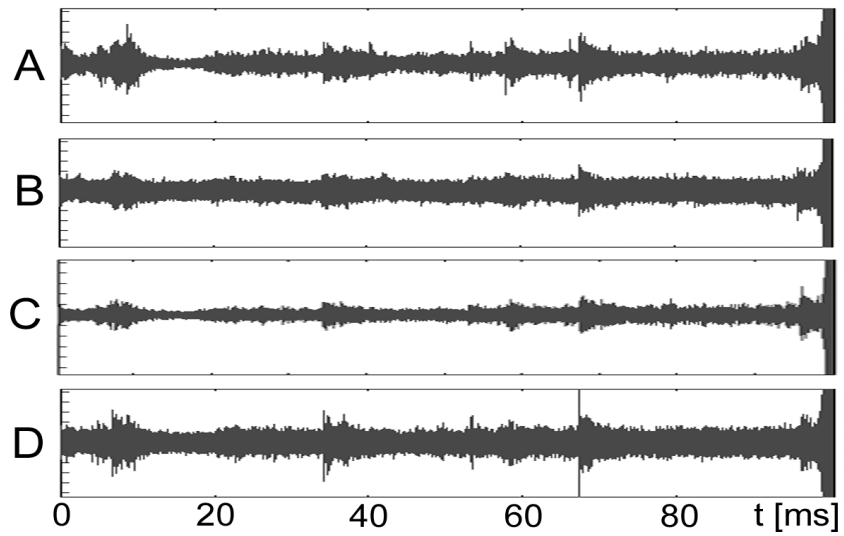


Fig. 1b. AE signals of metal punching process, recorded by four AE transducers (zoomed part b of the process in Fig. 1a) placed on cutting tool [9].

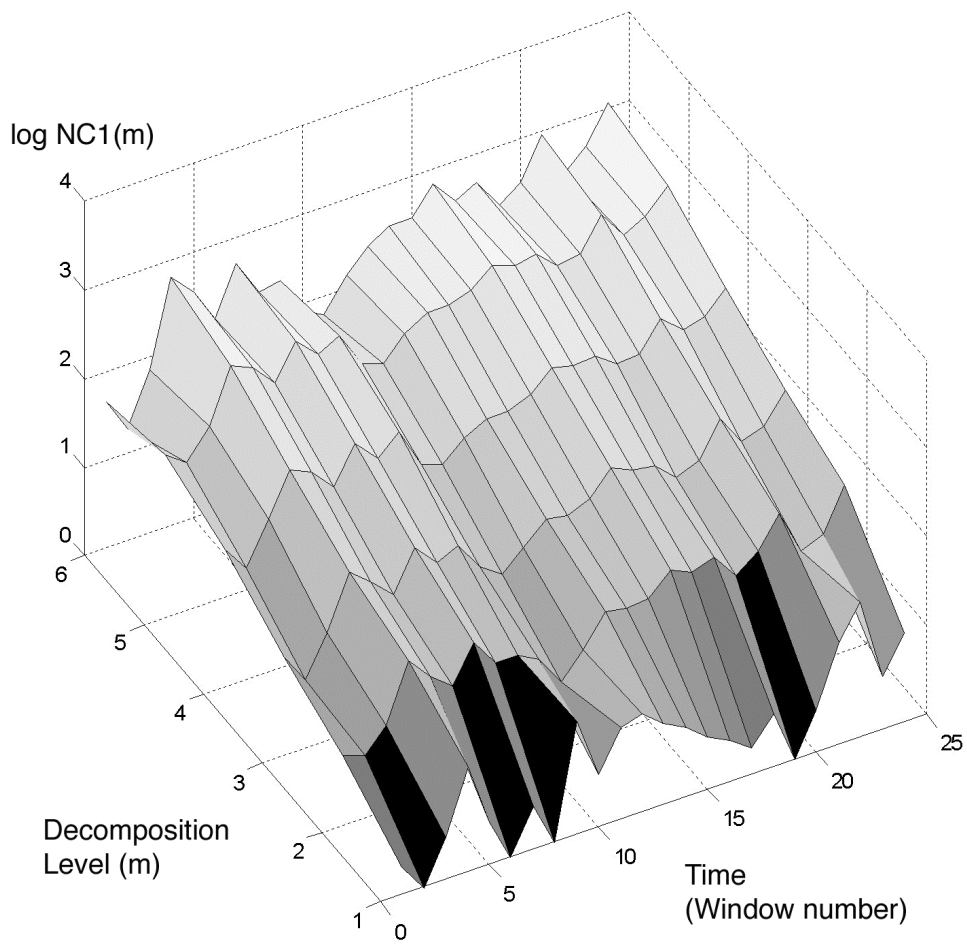


Fig. 2. Time development of AE signal parameters NC_1 ($m = 1$ to 6) during the metal sheet punching ($NC_i(m)$ are plotted in logarithmic scale).

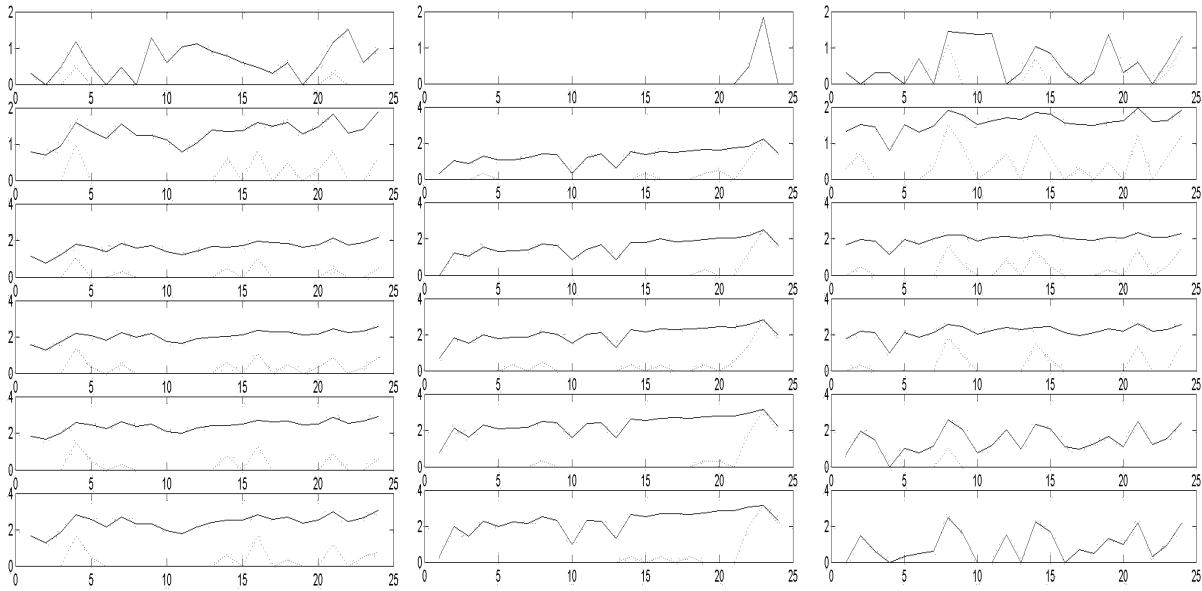


Fig. 3. Logarithmic NC_1 and NC_2 curves (solid and dashed lines, respectively) during the tests #V005 (left), #V007 (middle), and #V010 (right). Counts of the wavelet approximations are at the top, and counts of wavelet details $m = 2$ to 6 are below.

of about 400 ms was first eight-times down-sampled, which resulted in 500,000 signal samples. Down-sampled signal was then divided into 24 equidistant time intervals (windows), and the wavelet decomposition was applied to each interval (mother wavelet db1, $L=5$ detail levels). Subsequently, two-level threshold counting was performed on the wavelet coefficients of five details and low frequency approximation, which resulted in $2(L+1)$ parameters in each time interval (144 data in sum). This procedure represents ca. 3500 times data reduction, saving a global information on time and frequency changes of the whole process. The detailed $NC_{1,2}(m)$ curves are shown in Fig. 3: The wavelet parameters $NC_1(m)$ and $NC_2(m)$, evaluated in 24 time windows, are plotted so that counts of the wavelet approximation ($m=1$) are on the top, and below are counts of wavelet decomposition details of $m = 2$ to 6 (down from low to high frequency details). Low-amplitude level counts NC_1 are plotted as solid lines, and high-level NC_2 curves as dashed lines. NC_i curves, evaluated at all three tests in the same manner, can be compared. Threshold counting levels and other parameters of all tests were the same. Punching tests were performed using the cutting tool with very small damage. The only difference was the quality of punched metal sheets (degree of surface corrosion), which is pronounced mainly at the wavelet approximation level (no visible corrosion was at the sheet #V007 in the middle of Fig. 3). At all three parts of Fig. 3 we can see that NC_i curves have very similar form at all wavelet decomposition levels. This means that no remarkable changes in signal spectrum are observed during the running process, and an attempt to recognize different process stages by using spectral parameters has no sense.

3.2 Classification of simulated AE data

In this section, the use of new wavelet-domain parameters is demonstrated also on a simulated AE data, generated for the testing of NN-based AE source classification procedure [10]. Different time functions of AE sources were assumed to simulate and classify various emitting defects. At first, it was necessary to train a BP-NN, to classify the original source functions, and finally, the most significant AE parameters of generated waveforms were tested.

The training AE waveforms (input data) were generated as a convolution of the source function (having different forms) with a Green's function. The Green's function has been obtained experimentally as a transfer function between the AE source and sensor measured during the pulse laser excitation of a steel plate (representing the impulse source of propagating elastic waves) at a distance 140 mm from the source [10]. Its graph is shown at the top of Fig. 4. Input patterns for the classification BP-network are composed of the following 14 parameters extracted from the "input signal" $z(t)$: amplitude, rise time, RMS value, energy moment, ASL, gravity center of signal, second to fourth statistical moments, six spectral parameters, and above defined parameters in wavelet domain.

Different AE signal sources S_p (p indicates the pattern index) were simulated as a linear combination of three source functions ("waves"): $wave_1, wave_2, wave_3$, weighted by randomly generated coefficients a_p, b_p, c_p :

$$S_p = a_p \cdot wave_1 + b_p \cdot wave_2 + c_p \cdot wave_3$$

In order to obtain more comparable results, these coefficients are normalized so that their sum equals to one. The graphs of the source "waves" and their combination are also shown in Fig. 4, along with the "input signal" $z_p(t)$ computed as a convolution of the AE source function S_p with the Green function G :

$$z_p(t) = conv(S_p, G).$$

500 training patterns were generated for the training of 50 neural networks of the same architecture (topology 45-19-3, resulting error < 0.01). Only initial weights were set differently among the trained NN's. The averages of sensitivity coefficients calculated for all tested networks are presented in Table 1 (shaded by values).

Each of the three columns in Table 1 contains 24 values corresponding to input signal features. Only 9 wavelet parameters at 3 highest frequency detail levels were considered in this analysis, as the low frequency wavelet coefficients differ little for various model sources. From Table 1 we can see that the most important are pattern features number 6, 11, 14, 15 and 24. It means that the generated signal waveforms differ mostly at higher frequencies and a linear combination of different source "waves" can be estimated ("source classification") using the relative signal gravity centers in time domain and gravity centers of wavelet decompositions.

The application of PCA has proven (see Table 2) that the new "wavelet counting parameters" (parameters number 16 to 24) represent new, linearly independent information. Nevertheless, this information seems to be unimportant for the estimation of the composed signal "weights" as expected, while the linearly dependent classical parameters appear to be more important in this case.

Finally, numerical experiment with NN training has proven that for successful learning it is possible to use only the spectral parameters (features number 10 - 15) or just wavelet decomposition parameters (features number 16 - 24) giving very similar results.

3.3. Recognition of AE sources in polymer composite samples

The last example demonstrates importance of various AE parameters in recognition of AE signals coming from three types of model GFRP composite specimens. Unidirectional reinforced composite samples of three special forms were prepared and tested in [11] so that the three different damage mechanisms prevailed during the specimen loading (delamination, fiber breaks,

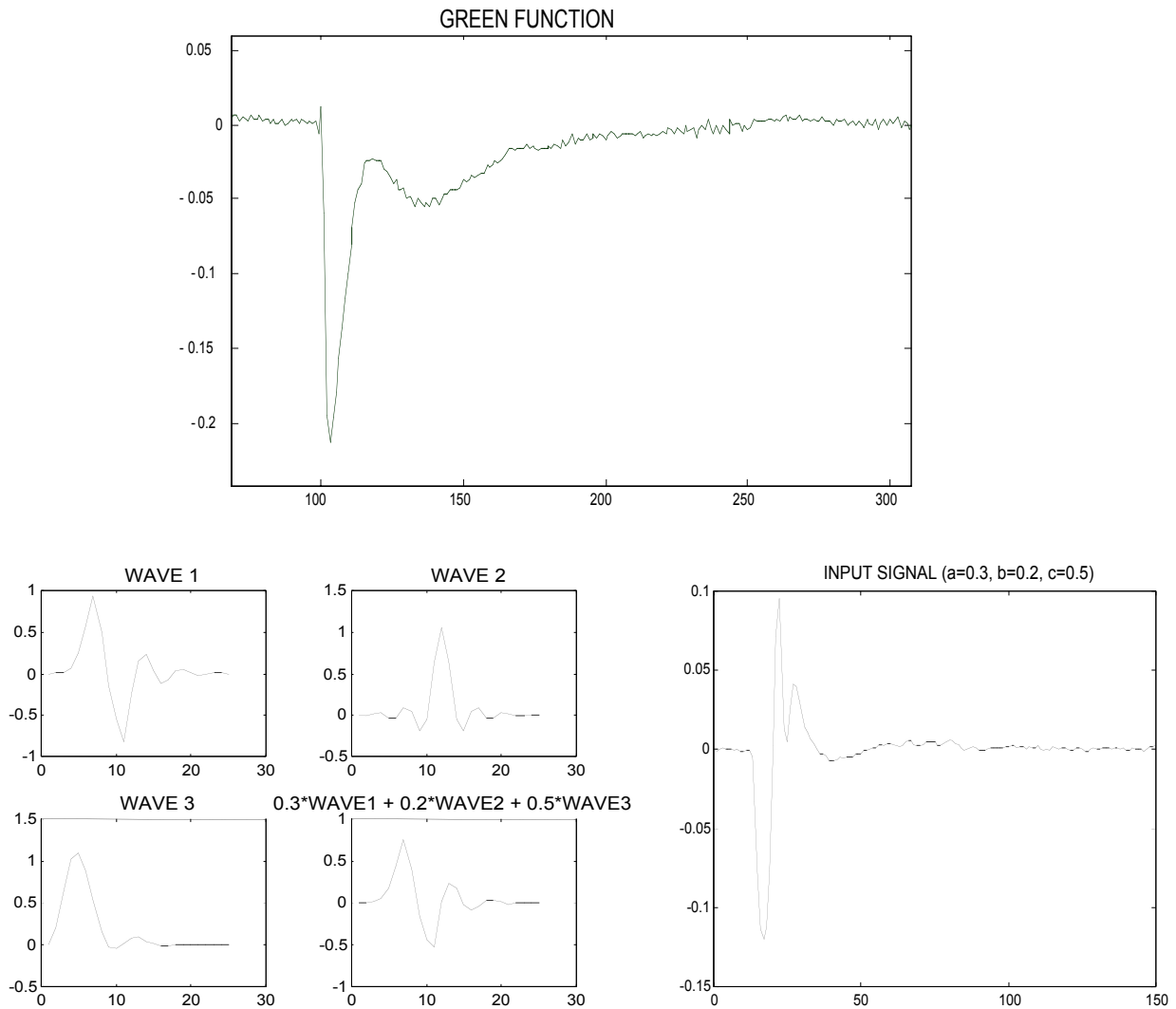


Fig. 4. Graphs of the source model functions ("waves" 1,2,3, and their linear combination) and the input signal resulting from the convolution of the source and Green's function.

and matrix cracks). The data (AE signal parameters) from specimens of different forms are used to see the significance of various AE parameters for the recognition of the three different AE source mechanisms. The NN with AE parameter inputs was trained to indicate the highest value on particular output corresponding to each specimen form (AE source mechanism). In Table 3 we can see that resulting NN sensitivity coefficients show similar picture as in Table 1 for simulated signals. Again, as the most important features (all five wavelet decomposition levels were considered in this case) seem to be the centers of gravity of spectral or wavelet parameters.

4. Conclusions

The wavelet transform of AE signal is now broadly used as very useful tool for AE signal analysis in time-frequency domain. New AE signal parameters based on wavelet transform (wavelet counts) were introduced here as a logical extension of commonly used AE signal

Table 1. Sensitivity analysis of trained BP-networks.

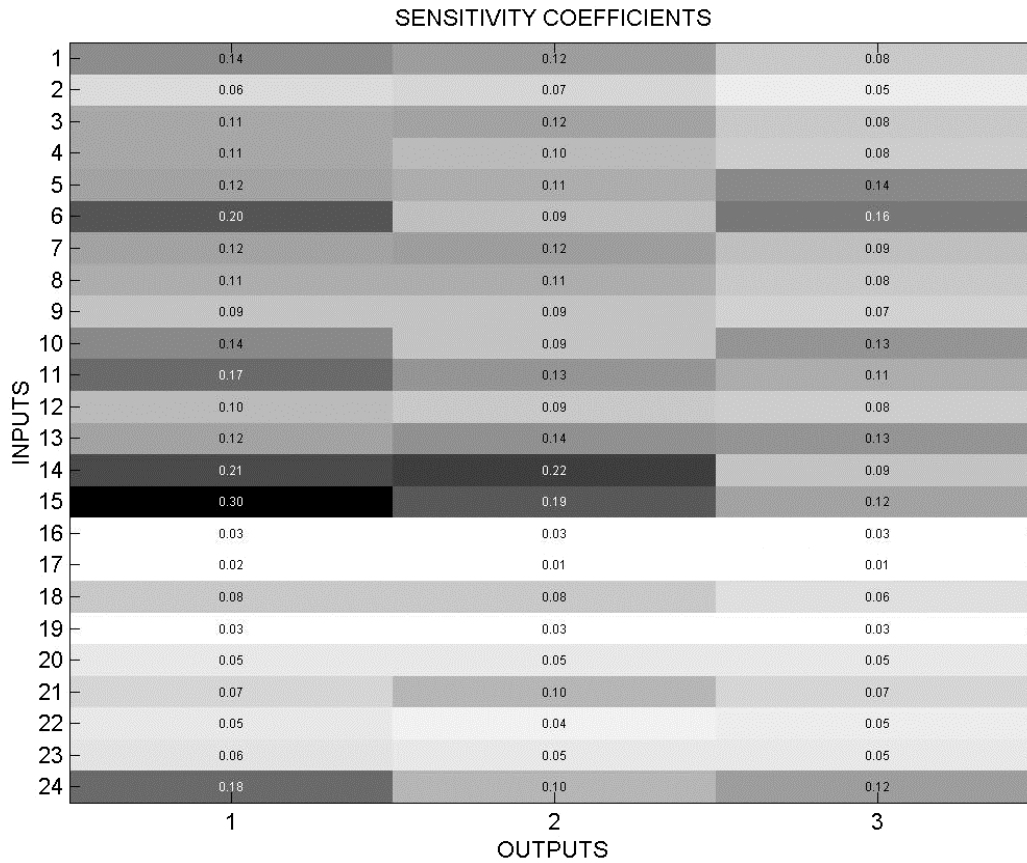
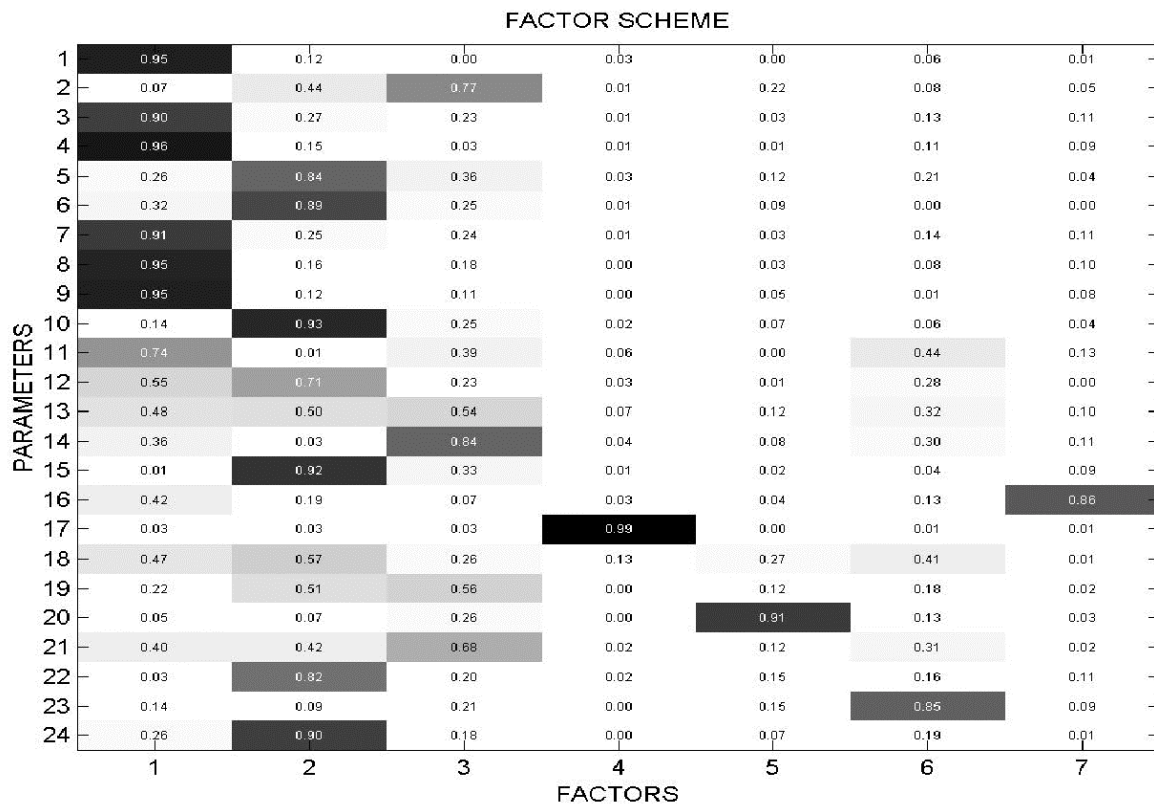
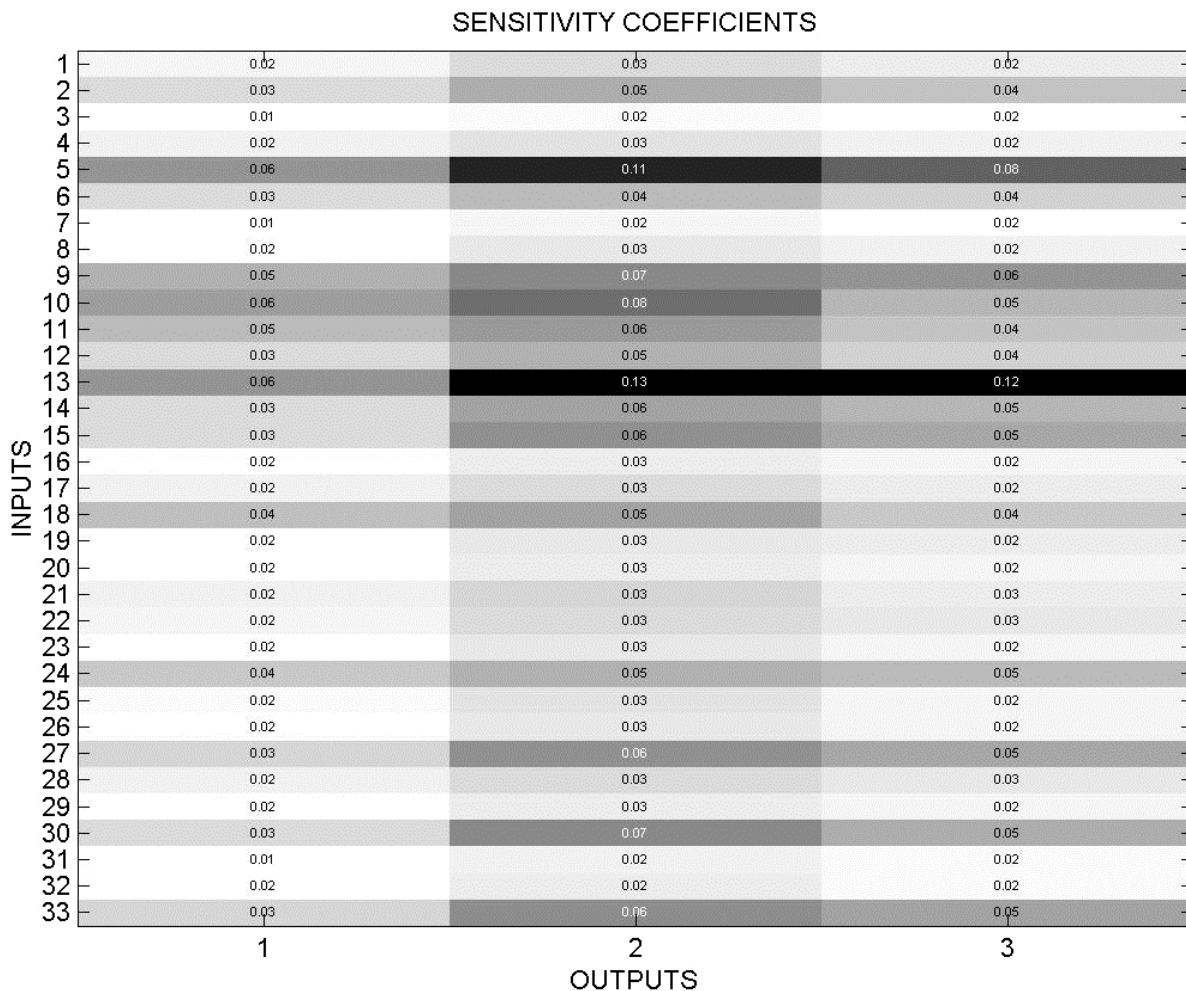


Table 2. Factor scheme (PCA) of tested signal parameters.



threshold counting procedures. These new AE signal parameters are defined as numbers of threshold crossing counts of wavelet coefficient amplitudes at various wavelet decomposition levels. Two predetermined threshold values are used in a simplest case, which can differ at various wavelet decomposition levels. Thresholds should be selected in a similar way as recommended in standard threshold counting of original AE signal. The applications of wavelet counts have been illustrated on three examples of both real and simulated AE data. Numerical tests have been performed using the neural-network sensitivity and factor analyses. Test results show which of various classical and newly introduced AE signal features are significant for AE source identification procedures. As the most important features seem to be the centers of gravity of spectral or wavelet parameters. The wavelet counts, carrying the global information in both time and frequency domains, can replace ill-defined frequency spectrum parameters of AE signal in a more efficient way. The strategy of neural network sensitivity analysis seems to be very useful to reveal the most significant AE signal features in various applications.

Table 3. NN sensitivity analysis results of tested AE parameters significance for the recognition of three different AE source mechanisms acting in loaded composite samples.



References

- [1] Standard Practice for AE Examination of FRP Tanks/Vessels. (ASTM E 1067).
- [2] Mertins A.: *Signal Analysis: Wavelets, Filter Banks, Time-Frequency Transform and Applications*. J. Wiley & Sons, Ltd., Chichester, 1998.
- [3] Poularikas A.D.: *The Handbook of Formulas and Tables for Signal Processing*. CRC Press & IEEE Press, 1998.
- [4] Ou-Yang Kwon, Young-Chan Joo: "Source location in plates by using wavelet transform of AE signals." *Progress of AE IX, The Proc. of 14th Internat AE Symp. and 5th AE World Meeting*, Ono K., ed., Hawaii, August 9-14, 1998.
- [5] Kinjo T., Suzuki H., Saito N., Takemoto M., Ono K.: "Fracture-mode classification using wavelet-transformed AE signals from a composite." *J. of Acoustic Emission*, **15**(1-4), pp.19-32, 1997.
- [6] Yamaguchi K., Oyaizu H.: "Advanced AE Instrumentation System for Versatile and Precise Use by Waveform Microdata Processing." *Proc. of the 3rd Congress on AE from Composite materials AECM 3*, Paris, July 17-21, 1989.
- [7] Bishop C.M.: *Neural Networks for Pattern Recognition*. Oxford University Press, 1996.
- [8] Fidalgo, J.N.: "Feature Subset Selection Based on ANN Sensitivity Analysis – a Practical Study." *Advances in Neural Networks and Applications*, Mastorakis N., ed.: WSES Press, pp 206-211, 2001.
- [9] Prevorovsky Z., Fischer J., Krofta J., Chlada M., Blaháček M.: "Fuzzy-Probabilistic Evaluation of AE During Steel Plate Punching." *Proc. COST P4 Conf. on Characterization of Manufacturing Processes "Synergetics and Data Processing Methods"*, Govekar E, ed., Ljubljana, Slovenia, 25-26 May 2000, pp. 279-285.
- [10] Krofta, J., Chlada, M., Prevorovsky, Z.: "Probabilistic and Neural Network Classification of Simulated AE Data," *EUROMECH 419 Colloquium on Elastic Waves in NDT*, Prague, 3-5 Oct. 2000, Book of Abstracts, p. 47.
- [11] Klimes O.: "Modeling of AE sources in fiber reinforced composites." MS Thesis, Faculty of Nuclear Sci. and Phys. Eng., Czech Technical University, IT CAS, Prague, 1996.

DAMAGE DIAGNOSIS TECHNIQUE FOR BRICK STRUCTURES USING ACOUSTIC EMISSION

TAKUO SHINOMIYA¹, YASUHIRO NAKANISHI², HIROYUKI MORISHIMA¹ and TOMOKI SHIOTANI³

¹ Technical Center, East Japan Railway Company, Tokyo, Japan

² Research Institute of Technology, Tobishima Corporation, Chiba, Japan

³ Faculty of Civil Engineering and Geosciences, Delft University of Technology, The Netherlands (on leave from Tobishima Corporation)

Abstract

Acoustic emission (AE) is known as a non-destructive test under external load/variation of stress distribution within materials; AE waves are difficult to generate without those stress variation. Railway bridges are the structures where the external load variation can be easily applied due to over-passing railway traffic. In this study, in order to apply AE technique to the damage evaluation in railway brick structures, fundamental experiments using brick specimens sampled from an actual old brick foundation of a bridge are carried out. This is performed to find the applicability of AE technique to brick materials. Next, in order to know the deterioration process and to establish a damage evaluation table, brick specimens made in laboratory are subjected to cyclic loads, and AE activities with crack growth are examined. Finally, in-situ AE monitoring is performed on an "elevated arch railway bridge" where obvious penetration-cracks are observed. For in-situ monitoring, AE activities directly generated from the observed cracks are distinguished from those induced by the railway traffic.

Key words: brick, calm ratio, damage diagnosis/degree, load ratio, railway structures

1. Introduction

In Japan, many masonry structures using bricks have been constructed over 60 years ago. During service, they have sustained damage from several earthquakes and long-term weathering. In order to confirm the safety for service, it is essential to investigate the deterioration and degree of damage of the structures. Also the investigation result is important in performing appropriate rehabilitation/reinforcement for the deteriorated structures. Thus far, such techniques as visual observations and crack displacement have been used in the investigation of elevated bridges made of bricks. As for the lower portions of the elevated bridges, however, since they are normally utilized as commercial buildings, the same techniques are difficult to apply. Again, it is required to establish another technique to diagnose the integrity of brick structures even where conventional techniques are difficult to apply. Several NDT techniques, radar, ultrasonics, electric exploration and acoustic emission (AE), had been performed in brick structures as preparation. However, the results except from the AE technique were useless. Thus, this study only focuses on the AE technique.

When the AE technique is applied to railway brick structures, it has the following unresolved points:

- 1) How the external loadings or variation of internal stress are applied to induce AE activity?
- 2) Is AE signal from cracking in bricks really obtainable?

- 3) How do the types of crack affect AE activity?
- 4) AE activity might decrease with repetition of loads; i.e., Kaiser effect may exist.
- 5) Detected AE activity might include AE signals, which is not related to crack behavior directly but related to the dynamic behavior due to railway traffic loads.

In this paper, answers to these points are explained with the following procedure. First, fundamental experiments using brick specimens that are sampled from an actual old brick foundation of bridge are carried out (answer point 2). Second, in order to evaluate the deterioration process and to establish the damage evaluation method, brick specimens made in laboratory are subjected to cyclic loads, and AE activities with crack growth are examined (for points 3 and 4). Finally, in-situ AE monitoring is performed in an “elevated arch railway bridge” where obvious penetration cracks are observed (for points 1 and 5).

2. Experiments

2.1 Fracture tests using sampled specimens [1]

There exists a brick bridge of over 80 years old. Four beam specimens were sampled from the substructure of the bridge. Figure 1 shows the configuration of the specimen with the arrangement of AE sensors. The tests are performed with 4 different specimens and 3 different conditions of axial force as shown in Table 1. The axial stress of 1.0 MPa in No. 1 specimen is the maximum load when the train passes on the arch, in which the span is 7.8 m; the axial force of No. 2 is 50% of the assumed maximum load. Monotonic bending load was applied to the specimen with AE monitoring. 12 AE sensors of 60-kHz resonance were placed on the surface with wax couplant (see Fig. 1). The signals detected were pre-amplified 40 dB and processed by a DSP-based MISTRAS AE system (Physical Acoustics Corp.) with the 40-dB threshold (ref. 0 dB = 1 μ V at sensor). Both AE parameters and waveforms are recorded; the latter with 1-MHz sampling and 1-kword length. In this experiment, the AE activity corresponding to the fracture stages classified by using the load-displacement relation is studied, considering with/without axial force. The monotonic load was applied in a step-wise manner with 5 kN increment.

Table 1. Specification of specimens.

No.	b (mm)	h (mm)	L (mm)	a (mm)	<i>Axial force</i> (MPa)
1	350	350	1,000	350	1.0
2			1,200	450	0.5
3			1,350	525	0.0
4			1,500	600	0.0

2.2 Cyclic tests using laboratory-made specimens

In general, AE activity generated due to crack nucleation and formation is referred to as “primary AE activity,” whereas AE activity due to the friction of pre-existing crack interfaces is referred to as “secondary AE activity.” In this cyclic test, in order to study the secondary AE activity, the cracks are first introduced into the newly made specimens with loading. The specimen has a length of 1776 mm, a width of 360 mm and a depth of 330 mm as shown in Fig. 2. 12 AE sensors are placed on the surface. The condition of AE monitoring system is the same as in the previous test. Lateral force (i.e., axial stress) of 0.33 MPa was first applied to the specimen, then the vertical load was applied until a penetration crack was observed. Changing the shear span,

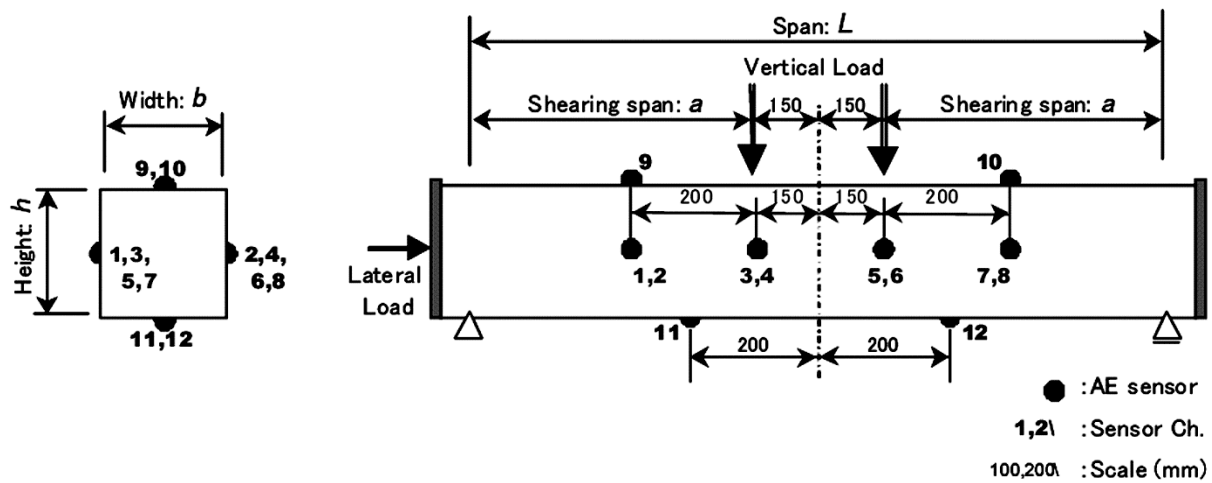


Fig. 1. Configuration of sampled specimen in fracture test.

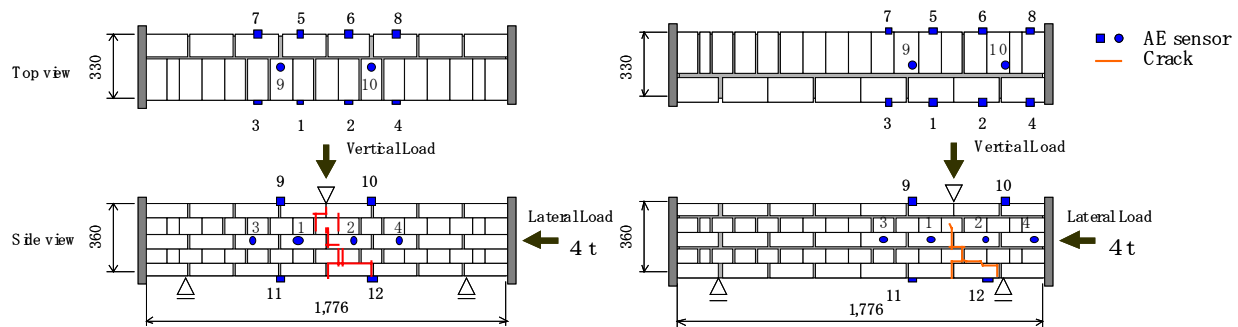


Fig. 2. Specimens and arrangements of AE sensors in cyclic tests. (left: bending, right: shear)

bending and shear loads were applied (see Fig. 2). After introducing the penetration crack, the specimen was subjected to cyclic loads. We applied five repetitions of cyclic load at 10, 50 and 75% of the load, at which the penetration crack was observed. After cycling, monotonically increasing load was applied until the specimen broke and dropped from the stand.

2.3 In-situ AE monitoring at an *elevated arch railway bridge*

In order to generate AE activity, it is essential to apply the external load or to give the variation of stress distribution within materials. For railway structures, both can be possible by the train passage. The monitored structure is a *double-tracked brick arch elevated bridge* constructed in 1910. The bricks used for the foundation are laid by means of English bond. A penetration crack was already visible in the direction of railway (see Fig. 3), and out-of-plane displacement of approximately 0.2 mm was measured with each train passage. Thus, the AE activity from the bridge is expected due to the crack movement. A set of AE sensors with 15-kHz resonance were placed on the bridge bottom as shown in Fig. 3. Subsequently, these were exchanged with 60-kHz sensors. To monitor the acceleration due to the train passage, accelerometers were also set up. The AE system used and the monitoring condition are the same as in the previous tests.

3. Results and Discussion

3.1 Fracture tests using sampled specimens

A typical behavior of displacement and AE activity are shown in Fig. 4. This is the result of specimen No. 1, where axial force was applied. In the chart, the vertical displacement at the

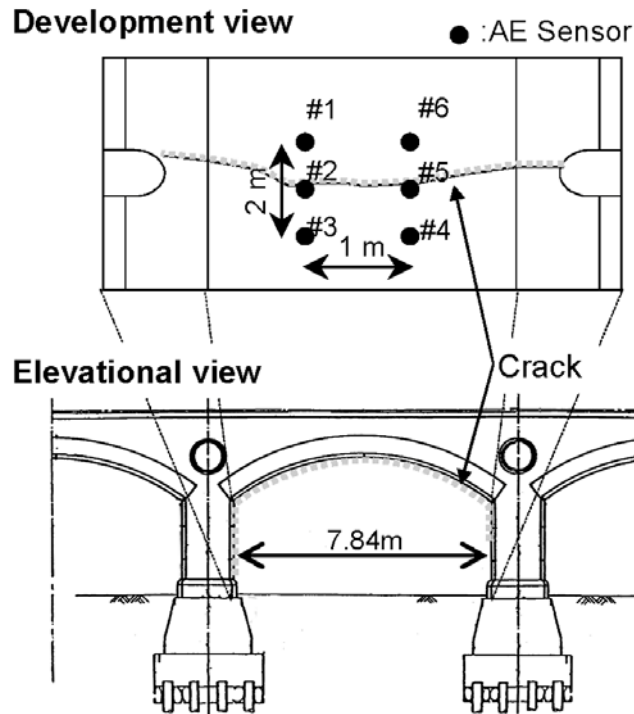


Fig. 3. A penetration crack and an arrangement of AE sensors in an arch bridge.

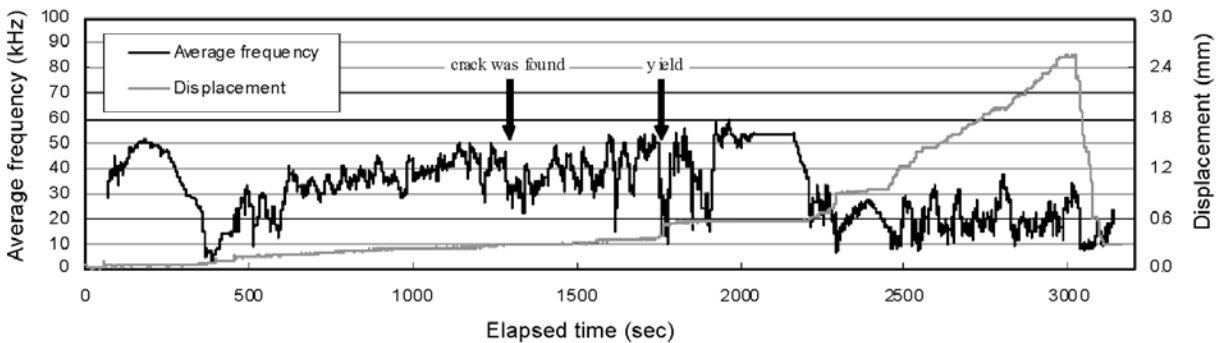


Fig. 4. Displacement and average frequency in specimen No. 1 with axial force. The arrows show the times when a crack was first observed and then reached the yield point.

loading point and AE average frequency obtained by AE (ring-down) counts and duration are given as a function of elapsed time. The average frequency is the average of the latest 100 AE hits; i.e., using a method of *moving average* [2]. As seen in Fig. 4, the axial force was imposed during the initial 430 s. With subsequent loading, the average frequency increased, accompanied by the repetition of rise and fall until a crack was observed. The manner of the repetition corresponded well with the stepwise increase of the load step of 5 kN. The average frequency ranges from 20 to 60 kHz in the cracking process (i.e., 430 - 1775 s). The repetition was also found after the yield point at 1775 s. However, the average frequency became smaller to around 20 kHz. Thus, the progress of fracture in brick structures can be classified into the following three processes: 1) Micro-cracking due to tensile/shear stresses accompanied by the AE activity of high average frequency; 2) Formation of macro-cracks by connecting the micro-cracks, and local generation of macro-scale shear fracture due to yielding, accompanied by the AE activity of low average frequency; 3) The friction between pre-existing fracture planes, accompanied by the AE activity of low average frequency.

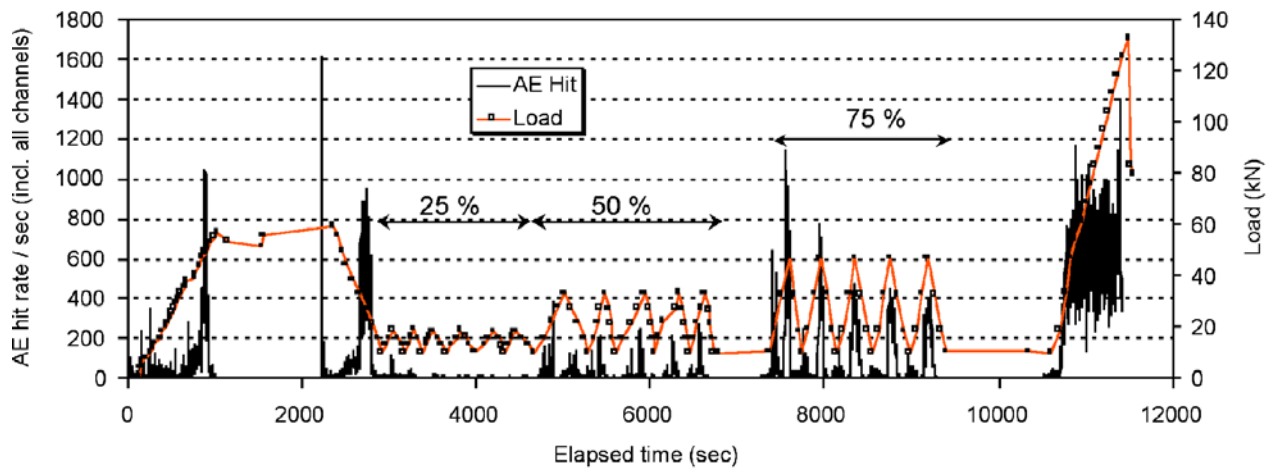


Fig. 5 AE hit rate and load applied with elapsed time in the shear cyclic test.

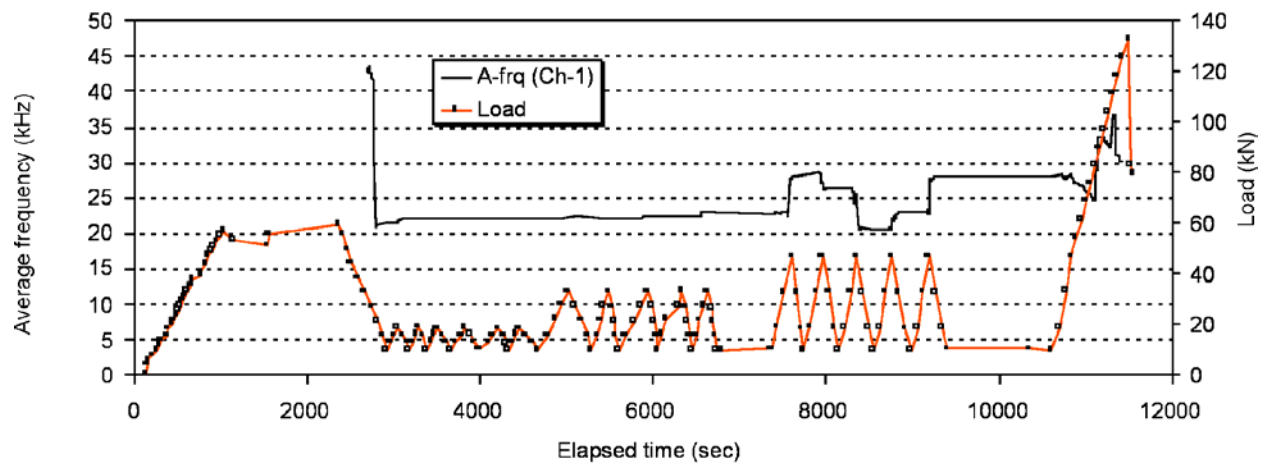


Fig. 6 Average frequency and load applied with elapsed time in the shear cyclic test.

3.2 Cyclic tests using laboratory-made specimens

Figure 5 shows the applied load and AE hit rate per 10 s against elapsed time in the shear cyclic test. In this figure, the AE activity increases with the first applied monotonic load, and there is no active AE occurrence during cyclic load at 25% of the nominal cracking load. The no AE activity during the cyclic load at 25% was caused by the following: 1) Shear stress due to bending was too small. 2) Kaiser effect was observed. During cyclic load at 50%, however, AE activity with loading can be observed in every repetition. AE hits are actively generated during 75% cyclic load both in loading and unloading. These suggest that Kaiser effect started to break down from 50% of the cracking load, and continuous AE activity was obtained not only in loading but also in unloading to and from 75% of the maximum load.

Figure 6 shows the average frequency and the load applied against elapsed time. After the penetration of cracks, the average frequency increases from 20 to 30 kHz without the final buckling process. This range of the average frequency is almost the same as in the bending specimen, and agrees well with the result in the sampled specimen after yielding (see Fig. 4). Figure 7 shows results of 3D source locations projected to the front surface of the specimens with observed cracks. The sources are classified with scale of the peak amplitude. In both bending and shear specimens, cracks are generated not only in direction of the axial load (i.e., vertical), but also parallel to the axial force. This implies that even when the bending loads are applied, cracks

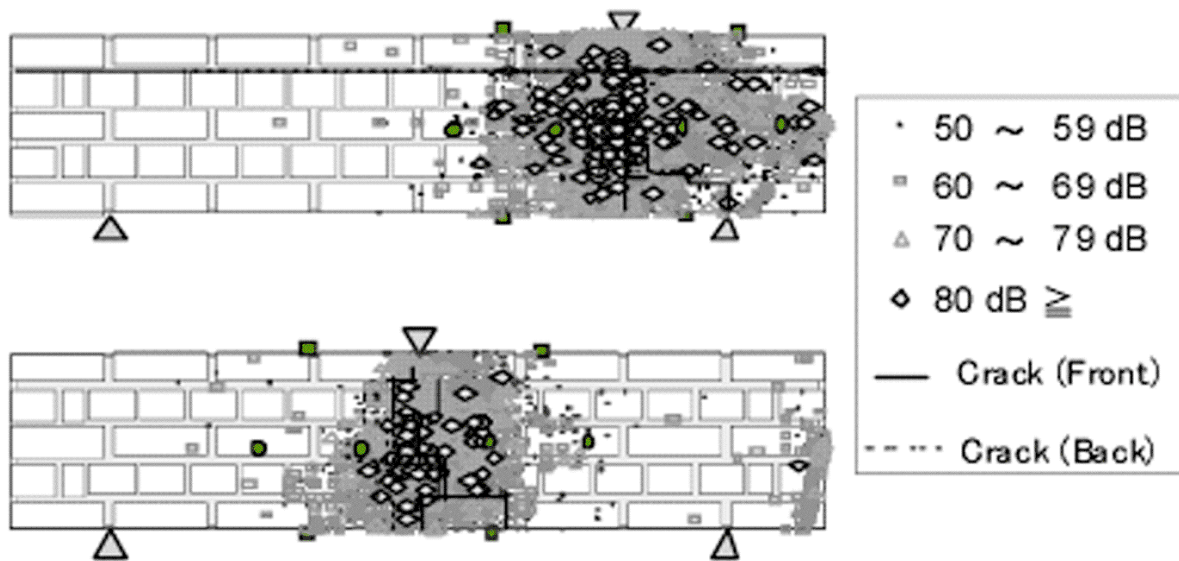


Fig. 7. 3D source locations projected to the front surface. AE sources are classified with the peak amplitude.

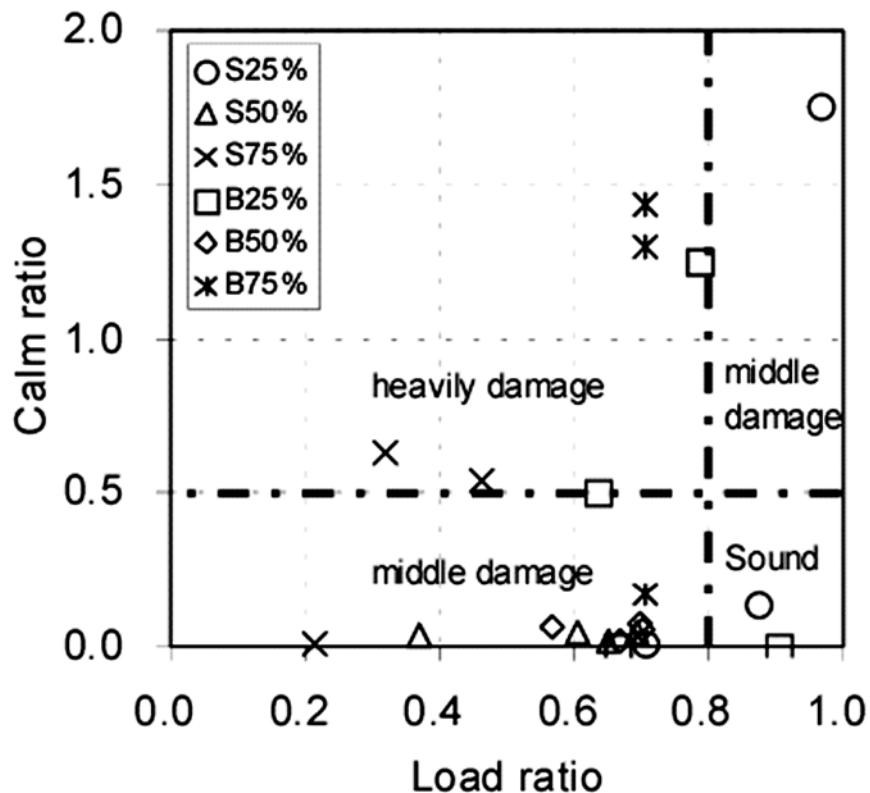


Fig. 8. Damage degree map. (S: damage is given by shear load. B: damage is given by bending load)

are sometimes generated horizontally along the interfaces among bricks; the shear type of cracks also occurred even in the bending test. Thus, the reason why the same average frequency was obtained in both types of specimens is that the same shear fracture had occurred in both bending and shear specimens. In addition, the location of cracks observed is identical to the AE sources with large peak amplitude. This leads to a conclusion that macro-scale cracks could be estimated from AE activity with large peak amplitude.

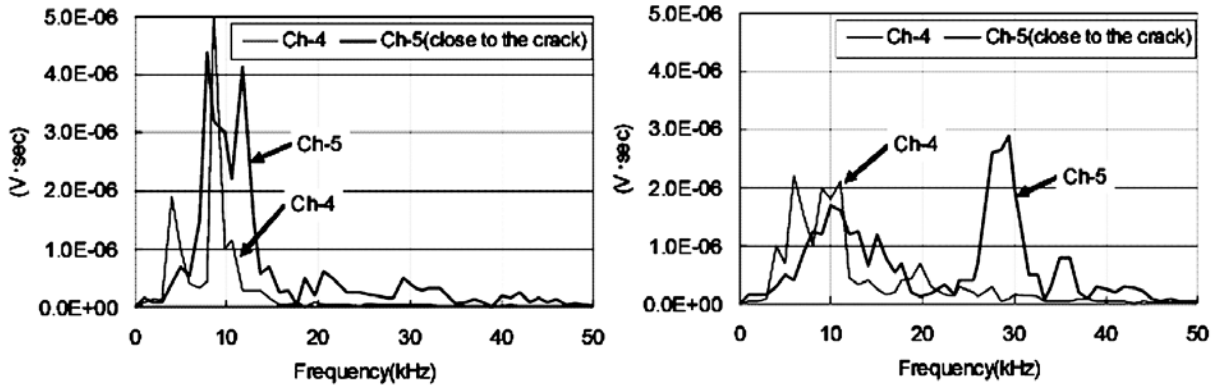


Fig. 9. Typical frequency spectra of detected AE waves with 15-kHz (left) and 60-kHz (right) resonant AE sensors.

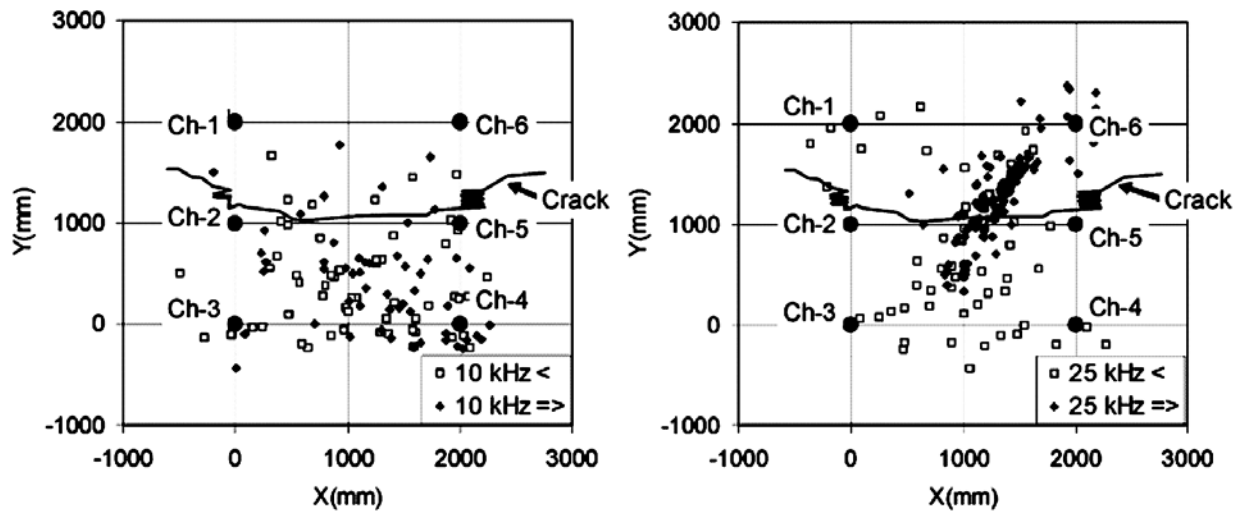


Fig. 10. 2D AE sources classified with the average frequency (left: with 15-kHz, right: with 60-kHz resonant AE sensors).

From all of the results, a damage map of brick structure is constructed as shown in Fig. 8. The map is based on the NDIS 2421 [3], “Load” stands for ratio of load at the onset of AE activity to previous load, and “Calm” stands for ratio of cumulative AE activity under unloading to that of previous maximum loading cycle. With an increase of the degree of damage, the plots distributed toward the upper left side of the map, irrespective of the types of loading conditions. Thus, it is found that evaluation of integrity in brick structures is possible using the damage degree map based on the AE activity.

3.3 In-situ AE monitoring at an *elevated arch railway bridge*

With each train passage, AE signals could be detected in AE sensors of both 15-kHz and 60-kHz resonance. Figure 9 shows the typical frequency spectra of detected AE waveforms with 15-kHz (left) and 60-kHz (right) sensors. In each chart, a comparison is made between Ch-4 and Ch-5, which are the AE sensors close to the observed crack and far from the observed crack, respectively. Both sensors have the common frequency component of 10 kHz, irrespective of the location from the crack. In the 60-kHz sensor data, however, the frequency component from 25 to 35 kHz is only found at Ch-5 being close to the crack. This implies that AE signals having the

frequency component ranging from 25 to 35 kHz are generated from the existing crack. Here, the 2D source locations obtained are classified with average frequency as shown in Fig. 10. The AE signals for the first arrival are used in the classification. In the arrangement of 15-kHz resonant AE sensors, AE sources disperse over the monitoring area, whereas for 60-kHz resonant AE sensors, AE sources higher than 25 kHz are distributed around the center of the monitoring area. The AE sources distributed in the center area appear to be the AE events generated from the existing cracks, although this area is not completely identical to the location of the crack observed. This is because; 1) the heterogeneous velocity-distribution existed in the vicinity of the large cracks, and 2) the actual cracks distributed in 3D space, normally with curved crack surfaces. Thus, it seems reasonable that the distribution of AE sources, higher than 25 kHz, may not be completely identical to the position of the surface-breaking crack. It becomes clear that by using AE sensor of 60-kHz resonance and focusing on AE signals around 30 kHz, the secondary AE activity due to the friction between the pre-existing crack interfaces can successfully be detected.

4. Conclusions

In this study, the AE technique was applied for the damage evaluation in brick structures. It can be concluded that:

- (1) AE signals could be obtained during the cracking process of bricks, and there exists the secondary AE activity generated due to the friction of pre-existing crack faces;
- (2) Deterioration/cracking process could be evaluated using AE parameters;
- (3) Using the proposed damage map based on AE activity, the degree of damage of brick structures could be reasonably evaluated;
- (4) With the sensor of 60-kHz resonance and using the high pass filtering over 25 kHz, AE activity directly related to the crack behavior could be distinguished from those related to the dynamic behavior due to railway traffic loads;
- (5) Railway traffic could induce AE activity generated from pre-existing crack faces, and the damaged area could be estimated as a distribution where higher frequency AE sources over 25 kHz were generated; and
- (6) From all of the findings, the AE monitoring range is limited to 1.5 m using AE sensor of 60-kHz resonance, and the threshold of 40 dB. For the future work, additional ideas to expand the monitoring areas would be needed.

References

- [1] Kino, J., Kanno, T. and Furuya, T., "The strength test of cored samples from brick structures," *Proceedings of 56th JSCE Annual Conference*, Japanese Society of Civil Engineers, pp. 222-223, 2001, (in Japanese).
- [2] Shiotani, T., Ohtsu, M. and Ikeda, K., "Detection and evaluation of AE waves due to rock deformation," *Construction and Building Materials*, **15**, 235-246, 2002.
- [3] The Japan Society for Non-Destructive Inspection, "*Recommended practice for in situ monitoring of concrete structures by acoustic emission*," Standard of the Japan Society for Non-Destructive Inspection (NDIS), NDIS 2421, 2000, (in Japanese).

EVALUATION OF DRYING SHRINKAGE MICROCRACKING IN CEMENTITIOUS MATERIALS USING ACOUSTIC EMISSION

TOMOKI SHIOTANI^{1,2}, JAN BISSCHOP¹ and J. G. M. VAN MIER³

¹ Microlab, Faculty of Civil Engineering and Geosciences, Delft University of Technology, The Netherlands. ² Research Institute of Technology, Tobishima Corporation, Chiba, Japan.

³ Institute for Building Materials, ETH, Zürich, Switzerland.

Abstract

To determine the temporal evolution of shrinkage microcracking in cementitious materials, acoustic emission (AE) technique is applied to the materials during drying process. Initial studies on wave propagation are carried out for the materials. Geometry of generated cracks is recorded with FLM (fluorescent light microscopy) both in plain cement paste and glass-particle cement composites. The results indicate two mechanisms of drying shrinkage microcracking; self-restraint of the specimen/structure and aggregate restraint. In plain cement paste, the cracks due to self-restraint initially develop perpendicular to the drying surface, but may subsequently grow parallel to the drying surface. AE monitoring has revealed that the self-restraint cracks have developed almost instantaneously at the onset of drying. In composites containing glass particles, however, aggregate-restraint cracking continuously develops throughout the experiment.

Keywords: cementitious materials, cracking, drying shrinkage, restraint, temporal evolution

1. Introduction

Drying shrinkage leads to stresses and cracking in cement-based materials when the deformations are restrained. The mechanism of drying shrinkage cracking strongly relates to the type of restraint that is caused by the material and structure. This paper focuses on only the cracking due to internal restraining of the material. There are two internal restraint mechanisms of microcracking due to drying shrinkage in cement-based materials [1]. The first mechanism is called self-restraining of the material, and is caused by moisture/shrinkage gradients that develop in a specimen/structure. This mechanism is studied in plain hardened cement paste specimens. The second type of internal restraint in cement-based composites is caused by the presence of stiff aggregate particles. Composites containing glass particles are used for studying this type of restraint. In this paper, AE technique is applied to determine the temporal evolution of shrinkage cracking. Fundamental issues on wave propagation within the materials are studied first. Two types of specimens, hardened plain cement paste and cement composite containing mono-sized glass spheres, are used to reproduce shrinkage due to the self-restraint and due to the aggregate-restraint respectively.

2. Experiment

2.1 Materials

As mentioned, drying shrinkage micro-cracking is studied in two types of materials: plain hardened cement paste and cement-based composite with mono-sized 6-mm glass spheres. The cement paste consists of ordinary Portland cement (CEM I 52.5R) with a water-cement ratio of 0.45. The composite consists of the same cement paste with a 35% volume percentage of 6-mm

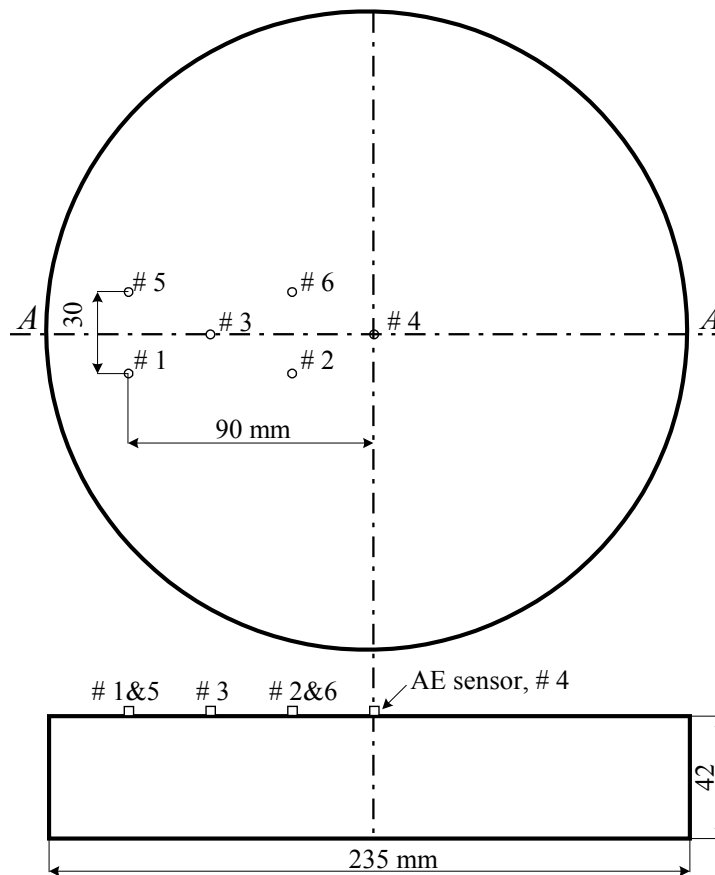


Fig. 1. Cylindrical specimen with the location of AE sensors.

glass spheres with smooth surfaces. The Young's Modulus of the glass spheres is 77 GPa. The cement-based materials are cast in cylindrical moulds as shown in Fig. 1. Note that the specimens for the initial studies are cast in smaller prismatic moulds ($h \times w \times l = 40 \times 40 \times 160$ mm). The specimens remain in the moulds for 24 hours at room temperature, sealed with a plastic foil. After demoulding, the specimens are placed for 6 days in calcium hydroxide saturated tap water at room temperature. At an age of 7 days, the specimens are removed from the water and all sides, except the top-surface, are sealed with 3 layers of adhesive tape, creating one-dimensional drying in the specimens. Subsequently, six AE sensors (M65, Fuji Ceramics Corp.) with a 500-kHz resonant frequency are placed with wax couplant onto the drying surface in the arrangement given in Fig. 1. The specimens are dried in an environmental cabin ventilated with air of $25\% \pm 5\%$ RH, at temperature of $31^\circ\text{C} (\pm 0.5^\circ\text{C})$. The drying continues for 16 hours.

2.2 AE monitoring

The used AE monitoring system is a MISTRAS AE system (Physical Acoustics Corp.). The detected AE signals are amplified 40 dB using preamplifiers (PAC, 1220). Both parameters and waveforms of AE signals over the threshold of 30 dB (ref. 0 dB at $1 \mu\text{V}$ at sensor) are recorded. Three parameters; grade [2], initial frequency [3] and improved b -value [4], are employed to study the fracture behavior during shrinkage. The initial part of the AE waves is extracted from the waveforms because it is least affected by the resonance characteristic of AE sensors and contains the cleanest information about fracture characteristics. A higher initial frequency is expected to occur in a situation where cracks rapidly generate (e.g. mode I), while a lower initial frequency is expected when the cracks develop slowly (e.g. mode II). Grade is defined as a gradient of the AE waveform up to the peak amplitude. A rapid growth/development of cracks

corresponds to large values of grade. In contrast, slow development of cracks corresponds to small values of grade. The improved b -value, which is defined as the negative slope of peak amplitude distribution, is used to quantitatively evaluate the fracture state. Improved b -values tend to increase where small-scale fracturing occurs in comparison to large-scale fracturing. When predominantly large-scale fractures are generated in place of small-scale fracture, improved b -values tend to decrease [4].

After experiment, the generated crack-pattern of the specimen is recorded by FLM [1]. Manual crack tracing is subsequently applied to obtain a detailed crack map, which is digitized to extract characteristic crack data.

3. Initial Studies for AE Monitoring

3.1 Wave velocity

The velocity of elastic waves within the hardened plain cement paste is studied first. Two conditions of the specimen: before drying (intact state) and after 16 hours drying (cracked state) are prepared. The measurement of the velocity was carried out in the transverse direction of the specimen using AE sensors. With an artificial pulse generator of 240-V peak voltage, signals were excited 30 times. The measured wave velocities in both the intact and cracked specimens are shown in Fig. 2. A slight decrease of wave velocity is observed with progress in micro-cracking. The difference of wave velocities between intact and cracked specimens is approximately 340 m/s. How does the velocity difference influence the source location? If the distance between AE sensors is 5 cm, the maximum difference of arrival times would be 14.3 to 15.6 μ s when the wave velocity ranges from 3200 to 3500 m/s. This error of the time difference is equivalent to 4.2 to 4.6 mm and the source location error due to variation of wave velocity (i.e., progress of cracks) would be 4.2 to 4.6 mm.

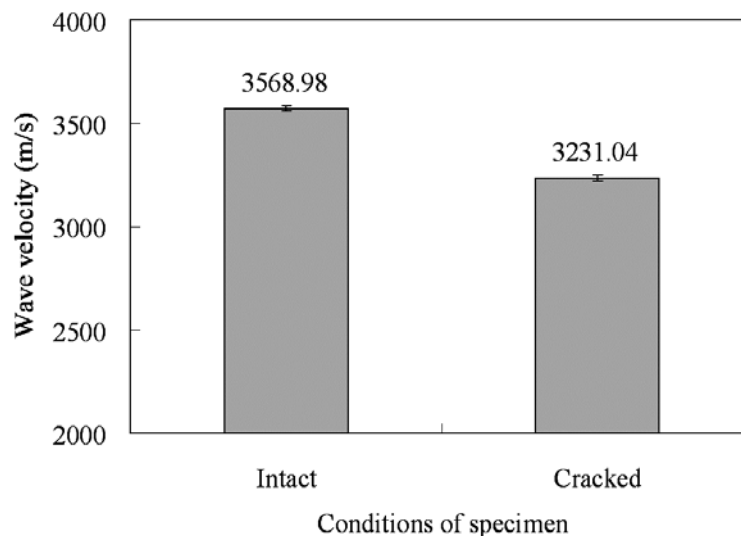


Fig. 2. Measured wave velocities. The height of bars shows the average of 30 waves with standard deviations (12.75 for intact and 13.06 for cracked).

3.2 Wave attenuation

To obtain the attenuation characteristics of the AE waves, six AE sensors are placed in three dimensions on a plain cement paste specimen. The enlarged view of the arrangement of the AE sensors is shown in Fig. 3. The prismatic specimen is subjected to 16 hour drying and AE signals due to cracking are detected. The attenuation characteristics are determined as follows:

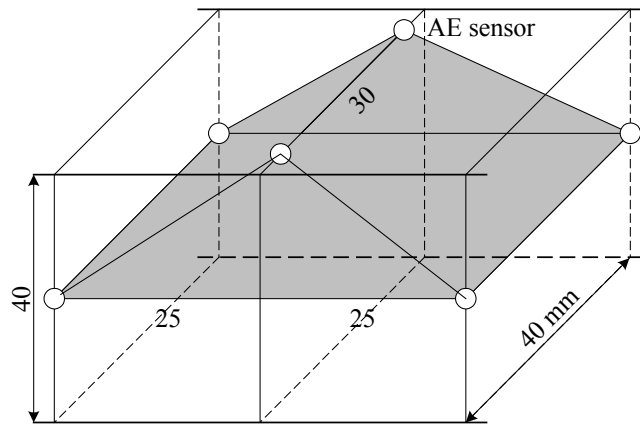


Fig. 3 Enlarged view for the arrangement of AE sensors.

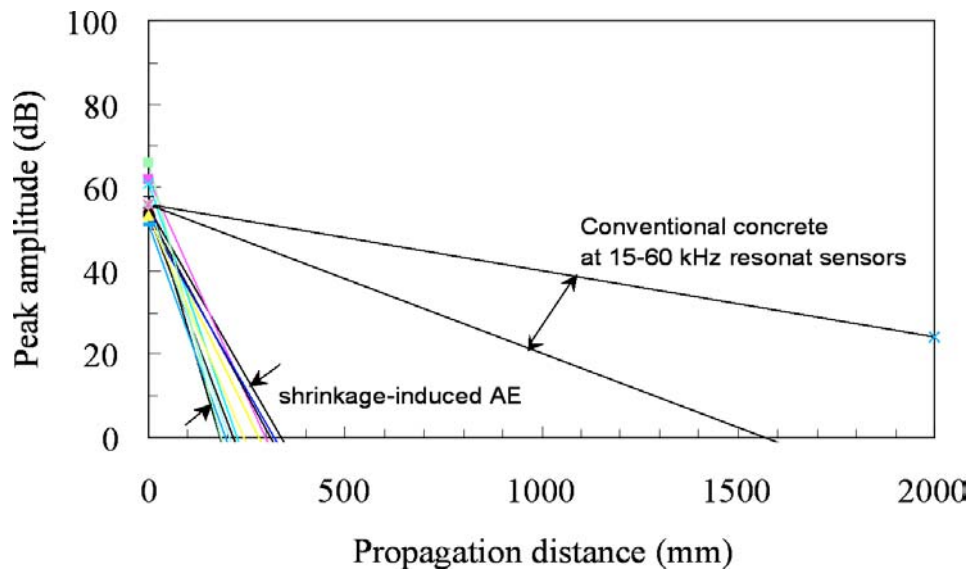


Fig. 4. Attenuations of 12 AE sources.

1) 3D source locations are performed; 2) The distances between the source and each AE sensors are calculated; 3) The relation between peak amplitude (dB) and propagation distance (mm) is plotted and a linear approximation is carried out, and 4) The attenuation characteristics are obtained. Figure 4 shows the attenuation characteristics of 12 AE sources. With extrapolations, the peak amplitudes of AE sources range around 60 dB. This suggests that AE signals with large amplitude are difficult to generate/obtain due to the shrinkage cracking. For a threshold of 40 dB, the monitoring area is limited to 5-15 cm. If a comparison is made with conventional concrete [5], AE signals generated by shrinkage cracking is observed to attenuate sharply.

4. Results

Figure 5 and 6 show the digitized crack maps on the drying surface and cross-sections of plain cement paste and the composite specimen, respectively. In the plain cement paste, a cell-like crack-pattern developed. The crack-widths ranged between 20 and 40 μm . In the composite, there is no clear cell-like crack-pattern as on the surface of the plain cement. However, a similar cell-like pattern is believed to exist as in the cement paste, but since the top layer of the composite specimen was removed by grinding, just lightly to remove the upper cement layer to reveal the positions of the glass spheres, the original pattern can only be inferred. Cracks were generally

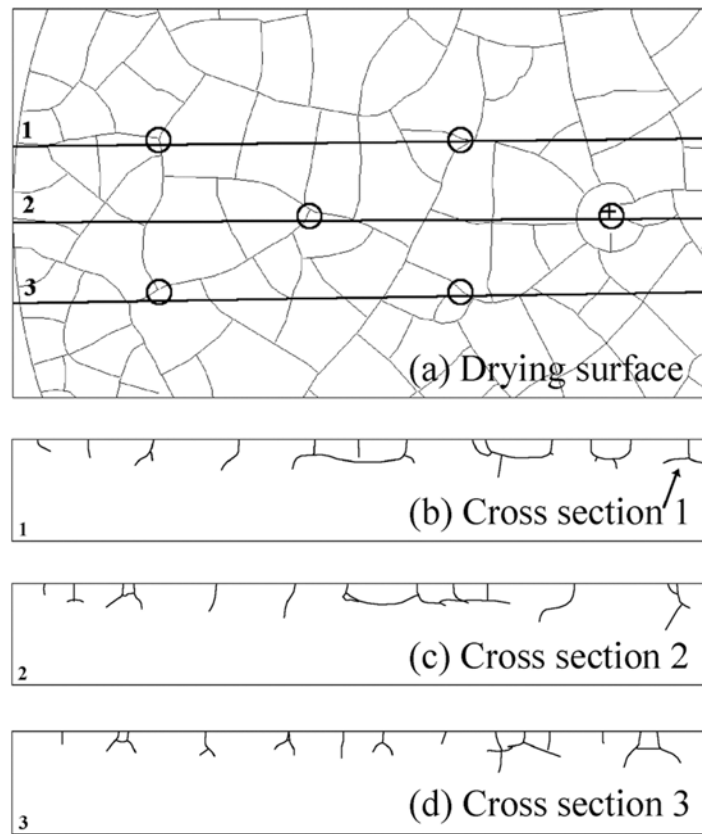


Fig. 5 Digitized crack-map in the plain cement.

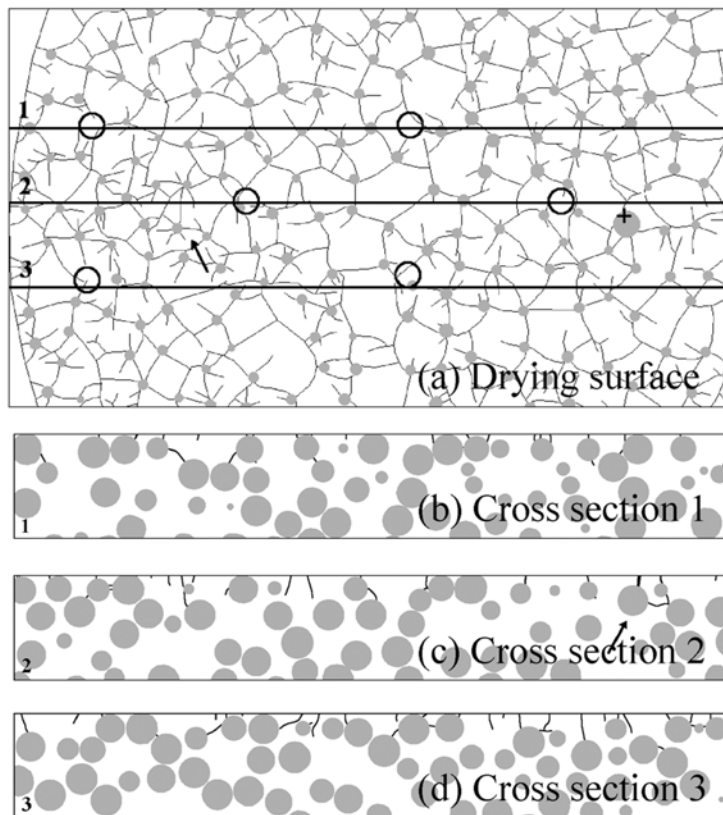


Fig. 6 Digitized crack-map in the composite.

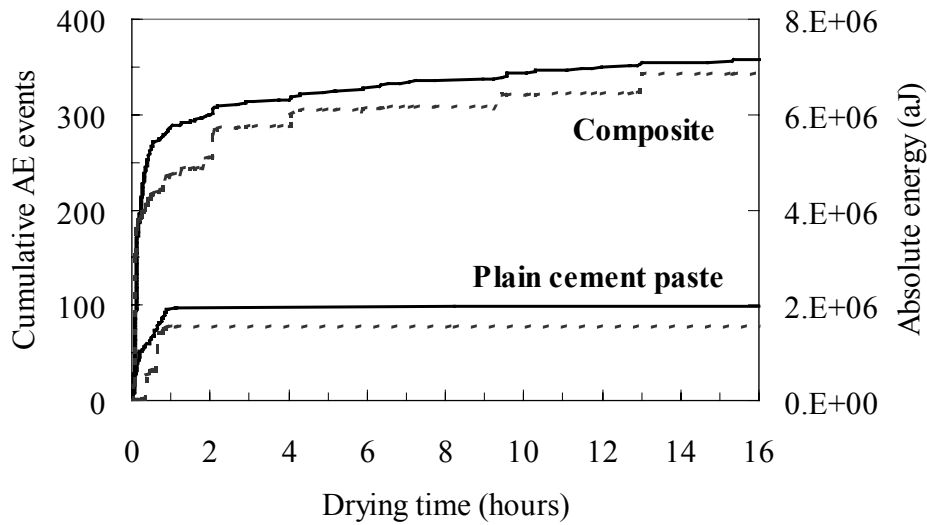


Fig. 7. Cumulative AE events and absolute energy.

perpendicular to the boundary of glass spheres indicating that they were partly caused by aggregate restraint. Self-restraining also took place in this composite (see Fig. 6b-d): a significant part of cracking had an orientation perpendicular to the drying surface.

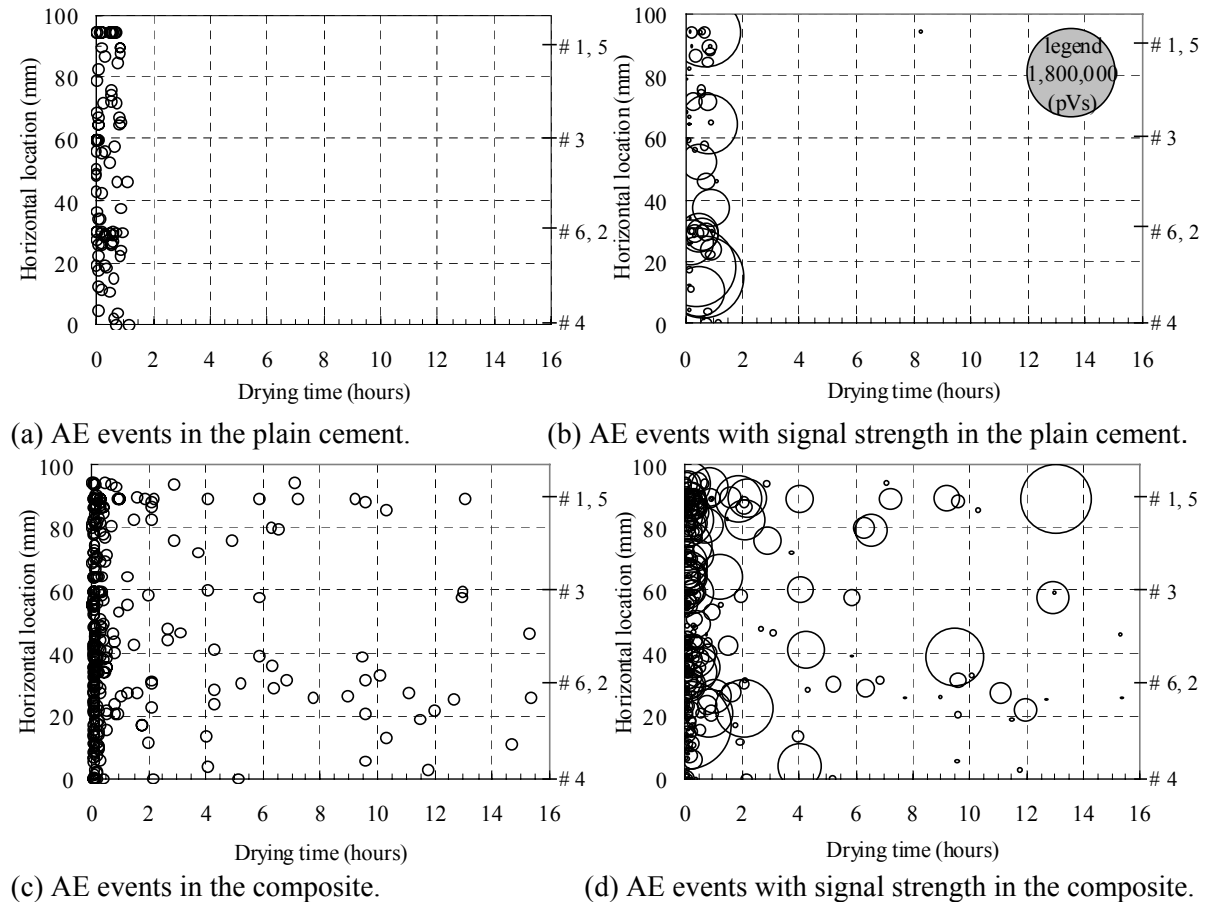


Fig. 8. One-dimensional source locations as function of drying time.

Figure 7 shows the cumulative AE events (black lines) and cumulative absolute energy (dotted lines) as function of drying time for plain cement paste and the composite. In comparison to the plain cement paste, approximately 3.5 times more AE events (accompanied by 4.5 times more absolute energy) are recorded in the composite after 16 hours drying. In both specimens, a rapid increase of AE events is observed in the first hour of drying. In the plain cement after this initial activity during approximately one hour drying, no further AE events are recorded. In contrast, AE events are continuously recorded, and a stepwise increase of absolute energy is found in the composite throughout the 16-hour drying experiment.

Figure 8 shows 1D source locations as a function of drying time for plain cement paste and composite. Source locations projected along line A-A in Fig. 1 are shown along the y-axis in Fig. 8. Figure 8b and d are shown with the scale of signal strength using the first arrival AE signals. In the plain cement (see Fig. 8a), AE events are dispersed along the A-A-axis in the first hour of drying. In the composite, more AE events are recorded from the start of drying and continue to be generated throughout the drying experiment. An important aspect is also found when the comparison is made between AE sources (see Fig. 8a) and those with signal strength (see Fig. 8b) in the plain cement. There are a number of AE sources observed in instantaneous drying in Fig. 8a, although they could not be found in Fig. 8b. This implies that the instantaneously generated AE sources had very small signal strength.

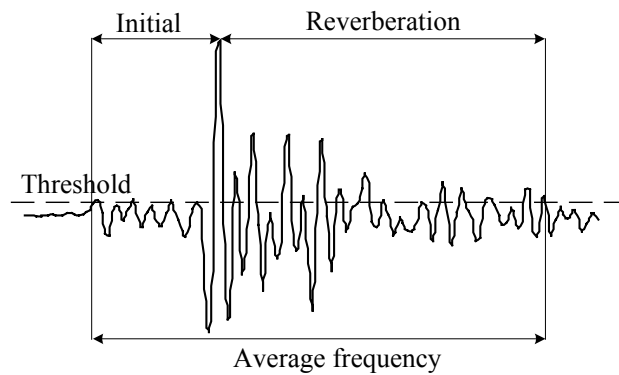


Fig. 9. Three extracted components of AE waveform to obtain individual frequencies.

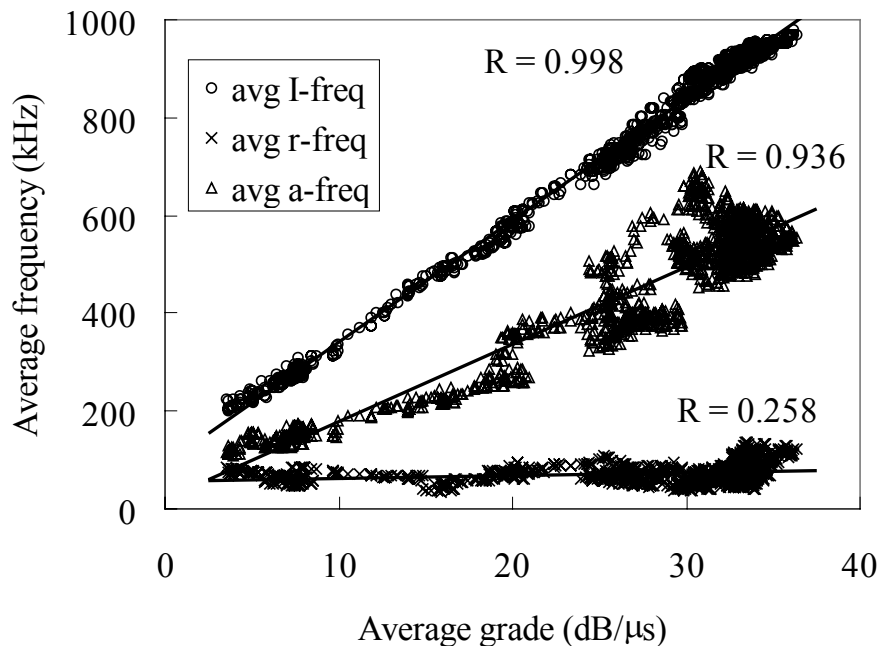


Fig. 10. Relationships between average frequency and grade.

Figure 10 shows the relations between average frequency and average grade. 1515 AE signals obtained from shrinkage cracks of 16 hours drying are used for constructing the chart. Three components of the waveform as shown in Fig. 9 are extracted to obtain the frequencies. Note that these are apparent frequencies based on threshold-determined parameters such as ring-down-counts, rise time and duration. As mentioned before, the initial part of the AE waves (initial frequency) and gradient of the AE waves up to peak (grade) are supposed to be closely related each other. Consequently, the correlation coefficients are 0.998, 0.936 and 0.258 for initial frequency, average frequency and reverberation, respectively. These results show explicitly the close relationship between initial frequency or average frequency and grade. As expected, reverberation remains essentially unchanged with grade.

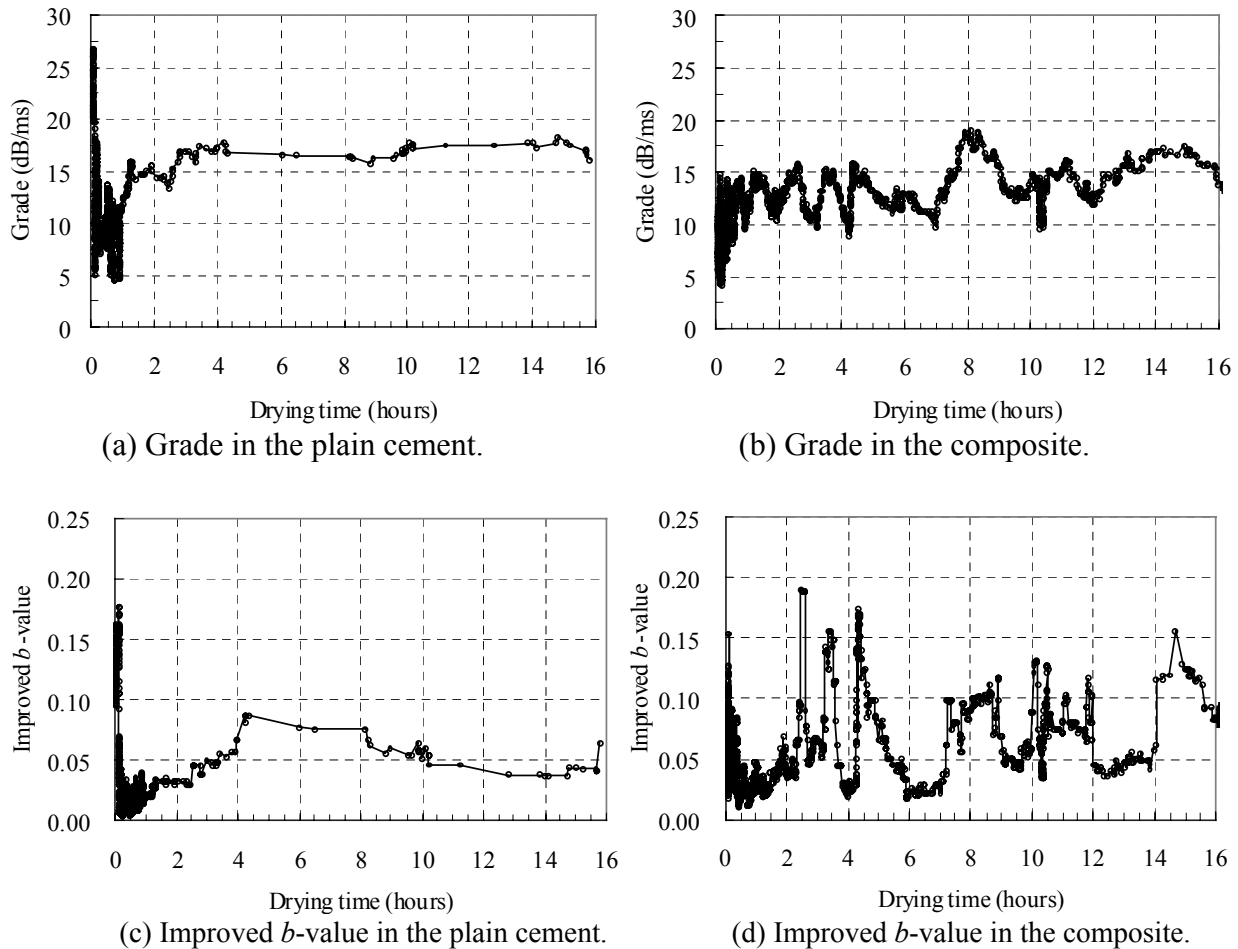


Fig.11. Grade and improved b -value as function of drying time.

Figure 11 shows the grade and the improved b -value with respect to the drying time. The grade sharply decreases only for the first one-hour of drying in the plain cement, whereas repetition of rising and falling values is found in the composite. The same trends are also observed in the charts of the Ib -value (see Fig. 11 c and d).

Finally in Fig. 12, the AE activity for the first one-hour of drying in the plain cement is enlarged showing Ib -value and initial frequency. A sudden drop is found after 0.1 hour (6 minutes) drying in both parameters, which suggests that a large scale fracturing and a slower deformation due to cracking have started at that moment.

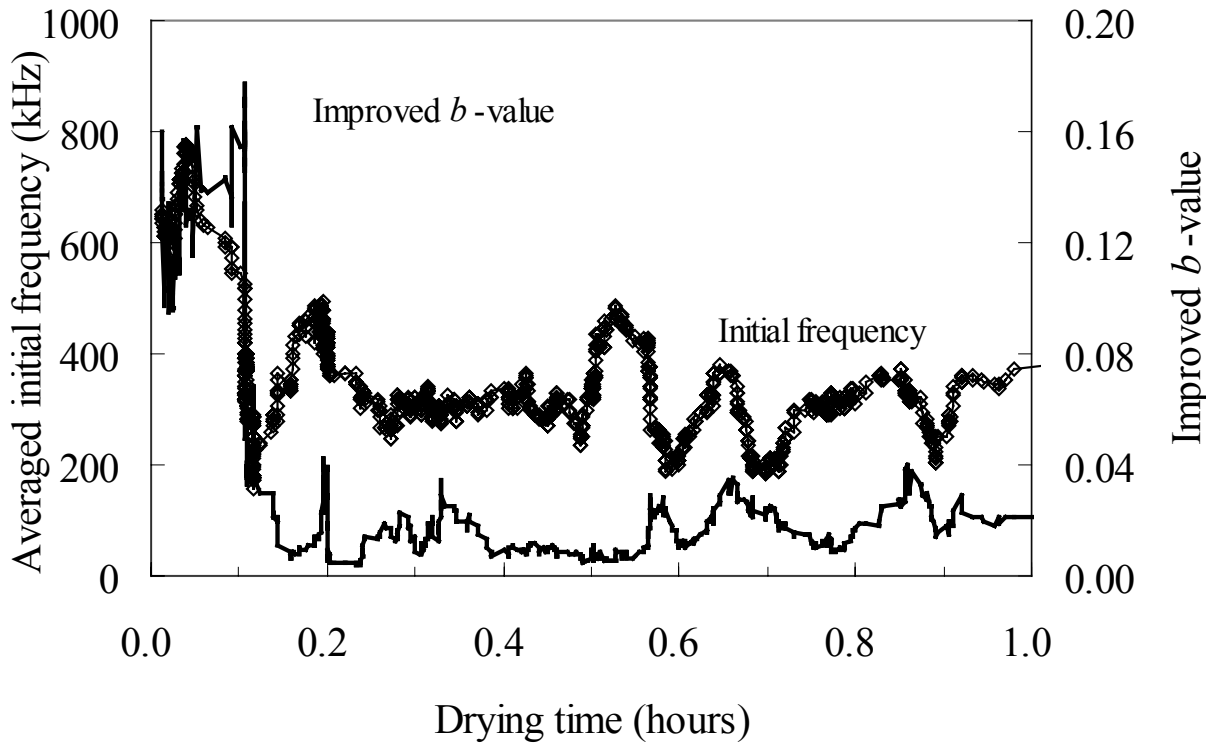


Fig. 12. AE activity for the first one-hour of drying showing Ib -value and initial frequency.

5. Discussion

The microscopy result shows that cracking in plain cement paste is due to self-restraining only, while cracking in composite is the result of combined self-restraint and aggregate restraint stresses. The AE event data show that in the plain cement paste most micro-cracking was generated within 1 hour, while micro-cracking in the composite continued throughout the drying experiment of 16 hours. The grade, initial frequency and the Ib -value analysis confirm this early behavior; large scale fracturing has already started at 6 minutes and continues to occur up to one hour in the plain cement paste. Similarly in the composite, large scale fracturing has started just after 6 minutes. Consequently, the self-restraint cracking in the plain cement paste is a very early drying phenomenon, while cracking due to aggregate restraint is a continuous process upon further drying. The development of the moisture gradient seems to be the main cause for the early crack-growth due to self-restraint in plain cement paste. The moisture gradient is steepest at the onset of drying, and starts to flatten already from (at least) 8 hours onwards [6]. This means that from this moment onwards, self-restraint stresses become less and cracking comes to a halt. In the composite, an initial peak in cracking is also observed, which can be explained by a significant contribution of self-restraint stresses. At later ages, aggregate restraint is the cause of cracking in the composite. Aggregate restraint cracking is not related to the moisture or shrinkage gradient and depends only on the 'local' magnitude of matrix shrinkage.

For the AE activity, which was generated during the initial 6 minutes of drying, the mechanisms producing the AE activity could not be ascertained. However, these initial AE signals have very small energy (from the observed absolute energy, signal strength and Ib -values), and they are caused by rapid phenomena judging from the observed initial frequency and grade. This AE mechanism will be clarified in a future paper.

6. Conclusions

Early behavior of micro-cracking due to drying shrinkage in cementitious materials has been studied by means of acoustic emission. The results are compared to findings from fluorescent light microscopy, and are summarized as follows:

(1) Self-restraining caused cracking in the very early stage of drying in both the plain cement paste and the composite; surprisingly and quite unexpectedly, drying cracks already were shown to form after 6 minutes of drying.

(2) Aggregate restraining occurred continuously throughout the drying experiment of the composite up to 16 hours.

(3) AE parameters such as grade, initial frequency and improved b -value provide valuable information on fracture mechanisms.

Acknowledgement

T. Shiotani received a TU Delft Senior Fellowship, which is gratefully acknowledged.

References

- [1] Bisschop J, van Mier J G M. "How to study drying shrinkage micro-cracking in cement-based materials using optical and scanning electron microscopy," *Cement Concrete Research*, **32**, 279-287, 2002.
- [2] Shiotani T, Ohtsu M, Ikeda K. "Detection and evaluation of AE waves due to rock deformation," *Construction and Building Materials* **15**, Elsevier Science, pp.235-246, 2001.
- [3] Shiotani T, Bisschop J, van Mier J G M. "Temporal and spatial development of drying shrinkage cracking in cement-based materials", *Engineering Fracture Mechanics* (in press).
- [4] Shiotani T, Yuyama S, Li Z W, Ohtsu M. "Application of AE improved b -value to quantitative evaluation of fracture process in concrete materials," *Journal of Acoustic Emission*, **19**. 118-133. 2001.
- [5] Shiotani T, Miwa S, Monma K. "Characteristics of elastic waves induced by raindrops," *Proc. 6th Domestic Conference on Subsurface and Civil Engineering Acoustic Emission*, MMII, pp. 7-12. 1999 (in Japanese).
- [6] Bisschop J, Pel L, van Mier J G M. "Effect of aggregate size and paste volume on drying shrinkage microcracking in cement-based materials," *Creep, Shrinkage and Durability Mechanics of Concrete and Other Quasi-Brittle Materials, Proc. CONCREEP-6*, Elsevier Science, pp. 75-80, 2001.

TRANSFORMATION PROCESSES IN SHAPE MEMORY ALLOYS BASED ON MONITORING ACOUSTIC EMISSION ACTIVITY

MICHAL LANDA¹, VÁCLAV NOVÁK², MICHAL BLAHÁČEK¹ and PETR SITTNER²

¹ Institute of Thermomechanics, AS CR, Dolejskova 5, 182 00, Praha 8, Czech Republic

² Institute of Physics, AS CR, Na Slovance 2, 182 21 Praha 8, Czech Republic

Abstract

Stress induced martensitic transformations (MT) in Cu-based shape memory alloys at room temperature were studied by acoustic emission method (AE). AE phenomenon is indicative particularly of the kinetics of MT's and can be used for nondestructive in-situ recognition of the various transformation processes. In this paper, correlations of structural processes and accompanied AE activity during forward and reverse MT in single crystals are shown and discussed.

Introduction

The functional materials are not being produced for their structural properties but for the unique functions they exhibit in thermomechanical loads. Shape memory alloys (SMA) are generic class of intermetallic alloys that display mechanical memory effects upon stress/thermal cycling. These properties are derived from a solid phase change - thermoelastic martensitic transformation (MT) taking place upon changing external stress and/or temperature. Nondestructive investigation of such materials requires novel experimental and theoretical approaches particularly in-situ studies under the external loads.

The ultrasonic techniques are based on detection and evaluation of acoustic properties changes taking place during MT's. Changes of acoustic wave velocities and attenuation bring information about the elastic moduli and structure variations (direct structure state characterization) [1]. Structure anisotropy and elastic properties of phase compositions, changing in the transformed polycrystalline material, need to be known and this is why single crystal experiments play an important role. The ultrasonic nondestructive techniques have a potential to provide (namely bulk) phase information complementary to classical phase identification methods (e.g. chemical analysis, TEM, X-ray).

Kinetics of MT's is characterized by acoustic emission (AE) activity. AE studies available in the literature (e.g. [2]) mainly focus on the thermally induced transformation. We have been studying AE accompanying stress induced MT in [011] and [001] oriented Cu-Al-Ni single crystals loaded in compression at a constant temperature.

Specimens

In the particular case of Cu-based SMA's, the high temperature austenitic ordered phase of high symmetry bcc structure (β_1) transforms mainly into lower symmetry martensitic phases with 18R monoclinic (β'_1) and/or 2H orthorhombic structures (γ'_1).

The different processes of MT are demonstrated on prismatic specimens ($10 \times 3 \times 3 \text{ mm}^3$) prepared from Cu-Al-Ni single crystals with orientation near $[001]$ (sample C110t) and $[011]$ (sample C101t) directions. Depending on temperature, the three stage may be distinguished: above A_f , between A_f and M_s and under M_s . The stress-free specimen above the temperature A_f is in the austenite phase (β_1) and its deformation exhibits super-elasticity effect; i.e. after unloading, the structure returns again to the austenite. Both specimens studied display this phenomenon at room temperature (RT), as shown in Fig. 1. The hysteresis of the stress-strain loop depends not only on the loading orientation but also on the maximal strain level (ϵ_{\max}). The four different transition processes ($\beta_1 \rightarrow \beta'_1$, $\beta_1 \rightarrow \gamma'_1$, $\beta'_1 \rightarrow \beta_1$ and $\gamma'_1 \rightarrow \beta_1$) were realized during the first (partial) and the second (complete) loading cycles. Accompanying AE activity of these separate processes is analyzed below.

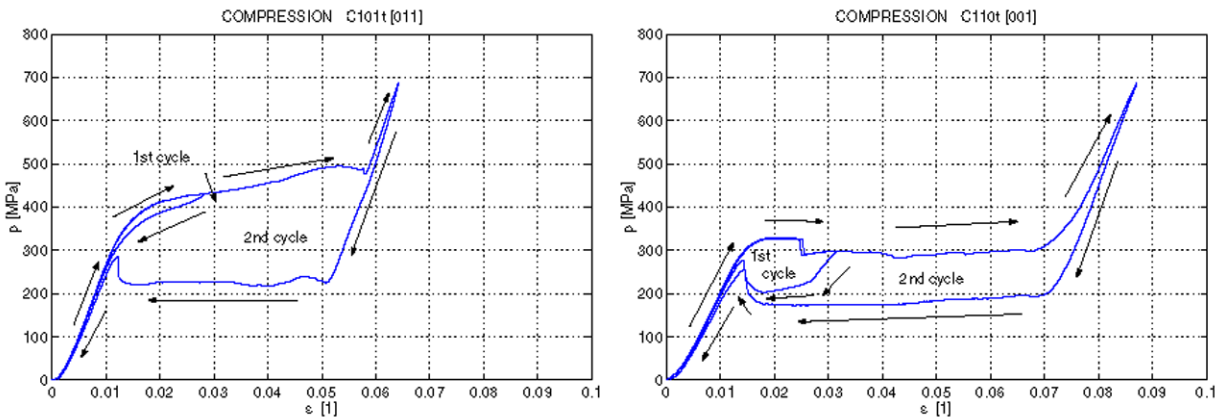


Fig. 1. Compression tests of Cu-Al-Ni single crystals. Samples C101t (left) and C110t (right).

Experimental Procedure

The experimental arrangement is described in [3]. Miniature AE sensors (PZT transducers, frequency band 1.4 MHz) were placed in the special designed loading heads of the testing machine TiraTest 2300. The heads had a shape of hollow rods, which enable one to place the sensors in the specimen axis. The strain rate control of compression tests was 0.1%/min. The classical AE parameters (count rate dN_c/dt , event rate dN_E/dt , AE amplitude distribution) were monitored each time step (0.5 s) by AE analyzer Dunegan-Endevco 3000 interfaced to PC via GPIB. The AE waveforms were recorded (12 bits/10 MHz) simultaneously by a transient recorder ADAM (Maurer). The AE events recording rate of the system is very low (several events per second). The AE parameters were resumed to the period $\Delta\tau = 5 \text{ s}$ and additional AE parameters were evaluated by post-processing: averaged count rate per events $\Delta N_c/\Delta N_E$ during the time interval $\Delta\tau$ and characteristics of AE amplitude distribution in the interval $\Delta\tau$ (see Fig. 2; the maximum amplitude A_{\max} , the averaged amplitude A_{AVG} and the best-fit slope b of the cumulative amplitude distribution; Fig. 2b). The AE amplitude is restricted by the threshold level of 44 dB and by the maximum of 100 dB. (In Fig. 2b, this range is from 2.2 to 5.0.)

The AE activity from forward and reverse MT's of both crystal orientations in the form of the AE parameters history and the stress curve are plotted together in Figs. 3 and 4. The observation of optical changes on the specimen surface was recorded, synchronously with the acousto-mechanical measurements (Fig. 5). The snapshots were obtained during the first loading cycle at the marked times in Figs. 3 and 4.

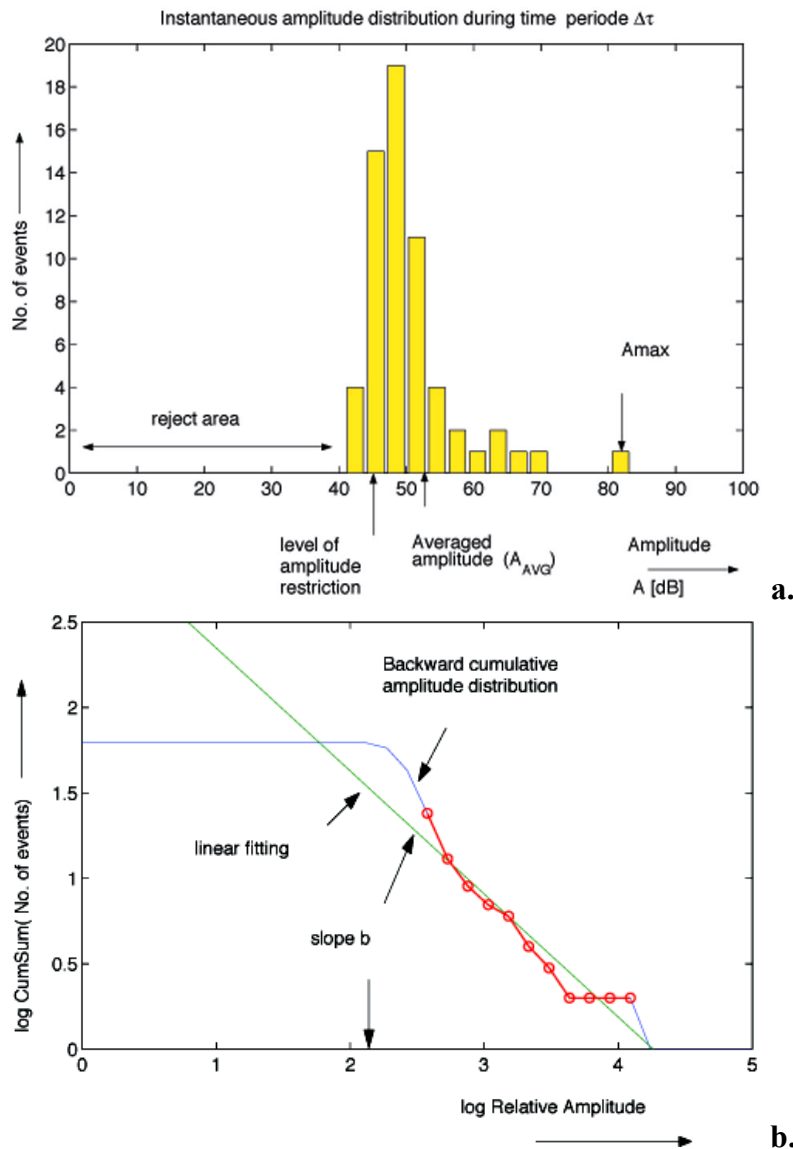


Fig. 2. Parametrization of instantaneous AE amplitude distribution. a. Differential; b. Cumulative distribution. Note Amplitude A (dB) = $20 \log$ Relative Amplitude.

Results and Discussion

Sample C101t

At first, we notice the partial loading cycle of the sample C101t in Fig. 3. The AE indicates formation of the thin individual lamellae of the martensite β'_1 , in the austenite single crystal (Fig. 5b). The martensite appears randomly at the characteristic orientation along the whole length of the sample. AE may be characterized by relatively averaged level of count and event rate, higher amplitudes and low level of the slope b of 1.5. During the process, the number of newly arisen lamellae decays and lamella width grows. This advanced stage of the forward MT is accompanied by lower AE activity (namely $\Delta N_c/\Delta N_E$ and A_{max} , note also dN_c/dt). During the unloading part of the first cycle AE activity changes dramatically: High level of dN_c/dt , dN_E/dt , $\Delta N_c/\Delta N_E$; i.e. high number of low amplitude events causes a higher level of the averaged amplitude A_{AVG} and high values of b up to the value of 6.1. The martensitic lamellae transform by the same way and synchronously.

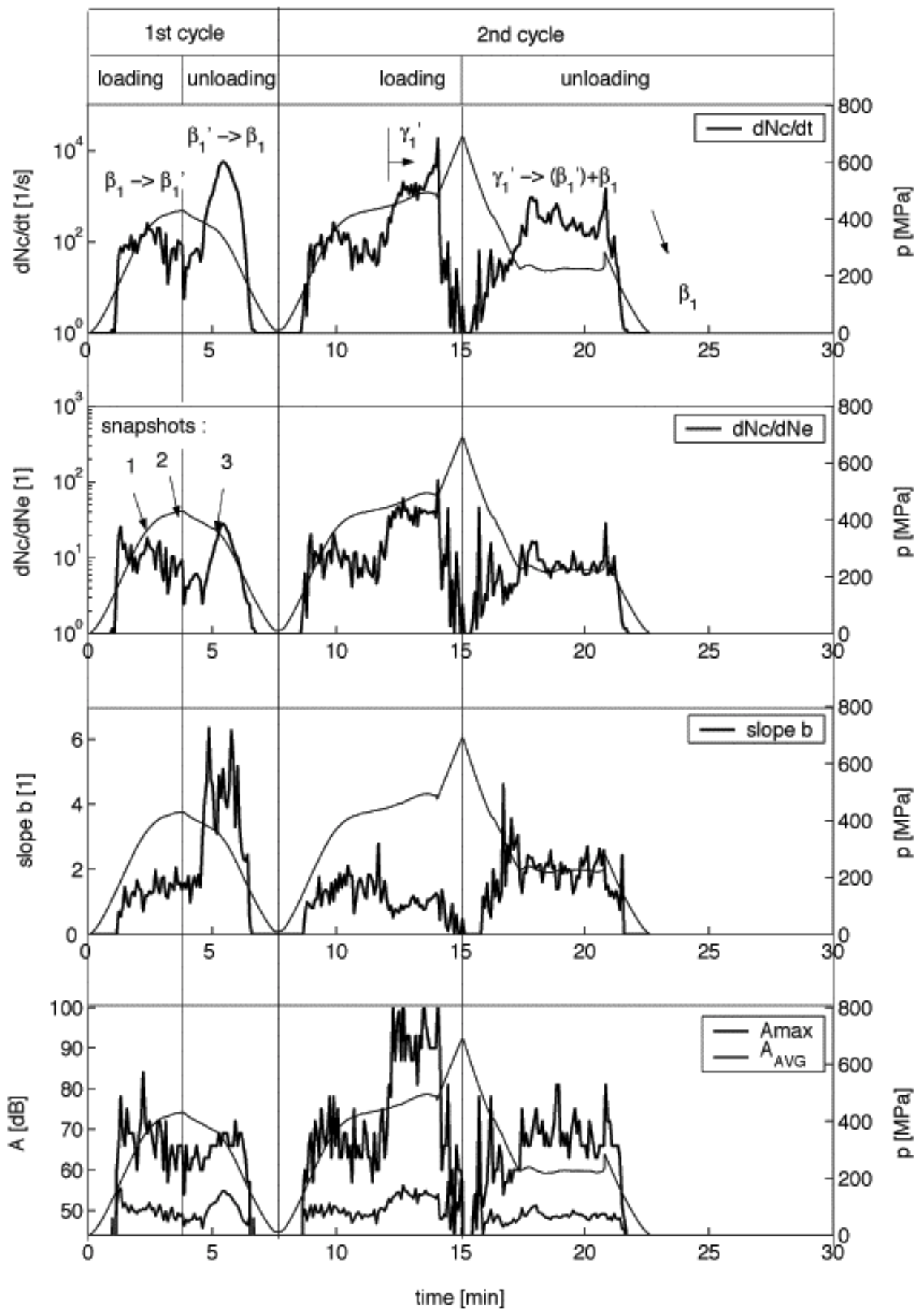


Fig. 3. AE activity during partial and full compression cycles of the sample C101t.

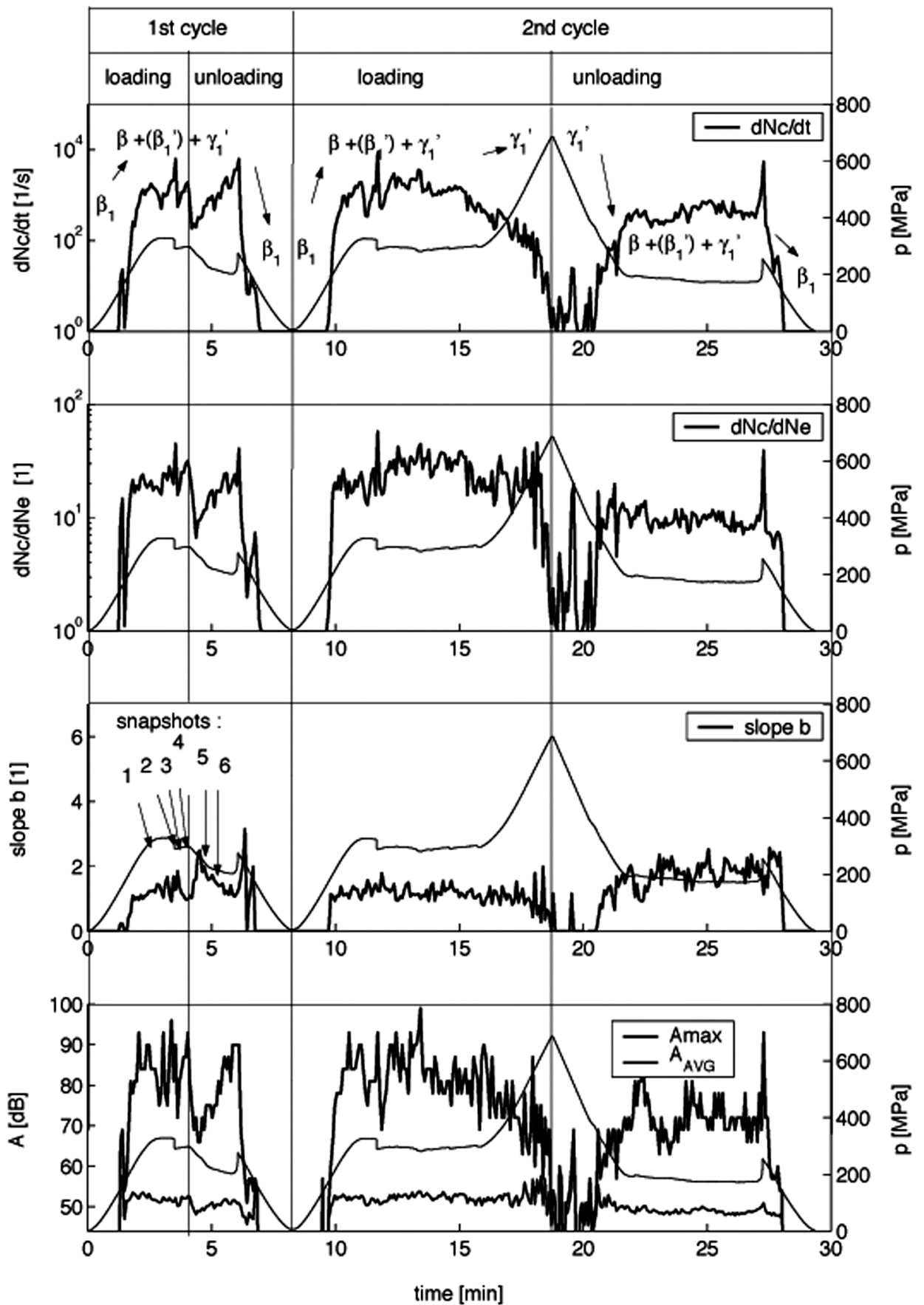


Fig. 4. AE activity during partial and full compression cycles of the sample C110t.

Higher level of AE activity indicates formation and growth of the martensite. It is in agreement with the expectation of the 2H-phase in the sample loaded over strain level 5%. The existence of high amplitude signals up to 100 dB causes lower values of b or the slope of cumulative amplitude distribution and higher values of A_{AVG} . High amplitude AE events correspond also with the optical observation. The γ'_1 martensite growth in the whole cross-section is found along the sample length, alternatively in both directions from the origin area. The AE decays quickly during the final linear part of the stress-time curve, as the forward MT is finished. The resulting structure is a single crystal of the γ'_1 -martensite having the orientation forced by the unidirectional stress. The AE from the reverse transformation ($\gamma'_1 \rightarrow \beta'_1 + \beta_1$) of the second circle is different from the process $\beta'_1 \rightarrow \beta_1$ (the first cycle). The reverse MT from the γ'_1 -martensite is more or less symmetric to the forward MT in the sense that γ'_1 -phase area transforms in whole cross-section and decreases along the sample axis. Nevertheless, the unloading path is longer (greater hysteresis in the stress-strain diagram), the MT is distributed over longer time and AE is less intensive than during the forward process. AE amplitudes of up to 80 dB are found and the parameter b reaches up to the value of 4.5 at the starting part and then moves around the value of 2 during the following constant stress period.

Sample C110t

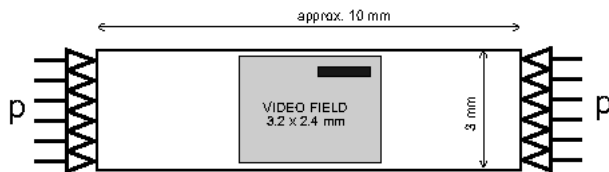
The MT of the sample C110t (Fig. 4) differs from that of C101t described above. The 2H martensite appears shortly after starting $\beta_1 \rightarrow \beta'_1$ transformation, Fig. 5c. The phase β'_1 exists for a short period and the martensitic transformation proceeds to $\beta_1 \rightarrow \gamma'_1$ directly after the stress step, which is notable in the loading curve (Fig. 4). From this moment, the continual martensite area spreads along the specimen. The β_1/γ'_1 interfaces move gradually in parallel planes.

The AE activity reaches the same level during the final unloading stage of the first partial cycle. The reverse MT from single martensite γ'_1 (the second full cycle) is accompanied by relatively stable AE activity with notable increase of high amplitude AE events the moment after starting and before finishing the reverse transformation process. The complete forward MT into the 2H-phase seems to be more acoustically efficient than the reverse one, but not as radically as in the case of $\beta_1 \leftrightarrow \beta'_1$.

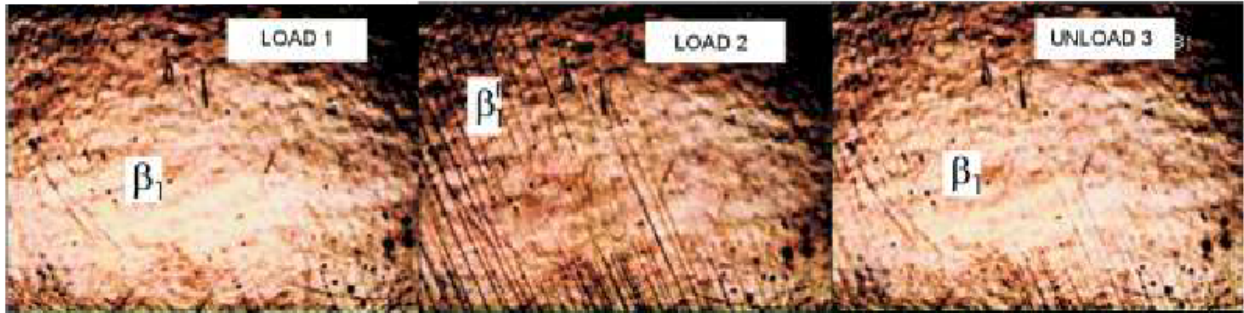
AE source localization

The character of the $\beta_1 \rightarrow \gamma'_1$ transformation in the form of the interfaces movement along the specimen length leads us to an idea of localizing this process by AE. The first wave arrivals were determined by AE signal records from the two AE sensors placed in the loading heads. The numerical procedure utilized adaptive threshold and denoising technique described in [4] and modified in [5]. The obtained results are plotted in Fig. 6a. The localization map brings only qualitative information; therefore the initial austenite structure is strongly anisotropic (anisotropy factor is about 12) and the elastic properties changed during MT. Nevertheless, the specimen length is dominant (prismatic bar shape), reducing anisotropy effect, and directions of the austenite/martensite interfaces (marked by arrows) are notable.

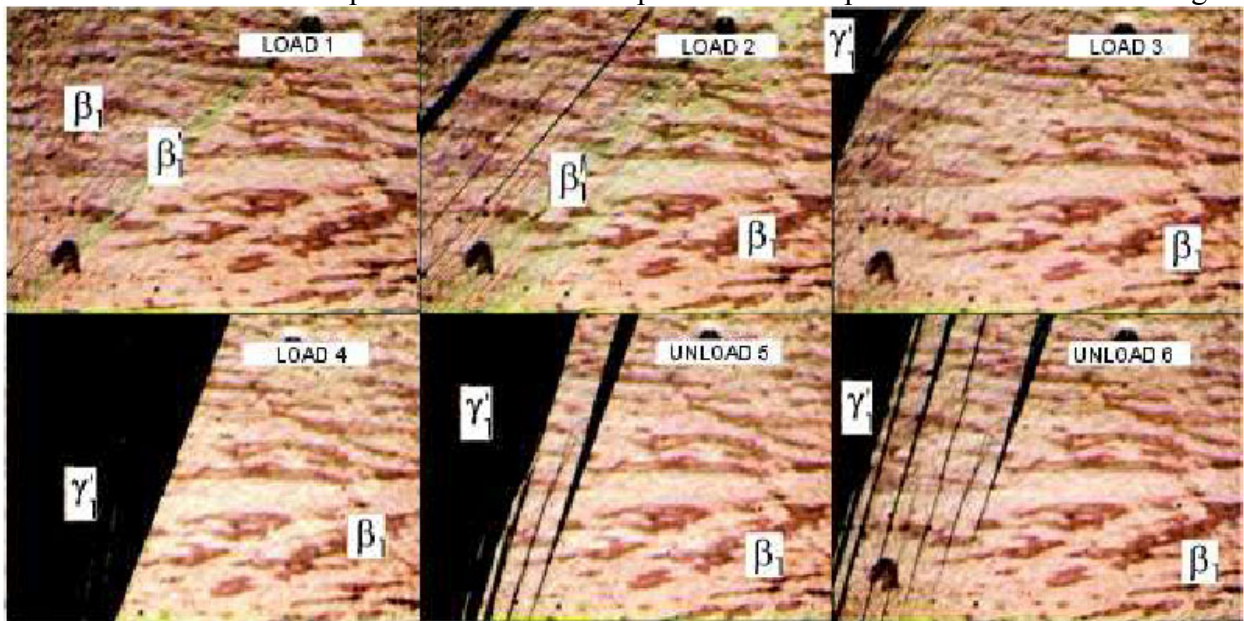
The more convincing result is obtained from the test of the sample C44t, which can be seen in Fig. 6b. The specimen is made also of the Cu-Al-Ni alloy and with the same orientation as C110t ([011]), but the transformation temperature A_f is shifted to $\sim 40^\circ\text{C}$ by a thermal treatment. It exhibits the shape memory behavior at RT. The specimen is driven to the martensite (2H) by compression and the structure stays permanent after unloading. The γ'_1 -phase is formed after the main peak during the loading stage and the only one interface, bordering the γ'_1 phase,



a. Observed field position on the specimen.



b. Sample C101t. Title corresponds to the snapshot number marked in Fig. 3.



c. Sample C110t. Title corresponds to the snapshot number marked in Fig. 4.

Fig. 5. Optical observation of MT-induced surface changes during compression.

propagates dominantly from the one side of the specimen to the other. The AE localization corresponds to only one active place, in contrast to the previous case of the sample C110t, where both sides of the γ'_1 area are active at the same time.

Conclusions

Acoustic emission during stress induced martensitic transformations in Cu-Al-Ni single crystals at room temperature was analyzed and correlated with structural changes observed on the specimen surface by optical microscopy. Understanding of martensite transformation processes in single crystals contributes to identification of structure changes in polycrystalline SMA's from acoustic emission.

AE signals of the forward and reverse $\beta_1 \leftrightarrow \beta'_1$ MT were found to be different. This indicates that this transformation, though otherwise fully reversible, has different kinetics in the forward

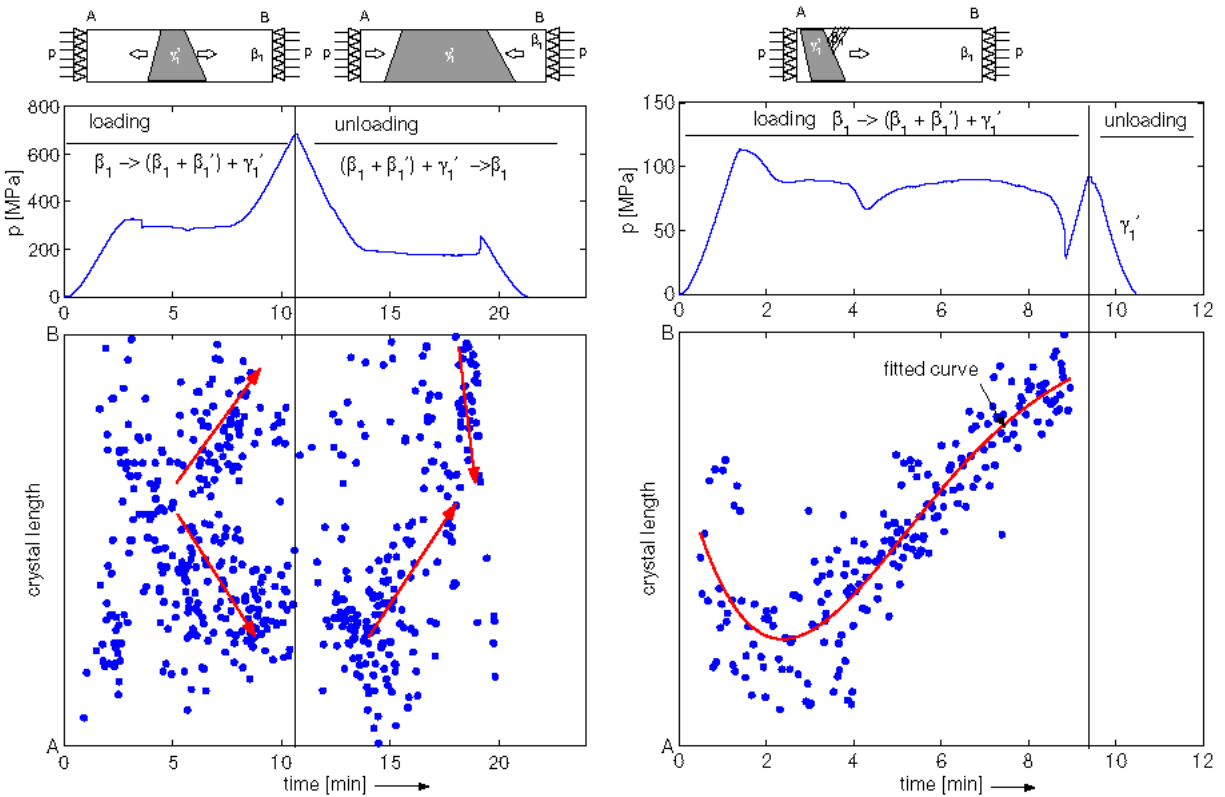


Fig. 6. Results of AE source localization and interpretation. C110t (left) and C101t (right).

and reverse processes. Similar behavior of AE activity was observed also during tensile tests of single crystals [6]. A bi-crystal with crystalline interface along the specimen axes has the same character of AE.

AE signals of the $\beta_1 \leftrightarrow \gamma_1$ MT in forward and reverse compression loads are similar. But complete and partial loading cycles give different results due to difficult nucleation of the stress induced γ_1 phase. By changing of the loading direction, the martensite phase may be reoriented (it is symbolized like $\gamma_1 \leftrightarrow \gamma_1'$). The reorientation is a much less active AE source than transformation processes described above [7].

Acknowledgements

The authors wish to express their thanks to Ing. Premysl Urbánek (Inst. of Thermomechanics, AS CR) for assistance during the experiments, Mr. Vladimír Novák (Inst. of Physics, AS CR) for preparation of the specimens. This work has been supported by Grant Agency of the Czech Republic under the project No. 106/01/0396.

References

- [1] M. Landa, V. Novák and P. Sittner, *Proceedings of 15th World Conference on Non-Destructive Testing*, Rome 2000, <http://www.ndt.net/article/wcndt00/index.htm>
- [2] E. Vives, I. Raifols, Ll. Mañosa, J. Ortín and A. Planes, *Phys. Rev. B*, **52** (1995), 12,644-12,650.
- [3] M. Landa, M. Chlada, Z. Prevorovsky, V. Novák and P. Sittner, *J. Acoustic Emission*, **17** (1999), S57-S64.

- [4] M. Landa, F. Chmelík and Z. Prevorovsky, Linear localization of acoustic emission sources, Research Report Z1219/96, IT AS CR Prague 1995.
- [5] M. Blaháček , AE source localization using artificial neural network approach (in Czech), PhD Thesis, IT AS CR, Prague 2000.
- [6] Novák, M. Landa and P. Sittner, *Proc. International Conference on Martensitic Transformations (ICOMAT'02)*, Helsinki, June 10-14, 2002 (in press).
- [7] V. Novák, M. Landa and P. Sittner, *Proceedings of 1st European Conf. on Shape Memory and Superelastic Technologies (SMST'99)*, Antwerp 1999, pp. 242-247.

CHARACTERIZATION OF STRESS CORROSION CRACKING OF CuZn-ALLOYS BY ACOUSTIC EMISSION TESTING

U.-D. HÜNICKE¹, M. SCHULZ¹, R. BUDZIER¹ and J. EBERLEIN²

¹ University of Rostock, Rostock, Germany

² Mecklenburger Metallguss GmbH, Waren, Germany

Abstract

This paper presents the results of the investigation for the characterization of stress corrosion cracking of CuZn-alloys using acoustic emission (AE) testing. The slow strain-rate test and the constant load test of various brass-alloys in a 0.5-molar sodium nitrite solution are carried out and the AE activity during these tests is recorded. The information provided by the AE hit counts, the amplitude and AE energy as well as the waveform of the AE signal is analyzed. The results show the possibility to predict the SCC-susceptibility of brass using AE testing.

Keywords: stress corrosion cracking; acoustic emission; CuZn-alloys

Introduction

The stress corrosion cracking (SCC) is an important engineering problem especially in the nuclear power and chemical industry. CuZn-alloys are known to undergo SCC both in ammoniacal and in some non-ammoniacal solutions. NaNO₂ was found to be one of the strongest promoters of SCC of brass in the non-ammoniacal solutions [1]. The process of SCC of brass in sodium nitrite solution has been extensively studied. Several models were suggested for the SCC mechanism of brass in sodium nitrite solution. The following models have achieved the widest acceptance: The film-rupture and dissolution model [2-7], the film-induced cleavage model [2-4, 7, 8] and the surface-mobility model [2, 4, 9]. Also some authors investigated the surface reaction of NO₂-solutions on metals [10-13].

The SCC is a process of microcracking and crack propagation. The initiation, multiplication and propagation of micro-cracks act as acoustic emission (AE) sources. Therefore, the AE analyses can be applied to evaluate the SCC-process in brass [14].

This paper describes the first part of a methodical investigation of AE signals for the characterization of SCC-susceptibility of different CuZn-alloys in sodium nitrite solution, which was realized by a slow strain-rate test and a constant load test.

Experimental Details

The specimens were cut from commercial rolled plates of brass with different Zn-contents with a thickness of 1 mm. The chemical composition of the test materials obtained by emission-spectroscopy and some mechanical properties are given in Table 1. The dimension of the tensile specimen is 250 mm x 30 mm. The width of the sample, which is exposed to the medium, is reduced to 12 mm.

Table 1. Chemical composition and mechanical properties of the tested brass.

	Chemical composition			Mechanical properties		
	Cu [wt%]	Zn [wt%]	Pb [wt%]	Tensile strength R_m [N/mm ²]	Yield strength $R_{p0.2}$ [N/mm ²]	Elongation A_{10} [%]
CuZn20	80.45	19.49	0.009	517	463	13
CuZn30	70.47	29.48	0.006	538	493	16
CuZn37	64.58	35.33	0.012	525	497	12
CuZn40	61.88	37.91	0.137	545	495	17

A resonant piezoelectric sensor (PAC R80, resonant frequency 200 kHz) was mounted directly on the test specimens above the liquid level preventing a destruction of the sensor due to the aggressive medium. The AE signals are pre-amplified (40 dB, 100-1200kHz) and processed using PAC's PCI-DISP4 AE-System. The threshold was set as low as possible.

The test medium of 0.5-molar sodium-nitrite solution is prepared from reagent grade chemical and distilled water, and the pH-value was 6.8.

Two different test techniques were used: The slow strain-rate test (SSRT) with a nominal strain rate of $1.5 \times 10^{-4} \text{ s}^{-1}$ and a constant load test (CLT). During the tests the samples are strained to rupture although the attention is directed to the first part of the experiment. Figure 1 shows a general overview of the experimental set-up.

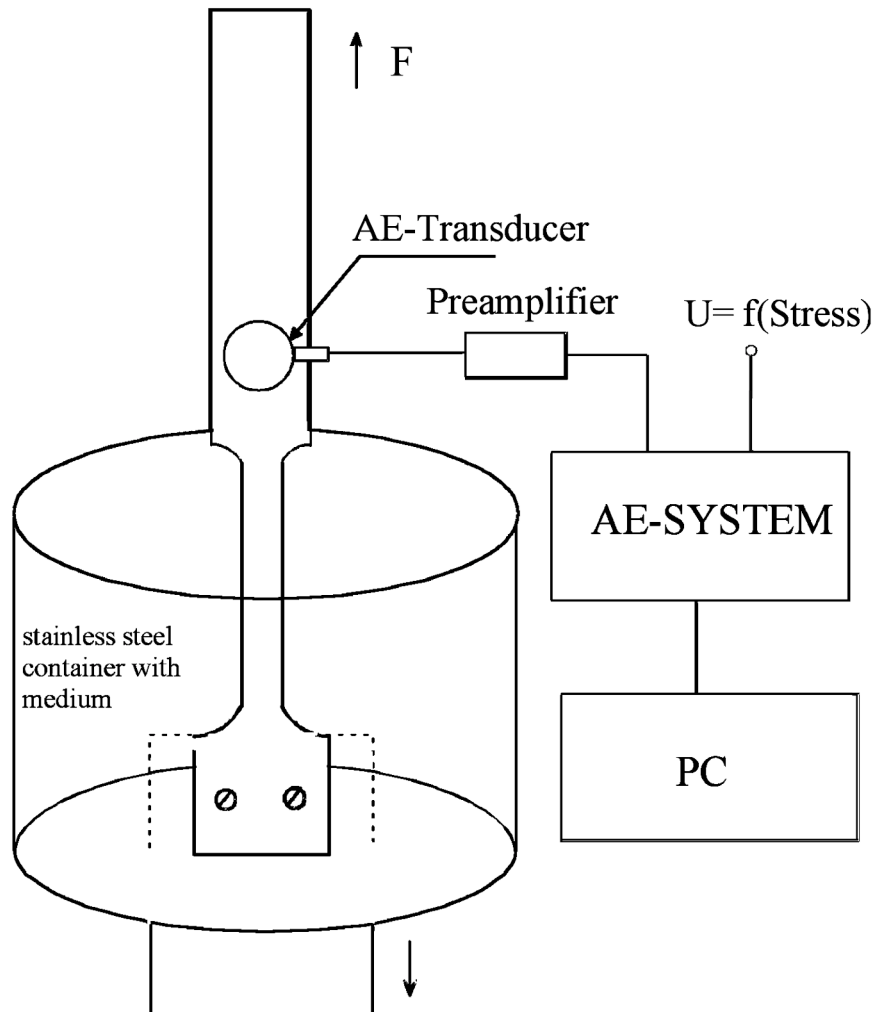


Fig. 1. Schematic experimental set-up for tensile tests in 0.5-mol NaNO_2 solution.

The CuZn-alloys, CuZn37 and CuZn20, were used for the SSRT in air and in a 0.5-molar NaNO₂ solution. Due to some noise emissions at the beginning of the tensile test caused by the set-up the analysis of the registration of the AE was started at a stress of R = 200 MPa.

The change of AE (ring-down) counts, hit counts, peak amplitude, energy, duration and other waveform parameters were evaluated. The CLT with an applied stress of $R = 0.9 \cdot R_{p0.2}$ and immersed in the solution of 0.5-molar NaNO₂ was performed for CuZn20, CuZn30 and CuZn40.

Results and Discussion

Slow strain rate test

The AE-signal-analyses represented by the cumulative hit counts during a SSRT at CuZn37 in air and in 0.5-mol NaNO₂ is shown in Fig. 2. An increase of the AE activity near the yield strength could be detected in both media. During the plastic deformation the specimen tested in air shows only a small amount of AE signals, while the AE in NaNO₂ intensified when the incubation time is reached.

Compared to the tensile test in air the influence of the sodium-nitrite solution caused a decrease of the tensile strength, yield strength and fracture elongation. The step-growth of the cumulative hit counts indicates the process of crack propagation and arrest during SCC of brass in the NaNO₂ solution.

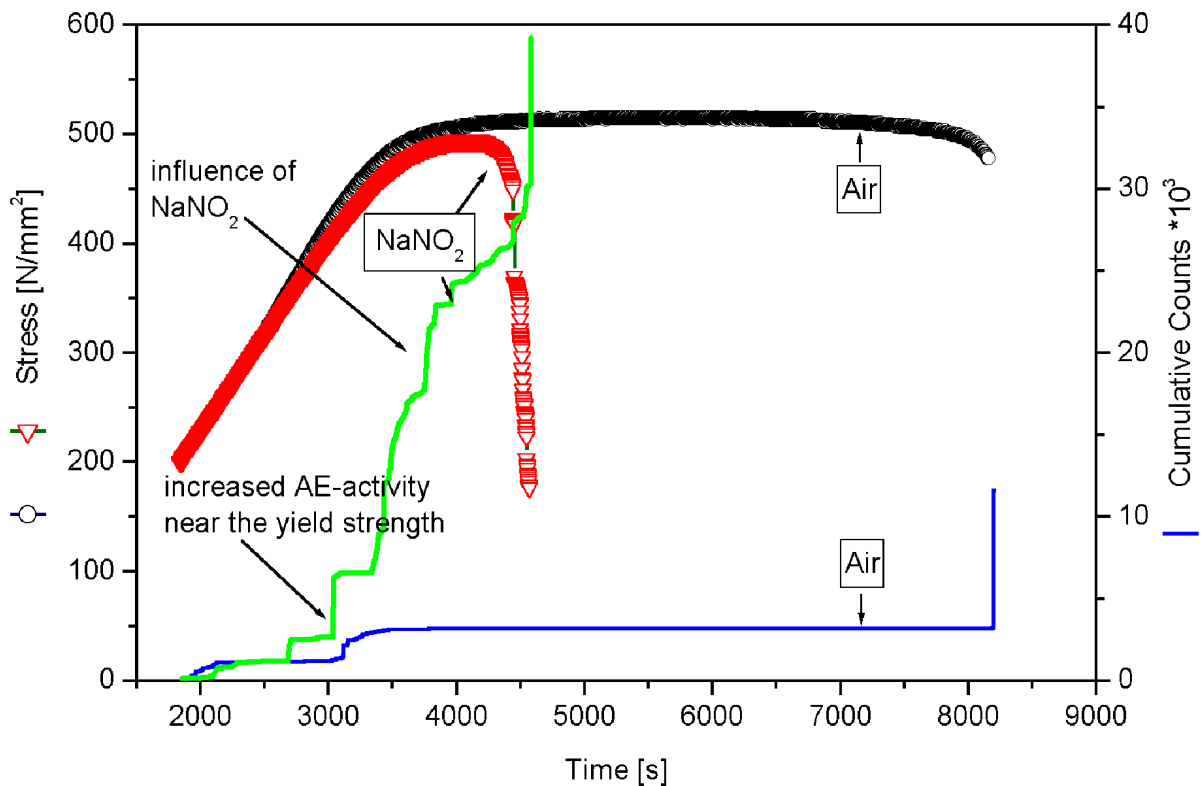


Fig. 2. Cumulative counts of AE signals during SSRT for CuZn37 in air and in 0.5-molar NaNO₂ solution.

The aggressive influence of the 0.5-mol NaNO_2 solution is also verified by SEM technique of the sample surface near the fracture zone, which is shown in Fig. 3. The sample stressed under the NaNO_2 solution features typical stress corrosion cracks normal to the applied tensile stress.

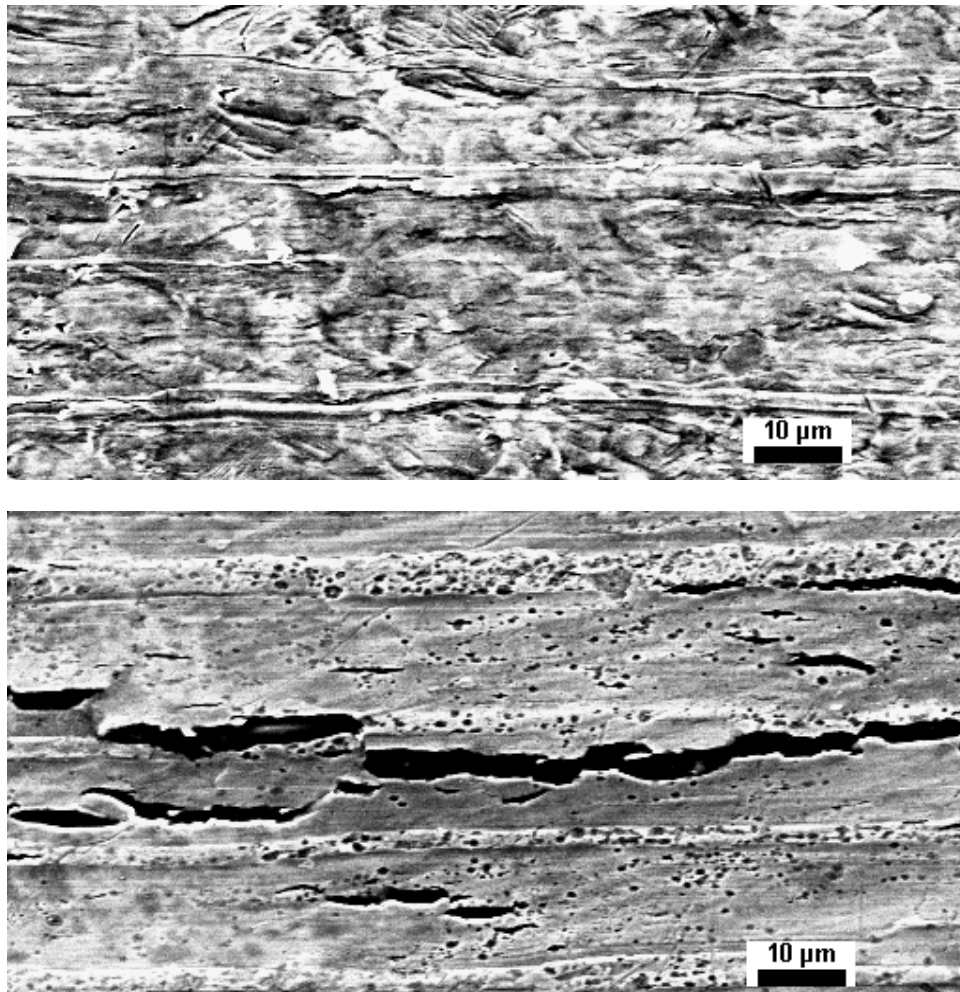


Fig. 3. Scanning electron micrograph of a CuZn37 near the fracture zone. a) in air (top) b) in 0.5 molar NaNO_2 (bottom).

The slow strain-rate technique is only useable for a characterization of an SCC-susceptibility when the incubation time, which in this case is defined as the time an increase in AE-activity can be detected, is shorter than the duration of the test. This is demonstrated in Fig. 4, which shows the cumulative counts during the SSRT in sodium-nitrite solution of CuZn20. Due to the low Zn-content the SCC-susceptibility is much lower. No significant AE activity could be detected after the increasing AE activity around the yield stress because the test duration was too short.

Constant load test

To characterize brass with a low SCC-susceptibility, a constant load test is more appropriate. The results of the CLT at a stress of $R = 0.9 \cdot R_{p0.2}$ in 0.5-molar NaNO_2 solution of the α -brass (CuZn20 and CuZn30) and the $(\alpha+\beta)$ -brass (CuZn40) are illustrated in Fig. 5. During the tests the applied stress is falling at first caused by the relaxation and later due to the crack propagation. The time to final fracture decreases with increasing Zn-content of brass. Also the time where the AE-activity increased visibly depends on the Zn-content. The higher the Zn-

content of the brass the earlier starts the AE-activity. Therefore, the point, where the graph of the cumulative counts is rising noticeably, could be interpreted as the incubation time. This could be used to characterize the SCC-susceptibility of brass.

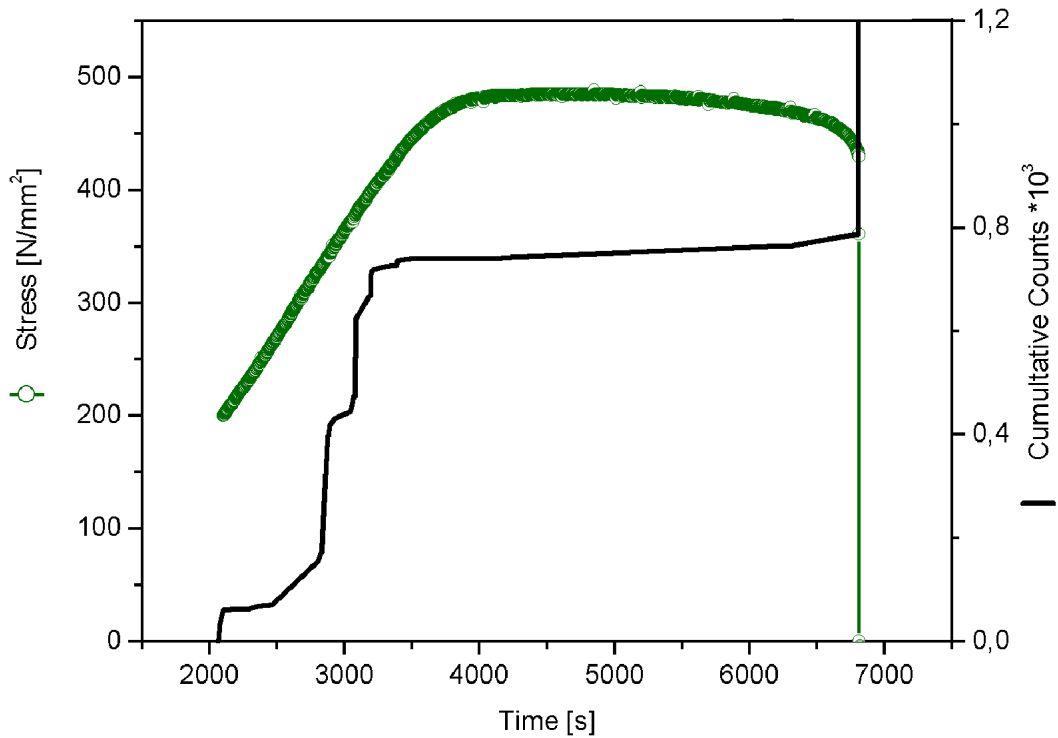


Fig. 4. AE cumulative counts during an SSRT for CuZn20 in 0.5-mol NaNO₂ solution.

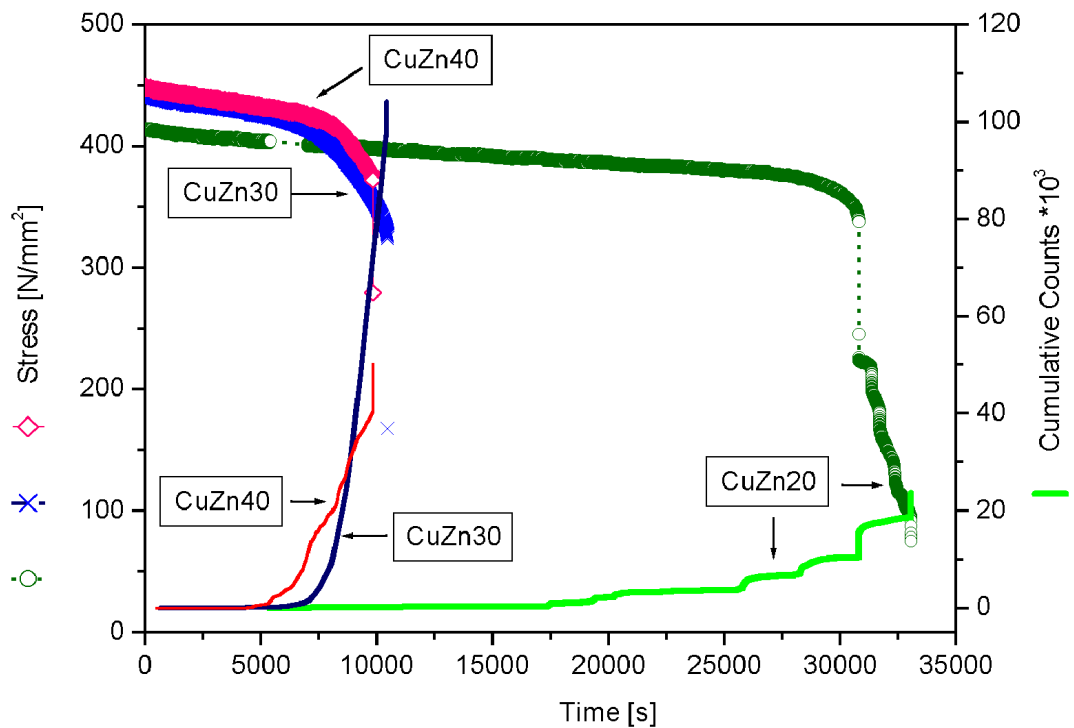


Fig. 5. AE cumulative counts during a CLT with $R = 0.9 \cdot R_{p0.2}$ for 3 CuZn alloys in 0.5-mol NaNO₂ solution.

The influence of the β -phase in CuZn40 is evident. Although the SCC-susceptibility of CuZn40 is higher ($t_{inc} \sim 1.4$ h) than for the single-phase CuZn30 ($t_{inc} \sim 2$ h), the AE activity is lower in CuZn40. This could be explained by the differences of the microstructures. The CLT of CuZn20 shows a SCC-susceptibility to NaNO_2 even though it is much less than for the alloys with higher Zn-content.

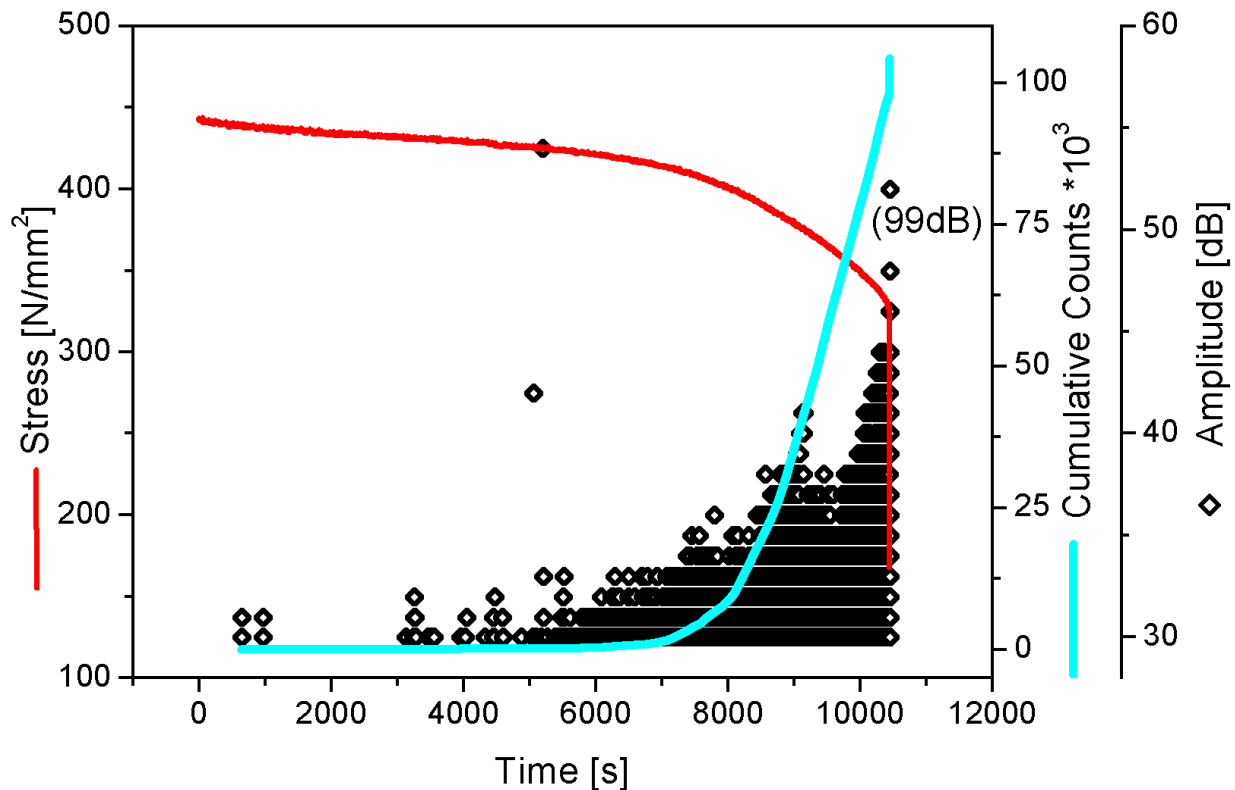


Fig. 6. Cumulative counts and peak amplitude of AE-signals during a CLT with $R = 0.9R_{p0.2}$ for CuZn30 in 0.5-mol NaNO_2 solution.

A more specific view to the character of the AE signals detected during the CLT of CuZn30 is given in Fig. 6 and Fig. 7. As a result of the increasing crack propagation the peak amplitude of the AE signals is also rising (Fig. 6). The same observation could be made for the duration of the signals shown in Fig. 7. Although there are two areas with an accumulation of AE signals, the majority of the detected AE signals possess a short duration up to $40 \mu\text{s}$ or between 150 and $200 \mu\text{s}$. This could indicate two different processes during the SCC.

Conclusion

The presented results show the possibility to characterize the SCC-process for brass in 0.5-molar NaNO_2 -solution by AE testing. Depending of the SCC-susceptibility of the specimen, it is possible to use the SSRT or CLT method with a load near the yield strength. The AE analysis is able to evaluate the SCC-susceptibility of various brass alloys under different conditions.

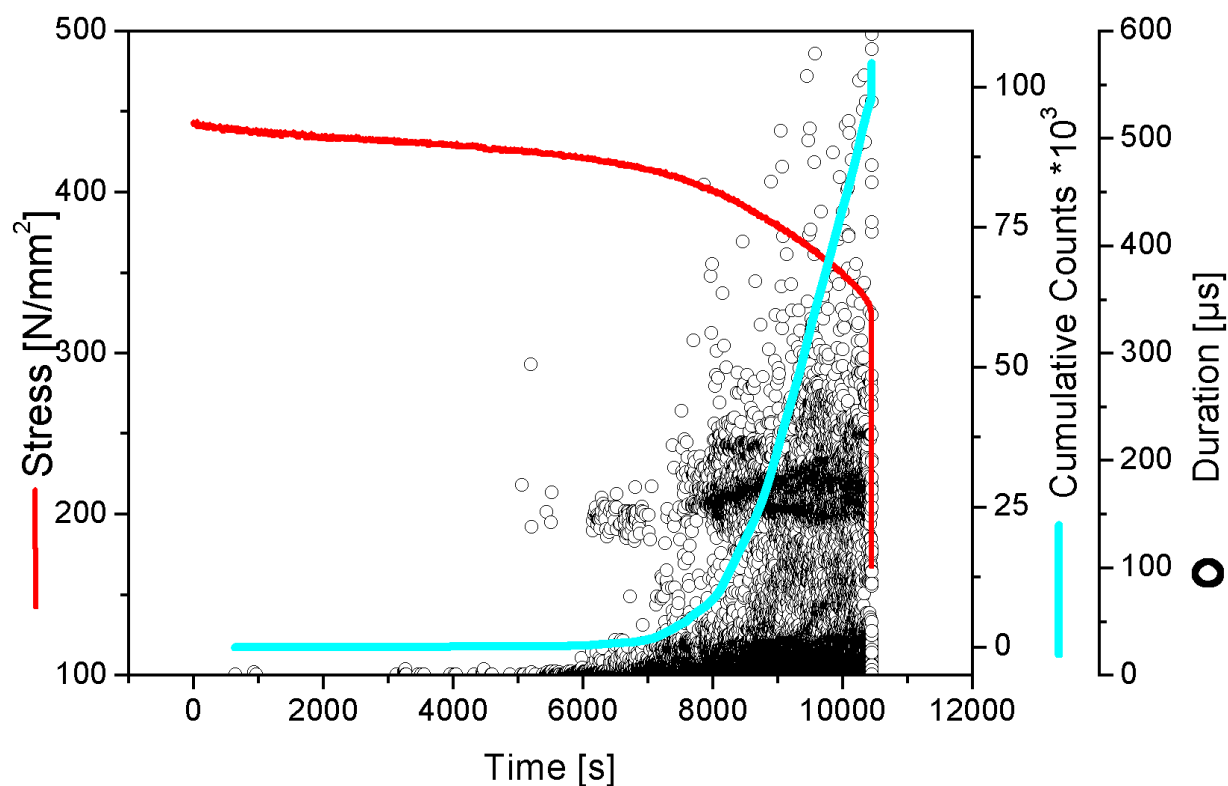


Fig. 7. Cumulative counts and duration of AE signals during a CLT with $R = 0.9R_{p0.2}$ for CuZn30 in 0.5-mol NaNO₂ solution.

References

- [1] M.G. Alvarez, C. Manfredi, M. Giordano and J.R. Galvele, *Corros. Sci.*, **23**, 769-780 (1984).
- [2] A.J. Bursle and E.N. Pugh, *Environment-Sensitive Fracture of Engineering Materials*, AIME, Warrendale, Pennsylvania, pp. 18-47 (1979).
- [3] E.N. Pugh, *Corrosion NACE*, **41**(9), 517-526 (1985).
- [4] F. King, The Potential for Stress Corrosion Cracking of Copper Containers in a Canadian Nuclear Fuel Waste Disposal Vault, AECL-11550, COG-96-94, 1996.
- [5] J. Yu and R.N. Parkins, *Corros. Sci.* **27**(2), 159-185 (1987).
- [6] J. Yu, R.N. Parkins, Y. Xu, G. Thompson, *Corros. Sci.*, **27**(2), 149-157 (1987).
- [7] D. Wu, H.S. Ahluwalia, A. Cai, J.T. Evans, R.N. Parkins, *Corros. Sci.*, **32**(7), 769-794, (1991).
- [8] K. Sieradzki, R.C. Newman, *Philos. Mag. A.* **51**(1), 95-132 (1985).
- [9] K. Sieradzki et al., *J. Electrochem. Soc.*, **134**, 1635-1639 (1991).
- [10] R.B. Rebak, R. M. Carranza, J.R. Galvele, *Corros. Sci.*, **28**, 1089-1106 (1988).
- [11] P. Eriksson et al. *J. Electrochem. Soc.*, **138**(5), 1227 (1991).
- [12] R. Holm, E. Mattsson, *Metal corrosion in the atmosphere*, ASTM STP 767, pp. 85-105 (1982).
- [13] R. Schubert, *J. Electrochem. Soc.*, **125**(7), 1114-1116 (1978).
- [14] U.-D. Hünicke, M. Schulz, R. Budzisz, *Proceedings of the DGZfP, Jahrestagung, Weimar*, 6-8 May 2002.

ACOUSTIC EMISSION TESTING ON FLAT-BOTTOMED STORAGE TANKS: HOW TO CONDENSE ACQUIRED DATA TO A RELIABLE STATEMENT REGARDING FLOOR CONDITION

G. LACKNER and P. TSCHELIES NIG

Institute for Technical Physics, TÜV Austria, Vienna, Austria

Abstract

Acoustic emission testing on flat-bottomed storage tanks is a beneficial method for tank operators to obtain information about possible corrosion or even leakage of the floor without opening the tank. Within a research project funded by the European Commission (SMT4-CT97-2177), a new testing technique was developed. It is based on specially designed measuring equipment as well as on sensor arrangement in combination with suitable location algorithms and on frequency analysis of the waveforms. After successful completion of the research project, the method is now in its introduction phase on the European market. Many tanks have been tested in refineries and tank farms. The new technique is described, including the outlines of AE testing, evaluation principle, data treatment, test examples and final report.

Keywords: Acoustic emission testing, storage tank, corrosion, leakage, maintenance.

1. Introduction

To have the necessary storage capacity available is of vital importance for every tank operator. One main task of the maintenance department is to take proper actions for ensuring the availability of the tanks. There are different methods to estimate the duration of a service period for a certain tank, most of which are based on experience. The common link between the experience-based methods is that they do not take into account the actual tank condition. Knowing the actual tank condition would enable the maintenance department to point out the tanks, which have to be repaired while leaving the others in operation. That would give an economic advantage by opening only tanks in bad condition for inside inspection and appropriate repair.

Tank degradation is mainly caused by corrosion. Physical and chemical conversions take place at the boundary area between the liquid storage product and the floor sheet. These processes are non-ideal. Therefore, some parts of the process energy are transformed into acoustic emission (AE) and may be detected with an appropriate measuring system. Within a research program funded by the European Commission (project identification: SMT4-CT97-2177, project partners: TÜV Austria/ENEL, Italy/Vallen-Systeme and Dow, Germany/Shell, Netherlands), a measuring system for detecting active corrosion and active leakage was developed. It was shown by laboratory and on-site measurements that AE signals contain information to obtain the actual tank condition [1-3].

Based on these results a suitable AE testing technique was developed. It consists of two parts:

1. Testing procedure to set up and to perform the measurement.
2. Evaluation procedure to process the acquired data and to grade the tank floor.

The tested tank floor is assigned to one out of four possible grades given in Table 1. The recommended duration of the following service period after the AE test is with reference to the service conditions given before and at the test. If the tested tank is grade IV, it is recommended to open the tank in order to clarify the indications found with AE. Costs for opening a tank and preparation for inside inspection differ according to the size and the storage product. In any event, significant expenses have to be spent. A loss of storage capacity for weeks or months might have a serious effect on production facilities. Therefore, a negative test result has to be as reliable as possible. However, a positive result has to be of highest confidence as well, because unexpected problems are even worse than an expected shut-down of a tank.

Table 1: Grading system for AE testing on flat-bottomed storage tanks.

Grade	Description	Recommended service period duration
I	No active sources	5 years
II	Low active corrosion	3 years
III	Medium active corrosion	1 year
IV	Leaks and/or high active corrosion	--

2. The AE Equipment

As an example for the standard sensor arrangement, 24 sensors have to be applied on a 100-m diameter tank, equally distributed along the circumference and at a level of 1 m above the tank floor. The used sensor is the VS30-V of Vallen-Systeme, which has a flat response especially within the used bandwidth centring at 30 kHz. The sensitivity of each measuring channel is checked with the Hsu-Nielsen source before the test. The AE system is an AMSY4 of Vallen-Systeme, which is capable of acquiring AE data and waveform data simultaneously for each channel. It has an internal pulsing unit, which sends on request an electric pulse to a sensor. That electric pulse is transferred into an acoustical pulse by the sensor. The other sensors may detect the emitted pulse after transmission through the liquid stock product and along the metallic tank shell. The AE system measures the time period for travelling from the emitting to the receiving sensor and that gives together with the distance between emitter and receiver the speed of sound.

The software for data acquisition, visualisation and frequency analysis are also provided by Vallen-Systeme. With VisualAE™ 2D and 3D plots may be produced to show the tank floor activity. With VisualClass™ classifier, files for analysing waveform data were created in order to identify the source mechanism, as shown in Figs. 1a and 1b. That may be either leakage or corrosion. If corrosion is given, further analysis assigns the corrosion process to either the onset of corrosion or to an already established 'old' corrosion indicated by the presence of a scaling layer.

One can take from Fig. 1 that the source mechanism is given in x-direction. The classifier file was created by using well-known and reliable training data sets. Then, independently acquired test data given at the y-axis were classified and the resulting assignment percentages given in z-direction

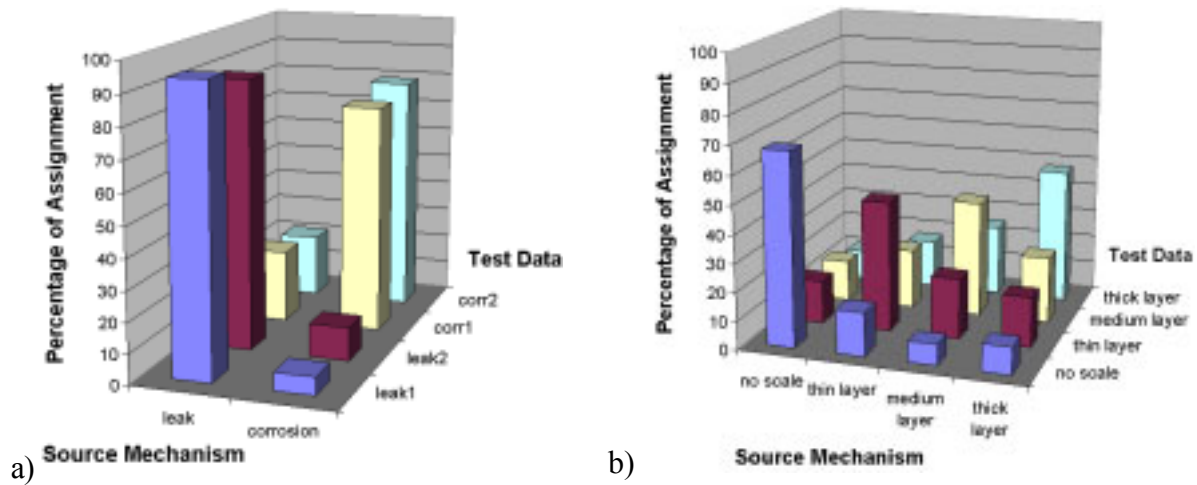


Fig. 1. Source mechanism identification with VisualClass™ classifiers.

a) leakage - corrosion, b) old corrosion - new corrosion.

were obtained. Due to the fact that the method is based on statistical methods it is very unlikely to get a 100 % assignment. The identified source mechanism is indicated by the maximum assignment percentage. The source mechanism was identified properly for every test data set in Fig. 1.

3. The Test Set-Up

Today's AE systems offer many features to filter the acquired data in order to eliminate noise as well as signals related to effects different from corrosion and/or leakage of the tank floor. There are possibilities for data filtering of each AE channel independently using criteria derived from combinations of various AE signal parameters. Optimised sensor arrangements in combination with appropriate location algorithms enable to focus on sources located on the tank floor by rejecting AE events with origins on the floating roof or drops falling from the fixed roof onto the liquid.

All these AE system capabilities may lead to the conclusion that the data treatment during the evaluation procedure is the most important part of the testing technique. But this is definitely not the case. The key to a successful test is always a proper set-up. The better the raw data of the test, the easier and more reliable is the data reduction down to the tank-floor condition representing located AE data. Following this straightforward concept, no measurement shall be taken during and shortly after periods of rain and/or strong wind. Furthermore, it is the aim before every test to identify and eliminate noise sources at and in the surrounding of the tank. The next step to avoid too much noise within the raw data is to find the best suited testing period. Very often this is during night; therefore a working permission covering 24 hours a day has to be provided. The AE sensors have to be applied onto the metallic surface of the tank shell; therefore small areas of the coating have to be removed at the sensor positions. The benefit of all these efforts is to be able to test the tank with the lowest possible threshold and with the highest possible sensitivity of the measuring channels. It has to be stressed that at the time being no data treatment is able to convert bad raw data into useful data.

To perform the test after a proper set-up is the easiest task of the testing technique. During the test the boundary conditions of the measurement have to be observed and remarks have to be writ

ten into the measuring file to identify periods of disturbance. These periods are rejected from evaluation and do not add to the minimum data recording time of 60 minutes. That gives up to 650 MB data (AE data and waveform data) for one measurement, which has to be stored on CD-R afterwards.

4. The Evaluation Principle

At the beginning of the research works, the demands for the testing technique were defined. Source mechanism identification was one of the main demands of the industrial partners. One possible approach was to use AE parameters like signal duration or peak amplitude for this purpose. One weak point of this approach was that the dependence of these parameters on the distance between source and sensor had to be estimated somehow. Since the frequency content of the emitted sound wave may be regarded as nearly unaltered starting from the source to the sensor on the tank shell, the partners have chosen another approach for source identification: the frequency-domain-based pattern recognition. Therefore, the evaluation of the test focuses on source location. This is again a straightforward concept. One can keep the link between the active source of the tank floor and its visualisation by location plots. Figure 2 shows as an example a 55-m diameter crude oil tank (floating roof) with a high active source near sensors 1 and 2.

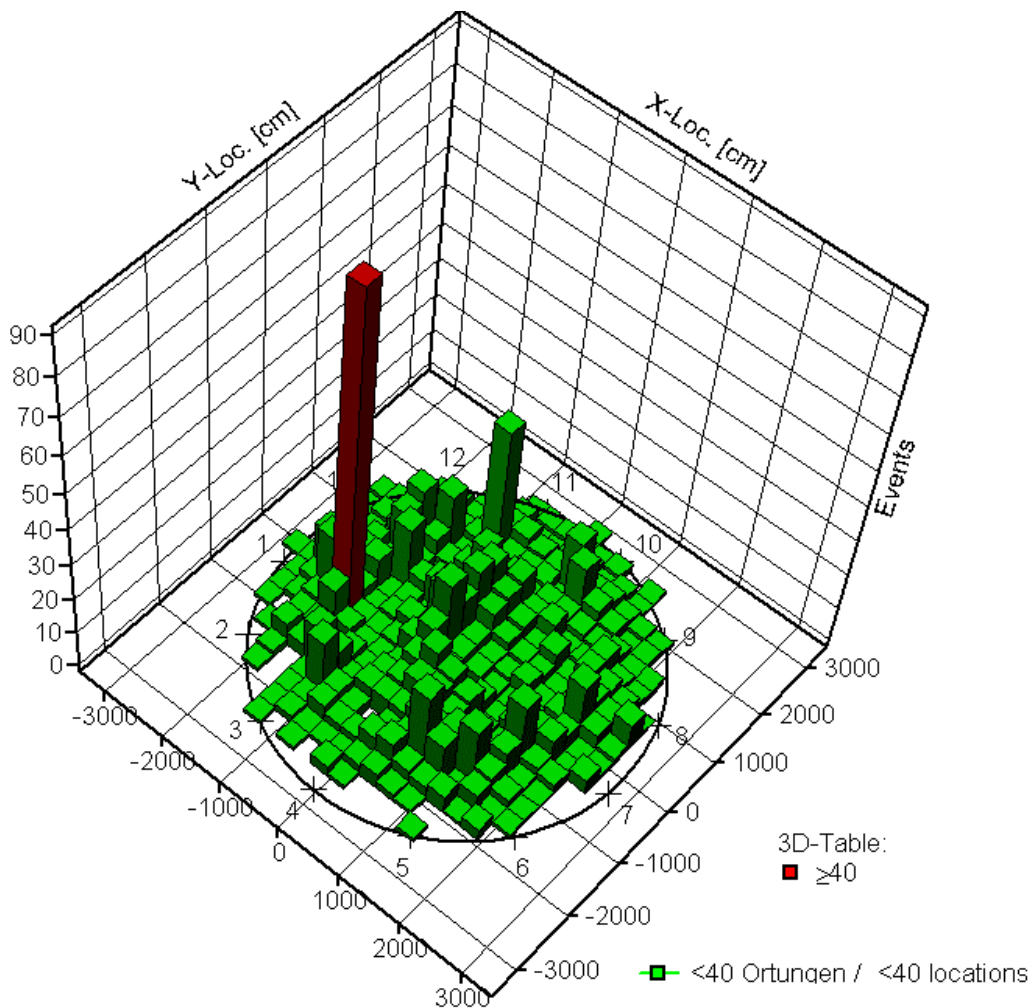


Fig. 2. Tank floor activity, 3D view of located AE events, 55 m diameter, floating roof.

The evaluation results in the location (coordinates) of the sources and their activity (low, medium, high). Moreover, it is obtained by frequency-content analysis of the acquired waveforms, if the sound waves were emitted by corrosion or leakage sources. In case of a corrosion source the presence of a scaling layer will be examined in another evaluation step. If a scaling layer is indicated, the source is assigned to an already established long-term corrosion process. If no scaling layer is indicated, then the source is identified as the onset of corrosion, which does affect the tank floor condition less than 'old' corrosion. But of course, if the activity is high, it has to be taken into account, lest this source might turn into a serious defect soon.

5. Measuring Data Treatment

Before the location result is ready for activity and frequency analysis, the measuring data has to be filtered in order to reject noise data or other signals not related to corrosion and/or leakage of the tank floor. Figure 3 shows the different stages of data reduction.

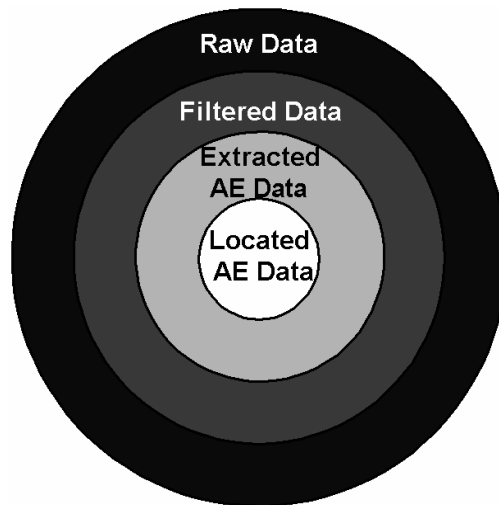


Fig. 3. Data reduction of raw data down to located AE data.

The first filtering step is applied to the raw data in order to get rid of spike signals. These signals are characterised by a very short rise time and are acquired in large numbers due to the fact that the measuring threshold is set very low. As already mentioned above, every test shall be performed with the lowest possible threshold. One consequence is that the test sensitivity is at its maximum; on the other hand, many acquired signals are related to arbitrarily occurring spikes of the background noise. Since these signals are without any significant source location potential, they are rejected from further evaluation. The remaining data is called filtered data.

The second filtering step is aimed at noise signals. These are AE signals, which are not related to corrosion or leakage sources. It was shown by laboratory tests that AE activity due to corrosion or leakage is evolving steadily in time without any sudden activity steps. Hence, it follows that every sudden step in AE activity indicates noise interference. One example of this noise interference during on-site tests is floating roof movement caused by gusts. Besides wind, electronic noise interference may lead to such a fluctuation in AE activity. In any case, noise shall not have an influence on the grading of the tank floor and those data has to be rejected from further evaluation. The remaining data after this step is called extracted AE data.

The final step of the data reduction process is the application of the location algorithm. It analyses the extracted AE data for hit sequences (AE events) with proper differences in arrival time. The main parameters of the calculations are the speed of sound, the size of the tank and of course the sensor positions. An AE event turns into a located AE event, if the algorithm finds correspondence of the measured arrival time differences with values derived from a certain location within the tank. The remaining data after this filtering step, the located AE data, are represented in Fig. 3 by the centre area of the disk.

At this stage one can be sure that the data is cleared from spikes, noise and signals, which cannot be combined to one single sound wave emitting physical event within the tank floor area. Figure 4 shows the extent of data reduction for some tank floors of different conditions according to the described filtering steps.

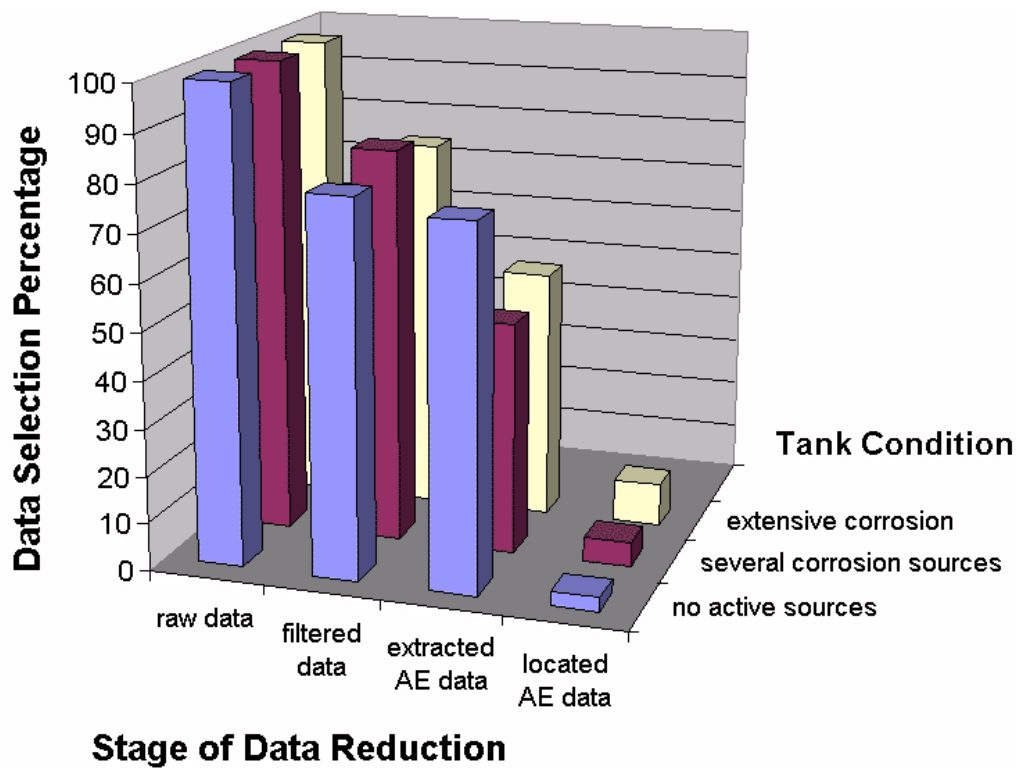


Fig. 4. Data reduction according to filtering stage.

It can be taken from Fig. 4 that the raw data contain only a few locatable AE data in the range of some percents (3 % for ‘no active sources’ to 9 % for ‘extensive corrosion’). But still the located AE data are not necessarily representing the actual tank floor condition regarding corrosion and/or leakage. In some cases further considerations are required.

6. Examples of Tested Tanks

Assuming a highly active corrosion source is located within a tank like that shown in Fig. 2, then the recommendation for tank maintenance according the grading system given in Table 1 would be to open the tank as soon as possible. Before presenting this kind of result to the tank operator

other possibilities for corrosion within the tank should be taken into account. One potential source of corrosion influencing the test result is the floating roof. An inspection of the roof can solve this problem only partly; much better is to use a sensor arrangement consisting of two rows of sensors. Figure 5 shows the same floating roof tank like Fig 2 but the measurement was evaluated with the help of the applied second row sensors.

The first row sensors are applied at a height of 1 m above the tank bottom as usual, and the second row sensors are mounted above the bottom row sensors in a vertical distance of 2 m to 4 m. The value depends on the filling height and the tank size. With this set-up AE events from above may be identified easily and reliably by using the second row sensors to guard the bottom row. It can be taken from Fig. 5 that no active source is remaining after this final evaluation step, the located AE source in Fig 2 was identified as defect of the weld between two roof sheets.

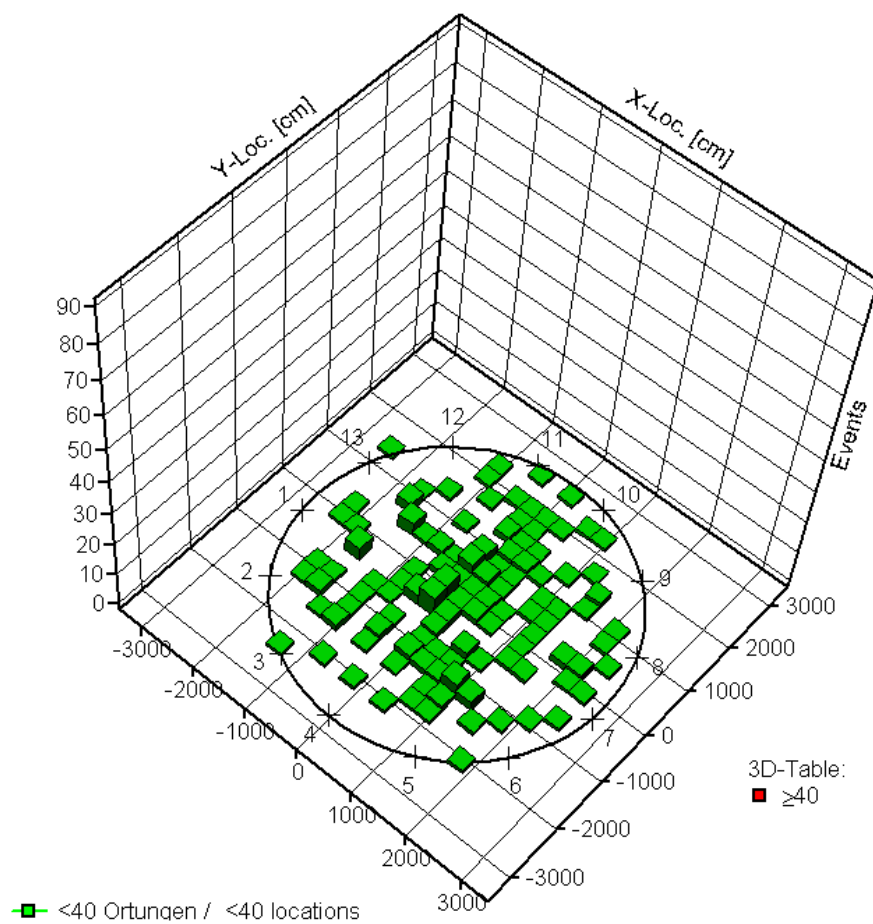


Fig 5. Tank floor activity, 3D view of located AE events, 55-m diameter, floating roof, evaluation with two rows of sensors to reject AE events from the roof.

Another application of the second row of sensors is for identifying drops falling on the liquid product inside a fixed roof tank. This might occur if the gaseous phase of the product condenses at cold parts of the roof structure. Some drops interfering the measurement may be identified manually; for large numbers of drops more efficient methods have to be used in order to finish evaluation within a reasonable period of time. Figure 6a shows the tank floor activity of a test interfered by

drops obtained by the bottom row only. Figure 6b shows the same tank but evaluated with the help of two rows of sensors, and no active source is remaining.

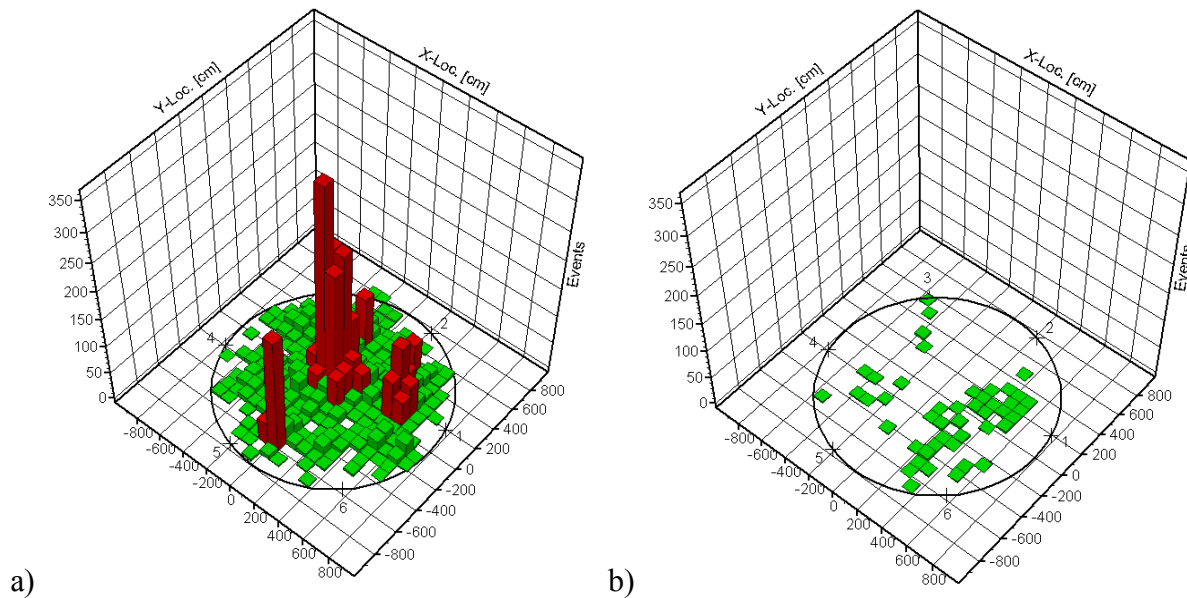


Fig. 6. Test interfered by drops, evaluation using a) one row and b) two rows of sensors.

The feasibility of the application of this special sensor arrangement is limited only by the increase of the background noise caused by countless drops. The corrosion or leakage signals would be drowned by noise signals without any chance to get them by a threshold depended AE system. But for the time being this is the same for all other noise sources, which cannot be eliminated.

7. Conclusion

Acoustic emission tests are suited for obtaining the actual tank floor condition of flat-bottomed storage tanks regarding active corrosion and/or active leakage. The presented testing technique focuses on location of AE sources and the identification of the source mechanism, either leakage or corrosion, by frequency-content analysis of the gathered waveforms. If corrosion is detected, further analysis results in distinguishing the onset of corrosion (no scaling layer) from already established long-term corrosion (presence of a scaling layer).

Several demands have to be fulfilled to obtain a test result, which represents the actual tank floor condition. One important part is to filter the raw data of the performed measurement subsequently in different steps. The strongest filter criterion is given by the location algorithm. It was shown that the raw data of the measurement contains from 3 to 9 % locatable AE data depending on the tank floor condition and the boundary conditions of the measurement. It follows that the location algorithm and the parameters to be set for its application have to be well known and well chosen. The standard sensor arrangement is able to locate within a horizontal plane and does not give any information about the position of the source origin in vertical direction. With a second row of sensors the location algorithm used is capable of rejecting AE events located above the sensor arrangement.

Meanwhile more than 100 tanks have been tested with this testing technique within the EU. The database and the knowledge of the given tank populations increase steadily. This again enables further improvements of the testing as well as the evaluation procedures, which shall lead to a broad acceptance of AE testing.

References

- [1] P.J. van de Loo and B. Herrmann, “How Reliable is Acoustic Emission (AE) Tank Testing?” - The Quantified Results of an AE User Group Correlation Study, presented at the 7th European Conference on NDT, 1998, Copenhagen (DM).
- [2] P. Tscheliesnig, G. Lackner, M. Gori, H. Vallen, P.J. van de Loo, and B. Herrmann, “Inspection of Flat Bottomed Storage Tanks by Acoustical Methods. Classification of Corrosion Related Signals”, presented at the 24th EWGAE Conference, 2000, Senlis (F)
- [3] Synthesis Report of the EC Standards, Measurements and Testing Contract Nr. SMT4-CT97-2177, “Inspection of Flat Bottomed Storage Tanks by Acoustical Methods“, issued November 1st, 2000

ACOUSTIC EMISSION MEASUREMENTS ON SHELL STRUCTURES WITH DIRECTLY ATTACHED PIEZO-CERAMIC

FRANZ RAUSCHER and MULU BAYRAY

Institute of Pressure Vessels and Plant Technology
Vienna University of Technology, Vienna, Austria

Abstract

When coupling acoustic emission sensors to curved shells by means of fluid coupling media, as often done in pressure equipment applications, disadvantages arise. Due to fluid coupling, the in-plane movements are not transferred to the sensor, and due to the coupling to a curved surface the repetitive accuracy is relatively low. The investigation dealt with the idea to build a simple sensor by gluing a piezo-ceramic directly to the vessel. To protect the simple sensor from electrical noise, a simple case was also glued to the shell, such that a shield was built around the ceramic by this case and by the tested shell itself. To compare with a sensor using the same piezo-ceramic, a simple sensor was built. This simple sensor was coupled by gluing, and also, in a separate test, with silicon grease to the test specimen. The response of the investigated arrangements to narrow-band pulses was recorded and plotted versus the centre frequency of the pulses. The ratio of the sensitivity to the in-of-plan waves to the sensitivity to the out-of-plane wave was evaluated using pencil lead breaks. In addition, the sensitivity to electrical noise of the arrangements was checked.

Keywords: Acoustic emission, sensors, plate waves, shell structure, pressure vessel

1. Introduction

Recent investigation [1-6] showed that the ratio of amplitude of the in-plane wave (S_0) to the out-of plane (A_0) wave is a good parameter for the evaluation of acoustic emission (AE) signals measured on shell structures like pressure vessels. The in-plane wave (S_0) in this context is the first symmetrical mode of the Lamb waves and the out-of-plane wave is the first asymmetrical mode of the Lamb waves.

To evaluate this ratio, it is necessary to detect the in-plane wave and to separate it from the out-of-plane wave. When using the usual AE sensors, coupled by some fluid to the vessel, the sensitivity to the in-plane wave is relatively low. Since in the case of the in-plane wave the in-plane movement at the surface is larger than the out-of-plane movement, a connection of the sensor to the vessel, which can carry shear forces, is desirable. This can be achieved by a sensor, which is glued to the surface of the structure, or even better by gluing the piezo-ceramic itself directly to the structure.

2. Tested Arrangements

2.1 Commercial sensor VS150 coupled by silicon grease

As a reference a commercial sensor (Vallen VS150) was coupled by silicon grease, as usual when testing pressure vessels. This sensor was not coupled to the vessel by gluing, because in this case it would not be possible to remove it without damage. Like in all the arrangements

tested here, at the location of the sensor the painting was removed and the surface was ground almost flat (as far as possible with simple means).

2.2 Directly glued piezo-ceramics

All the painting was removed from the metallic surface before gluing the piezo-ceramic to the surface. The glue and the gluing procedure were similar to the ones, which are used when applying strain gauges. Afterwards, for shielding the sensor from electrical noise, a case was glued to the surface of the tested plate in such a way that the piezo-ceramic is enclosed by a metallic shield (Fig. 1). A cable connected to the case by a BNC-connector and a short piece of bare wire, which touches the upper electrode of the piezo-ceramic, builds the electrical contact to the piezo-ceramic. The whole procedure of applying this kind of arrangement is as simple as applying strain gauges. No damping was applied to achieve high repetitive accuracy, but, because of this arrangement only narrow-band resonance sensors can be built. The resonance frequency of the arrangement can be corrected by adding mass at the top of the piezo-ceramic. The tested configuration is shown in Table 1.

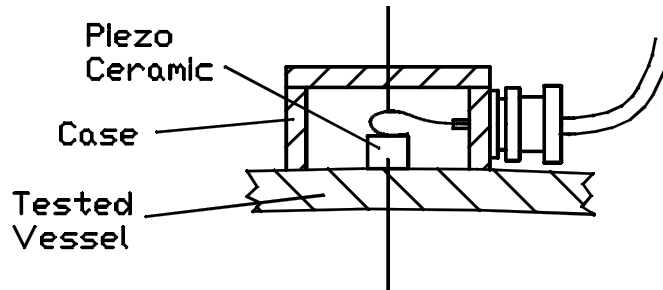


Fig. 1. Directly glued piezo-ceramics.

Table 1: Tested configuration with directly glued piezo-ceramics

Abbreviation	Form of piezo-ceramic	Dimensions
CD54-dir	Circular disc	D5 x 4 mm

2.3 Simple self made sensor

To determine the influence of some layers between the piezo-ceramic and the tested plate, a simple sensor based on the same piezo-ceramics as above was built. The whole arrangement was the same as above, only the piezo-ceramic was glued to the sensor case instead of gluing it directly to the tested plate (Fig. 2). This case is called CD54-sen because the same piezo-ceramic as in the configuration CD54-dir was used. When the sensor is glued to the vessel a “-gl” and when it is coupled by silicon grease a “-sil” is added to the name of the sensor to describe the arrangement (CD54-sen-gl, CD54-sen-sil).

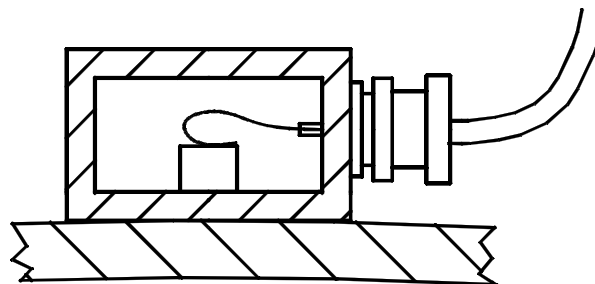


Fig. 2. Simple self-made sensor.

3. Test Procedures

All the tests were performed on an old vessel with an outside diameter of about 600 mm and a wall thickness of 5 mm. There were cut-outs in the vessel, so that pencil lead breaks could be performed in in-plane direction at the edge of the shell. The arrangement of the different sensors is shown in Fig. 3.

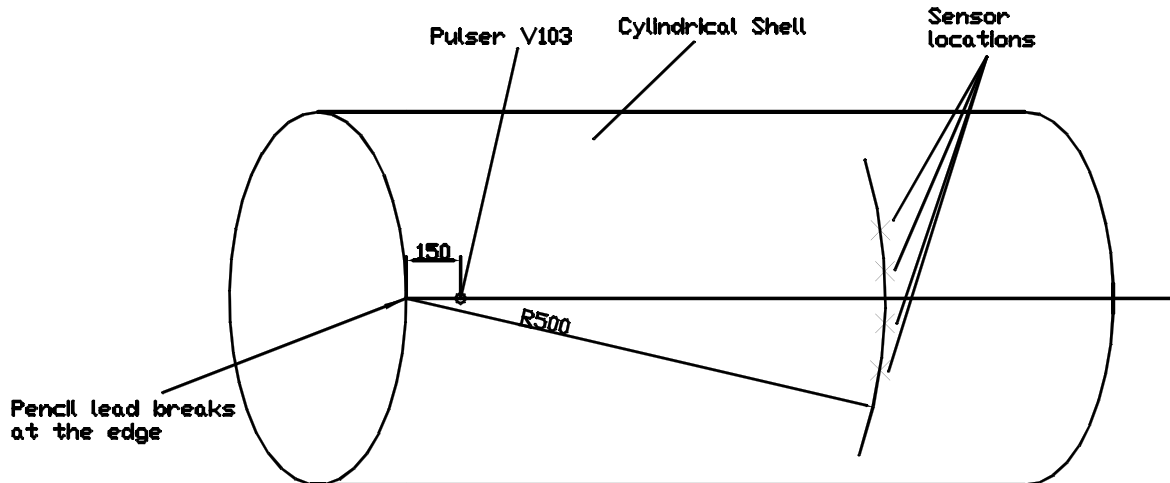


Fig. 3. Sensor arrangement for the different tests (drawing of shell simplified).

3.1 Sensitivity tests with narrow band pulses

For this test, narrow-band pulses were generated using a reference pulser (PANAMETRICS V103 ultrasonic transducer). The narrow-band electrical pulse has the modulated sine waveform (Fig. 4) with 10 oscillations and maximum peak-to-peak amplitude of 2 V. The centre frequency of the pulse was changed from 100 kHz to 1 MHz in steps of 10 kHz.

The maximum amplitude of the signal received at the tested sensor was plotted against the centre frequency of the electrical pulse (Fig. 5). When a pulser is coupled to the surface, like here, only a very small in-plane wave component is generated. Therefore, the results of this test are dominated by the sensitivity of the tested sensor to the out-of-pane wave.

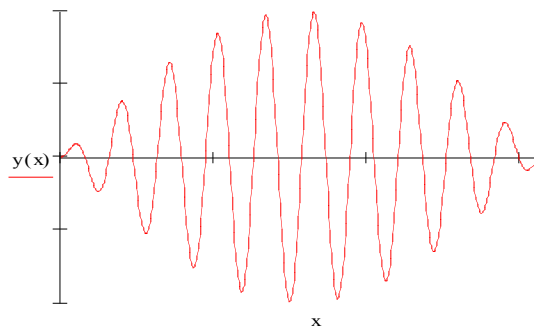


Fig. 4. Narrow band electrical pulse for input to V103 (voltage vs. time).

Due to the coupling with silicon grease to the vessel surface, which was not perfectly plane, the response of the VS150 is worse than when it is coupled to a perfectly flat surface. The sensitivity of all the arrangements with the circular disc CD54 is relatively high, but it should not be directly compared to the commercial sensor VS150, which is much better with respect to other properties.

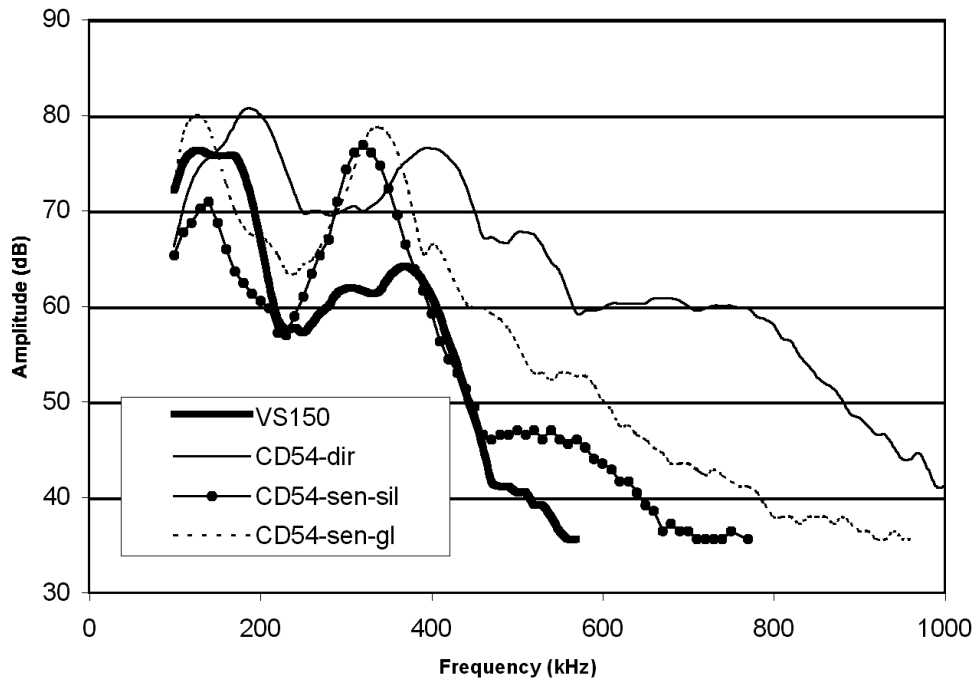


Fig. 5. Results of the tests.

When the data for the directly glued piezo-ceramic (CD54-dir) is compared to that of CD54 sensor, glued to the vessel and using the same piezo-ceramic (CD54-sen-gl), the peak sensitivities at the resonance frequencies are almost identical. Between the two resonance frequencies and in the high frequency range the directly glued piezo-ceramic is more sensitive than the CD54 sensor. When silicon grease is used for coupling the sensor (CD54-sen-sil), the sensitivity at high frequencies further decreased and also the sensitivity at the first resonance frequency decreased.

3.2 Ratio of the sensitivity to in-plane waves to the sensitivity to out-of-plane waves

To determine the sensitivity of the tested sensors to in-plane waves, pencil-lead breaks were performed at the edge of the shell (Fig. 3). To generate in-plane as well as out-of-plane waves the pencil-lead breaks were performed one quarter of the wall thickness from the surface. At the selected sensor locations, which are about 500 mm from the source of the pencil-lead breaks the in-plane wave can be easily distinguished from the out-of-plane wave and the amplitudes of the generated signals due to both waves can be evaluated.

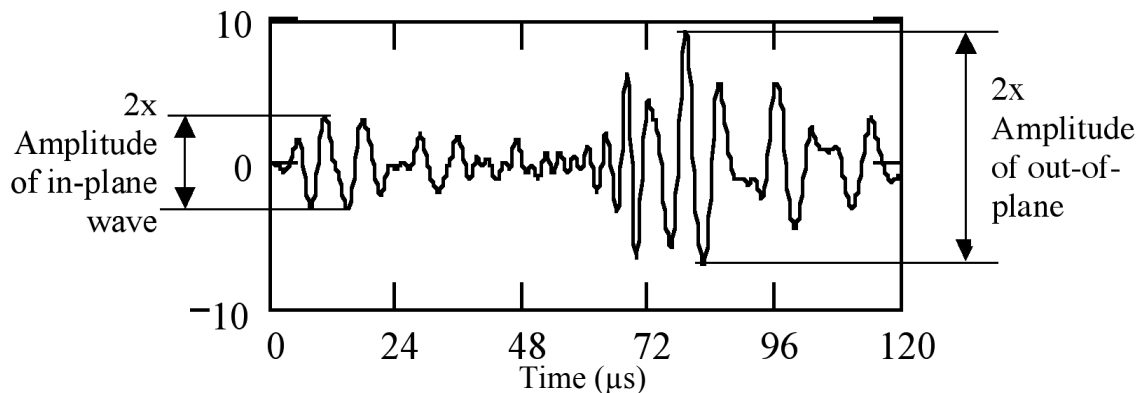


Fig. 6. Evaluation of the amplitude of the in-plane and out-of-plane waves.

Table 2: Sensitivity to in-plane and out-of-plane waves (pencil-lead breaks).

Sensor and Configuration	Number of pencil-lead breaks	Min/average/max amplitude of in-plane wave [mV]	Min/average/max amplitude of out of plane wave [mV]	Min/average/max ratio of amplitude: in-plane to out-of-plane waves
VS150	5	2.8/3.16/3.5	6/7.3/9	0.33/0.44/0.47
CD54-dir	5	14/15.6/17	18/23.6/27	0.56/0.67/0.83
CD54-sen-sil	5	3.5/3.6/4	6/9/12	0.29/0.42/0.58
CD54-sen-gl	5	8/9/10	8/9.2/10	0.8/1.0/1.25

Considering the arrangements with the CD54 ceramic, the following conclusions can be drawn: The best sensitivity is reached with the directly glued piezo-ceramic (CD54-dir). Using a simple sensor based on this ceramic and gluing it to the surface (CD54-sen-gl) decreases the sensitivity, but the ratio of the sensitivity to the in-plane wave to that to the out-of-plane wave improved. When the same sensor is coupled by silicon grease (CD54-sen-sil) the sensitivity as well as the amplitude ratio decreased.

3.3 Noise tests

To achieve comparable numbers for the sensitivity to noise, especially to electrical noise is not simple. Here, two tests were used: At first the RMS-level of the sensors was recorded. Because always a VS150 was used at the same time and it had an almost constant RMS level, these values can be compared. To check for the sensitivity to electrical noise, electrical pulses with amplitude of 10 V in the same form as used for pulsing a V103 in Sec. 3.1 were applied to the vessel. A galvanic isolated waveform generator was used, with the plus pole connected to the tested vessel and the minus pole was not connected at all. The vessel itself was connected to the ground of the AE measurement equipment.

Table 3: Results of noise tests.

Configuration	RMS-Level μV	Electrical noise test
VS150	0.3	Hits up to 37dB from 800kHz to 1 MHz, from 100kHz to 800kHz no hits above 35 dB
CD54-dir	1.5	Hits of 45 dB at 150kHz, increasing amplitude with frequency and 57dB max. at 850kHz
CD54-sen-sil	1.1	Similar to VS150
CD54-sen-gl	1.1	Similar to VS150

Table 3 shows that the RMS noise of the self-made sensor is twice the RMS noise of the VS150 (+6dB). The arrangement using the directly glued piezo-ceramic is relatively sensitive to electrical noise. Using a closed sensor case improves this. If the ground connection of the vessel is removed, the sensitivity evaluated in the electrical noise test of all the arrangements increased, but, in this case, VS150, which is isolated from the vessel, performs much better than the rest.

This noise tests are very sensitive to small changes in the configuration (small gaps in the cases, etc.) so that the results can only give some hints on what is going on.

4. Conclusions

Direct gluing of piezo-ceramics to a test specimen improves the overall sensitivity, especially the sensitivity to the in-plane wave. The disadvantage of this arrangement is, beside the relatively

complicated application procedure, the high sensitivity to electrical noise. A considerable improvement to the sensitivity to the in-plane waves can also be reached, when the sensor is glued to the vessels surface instead of liquid coupling. In most cases, direct gluing of a sensor to the test vessel seems to be the better alternative, but sensors need to be robust so that they could be removed after gluing them to the vessel. All the tests described here were performed with simple arrangements. Thus, modification of the procedures, especially the sensor case design, likely improves the results.

References

- [1] Bayray, M., "Crack growth investigations in pressure vessels using acoustic emission technique," Ph.D. dissertation, Vienna University of Technology, April 2002.
- [2] Bayray, M., "Investigation of AE waveforms in a pressure vessel," *Journal of Acoustic Emission*, **19**, 246-257, 2001.
- [3] Gorman, M. R., "Plate wave acoustic emission," *Journal of Acoustical Society of America*, **90**(1), 358-364, 1991.
- [4] Dunegan, H. L., "Modal analysis of acoustic emission signals," *Journal of Acoustic Emission*, **15**, 53-61, 1997.
- [5] Huang, M., "Application of Mindilin plate theory to analysis of acoustic emission waveforms in finite plates," *Review of Progress in Quantitative Non-destructive Evaluation*, **107**, 493-500, 1998.
- [6] Bayray, M. and Rauscher, F.: "Window Fourier Transform and Wavelet Transform in Acoustic Emission Signal Analysis", *Proc. EWGAE 2002 25th European Conference and Exhibition*, 11-13 September 2002 – Prague. pp. I/37-I/44.

AE MONITORING OF CRYOGENIC PROPELLANT TANK

YOSHIHIRO MIZUTANI¹, TAKAYUKI SHIMODA¹, JIANMEI HE¹,
YOSHIKI MORINO¹ and SOUICHI MIZUTANI²

¹ National Space Development Agency of Japan, Sengen, Tsukuba, Ibaraki 305-8505, Japan

² Advanced Engineering Services Co., Ltd., Takezono, Tsukuba, Ibaraki 305-0032, Japan

Abstract

In order to study the cryogenic properties of CFRP tank, we conducted pressurization test of a small filament-wound (FW) tank at cryogenic temperatures. We first investigated the orientation dependence of acoustic emission (AE) signals at both room temperature and LN₂ temperature by using artificial source. Lamb-mode dispersive AE signals were monitored in the CFRP tank. In tests at room temperature, we used A₀-mode Lamb waves for source location. However A₀-mode Lamb waves at several angles were hardly observed at LN₂ temperature. In this study S₀-mode were used for source location. 60% of tank wall was damaged before this test, and many AE signals are generated from this damaged zone. We developed a new method to separate AE signals generated at damaged zone utilizing signal duration. When the AEs from monitoring (or non-damaged) zone are evaluated, detail source location is possible using arrival time differences of AEs. Next we conducted pressurization test of the CFRP tank at LN₂ temperature. About 660 AE events were visually extracted from detected 2800 AE hits. We then investigated the duration of AE events and 100 AE events are evaluated as AE generated at non-damaged zone. Source locations of 7 AE events are obtained from the area where leakage was identified by snoop test conducted after the pressurization test.

Keywords: CFRP tank, Lamb wave, cryogenic pressure test, source location

Introduction

It is essential to develop a cryogenic CFRP tank in order to realize the drastic weight reduction needed for reusable launch vehicle (RLV) [1]. In order to study the cryogenic properties of such CFRP tanks, we conducted pressurization test of a small filament-wound (FW) tank [2] and monitored micro-cracks, which possibly grow to provide leak path of the propellant. We used acoustic emission technique for micro-crack monitoring. Several studies regarding AE monitoring of FRP tank were reported [3 - 6], but the study under cryogenic temperature is limited. We conducted 4-channel AE monitoring during cryogenic pressurization test of a CFRP tank. We first compared characteristics of AE signals detected at room temperature and LN₂ temperature by using artificial AE source. After that, we constructed source location method, which utilizes the signal duration and arrival time difference of AE signals. The proposed source location method is applied to the AEs detected during a cryogenic pressurization test of the CFRP tank. Estimated source location is compared to the leak point, which was found by snoop test conducted after the pressurization test.

CFRP Tank and Experimental Setup

A 300-mm-diameter CFRP tank was fabricated using filament-winding method. The prepreg tape was BESFIGHT IM600#133 with 3.5-mm width. The tank shape was 320-mm long cylin-

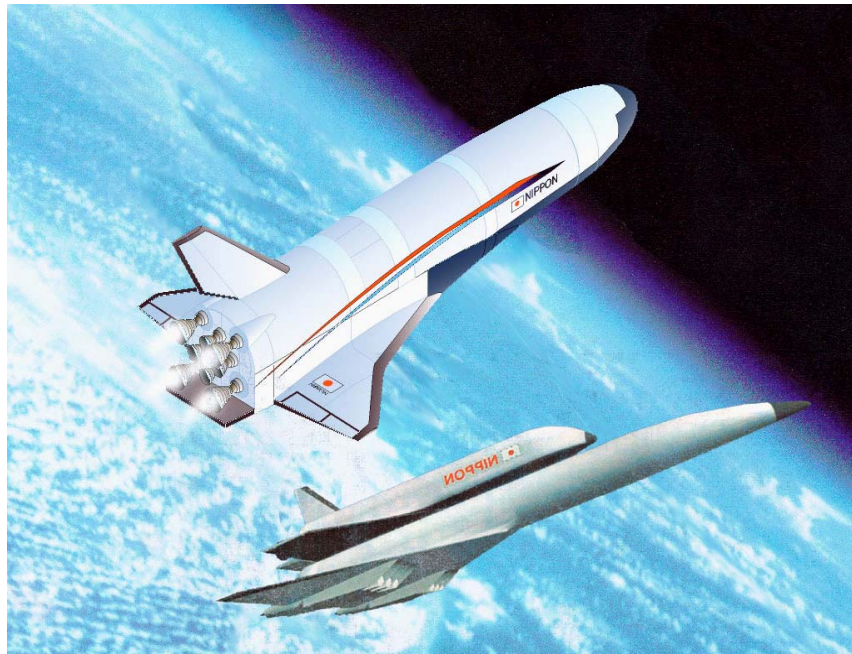


Fig. 1. Typical RLV concepts. Drastic weight reduction is needed for realization.

der with isotensoid dome at both sides (see Fig. 2). The tape was wound on a plaster mandrel and cured in autoclave at 180°C for 2 hours. The layer construction of the cylindrical part is $[\pm 30^\circ, 90^\circ_2, \pm 30^\circ, 90^\circ_2, \pm 30^\circ]$. The thickness of the cylinder is 1.2 mm.

We conducted water-proof testing and cryogenic low-level pressurization tests on this tank in the past two years. After these tests, some areas were damaged and we patched additional prepreg sheets on these areas from the inner side of the tank wall. Epoxy resin adhesive (HYSOL EA9394) was also pasted on the serious damage zone on the outside surface to prevent leakages. The photo images of damaged and non-damaged zones are shown in Fig. 2. In this study, we investigated cryogenic characteristics of the non-damaged zone. We call non-damaged zone as “monitoring zone” in this paper.

Figure 3 shows the schematic illustration of the CFRP tank used and experimental setup for cryogenic pressurization. Nickel-steel flanges are attached to both sides of the tank. Five pipes are connected to the top flange. Three of the five pipes are connected to pressure gauge, liquid level meter and safety valve. The other two pipes are used for filling and exhausting liquid nitrogen. These two pipes are also utilized for controlling the internal pressure during pressurization tests.

Liquid level meter output was connected to the monitor. The meter roughly indicates the liquid nitrogen level. The pressure gauge was connected to a digitizer and the data was digitized at 1-Hz sampling rate. Digitized data was fed to the computer. Strain and temperature of the outer surface were also measured, but we will not discuss these data here.

We used four 150-kHz resonant-type AE sensors (PAC, R15) in the test. These sensors were mounted on the corners of a 200-mm square on CFRP tank as shown in Fig. 3. Outputs of the sensors were amplified 40 dB and digitized at an interval of 250 ns with 4096 points at 16-bit amplitude resolution, and fed to a PC for analysis. We set the threshold level at 65 dB (1.78 mV at sensor output) during the pressurization test.

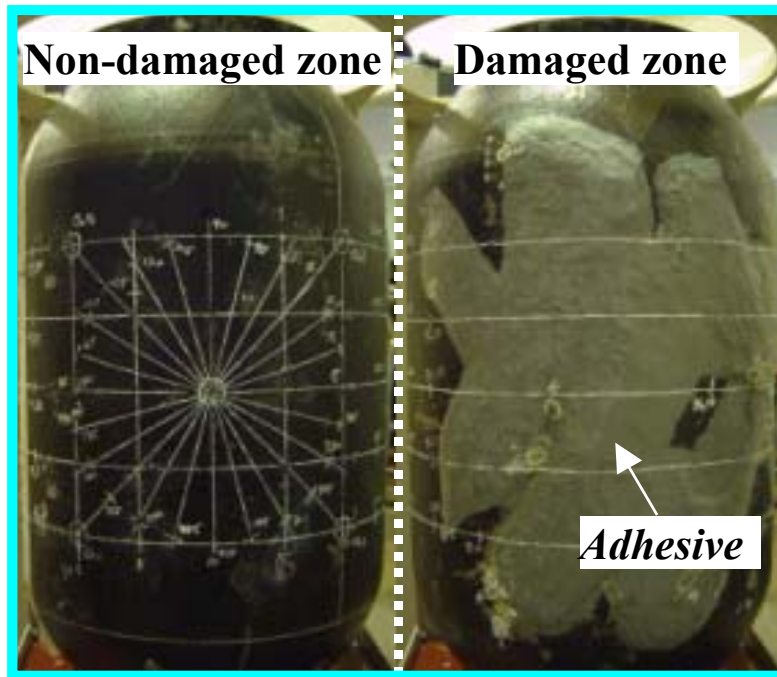


Fig. 2. Appearances of the non-damaged and damaged zones. Epoxy resin was pasted on the damaged zone. In this study, we evaluated non-damaged (monitoring) zone only.

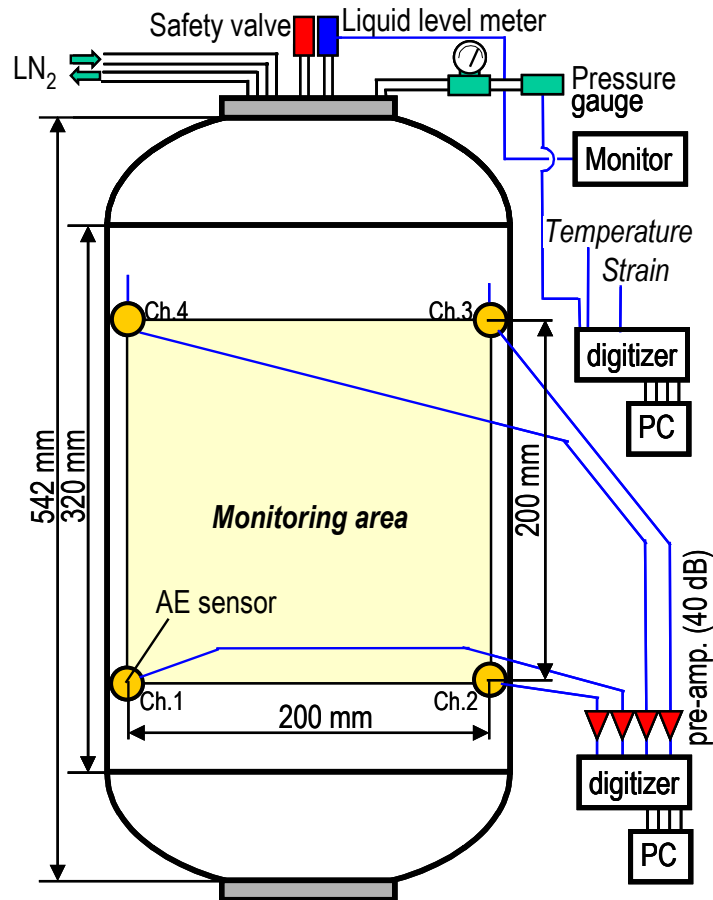


Fig. 3. Schematic illustration of the CFRP tank and experimental setup. 4-channel AE monitoring used 40-dB preamplifiers and Mistras system (PAC).

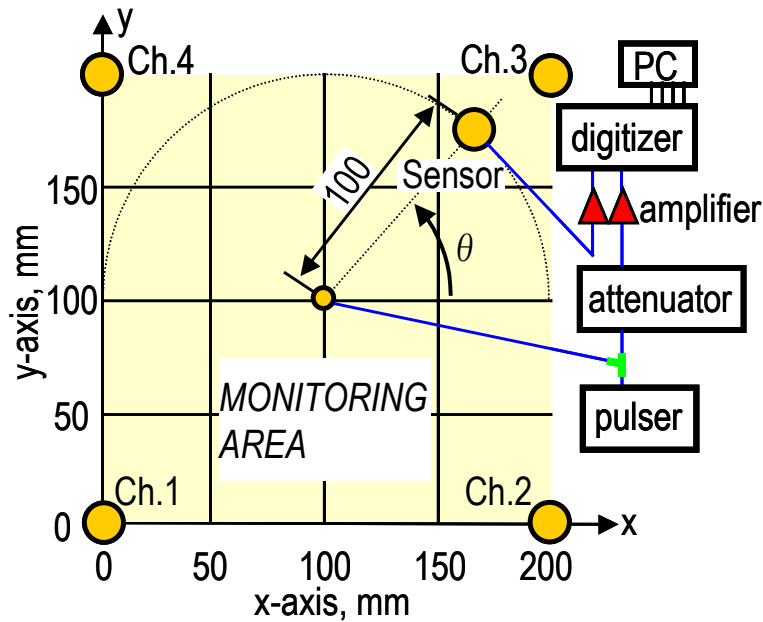


Fig. 4. Experimental setup for measuring orientation dependence of AEs on the shell wall of cylindrical section (see Fig. 2). Artificial sources generated by small transducer were used.

Procedure for AE Monitoring

We first measured the orientation dependence of AE signals propagating in CFRP tank at both room temperature and LN₂ temperature. We filled water or LN₂ into the tank at atmospheric pressure. As shown in Fig. 4, pulses were generated by a compression-type piezoelectric transducer (PAC, PICO, 4-mm diameter, nominal resonant frequency 0.45 MHz) and detected by an R15 AE sensor mounted on circles of 100-mm radius at angle θ . Examples of detected AEs are shown in Fig. 5. Left figure represents AEs at room temperature and right at LN₂ temperature. Small amplitude S₀-mode Lamb waves followed by large amplitude A₀-mode are observed at room temperature, but A₀-mode Lamb waves are hardly observed for several direction ($\theta = 150^\circ, 180^\circ$ in Fig.5) at LN₂ temperature. In a previous paper, Mizutani et al. [4] used wavelet coefficients of a specific frequency of A₀-Lamb waves for source location in room temperature tests, but this method cannot be applied to the cryogenic tests. Though some difficulties were expected (large source location error due to fast velocity of AEs, arrival time reading error due to small S/N ratio, etc.), we decided to use the arrival times of initial S₀-mode Lamb AEs in this study. The orientation dependence of the S₀-mode velocity was determined by dividing the inter-transducer distance (100 mm) by the first-peak arrival time. Measured orientation dependence is shown in Fig. 6. We fitted data by a quadratic equation, $V(\theta) = 7.97 \times 10^{-2}\theta^2 - 1.49 \times 10 \theta + 6.40 \times 10^3$ (m/s), shown by a solid line in Fig. 6 and used this function for the source location.

Next, we examined the accuracy of the source location method by using two types of artificial sources. Figure 7 shows top view and development of the tank. Monitoring area surrounded by 4 sensors is shown in tan color. About 60 % of the tank wall was patched by additional CFRP prepreg sheets from inside. The area which epoxy resin adhesive (HYSOL EA9394) was pasted from the outer surface is also indicated in the figure (shown in green color). We artificially generated AEs by pencil-lead breaks and a PICO sensor in the monitoring zone and damaged zone. Source location is shown by the symbol “X” in the figure.

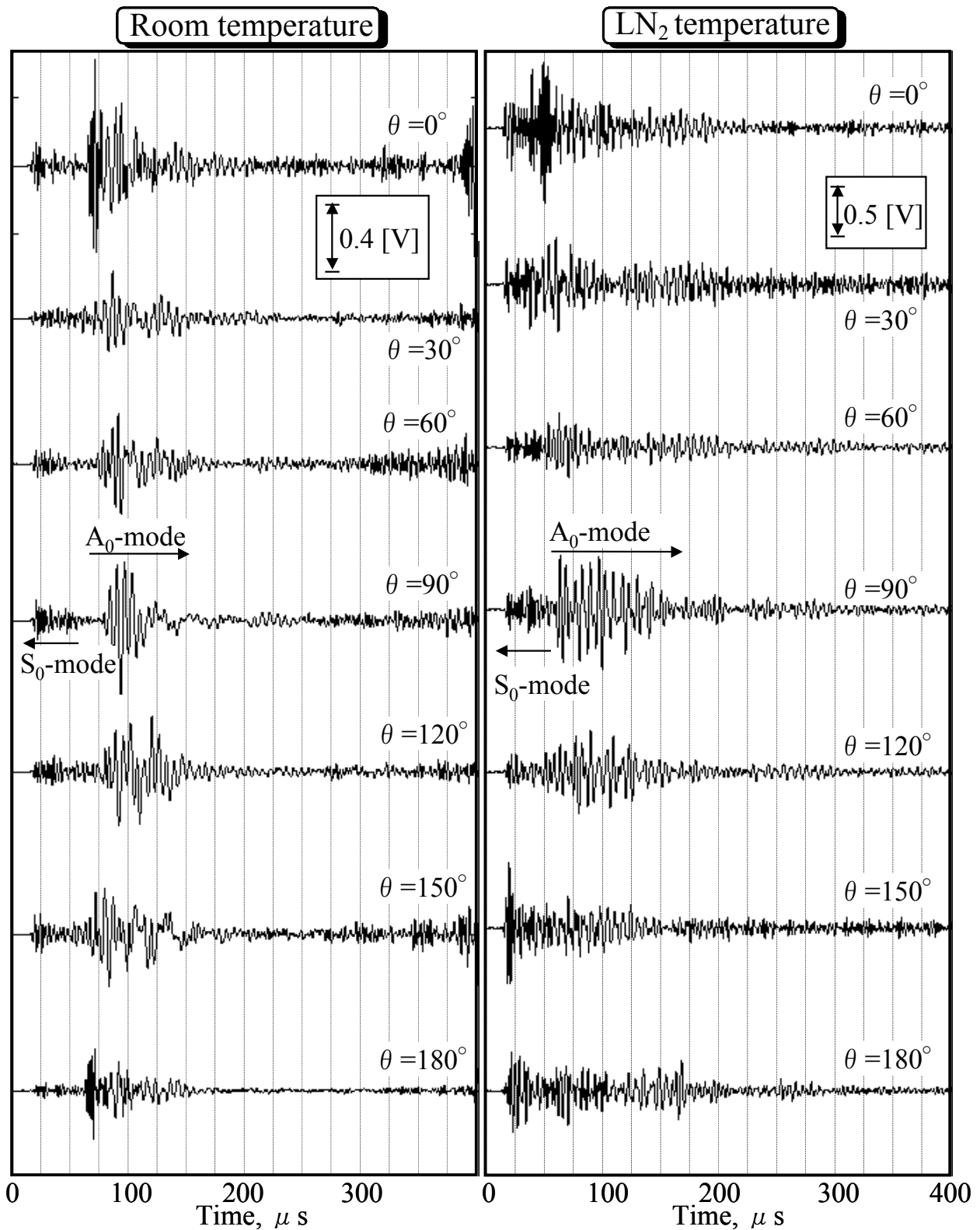


Fig. 5 Examples of Lamb wave AEs detected at room temperature (left) and LN₂ temperature (right) as a function of the propagation direction θ . A₀-mode Lamb waves are hardly observed in some directions at LN₂ temperature.

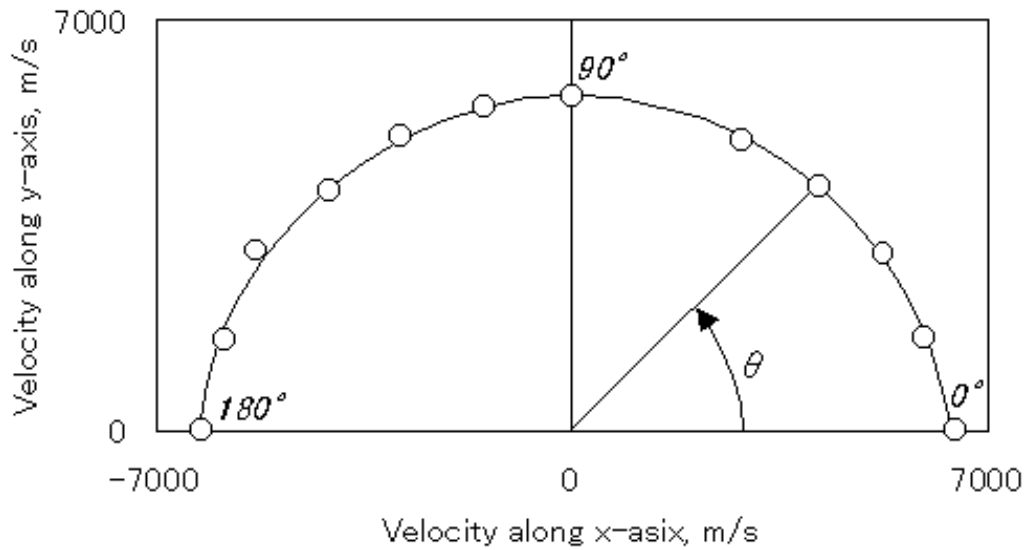


Fig. 6 Orientation dependence of S_0 -Lamb velocities in the tank. Solid line indicates fitted curve used for the source location.

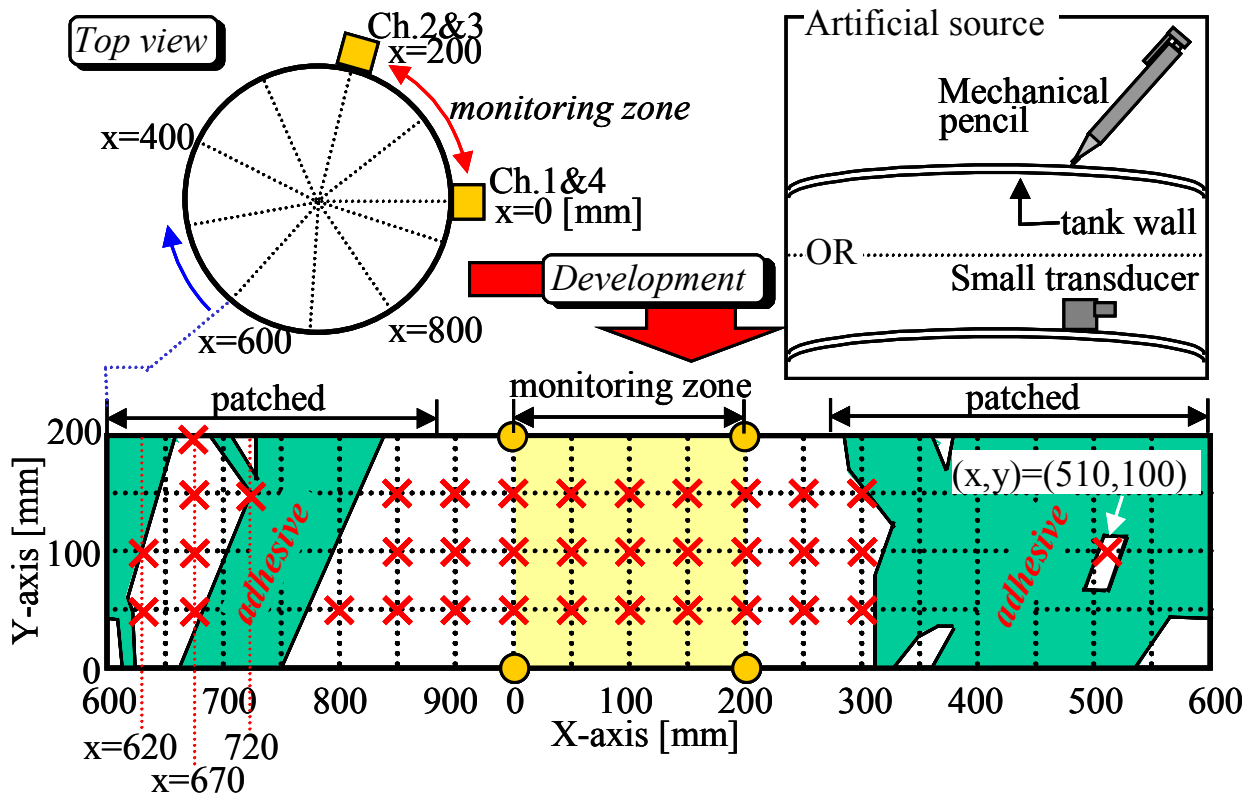


Fig. 7 Top view and development of the tank with AE sensor locations. The monitoring zone is shown in the figure by tan color. Source locations are indicated by symbol “X”. Two types of artificial sources are shown in top right.

Figure 8 shows detected AE signals induced at $(x,y) = (50,50)$ and $(620,100)$ by a sensor (left) and pencil-lead breaks (right). It is noted that arrival-time differences of AEs induced at damaged zone $(620,100)$ is at the same level as AEs induced at the monitoring zone $(50, 50)$.

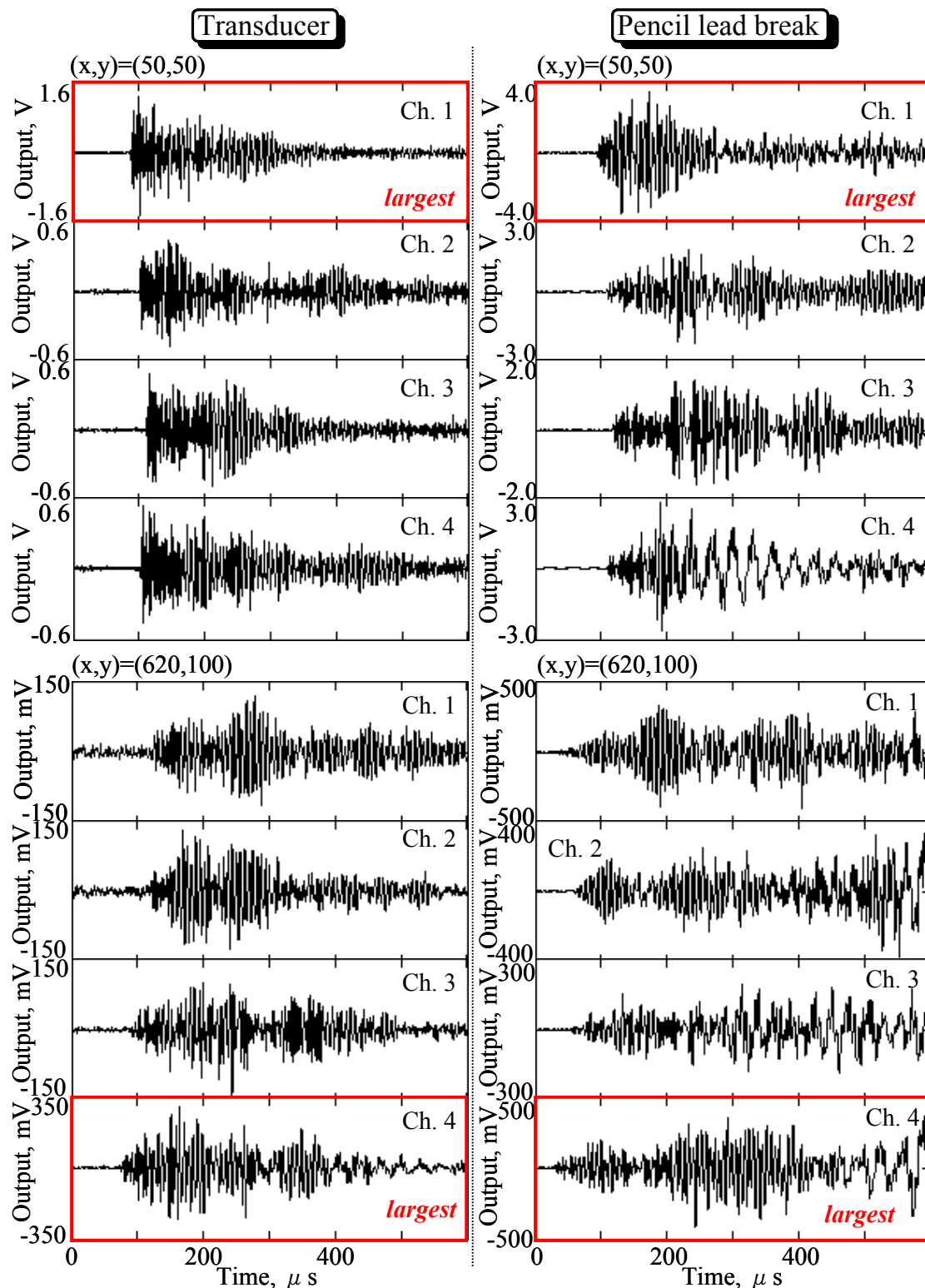


Fig. 8 Detected AEs induced at the monitoring zone $(x,y)=(50,50)$ and damaged zone $(620, 100)$ due to artificial source. Two types of artificial sources were used.

Therefore, we have to separate AEs generated at the damaged zone before the source location is conducted. Duration of the largest amplitude AEs for all events are investigated. The result is shown in Tables 1 and 2. Definition of duration is shown in Fig. 9. We defined the threshold as

50 % of the maximum value. Duration of AEs generated far from the monitoring zone is much longer than those for AEs from the monitoring zone. It is also noted that the duration of AEs generated by the PICO sensor (possibly generated high frequency AEs) and by pencil-lead breaks (generated low frequency AEs) is similar. This is due to the narrow-band AE sensor working as a band-pass filter. We set the threshold duration as 200 μs and try to separate AEs from the damaged zone. The result is shown in Table 1 and 2. Colored areas in the tables indicate the long duration AE. This clearly shows that AEs generated far from the monitoring area can be separated by utilizing duration.

Table 1 Duration of AEs produced by transducer Unit: μs

	0	50	100	150	200	250	300	510	620	670	720	800	850	900
50	18	101.25	45.25	110	102.25	102.5	117.75		966.75	896		314	93.75	73.25
100	109	118.5	105.25	106.75	76	151.5	62.5	1004	258	914			117.5	16.5
150	66.5	105.5	52.5	39.75	128.25	60	101.5			237.75	482.75		90.75	101
200										227.75				

Table 2 Duration of AEs produced by pencil-lead break Unit: μs

	0	50	100	150	200	250	300	510	620	670	720	800	850	900
50	31.5	91	49	54	147.25	47.75	97.25		790	837.75		238	57.75	84.25
100	65.5	161.75	52.5	106.5	1.25	93.75	189.75	641	850.5	520			93.75	149.25
150	115.25	51.75	25.75	104	113	73.5	201.25			571.25	609.25		94.5	111.25
200										339.75				

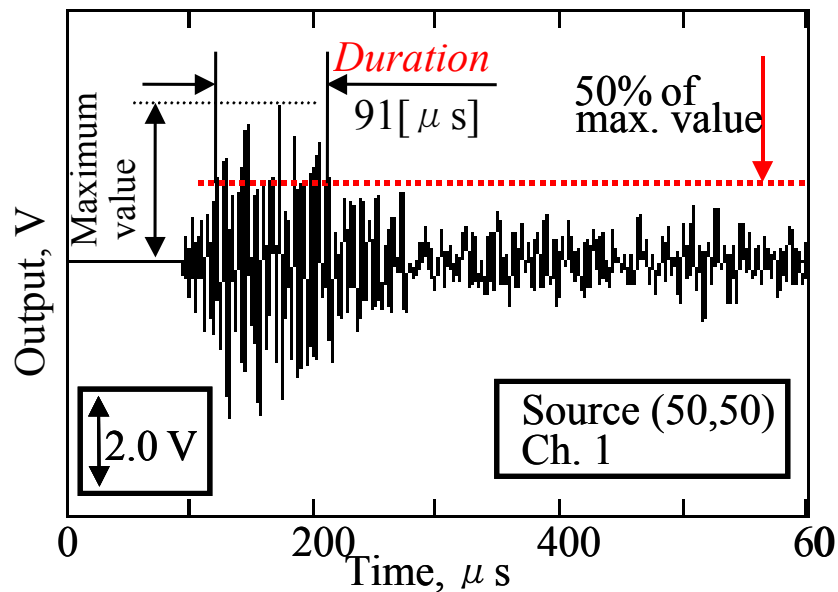


Fig. 9. Procedure for determining AE signal duration.

When detected AE is determined as AE from the monitoring zone, detail source location is conducted by the following steps; 1) Monitoring area is divided into 4 areas as shown in Fig. 10. 2) The channel that detected the largest AE is searched. The area that involves the maximum channel is selected. 3) One size larger area is defined as a scanning area of virtual source. (shown by dark rectangular in Fig. 9.) 4) Determine the arrival times of detected AEs (S_0 -mode arrival time). 5) Determine the source location by minimizing the differences of the measured arrival times and the arrival time differences computed by moving a virtual source position in the scanning area in 1.0-mm step. Orientation dependence of the S_0 -mode velocities (Fig. 6) is incorporated.

Detailed results of source location are shown in Fig. 11 for transducer (left) and pencil-lead break (right). A square indicates an original position and a circle the located source position. The source locations agree well with the input positions. The maximum error of 12.1 mm and average error of 6.2 mm were obtained for the transducer sources. For the pencil-lead break sources, the maximum error of 18.0 mm and average error of 9.2 mm were obtained.

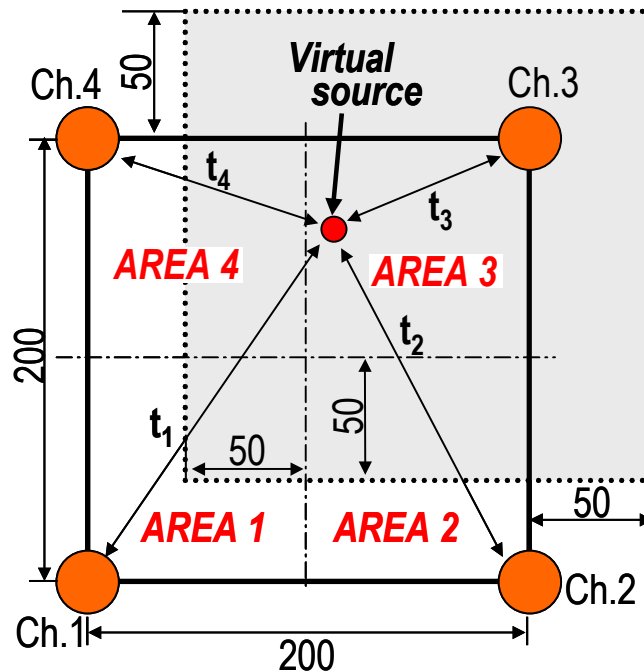


Fig. 10. Algorithm for source location. Virtual source is moved in 1-mm step. Arrival time is theoretically calculated by using the fitted curve shown in Fig. 6.

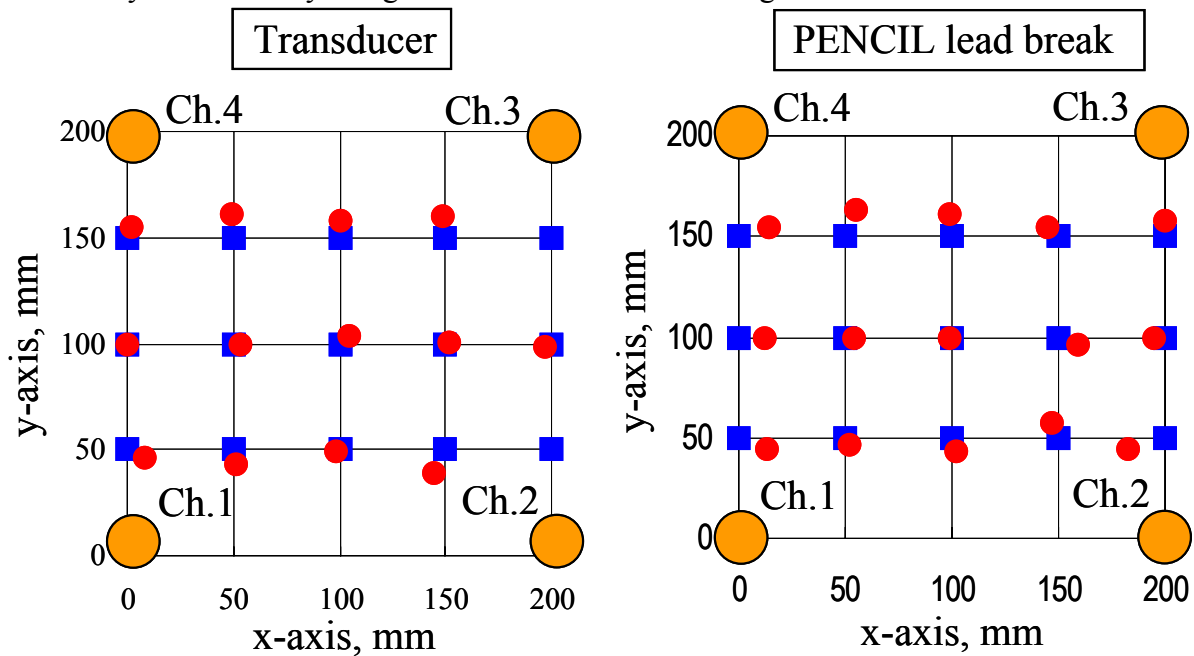


Fig. 11. Comparison of input location (■) and source location (●) of transducer (left) and pencil lead break (right) on the tank wall.

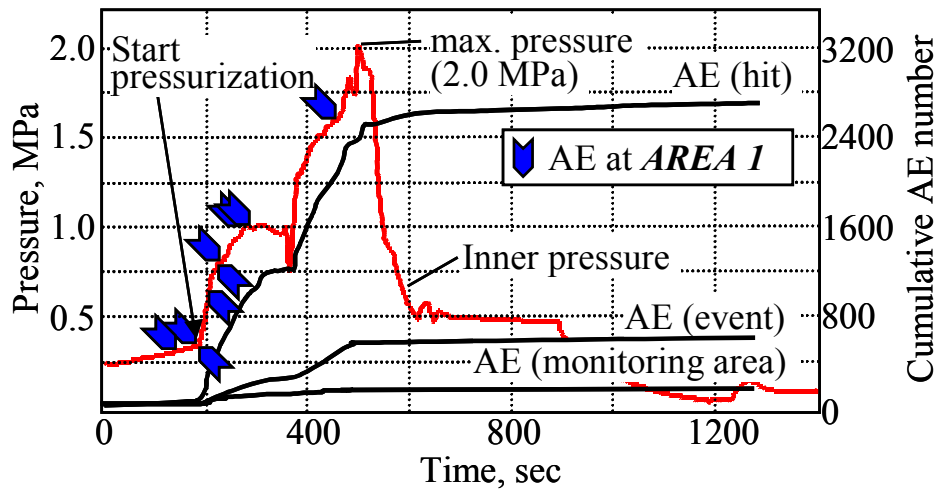


Fig. 12. The time history of an inner pressure and the cumulative AE counts. The timing of AE occurrence in area 1 is indicated by the blue arrow symbol.

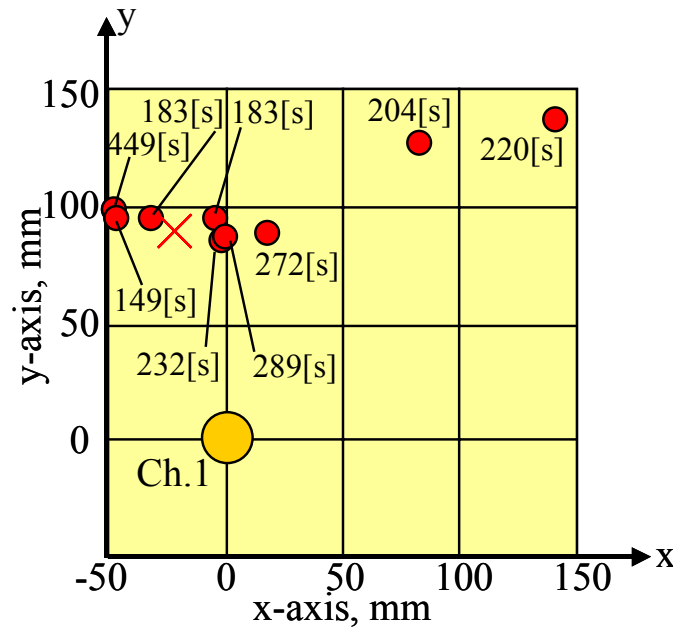


Fig. 13. Overlapping of source location result (indicated by symbol “●”) and leak point (“×”) at area 1.

Cryogenic Pressurization Test

The tank was filled with liquid nitrogen under atmospheric pressure. After the filling, we closed the valve and kept it for 5 minutes. The tank was chilled down to LN₂ temperature and boiling of LN₂ stopped. After that, we started AE monitoring and the tank was pressurized by gaseous N₂ to 2.0 MPa. Figure 12 shows the pressure history and AE counts. When the inner pressure reached 1.0 MPa, the pressure was held for 60 seconds. Pressurization was stopped at 2.0 MPa when a serious leakage from the damaged zone occurred. After the cryogenic pressurization test, we conducted snoop test by using soapsuds for identifying the leak points. Several leak points were observed in the damaged zone ($x = 300$ to 850 mm) and doom parts. Only one leak point was found near the monitoring area at $(x,y) = (-20,90)$ on a wrinkle. (shown by symbol “×” in Fig. 13).

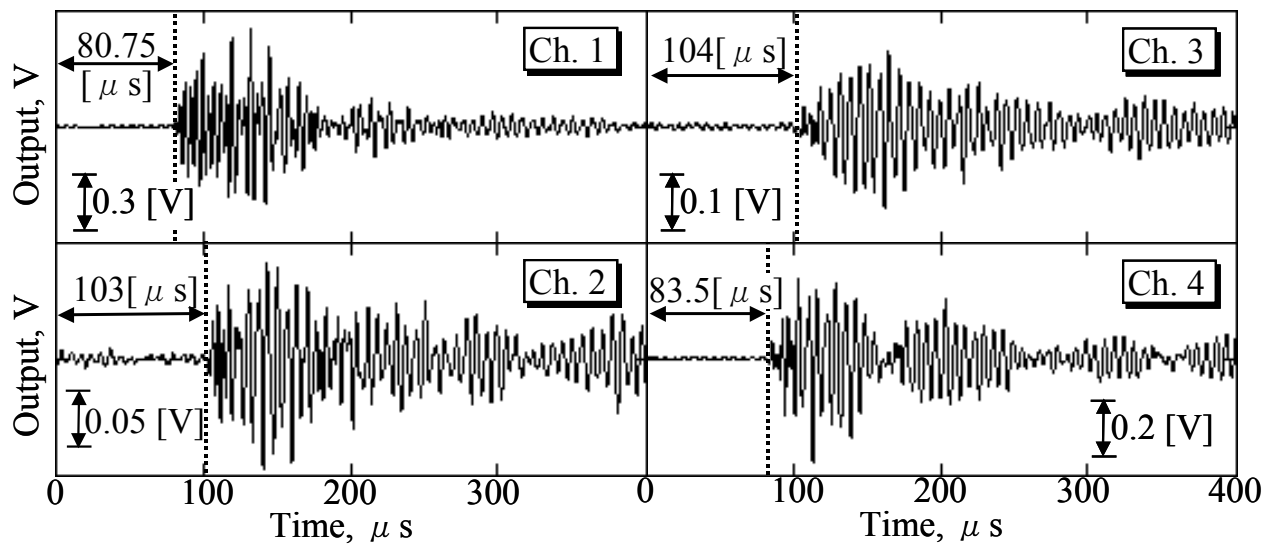


Fig. 14. Detected AEs located at area 1. Arrival time differences were used for detailed source location.

Each AE sensor detected about 2800 AEs. After the test, we visually extracted 663 AEs due to fracture (event), separating them from noise AEs and continuous AEs due to leakage. 123 AE are estimated to be the AEs generated within the monitoring zone by the zone location method explained previously. The time history of AE event and AEs in the monitoring zone are also shown in Fig. 12. An example of detected AEs from the monitoring zone is shown in Fig. 14. Detail source location is estimated for 9 AEs that were found to be in area 1. Source location results are shown in Fig. 13. Seven of the 9 AEs are located near the leak point. The timing of these 9 AEs are shown in Fig. 12 by arrows. It is noted that most AEs were generated at low pressure levels (<1.0 MPa) and this result shows that micro-cracks were produced at low stress levels under cryogenic condition at wrinkled parts.

Conclusion

AE monitoring was conducted during cryogenic pressurization test of a CFRP tank. Before the test, we investigated characteristics of AEs in the CFRP tank using artificial source and develop source location method. The results are summarized below.

- 1) A_0 -mode Lamb waves were hardly observed at several directions at LN_2 temperature and could not be used for source location.
- 2) Duration of AE signals produced at sources far from monitoring zone became longer. AE signals from non-monitoring zone can be separated by using signal duration.
- 3) Virtual source scanning method is used for source location. The source locations of transducer inputs were determined with the average error of 6.2 mm. Pencil-lead break sources were located within 9.2 mm on average.
- 4) 7 AE events monitored at low inner pressure levels are located near the leak point on the wrinkle on the tank. Micro-cracks were possibly produced at low stress levels at cryogenic temperature.

Acknowledgment

Professor K. Ono of UCLA gave valuable advice regarding this test and also kindly revised this paper.

References

1. Y. Morino et al., "Applicability of CFRP materials to the cryogenic propellant tank for reusable launch vehicle (RLV)," *Adv. Composite Mater.*, **10-4**, 339-347 (2001).
2. T. Shimoda et al., "Study of CFRP Application to Cryogenic Fuel Tank for RLV," *Proc. 23rd Intl. Symp. Space Tech. and Science*, ISTS 2002-c-13, (2002).
3. Y. Promboon and T.J. Fowler, "Source Location on Fiber Reinforced Composites", paper delivered at *6-th Int. Sym. on AE from Composite Materials* at San Antonio, Texas, (1998).
4. Y. Mizutani et al., "Damage Zonel Location in a GFRP Storage Tank by Lamb Wave AE Analysis," *J. of the Japanese Society for NDI*, **50-5**, 314-320 (2001). (in Japanese)
5. H. Yamada et al., "Lamb Wave Source Location of Impact on Anisotropic Plates," *Proc. EW-GAE 2000 European Working Group on Acoustic Emission*, CETIM, Senlis, France, (2000), pp. 77-83.
6. Y. Kwon et al., "Source Location in Plates by using wavelet transform of AE signals," *Progress in Acoustic Emission IX*, AEWG/AEG, Los Angeles, (1998), pp. IV9-IV17.

NON-DESTRUCTIVE TESTING FOR CORROSION MONITORING IN CHEMICAL PLANTS

M. WINKELMANS¹ and M. WEVERS²

¹ BASF Antwerpen N.V., Haven 725, B 2040 Antwerpen 4, Belgium

² Departement MTM, KU Leuven, B 3001 Heverlee, Belgium

Abstract

An appropriate and reliable tool for corrosion monitoring is necessary to guarantee the structural integrity of chemical production units. By combining the electrochemical noise measurements and the acoustic emission technique, the active corrosion processes are revealed. By combining acousto-ultrasonics and fibre optics a reliable quantification of the corrosion damage can be obtained. Electrochemical noise measurements, the acoustic emission technique, acousto-ultrasonics and fibre optics are very complementary non-destructive testing methods for monitoring the ongoing corrosion in chemical production units.

Keywords: Corrosion monitoring, electrochemical noise measurements, acoustic emission technique, acousto-ultrasonics, optical fibres

Introduction

Every day the chemical industry has to face new failures due to corrosion. In fact the major part of failures in the chemical industry are due to corrosion. In this way corrosion costs a lot to the chemical industry. Corroded parts of the production units have to be replaced and bring about production losses due to the shutdown of facilities. Corrosion failures also imply a considerable hazard to people and the environment. An appropriate and reliable tool for corrosion monitoring is necessary to guarantee the structural integrity of chemical production units.

Since 1999, BASF Antwerpen N.V. (Belgium) and the research group "Materials Performance and Non-Destructive Evaluation" of the Department of Metallurgy and Materials Engineering, K.U. Leuven (Belgium) are partners in developing a sensor to identify the active corrosion processes destructive to the equipment and to quantify the degree of corrosion damage in an industrial environment.

The research project is focused on the most important types of corrosion for the chemical industry. General corrosion of carbon steel, general corrosion of stainless steel, pitting of stainless steel, stress corrosion cracking of carbon steel and stress corrosion cracking of stainless steel are studied by four non-destructive testing methods. Electrochemical noise measurements, the acoustic emission (AE) technique, acousto-ultrasonics (AU) and fibre optics are the non-destructive testing methods used in this research project.

Experimental set up

Two completely different measurement principles are possible for a corrosion sensor. On the one hand a sensor can be developed so that it has to be fixed on the outside of the structure whose corrosion behaviour is of interest. The structure itself corrodes and the sensor reveals

information about this corrosion behaviour. On the other hand it is possible to develop a sensor, whose sensor body itself corrodes. Information can only be obtained about the corrosion behaviour of the sensor body itself. In this case the sensor has to be built in such a way that its corrosion behaviour is representative for the ongoing corrosion in the equipment of interest.

The decision has been made to develop a sensor, whose sensor body itself corrodes and reveals information about the ongoing corrosion. Figure 1 illustrates this principle. The four measurement techniques are incorporated on the same sensor body. The two passive non-destructive testing methods (electrochemical noise measurements, the AE technique) are activated during the whole life-cycle of the sensor body. The two active non-destructive testing methods (AU and fibre optics) are periodically activated. The periodicity is adapted as a function of the information revealed by the two passive non-destructive testing methods.

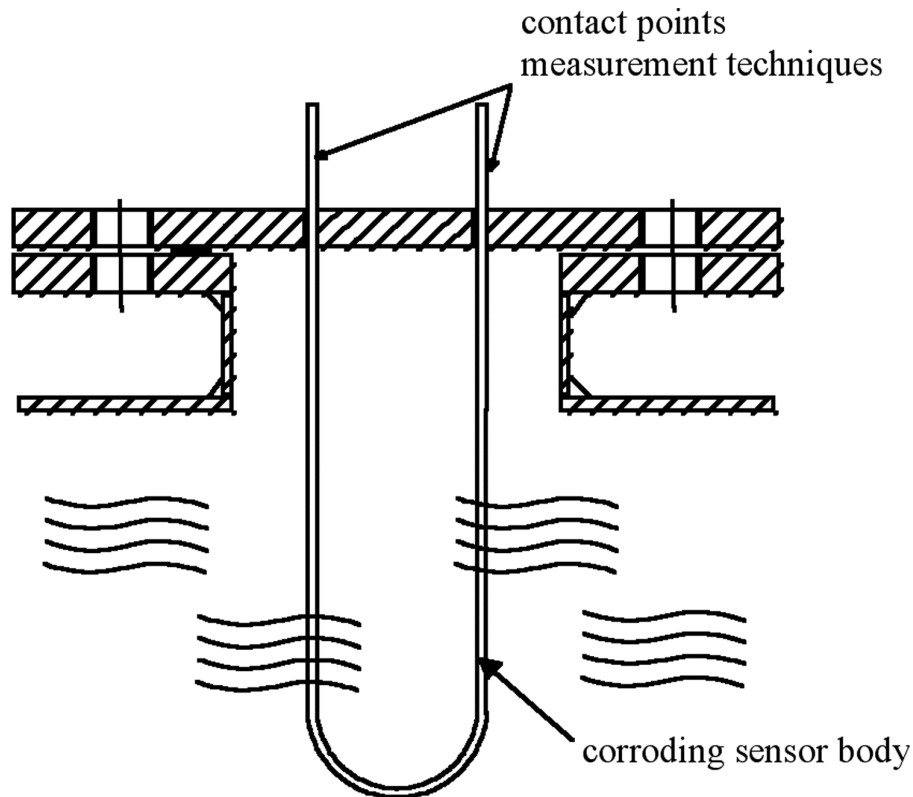
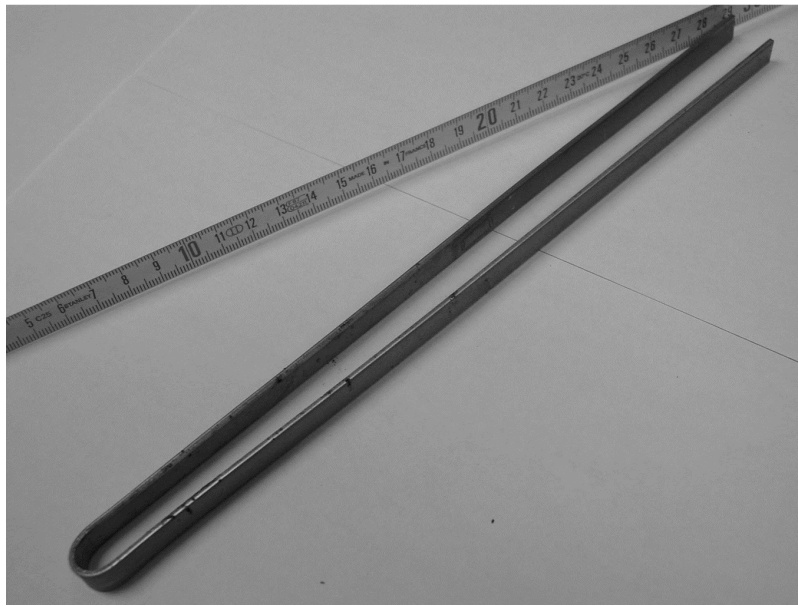


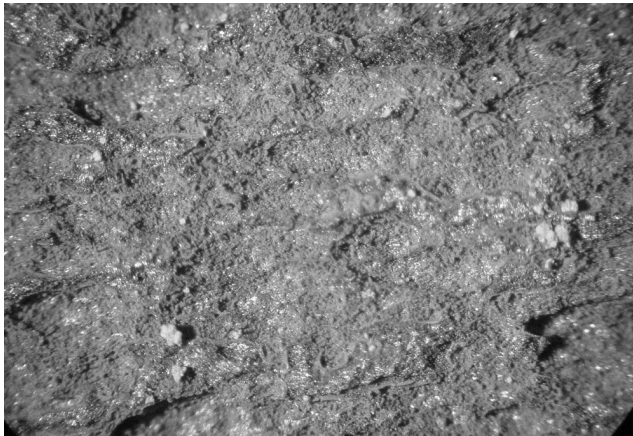
Fig. 1. Sensor principle

The basic research was done in the laboratory. The corroding sensor body was placed in a Faraday cage to prevent electromagnetic interference. Temperature and flow rate were controlled. The conversion to industrial environment has been done in two steps. First a mini-plant was built to study the influence of temperature fluctuations, fluctuations in flow rate and interference by other measurement equipment, pumps, heating systems, etc. Finally there were some experiments in a bypass of the chemical facilities themselves. Here the basic measurement concept was tested under the rough industrial conditions.

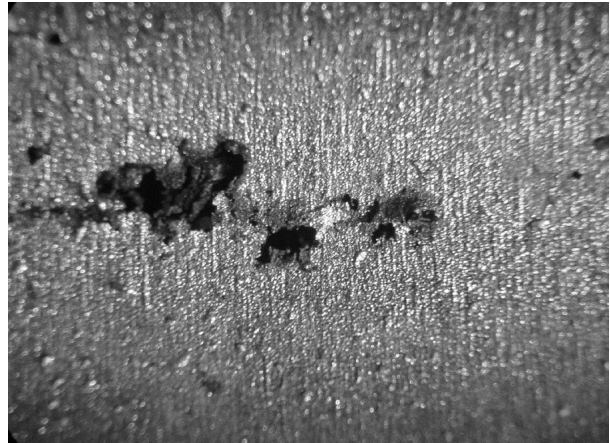
Carbon steel 1.0038 according to DIN EN 10025 and stainless steel 1.4541 according to DIN EN 10088 part 1 are used in the experiments. Figure 2 gives an overview of the sample geometry used for the experiments.



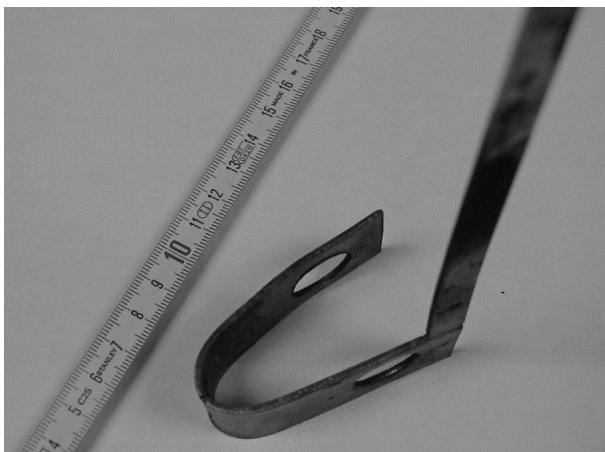
(a) Sample geometry for corrosion monitoring (general and pitting).



(b) General corrosion.



(c) Pitting corrosion.



(d) Sample geometry for SCC monitoring.



(e) Stress corrosion crack.

Fig. 2. Sample geometries used for the corrosion and SCC experiments.

Electrochemical Noise Measurements (EN)

Due to the oxidation and reduction reactions of the corrosion processes at the interface of metal and electrolyte, a potential difference arises across this interface. The short and long-term evolution of this potential reveals information about the active corrosion processes [1, 2].

A nanovoltmeter (Keithley 2182) with an input resistance $> 10 \text{ G}\Omega$ and a resolution of 100 nV is used for the potential noise measurements. The nanovoltmeter is connected to a computer by a GPIB-interface. The nanovoltmeter is controlled by the computer and the measured data are stored on the hard disk. The sample frequency is 10 Hz. The potential differences are measured between the sensor body and an Ag/AgCl reference electrode (Fig. 3).

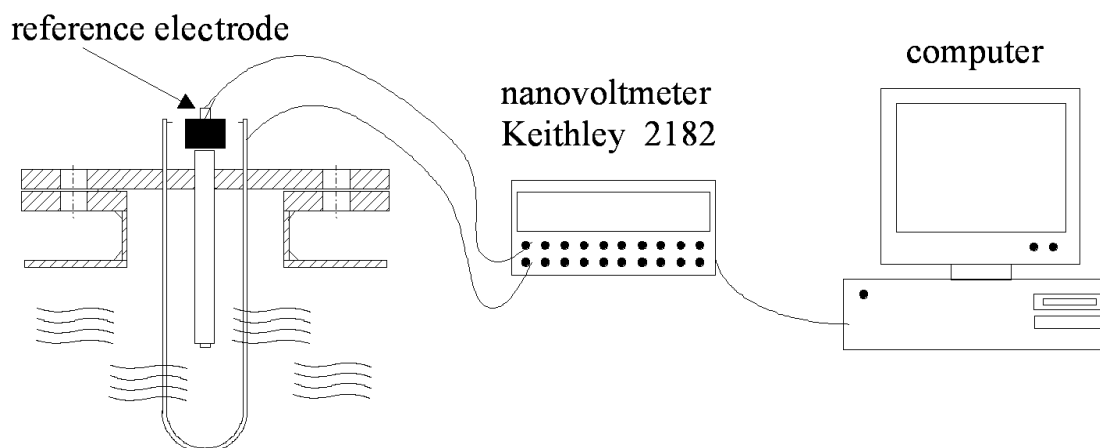


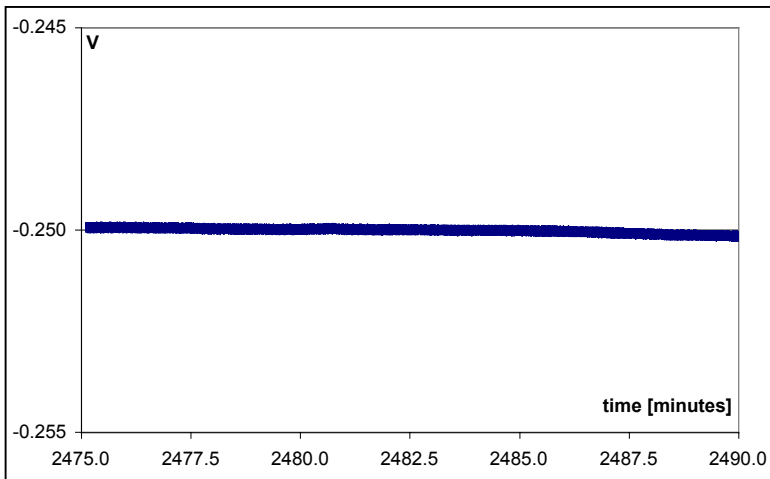
Fig. 3. Experimental set up electrochemical noise measurements.

Figure 4 shows typical EN signals. General corrosion of carbon steel, general corrosion of stainless steel, pitting of stainless steel and stress corrosion cracking of stainless steel can be distinguished by pattern recognition techniques in combination with statistical analysis in the time domain. Any information about pit growth during pitting and about crack growth during stress corrosion cracking cannot be obtained. Electrochemical noise measurements have a higher accuracy than more conventional non-destructive testing methods like dye penetrant, magnetic interference or ultrasonic testing.

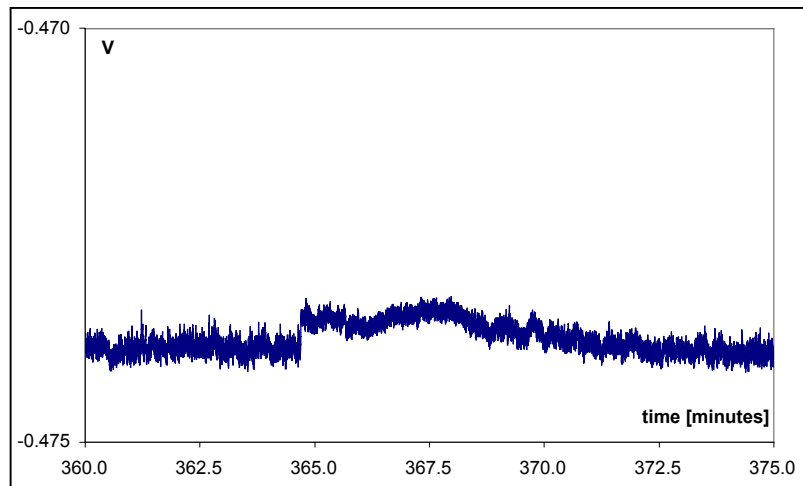
During the scaling-up of the experiments the potential noise measurements have been found to be very reliable. No additional difficulties arose. In fact no additional filtering of the measured data was necessary. Apparently the developed measurement concept for the potential noise measurements can be used in an industrial environment.

Acoustic Emission Technique

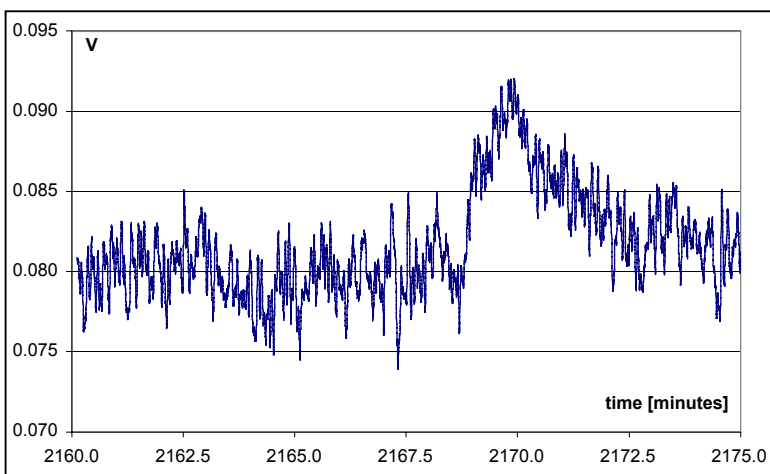
Corrosion processes cause microstructural changes at the metal/electrolyte interface. The energy released by these microstructural changes results in transient elastic waves. Sounds of higher frequency and lower intensity than audible sounds can be measured by the acoustic emission technique [3, 4]. The Fracture Wave Detector (Digital Wave Co., U.S.) is used for the experiments. Figure 5 shows the basic components of this system. The typical sample frequency for the experiments is 20 MHz. Broadband sensors (Digital Wave B1025) with a frequency range from 50 kHz to 2 MHz are used.



*no corrosion
stainless steel - CaCl₂ 40% - 85°C*

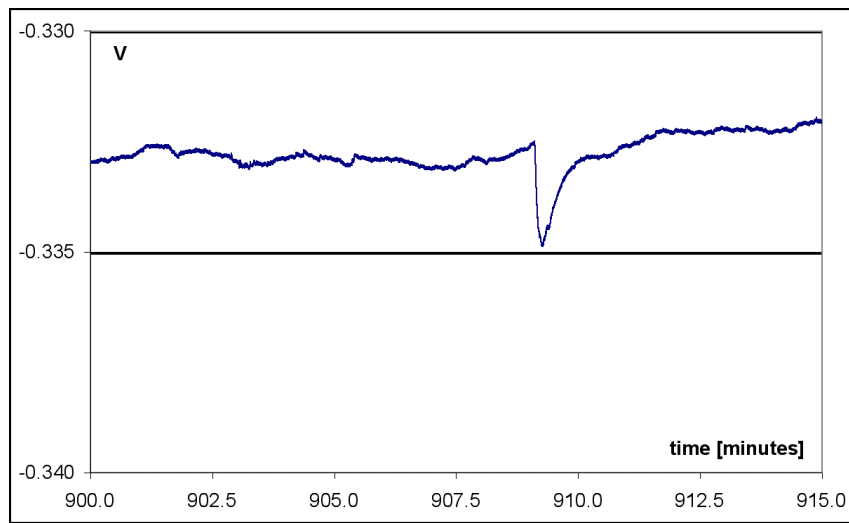


general corrosion carbon steel - H₃PO₄ 10% - 20°C



pitting - stainless steel brackish water + FeCl₃ 1% - 45°C

Fig. 4. Electrochemical noise measurements - typical signals.



stress corrosion cracking stainless steel - CaCl₂ 40% - 85°C

Fig. 4 (continued). Electrochemical noise measurements - typical signals.

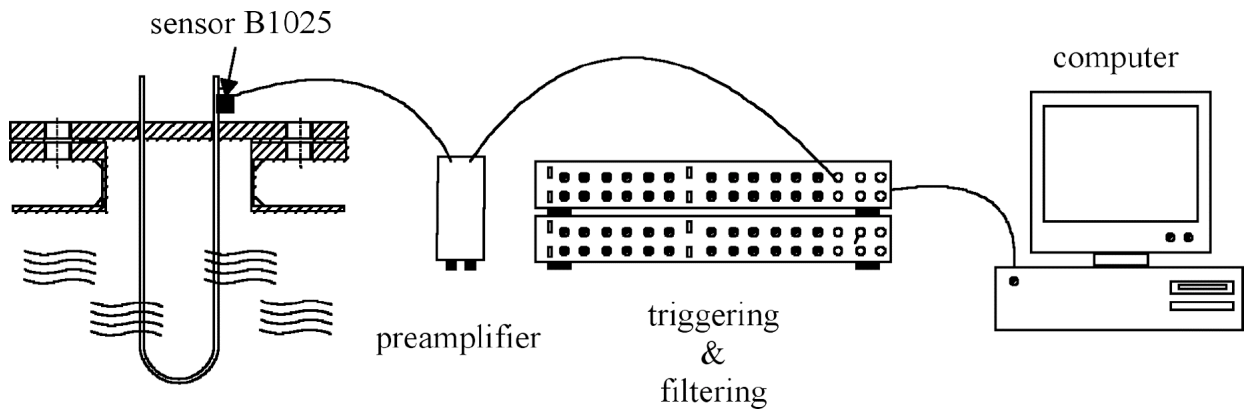
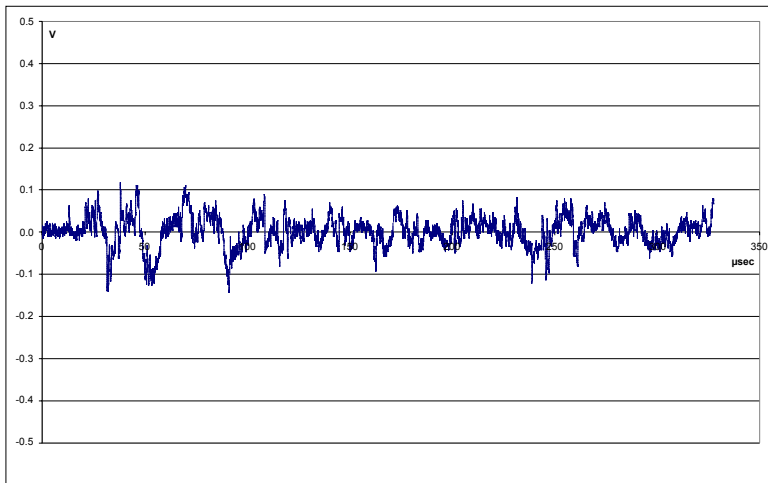


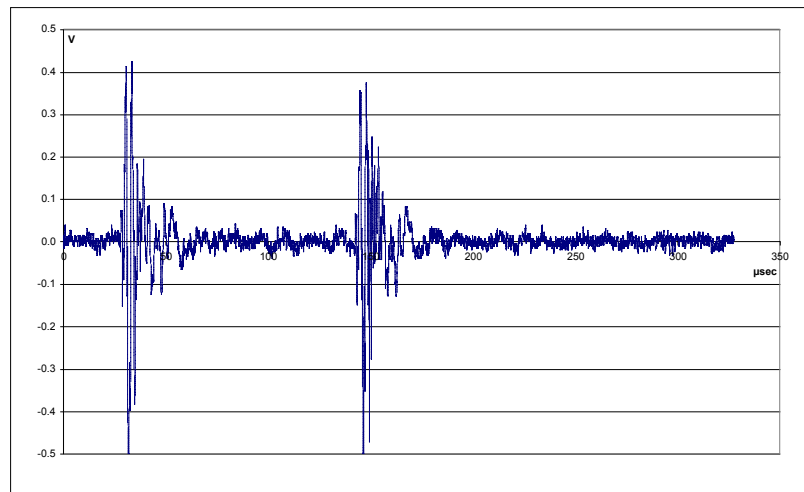
Fig. 5. Experimental set up for AE technique.

Figure 6 shows typical AE signals. General corrosion of carbon steel, general corrosion of stainless steel, pitting of stainless steel, stress corrosion cracking of carbon steel and stress corrosion cracking of stainless steel can be distinguished by pattern recognition techniques, statistical analysis and the energy content in the time domain in combination with frequency analysis. The pit initiation or crack initiation as well as the pit growth or crack growth can be monitored by the acoustic emission technique. This is important additional information revealed by the acoustic emission technique in comparison to the electrochemical noise measurements. Apart from this additional information, the accuracy of the acoustic emission technique is higher than that of more conventional non-destructive testing methods like dye penetrant, magnetic interference or ultrasonic testing.

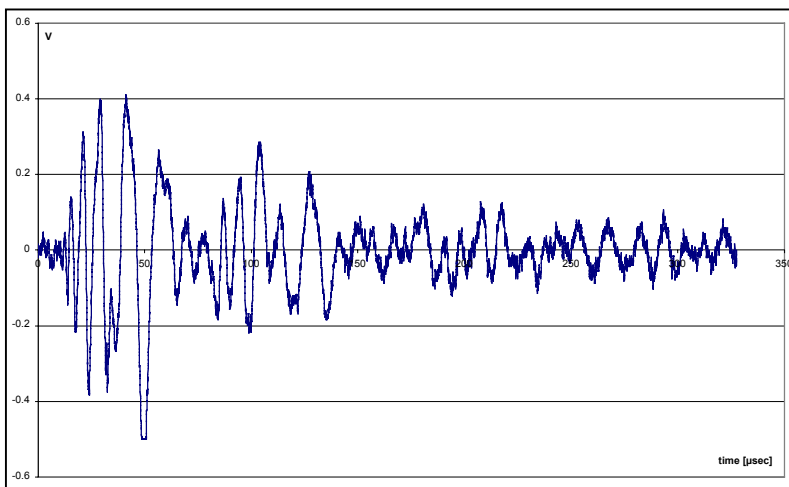
The scaling-up of the AE experiments turned out that the development of an additional and very accurate filtering system is necessary to use the AE technique as a reliable measurement tool in an industrial environment.



*general corrosion
carbon steel - H_3PO_4 10% - 20°C*



*pitting - stainless steel
brackish water + $FeCl_3$ 1% - 45°C*



*stress corrosion cracking
stainless steel - $CaCl_2$ 40% - 85°C*

Fig. 6. AE technique - typical results.

Acousto-Ultrasonics

A calibrated ultrasonic pulse with a frequency of 300 KHz (Fig. 7a) is introduced in the metal. This ultrasonic pulse is introduced by a function generator (PHILIPS PM 5138). Changes in the metal morphology, the metal thickness and the metal microstructure change the wave propagation and therefore the signal measured after propagation through the metal (Fig. 7b) [5, 6]. The propagated signal is measured by Fracture Wave Detector (Fig. 5). The typical sample frequency is 20 MHz. The complete experimental set up for the acousto-ultrasonic technique is shown in Fig. 8.

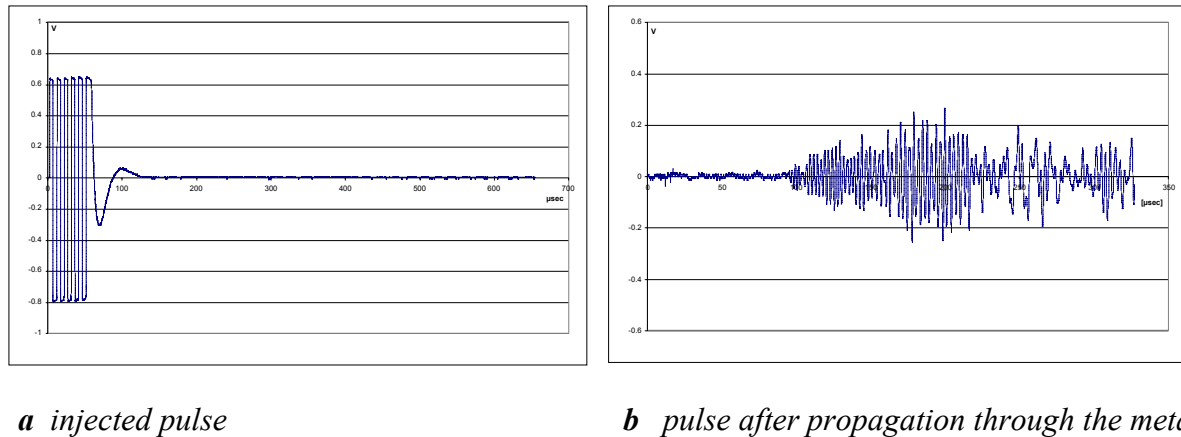


Fig. 7. Injected pulse and pulse after propagation through the metal; general corrosion, carbon steel - H_3PO_4 10% - 20°C.

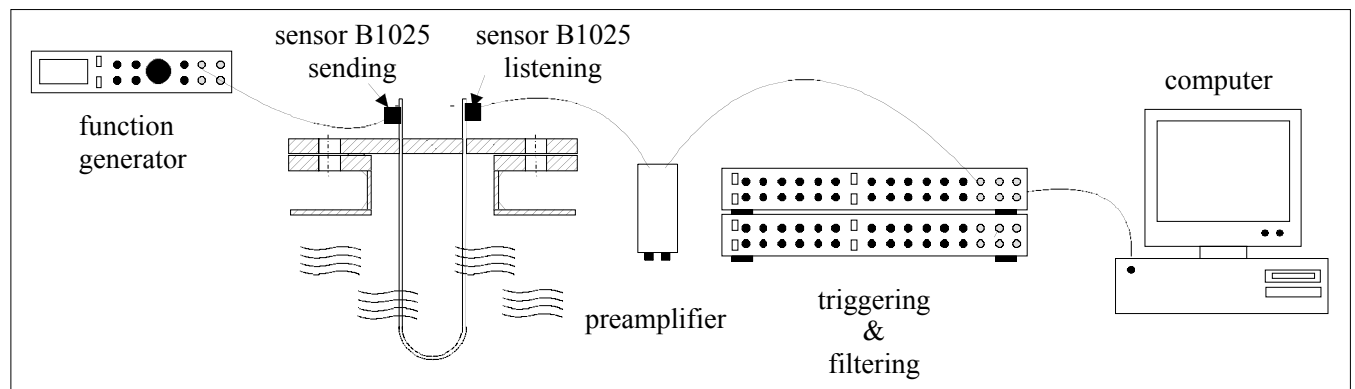
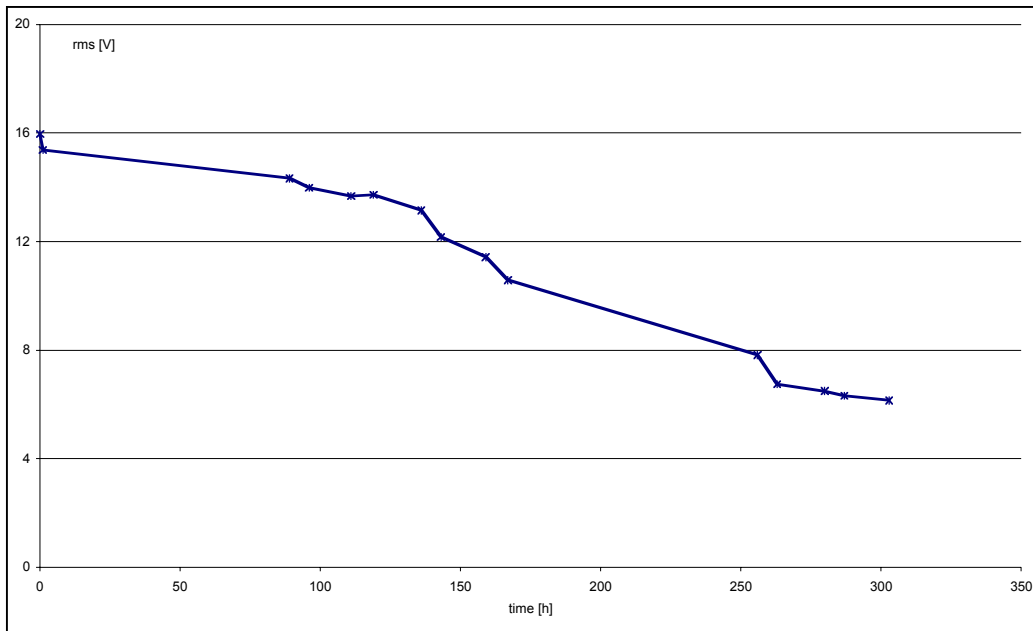


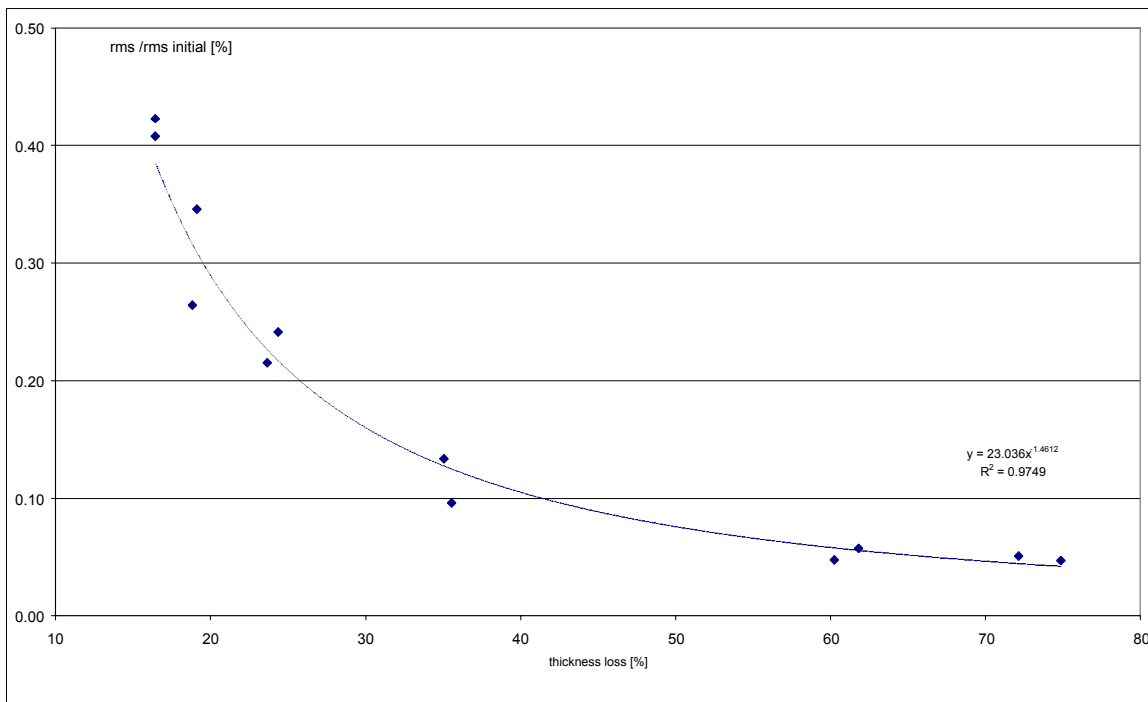
Fig. 8. Experimental set up acousto-ultrasonic technique

Knowledge of the wave type and the interference between several wave types is necessary to select the most interesting part of the signal for further calculation. An energy loss in this particular part of the signal is measured during ongoing corrosion. (Fig. 9) Corrosion damage due to general corrosion, pitting or stress corrosion cracking can be quantified in this way. Figure 10 illustrates this quantification for general corrosion. The correlation between the calculated energy losses of the acousto-ultrasonic measurements and the calculated loss in thickness based on the weight loss of the specimens during the tests has a very high accuracy. The highest accuracy is obtained for intermediate and high corrosion rates. For low corrosion rates the accuracy is not that high.



general corrosion carbon steel – H₃PO₄ 10% - 20°C

Fig. 9. Energy loss during corrosion attack.



general corrosion carbon steel – H₃PO₄ 10% - 20°C

Fig. 10. Correlation energy loss - thickness loss.

The highest regression coefficients (Fig. 10) could be obtained in the laboratory. However also for the experiments in the mini-plant and in the industrial environment high regression coefficients can be obtained when additional filters are applied. In fact an accurate band-pass filter centred around 300 kHz turned out to be very efficient.

Optical Fibres (OF)

An optical fibre is attached on the surface of interest. A laser-diode forces a light pulse through the fibre. Changes in the stress conditions on the surface due to the corrosion activity change also the stress conditions of the optical fibre. The changing stress conditions of the optical fibre modulate the light pulse. Analysis of this modulation is very useful in quantifying the corrosion damage [7, 8].

Figure 11 shows the experimental set up. The main components are a 30-mW laser, a trans-impedance photodiode preamplifier with a DC bandwidth of 2 MHz and a gain of 1-10 MV/A and the silica/silica optical fibre. The photodiode is connected to the computer by a PCI Bus high-speed A/D board (Keithley KPCI-3110). The typical sample rate is 110 Hz.

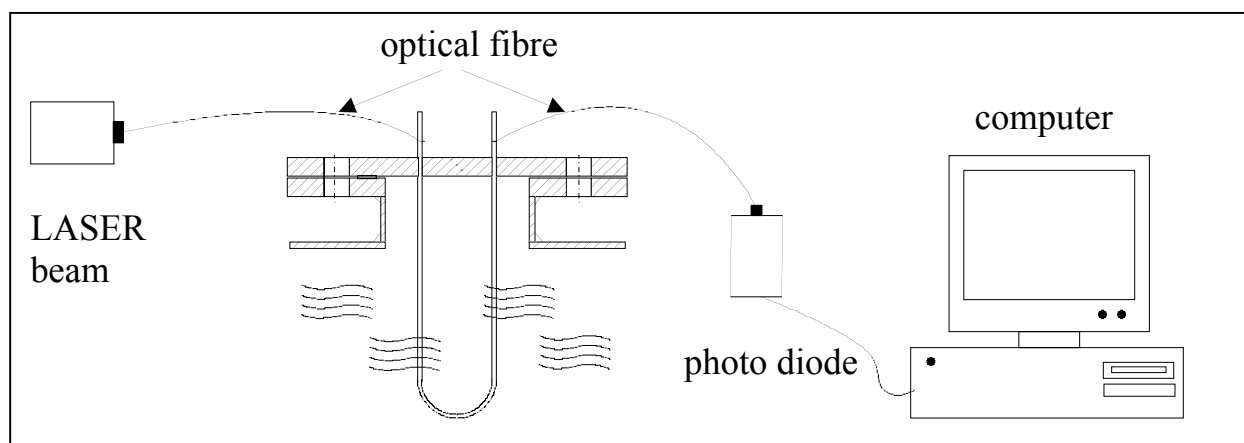


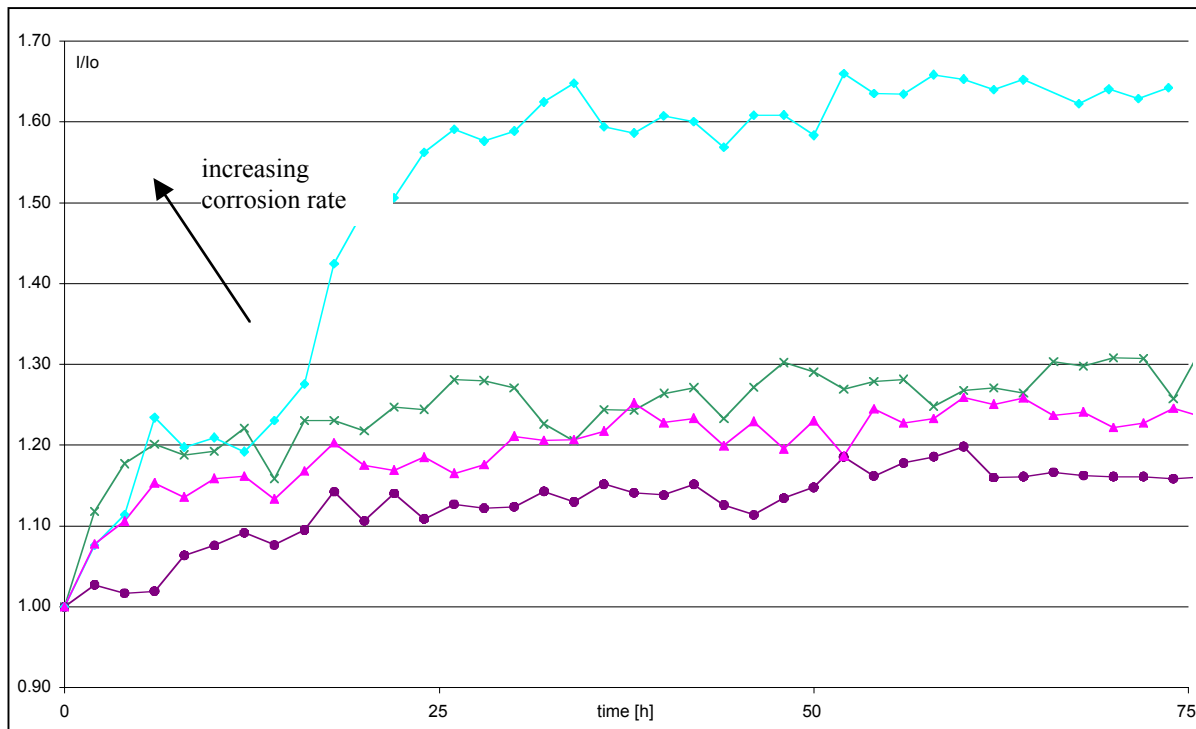
Fig. 11. Experimental set up of optical fibres.

The variation in intensity of the light pulse is an appropriate tool for the quantification of the ongoing corrosion. Figure 12 illustrates the rise in intensity for several experiments. The fibre is fixed on the surface of interest under a certain prestress. During ongoing corrosion the prestress diminishes and the intensity of the laser pulse through the fibre will rise. The linear curve fitting at the initial part of this curve correlates with the corrosion rate. Optical fibres are very interesting to monitor general corrosion with relative low corrosion rates. In this way the optical fibres are complementary to the acousto-ultrasonics. During the scaling-up of the experiments the optical fibres has been found to be very reliable. No additional difficulties arose.

Conclusion

Electrochemical noise measurements, the acoustic emission technique, acousto-ultrasonics and optical fibres are very complementary non-destructive testing methods for the monitoring of general corrosion of carbon steel, general corrosion of stainless steel, pitting of stainless steel, stress corrosion cracking of carbon steel and stress corrosion cracking of stainless steel (Fig. 13).

By combining the electrochemical noise measurements and the acoustic emission results the active corrosion processes are revealed. The electrochemical part of the corrosion processes is visualised by the electrochemical noise measurements. The acoustic emission technique moni-



general corrosion
carbon steel - H₃PO₄ 10% - 20°C

Fig. 12. Intensity rise in optical fibres. (I_0 is the initial intensity).

tors the mechanical part of the corrosion processes like the breakdown of passive films, crack growth, pit growth.

By combining acousto-ultrasonics and fibre optics the corrosion damage can be quantified. Acousto-ultrasonics have the highest accuracy for intermediate and relative high corrosion rates. Optical fibres have the highest accuracy for relative low corrosion rates.

By combining electrochemical noise measurements, the acoustic emission technique, acousto-ultrasonics and fibre optics a sensor to identify the active corrosion processes and to quantify the corrosion damage in chemical production units has born.

This combination of non-destructive testing methods has accuracy higher than that of more conventional non-destructive testing method like dye check, magnetic interference or ultrasonic testing.

Acknowledgements

This research has been realised with financial support from the Flemish Institute for the promotion of scientific-technological research in industry (IWT), project 010261/BASF Antwerpen.

	Identification	Quantification
no corrosion	EN, (AE)	
general corrosion carbon steel	EN, (AE)	AU, OF
general corrosion stainless steel	EN, (AE)	AU, OF
pitting stainless steel	EN, AE	AU, (OF)
stress corrosion cracking carbon steel	AE	AU, (OF)
stress corrosion cracking stainless steel	EN, (AE)	AU, (OF)

Fig. 13 Four complementary non-destructive measurement methods.

References

- [1] C. Gabrielli and M. Keddam, "Review of Applications of Impedance and Noise Analysis to Uniform and Localized Corrosion", Corrosion, National Association of Corrosion Engineers, October, pp. 794- 811 (1992).
- [2] J. Göllner und A. Burkert, „Untersuchung der Korrosionsneigung mit Hilfe des elektrochemischen Rauschens“, Materials and Corrosion, **49**, 614-622 (1998).
- [3] R.V. Williams, 'Acoustic emission', Adam Hilger Ltd, Bristol, 1980.
- [4] M. Wevers, I. Verpoest, P. De Meester, and E. Aernoudt, *Acoustic emission: current practice and future directions* (ASTM STP 1077), eds. W. Sachse, J. Roget and K. Yamaguchi, American Society for Testing of Materials, 1991, pp. 416-423.
- [5] J.H. Williams Jr. and S.S. Lee, Promising quantitative nondestructive evaluation techniques for composite materials – Materials Evaluation **43**, April 1985, 561-565.
- [6] A. Vary and R.F. Lark, Correlation of fibre composite tensile strength with the ultrasonic stress wave factor, Journal of Testing and Evaluation, **7**(4), 185-191.
- [7] A. Mendez, T.F. Morse, and F. Mendez, "Applications of Embedded Optical Fiber Sensors in Reinforced Concrete Buildings and Structures", Proc. SPIE Fiber Optic Smart Materials and Structures, Vol 1170, Sept. 1994.
- [8] Monitoring Corrosion On-Line With Fiber Optics, EPRI Journal, November/December 1995, p. 5.

AE TECHNOLOGY AS A KEY ELEMENT OF THE OPERATION SAFETY SYSTEM AT REFINERY

B. S. KABANOV, V. P. GOMERA, V. L. SOKOLOV, A. A. OKHOTNIKOV
and V. P. FEDOROV

KIRISHINEFTEORGSINTEZ / Kirishi, Leningrad region, 187110, RUSSIA

Abstract

Experiences of AE inspections of pressure vessel at Kirishi refinery are summarized. This is to demonstrate AE method despite rather complicated interpretation of results can become an important part of refinery NDT department. AE is shown to be a useful tool in the production equipment safety system.

Introduction

Pressure vessel AE inspections started at Kirishi refinery at the end of 1980s. At first, such jobs had been carried out by outside research centers and independent service companies. In 1991, the refinery organized its own AE inspection laboratory, the first one among Russian refineries. Since 1992, the AE inspection laboratory has conducted the AE monitoring of refinery equipment. In some cases, some research centers had been involved in complicated vessels tests, but since 2000 the refinery AE inspection laboratory conducted all the tests.

Some results of 10-year activity of our AE inspection laboratory are presented in this report. The main purpose of this article is to demonstrate AE method (despite the fact that results interpretation are rather complicated) can become an important part of refinery NDT department. Moreover, it is quite reasonable for the petroleum and chemical industries, where a large number of pressure vessels and storage tanks must be tested, to have a specialized AE laboratory.

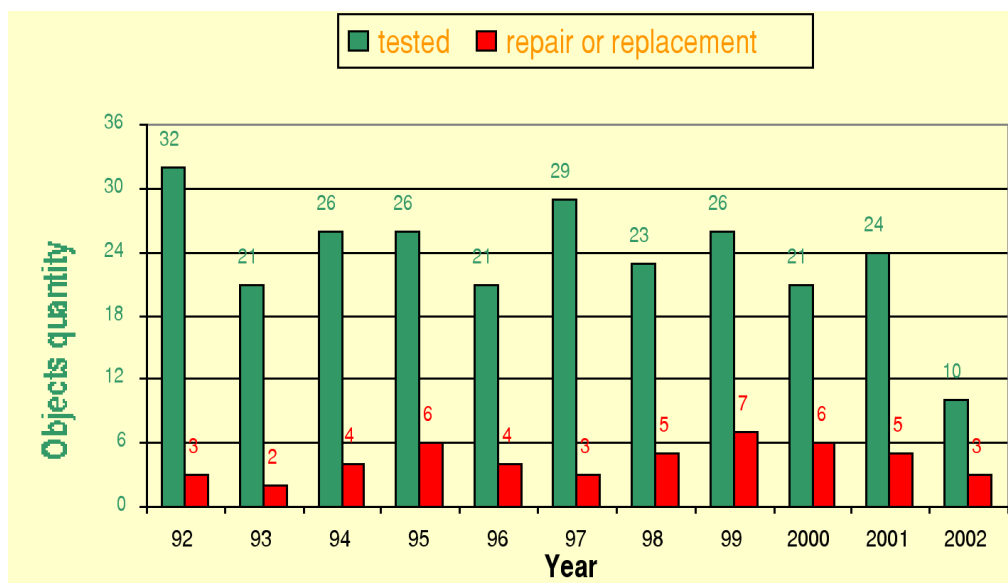


Fig. 1. Pressure vessels AE inspection results at Kirishi refinery from 1992 to 2002.

Statistics

For AE tests we use two inspection systems – LOCAN AT (PAC, USA) from 1991 and AMSY4 (Vallen-Systeme, Germany) since 1997. Depending on the test tasks, one or both of the systems have been used. For example, when we test the large-size vessels, we inspect the upper part with the help of one, and the lower part with the second system. To the present, we have tested more than 250 vessels. Some statistical data are presented in Figs. 1 and 2. The list of the most serious defects, detected with AE method, is shown in Table 1.

Some Application Techniques

On the basis of our experience, we point out some aspects of AE applications at the plant site. These notes can be useful for the AE specialists involved in similar tests in different branches of industry.

1. Some important notes of organization procedure

1.1. Test planning

Based on the recommendations of corrosion engineers, a safety department manager issues a list of pressure vessels to be tested with AE technology within upcoming year. This list is included in an Annual Preventive Refinery Maintenance Plan. The presence of process causing alkaline cracking is the reason for the vessel to be included in such a Plan. The vessel preparation for AE tests is also included in the maintenance documents.

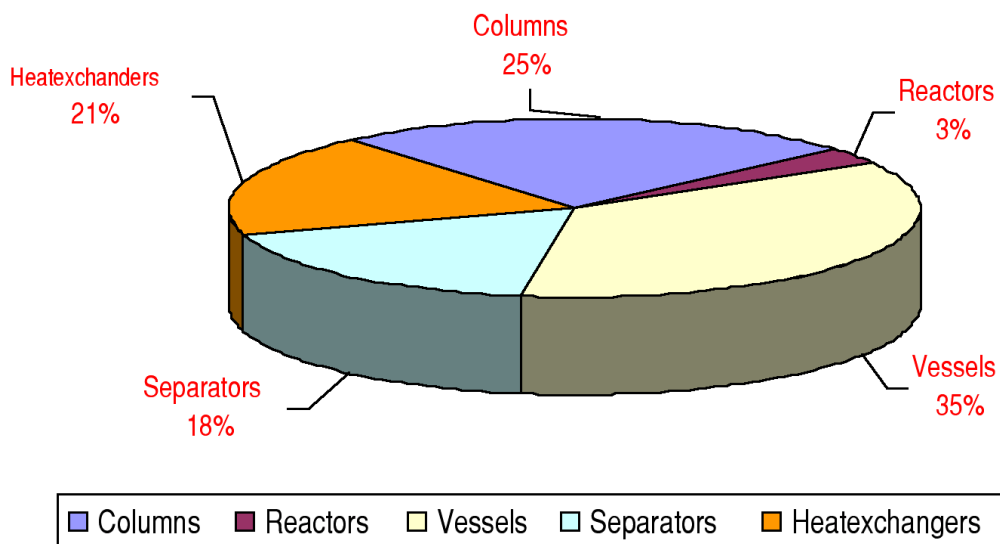


Fig. 2. Pressure vessels AE inspection structure according to equipment type.

1.2. Preparation instruction for the AE test of a vessel.

AE test procedures demand the preparation of the object, involving various activities by technical staff. A manual for AE test preparation procedure was created in order to avoid the possible subjective factors, affecting the quality of preparation. In the manual, the order of preparatory steps and the persons responsible for those steps are prescribed.

1.3. Vessel pressurization equipment

At the beginning we used vessel's own capabilities to pressurize itself. It created some problems connected with the rate of pressurization, keeping the pressure and releasing it. In order

to avoid all these issues, AE inspection laboratory is equipped with a portable electric pump. Initially, the tested vessel is filled with water. Then we use the pump to create excessive pressure inside the vessel. The process of pressurization is fully under control by AE laboratory specialists.

2. Positive image creation for AE

The creation of a positive image of AE laboratory and finding allies among refinery specialists are very important. We use any opportunity to inform them about capabilities, advantages and even physical principles of AE method. It is impossible to overestimate popularization of AE method.

To achieve these goals the advantages of the method should be shown and proved (through literature examples and/or experience) to the specialists, who are responsible for the safe and reliable performance of vessels and pipelines and also to those who are experts in corrosion protection of equipment. The most effective are the cases, where the emergencies are prevented with help of AE technology. There have been some cases in our practice, when very serious defects were detected, which could lead to dangerous emergencies. More over, these defects could not be detected with any other methods. For example, dangerous defects had been detected at the amino-treatment absorber just a few hours before the production process started up (Appendix, Table 1, Item 23). Due to the nature of the detected defects, the probability of an emergency was high. Later, it was found that the defects were similar to those defects, which caused the accident of amino-treatment absorber in Romeoville, Illinois, USA, in 1984. There were 17 victims in that accident and refinery lost more than US\$100 million [1, 2].

3. Results interpretation

Formal use of any known system of AE results interpretation for pressure vessel condition estimation is not the most successful approach. AE method is based on probability approach (as others NDT methods of complicated objects). Thus, an AE specialist who is in charge for analyzing AE data has to treat the formal rules, traditional approaches etc as only as a guide. He must take into account his own subjective thoughts, guesses, feelings etc because they reflect his experience, knowledge about particular objects under the test.

Applying Bayes approach (subjective/objective approach) we can take "non-formal" information (such as thoughts, guesses, feelings etc) as an analogue of *a priori* density distribution probabilities of Bayes approach, while real data collected during AE test, formal techniques etc can be taken as an analogue of objective component (truth function) in expression for *a posteriori* distribution.

In this connection the ability to use non-formal information can be considered as one of the key professional skill of AE specialist. Accordingly, the AE equipment has to have capabilities for developing and applying such skills, for instance, providing maximum options of data collection and its interpretation. The best modern systems meet this condition and allow building up any desired structure of data evaluation in accordance to specialist's skills.

Some Pros and Cons of AE Inspections Implemented by Refinery Specialists

Among the main advantages of AE, it may be pointed out:

1. It has provided the maximum flexibility in actions.

2. Many Russian refineries are equipped much better than research centers and third party service companies in Russia.

3. The variety of the objects for AE testing at refinery provides the excellent opportunity for AE applications research. On the other hand it is difficult to simulate in laboratory conditions or in theoretical model all the variety of real objects.

4. As a rule, the plant specialists know the object's specific features and their characteristics to be inspected with AE method very well.

Points mentioned in items 3 and 4 lead to the formation of specialized experience of AE technicians. This experience is limited, perhaps. However, it is often enough for reliable and successful AE inspections of plant equipment. It forms a good base for a comprehensive approach to the object inspection. Within refinery it is possible to get any operational and agreed information, instrumental support concerning the vessel operation from technologists, mechanics, maintenance and NDT personnel. The usage of complex approach allows extending database of knowledge involved into inspection results analysis. In some cases, it allows to detect the defects, which may be missed in the event that traditional approach would be applied. As a result, the quality of AE inspections is increasing.

The following disadvantages of AE can be mentioned:

1. The main distinctive feature of AE inspection at the refinery is a tight maintenance schedule and as a result - a shortage of time for results analysis. As experience says, there is enough time for defect detection, but sometimes there is no time for their detailed investigation. Moreover, the defects are not investigated at the refinery, but they are fixed, and often, very fast. It is evident that a part of information concerning the defects is lost, but the production has higher priority than defects research.

2. Sometimes the AE tasks can be complicated thus leading to mismatching to the knowledge and experience of refinery personnel. In some cases quick requests to the experts are not possible and their responses are not available. However, with gained experience, this problem disappears.

Examples

The above written thesis may be illustrated with examples from our practice. Let's consider the case, when the information about the specific properties of inspected object helps to assess the inspection results, while the formal approach can lead to mistakes in results assessment. For example, traditionally, the remarkable emission at low load is related to "bad emission" and is related to mechanical noise [3]. But it is not always correct.

In Figs. 3 and 4 the results of AE sources planar location for two different vessels shells are presented. In the first case, it is the gas fractionation vessel of 40 cubic meters capacity; in the second one it is the top distillation column with 200 cubic meters volume.

In Fig. 3, there are 3 zones marked out where the following defects were detected:

(1) - the crack in the weld root of T-weld with 55 mm long and 20 mm depth (wall thickness is 30 mm);

(2) - the group of blisters on the inner surface of the shell within area of 170 x 40 mm, 2-3 mm depth;

(3) - crack of 30 mm length, 5 mm depth in the root of T-weld.

Defect localisation in zones (1) and (2) was performed by planar location. The crack on zone (3) was detected by analysing relative activity of inspection channels at the different load stages.

In Fig. 5, there are also 3 defective zones marked out. The zones are numbered from 4 to 6. Those zones contained the following defects:

- (4) and (5) - multiple developed pores in inner side of the shell at 2-3 mm depth,
- (6) - defect in the weld (large non-metal inclusion, due to which the crack developed).

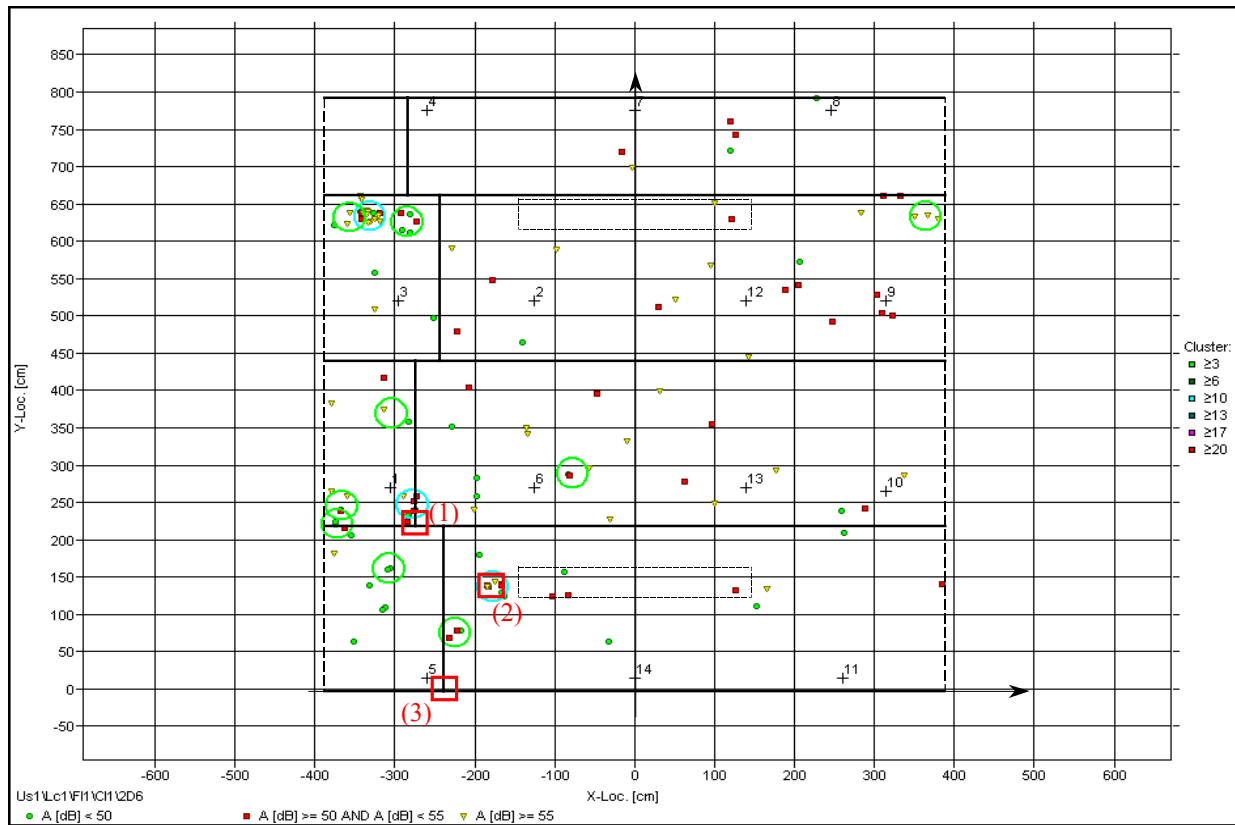


Fig. 3. Vessel V= 40 m³ AE inspection results of planar location sources.

Pores located on two areas with 120 x 120 mm and 120 x 135 mm sizes near the welding zone. These pores have been located with help of liquid penetrant inspection (LPI) method. These defects were eliminated by blasting (wall thickness 36 mm). Defect presence in zone (6) was confirmed with ultrasonic method (Fig. 8). LPI method did not give any results for zone (6).

As it may be seen in Figs. 4 and 5, the defect in zone (6) was detected with planar location, but defects in zones (4) and (5) were detected by means similar to that used for zone (3): defects were detected by analysing relative activity of inspection channels at the different load stages. The most important of given examples is the following: the periods of major relative AE activities, connected with sources located in zones (3), (4) and (5), were registered when the pressures were less than maximum operation pressure of the vessel. It may be seen in Figs. 6 and 7. Moreover, these AE activities had the highest values among all AE activities registered during whole AE inspection, including higher pressure loads.

The change of the behavior of AE activity after applying the excessive operation pressure does not match the conception which is considered to be the traditional one. In such way, the expected source activity at channel #5 of the first example, did not increase at all, on the contrary it decreased greatly.

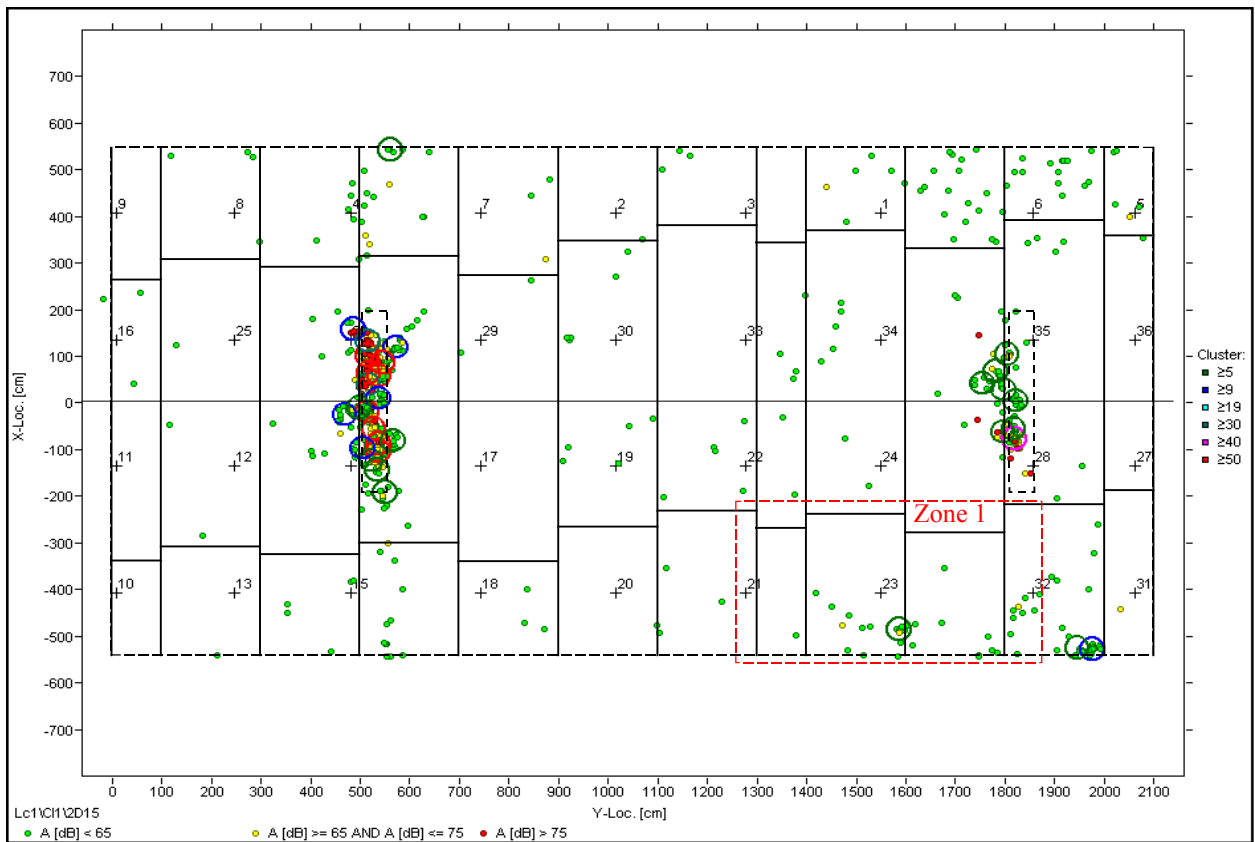


Fig. 4. Vessel V= 200 m³ AE inspection results of planar location sources.

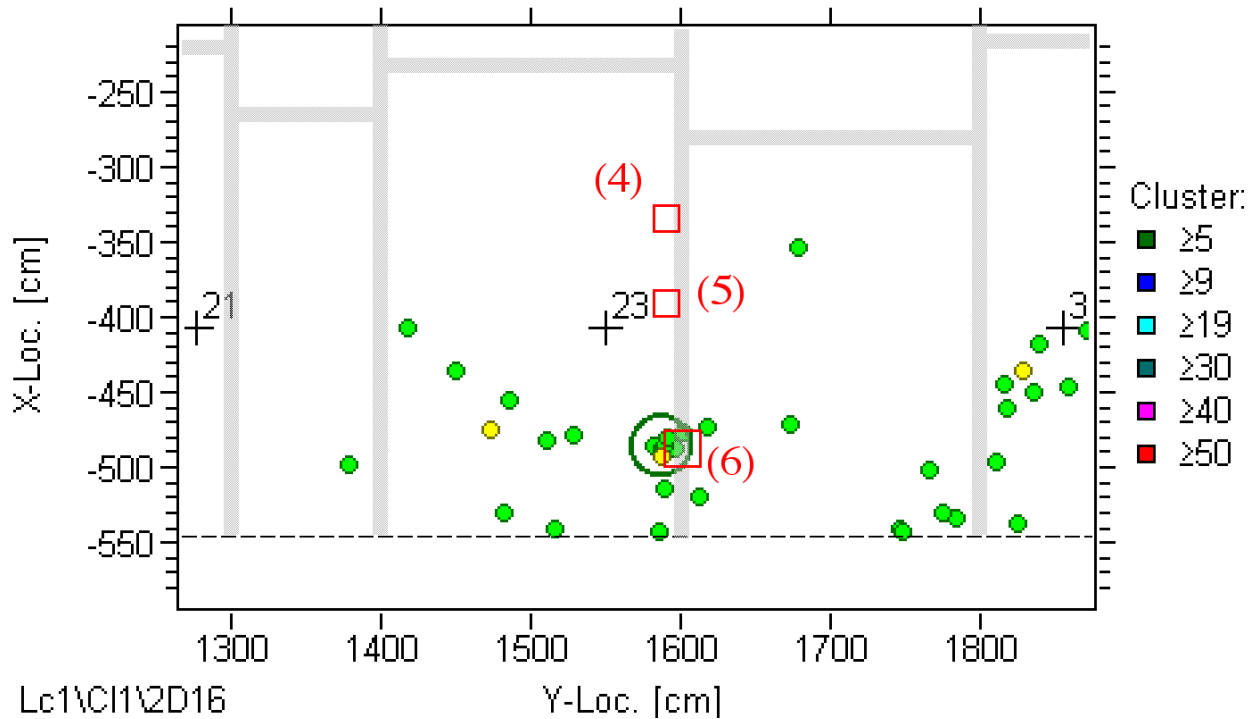


Fig 5. Vessel V=200 m³ shell segment with defects (Zone 1 in picture 4). Zones (4) - (5) contain pores, zone (6) has defect in the weld.

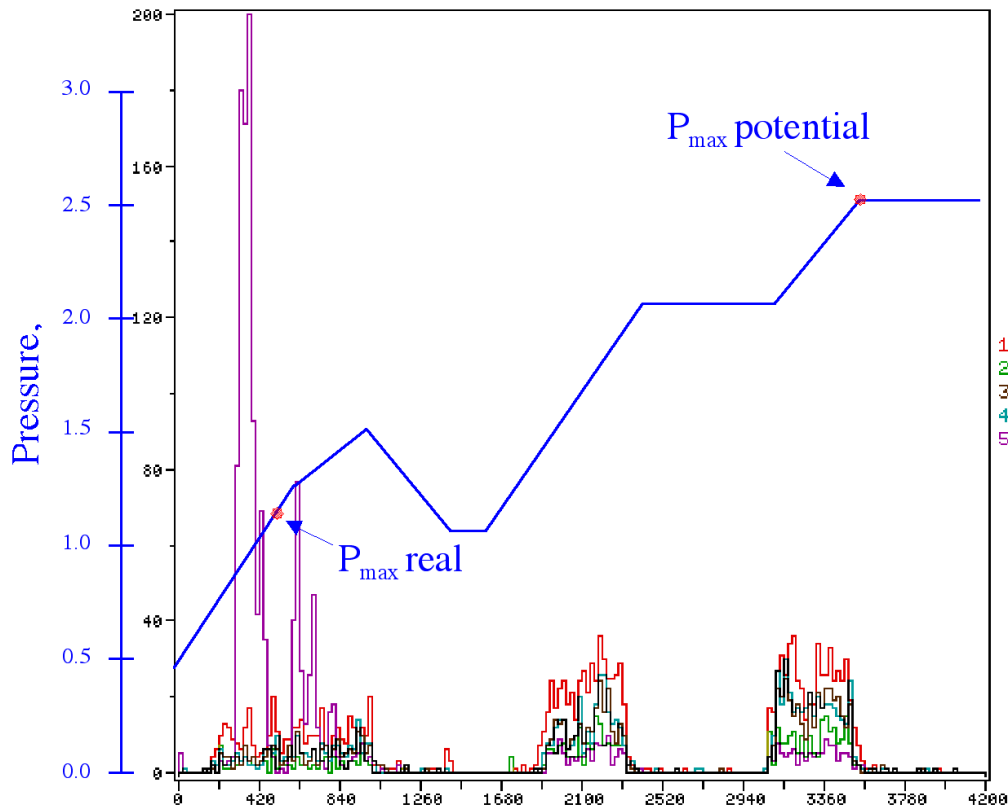


Fig. 6. Relative activity behavior of channels 1-5 at different load stages for vessel $V = 40 \text{ m}^3$.

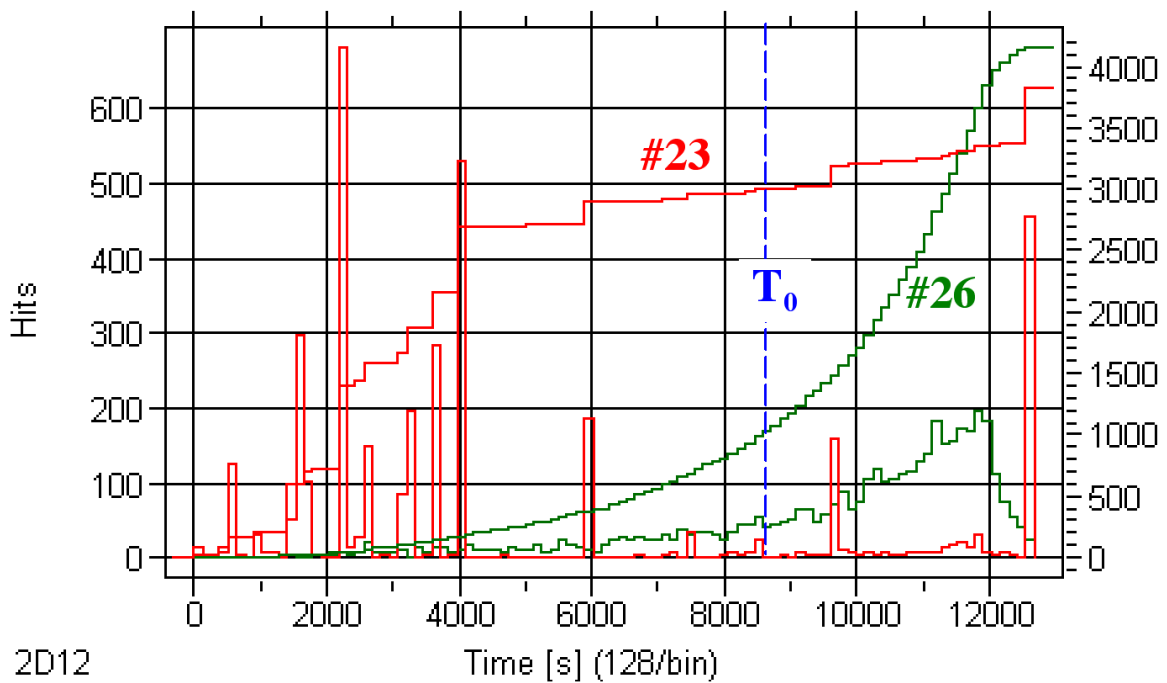


Fig. 7. Relative AE activity. Vessel $V = 200 \text{ m}^3$. Sensor #23 is located near a group of defects. Sensor #26 is located in the zone of high AE activity near the left support. T_0 is the time when the maximum operation pressure was achieved.

The most probable reason of the obtained effect was determined after joint study with technology and corrosion engineers where sequence of preparation steps had been discovered. During shut-down procedure and discharging of the vessel, the oxygen and atmospheric humidity went into the vessel and the temperature dropped. During steaming process, condensate formed and this was aggressive in terms of corrosion. These factors created the conditions for fast defects development. During the shut-down of a top distillation column, the corrosion speed can be 10-20 mm per year, whereas in case the vessel is in production stage, the speed of corrosion is only 0.02 mm per year. This should be taken into account, otherwise the information can be lost.

The above described situation is a typical one for refineries. That is why high AE activity registration at the early stages of vessels load should not be considered as a “bad emission”. Moreover, this effect may be used as one of helpful criteria during defect detection.

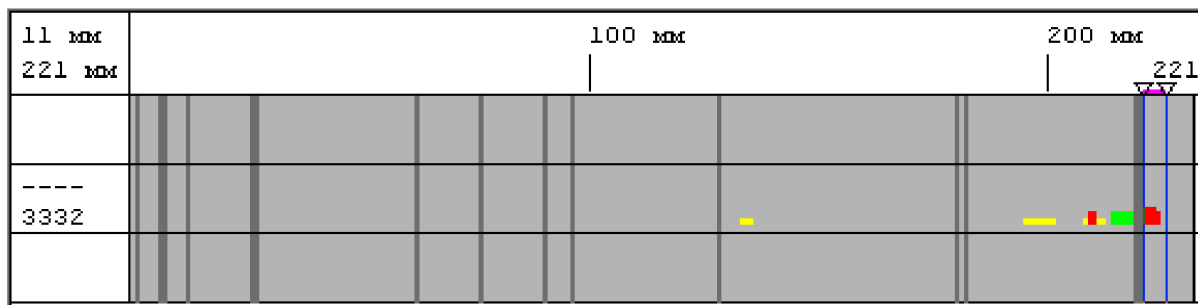


Fig. 8. Results of ultrasonic test method. Weld fragment from zone (6) in Fig. 5. Fragment length is 232-mm. Color index: red - plane defect (crack); green - volume defect (non-metal inclusion); yellow - volume/plane defect. Defect height ≥ 3 mm (3 mm the high limit of equipment sensitive).

Conclusion

The experience of AE laboratory at Kirishi refinery demonstrates that activity of such laboratory can be a very useful tool in the production equipment safety system. The most important condition for effective implementation of AE method at an industry plant is the permanent cooperation and communication of AE specialists with all other departments of the plant who are responsible for safe equipment operation.

References

1. M.G. Mogul, "Reduce corrosion in amine gas absorption columns", *Hydrocarbon Processing*, **78**(10), October, 1999.
2. "Amine Absorbers: Chemical Time Bombs", *Science News*, **130**(265), October 26, 1986.
3. A.A. Pollock, "Acoustic Emission Testing", *Metals Handbook*, Volume 17 (9th Ed.), ASM International, 1989, pp. 278-294.

Appendix

Table 1 List of the most severe defects, found in vessels with the help of AE method.

Year	Control objects	Detected defects	Actions	Remarks
1992	1. Ammonia storage tank.	Longitudinal cracks (3) with 20-30 mm length in weld, inside.	Weld repair.	After weld opened, defects were confirmed; could not be detected with other methods.
	2. Reforming unit column	Local non-metal intrusions in the low part of column in zone 600x600 mm.	Ultrasonic control, Defects sizes were determined.	Defects were registered in a distance of 8 m.
	3. Carbonization unit column	Multi micro cracks distributed in the body of material. Common material degradation.	Column replaced.	
	4. Paraffin production reboiler	Several parts of intensive alkaline cracking. Common metal degradation.	Defects elimination followed by apparatus change.	
1993	5. Gas fractionation unit separator.	Nozzle welding zone crack, some zones near welding had corrosion cracks.	Defects elimination followed by apparatus change..	
	6. Paraffin production reboiler	Sore type defects. (2).	Defects elimination	
1994	7. Top & vacuum distillation column AVT	Some crack zones in plucking welds.	Defects elimination	Cracks maximum size: $l=3\text{mm}$, $a=130\text{ mm}$.
	8. Reformer unit drum	Inner side sore corrosion (2).	Defects elimination	
	9 Hydro treatment column	Fatigue crack in charge pipeline weld.	Weld repair. Scheme of pipeline fixation changed.	For the vessels NN 9,10, the defects were similar and related to their construction features.
	10. Hydro treatment column	Fatigue crack in charge pipeline weld.	Weld repair. Scheme of pipeline fixation changed.	
	11. Sphere drum for liquefied gases storage	1) Low part of the drum, weld defect with the length 500 mm, containing cracks, pours, sludge intrusions. 2) Middle part of the drum, weld defect containing pours and sludge intrusion with the length of 800 mm.	1) Defect is confirmed with ultra sonic method. Repair. 2) Defect is confirmed with ultra sonic method. Weld repair.	Thickness of the wall is 30 mm.
	12. Sphere drum for liquefied gases storage	Weld zone 100x120 mm, containing pores and cracks 2-3 mm depth.	Elimination of the defect.	
	13. Gas fractionation unit drum	Cracks in T-route weld (2) zone 170x40 mm, 2-3 mm depth.	Weld repair.	One of cracks dimension: $a=55\text{ mm}$; $l=20\text{ mm}$ (wall thickness is 30 mm).
	14. Benzene production drum	Large corrosion zones in low part of the drum. Wall decreases from 20 to 7-10 mm.	Drum is replaces.	
	15. Gas fractionation unit drum	Zone with corrosion cracks $a=5-10\text{ mm}$., $l=2-4\text{ mm}$ in low part of the drum.	Repair.	

	16. Hydro treatment separator	150 mm of a bad welded weld.	Weld repair.	
	17. Reforming unit column	The dispersed caverns in zone of 200x300 mm in low part of the column.	Defects elimination.	
	18. Top distillation drum	Cross cracks of the weld, connecting shell with low bottom.	Weld repair.	
1996	19. Reforming unit column	Crack $l=4$ mm., $a=25$ mm, along the upper bottom weld.	Defect elimination.	
	20. Top distillation unit AVT	Cracks in cladding near welds.	Defect elimination.	
	21. Reforming unit column	Intensive corrosion cracking of cladding near welds in upper and middle zones of the column.	Defects elimination.	The solution- the column should be changed.
	22. Liquefied gases storage drum	Cross crack of the weld, $l=3$ mm. Stressed weld.	Defects elimination.	
1997	23. Hydro treatment column	Cracks, including, through, arranged on circumferences in several cross-sections of low part of column.	Column dismantled immediately.	The defects could be detected only with AE method.
	24. AT unit column	Some zones with cracks in cladding.	Defects elimination.	
	25. AT unit column	Perforation in low bottom, some zone with cracks in cladding.	Defects elimination.	
1998	26. Paraffin production unit column	Some zones of corrosion cracks in cladding.	Defects elimination.	
	27. Paraffin production unit drum	A lot of non-metallic intrusions, distributed along the large square.	Confirmation by USC.	The solution - the drum should be changed.
1998	28. Hydro treatment separator	Cracks in cladding.	Defects elimination.	
	29. AVT unit column	Cladding cracks near the upper bottom weld.	Defects elimination.	
	30. Reforming unit column	Cladding cracks in upper part of the column.	Defects elimination.	
1999	31. Reformer unit drum	Cross-cracks in joint welds of bottoms.	Defects elimination.	The solution - drum should be changed.
	32. Reformer unit column	Long zones with cracks in cladding.	Defects elimination.	The solution – to change column.
	33. Reformer unit heat exchanger	Round crack in weld of boss.	Defects elimination.	Crack depth 8-10 mm (wall thickness is 30 mm).
	34. Sphere storage tank for liquefied gases	1) Defect weld zone ($l=900$ mm) in the middle part of the vessel. 2) Cross crack of the weld ($l=6-7$ mm). 3) Damaged part of inner surface during mounting (low part of the vessel). 4) Zones (2) with active sources in upper part of the vessel.	1) Additional USC. Defects confirmed, weld repair. Defects elimination. 2) Defects elimination 3) Defect eliminated. 4) Defects allowed in size.	
	35. Sphere storage tank for liquefied gases	Zones (3) with active sources in low part of the vessel.	4) Defects allowed in size, confirmed with USC.	

	36. Sphere storage tank for liquefied gases	1) Cross-cracks (3) in upper part ($L=3-4$ mm) 2) Zones with active sources in low part of the vessel.	1) Defect eliminated. 2) Defects confirmed with USC, allowed in size.	
	37. AT unit column	1) Cladding cracks near welds. 2) Penetration of the bottom.	Defects elimination	The solution – to change column
	38. AT unit column	Long zones with cracks in cladding near several welds.	Defects elimination	The solution – to change column
2000	39. AT unit column	Long zones with cracks in cladding near several welds.	Defects elimination	The solution – to change column
	40. At unit drum	A lot of micro defects distributed in all of the material	Defects elimination.	The solution – to change the drum.
	41. Hydro treatment separator	Zone with cladding cracks.	Defects elimination	
	42. Hydro treatment unit heat exchanger	Bundle defects localization (brass corrosion).	Additional bundle revision. Defective tubes removal.	The main purpose was the shell revision. Tube defects localization was the additional result. Used the 3-D location algorithm
2001	43. AVT unit column	Cladding cracks near the welds of the upper bottom.	Defects elimination.	
	44. Reformer unit column	Zones of cladding cracks in the upper part of the column.	Defects elimination.	The solution - to change column
	45. Reformer unit column	Intrusions in the upper part of the vessel.	USC; defects size is allowable.	
	46. Alkylation unit apparatus	Intrusions in shell	Defects elimination	The solution – to change apparatus.
	47. Reformer unit heat exchanger	Bundle defects localization (brass corrosion)	Defects elimination.	The experience from item 42 utilized. Carried out the complex testing: both shell & bundle. Used the 3-D location.
2002	48. AVT unit column	Long zones with cracks in cladding near several welds.	Elimination of the considerable defects.	The solution – to change column.
	49. AVT unit column	Long zones with cracks in cladding near several welds.	Elimination of the considerable defects.	The solution – to change column.
	50. AVT unit drum	1) Inner defect of the weld (non-metal intrusion + crack). 2) Zones (2) with pores.	Defects elimination	

STRUCTURAL INTEGRITY EVALUATION OF WIND TURBINE BLADES USING PATTERN RECOGNITION ANALYSIS ON ACOUSTIC EMISSION DATA

A. A. ANASTASSOPOULOS¹, D. A. KOUROUSSIS¹, V. N. NIKOLAIDIS¹, A. PROUST²,
A. G. DUTTON³, M. J. BLANCH³, L. E. JONES³, P. VIONIS⁴, D. J. LEKOU⁴, D R V VAN
DELFT⁵, P. A. JOOSSE⁵, T. P. PHILIPPIDIS⁶, T. KOSSIVAS⁷ and G FERNANDO⁸

¹Envirocoustics S.A., El. Venizelou 7, 14452 Metamorphosi, Athens, Greece

²Euro Physical Acoustics SA, ZAC des Portes de Sucy, Sucy-en-Brie F-94373, France

³Energy Research Unit, CLRC Rutherford Appleton Laboratory, Chilton, Didcot, Oxon, OX11 0QX, UK

⁴CRES, Wind Energy Department, Pikermi 19009, Attiki, Greece

⁵Delft University of Technology, WMC-Group, 2628 CN Delft, Netherlands

⁶Dept of Mechanical Engr. & Aeronautics, University of Patras, Patras 265 00, Greece

⁷Geobiologiki S.A., 136 71 Acharnai, Athens, Greece

⁸Engineering Systems Dept., Cranfield Univ. (RMCS), Shrivenham, Swindon SN6 8LA, UK

Abstract

Current wind turbine (W/T) blade certification practices require static and fatigue testing on new blades in order to assess whether the blade can sustain the applied loads. Within the scopes of a current EC-funded research project, acoustic emission (AE) monitoring has been extensively applied during testing of various W/T blades of similar design. All blades were loaded to failure by, either, gradually increasing the static test loads, or fatiguing the blade until it failed. It has already been reported that AE could locate the damage imposed on the blade during such tests (static and fatigue), and in most cases before the damage had become visible or audible, enhancing the assessment capabilities and the understanding of the failure process of the blades. Additionally, application of typical AE load-and-hold proof tests at intermediate loading stages, prior to failure, has enabled the assessment of the damage criticality for the particular proof load, denoted by high AE rates during load-holds. Furthermore, it has been observed that the AE behaviour of all tested blades during load-holds exhibited very similar trends right prior to failure, despite the fact that blades failed differently. The present paper reports on the use of (specially created for the Project) pattern recognition (PR) software, which has revealed the existence of a “critical” class of AE data appearing close to failure. This has enabled the formulation of evaluation criteria used for the automated assessment of the blade’s integrity, based on the amount of hits from critical classes appearing during the hold period. It is shown that, for similar blades, common grading criteria can be applied successfully, enabling a fast and effective “grading” (from “good” to “severely damaged”), and providing successful warnings of impending failure. This is particularly important for an effective analysis of fatigue tests that have lasted for months and have produced huge amounts of AE data. The software and the automated blade evaluation will be verified with future tests on large, commercial scale blades.

Keywords: acoustic emission, wind turbine blade certification testing, pattern recognition

Introduction

Wind turbine (W/T) blades, while in operation, encounter very complex loading sequences, due to the stochastic nature of wind conditions on wind turbines sites. The suitability of a par-

ticular W/T blade to operate on a specific site is assessed through a certification procedure, which entails the conduction of a series of static and fatigue laboratory tests on the W/T blade. The purpose of such tests is to ascertain that the blade can survive the applied (static and fatigue) loads according to the applicable design standards [1, 2], while the applied static loads aim to simulate the 1-in-50-years gust (and is applied on the blade for ten seconds during testing), followed by fatiguing the same blade for an accelerated 20-years fatigue lifetime test.

In the aforementioned procedures the pass/fail criteria for W/T blades have been based on deflection measurements and strain measurements on the blade's surface, during static loading. Damage characterisation is usually performed by visual inspection for evaluating surface damage. Audible sound emissions heard during such certification tests are considered as potential damage indications; however, on most occasions, the source of such noises cannot be located.

It has already been shown and reported [3-6] that application of AE monitoring during loading of W/T blades has offered considerable advantages towards the understanding of the complex damage mechanisms occurring on the blade, as the loading gets more severe, and, subsequently, has enhanced the tester's ability to evaluate the tested blade's condition. Damage occurring during certification testing (both static and fatigue) can be located with AE, while "weak" areas of the blade are pin-pointed at early loading stages. Additionally, the application of AE "proof-type" tests (with ten-minute load-holds) before and after each certification-type static tests as well as before and during the fatigue tests (at various times during testing) has enabled the assessment of the criticality of the damage (if any) introduced by the test, based on the traditional "emission during load-hold" criterion.

Within the scope of a current, EC-funded research project (AEGIS) aiming to provide a reliable methodology for the assessment of W/T blades' structural integrity, AE monitoring was extensively applied during both static and fatigue certification-type testing of W/T blades. Various proof tests have also been conducted for each blade and at various loading stages prior to failure. It has been verified that, as damage was propagating and as the load was approaching the ultimate failure load, emission during load-hold demonstrated increasing trends. Furthermore, it has been observed that the qualitative characteristics of the recorded AE signals during load-holds (e.g. Amplitude, Duration, etc.) exhibited similar "patterns" close to failure loads. In general, the intensity of the recorded signals increased as damage was becoming more critical and as the loads were approaching the failure loads. The consistency in the presence of a distinguishable family of AE data right before failure has enabled the formulation of specific criteria for the assessment of the blade's ability to withstand specific loads. In other words, the absolute amount of intense AE data on a specific section of the blade during load-hold at a specific load has been proven to be a very good measure of weakness of this section of the blade to withstand such load.

With the use of a PR and blade grading software (AEGIS software, especially created for the Project), critical AE data can be automatically identified and quantified, for any given AE data set, and the tested blade can be sectionally (zonally) graded from "A" (minor damage) to "E" (severe damage) for a specific load, based on the number of critical AE data recorded per zone (i.e. per AE sensor) during the ten-minute load-hold.

Experimental Procedure

In a series of ten (10) similar, small-scale blades, made of fibre reinforced plastic (FRP), (Fig. 1), specifically manufactured for the project, various loading envelopes have been applied, while all blades were loaded up to final failure. Four blades were fatigued up to catastrophic failure, while six blades were deliberately loaded to failure by gradually increasing static loads, using various loading envelopes. The static testing loading envelopes varied and started from simple, monotonic, stepwise load increases (Fig. 2, top) up to failure with 10-min. load holds at various load levels, while, at later project stages, more complex loadings were applied, incorporating both “certification-type” loadings (10-s load increase, 10-s load hold, load decrease) to gradually increasing loads until failure and, intermediately, 10-min. load-holds (AE examination or “proof-type” tests) at increasing load levels, to certain percentages of the previously applied certification-type test load (Fig. 5, top).

Results from the test to failure of three different blades will be presented below. Blade #1 was monotonically loaded to failure with gradual load increases and 10-min. load holds. The results from this blade were used to “calibrate” the grading technique. Blade #7 was statically loaded to failure, following a complex loading envelope with certification-type tests of gradually increasing load and intermediate AE-proof tests with 10-min. load-holds, which were used to grade the blade at various loading stages. Blade #8 was fatigue-loaded to failure, but before the application of the fatigue test, it had been subjected to AE-proof tests at two load levels, which were used to grade the blade.

The tested blades presented herein were manufactured by Geobiologiki S.A. and were tested to failure at the Centre for Renewable Energy Sources, while additional blades (not presented) were loaded at Delft University of Technology. For all tests presented, a 10-channel SPARTAN-2000 Acoustic Emission system by Physical Acoustics Corporation (PAC) was used, with PAC-R6I AE sensors.

Unsupervised Pattern Recognition on Blade #1

The blade layout, sensor positions and load application point are presented in Fig. 1. The applied loading envelope is shown in Fig. 2. The blade final failure area was at 2300 mm from the root, between sensors 7 and 8. Delamination was observed at the bottom section of the root area (sensor 2, not shown). The blade failed by buckling at 7-kN load.

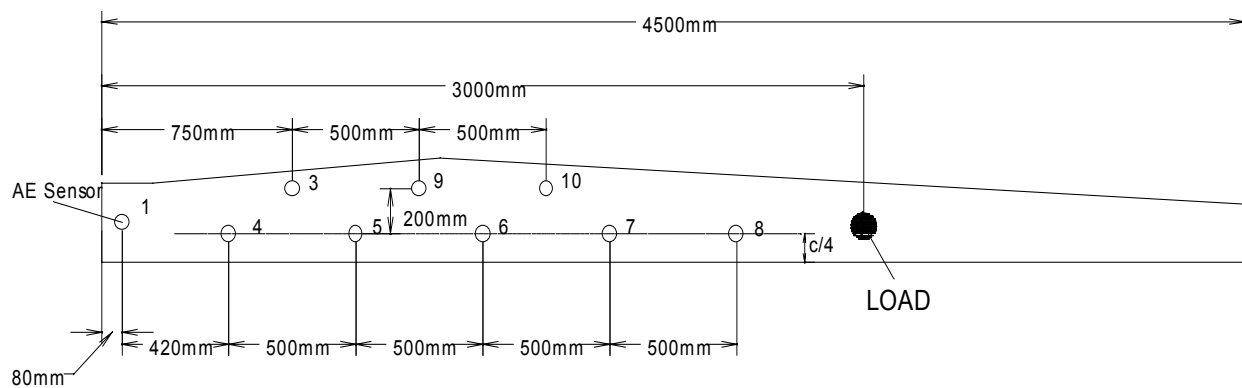


Fig. 1. AE sensor positions, AE channel numbers, and load application point of Blade #1.

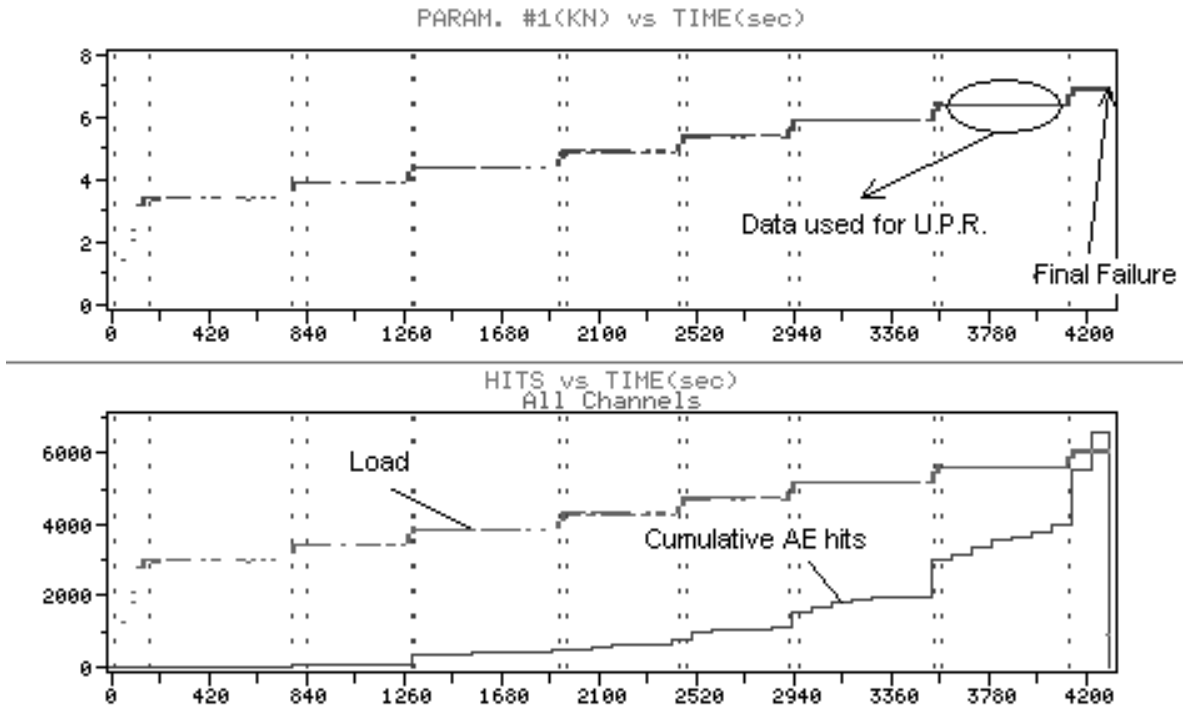
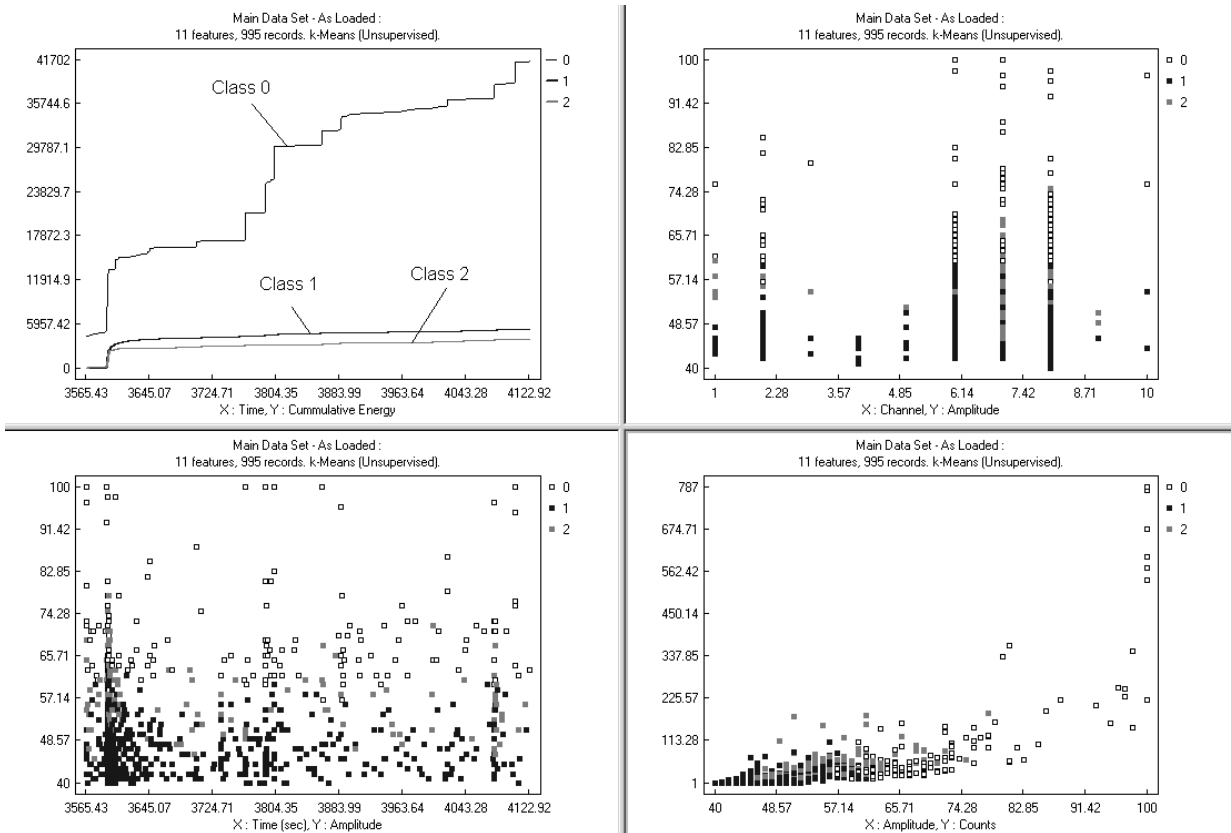


Fig. 2. Applied loading envelope of Blade #1 (top) and cumulative AE hits vs. time (bottom), with load superimposed.



Unsupervised pattern recognition (UPR) was applied on the data of the last load-hold (at 6.5KN) prior to failure using the AEGIS software [7]. A “first-hit” analysis was followed. A representative set of AE features was used, comprising Counts to Peak, Energy, Duration, Amplitude and Average Frequency. Furthermore, all features were normalised individually to a range from 0 to 1, in order to avoid biasing the classification towards the feature exhibiting the highest physical dimensions. UPR was performed using the K-Means algorithm and yielded three different classes of AE data [8].

Figure 3 refers to the data from the load-hold at 6.5 kN, which was classified into three classes by UPR. A thorough examination of the data of Class “0” reveals the following:

- a. Data has an intense rate of AE Energy throughout the load-hold, as opposed to the other classes (see Fig. 3, top left graph),
- b. AE hits have high Amplitude throughout the load-hold (Fig. 3, bottom left graph),
- c. The class appears mainly in the channels close to the failure area (Fig. 3, top right graph),
- d. The AE hits in this Class have high Amplitude and Counts values (Fig. 3, bottom right graph).

Class “0” was characterized as the “critical” AE class; based on it, the grading strategy was formulated. Following the clustering performed by UPR on the 6.5-kN load-hold AE data, a “k-Nearest Neighbour” (k-NNC) Supervised Classifier [9] was trained to correspond AE hits, from any given data set, to one of the three classes based upon the values of their AE features. Subsequently, the data from each one of the load-holds of the loading envelope of Blade #1 (Fig. 2) was classified separately and the amount of data falling into the critical class was observed each time. As a result, a colour-coded grading strategy was formulated, which grades the blade (for a specific load) based on the number of AE hits that are classified with the critical class. For example, for a channel to get a “B” grade, this channel must have recorded 10-25 critical class first-hits during the 10-min. load-hold. This same grading strategy was applied on subsequent blades’ load holds, (at various loading stages) and results from Blades #7 and 8 are presented below.

Supervised Pattern Recognition and Grading of Blade #7

The blade layout, sensor positions and load application point are presented in Fig. 4. The applied loading envelope is shown in Fig. 5, where the loading stages and the sustained damage are indicated. It can be observed that the loading envelope included both certification-type tests (e.g. the MTL11 test) and AE proof-type tests (e.g. tests AE7a to AE7d). Apart from an artificially imposed skin delamination, which was located between 2 m and 2.2 m from the root on the sensors’ line, the blade sustained damage during the test at various positions. Visual inspection during and after the test revealed (see also Fig. 5 bottom):

- Delamination at the root area, visible at later stages of the test,
- Two cracks at the compressive side, perpendicular to the blade axis, at 1.1 m and 1.2 m from the root, visible after the MTL11 certification-type test and,
- One crack at the compressive side, perpendicular to the blade axis, at 2.2 m from the root, developed after the MTL11 certification-type test.

The blade failed at the position of the crack at 2.2 m, during the MTL21 certification-type test at 22.8 kN, slightly before this load was achieved.

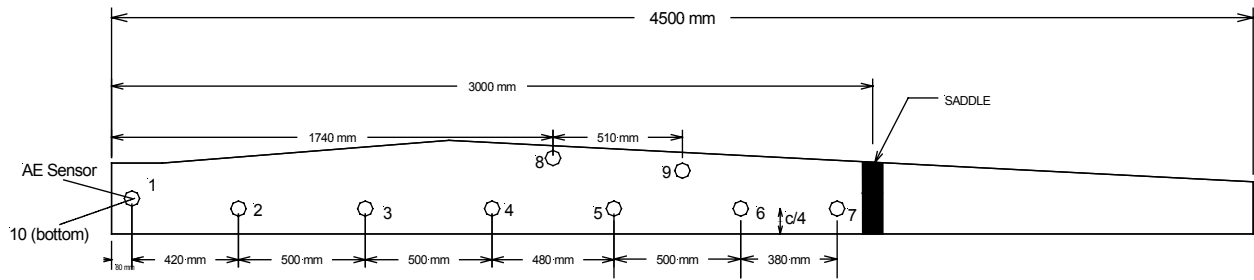


Fig. 4. AE sensor positions, AE channel numbers, and load application point of Blade #7.

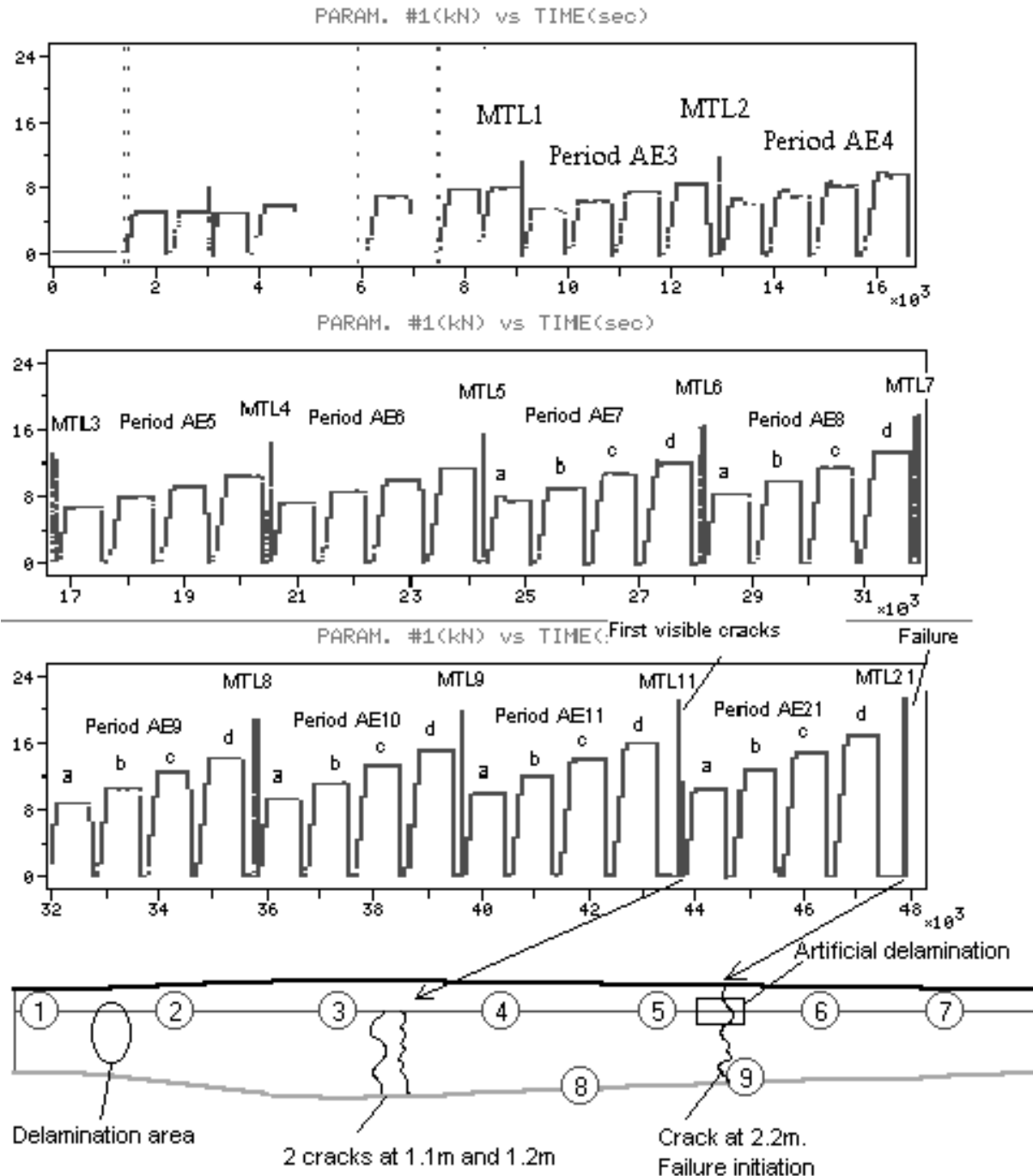


Fig. 5. Loading envelope of Blade #7 indicating loading stages, and damage information.

Each AE proof test was graded using the AEGIS software and the grading strategy defined in the previous paragraph, herein. Grading of some characteristic periods is presented in Table 1. It is worth noting that, prior to loading MTL5, the grading did not reveal any grades other than “A” or “no-grade”, meaning complete absence of critical AE data and the blade did not exhibit any visible damage. The grading of sensor 1 (closest to the delamination area) and sensor 3 (closest to the crack formed during MTL11 test) gradually increases from “A” (period AE7D) to “E” (period AE11E) giving a very good warning of the impending damage, i.e. the crack first seen after period MTL11. During the periods AE21A to E, sensor 5 was graded “E”, while the blade failed catastrophically during the next test (MTL21) exactly in the area of sensor 5. Grading of the rest of the periods is not presented due to space limitations.

Table 1. Graded Blade #7 ■ ■ ■ ■ ■		Period/Load-hold level (kN)
		AE7D 12.48
		AE8D 13.44
		AE9D 14.4
		AE10D 15.36
		AE11D 16.32
		AE21D 17.28

Supervised Pattern Recognition and Grading of Blade #8

The blade layout, sensor positions and load application point of Blade #8 were identical to Blade #7 (see Fig. 4). The blade was fatigue-tested with a sinusoidal load ranging from 1.2 to 12 kN, at a frequency of 1 Hz (Fig. 6 middle). Prior to fatigue testing, static AE proof-type tests were applied to assess the ability of the blade to sustain fatigue loads. The applied static loading envelope is shown in Fig. 6, top, where the loading stages are, also, indicated. Apart from an artificially imposed skin delamination, located from 2 m to 2.2 m from the root, there was no other visible damage present on the blade during the last visual inspection prior to failure, which was estimated to have taken place less than one hour prior to failure. The blade failed after about 75K cycles into fatigue testing. Visual inspection after the test revealed that the blade failed with a crack on the compressive side between 1.8m and 2.0m from the root, close to sensor 5 (Fig. 6 bottom). Each preliminary AE proof test was graded using the AEGIS software and the grading strategy defined in the previous paragraph, herein. Grading results are presented in Table 2 and are summarized below. Here, note that:

- a. Grading of Periods AE1a and b, does not yield any severe grade, indicating that the applied load (6 kN) could probably be sustained by the blade.

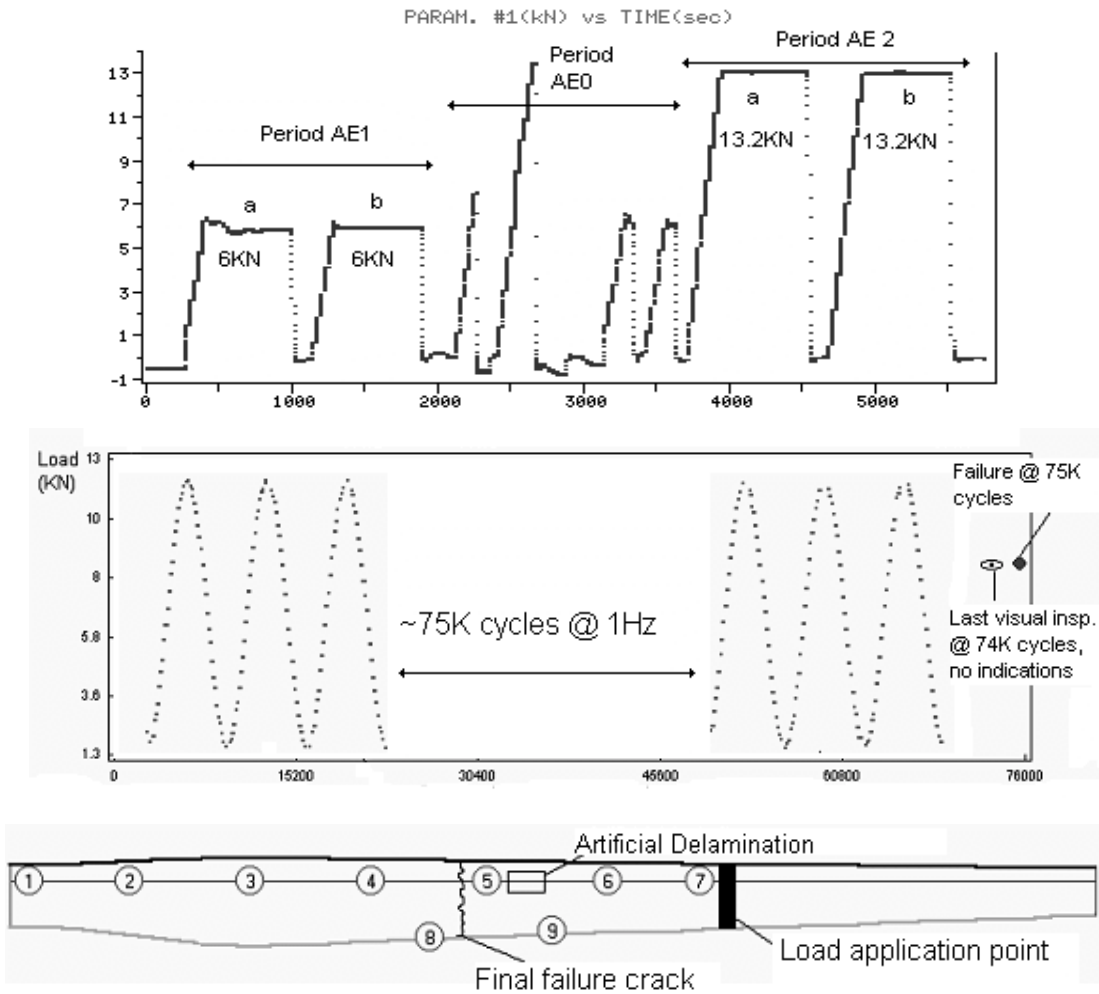


Fig. 6. Static loading envelope of Blade #8 indicating loading stages (top), fatigue envelope (middle) and damage information (bottom).

Table 2: Graded Blade #8	Period /Load-hold level (kN)
	AE1a 6 (50% of max. fatigue)
	AE1b 6 (50% of max. fatigue)
	AE2a 13.2 (110% of max. fatigue)
	AE2b 13.2 (110% of max. fatigue)

b. Grading of Periods AE2a and AE2b yield E grades, indicating that the applied load (13.2 kN) is severe for the blade.

Conclusions

An automated method for the assessment of the structural integrity of wind turbine blades and of their ability to withstand specific load levels has been developed and verified in a series of static and fatigue tests to failure of small-scale wind-turbine blades. The method involves static proof-loading of the blade and load-hold at the load of interest. AE activity during the load-hold is classified by a trained supervised classifier, to classes resulted from UPR classification performed on the AE data obtained from the last load-hold prior to failure of the first tested blade. Each zone of the blade is, subsequently graded, from “A” to “E” based on the number of AE hits classified with the critical class (revealed from the first blade) of each corresponding AE sensor. A grade “A” indicates that there is minor or insignificant (for the specific load) damage on the blade, while an “E” grade indicates that the applied load causes severe damage and cannot be properly supported by the blade. The same grading strategy was applied on all tested small blades under the AEGIS project with encouraging results, considering the fact that different blades failed in different ways (some of them very suddenly, with buckling) while different loading envelopes were applied. In most of the blades, including Blade #7, an “E” grade was assigned right before ultimate failure (or extreme damage), even during loading levels in which the blade did not exhibit any visible damage, and where it would have been otherwise unknown whether failure was pending. Additionally, the applied grading prior to fatiguing Blade #8, implied severity of the fatigue load levels and the blade failed after 75 k-cycles. Future work will include application of the same grading strategy during static and fatigue loading of large, commercial-scale blades, in order to assess whether the method can be applied to different blades, or further refinement and calibration of the method is required. A finalized version of such a method will provide manufacturers a tool to assist in blade design improvement and to users a fast and effective means for evaluating a blade’s condition (both new and in-service), increasing, thus, the overall reliability and cost effectiveness of wind turbines.

Acknowledgements

This work was supported by EC, Non-Nuclear energy program under contract number JOR3-CT98-0283.

References

- [1] IEC 61400-1, *Wind turbine generator systems - part 1: safety requirements*, 1998.
- [2] IEC 61400-23 TS ed. 1: *Wind turbine generator systems - part 23: Full scale structural testing of rotor blades for WTGS's*, draft 1999.
- [3] Sutherland, H., et al, “*The Application of Non-Destructive Techniques to the Testing of a Wind Turbine Blade*”, Sandia National Labs Report, Ref: SAND93-1380. UC-261, NM, U.S.A., June 1994.
- [4] Kouroussis, D.A. and Anastassopoulos, A.A., “*Analysis of Acoustic Emission Data from a 12-m F.R.P. Wind Turbine Blade During Flapwise Bending*”, Envirocoustics A.B.E.E., Technical Report, Ref: TR-001-8/98, Athens, August 1998.
- [5] Dutton, A.G., et al, “*Acoustic Emission Monitoring from Wind Turbine Blades Undergoing Static and Dynamic Fatigue Testing*”, Proceedings of the 15th World Conference on Non-Destructive Testing, Rome, Italy, 15-21 October, 2000.
- [6] Joosse, P.A., et al, “*Acoustic Emission Monitoring Of Small Wind Turbine Blades*”, 21st ASME Wind Energy Symposium, 14-17 January 2002, Reno, NV U.S.A.
- [7] Nikolaidis, V.N., Kouroussis, D.A., Anastassopoulos, A.A., “*AEGIS Software Manual*”, Envirocoustics A.B.E.E. Technical Report, Ref: TR-015-10/2000, Athens, October 2000.
- [8] Philippidis, T.P., Nikolaidis, V.N., Anastassopoulos, A.A., “*Damage Characterisation of C/C laminates using Neural Network Techniques on AE Signals*”, NDT and E International, **31**(5), 1998, 329-340.
- [9] Anastassopoulos, A.A., et al, “*A Comparative study of Pattern Recognition Algorithms for Classification of Ultrasonic Signals*”, Neural Computing & Applications, **8**, 1999, 53-61.

LOW ALLOY STEEL METAL DUSTING: DETAILED ANALYSIS BY MEANS OF ACOUSTIC EMISSION

P. J. VAN DE LOO¹, A. WOLFERT¹, R. SCHELLING¹, H. J. SCHOORLEMMER²
and T. M. KOOISTRA³

¹ Shell Global Solutions, Materials and Inspection, Amsterdam, Netherlands

² Physical Acoustics Limited, Rotterdam, Netherlands

³ HTS Haarlem, Aeronautics

Abstract

The process of metal dusting of low alloy steel subjected to an equal mixture of CO and H₂ gas at elevated temperatures has been monitored on-line with the aid of acoustic emission (AE). To a test tube a programmable temperature gradient was applied. Two AE sensors allowed continuous monitoring of AE activities as function of time and position/temperature. At regular intervals the tube was opened and examined for the presence of dusty powder. Two clearly distinctive metal dusting activities were identified: oxide dusting in the range of 380 to 420°C, and metal (bulk) dusting, being most reactive at temperatures from 425 to 500°C. On the basis of AE pattern recognition techniques, noise and relevant signals can be distinguished. The application of AE has considerably contributed to the identification of the dusting processes and interpretation of the test results. AE will further be used to study different process conditions and inhibition effectiveness.

Keywords: metal dusting, oxide dusting, AE monitoring, pattern recognition, process parameters

1. Introduction

Metal dusting is a detrimental chemical process by which low and high alloy steels can rapidly disintegrate into powdery dust consisting of carbon and metal particles. Detailed information about this phenomenon is given in References [1 – 9]. Because many processes contain synthesis gas, consisting of a CO and H₂ mixture at various temperatures, material and process engineers need a better understanding of all parameters which may lead to this detrimental process. This is required to avoid the critical process conditions, to enable proper material selection, and, when appropriate, to study the effectiveness of inhibition measures.

In the past, a number of coupon tests had been performed in the Shell laboratories. Effects of the test parameters applied were mainly judged at the end of a pre-defined test period. This gave insufficient insight in the process dynamics. At the EWGAE2000 at Senlis 2000, Elf Autochem paper showed the feasibility and advantages of the application of AE during metal dusting tests [10]. We decided to apply a similar test set up in our Shell laboratory. Main difference was the selected steel type and cooling of the tube ends where the sensors were mounted (see Sec. 2). Apart from protecting the sensors to overheating, a temperature gradient was introduced in this test set up.

Together with the linear localisation technique of the two AE sensors, AE activities could be correlated to both position and discrete temperature regions on the tube. This appeared to be an effective approach to get insight in the temperature dependence of the dusting process.

2. Experimental Set-Up

The material of main interest is steel 13CrMo44 with the following composition:

Chemical composition (% weight)								
C	Si	Mn	Cr	Mo	Ni	V	W	Others
0.14	0.2	0.55	0.98	0.6	-	-	-	-

The test tube dimensions and external furnace are given in Fig. 1. Details of the AE sensor mounting and the cooling part are given in Fig. 2.

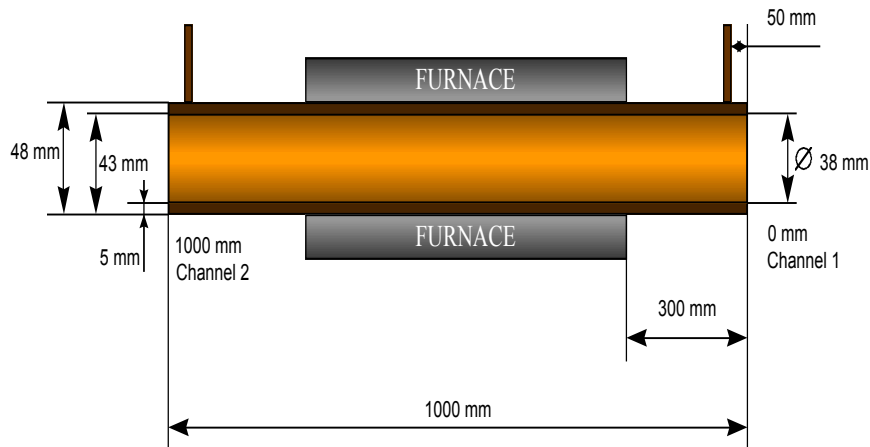


Fig. 1. Tube dimensions.

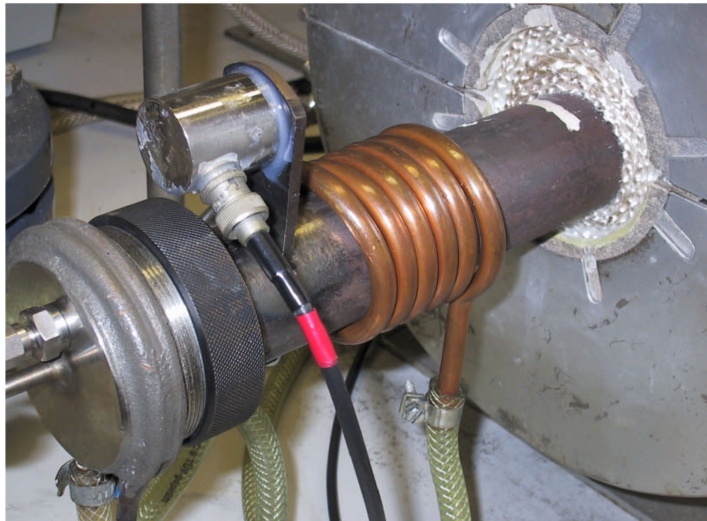


Fig. 2. AE sensor & cooling part.

The heating and cooling of the furnace is computer controlled. The maximum temperature in the furnace is set and by calibration measurements the resultant tube skin temperature (which is equal to the internal gas temperature) has been determined. An example of a measured temperature profile is given in Fig. 3. Away from the centre one can observe very steep temperature gradients. This implies that with a limited localisation accuracy the correlation with absolute temperature may have limited accuracy (see Sec. 3).

In all tests, an equal CO/H₂ gas mixture was applied at an injection rate of 100 ml/min. In future tests the mixture will be varied.

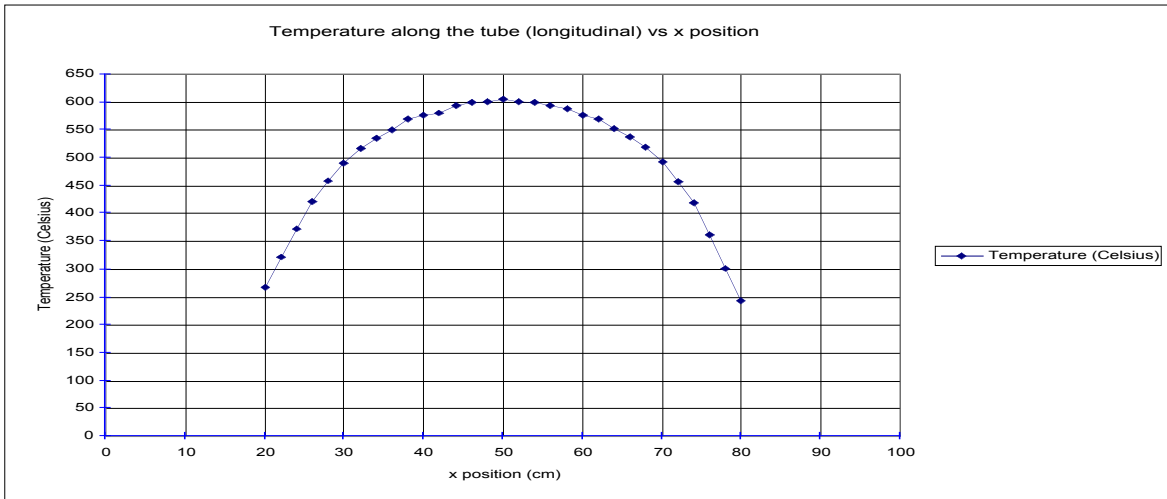


Fig. 3. Temperature profile along the tube.

We used PAC R15I resonant sensors with a peak sensitivity of 109 dB, operating frequency 70 – 200 kHz, resonance frequency 125 kHz, 40 dB gain integral pre-amplifier for 50 Ω load. The attenuation over the tube section between the sensors was 3.3 dB. Sensor 2 is 1.4 dB more sensitive than sensor 1. Data handling and analysis is done with PAC's Mistras and Noesis system [11]. For all tests the threshold was set at 43 dB. The filter range from 10 kHz to 400 kHz was used. Sample rate was 4 MHz, pre-trigger time 20 μ s (= 7.8 % hit length) and hit length 1 k-sample (= 256 μ s).

3. Results

On the basis of experience and the available literature data initial tests were started at relatively high temperatures ($> 500^{\circ}\text{C}$). We then observed that directly after start-up of the experiment AE activities were not registered in the middle of the tube where the highest temperature is present, but observed 20 to 30 cm left and right from the centre (Fig. 4). After various repetitive tests at the same tube the activity rate decreased and finally stopped.

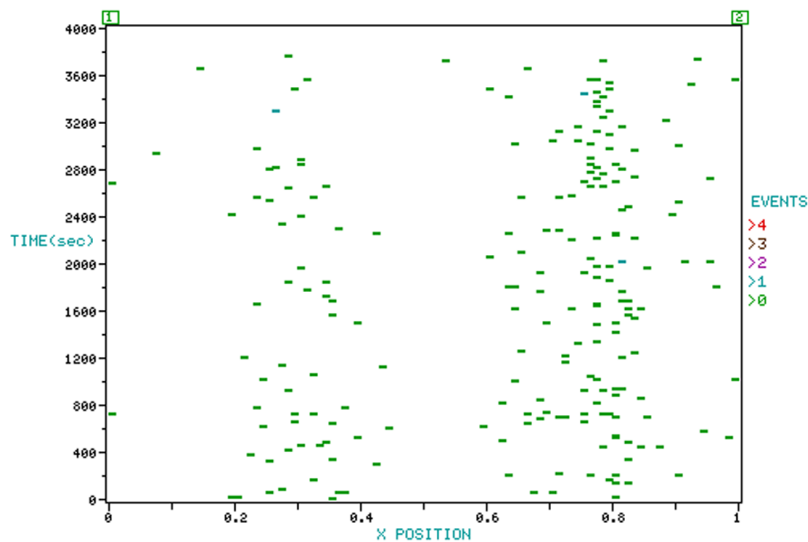


Fig. 4. AE events as a function of time (vertical axis) and position (horizontal axis). Maximum tube temperature at the centre (x position = 0.5 m) = 500°C . Approximate temperature at active areas: $380 - 420^{\circ}\text{C}$. At these positions dusty powder was found.

This could be explained and was later confirmed by more systematic tests: the observed dusting activities were related to dusting of the tube's oxide layer. The oxide scale is reduced by the gas mixture, resulting in highly dispersed iron particles. Iron concentrations of 70 % were measured. When this layer was consumed, the process stopped. By applying different temperatures different sections of the tube were consecutively consumed. Figure 5 shows a long duration tests with the maximum tube centre temperature at 400°C. We see initially most AE activities slightly left from the centre (left is the gas inlet side). Figure 5 indicates that most AE activities at this position occurred in the first 10 000 s (roughly 3 hours). The tube was almost blocked with loose dust at that position. From 15 000 to 25 000 s, an increased number of events was observed at the right (downstream) side of the centre. Maybe by the left hand (upstream) blockage, this process went slower, but also at this position dust was found. The oxide layer had disappeared. The rest of the signals may be related to scatter by localisation limitations: various dispersive modes, shifts in threshold passing by attenuation, etc. and maybe some slow dusting activities (much less active below 380°C). It is very unlikely that outside the furnace area, metal dusting will be active.

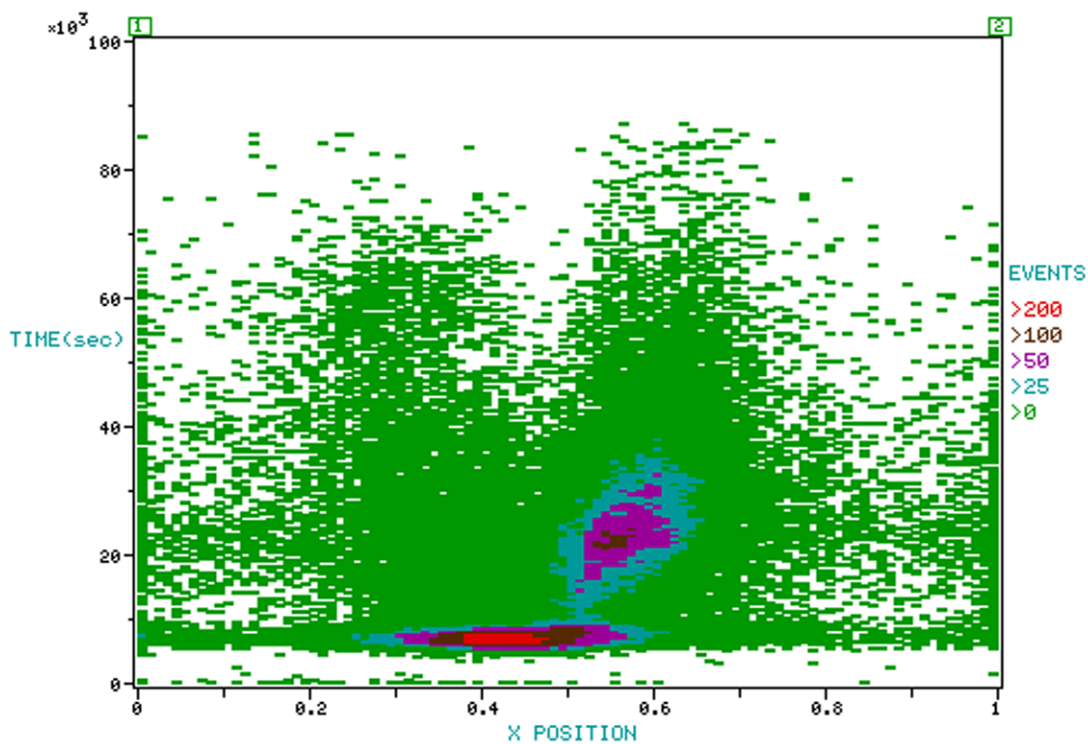


Fig. 5. Registered events during the oxide dusting process as a function of time and x position. Maximum tube temperature at the centre of the tube is 400°C.

The observations that the dusting was limited to the oxide layer alone and that it happened at relatively low temperatures of the process were rather unexpected. However, we do know that metal dusting of the bulk material is an existing problem, with indications that this happens at higher temperatures. Therefore, long-duration experiments at higher temperatures were performed on tubes where the oxide layer had been consumed by the above-described process. Figure 6 shows a typical example. The maximum temperature at the tube centre was 550°C. The activities left of the centre (at the gas inlet side) occur in an estimated temperature range of 425 to 500°C. Another interesting phenomenon is that the AE event rate increases as given in Fig. 7. This shows that the whole process requires a certain incubation time and then progresses at constant rate.

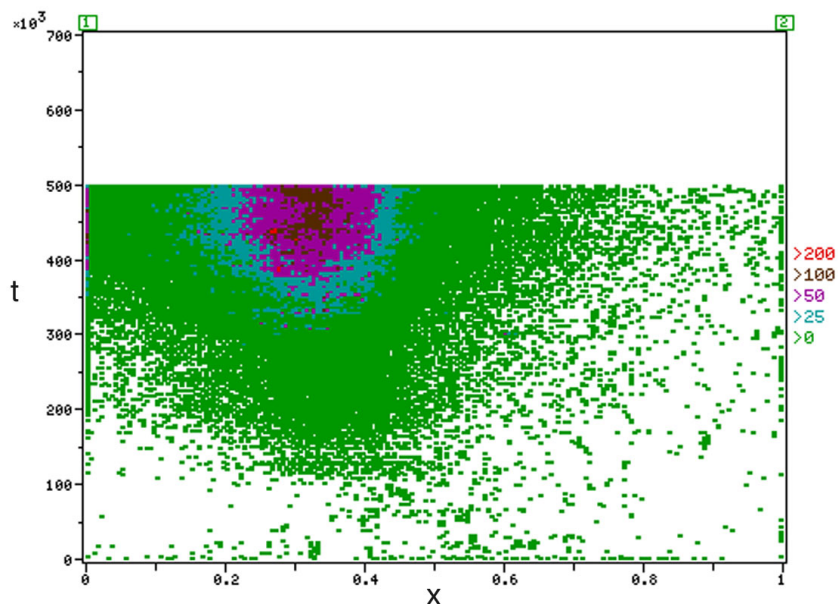


Fig. 6. Metal dusting AE events (color scale) on time (s) vs. x-position (in m) plot. Maximum tube temperature at the pipe centre: 550°C.

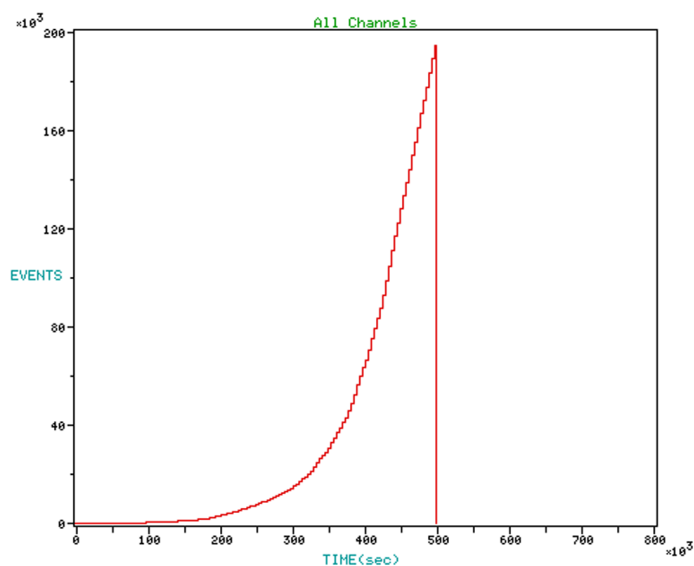


Fig. 7. Events (cumulative) vs time. Maximum tube temperature at the pipe centre: 550°C.

More tests were done. Figures 8 and 9 show test results where the maximum temperature of the tube was kept at 650°C. We observe that without incubation first AE activities occur close to the centre, thus in the temperature range from 600 to 650°C. After 150 000 s (= 42 hours) increased activities start further left from the centre (estimated temperatures between 425 and 500°C). With a symmetric temperature profile one would expect also activities at the right (gas outlet) side of the tube. A rough estimate of the C-balance from the CO injection and the carbon formation indicates that most of the reactive gas components have been consumed at the left part and that “downstream” a different gas composition will be present. This may explain the asymmetric behaviour.

At the end of the test, black powder and hard solid material (coke formation in a confined space) was found at the region of AE activities.

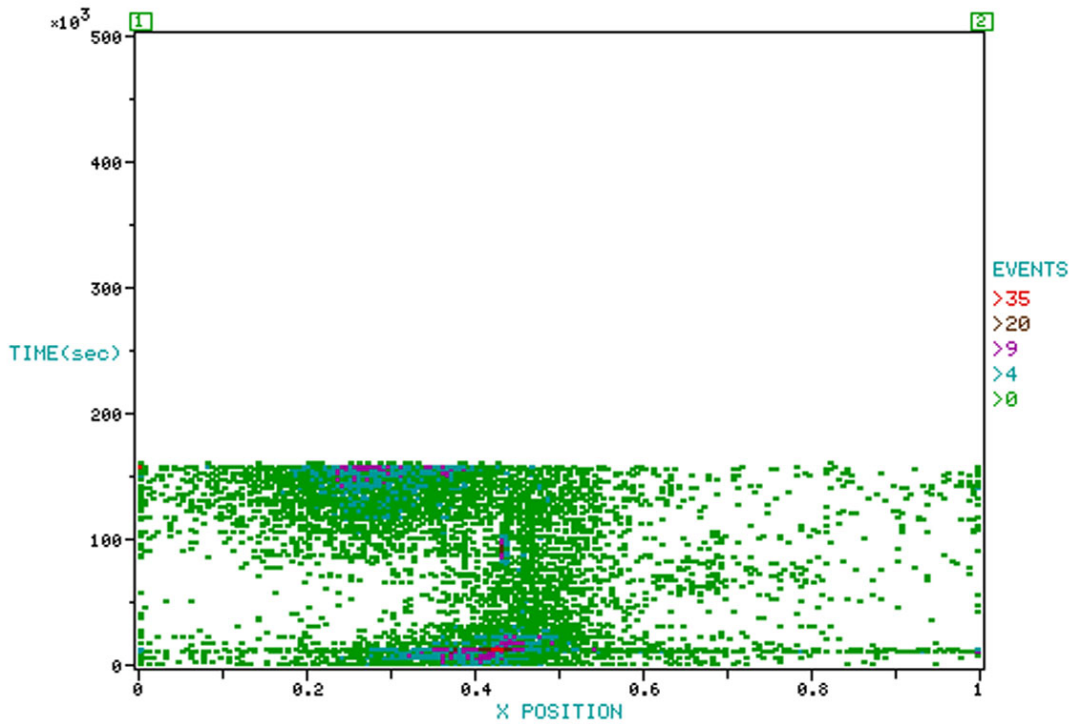


Fig. 8. Time vs x-position and metal dusting events. Maximum tube temperature: 650°C.

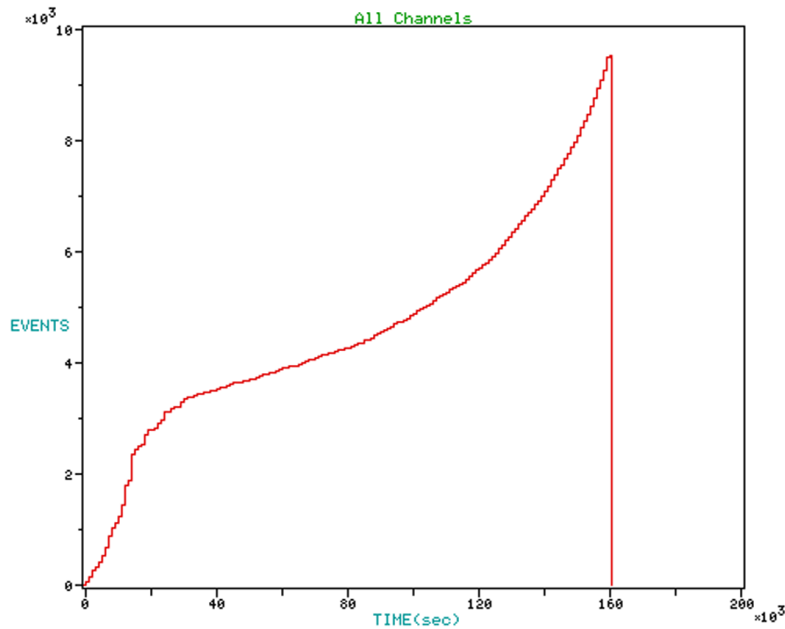


Fig. 9. Metal dusting events (cumulative) vs time. Maximum tube temperature: 650°C.

Finally we want to show test results, which were obtained when stepwise temperature changes (25°C) were applied (see Fig. 10). We observe that the first significant increase of AE activities happens when the temperature in the middle of the tube drops from 500 to 475°C. The activities are slightly left from the centre, thus at slightly lower temperature than the reported maximum temperatures. The increments are only for a very small amount related to shrinkage activities: see the minor steps at higher and lower temperatures. This is also confirmed by the signal characteristics as derived from pattern recognition.

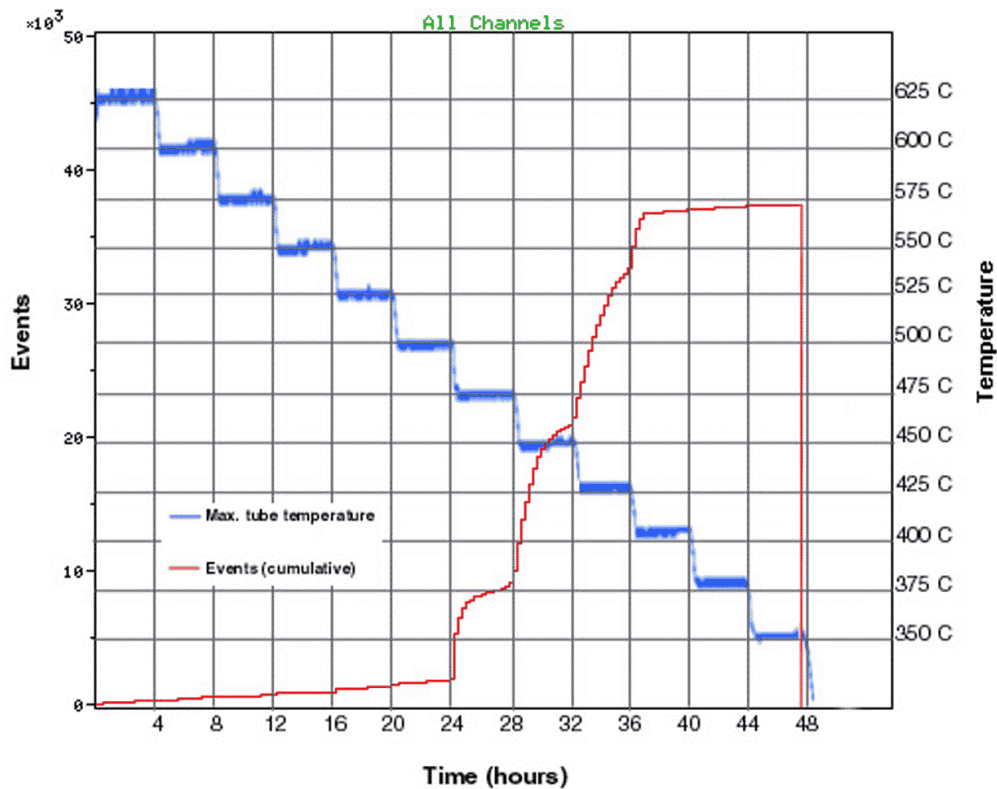


Fig. 10. Cumulative events in relation to temperature steps. Events are related to metal dusting (confirmed). Temperatures are maximum tube temperatures at the tube centre.

We have to keep in mind that the duration of the periods with constant temperature was only 4 hours. From Fig. 9 we learned that the incubation time for the metal dusting process may be over 40 hours. So this test cannot be conclusive about process reactivity and temperature. However, the reason for presenting these test results here is to draw attention on a more interesting phenomenon: within the temperature range from 500 to 400°C the increments in activities occur at the short periods of the temperature steps and level out when the temperature is kept constant (faster at 475 and 400°C and slower in the mid-temperature region). The rate of change is very significant. This may indicate that vulnerability to metal dusting is largest when favourable process conditions are combined with the presence of certain strain rates, shrinkage or expansion due to temperature variations. This phenomenon requires further attention, particularly because this seems to be the fastest process. When the tube was opened, a hard ring of dusty powder was found, which almost fully blocked the tube.

4. Detailed Analysis/Pattern Recognition

In the previous section, the observed AE events were mainly related to three types of activities: oxide dusting, metal (bulk) dusting and noise, mainly due to shrinkage and expansion of the tube during temperature changes. By the controlled tests and follow-up investigations (dust powder analysis) the periods and conditions can be correlated to the distinctive processes. Now it is interesting to see whether these processes can be distinguished on the basis of their signal characteristics. To this end the pattern recognition programme Noeses has been used. First manual clustering was applied. Within Mistras it is very hard to select a set of data on the basis of their localisation. By judgement it appeared that dusting activities (from the furnace section of

the tube, where dusting was identified) mostly had energies >50 , whereas over the rest of the tube more random characteristics were present. These data were selected for further analysis.

Figure 11 shows that the counts and duration distribution plots (signals with energy >50) of the oxide and metal dusting process can clearly be distinguished. (Counts and duration are strongly correlated). The same can be done, to a lesser degree, on the basis of the other characteristics.

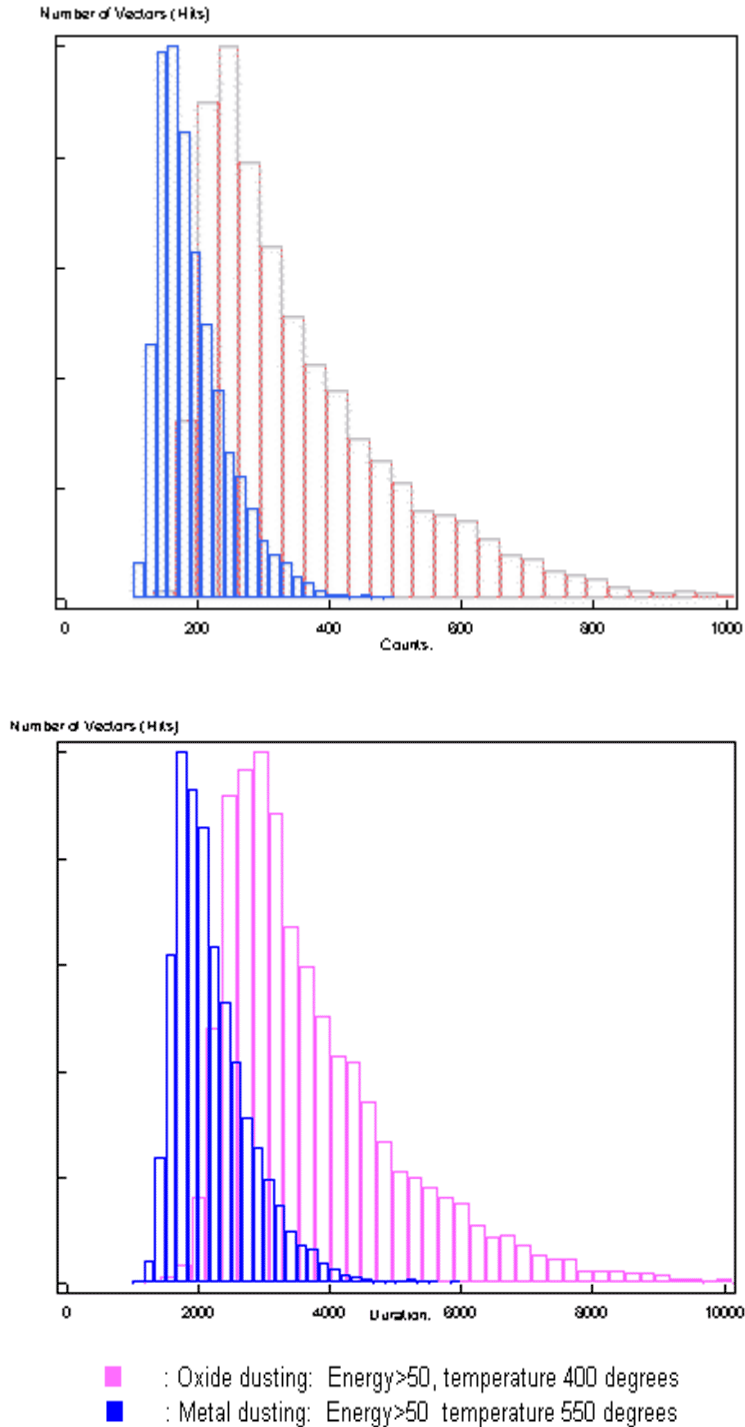


Fig. 11. Frequency distribution of counts (top) and duration (bottom). Oxide and metal dusting can clearly be distinguished.

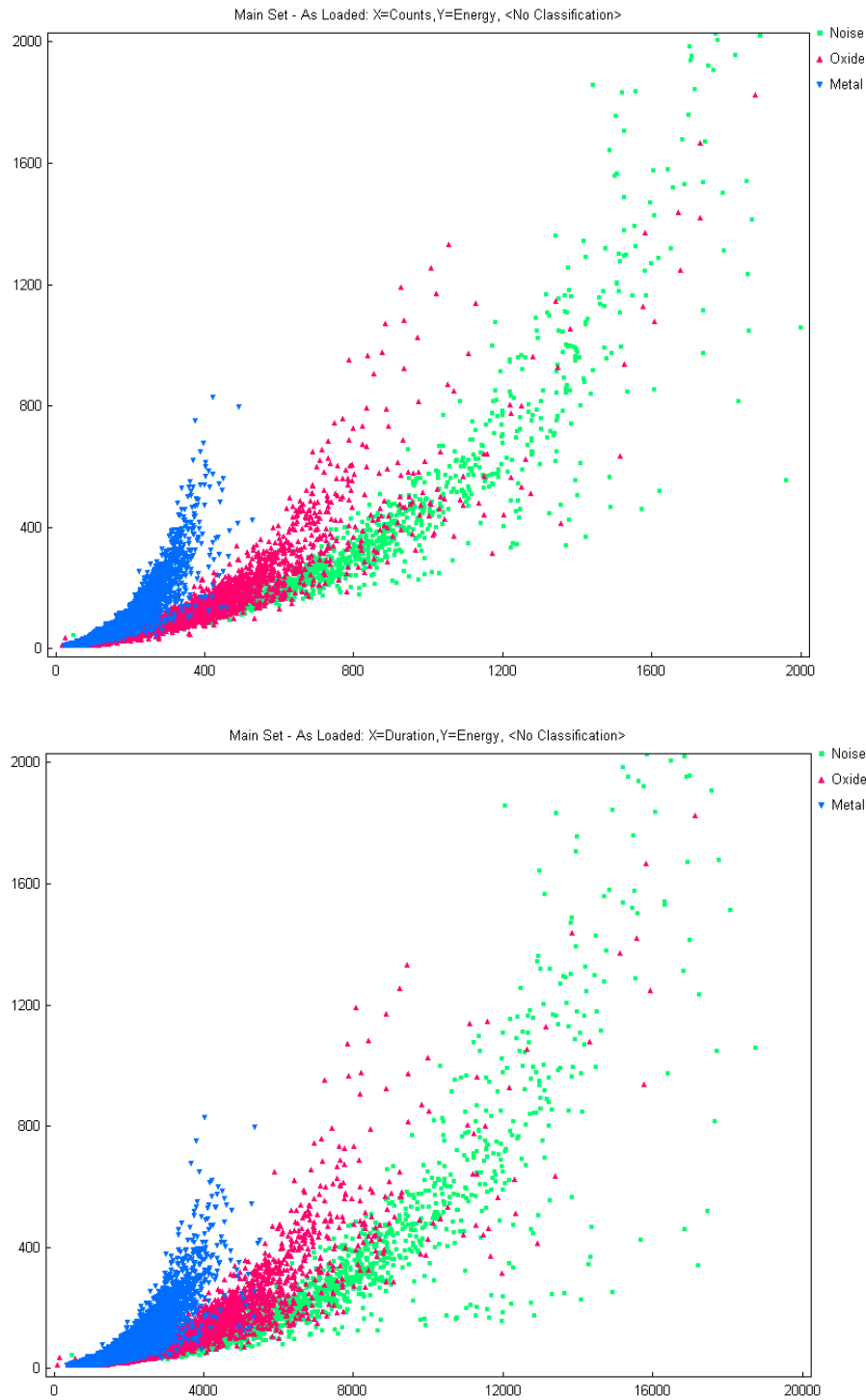


Fig. 12. Vector projection from unsupervised clustering: energy versus counts (top) and energy versus duration (bottom). The three clustered, related to noise, oxide dusting and metal dusting can clearly be distinguished.

Based on single characteristics we get the following discriminating power between the two dusting process activities:

- If the duration $>6000 \mu\text{s}$, then the chance that the hit is related to oxide dusting is 160 to 1.
- If the counts >500 , then the chance that the hit is related to oxide dusting is 70 to 1.

- If the average frequency >120 kHz, the chance that the hit is related to oxide dusting is 8 to 1.
- If the energy >500, then the chance that the hit is related to oxide dusting is 4 to 1.

Better distinction can be obtained when a combination of parameters will be used. To investigate this, unsupervised clustering has been applied to the complete data set of a mixture of oxide dusting, metal dusting and noise, mainly due to temperature variations. Figure 12 shows vector projection of energy vs. counts and duration vs. counts. The three distinctive phenomena are clearly separated. As was done with the manual clustering, best separation is obtained at higher energy levels.

5. Concluding Remarks

Two clearly distinctive metal dusting activities were identified: oxide dusting in the range of 380 to 420°C, and metal (bulk) dusting most reactive at temperatures from 425 to 500°C. On the basis of AE pattern recognition techniques, noise and relevant signals can be distinguished. The application of AE has considerably contributed to the identification of the dusting processes and interpretation of the test results. Insight was gained in the process dynamics, incubation times, etc. AE will further be used to study different process conditions and inhibition effectiveness.

References

1. R. F. Hochman, "Catastrophic deterioration of high temperature alloys in carbonaceous atmospheres", *Proceedings of Symposium on Properties of High Temperature Alloys*, Z.A. Foroulis and F.S. Petit, eds, Elec. Chem. Soc., 1976, pp. 715 - 732
2. H. J. Grabke, C. B. Bracho-Troconis and E. M. Muller-Lorenz, "Metal dusting of low alloy steels". *Werkstoffe und Korrosion*, **45**, 215-221 (1994).
3. R. J. Gommans and T. L. Huurdeman, "Experience with Metal Dusting in Waste Heat Boilers". DSM Fertilizers, Geleen, The Netherlands, pp. 145-162.
4. P. F. Tortorelli, J. H. DeVan, R. R. Judkins and I. G. Wright, "Solid-state phase stabilities of relevance to metal dusting in coal gasifier environments". *Materials and Corrosion*, **49**, 340-344 (1998).
5. M. Maier, J. F. Norton and P. D. Frampton, "Metal dusting of 9 - 20% Cr steels in increased pressure environments at 560° C". *Materials and Corrosion*, **49**, 330-335 (1998).
6. H. J. Grabke, D. Monceau and E. M. Muller-Lorenz, "Metal Dusting resistance of steels in the temperature range 500 - 600°C", MPI für Eisenforschung, Düsseldorf, Germany.
7. M.J. Bennett, "Carbon deposition: A major technological problem". *Materials and Corrosion*, **49**, 345-351 (1998).
8. P.A. Lefrancois and W. B. Hoyt, "Chemical Thermodynamics of High Temperature Reactions in Metal Dusting Corrosion". *Proc. the 19th Annual Conference of the National Association of Corrosion Engineers*, March 11-15, 1963, New York. pp. 360t - 368t.
9. M. L. Holland and H. J. de Bruyn, "Metal dusting failures in methane reforming plant". *Int. J. Press. Vessels and Piping*, **66**, 125-133 (1996).
10. F. Ferrer, E. Andres, J. Goudiakas and C. Brun, "Using acoustic emission to monitor metal dusting". *Proc. 24th European conference on Acoustic Emission Testing*, EWGAE, Senlis 2000.
11. Mistras and Noesis: Acoustic emission data analysis and pattern recognition systems of Physical Acoustic Corporation.

RECONSTRUCTION METHOD OF DYNAMIC FRACTURE PROCESS INSIDE THE MATERIAL WITH THE AID OF ACOUSTIC EMISSION

YASUHIKO MORI¹, YOSHIHIKO OBATA¹ and TAKATERU UMEDA²

¹ College of Industrial Technology, Nihon University, Narashino, Chiba 275-8575, Japan

² Faculty of Engineering, The University of Tokyo, Tokyo, Japan; now at Faculty of Engineering, Chulalongkorn University, Bangkok 10330, Thailand

Abstract

A method, which combines a confocal-optics-based scanning laser microscope (SLM) and computer software to match three-dimensional features of conjugate fracture surfaces and reconstructs microscopic fracture processes that occurred inside the materials, has been developed. This method can visualize the location of crack initiation and successive micro-crack extension behavior. The quantitative information about crack, such as length, displacement between crack surfaces and direction of crack extension are also obtained from the method. The method, however, is unable to evaluate the forces required to initiate or extend a crack observed. In order to resolve this problem, acoustic emission (AE) test was combined with the method. Pearlitic spheroidal graphite cast iron was selected as a model material for this study, and its notched bar sample was broken in tension, where the AE was simultaneously measured. Reconstructed fracture process revealed that crack initiation and growth started in the middle of the specimen. Micro-fracture onset load level and successive fracture processes inside the specimen were estimated and traced by the AE signals measured. This study demonstrates the utility of the AE technique, which rectified the deficiency of another material evaluation method.

Keywords: fracture process, internal crack, cast iron, scanning laser microscope, AE

1. Introduction

Materials development requires an understanding of detailed micro-fracture mechanisms; i.e., in what part of the material a micro-crack starts, how the growing crack interacts with various constituents, and what mechanism resists crack growth. Crack observation of the sample under stress is needed to give answers about these fracture processes.

There are a number of reports that *in-situ* crack growth observation has been done during fracture toughness test, which was conducted under the scanning electron microscope or ultrasonic microscope [1 - 5]. These applications, however, gave us only the surface or subsurface information of crack growth behavior. On the other hand, acoustic emission (AE) is a promising method for monitoring changes that occur inside a material. In addition, in some cases, it is possible to estimate the size and fracture mode of a micro-crack by analyzing the signal waveform of AE signals [6, 7]. However, the AE method is limited to make a complete trace of crack growth in relation to the material constituents on a crack path, with which the growing crack might interact.

The fracture surfaces of a broken part record the details and sequence of micro-fracture processes that led to the failure. Kobayashi and Shockey [8] developed a fracture-surface topography analysis technique, FRASTA, which combines a confocal-optics-based scanning laser micro-

scope (SLM) and computer software to match three-dimensional features of conjugate fracture surfaces. This leads to the reconstruction of detailed fracture processes that occurred inside the material. We also have developed a technique, which can reconstruct the fracture process in microscopic details by using the computer aided image processing for the topography of conjugate fracture surfaces obtained by an SLM [9]. However, though the method can characterize the growth of micro-fracture events from evaluation of the fracture surface, the method is unable to evaluate the stress or strain level, at which the crack initiation or growth occurred. Thus, the AE method was combined with the reconstruction method. By comparing AE signals generated from the fracture surface with the results of fracture surface analysis, it is possible to relate each micro-fracture event to a specific AE event; i.e., the stress state at which the micro-fracture event occurred. This combination technique eventually will make it possible to interpret the physical meaning of an AE signal. It should make AE monitoring a more effective method to evaluate the condition of structure.

This paper reports that the combined SLM/AE method was applied successfully to answer a problem existed in cast iron. In ductile cast iron, spheroidizing the graphite distributed in the matrix increases the strength of the material. The strength of the cast iron, however, depends on the sample shape. For instance, in the case of a bar specimen, it has been reported that the existence of notch did not decrease the strength substantially and in fact increased the strength in some cases [10-13]. Several models have been proposed for the explanation of this notch strengthening; e.g., the effect of the non-uniformity of stress distribution around the notch root [12, 14, 15], or the internal notch effect of graphite nodule distributed in the matrix [16]. Therefore, the dynamic behavior of the graphite nodule and the internal fracture process are needed to determine the fracture mechanism of the material.

In the present paper, tensile tests and AE measurements were conducted on bar specimens of pearlitic spheroidal graphite cast iron. SLM technique was applied for the broken sample to examine how the graphite nodules in the matrix contributed to the fracture process in the material. Actual dynamic fracture events were estimated by the AE signals. This paper visually demonstrates that the graphite nodule acts as internal crack and proposes a fracture model built around the graphite nodule.

2. Experimental

The material used was a pearlitic spheroidal graphite cast iron, having retained pearlite of 98.9%, nodularity of graphite of 81%, graphite area of 9.5%, number of graphite nodule per area of $244/\text{mm}^2$, and mean graphite nodule diameter of 22 μm .

Smooth bar with gage diameter of 6 mm and circumferentially notched bars with outer diameter of 10 mm were stressed and fractured in tension. Shape of notches was U- and V-type, and the elastic stress concentration factor of notches, K_t , was estimated to be 2.0 and 3.8, respectively. Tensile test samples showed that all the specimens ruptured in flat fracture. Fracture strength (= tensile strength) of the smooth bar specimen was 940 MPa, showing the elongation of 6.6 %. Fracture strength of V-notched (stress concentration factor $K_t = 3.8$) specimen was 880 MPa. The observed decrease was 6% compared to the expected value of 74% due to the effect of K_t , implying that the notch strengthening exists. On the other hand, the sample failure of the U-notched specimen ($K_t = 2.0$) occurred at stress of 980 MPa, which exceeded the tensile strength of the smooth specimen by approximately 4 %. Again, the notch strengthening exists.

Figure 1 shows the applied stress, σ , and the cumulative counts of AE events, N , as a function of elapsed time of tensile test, t , for the U-notched specimen. Applied stress increases continuously until the specimen fractures. Acoustic emissions start at the stress level of about 90 % of the fracture strength of the specimen and increase continuously until the specimen fracture.

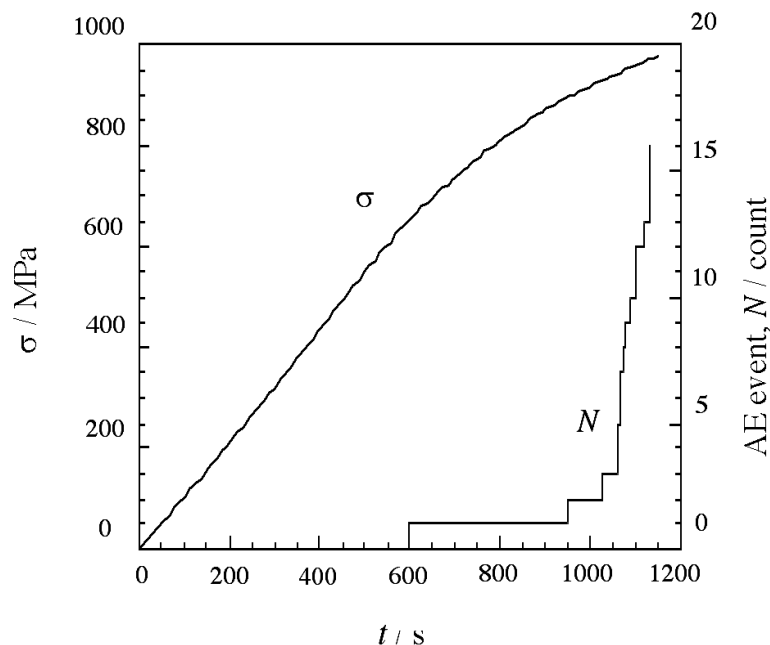


Fig. 1. Applied stress, σ , and AE event counts, N , vs. testing time, t . (U-notched specimen).

Fracture surface analysis by using an SEM showed that in the case of the V-notched specimens, fracture initiated at the notch root. AE in the V-notched specimens started at 85% of the fracture stress, similarly to Fig. 1. However, the stress-time curve was linear to fracture (at 880 MPa). V-notch fracture initiated at the notch. In the U-notched specimens, however, the traces of crack initiation site were not clearly left on the fracture surface. So the fracture process of the U-notched specimen was reconstructed and analyzed by using SLM technique.

3. Reconstruction of Fracture Process

Figure 2 shows the macroscopic features of conjugate fracture surfaces of the U-notched sample. SLM observations were performed on the five locations on the conjugate surfaces, which are labeled I to V in Fig. 2, because of the limitation of SLM field of view.

Figure 3 shows SLM micrographs (top) and corresponding gray-scale image topographs (bottom) of conjugate fracture surfaces of the area location III in Fig. 2. Scanning-laser micrographs show that the graphite nodules are individually distributed in the matrix. Gray-scale images show that lighter areas are higher in elevation than darker areas.

The fracture process of this area was reconstructed using topographic information from Fig. 3 (bottom) in digitized form. Maximum elevation resolution is $0.03 \mu\text{m}$, which is determined by dividing a specified range, i.e., the difference in elevation between the highest and lowest point within the observation field, by 256. Reconstruction of fracture process is accomplished by the following procedure. (1) Matching the three-dimensional features of conjugate fracture surfaces in a direction vertical to the specimen axis with the aid of a computer (Fig. 4a through 4d). This makes a reference state (Fig. 4d) for the successive procedure. If the surface irregularity, i.e., an

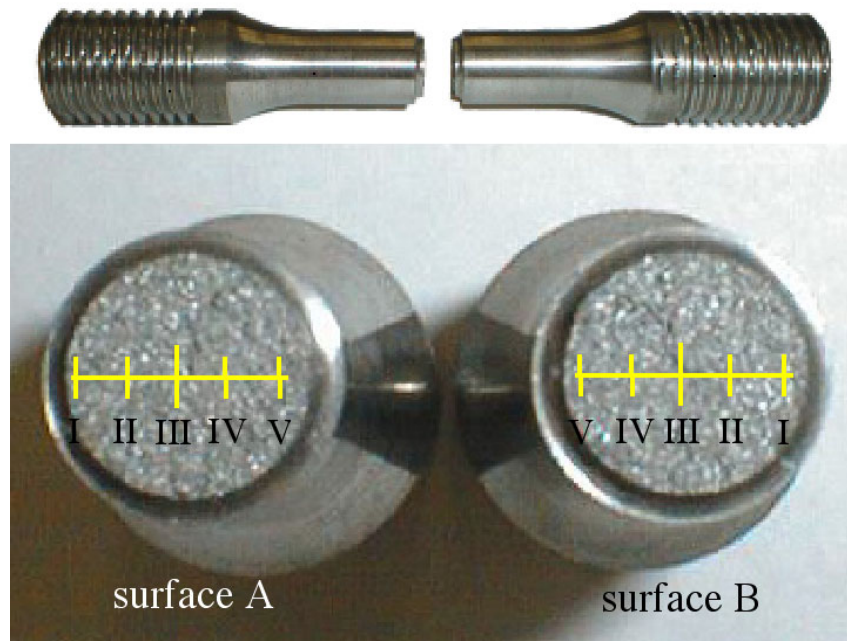


Fig. 2. Macroscopic fracture surfaces of U-notched specimen broken in tension.

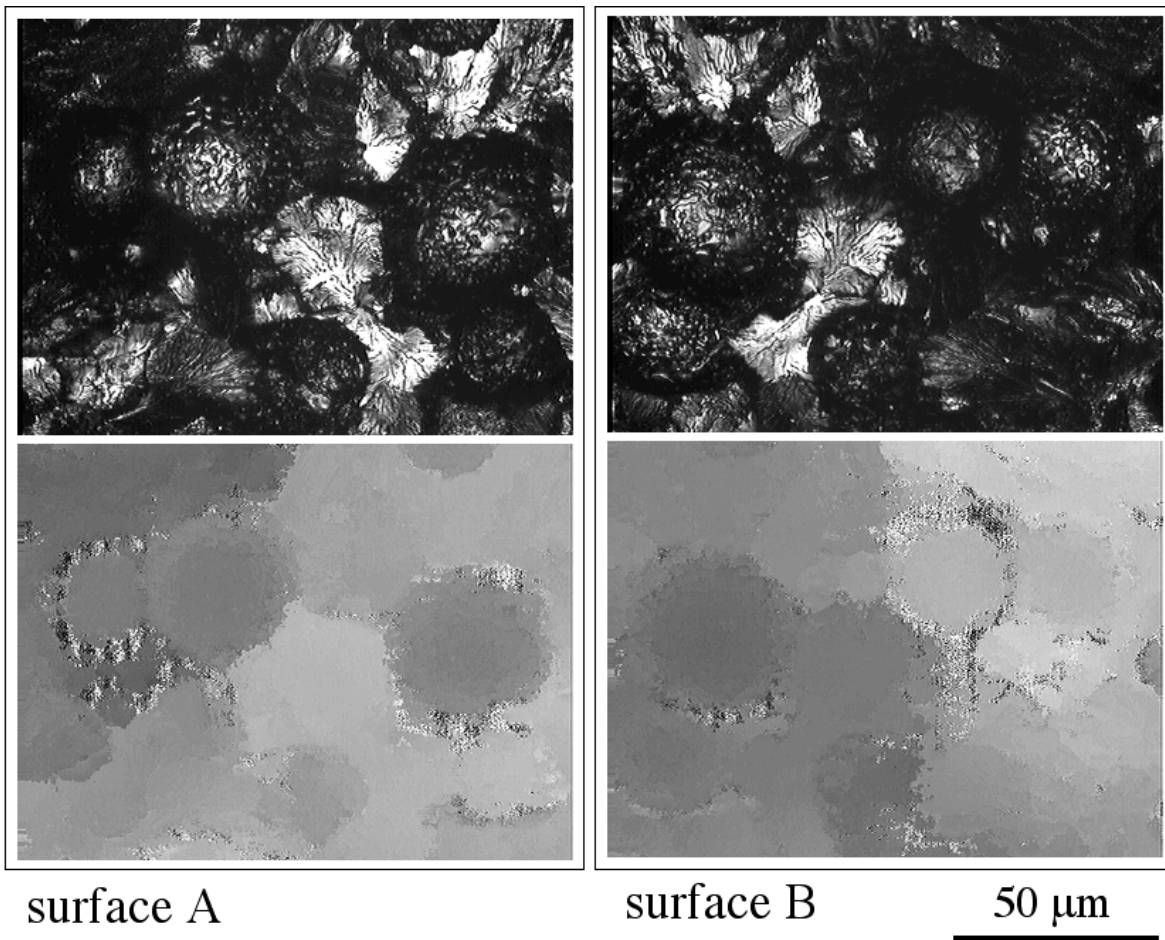


Fig. 3. Scanning-laser micrographs, top, and corresponding topographs, bottom, of conjugate fracture surfaces of the location III in Fig. 2.

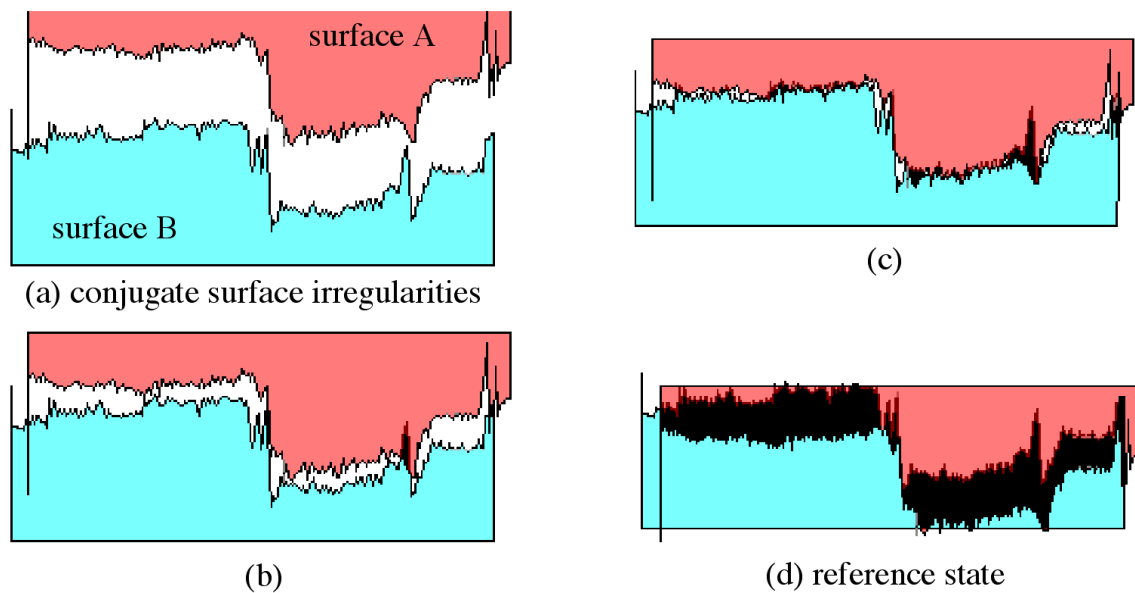


Fig. 4. Procedure of fracture process reconstruction, showing conjugate surface irregularities in two-dimension. Matching process, (a) to (d); reconstruction of fracture process, (d) to (a).

elevation profile on the fracture surface is caused only by the interaction of the crack tip with the microstructure and without inelastic deformation, the conjugate surface profiles should match precisely. Any mismatch appearing as overlap between the conjugate surface profiles indicates inelastic deformation (Fig. 4d). (2) Separating the two surface irregularities from a matching reference state in a direction vertical to the specimen axis using computer software (Fig. 4d through 4a). Displacement of the separation (ds) is increased step-by-step at a certain increment. Gaps, which appeared between the two surface irregularities in this sequential process, are projected on display equipment.

Figure 5 is a result of fracture process reconstructed for the location III shown in Fig. 2, showing the step-by-step development of the fracture. Black areas, where the conjugate surface profiles overlap, denote intact material. White areas, where the surface profiles do not overlap, are considered locations where the fracture surfaces are separated, i.e., cracked. Projection diagrams of fractured areas show that cracking initiated in the matrix around graphite nodules (Fig. 5a). As the applied stress is increased (see Fig. 1), i.e., as the conjugate fracture surfaces are displaced relative to one another, as denoted as “ ds ” in Fig. 5, micro-cracks grow slightly, debonding starts at the graphite/matrix interface (Figs. 5b and 5c). Increasing the stress further causes coalescence of micro-cracks (Fig. 5d) and development in the matrix forming a crack (Fig. 5e).

In order to estimate the entire fracture processes in the specimen, fracture processes for the locations I to V shown in Fig. 2 were reconstructed with a single reference state. The reference state, that is, the state of the specimen before loading, was found in the location III, at which the matching of the conjugate surface profiles was completed. A series of fractured area projection diagrams in Fig. 6 show the step-by-step development of the fracture. The reference state is the top of location III (center of the specimen) in the diagram. The displacement ds , in Figs. 5 and 6, is correlated with the applied stress level, since the applied stress continuously increased until the specimen failure, as seen in Fig. 1. Therefore, the result of reconstructed fracture process shown in Fig. 6 clearly demonstrates that as the stress is applied, micro-crack initiates at around the graphite nodules distributed in the middle of the specimen (location III), as seen in Fig. 5 in de-

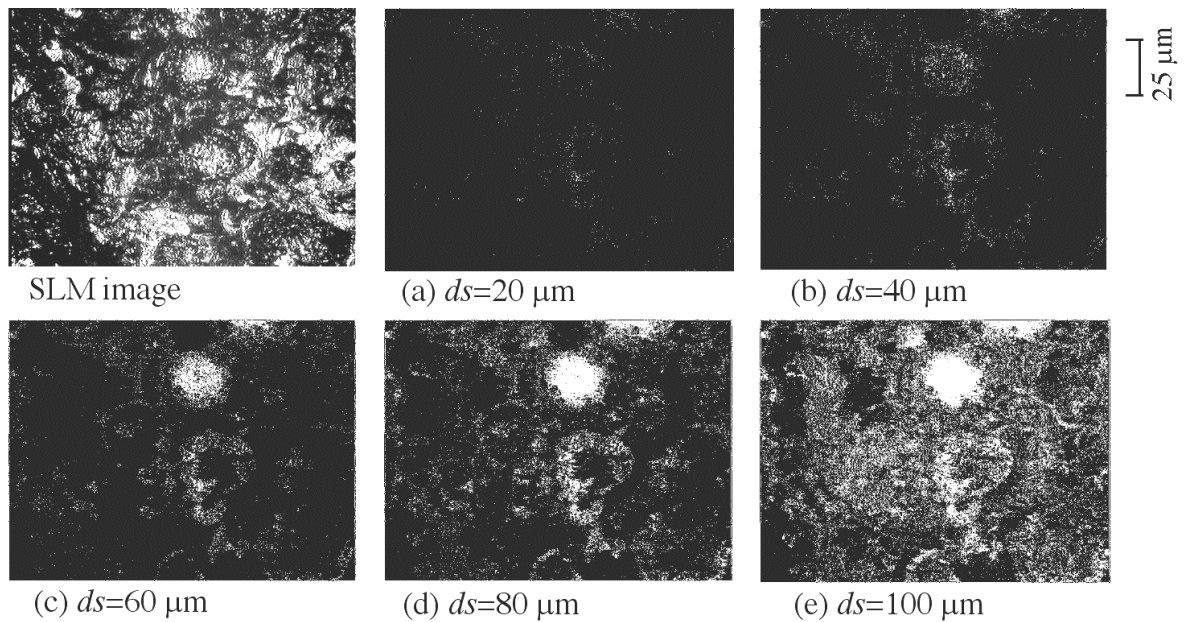


Fig. 5. Scanning-laser micrograph, left top, and a series of projection diagrams of fractured areas, (a) to (e), of the location III shown in Fig. 2.

tail. With increasing the stress further, the micro-cracks are also created successively at the graphite nodules in the locations of II, I, IV and V. Then, a crack is formed by the coalescence of these micro-cracks and grows outward (toward the notch root of locations I or V), and the specimen ruptures.

4. Approach from Acoustic Emission

Result of AE measurement during the tensile test of the specimen, of which fracture process was reconstructed, has been shown in Fig. 1. Generation of AE started at stress level about 90 % of the fracture strength of the specimen and increased continuously until the specimen rupture. The stress applied to the specimen also continuously increased until the specimen failure. From the fracture process shown in Fig. 6, the crack initiation and growth started inside the specimen and successive micro-fracture processes led to the failure. From the AE measurement, the nominal stress level of crack initiation was estimated to be approximately 850 MPa (Fig. 1).

Microstructure of the material tested showed that the graphite area amounted 9.5 % of the total and the number of graphite nodule was 244 nodules/mm². A total of 16 AE events were detected during the tensile test (Fig. 1). Though the number of AE events depends on the threshold level of AE discrimination, AE event counts measured were so small compared to the number of graphite nodules distributed over the crack path in the material. Therefore, it is expected that the generation of measured AE events were due to the matrix cracking; i.e., coalescence of micro-cracks initiated from each graphite nodule, formation of main crack, or successive crack growth, rather than micro-crack initiation around each graphite nodule.

5. Fracture Model

Fracture reconstruction revealed that the graphite nodule in the matrix behaves as void or pore in the ductile matrix stressed in tension. A model shown in Fig. 7 could be proposed to explain the fracture process around the spheroidal graphite nodule. As the material (Fig. 7a) is

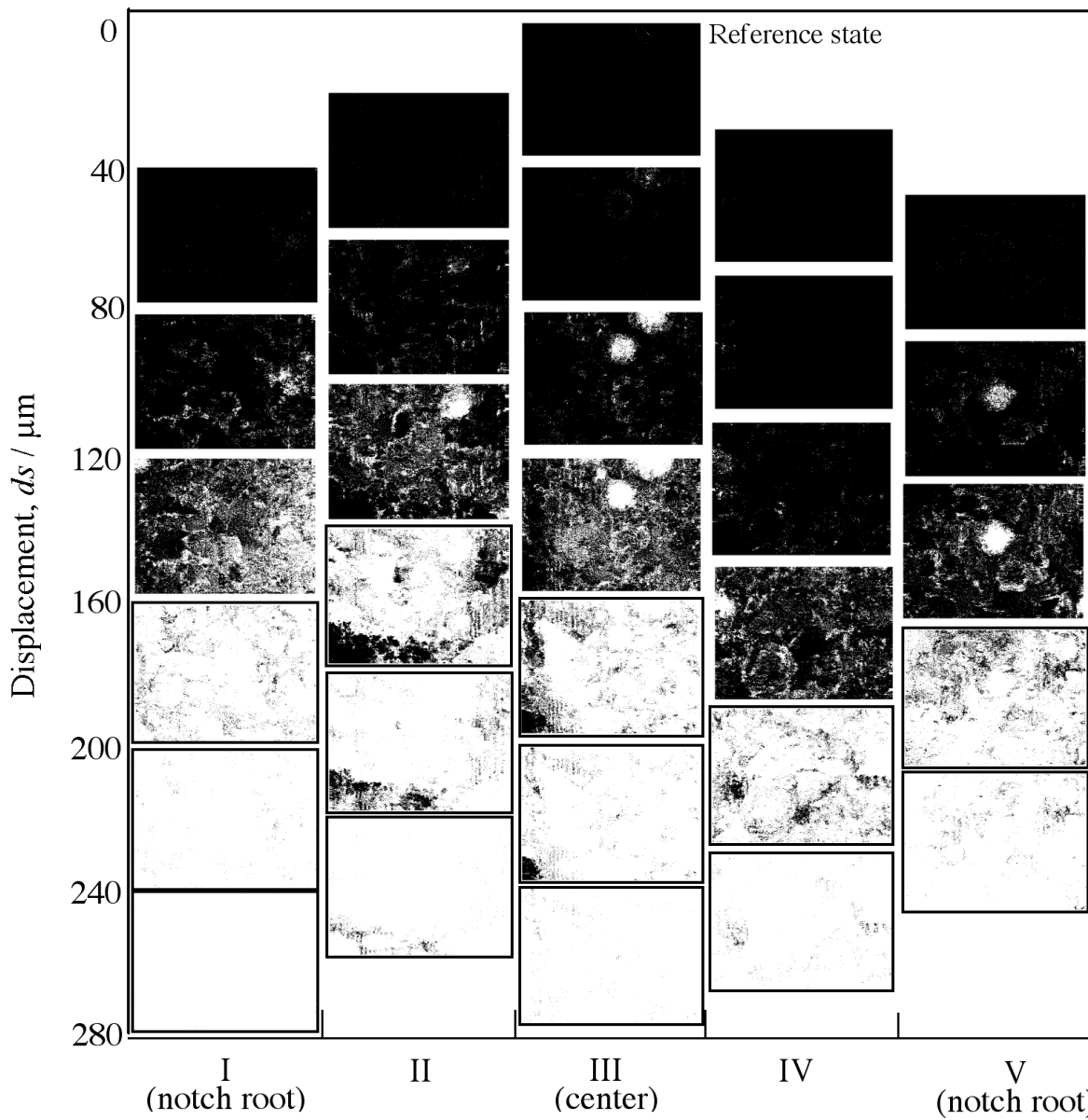


Fig. 6. Fractured area projection diagrams for the locations I to V shown in Fig. 2. Reconstructions of fracture process were performed with a single reference state (location III).

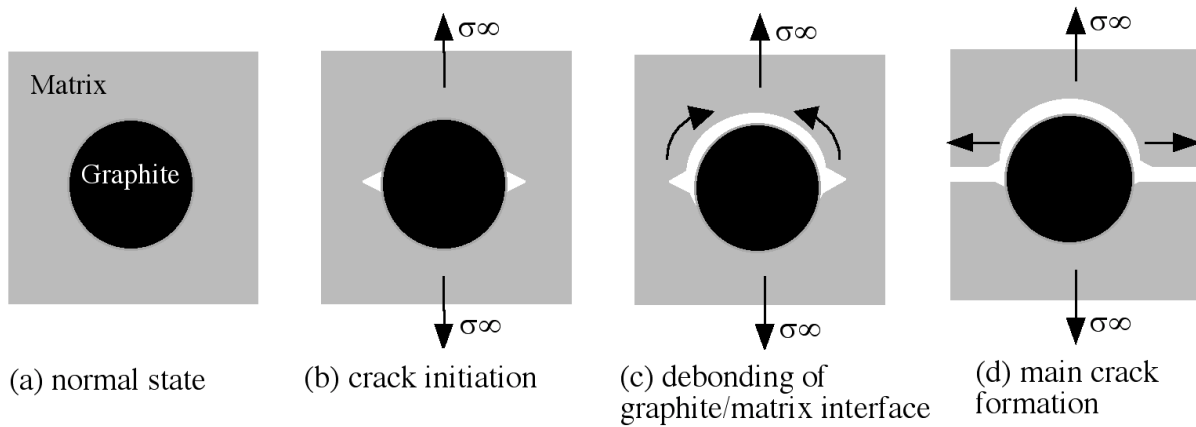


Fig. 7. Model of fracture process occurred around the spheroidal graphite nodule.

stressed in tension and the stress reaches a critical level, a micro-crack initiates in the matrix around graphite nodule (Fig. 7b). Such Saturn's-ring-shaped crack perpendicular to the stress axis could be created where the stress is the maximum. The next step of debonding at the graphite/matrix interface (Fig. 7c) exists only nominally as the graphite strength is so much lower. The crack grows into the matrix, forming a main crack (Fig. 7d). When this last step occurs almost simultaneously at neighboring nodules, an observable AE signal is expected.

Cross sectional observation of the fractured specimen by an SEM showed that the crack path twisted around the surfaces of graphite nodules. Traces of an internal crack initiated from a graphite nodule were also found near the main crack path. These observations suggest the validity of the model proposed in Fig. 7, but further improvement in resolution is needed to follow the crack spreading that is expected to generate AE.

6. Summary

In order to determine visually how the graphite nodules in the matrix contributed to the fracture process, tensile testing was conducted on notched bar specimens of pearlitic spheroidal graphite cast iron. Fracture processes were reconstructed by the computer-aided image processing for the topography of conjugate areas of the fracture surfaces observed by a confocal-optics-based scanning laser microscope. Acoustic emission was simultaneously measured during the tensile test, in order to obtain the dynamic information about the stress state and interpret the reconstructed fracture process occurred inside the material.

Reconstructed fracture process revealed that crack initiation and growth started in the middle of the specimen. Initial micro-crack was created in the matrix around a graphite nodule at a stress level of approximately 90 % of the specimen failure strength, estimated by AE. A model, which explains the fracture process occurring around the spheroidal graphite nodule, was proposed.

This technique, combining AE with SLM, eventually will make it possible to interpret the physical meaning of an AE signal and make AE monitoring a more effective method to evaluate the condition of structure.

Acknowledgement

The authors wish to acknowledge the invaluable discussion in this work of Prof. Kanji Ono of University of California, Los Angeles.

References

- [1] N. Niwa, Bulletin of the Iron and Steel Institute of Japan, **78**(4), 1992, 673-679.
- [2] A. Nozue, T. Uchimura and T. Okubo, J. Materials and Environment, **40**(11), 1992, 728-733.
- [3] K. Kouyama, S. Sato and K. Saka, J. Japan Institute of Light Metals, **42**(7), 1992, 418-426.
- [4] N. Niwa, M. Gunji and K. Itoh, Annual Report of General Institute of Faculty of Engineering, University of Tokyo, **45**, 1986, 255-262.
- [5] Y. Obata, K. Aoki, Y. Mori and A. Nozue, *Progress in Acoustic Emission VIII, Proc. of 13th Int. Acoustic Emission Symp.*, JSNDI, Tokyo, 1996, pp. 231-236.
- [6] T. Ohira and T. Kishi, Bulletin of the Iron and Steel Institute of Japan, **70**, 1984, 2188-2195.

- [7] M. Ohtsu, *Journal of Geophysics Research*, **96**, 1991, 6211-6221.
- [8] T. Kobayashi and D. A. Shockey, *Metallurgical Transactions A*, **18A**, 1987, 1941-1949.
- [9] Y. Mori, Y. Obata, S. Nose, P. Kriengsak and T. Umeda, *Proc. of the 10th Intl. Congress on Fracture*, Honolulu, 2001, Elsevier Science, CD ROM, Ref. No. 1014.
- [10] Amer. Foundry Soc., *Cast Metal Handbook*. Des Plaines, Illinois, 1957, p. 92.
- [11] F. Nakanishi and S. Okamoto, *Trans. of Japan Society of Mechanical Engineering*, **17(61)**, 1951, 103-107.
- [12] T. Noguchi, *J. Society of Materials Science, Japan*, **29**, 1980, 387-393.
- [13] K. Kriengsak, K. Satoh, Y. Mori, B. Paritud and T. Umeda, *Proc. of the 3rd. Asian Foundry Congress*, The Korean Foundrymen's Society, 1995, pp. 296-303,
- [14] T. Noguchi, *Transaction of Japan Society of Mechanical Engineering, A*, **54-507**, 1988, 1962.
- [15] T. Takao and H. Nisitani, *J. Society of Materials Science, Japan*, **36(409)**, 1987, 1060-1064.
- [16] T. Ishibasi, *Transaction of the Japan Society of Mechanical Engineering*, **18**, 1952, 87-88

NON-DESTRUCTIVE EVALUATION OF BRAZED JOINTS BY MEANS OF ACOUSTIC EMISSION

H. TRAXLER¹, W. ARNOLD², W. KNABL¹ and P. RÖDHAMMER¹

¹PLANSEE Aktiengesellschaft, Technology Center, A-6600 Reutte, Austria

²Fraunhofer Institut für Zerstörungsfreie Prüfverfahren (IZFP),
D-66123 Saarbrücken, Germany

Abstract

Brazing is a key technology in the production of components made of high performance materials. Due to the extreme operating conditions and stringent safety requirements, there is a strong demand for quality assurance by non-destructive evaluation of brazed components such as composite X-ray targets. An established method for non-destructive testing is ultrasonic C-scanning in the pulse-echo mode. This method allows one to detect voids in the brazing interface such as voids, which are caused by inhomogeneous wetting by the filler metal of the parts to be brazed. Additionally there is an interest for the microstructure of the braze alloy and for testing its loading capacity. To get information on these properties at present metallography or loading tests up to destructive load levels are required. The results presented here show that acoustic emission (AE) during a loading test to a subcritical load level is sensitive to deviations in the process parameters causing embrittlement of the brazing alloy. The origin of the AE signals has been identified by the systematic exclusion of the various possible sources in a comparative experimental study. Furthermore, a correlation between the non-destructive AE test and the destructive load test has been established. Samples, which failed prematurely in the destructive load test, showed a strongly increased signal rate and a specific type of signals in the AE test.

Keywords: Acoustic emission, Non-destructive testing, Brazing, X-ray target

1. Introduction

The improvement of X-ray imaging systems for medical applications entails increasing power densities of the electron beam striking the X-ray target. Due to the large energies deposited on the targets, they must be rotated during the application to avoid melting of the target material. A typical design of X-ray targets consists of two major components, a metal disc made of the molybdenum alloy TZM (0.5 wt-% Ti, 0.08 wt-% Zr), onto which a layer of a tungsten-rhenium alloy facing the electron beam is attached, and a graphite disc, which is joined to the metal disc by brazing (see Fig. 1).

Temperature values above 1200°C and rotation speeds up to 10,000 revolutions per minute characterize a typical load cycle of X-ray targets. In view of safety risks during X-ray diagnosis no defect of the brazed joint is allowed. The demand for reliable quality assurance is met by the application of different testing methods for the brazed joint. One of them is the non-destructive evaluation (NDE) using ultrasonic testing in pulse-echo mode. This method allows us to detect voids in the brazing interface, but gives no information about its mechanical loading capacity. The latter may be determined by a destructive load test, such as the “crash test”. During this test

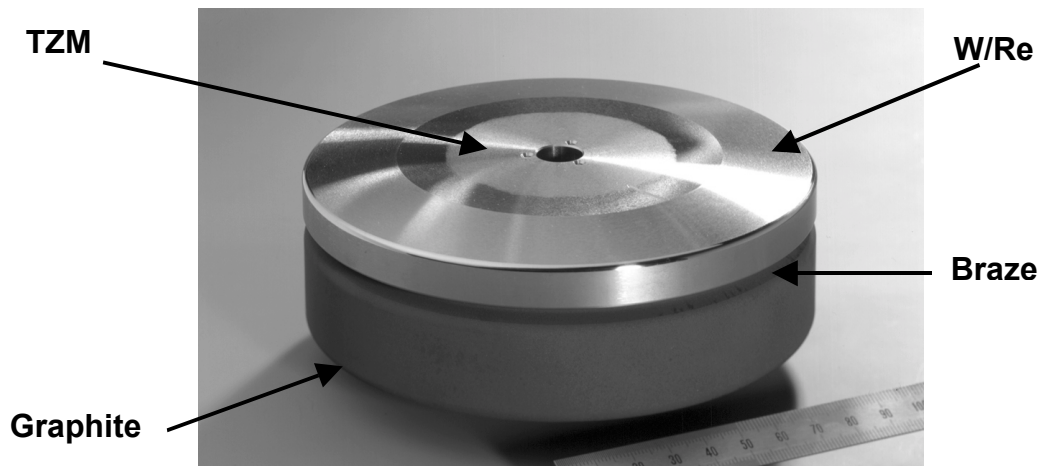


Fig. 1. Photograph of X-ray target studied.

a target of a production lot is heated up to some hundreds degrees C and afterwards shock-cooled by immersion in cold water. If there is no visible damage at the examined X-ray target after 20 cycles of thermal loading, the production lot is released.

The goal of the present work was the development of a non-destructive load test to gauge the bond strength of brazed X-ray targets by applying acoustic emission (AE), and in consequence the replacement of the crash test. The method applied in this test is to induce – by way of elastic deformation of the brazed composite – a specific pattern of tensile and shear stresses at the TZM – graphite brazing interface and to monitor the ensuing AE response of the interface in the high kilohertz regime. Until now, a few examples of NDE of material joints by AE are known [1, 2].

2. Experimental Set-Up

2.1 Mechanical loading of samples

For loading the samples, the outer perimeter of the metal component of the target is supported by a steel ring. When applied along the central axis of the target, a force (F) effects a bending with circular symmetry. The set-up and the coupling of the AE sensors to the part to be tested are shown in Fig. 2. This set-up is used because the graphite component cannot bear mechanical loads without surface damage. The stress distribution in the interface between the metal and the graphite component under maximum test load was calculated by means of finite element analysis. Pre-stresses present after cool-down from the brazing temperature were taken into account. The resulting distribution of normal and shear stresses is shown in Fig. 3. The stress distribution shows a pronounced maximum in the vicinity of the inner diameter for both normal and shear stresses. To validate the finite element simulation, the deformation under load was measured and compared to the calculations. A test load of 40 kN caused a 70 μm deformation in the center of the target, in good agreement with the calculations.

2.2 Measurement of acoustic emission

In the present work the AE signals were detected using piezoelectric sensors covering the frequency range between 200 and 900 kHz (Dunegan SE-650P). To minimize the influence of external noise in the measurement chain, and hence to improve the signal-to-noise ratio, the sensor signal was pre-amplified by 34 dB with the preamplifiers shielded and close to the AE sensors. For data acquisition, storage and analysis the system Vallen AMSY4 was used. Four AE sensors were attached to the sample to allow the location of the AE events. To accurately deter-

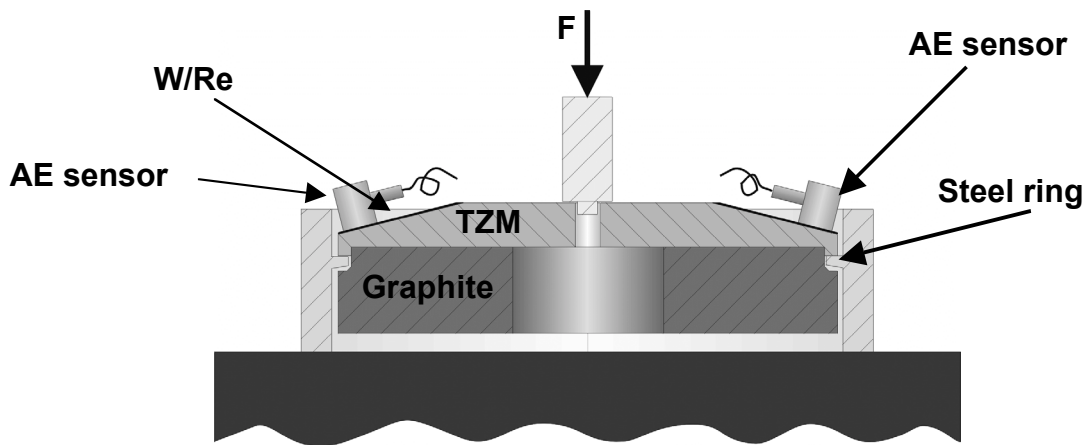


Fig. 2. Schematic view of the mechanical loading of X-ray targets and coupling of the AE sensors to the sample. The load F is introduced in the centerline of the target.

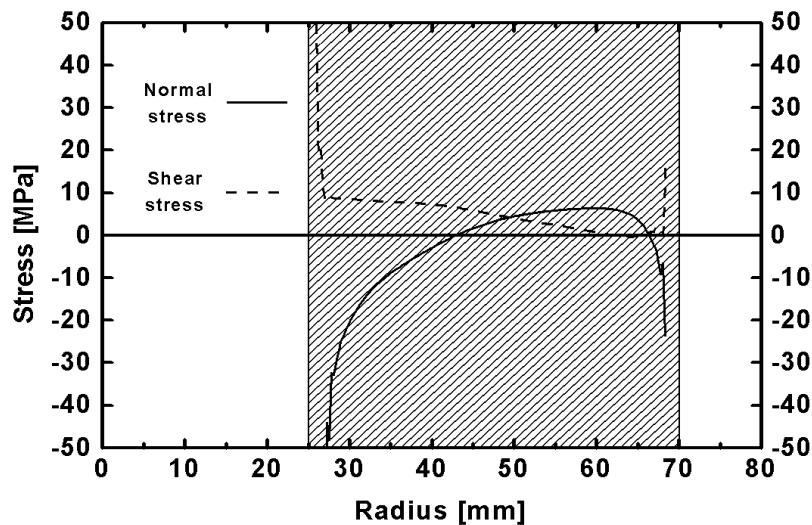


Fig. 3. Normal (solid line) and shear (dashed line) stresses in the interface between the metal and the graphite component of an X-ray target caused by mechanical loading up to 40 kN. The target has circular symmetry. The hatched area indicates the area of the brazed zone, which extends from 25 mm to the outer perimeter of the target at 70 mm.

mine the location of the AE signals, the threshold was set at the relatively low value of 25 dB (in reference to 0 dB at 1 μ V) to ensure that the mode of fastest wave propagation triggers all four channels. Experience showed that a higher threshold value led to unreliable results in locating the AE sources since the different channels were then triggered by different wave modes. With a high threshold value the fastest mode triggers only the sensor next to the signal source and the more distant sensors are triggered by a slower wave mode carrying higher signal energy. To avoid a saturation of the data recording a front-end filter at 40 dB was applied.

3. Results

3.1 Investigation of the signal sources

The first approach to investigate the AE behavior of the X-ray targets was to study the emission of the individual components. To this end the metal component and the graphite component

were loaded mechanically. The AE of these parts was then compared to that of the X-ray target, which had been brazed applying the standard brazing parameters. A micrograph of the metallographic section of the brazed interface of such a target (Fig. 4) shows that the braze metal, zirconium, upon solidification reacts with molybdenum and forms needle-shaped primary crystals of the brittle intermetallic phase (Mo_2Zr). Furthermore, a carbide layer forms at the interface to the graphite component. Also there exists a skeleton of ZrC within the graphite zone in the vicinity of the interface, due to infiltration of the zirconium melt into the porous graphite disc (10 % porosity). A target with altered production history was studied in this stage of investigation. This target was brazed at higher temperature, which caused a significant increase in the formation of both Mo_2Zr and ZrC brittle phases (Fig. 5).

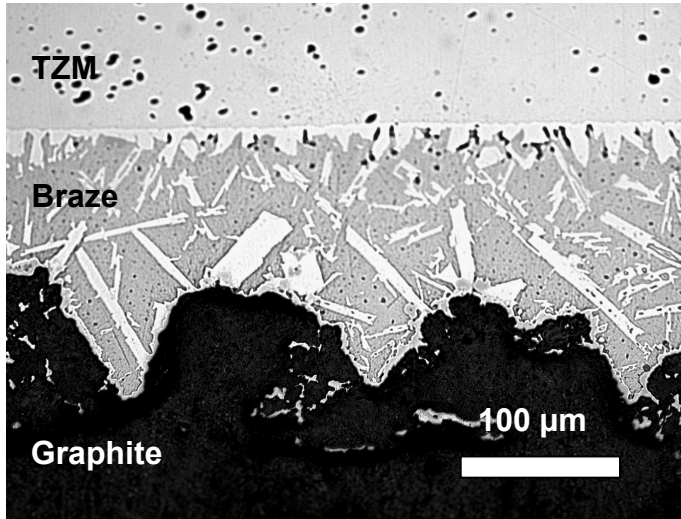


Fig. 4. Micrograph of a metallographic section of the brazing interface of an X-ray target brazed applying standard conditions.

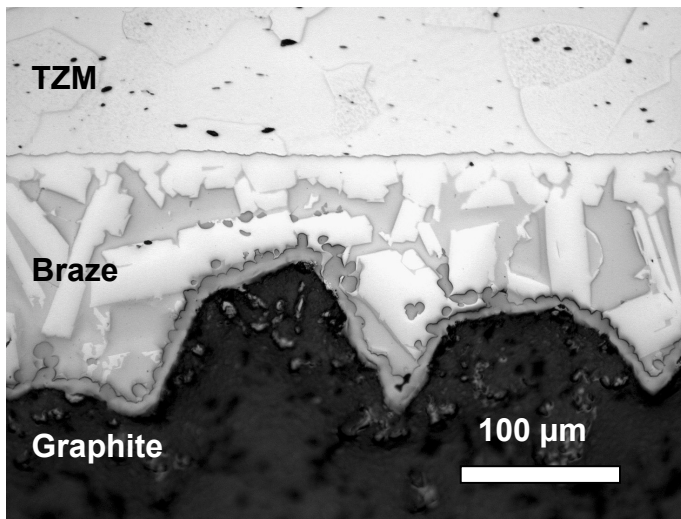


Fig. 5. Micrograph of a metallographic section of the brazing zone of an X-ray target brazed at higher temperature than standard. The larger content of Mo_2Zr -crystallites in the braze zone and the thicker carbide layer at the braze-graphite interface are clearly visible.

The signal energies of the AE from the metal and the graphite component and of the two target variants are compared in Fig. 6. The rapid increase between 8 and 9 kN in the AE-energy versus load graph of the graphite component (dashed line) indicates the fracture of the component, after which the test was stopped. Apart from this failure the individual components exhibit a negligible AE compared to the brazed targets (see Fig. 6). In the frequency range considered here, the elastic deformation of molybdenum did not cause significant AE also in earlier investigations [3]. Therefore, AE of the brazed composite may for practical purposes be attributed solely to the area of the braze interface. The elevated brazing temperature leads to a significant

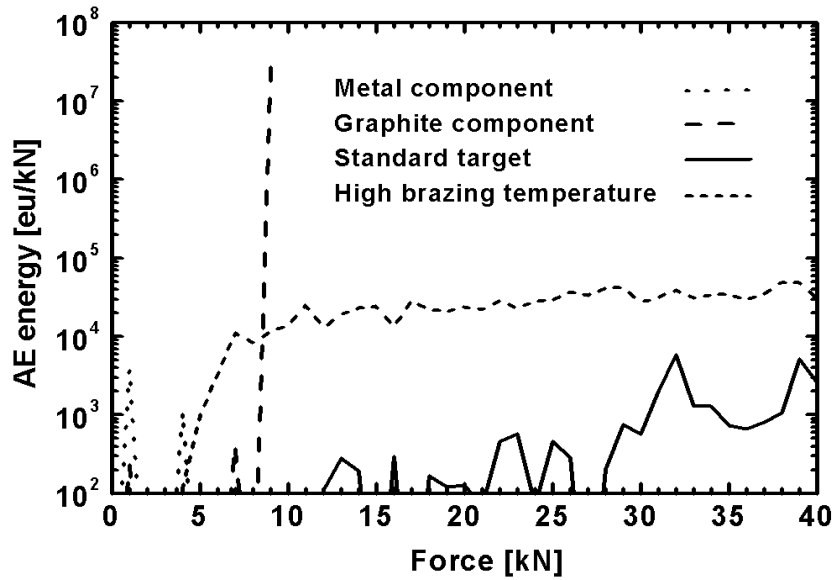


Fig. 6. Comparison of the rate of acoustic energy released during mechanical loading for the metal and the graphite component, and the two different types of brazed targets examined. On the y-axis the AE energy per 1 kN loading interval is plotted.

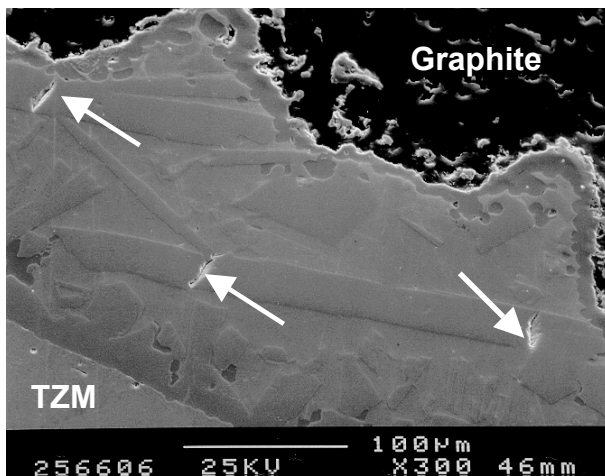


Fig. 7. Scanning electron microscope image of the zirconium braze after the mechanical loading test. The arrows mark micro-cracks in Mo_2Zr crystals.

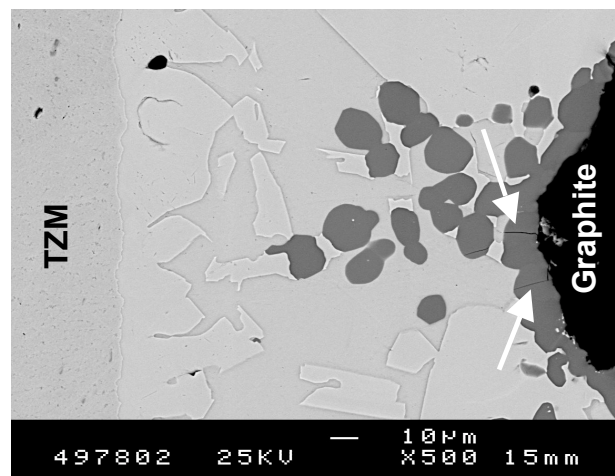


Fig. 8. Scanning electron microscopy image of the zirconium braze after the mechanical loading test. The arrows mark micro-cracks in the ZrC layer.

increase of AE during the mechanical loading test (cf. Fig. 6). Further tests showed that two source mechanisms could be identified: Micro-cracks in the Mo_2Zr crystals (see Fig. 7) and cracks in the carbide layer (see Fig. 8).

3.2 Signal location

Typical results for the distribution of AE activity over the brazing interface of an X-ray target (standard brazing configuration and parameters) are shown in Fig. 9. In this plot the number of

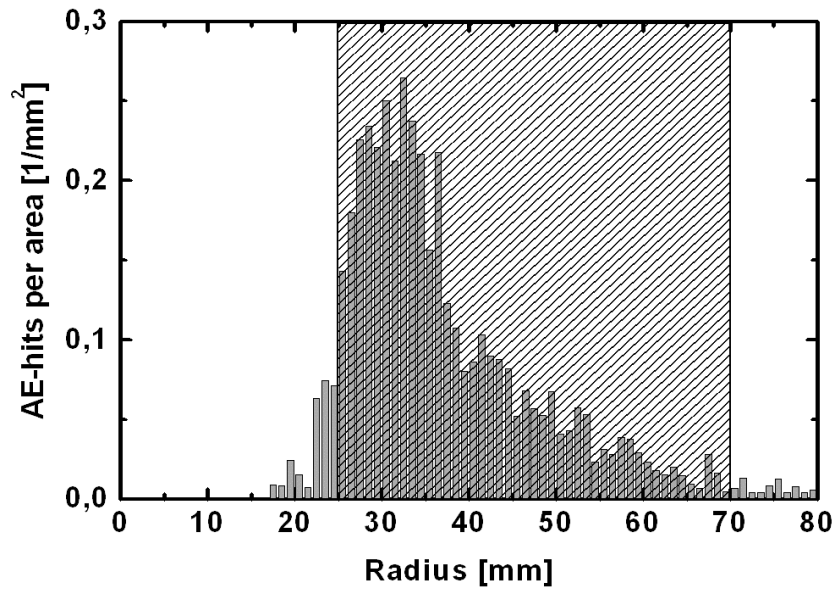


Fig. 9. Locations of AE signals during a mechanical loading test of an X-ray target up to 40 kN. The target is round. The hatched area indicates the area of the brazed zone, which extends from 25 mm to the outer perimeter of the target at 70 mm.

AE signals, called AE-hits, are measured in radial segments of 1-mm width and plotted as a function of radius. This source location plot shows a maximum at the inner perimeter of the brazed zone in agreement with the finite element simulation (see Fig. 3) where both the normal and shear stresses are highest at the inner perimeter. From the AE data it is not possible to distinguish whether the AE normal or shear stress caused the AE signal. Since compression at the stress levels calculated is not likely to cause micro-structural failures in the brazing interface, the shear stresses are held responsible for this damage on a microscopic scale. The signals located outside the brazing zone (radius smaller than 25 mm or larger than 70 mm in Fig. 9) are an indication for the relative number of false location due to triggering delays described in Sec. 2.2.

3.3 Correlation to established tests

To compare the results of the AE test with established testing methods, a series of 50 X-ray targets partially failed in the ultrasonic test (US) or in the crash test were examined further (see Table 1).

Table 1. Results of the established testing methods for a series of 50 X-ray targets.

Results of the US test	Results of the crash test	Number of targets
OK	OK	43
OK	failed	3
failed	OK	4

All targets listed in Table 1 had identical geometry and were produced using standard parameters. The results of the AE test on these targets are summarized in Fig. 10. The histogram shows the AE energy emitted by each target during the mechanical loading test. The distribution exhibits the maximum at the lowest AE-energy levels. The targets, which passed both the US and the crash test without failure, emit AE energies up to 2.3×10^6 eu with one outlier above 10^7 eu.

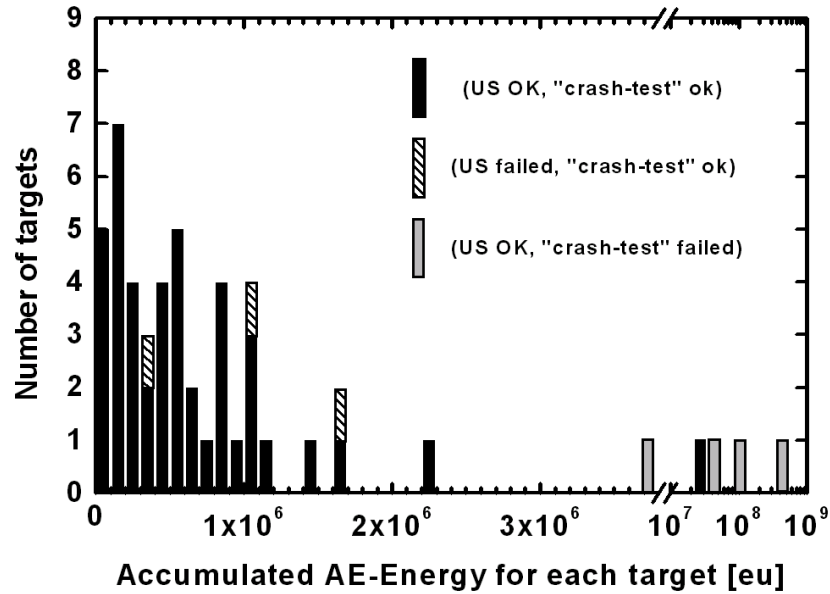


Fig. 10. Histogram of the AE-energy accumulated during a mechanical loading test up to a load level of 40 kN of the X-ray targets listed in Table 1.

The increase of the AE energy levels of the targets, which failed in the ultrasonic test, was insufficient to discriminate them against the distribution of flawless targets. However, targets, which later failed in the crash test, emitted significantly higher AE energies than the flawless ones. The increase in AE energy release is associated with the emission of a few specific signals showing amplitude values up to the saturation value of the data acquisition chain at 100 dB. We attribute such high amplitude bursts to avalanches of micro-failures involving very large numbers of micro-cracks.

4. Conclusions

AE stimulated by non-destructive bending deformation of brazed X-ray targets provides a valuable tool to sensitively detect variations in the brazing process; in particular, deviations in the temperature profile during the brazing operation. Upon statistical analysis, the results of AE tests obtained from large samples may be used to maintain the brazing parameters within the statistical process control window of tolerance.

In addition, we have demonstrated that the accumulated AE energy detected during the non-destructive mechanical load test of X-ray targets allows one to reject with a high confidence level those targets, which fail in the destructive crash test. Replacement of the latter by the AE test allows to increase the sampling of test parts up to 100 % at comparable costs, and thereby to eliminate the risk of passing flawed targets. Defects in the joining zone, such as voids, which can be detected by ultrasonic C-scans, appear to have influence on the AE, but insufficient for discrimination against flawless targets.

In summary, AE under mechanical loading has proven a valuable tool to gauge the mechanical integrity of braze joints.

Acknowledgement

We are grateful to H. Klocker for carrying out the finite element analysis and to A. Plankensteiner for fruitful discussions. The assistance of A. Wolf is gratefully acknowledged.

References

- [1] Schmitt-Thomas Kh. and Waterschek R., “Untersuchung der Güte von Weichlötstellen mit Hilfe der Schallemissionsanalyse”, *Proc. 8th Congress on Material Testing*, Vol. 1, Omikk-Technoinform, Budapest (1982), pp. 1180 – 1184.
- [2] Sell J. and Weiler L., “Quality Control Proof-test with Acoustic Emission of Ceramic Cooling Plates”, *Proc. 23rd European Conference on Acoustic Emission Testing*, TÜV Vienna, Vienna (1998), pp. 140 – 145.
- [3] Traxler H., “Schichtprüfung mittels Schallemissionsanalyse”, Diplomarbeit Technische Universität Wien (1997), pp. 56 – 64, unpublished.

DAMAGE MODE IDENTIFICATION AND ANALYSIS OF COATED GAS TURBINE MATERIALS USING A NON-DESTRUCTIVE EVALUATION TECHNIQUE

Y. VOUGIOUKLAKIS^{1,2}, P. HÄHNER², V. KOSTOPOULOS² and S. PETEVES¹

¹ European Commission, Joint Research Center, Institute for Energy, 1755ZG, The Netherlands.

² University of Patras, Applied Mechanics Laboratory, Rio GR-26500, Greece.

Abstract

The performance of coated high-temperature material systems under close-to-service conditions can be assessed by means of thermo-mechanical fatigue (TMF) tests, while acoustic emission (AE) can be applied for the in-situ monitoring of damage processes occurring during these tests. This work presents experimental methodologies adopted for assessing the damage behavior during TMF testing. In view of the complexity of these tests and the lack of detailed knowledge of the damage evolution in those material systems, AE monitoring has been used, in order to reveal and interpret the micromechanical behavior during TMF. The results are suggesting that the use of the AE technique during the thermal and mechanical solicitation is extremely powerful as it enables non-destructive damage monitoring and it offers possibilities for the life assessment of coated high-temperature material systems.

Keywords: Thermo-mechanical fatigue, AE activity, CM186

1. Introduction

The research and development efforts for enhanced performance of high-temperature materials for gas turbines is driven by the need to meet the demands for increased lifetimes and higher efficiencies at lower costs and reduced environmental impact. These ambitious goals can only be achieved through a combined approach comprising the development of new material systems and the use of advanced materials testing methods, in order to improve the understanding of the materials behavior and to allow for less conservative designs [1-4]. This work presents an experimental set-up optimized for assessing the materials systems behavior and life under thermo-mechanical fatigue (TMF) testing.

Acoustic emission (AE) is a non-destructive method that allows the in-situ monitoring of damage evolution during combined thermal and mechanical loading of a material. As compared to other non-destructive techniques, which provide information about the damage accumulated at a certain stage of life, AE gives access to damage processes inside a material in terms of the rate of damage accumulation, and it is a highly sensitive means for the early detection of impending failure [5]. Hence, the implementation of AE monitoring in a laboratory environment can be instrumental in interpreting the damage mechanisms, as these are triggered and progressing during TMF tests. Furthermore, AE is an extremely versatile technique to the experimental set-up, has no constraints concerning into the specimen geometry and can be applied even to complex material systems.

In this work, results from AE data analysis of TMF tests on single crystal and directionally solidified (DS) superalloys in the uncoated and coated conditions are described. Goal of this study is to establish the validity of the information obtained by AE monitoring during TMF and to correlate the AE data with specific damage processes (modes).

Currently, the efforts are focused on a simple material system (substrate with a diffusion type coating) in order to evaluate the contribution of AE into identifying the damage processes. Ultimately, the goal of our efforts is to apply this method to a more complex material system (a thermal barrier coating system) in order to scan all the damage processes that are activated during a TMF test.

2. Experimental Set-Up

Specimens were prepared from single crystal (SC) and DS Ni-based superalloy, CM 186 alloy bars, with the crystallographic orientation of the long axis of the samples in the [001] direction. Threaded end specimens with a solid rectangular cross-section of $12 \times 3 \text{ mm}^2$ and a parallel length of 9 mm were machined. The rectangular cross section was adopted to enable observation of the flat surface by means of a computer-controlled video imaging system during testing, as discussed later. Some of the SC and DS CM186 samples were coated with a modified aluminide coating, Sermalloy 1515, via an Al/Si slurry diffusion process, with an approximate thickness of 80 μm .

2.1 Mechanical testing set-up

The strain-controlled TMF tests were carried out in air on a computer controlled electro-mechanical closed loop-testing machine of 100 kN capacity (Schenck Trebel). Asymmetrical triangular out-of-phase cycles with mechanical strain ranges $\Delta\varepsilon_m$ of 0.8% and 1.0%, respectively, and a temperature range $\Delta T=600^\circ\text{C}$ with temperature cycled between 350°C and 950°C were chosen (minimum to maximum mechanical strain ratio $R=-\infty$, cycle period $\Delta t=200\text{s}$) (see Fig. 2). Temperature and mechanical strain both varied linearly with time, but with a phase shift of 180° . This cycle imposes maximum mechanical strain/stress at minimum temperature and minimum strain/stress at maximum temperature. Control of the testing machine, the high frequency induction heating system and data acquisition was performed by means of a dedicated computer system using LabVIEW. Compensation of the thermal strain was achieved by recording the thermal expansion under zero load as a function of time prior to TMF testing using the same temperature cycle as in the subsequent test. Prior to the actual TMF tests, the temperature dependence of the Young's modulus was also determined by isothermal static measurements in the TMF temperature range.

The tests were started at the minimum temperature and at zero mechanical strain, and conducted until failure, or stopped when the cyclic stress range had dropped at levels 50% below the stress range during the previously stabilized value. TMF life is then defined as the ultimate cycle number.

During TMF testing, images of the flat surface of the specimen were taken at pre-selected cycle numbers by means of a computer controlled video imaging system, allowing contact-less, in-situ and fully automated monitoring of the evolution of surface damage [6]. To enhance the detection of crack initiation (with a surface length $\geq 15\mu\text{m}$), the CCD camera with a flash unit was synchronized with the TMF cycle and images were taken when the imposed stress on the specimen exceeded 80% of the maximum tensile stress of the previous cycle. These images

covered the whole specimen width and the gauge length. All the images were digitized and stored for post-processing and analysis. More details on the TMF set-up can be found in Ref. [2].

2.2 Acoustic emission set-up

Two broadband piezoelectric transducers (PAC WD) were used as sensors to monitor the acoustic emission during the tests. The sensors were attached on the grips of the machine just after the two cooling plates used to protect the gripping system and to stabilize the temperature control. The AE signals were pre-amplified (PAC 1220A with 500-kHz high-pass filter) and fed into a two-channel AE digital signal processor. The acquisition of the AE signals was performed by a computer system using MISTRAS-2001 software configured with the specific mechanical set-up [7]. The initialization parameters of the AE set-up were optimized with respect to the external noise (ambient or induced by the induction heating system), the experimental set-up, the specimen geometry and volume of interest (the bulk inside the gauge length).

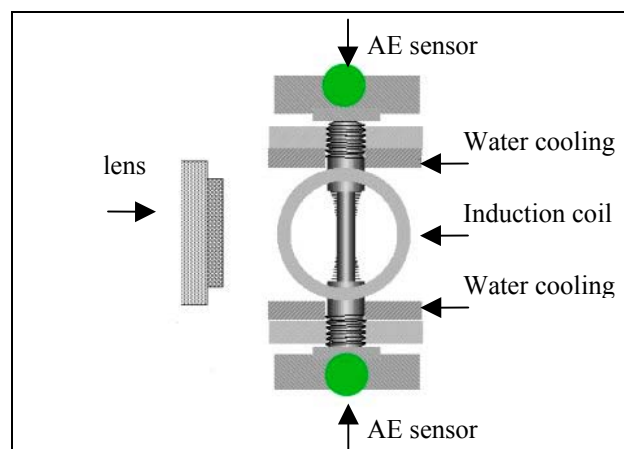


Fig. 1. Schematic drawing of the acoustic emission set-up.

The AE signals were collected in time-order and seven different AE features were monitored each time: rise time, counts, energy, amplitude, duration, average frequency, counts to peak, as well as the current stress value and the cycle number as input parameters. The evaluation and analysis of the received signals was performed using NOESIS and SPSS software packages.

3. TMF Tests

The TMF results and post mortem fractographic and microstructural analyses of the samples have been reported and discussed elsewhere [8]. The identified damage modes are named briefly as: (1) damage initiation sites, precipitate cracking at the substrate-coating interface, (2) subsurface-crack propagation in the coating and crack interaction, (3) surface cracking, crack coalescence, (4) oxidation-controlled fatigue crack growth.

As such a few relevant results will be presented here; namely, the pronounced cyclic creep during the first cycles caused by the accumulation of compressive inelastic deformation due to plastic flow at high temperature (Fig. 2). It was observed that the coatings crack in mode I (Fig. 3). These cracks initiate in the coating at the coating/substrate interface (Fig. 4), grow towards the surface and finally propagate also into the substrate by Mode I extension, producing a crack front almost parallel to the specimen surface and a crack path perpendicular to the loading direction.

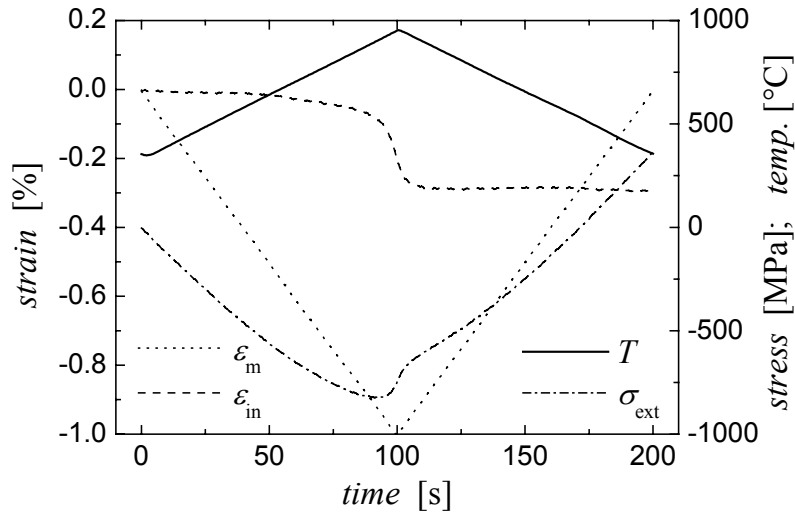


Fig. 2. Thermomechanical behavior of uncoated DS CM186 sample during the first cycle (ϵ_m : mechanical strain, ϵ_{in} : inelastic strain, T : temperature, σ_{ext} : external tensile stress).

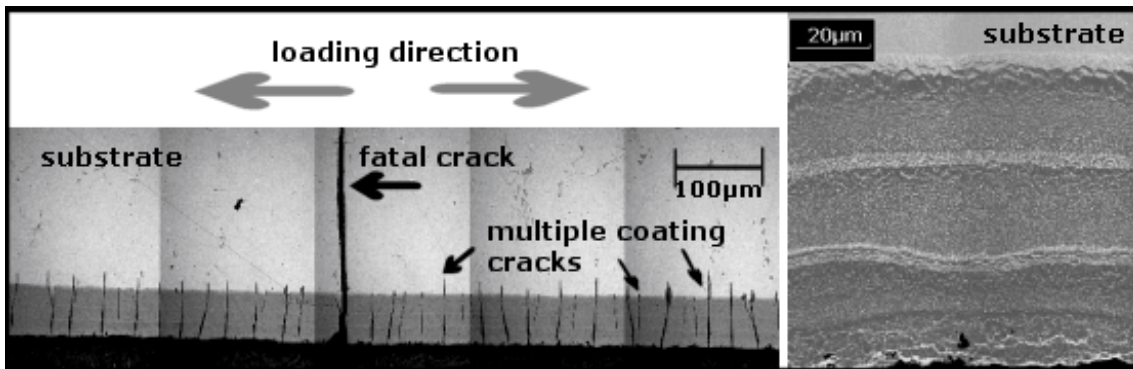


Fig. 3. Post-mortem scanning electron micrographs from a coated CM186 sample.

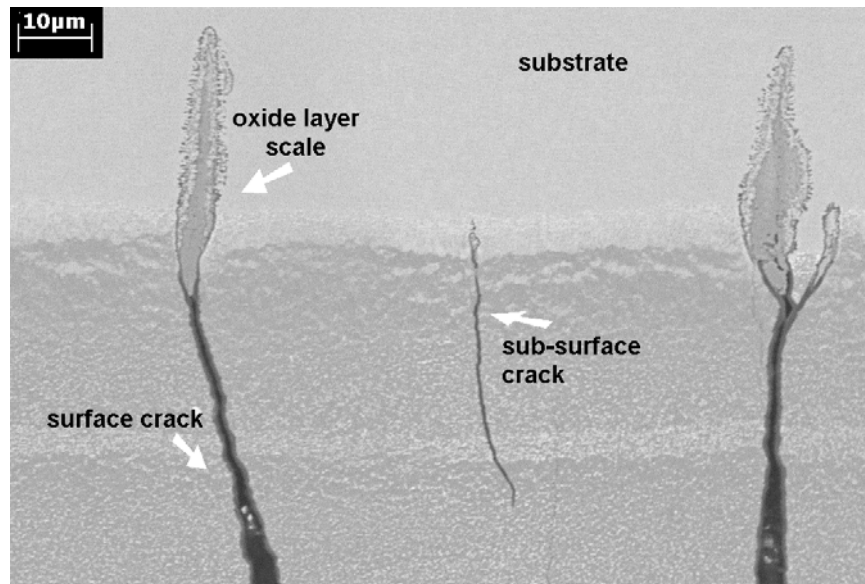


Fig. 4. Post-mortem scanning electron micrograph showing the initiation sites of cracks into the coating – substrate interface.

4. AE Analysis

The AE signals were separated according to the mechanical load state at their time of occurrence: compressive or tensile signals. Table 1 presents the global information for each test. A first conclusion resulting from Table 1 is that more AE signals were received from the coated specimens.

Table 1. Experimental conditions and AE activity in terms of number of AE events.

Material	SC	SC	SC, coated	SC, coated	DS	DS, coated
Mechanical strain range	1%	0.8%	1%	0.8%	1%	1%
TMF lives (# cycles)	1941	9165	1121	5300	1412	2404
AE events in tension	749	1309	2393	7022	742	14693
AE events in compression	2491	4238	4813	5918	850	2629
AE events in Region I						
in tension	1675	6484	...	6453
in compression	1475	1640	...	1892
End of Reg. I (cycle #)	335	2508	...	933
(% of TMF life)			(30%)	(47%)		(39%)
First crack at cycle #	600	1000	200	300	400	200

When the temporal evolution of the overall AE activity during the test is considered, two distinct regimes of AE activity are revealed; Regions I and II (see Fig. 5), which are sometimes separated by an inactive period. In the case of the coated samples, both regimes are present, whereas in the case of the uncoated samples only Region II is active during the last 20% of the TMF life (Fig. 5).

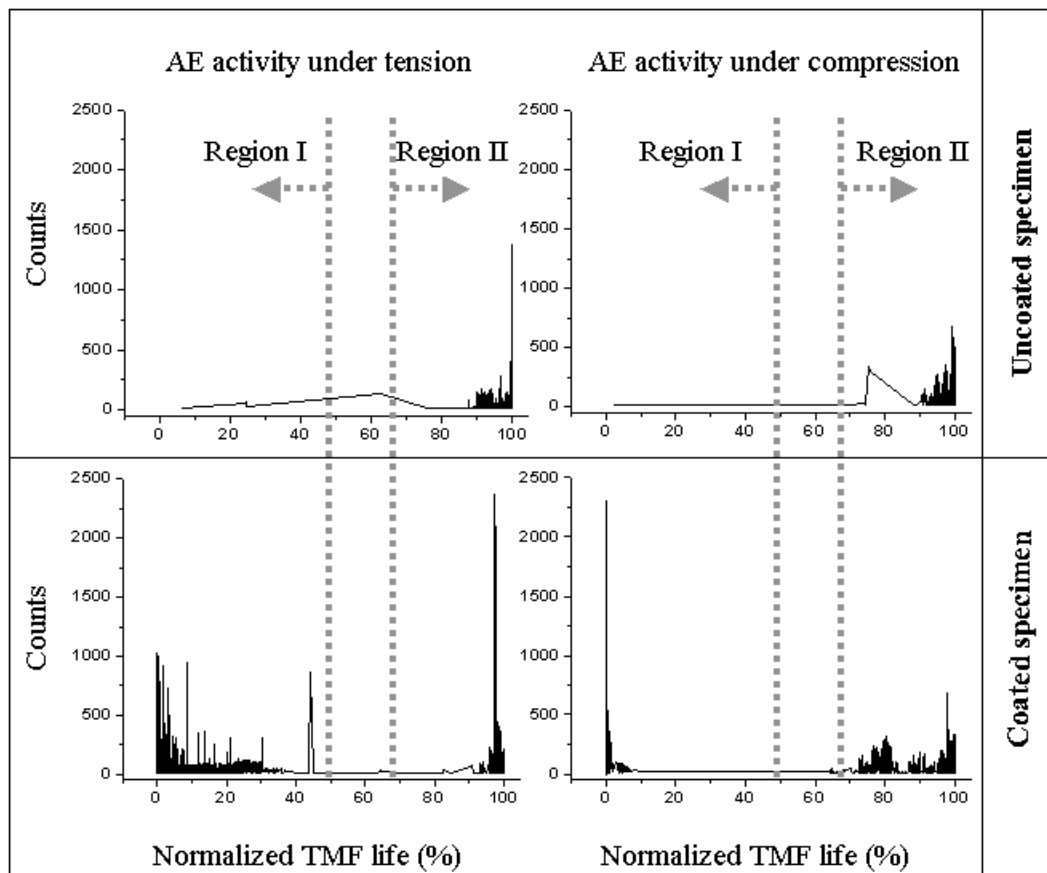


Fig. 5. AE activity for a coated and an uncoated specimen throughout the test.

This observation provides a clear distinction between signals originating exclusively from the coating (Region I) and those involving also the substrate (Region II). Therefore, signals from Region I relate to damage processes in, or induced by the presence of the coating [9], while signals from Region II reflect the behavior of the bulk material independently of the presence of the coating. These signals are associated with the final stage of the test before the failure of the specimen, which is brought about by the fatigue crack growth.

The AE data recorded during the late stages of the TMF tests, i.e. events from the aforementioned Region II, are considered for further analysis in terms of a supervised pattern recognition. This stage may reveal precursory events, before the imminent failure due to the fatal fatigue crack growth becomes obvious from the mechanical response of the specimens.

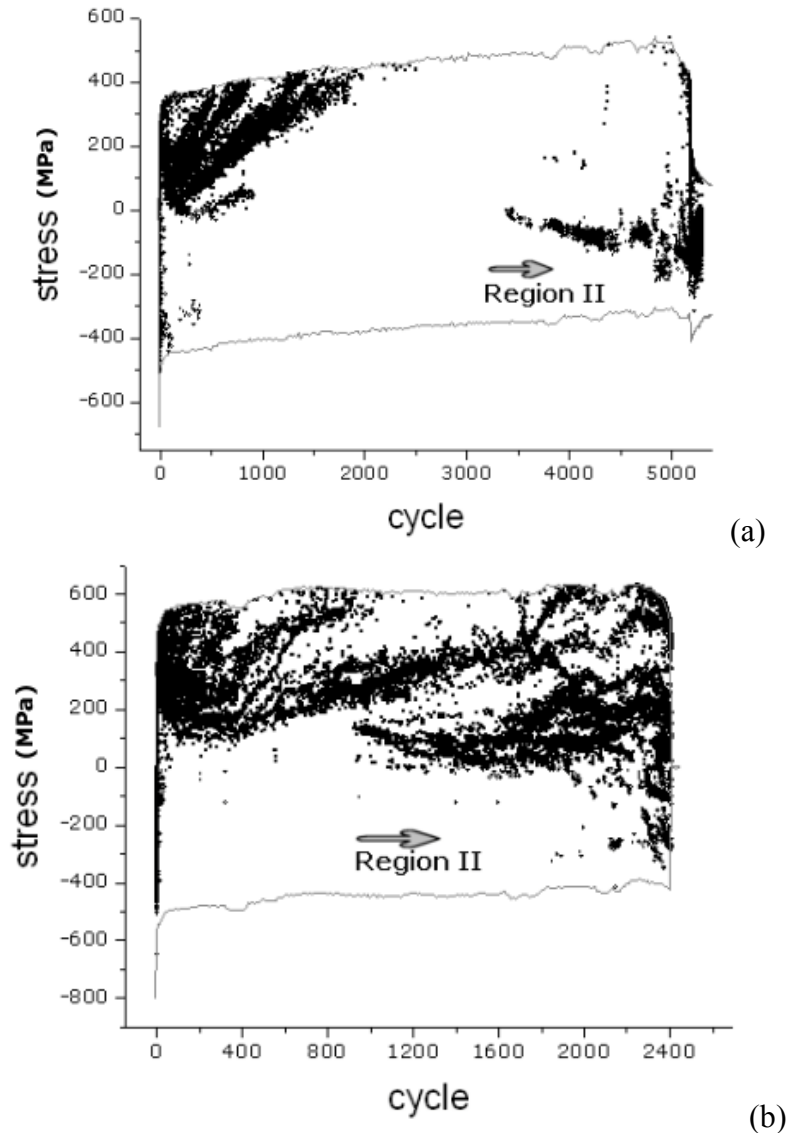


Fig. 6. AE events (symbols) and cyclic maximum and minimum stress envelopes (solid lines) during TMF tests for SC (a) and DS (b) coated samples.

Figure. 6 shows two examples of the AE activity in the stress vs. cycle number domain. For the SC sample, Region II is well separated from Region I by an inactive period, which is missing in the case of the DS sample. In both cases, AE activity in Region II starts at an intermediate

stress level (close to zero stress or slightly compressive stresses), it spreads with respect to its stress range of occurrence, while its rate of activity increases as TMF cycling continues. At a later stage of TMF life (80-90%) another type of AE activity emerges which relates to the maximum stresses (min. temp.) available within the TMF cycles. This AE activity accompanies the ultimate fatigue crack propagation (Fig. 7).

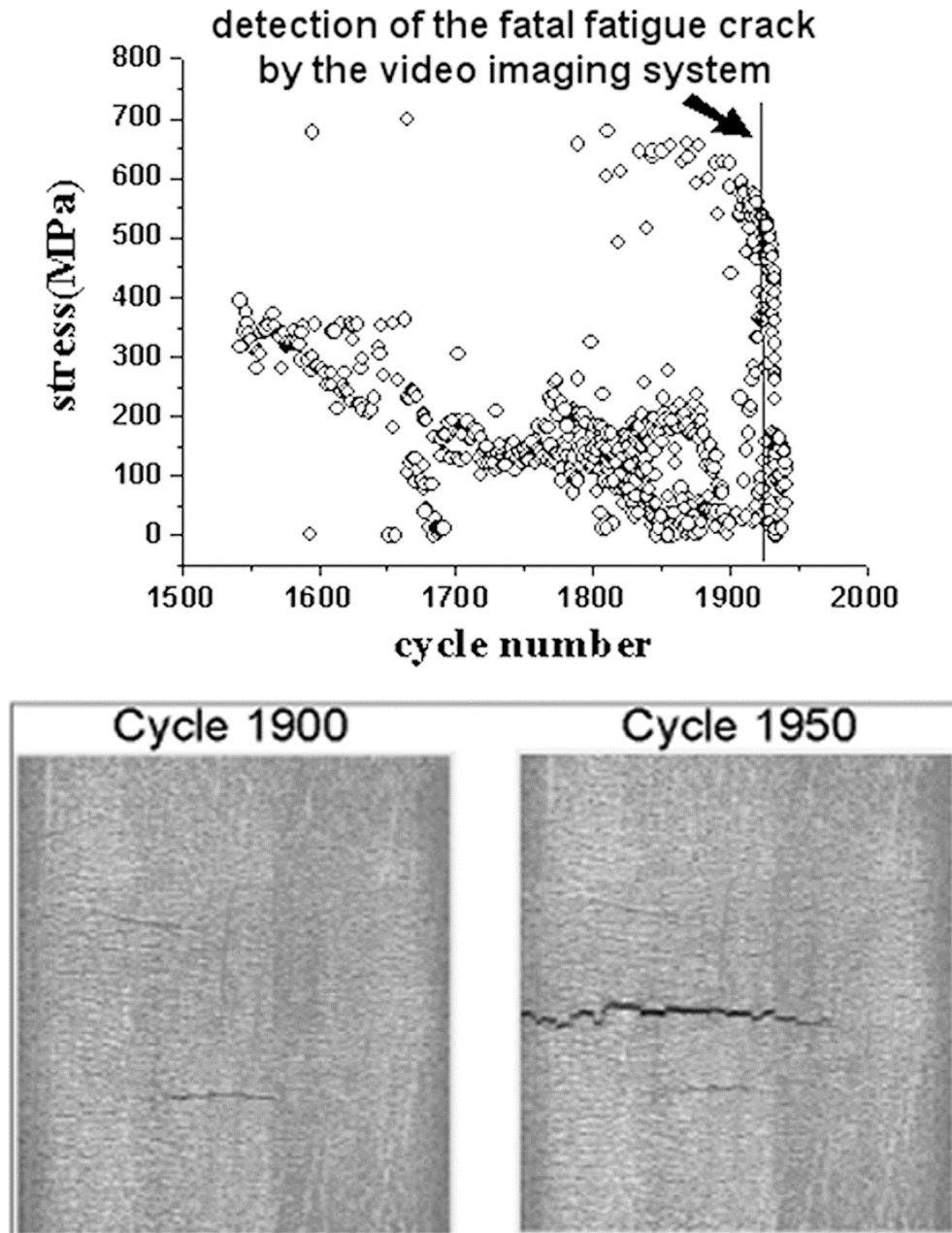


Fig. 7. Last stage (Region II) of AE data under tension for an uncoated sample. (top) Surface images from the video imaging system during the last cycles. (bottom)

Figures 6a and 6b show that Region II may start as early as approximately 40% of the ultimate TMF life, thus, providing important information about damage mechanisms preceding the propagation of the fatal crack. Further analysis of this last part of the AE data is needed, to consolidate the observed trend for these samples and to relate the Region II AE activity to specific damage mechanisms.

Based on the general understanding of the damage evolution inside the material and confirmed by post-mortem microstructural analysis (Figs. 4 and 8), it is expected that the propagation of cracks inside the substrate is initially controlled by the cyclic formation and fracture of an oxide layer grown at the crack tip during the high-temperature parts of the TMF cycles. This oxidation controlled crack growth will cease when a critical crack length is reached such that the toughness of the un-oxidized bulk material is exceeded. Then the crack will be free to propagate at a higher rate controlled by the mechanical loading during the low-temperature part of the cycles. The difference in nature of these two crack propagation mechanisms results in distinct clusters of AE signals in the stress vs. cycle number domain.

The oxidation-controlled crack growth relates to AE signals that are generated at intermediate applied stress levels, as low stresses are sufficient to crack the brittle oxide layer (note that appreciable tensile internal stresses may assist the cracking of the oxide scale, such that the local stresses at the crack tip are still tensile even if the applied stress is slightly compressive). Ultimately, when oxidation-controlled crack growth gives way to stress-controlled crack propagation, the AE signals related to latter growth mode occur close to the maximum cyclic stress values (Fig. 8).

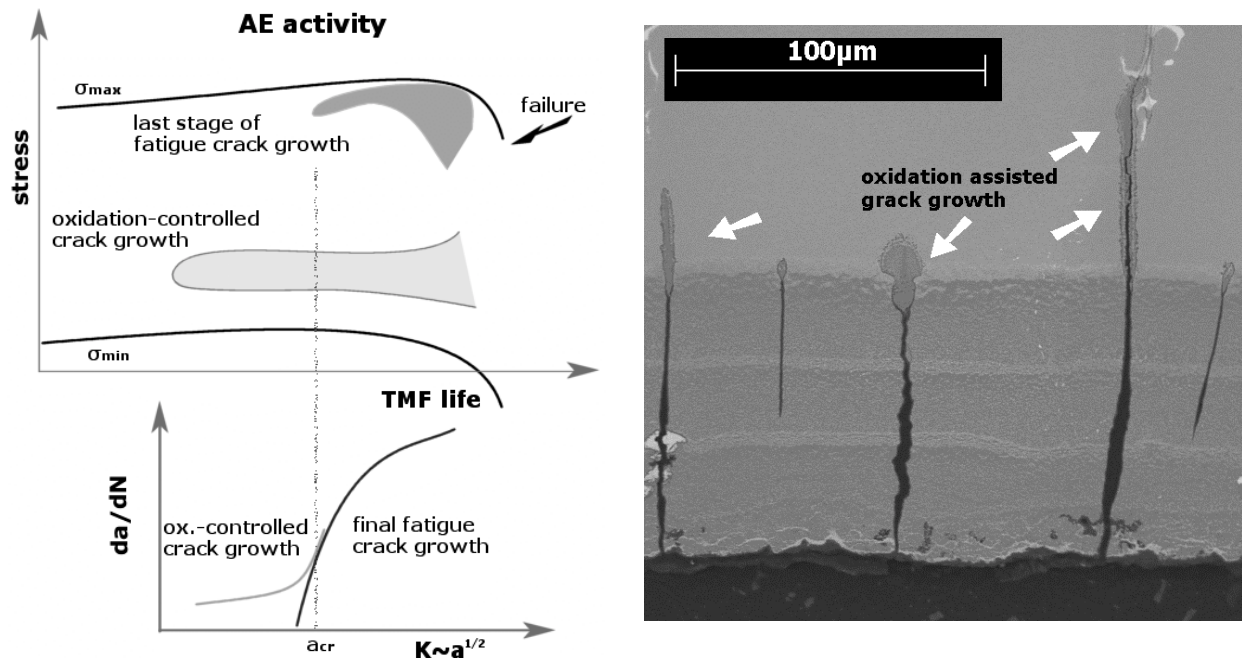


Fig. 8. Correlation of AE signals with hypothetical damage mechanisms during the last stage and verification of the existence of these mechanisms by a SEM micrograph.

By choosing stress and cycle number as descriptors in addition to the other physical AE features a supervised cluster analysis can be performed, the result of which will be the correlation of the two assuming damage mechanisms with different groups of signals, i.e. clusters. In this case, where clusters are clearly distinct already in the stress vs. cycle number domain (cf. Fig. 8) the important information provided by the AE activity does not so much relate to the physical AE parameters, but mainly to the mechanical state of the system and the time of their occurrence.

5. Conclusions

The analysis of the AE data generated during the previously described experiments revealed valuable information about the validity of AE as a method to monitor and identify damage processes. Utilizing these methodically analyzed AE data and combining the results with information provided by mechanical, video and post mortem microstructural observations, the damage evolution was assessed in terms of different damage mechanisms associated with distinct clusters of AE signals. Future analysis is expected to reveal common trends of material systems subjected to thermo-mechanical fatigue, as far as the signature of AE activity received prior to macroscopic damage visible on the surface or inferred from the mechanical response is concerned. This opens up possibilities for life prediction methodologies for high-temperature material systems during thermal and mechanical loading.

References

- [1] Affeldt E.E., "Influence of an aluminide coating on the TMF life of a single crystal Ni-base superalloy", *J. Engineering for Gas Turbines and Power*, **121**, 687, 1999.
- [2] Martinez-Esnaola J.M., Arana M., Bressers J., Timm J., Martin-Meisoza A., Bennett A., Affeldt E., "Crack initiation in an aluminide coated single crystal during thermo-mechanical fatigue", *Thermo-mechanical Fatigue Behavior of Materials*, Vol. 2, ASTM STP 1263, M.J. Verrilli and M.G. Castelli eds., West Conshohocken, PA (1995), p. 68.
- [3] Wood M.I., "The mechanical properties of coatings and coated systems", *Materials Science and Engineering A*, **A121**, 633-643, 1989.
- [4] Burgel R., "Coating service experience with industrial gas turbines", *Materials Science and Technology*, **2**, 302-308, 1986.
- [5] Pappas Y.Z., Markopoulos Y.P., Kostopoulos V., Paipetis S.A., "Failure mechanism analysis of ceramic matrix composites on the pattern recognition approach of acoustic emission", *1st Hellenic Conference on Composite Materials and Structures*, Ksanthi 1997, pp. 192-206.
- [6] Arrell D.J., Wieneke B., "An in-situ optical technique for surface strain evolution measurement", *Nontraditional Methods of Sensing Stress, Strain and Damage in Materials and Structures*, Vol. 2, ASTM STP 1323, G.F. Lucas, P.C. McKeighan, J.S. Ransom eds., West Conshohocken, PA, 2000, pp. 102-115.
- [7] *Mistras 2001 Manual*, Physical Acoustics Corporation, Princeton, NJ
- [8] Peteves S.D., De Haan F., Timm J., Bressers J., Hughes P.M., Moss S.J., Johnson P., Hendersen M., "Effect of coating on the TMF lives of single crystal and columnar grained CM186 blade alloy", *Proc. of the 9th Int. Symp. on Superalloys (Superalloys 2000)*, Sept. 17-21, 2000, pp. 655-665.
- [9] Vougiouklakis I., Hahner P., Stamos V., Peteves S., Bressers J., "Acoustic emission analysis of out-of-phase thermomechanical fatigue of coated Ni-base superalloys", *Temperature-Fatigue Interaction*, L. Remy, J. Petit eds., Elsevier, 2002, pp. 143-156.

ACOUSTIC EMISSION DURING STRUCTURE CHANGES IN SEMI-CRYSTALLINE POLYMERS

J. KROFTA¹, Z. PREVOROVSKY¹, M. BLAHÁČEK¹ and M. RAAB²

¹ Institute of Thermomechanics AS CR, Prague, Czech Republic

² Institute of Macromolecular Chemistry AS CR, Prague, Czech Republic

Abstract

Tensile tests of polypropylene and its blends with polyethylene and other additives have been recorded by digital camcorder. Acoustic emission (AE) was monitored during tests by two transducers attached to test samples, allowing linear location of AE sources. Tested materials exhibit large localized plastic deformation or necking, reaching hundreds of percent before failure. Image analysis procedure based on displacement of contrast markers on the surface has been used to quantitatively evaluate axial and lateral strains and strain rates along the sample. Correlation of AE activity with a set of plastic deformation, neck formation and defect development enables us to evaluate influence of additives on the whole stretching process.

Keywords: Acoustic emission, strain visualization, polymer drawing and necking

1. Introduction

The behavior of polymer materials beyond their elasticity limit is important for many technological operations, such as a production of reinforced fibers, sheets, plates and so on [1]. A plastic deformation of semi-crystalline thermoplastics is characterized by the creation and development of a neck. In such cases, the localized plastic deformation can reach hundreds or thousands of percents. The mechanisms of plastic or visco-plastic deformation of these polymers are strongly dependent on supra-molecular structure (content of the amorphous phase, the size and configuration of crystallites, etc.). The attention of plastic processing industry is in recent years focused on cost reduction and improvements of mechanical properties of plastics. It can be achieved by the usage of the controlled co-polymerization or various blending. Typical example of the newly developed material is the blend of polypropylene (PP) and polyethylene (PE). Both materials have different molecular and supra-molecular structure and as a result they also have different mechanical behavior. The main task is how to interconnect these two structures so that the resulting blend should have the best mechanical properties (the problem of blend compatibilization). Special compatibilizers have been developed for this purpose (copolymer additives). In this study, e.g., we used a modifier, VISTALON, with variable content of ethylene units.

The influence of compatibilizers or other additives (rubber particles, etc) is relatively small in the range of elastic (or linear visco-elastic) deformation. But it becomes important when the plastic deformation becomes large near the neck formation and with neck elongation, as well as in the case of defect (crack) initiation and growth. The creation and development of a localized plastic deformation under different strain rates can be well documented using video-recording of a sample during the standard tension test. Then it is possible to analyze the distribution of longitudinal and transverse deformation of the specimen in each moment of the video image record (it enables to localize the place of a neck formation and its continuous elongation). However, the

video-recording gives no local information about micro-mechanisms and structural defects related to the neck formation and elongation. Such information may be obtained by the acoustic emission (AE) method [2].

2. Tension Tests of Polymer Blends

Polymer specimens for standard tension test were prepared; a set was made of pure isotactic PP and further sets of PP and PE (HDPE) blends with various additives and modifiers. During tension tests under different strain rates (5 to 200 mm/min.), AE signals were detected by two sensors placed at the specimen ends. The goal was to monitor changes of plastic deformation mechanism and beginning of damage and fracture, dependent on the composition of the material and the strain rate. Many tests were performed with the following specimens: pure PP, PP+PE (50+50%) blend without compatibilizer, blend of PP+PE (47+47%) + 6% compatibilizer VISTALON 407 (i.e. copolymer PP+PE with 40% of ethylene units), blend PPR (PP+22.5% modifier ROYALEN), blend PPK (PP+22.5% amorphous rubber KELTON) and blend PPB (PP+22.5% semi-crystalline rubber BUNA).

Some experimental and procedural problems were encountered during the first tests: The first question concerned with the reproducibility of acoustic coupling of broadband AE sensors placed on a glassy surface of the specimen subjected to large plastic elongation and neck development. Next problem was related to the linear localization of AE sources during the continuous increase of the distance between both sensors. Also a relatively high attenuation of tested polymer samples (more than 1 dB/cm) and its growth during the test causes AE detection and evaluation difficult. The detailed analysis of material structure changes requires correlation of AE sources with the localized plastic deformation. Considering inhomogeneous distribution of plastic deformation along the sample (neck formation and elongation), and the fact that the total elongation of the specimens to the fracture can achieve tens to hundreds of mm (deformation is hundreds of %), it is evident that only a non-contact (optical) strain measurement method can be used. Equidistant marks were drawn on the specimen surface, and their changes were scanned by digital camcorder. Camera also scanned the position of the AE sensors. So the instantaneous distance between sensors, necessary for successful AE source location, was obtained from video-records. The video-record is synchronized with AE registration by the time code and also (for the fast check) by synchronous video-recording of the AE-analyzer audio-monitor output. Due to the high material attenuation and relatively noiseless deformation mechanisms, the AE analyzer had to be set on high total amplification (of about 85 dB). Also the threshold level for AE counting was set just above the background noise.

The experimental setup used in tension tests is shown in Fig. 1. Specimen is loaded using the computer-controlled electromechanical tensile testing machine TIRATEST 2300 with attached dynamometer of 10 kN capacity. Signals from AE transducers were parallel-processed by two 2-channel AE analyzers: The analog D/E 3000 analyzer served as a "stereo" audio-monitor and linear locator. Signal waveforms were recorded by the digital analyzer DAKEL-XEDO equipped with signal processors. It allows registration of global parameters, as well as digital recording and frequency analysis of sampled AE events. Low-frequency audio-monitor output was recorded by the digital camera (48 kHz/16 bit) at the same time with movies. After the test, the video and sound data from the camera are transferred through the interface IEEE1394 (firewire) into a PC. The changes of distances between calibration marks (initial spacing was 5 mm), changes of specimen widths (lateral deformation) and also changes of distance between AE sensors during the whole test are then analyzed by the special software designed for this purpose.

Analyzed details of specimen evolution during the test are shown in Fig. 2 (snapshots by steps of 200 s). Video-recording is synchronized with presence of emissive event detected by AE sensors with the accuracy of 40 ms. It makes it possible to correlate diagrams of heterogeneously distributed instantaneous specimen deformation (strain rates) with that of AE event occurrence.

EXPERIMENTAL ARRANGEMENT OF TENSILE TESTS

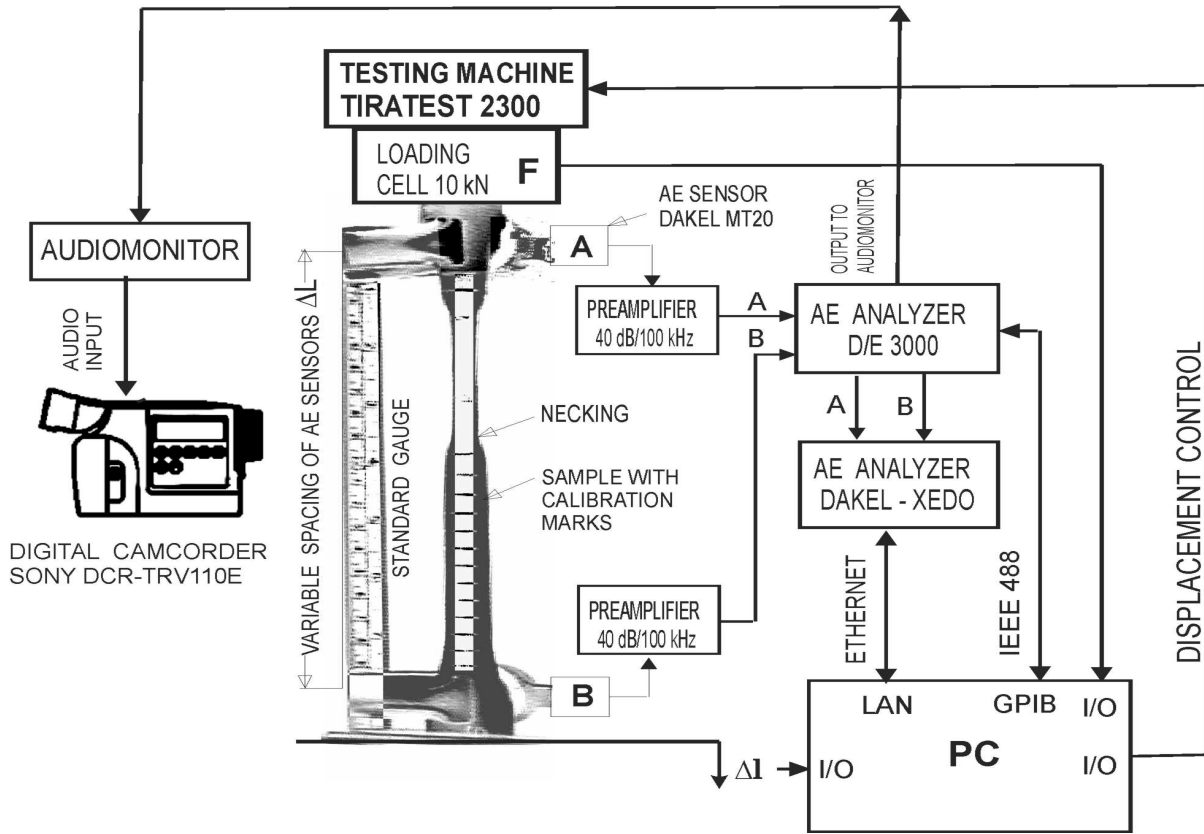


Fig. 1. Schematic drawing of experimental setup used in tension tests of polymer samples.

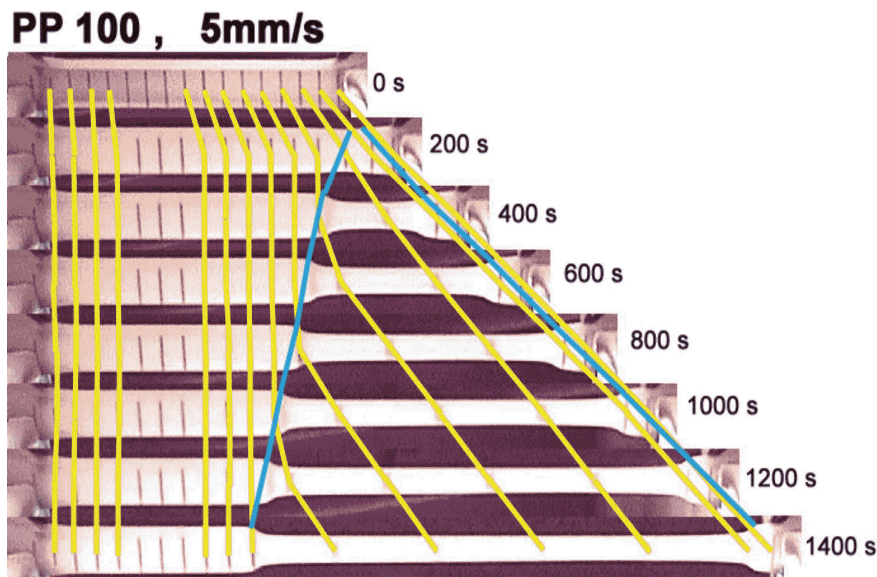


Fig. 2. Samples of videorecords during test of pure PP; the creation and elongation of the neck (5 mm spaced markers are connected by white lines and neck ends by black lines).

3. Evaluation of Video-Recordings

We used a digital camcorder that scans 25 frames/s, with resolution 720 x 576 pixels, and color depth 24 bit. Video and sound information are encoded using camera firmware (codec DV video). Resulting data flow recorded by the camera (DIGITAL-8 format) amounts to 3.6 MB/s. After the test, all data are transferred to a PC hard disk. One-minute recording matches AVI file with size of 216 MB. Total time of tension test until fracture of a specimen was as much as 30 minutes, which results in AVI-file size of about 7 GB. With respect to the main research objectives (deformation behavior of tested material, continuous plastic deformation and neck formation) the information content is inefficiently huge. Only selected frames were analyzed from video files (50 to 500 frames at equidistant time intervals of 3 to 30 s). Distribution of longitudinal and lateral strain along the sample was automatically analyzed in selected frames, showing the neck formation. At very high elongation rates (200 mm/min.) the test duration is only a few s, hence all saved frames were analyzed.

Algorithm used for automatic evaluation of deformation characteristics from video-records must take into account various problems associated with image recognition:

- a) Non-uniform scene illumination during the test (designed algorithm was sufficiently robust to eliminate that influence, so the contrast and brightness corrections were not necessary)
- b) Analyzed scene is distorted due to the short focal distance. Quite sufficient solution was based on a simple linear transform (rhomboid transformed to rectangle).
- c) During the sample stretching it is difficult to separate specimen from surroundings, and moreover, both sample heads are moving (constant position have only static parts, e.g. upper clamp). The problem is solved by suitable editing of the first and last frames (easily detectable crosses are added to the last markings on a sample). The relative movement of enlarged sample heads is influenced only by pure elastic deformation proportional to the strain rate and thereby the sample position in all other scenes can be well localized.
- d) The markers drawn on the specimen change not only their lengths (lateral contraction), but their widths (differently in various specimen parts). Variable width of markers disallows the use of classical line detection algorithm, and it must be replaced by the edge detection (left and right edges are detected and the line position is identified as their arithmetic mean). The edge detection is performed by the convolution of analyzed scene with a suitable mask.
- e) The light source is not placed in the camera axis, which results in shadowing of thickness changes (false lines has sometimes more contrast than detected lines). Presence of false lines requires to detect real edges only around their expected position. The prediction is realized using the edge position in previous scene and knowledge of exact strain rate.

Designed automatic algorithm consists of following steps:

1. Detection of the auxiliary crosses in the first and the last analyzed frame ($i = 1, N$).
2. Detection and localization of the left and right edges in the first frame.
3. For $i = 2$ to N :
Detection of the left and right edges in frame (i) using the knowledge about detected edges in figure ($i-1$). Determination of marker positions in frame (i).
4. For $i = 1$ to N :
Detection of top and bottom sample edges at places of detected markers in frame (i). Determination of specimens width in places of detected markers.

The accuracy of evaluated strain distribution depends primarily on a pixel resolution of camera used. Further errors are caused by the algorithm of video-recording compression, and by the precision of drawn markings.

4. Discussion of Results

Results of AE analysis revealed that AE activity during the heterogeneous plastic deformation is predominantly concentrated in areas of necking (neck boundaries). After the further neck drawing, especially if another deformation mechanisms start to develop, the other areas become also active. Intensity of AE increases rapidly when defects are formed in plastically exhausted zones. Development of crack-like defects lead to specimen rupture. The typical AE activity distribution along the sample of PP+PE blend is illustrated in Fig. 3a, where the AE activity is characterized by the number of events N_e (3 decades in logarithmic scale) emitted between two subsequent time snapshots taken at 30-s interval. The variation of loading rate from 0.1 to 50 mm/min has no substantial influence on the test history.

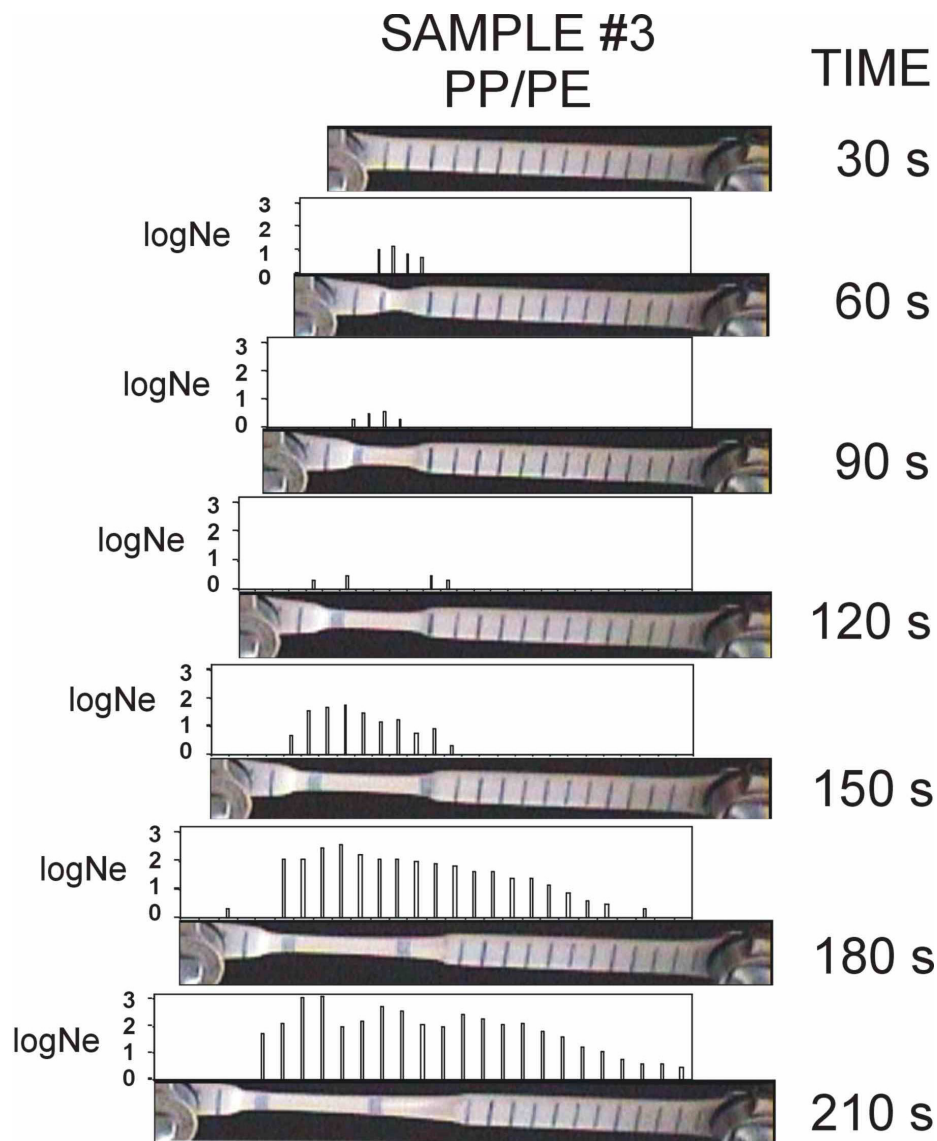


Fig. 3. AE activity during the test of blend PP (50%) + PE (50%).
a. Number of AE events N_e (log. scale) distributed along the sample snapshots.

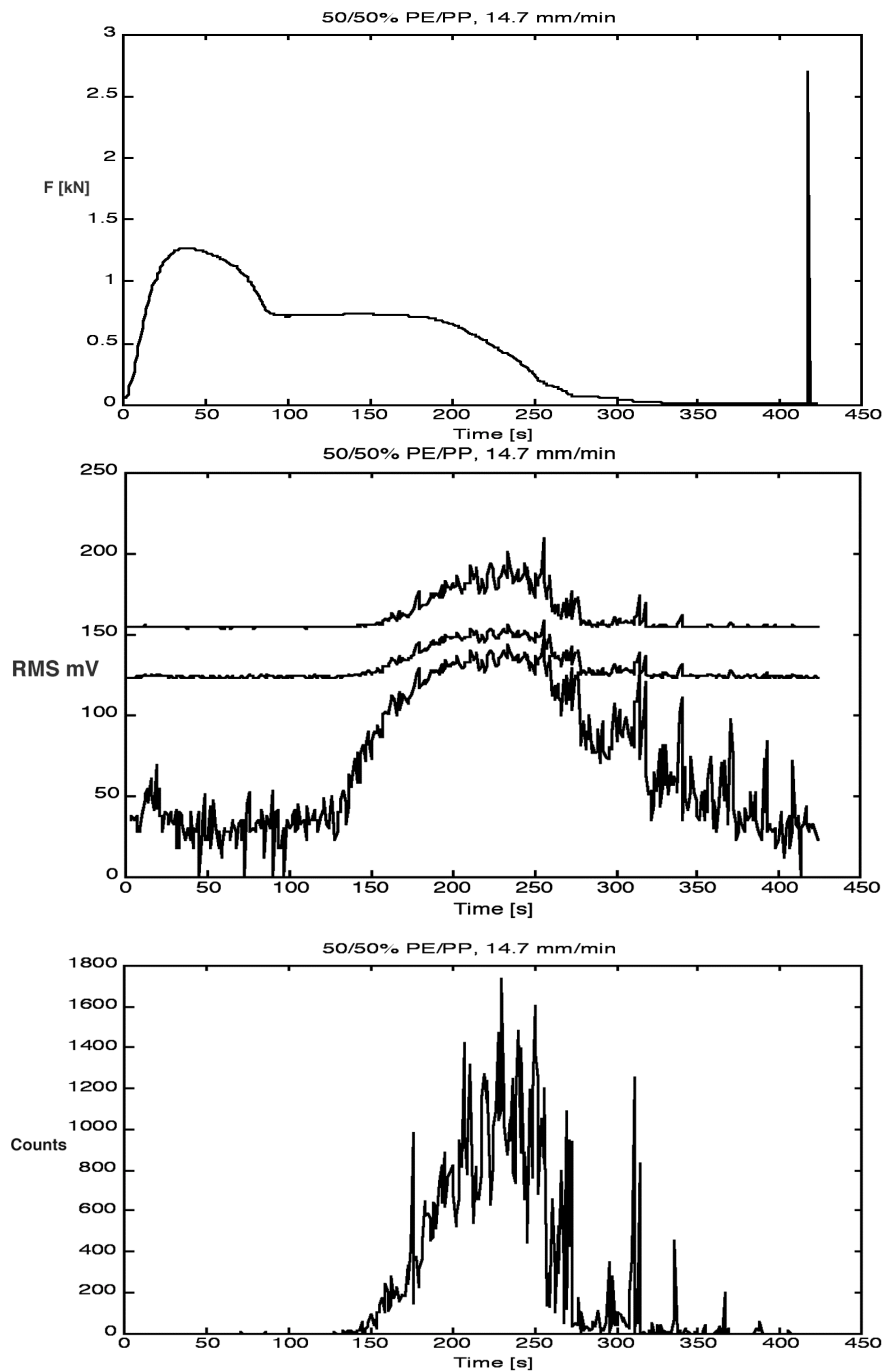
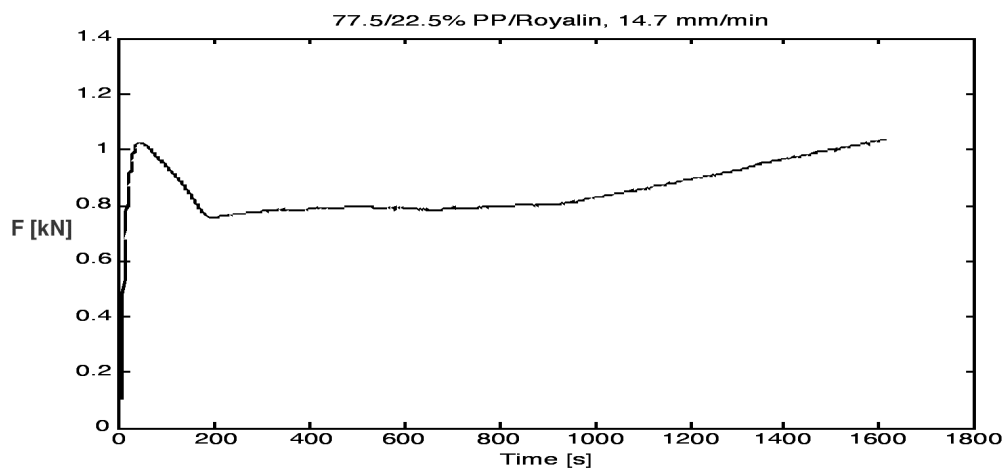
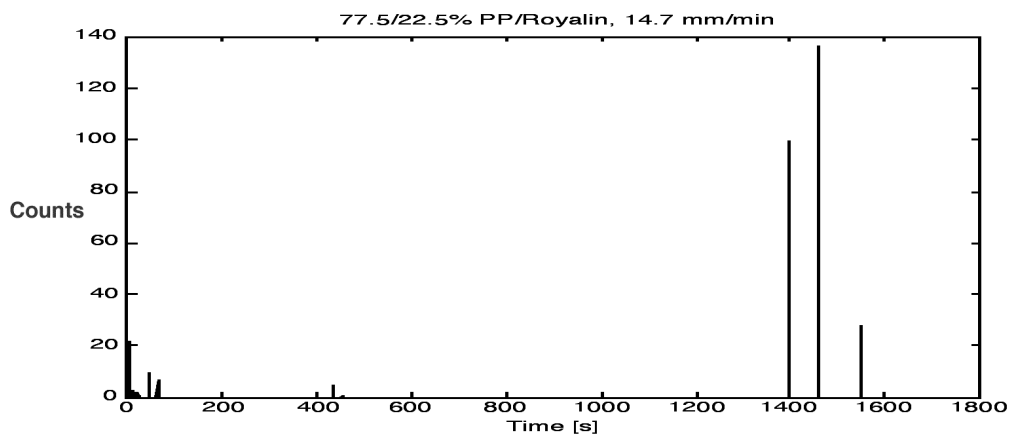


Fig. 3. AE activity during the test of blend PP (50%) + PE (50%). b. (top) Loading force vs. time. c. (middle) AE activity expressed by RMS values of both AE channels, A and B (upper and middle curves), and RMS recorded by camcorder (channel A). d. (bottom) Number of counts Nc1 in channel A.

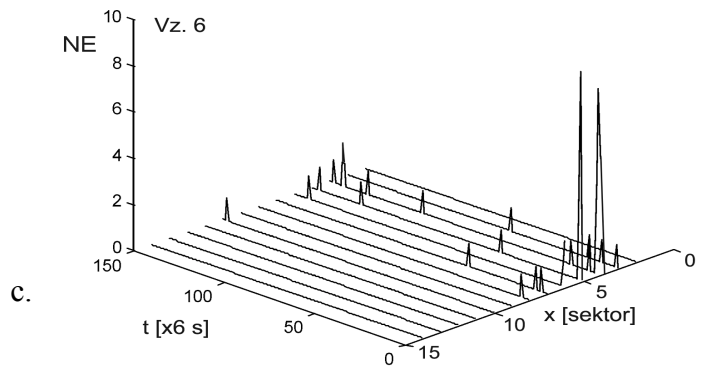
Samples made of pure PP exhibited very low AE activity, with the maximum in transition to plastic deformation, when the neck with sharp boundaries begins to form. When the neck elongates, the AE activity is rapidly reduced. It re-appears again just before the specimens rupture, when a fibrous structure forms and breaks (axial fibers are drawn out). If the displacement rate is higher than 100 mm/min, the deformation behavior of the PP specimen becomes completely different, and specimen breaks in a quasi-brittle manner.



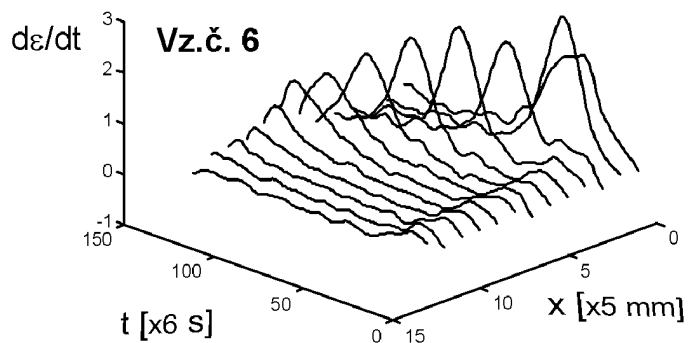
a.



b.



c.



d.

Fig. 4. Test of the blend PP (77.5%) + additive ROYALEN (22.5%)
a. Time dependence of the loading force F .
b. AE count rate dN_{c1}/dt .
c. Time development of axial distribution of AE events N_e .
d. Strain rates $d\varepsilon/dt$ vs. t and x . Distributions along the sample axis x are related to the initial markers spaced by 5 mm (sectors).

Blends made of PPR, PPK and PPB exhibited similar deformation behavior, but the formed neck had no sharp boundaries. They are also characterized by the relatively small AE activity as it is illustrated in Fig. 4.

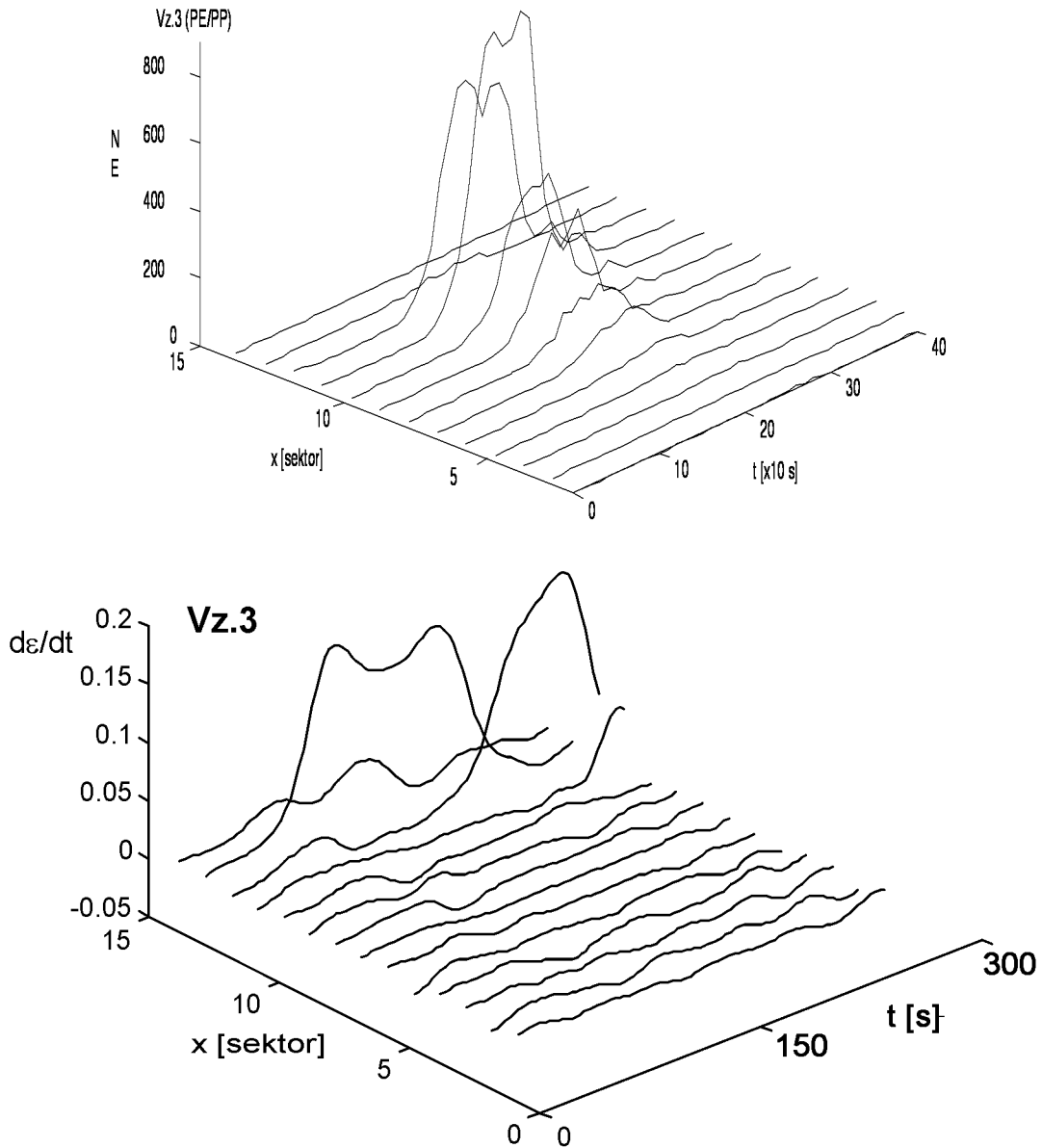


Fig. 5. Test of the pure blend PP (50%) + PE (50%) (for other characteristics, see Fig. 3). Top: Time development of axial distributions of AE events N_e . Bottom: Time development of strain rate $d\epsilon/dt$ distribution along sample axis. Distributions are related to initial markers spaced by 5 mm (sectors).

Quite dissimilar AE activity was detected for PP+PE blends. Already initial tests indicated differences in deformation behavior of blends with added compatibilizers. Test examples are shown in Fig. 5 (PP+PE without additives, see also Fig. 3) and in Fig. 6 (mixture with 6% of compatibilizer VISTALON 407).

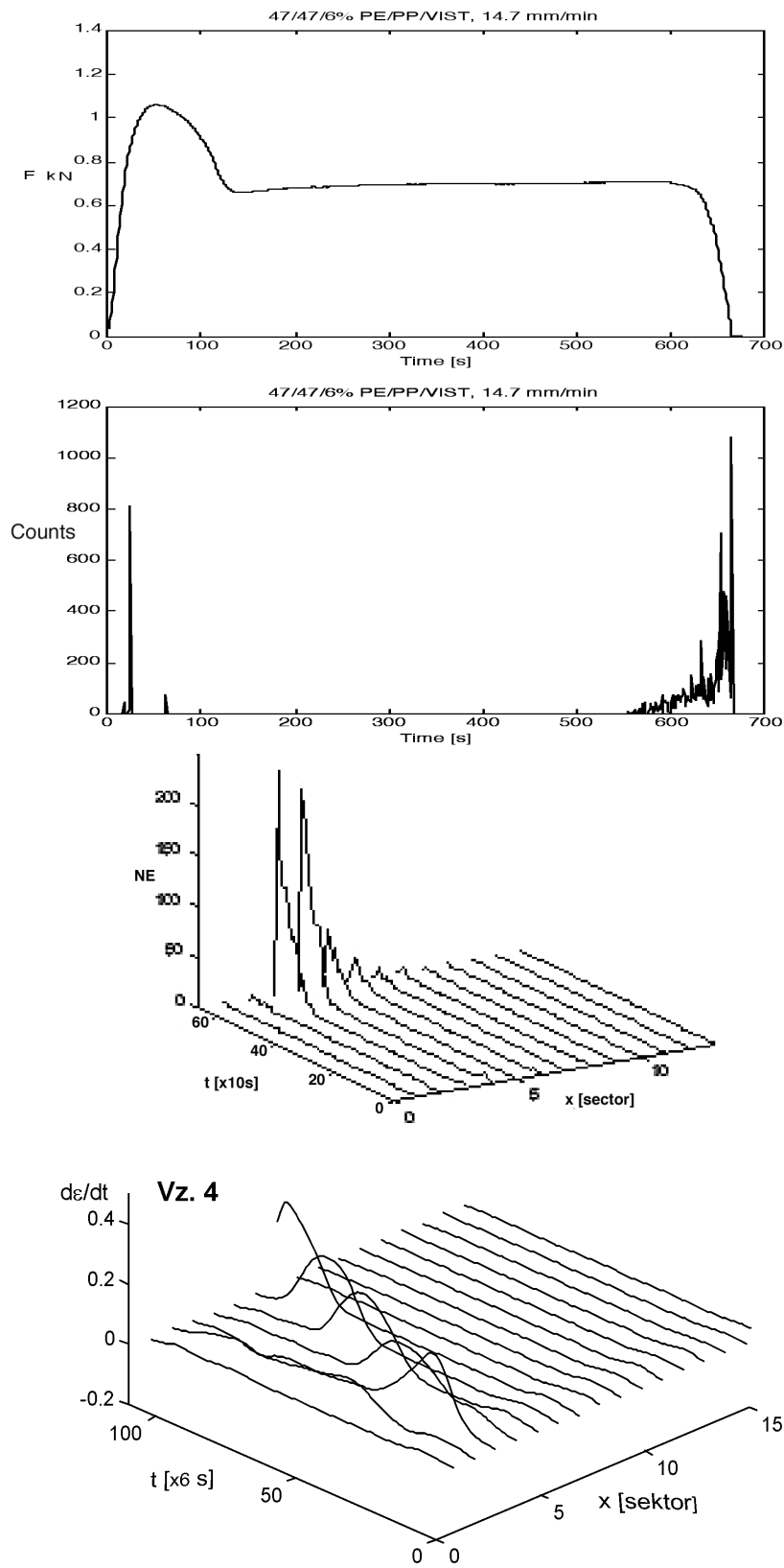


Fig. 6. Test of blend PP (47.5%) + PE (47.5%) + VISTALON (5%). Top: Time dependence of the loading force F . Middle: AE count rate dN_c/dt . Middle-lower: Time development of axial distributions of AE events N_e . Bottom: Strain rates $d\varepsilon/dt$, vs. t and x . Distributions are related to initial markers spaced by 5 mm (sectors).

Detailed analysis of considerably different AE activities at distinct periods of drawing process can help explain structural mechanism of compatibilizer effect. AE activity of samples without modifier markedly increases at the beginning of neck formation without sharp boundaries. This activity remains very high until the specimens rupture, and can be compared with AE of polymer composites. To explain AE activity, we must consider that PP and PE have different crystallite sizes and the structure with different crosslinks (tie molecules). In a blend, there are two different networks mechanically joined together, which must be rearranged and uncoupled during their deep drawing. In contrast to previous pure polymer, the blend PP+PE with added compatibilizer VISTALON 407, which is completely amorphous copolymer, had in the first deformation phase the behavior similar to the pure blend. When the neck started to draw, the AE activity became very low, similar to the pure PP. It may be caused by the presence of compatibilizer, which allows better sliding of networks through the amorphous phase. Nevertheless, after reaching a certain drawing limit, the AE suddenly starts to grow to the level of the blend without modifier. This relatively complicated AE behavior reflects very sensitively changes of structural mechanism during various deformation periods in the materials with complicated molecular network structure. Synchronous video-recording with the AE monitoring shows the instantaneous correlation of the heterogeneously distributed plastic strain rates with the occurrence of active AE sources.

Recorded AE signals were also subjected to frequency analysis and their evaluated parameters in time and frequency domain were used as input data for the source type classification. However, no sharply different classes have been recognized. It is probably caused by many geometrical factors affecting the way of elastic wave propagation:

- a) Dimensions of the active part of test specimen (100 x 10 x 4 mm, initially) are comparable to the length of detected elastic waves spreading from AE source to a sensor (2 to 20 mm in hundreds kHz frequency range). It results in strong wave dispersion and guided waves are mainly detected, which substantially modify the spectral and other characteristics of received signal (filtration effects) and partially implicate loss of information about the sources.
- b) Geometrical form and dispersion behavior of the specimen pass through considerable changes during the course of very large deformations (hundreds of percent). Moreover, the distance between AE sensors changes. It complicates the attempt of getting precise linear location of AE sources.
- c) Tested polymer materials exhibit relatively high attenuation in the used AE frequency range (100 kHz to 1 MHz). Only the AE events with higher amplitudes were detected by both transducers. This allowed localization of only about 30% of all registered events. To obtain correct interpretation of structural changes, it is therefore necessary to evaluate global AE characteristics in both channels separately, and make corrections to them for the attenuation changes.

5. Conclusions

Deformation behavior of semi-crystalline polymer materials, PP and PE, and their blends with various additives, was investigated by means of video-recording and AE monitoring during the tensile tests. The video-records were used to evaluate the localized plastic deformation distributed along the sample. Comparison of plastic zone expansion (necking) and spatial distribution of AE events shows that primary sources of AE are places, where the plastic necking starts to develop, areas of neck drawing, and finally locations where neck stopped its elongation and crack defects are created. It has been detected that deformation and AE behavior of pure PP and PP with small addition of rubber-like fillers (very low AE activity) markedly differs from the

behavior of polymer blends of PP with PE, whose plastic deformation is accompanied by very high AE activity. Tests also helped to clarify influence of blending compatibilizers on a plastic zone development: Compatibilizers prolong the first stage of plastic deformation with low AE activity (comparable with the pure PP), but after reaching some deformation limit, their AE behavior is similar to blends without additives.

Using the low-cost digital camera for video-recording of mechanical tests together with proper evaluation algorithms allows detailed analysis of AE source distribution connected with structural changes during the localized plastic deformation.

Acknowledgment

The project was supported by the Grant Agency of the Czech Academy of Sciences under the grant No. A 4050904.

References

- [1] Raab M., Sova M., Slízová M.: "Importance of polymer morphology in understanding technological processes", *Internat. Polym. Sci. Technol.*, **21**, T81-T88 (1994).
- [2] Raab M., Prevorovsky Z., Kardos J.L.: "Quiet and noisy polyethylenes: Birth and Failure of a composite", *17th Europhysics Conference on Macromolecular Physics "Morphology of Polymers"*, Prague 1985, Book of Abstracts, p. 95.

ACOUSTIC EMISSION CHARACTERISTICS OF SURFACE FRICTION IN BIO-MEDICAL APPLICATION

D. PREVOROVSKY¹, Z. PREVOROVSKY¹, J. ASSERIN², D. VARCHON³

¹ Institute of Thermomechanics AS CR, Czech Republic; ² EVIC France, Bordeaux, France
³ LMARC Université de Franche-Comté, Besançon, France.

Abstract

The paper describes the use of acoustic emission (AE) techniques in a study of surface friction properties. All dynamic friction processes generate quasi-continuous AE signal, which can be used to characterize surface friction. The AE signal is produced by stick-slip motion of two materials in contact. Signal intensity depends on contact force, motion velocity, molecular adhesion forces between both materials, and surface properties as roughness, hardness, elastic and plastic properties and surface layer properties (lubrication, dry friction).

A series of tests have been performed using a new prototype of friction brush probe combined with tangential force measurement. This probe has been designed for measurement of human skin friction coefficient, but can be applied also to other materials. Measured signals (AE signal, tangential and normal forces) were recorded and analyzed by digital processing analyzer DAKEL-XEDO. Various friction head materials were tested on samples made of different materials. The best results were obtained using carbon-fiber brush friction head. The contact force and motion velocity were optimized to produce maximal AE signal amplitude at a contact force as low as possible. Good correlation was observed between frictional forces and global AE activity parameters.

1. Introduction

Properties of a solid body surface (surface roughness, coarseness, abrasiveness, profile, topology, friction, adhesion tension, etc.) are often characterized by static or dynamic friction measurements. Friction can be defined as the resistance to the movement of one body in relation to another body with which it is in contact [1].

The degree of friction between two objects is greatest when they are at rest (static friction). The direction of static frictional force is along the contact surface and opposite in direction of any applied force. The magnitude of static friction force f_s is given by

$$f_s = \mu_s N, \quad (1)$$

where μ_s is static friction coefficient, and N is normal force acting between two objects. The frictional force equals the applied force (in magnitude) until it reaches the maximum possible value $\mu_s N$. Then the object begins to move as the applied force exceeds its maximum. When the object is moving the frictional force is kinetic (kinetic or dynamic friction) and roughly constant at the value $\mu_k N$, which is below the maximum static friction force. The direction of the kinetic frictional force is opposite the direction of motion of the object it acts on. The magnitude of the kinetic friction force f_k is proportional to normal force N and the coefficient of kinetic friction μ_k

$$f_k = \mu_k N. \quad (2)$$

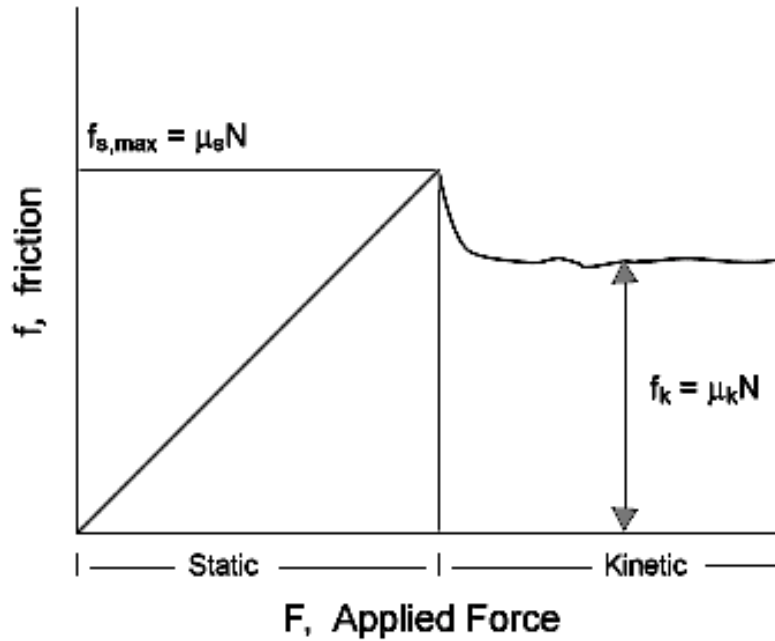


Fig. 1. General relation between frictional and applied force

The coefficients of friction depend on the nature of the surface, and the frictional force is nearly independent of the contact area between objects. The plot in Fig. 1 of the frictional force vs. the applied force illustrates some of the friction features. Friction depends upon the properties of the two surfaces in contact. The irregularities in surfaces (the degree of roughness) cause resistance to movement. The force of friction is a common but complex force. A simple model of the friction force can be built up assuming that the coefficient of friction is the sum of two terms, molecular and mechanical [2];

$$\mu = \mu_{\text{molecular}} + \mu_{\text{mechanical}}. \quad (3)$$

Molecular interactions take place in the surface 'film' and affect the surface layers to a depth of a few hundredths of μm . Mechanical interaction takes place in layers with a thickness of a few μm . As these processes occur at different levels, they are uncorrelated and hence can be mostly separated. Kinetic friction coefficient is measured throughout the displacement of body over the surface by a constant velocity v . It depends on normal acting pressure and movement velocity as well as on properties of both surfaces in contact (molecular adhesive forces, roughness, hardness, lubrication, etc.). Accompanying friction, physical effects such as thermal effects, electromagnetic and optical effects (triboluminescence), low frequency vibrations (1 Hz – 10 kHz) and acoustic emission (30 kHz - 5 MHz) are observed and are evaluated for surface characterization.

Excited by dry friction on a rough surface, AE is monitored using AE sensor attached to the moving body (stylus) and/or to the stationary surface base, as Dunegan reported in [3]. Detected AE signals have relatively broad frequency content ranging mostly from 1 kHz to a few MHz depending on surface roughness, and on frequency characteristics of AE transducer. It also depends on a wave-path from friction surface to the AE sensor.

In previous laboratory experiments, AE transducer was coupled with stylus (acting as a wave-guide) scanning tested surface. Different stylus materials (hard materials ranging from metals and ceramics to glass, sapphire, diamond and other crystals) of various quasi-point contact radius and form (ranging from sharp tip or needle to a ball) were used in these measure-

ments. Test results were similar to that from surface profilometry, where the registered vertical displacement of stylus is proportional to the surface roughness profile.

The newest contact methods of surface properties study are known as atomic force microscopes (AFM) based on diverse sensing devices. The main principle of AFM consists in 2-D surface scanning by a single stylus or a thin hard wire contacting tested surface. AFM's are highly precise, very sensitive, expensive and bulky laboratory instruments allowing to scan only few square mm of studied surface of a small body supported by a rigid base. Except for classical friction measurement (displacement of a body over the surface), all other reviewed methods give only local, instantaneous information (one contact point of stylus or wire with the surface), which is then spread over the line or area by the scanning. For area characterization, large amount of data must be analyzed. This led us to design a new approach as described below.

2. Design and Operation of the Acoustic Brush Probe (ABP)

The low-resolution alternative to AFM for the rough characterization of surface properties has been designed and patented as a "Friction Brush Probe" (ABP) [4, 5]. It represents new type of direct mechanical contact sensor designed for non-local surface characterization during the sensor movement along a surface line or other path. The basic element of probe is a fiber brush (line or multi-line bundle of thin fibers) joined with AE sensing element. The probe is mounted to the line or area-scanning device. During constant velocity brush movement over the analyzed surface, many of brush fibers are subsequently coming into and released from direct contact with the surface. These rapid processes of fiber-surface interaction (friction) are randomly exciting piezoelectric AE sensing element, which produces quasi-continuous AE signal. Simultaneously with AE signal acquisition, the classical friction parameters - tangential and normal forces acting on the probe - are sensed by external force sensing elements mounted on a probe holder or, in a combined probe version, directly by force sensing elements integrated with AE transducer in a common probe case. This enables direct correlation of AE signal parameters with classical integral surface friction variables, which are less sensitive to small surface disturbances. Schematic draw of ABP construction is shown in Fig. 2a.

The brush fibers in contact with the test surface are loaded by normal force N acting on the probe through the scanning head. Throughout the brush movement along the surface, AE transducer transfers the induced dry friction effects into electrical signal, recorded and processed by AE analyzer. Common AE signal processing methods are adopted in analyzing device (DAKEL - XEDO digital AE analyzer and transient recorder) including signal amplification and filtration. Standard and extended AE signal parameters (e.g., number of AE (threshold-crossing) counts, RMS, integral energy, average signal level, event counts and signal envelope parameters, as other selected signal features in time, frequency, time-frequency or wavelet domain) are evaluated by AE analyzer connected with a personal computer via LAN (ETHERNET). Evaluated parameters are used to characterize analyzed surface features and to correlate them with other commonly used surface properties (e.g., tangential and normal friction forces).

In the combined ABP design, the integrated tangential (shear) and normal force sensing elements are considered: The normal force sensing system is realized by deflection of spring membrane joined to the AE sensor. Deflected membrane acts on miniaturized pressure transducer connected to the A/D card installed in the DAKEL system. Hydraulic force multiplier is used to enhance pressure transducer sensitivity. Tangential force f_t is sensed by the deflection of a metallic foil attached to the AE sensor and semiconductor strain gauges connected to an interface

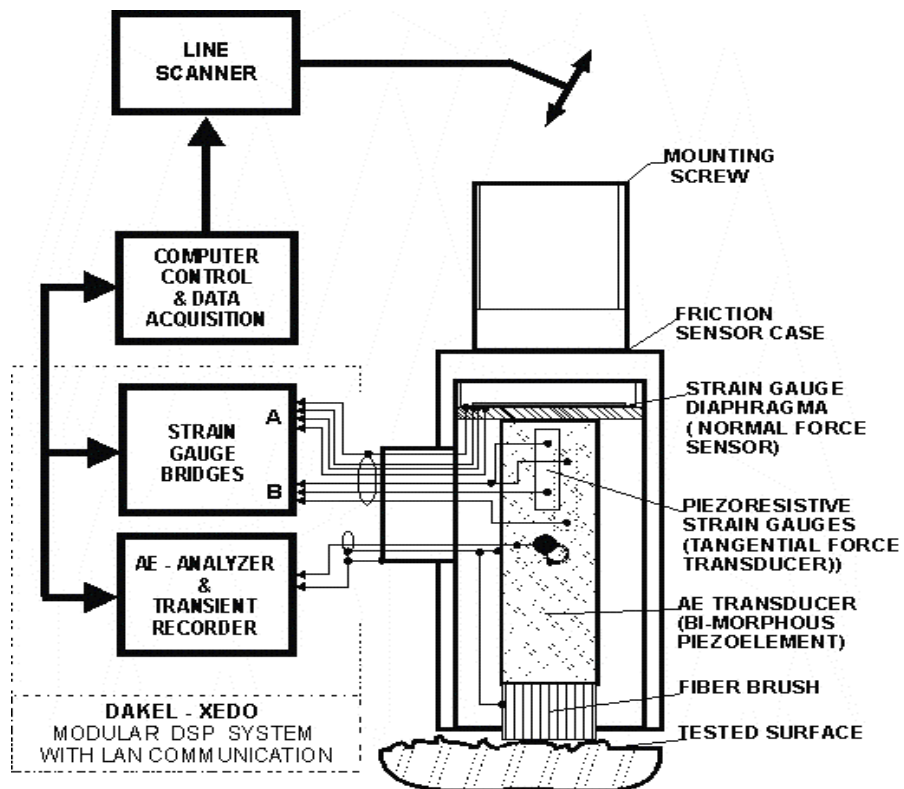


Fig. 2a. Schematics of acoustic brush probe.

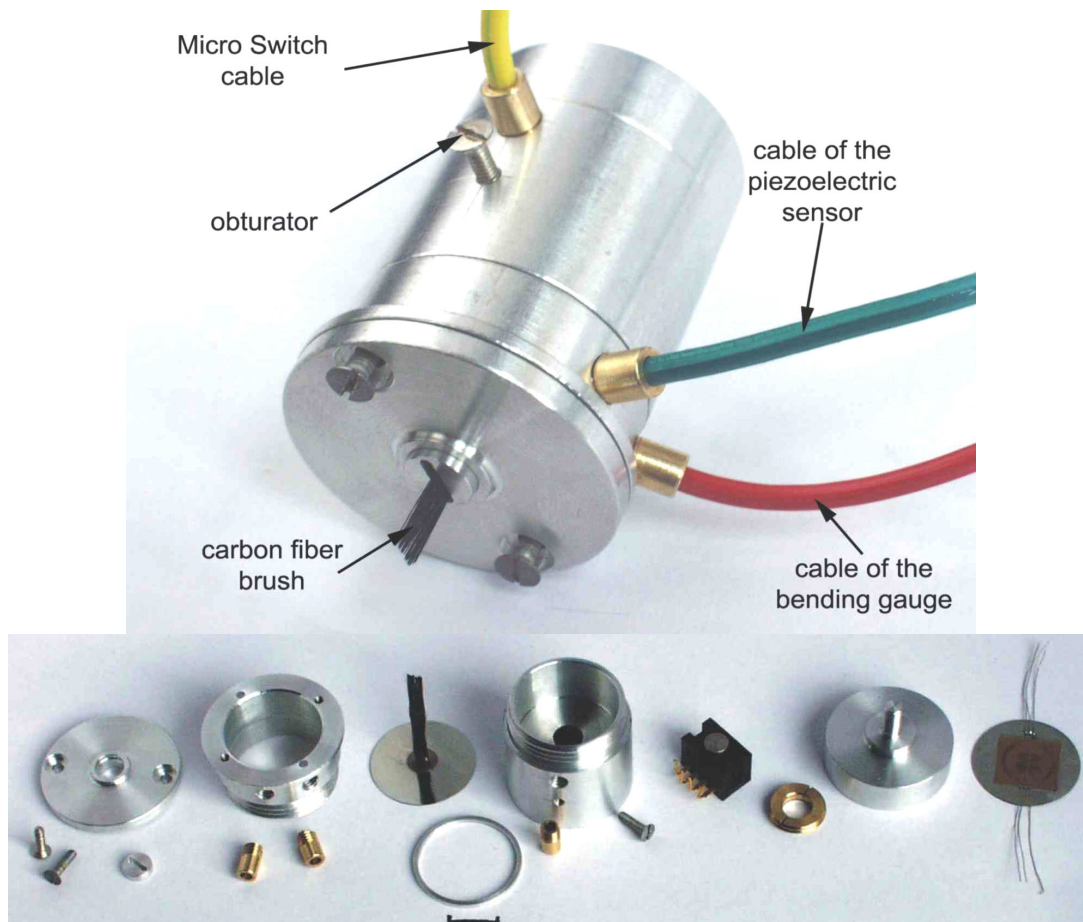


Fig. 2b. A prototype and detailed view of acoustic brush probe.

card of the DAKEL-XEDO device. The computer collects data from AE and force sensing elements and also controls the scanning device. One of ABP prototypes is shown in Fig. 2b.

3. Results Obtained by Acoustic Brush Probe

Measurements using ABP have been performed on two kinds of surfaces. First measurements were made on reference standards of surface roughness; here, we used abrasive papers of 120 to 1200-grit. In this case, the ABP was moved over the horizontally supported tested surface at a constant velocity $v = 10$ mm/s on a distance of approximately 50 mm using precisely controlled scanning device. Three kinds of line brushes have been tested, made from carbon, glass, and Kevlar fibers, respectively. Brushes were composed of about 1000 individual fibers of average diameter 2-10 μm . Best results were obtained with high modulus carbon fibers. Figure 3 illustrates AE activity detected through tests of abrasive papers (120- to 1200-grit with higher number for finer grains). AE activity is characterized by the sum of AE counts N_c . Slope of linear part of N_c -vs.- t plot, determined by linear regression, represents average count rate dN_c/dt .

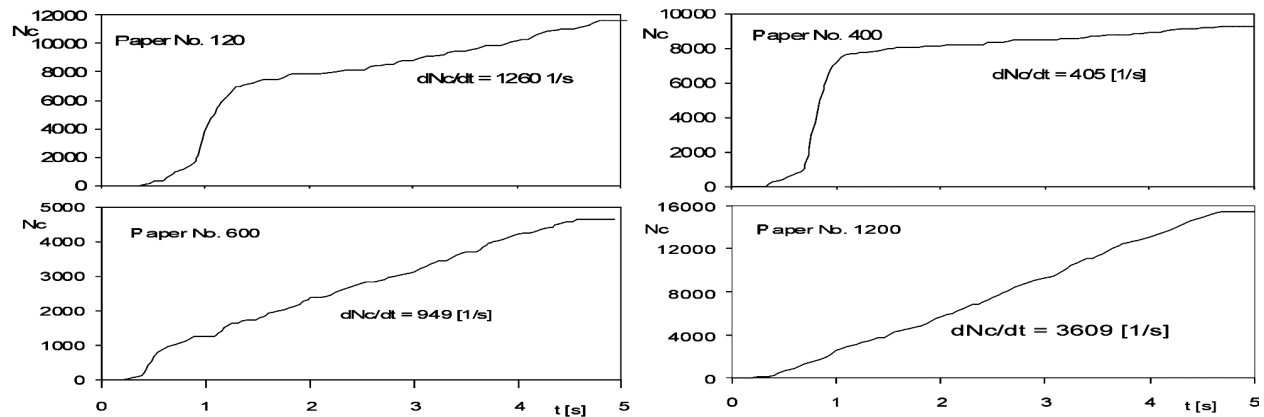


Fig. 3. AE activity recorded during ABP tests of papers with 120-, 400-, 600-, and 1200-grit.

Except for the roughest abrasive paper (120-grit), the tendency is increased AE activity with finer grains. The exception for 120-grit paper is explained by the effect of coarse grains causing stick-slip movement of individual brush fibers accompanied by relatively high-energy release. On finer surfaces, the fiber movement starts to be quasi-continuous with lower instantaneous energy release, but growing number of AE events with higher number of surface obstacles (grains) increases integral AE energy. Nevertheless, the growing trend of AE activity is limited by fibers diameter. When it becomes comparable or greater with respect to dimensions of surface crimps, then the AE activity decreases, reflecting sliding friction at molecular level only.

As ABP has been developed in particular for the characterization of human skin surface, second series of measurements were realized on human skin using specially developed scanning device. These measurements were performed in-vivo on 18 persons with various types of skin (normal, dry, diseased, etc.) at different places of the body (forearm and shank). Different normal loads and scanning velocities were applied to each measured person in order to study the influence of these two factors on AE results. Two main parameters, the number of AE counts N_{c1} and a signal RMS value, were evaluated from measured data to characterize skin properties. Figure 4 shows typical dependencies of AE activity on normal load (left) and on ABP displacement velocity (right). It can be concluded that average slope of N_{c1} (dN_{c1}/dt) is about linearly dependent on both factors in measured intervals.

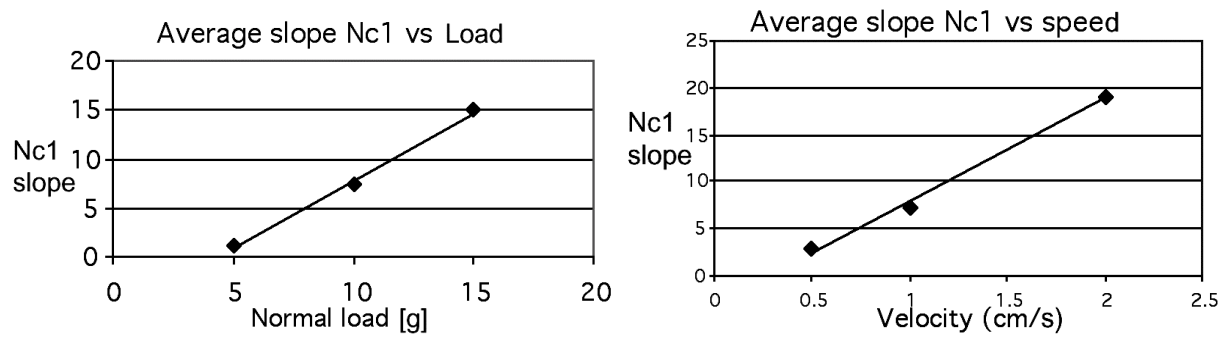


Fig. 4. Dependence of AE activity Nc1 on a normal load (left) and velocity (right).

A factor analysis has been performed to determine which are the main factors influencing the AE activity. Along with above mentioned velocity and normal load factors, the other parameters were also analyzed (test person's age, skin photo type, skin disease, test location, and interchangeable brush parameters). The brush type, loading force, and scanning velocity were the most important factors over the whole set of tests. Figure 5 illustrates the influence of the test person's age on the AE activity, when only tests having more parameter constants are considered. Average count rate in logarithmic scale (Fig. 5 - left) shows the growing global tendency with the person's age (five persons from 22 to 86 years old are classified), whereas the AE activity characterized by the average RMS value (Fig. 5 - right) tends to go down with the age during tests of younger persons between 22 and 35 years.



Fig. 5. Dependence of AE activity on the age of tested person.

Six persons with normal healthy skin were considered in the second group (right in Fig. 5), and results for two different scanning velocities (1 and 2 cm/s) are plotted. The differences between both plots in Fig. 5 can be explained by different information included in both AE activity parameters. While the count rate reflects more pronounced skin features (e.g. bumps), average RMS value integrates global skin friction properties. Another useful information has been drawn from AE records, e.g. concerning indication of some skin diseases, the ratio of AE activity parameters obtained in tests with different scanning velocities differs for healthy and ill skin. A more detailed and enlarged study under constant conditions is necessary to prove and elucidate the above findings. Also the frequency parameters of detected AE signals, which are evaluated in ongoing studies, seem to be useful for the characterization of skin friction properties.

The choice of brush-fiber material has shown to be of great importance as it determines molecular adhesion forces in friction. Elastic modulus and cross-section of fibers (brush rigidity) influence local forces acting on fibers, and energy stored and released during brush movement

over the surface. Hence, both the force and AE signal are dependent on brush rigidity. Low axial modulus and lower fiber cross-section (low brush rigidity) result in lower force and lower AE activity excited by surface friction. Fiber cross-section and stiffness also determine the resolution of surface characteristics (scale of details). Circular cross-section of fibers and rectangular form of brush (fiber bundle) are assumed in most cases but other forms may be considered, too. Concerning brush fiber material, the most practical (optimal) results are achieved choosing relatively short (some millimeters), small-diameter (1 to 10 microns) glass or high-modulus carbon fibers in a bundle containing thousands of fibers. To obtain well reproducible results, the brush should be prepared very carefully by the well-defined manufacturing procedure.

4. Conclusions

A new Acoustic Brush Probe (ABP) has been designed for the characterization of surface friction properties. Basic element of the probe is a brush of carbon fibers attached to AE sensor. A number of dynamic friction tests were performed using this probe, on both surface roughness standards (abrasive papers), and on the human skin surface of 18 persons at a dermatological clinic. The tests shown that registered AE activity depends on many influencing factors, whose importance was estimated by the factor analysis. Interesting relations between the global AE activity parameters and some external factors were found, which must be further proved in more detailed studies. ABP is suitable to design standard qualitative and quantitative method of rapid surface characterization and comparison. Standard measurement conditions and devices, along with evaluation procedures must be well defined for this purpose. In dermatological applications, the ABP can rapidly determine effects of a cosmetic product application or a clinical treatment. Evaluated integral AE activity parameters cannot render fine details of frictional behavior. Differences in spectral contents and time-frequency representation of AE signals, registered in ongoing experiments, seem to provide useful tool for more detailed characterization of material surface roughness and other surface friction properties.

References

- [1] Blau P. J.: *Friction Science and Technology*. Dekker, N.Y., 1996.
- [2] Persson B. N.: *Sliding Friction: Physical Principles and Applications*. Springer-Verlag, New York, 2000.
- [3] Dunegan H.L.: An Acoustic Emission Technique for Measuring Surface Roughness. The DECI Report No. 5, December 1998, <http://www/dec.com/report5.htm>.
- [4] Asserin J., Prevorovsky Z., Zahouanni H.: "Dispositif d'évaluation de propriétés acoustiques de friction d'un surface." Brevet d'invention No. 0009173, 33 INPI Bordeaux, 13 July 2000.
- [5] Prevorovsky Z., Prevorovsky D., Asserin J.: Characterization of Surface Friction by AE. *Proc. 6th Internat. Conf. of the Slovenian Society for NDT*, Portoroz, Slovenia, September 13-15, 2001, pp. 205-211.

ACOUSTIC EMISSION DURING MONOTONIC AND CYCLIC DEFORMATION OF A BRITTLE LIMESTONE

A. LAVROV^{1,2}, M. WEVERS³ and A. VERVOORT¹

¹ Katholieke Universiteit Leuven, Department of Civil Engineering, Leuven, Belgium

² Moscow State Mining University, Physical and Engineering Department, Moscow, Russia

³ Katholieke Universiteit Leuven, Dept. of Metallurgy and Materials Eng., Leuven, Belgium

Abstract

An overview of recent experimental research on acoustic emission (AE) during monotonic and cyclic tests of a brittle rock (crinoïdal limestone) is given. The AE and the Kaiser effect in 'Brazilian' tests are described. The results of experiments performed to reveal the directional and loading-rate sensitivity of the Kaiser effect are presented. The impact of the results on geotechnical applications of AE is outlined.

Keywords: acoustic emission, limestone, 'Brazilian' test, Kaiser effect, fracturing, rock mechanics.

1. Introduction

Deformation of rock specimens is accompanied by acoustic emission (AE). This is usually produced by the growth of micro- and macro-cracks, twinning processes and other structural changes. Together with other non-destructive techniques like electromagnetic emission, ultrasonic velocity and electric resistivity measurements [1-3], AE allows an insight into the fracturing process in rocks at mesoscale, at the early pre-failure stage.

The purpose of this paper is to give a review of our experimental research on AE in rock mechanics in various loading regimes. Special attention is paid to the Kaiser effect as a possible tool for stress estimation in rocks. The Kaiser effect takes place when rock is subjected to cyclic loading with the peak stress increasing from cycle to cycle [4, 5]. As long as the stress does not exceed the largest previously reached value, AE activity is sparse or there is no AE at all. As soon as this largest previously reached stress level is attained, AE activity increases dramatically. Yoshikawa and Mogi conducted a thorough investigation of temperature and water effects on the Kaiser effect recovery [6, 7]. The effect of sequential loading in mutually-perpendicular directions on the Kaiser effect in cubic specimens was studied by Michihiro et al. [8]. They also investigated the influence of time delay between loading cycles on the Kaiser effect recovery in brittle rocks.

The Kaiser effect seems to be applicable for stress measurements in rocks and soils. Such measurements are required in geological, geotechnical, mining and tunneling applications, e.g. for a proper design of underground workings, for regional seismic forecast and monitoring the rock mass stability in mines. First attempts of the application of the Kaiser effect for stress measurements in rocks were made by researchers from CRIEPI (Japan) in late 1970s [9].

Practical applications of the Kaiser effect for stress measurements require a firm understanding of its features under various loading conditions. One of the most important questions

concerns the manifestation of the Kaiser effect in cyclic loading regimes in which the directions of principal axes do not coincide in successive cycles. This question is important because all Kaiser-effect-based stress measurement techniques proposed so far imply that the specimen is recovered in the direction of the major in-situ principal stress, σ_1 . This direction is never known exactly. Very often, geological methods can provide some information on the approximate direction of the principal stresses in situ. Yet a possible deviation of the real major principal stress direction may not be excluded. To clarify what happens when the 2nd loading cycle is performed in a different direction than the 1st cycle, a series of tests is conducted. Specimens having the shape of thin disks are compressed along a diameter, then unloaded, rotated by an angle of θ and reloaded along the new diameter to failure. The loading scheme employed in these tests (diametrical compression of disk specimens) is usually called ‘Brazilian’ test and is widely used in order to estimate tensile strength of brittle rocks and concrete. Results of these tests are described in Sec. 5.

Another important question for practical applications of the Kaiser effect is its loading-rate sensitivity. Loading of rock in the Earth crust (in virgin rock masses or around underground cavities) can occur with different loading rates, from relatively slow (in geological history) to very fast (e.g. during rock blasting). The question is whether it is possible to estimate the first-cycle peak stress value by means of the Kaiser effect in the 2nd cycle, when the loading rates are different between the 1st and 2nd cycles? To clarify this question, a series of tests is performed on disk specimens in diametrical compression (‘Brazilian’ method). Results of these tests are described in Sec. 6.

2. Material and Equipment

Experiments are performed on a typical brittle rock, crinoïdal limestone. This low-porosity rock (porosity <1%) has a uniaxial compressive strength of 80 to 120 MPa, tensile strength of 15 MPa, and consists predominantly of calcite. Disk specimens are prepared for the ‘Brazilian’ tests with a diameter of 113 mm and a thickness of approximately 20 mm.

The loading is performed on the testing machine INSTRON 1196 with a constant displacement rate. The AE is measured by a two-channel AMS3 system (Vallen Systeme). Two wide-band sensors of type B1025 (Digital Wave) are coupled to the specimen using a high-vacuum grease. They are placed on the same plane of the disk, symmetrically with respect to the loaded diameter. This allows an approximate linear location of AE sources in the disk. The system provides a sampling rate of 5 MHz, with the ADC dynamic range of 78 dB. The preamplifiers have a gain of 40 dB. The built-in band-pass filters have a frequency range from 100 kHz to 1 MHz. The threshold level is chosen at 40 dB in all tests. Based on the AE data measured, the dependencies of cumulative hits versus load (stress) are plotted.

3. AE in One-cycle Brazilian Tests

A typical example of an AE signal measured in a ‘Brazilian’ test is shown in Fig. 1 together with its wavelet transform. Two energy maxima are well-pronounced in the wavelet, at about 20 μ s and 70 μ s. They correspond to the direct and the reflected wave, respectively.

Linear location of AE sources has shown that about 70% of all epicenters are located in the central zone of the disk. The width of this zone is about 30 mm, i.e., 15 mm on each side of the

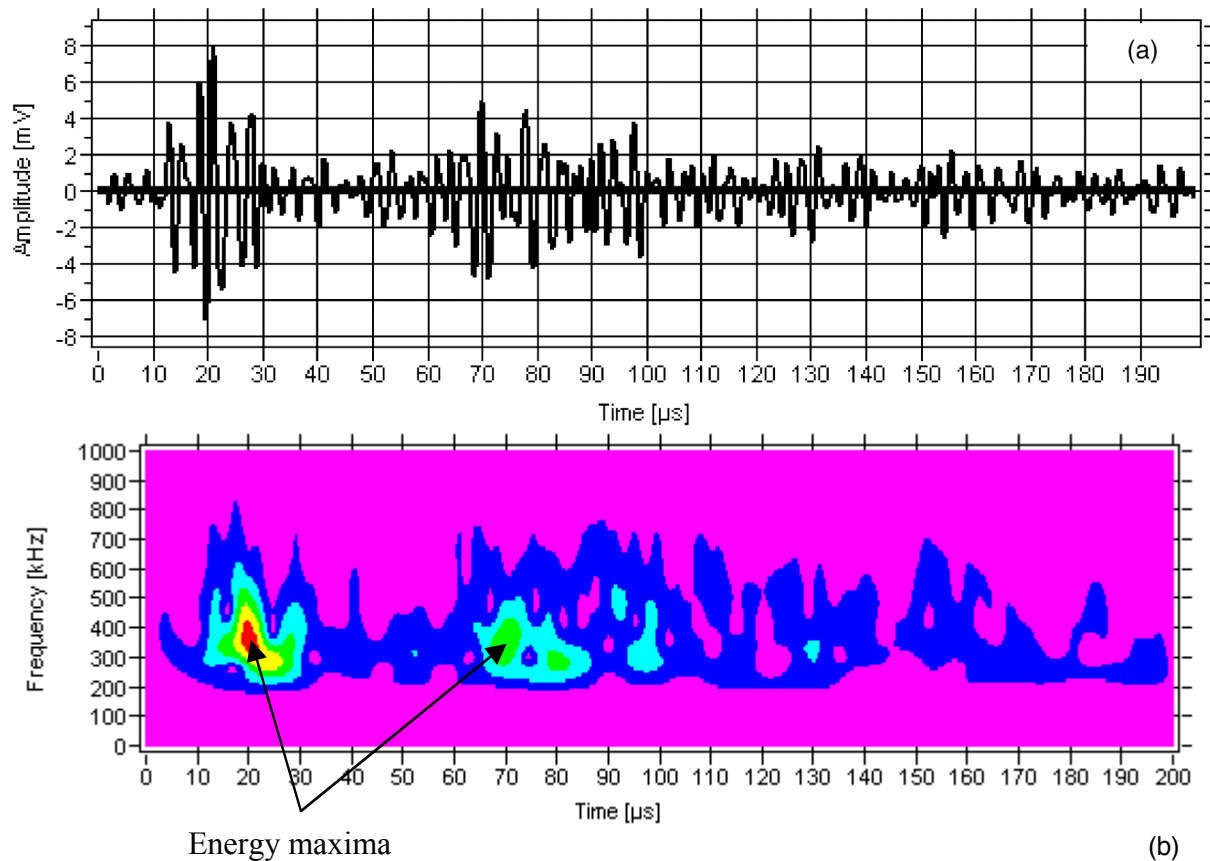


Fig. 1. An example of an AE full wave (a) and its wavelet transform showing the energy distribution with respect to the time and frequency (b) measured in ‘Brazilian’ test of a limestone specimen.

loaded diameter [10]. The concentration of AE sources in the central part of the disk is in agreement with the observed fracture forms, namely that the disks split along the loaded diameter.

In some of the tests, detectable AE starts from the beginning of loading, virtually from zero load. In other experiments, AE onset is observed at the load level corresponding to 10-30% of the ultimate strength of the specimen. AE hit rate measured as a number of AE hits per 1 kN load increment gradually increases with increasing load (Fig. 2b).

4. AE and Kaiser Effect in Cyclic Brazilian Tests

Cyclic loading of disks in diametrical compression is accompanied with the Kaiser effect: in each cycle beginning from the second one, AE starts when the load approaches the largest load value attained in the past (Fig. 3). This phenomenon is very similar to what has been observed in many other rocks and materials usually tested in uniaxial or triaxial compression (see [11-15] and references therein). In a ‘Brazilian’ test, a tensile principal stress is acting in the middle part of the disk, in the direction perpendicular to the loaded diameter. Parallel to the loaded diameter, a compressive principal stress is acting. This implies that while load increases, the rock undergoes a proportional loading in each point of the disk. Directions and ratio of the principal stresses are different at different points of the disk, but stay the same in each point during the loading. The observation thus shows that when two loading cycles are performed in proportional

regime (i.e. the ratio of principal stresses σ_1/σ_3 stays constant during the test), a very well-pronounced Kaiser effect takes place.

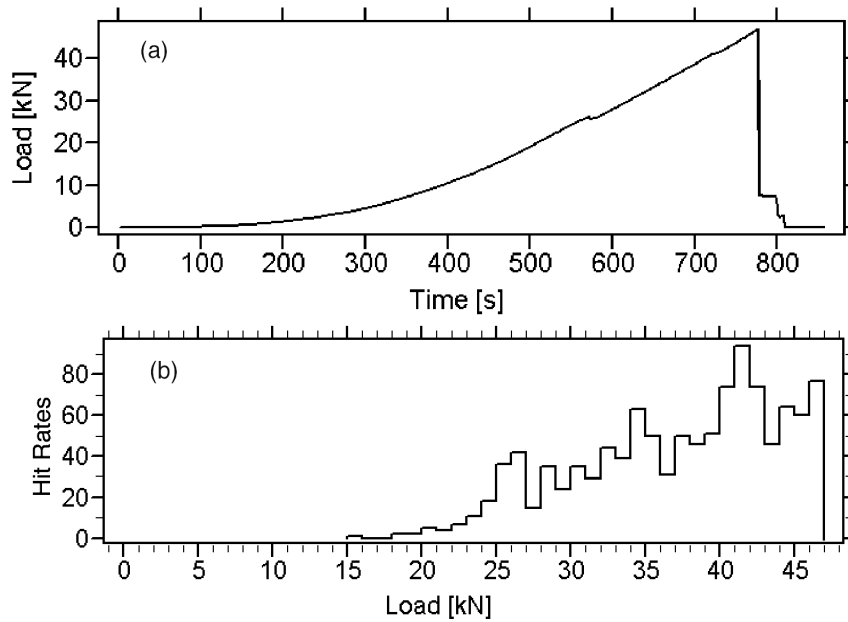


Fig. 2. Load vs. time (a) and AE hit rate vs. load (b) in a 'Brazilian' test of a limestone specimen.

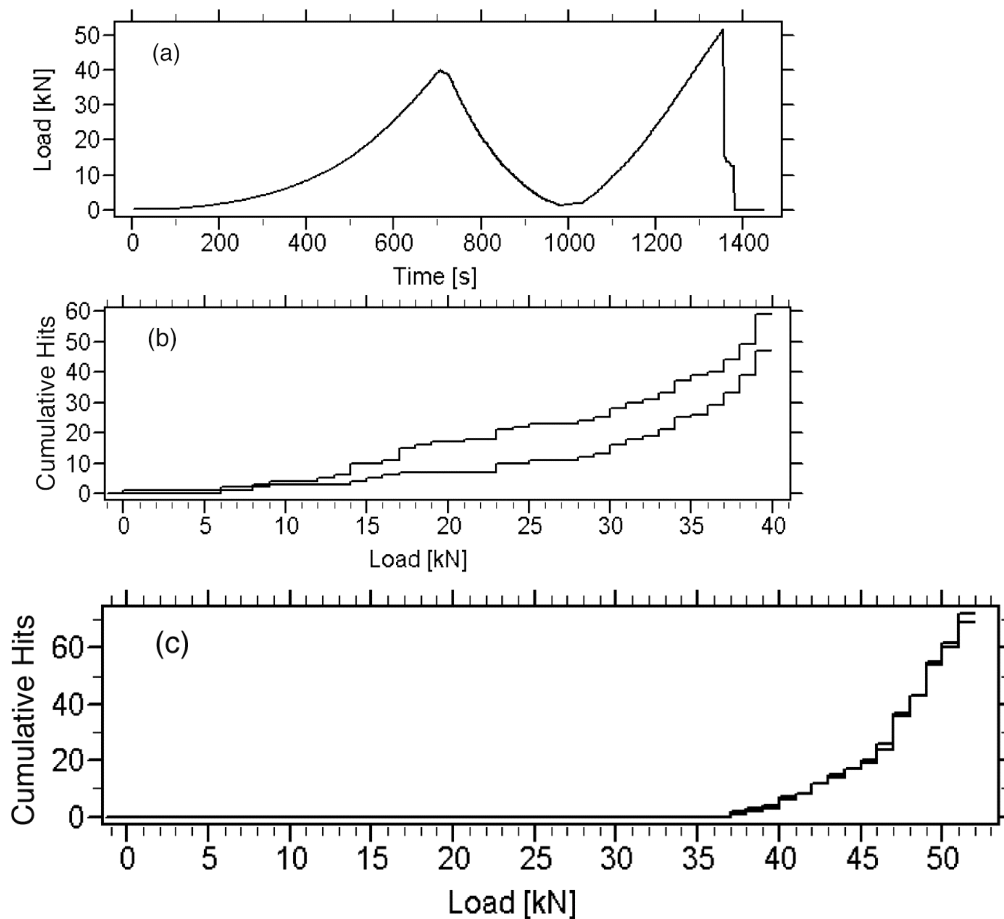


Fig. 3. Load vs. time (a), cumulative AE hits vs. load in the 1st (b) and 2nd (c) loading cycles of a disk specimen (the two curves in b, c correspond to the data measured by two AE-channels). Peak load in the 1st cycle 40 kN. Kaiser effect in the 2nd cycle at 37 kN.

5. Kaiser Effect Sensitivity against Principal Axes Rotation

A series of tests is carried out in order to clarify the question about the influence of the mutual orientation of principal stresses in successive loading cycles on the Kaiser effect. This is achieved by performing two-cycle experiments on disk specimens with disk rotation between the two cycles. In the 1st cycle, a specimen is diametrically compressed to a certain load level, usually corresponding to 50-80% of the rock's strength in a 'Brazilian' test. Then the specimen is completely unloaded, rotated by a certain angle θ and then reloaded, in the new direction. The following values of θ are studied: 3.5°, 7.5°, 15°, 30°, 45°, 60° and 90°. AE is measured in both cycles.

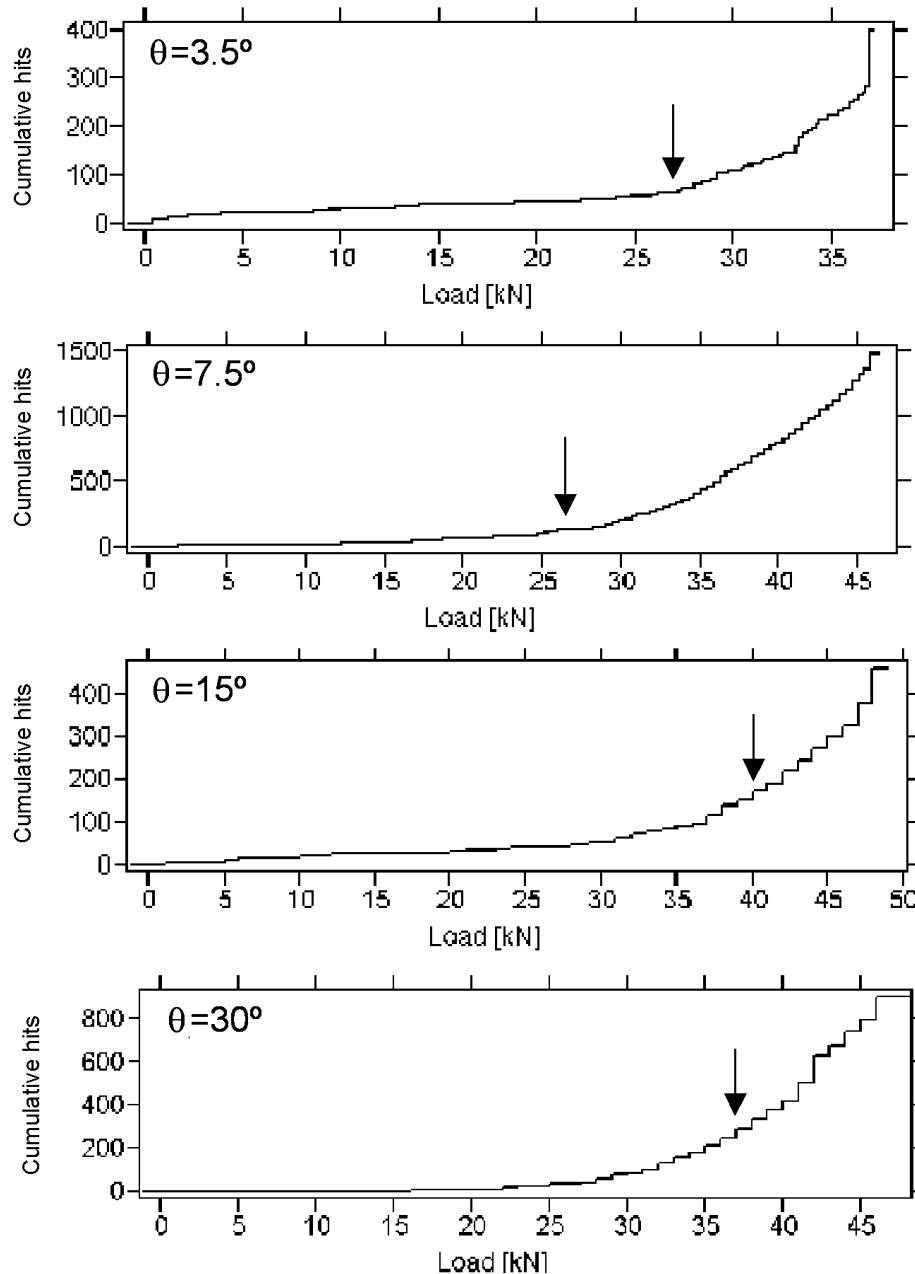


Fig. 4. AE in the second cycle in the tests with disk rotation between 1st and 2nd cycle. The value of the rotation angle θ is shown in each graph. The peak value of the first-cycle load is indicated by an arrow.

Experiments show that with increasing θ , the Kaiser effect becomes less clearly pronounced. The effect can still be recognised in the tests with $\theta = 7.5^\circ$, as Fig. 4 illustrates. As the rotation angle increases to 15° or more, the Kaiser effect disappears completely. This corresponds well to the results of the earlier simulation with a brittle fracture mechanics model (Fairhurst-Cook model) [15-18] as well as to the boundary-element computation carried out in [19].

6. Loading Rate Dependency of the Kaiser Effect

‘Brazilian’ tests described in the above sections are performed with the same loading rate in all cycles (typically 0.2 mm/min). In reality, cyclic loading of rocks may occur with different loading rates in different cycles. For example, the loading rate in situ can be higher or lower than that in the laboratory test. To clarify the question about the influence of the loading rate on the Kaiser effect in ‘Brazilian’ test, a series of experiments is performed in which disk specimens are subjected to three cycles of diametrical loading without rotation. The displacement rates in the first, second and third cycles are 0.2 mm/min, 5 mm/min and 0.2 mm/min, respectively. It should be noted that the maximum displacement rate of 5 mm/min used in these tests is still much lower than that occurring in blasting or impact processes. Typical results are shown in Fig. 5. The Kaiser effect in the second cycle, when the load rate is increased, is observed at the load value only slightly higher than the largest previously reached load. In the third cycle, when the load rate is decreased again, the opposite takes place: the Kaiser effect is observed at the load value only slightly lower than the largest previously reached load [20]. In both cycles, the peak value of the previous load can be estimated from the Kaiser effect with a reasonable accuracy. Further experimental and theoretical research should clarify the physics of the observed phenomena.

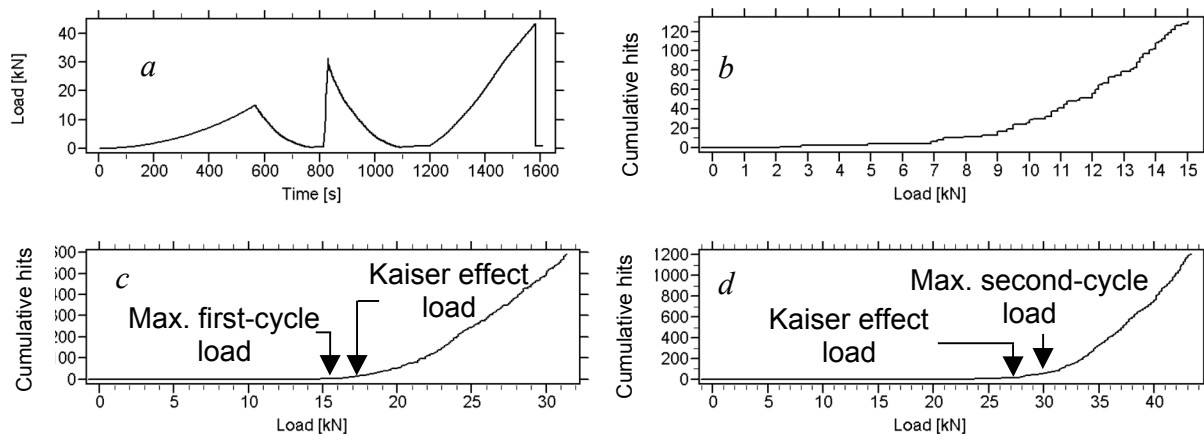


Fig. 5. Load vs. time in three loading cycles (a); cumulative hits vs. load in the first (b), second (c) and third (d) cycles of diametrical compression of a disk specimen. Displacement rate in the first and third (“slow”) cycles: 0.2 mm/min; displacement rate in the second (“fast”) cycle: 5 mm/min.

7. Impact of the Experimental Results on Stress Measurement Techniques

The results obtained in the experiments are of importance for the Kaiser effect applications for stress measurements in rocks and brittle materials like concrete. The high sensitivity of the Kaiser effect against a non-coincidence of the principal axes in successive loading cycles implies that it is necessary to know a priori the directions of σ_1 , σ_2 , σ_3 in order to be able to determine

their values by means of the Kaiser effect. For example, when measuring the value of σ_1 , the specimen must be oriented parallel to the direction of σ_1 . If the axis of the specimen is inclined to the direction of σ_1 by more than $\pm 10^\circ$, there will be no Kaiser effect. The absence of the Kaiser effect in this case may be misinterpreted by the experimentalist. The results presented above show that the absence of the Kaiser effect in some directions does not indicate the absence of stress memory in rock. It just means that the orientation of σ_1 is different from the orientation of the core specimen. To reveal stress memory, the orientation of the specimen should be parallel or close ($\pm 10^\circ$) to the direction of σ_1 .

The high sensitivity of the Kaiser effect to the mutual orientation of principal axes in successive loading cycles may be used as a basis for a precise determination of the directions of principal stresses *in situ*. Estimating the directions of principal axes *in situ* is important in many applications in geology, rock mechanics and tectonophysics. The results presented show that testing a series of specimens orientated in various directions may allow one to estimate the σ_1 -direction with an accuracy of $\pm 5^\circ$ provided that a sufficient amount of rock specimens is available. The direction of σ_1 corresponds to the direction of the specimen, which shows the best-pronounced Kaiser effect.

Varying loading rate between the cycles in the range 0.2 mm/min to 5 mm/min does not result in a disappearance of the Kaiser effect. Further study is necessary in order to estimate the Kaiser effect applicability for stress estimation in impact and blasting processes in rocks.

References

1. Rabinovitch A., Bahat D., Frid V. (2002) "Similarity and dissimilarity of electromagnetic radiation from carbonate rocks under compression, drilling and blasting." *International Journal of Rock Mechanics and Mining Sciences*, **39**(1): 125-129.
2. Couvreur J.-F., Vervoort A., King M.S., Lousberg E., Thimus J.-F. (2001) "Successive cracking steps of a limestone highlighted by ultrasonic wave propagation." *Geophysical Prospecting*, **49**(1): 71-78.
3. Van de Steen B., Wuytens B., Vervoort A., Van Geemert D. (1997) "Variation in resistivity with stress level in mineral building materials." *International Journal for the Restoration of Buildings and Monuments*, **3**: 75-85.
4. Leaird J.D., Dunning J.D., Miller M.E. (1985) "Kaiser experiment in sawcut rock." *Journal of Acoustic Emission*, **4**(2-3): S11-S16.
5. Lord A.E., Koerner R.M. (1985) "Field determination of prestress (existing stress) in soil and rock masses using acoustic emission." *Journal of Acoustic Emission*, **4**(2-3): S22-S25.
6. Yoshikawa S., Mogi K. (1981) "A new method for estimation of the crustal stress from rock samples: laboratory study in the case of uniaxial compression." *Tectonophysics*, **74**: 323-339.
7. Yoshikawa S., Mogi K. (1989) "Experimental studies on the effect of stress history on acoustic emission activity: a possibility for estimation of rock stress." *Journal of Acoustic Emission*, **8**(4): 113-123.
8. Michihiro K., Hata K., Yoshioka H., Fujiwara T. (1991/1992) "Determination of the initial stresses on rock mass using acoustic emission method." *Journal of Acoustic Emission*, **10** (1/2): S63-S76.
9. Kanagawa T., Nakasa H. *Method of estimating ground pressure*. U.S. Patent No. 4107981; 1978.

10. Lavrov A.V. (2001) "Acoustic emission in 'Brazilian' tests on brittle rock." *Proceedings of the 11th Session of the Russian Acoustical Society*. Moscow: GEOS, vol. 2, pp. 99-102 (in Russian).
11. Filimonov Y., Lavrov A., Shafarenko Y., Shkuratnik V. (2002) "Observation of post-failure Kaiser effect in a plastic rock." *Pure and Applied Geophysics (PAGEOPH)*, **159**(6): 1321-1331.
12. Filimonov Y.L., Lavrov A.V., Shafarenko Y.M., Shkuratnik V.L. (2001) "Memory effects in rock salt under triaxial stress state and their use for stress measurement in a rock mass." *Rock Mechanics and Rock Engineering*, **34**(4): 275-291.
13. Lavrov A., Vervoort A., Filimonov Y., Wevers M., Mertens J. (2002) "Acoustic emission in host-rock material for radioactive waste disposal: comparison between clay and rock salt." *Bulletin of Engineering Geology and the Environment* **61**(4): 379-387.
14. Li C., Nordlund E. (1993) "Experimental verification of the Kaiser effect in rocks." *Rock Mechanics and Rock Engineering*, **26**(4): 333-351.
15. Holcomb D.J. (1993) "General theory of the Kaiser effect." *International Journal of Rock Mechanics and Mining Sciences & Geomechanics Abstracts*, **30**(7): 929-935.
16. Lavrov A.V. (1997) "Three-dimensional simulation of memory effects in rock samples." *Proceedings of the International Symposium on Rock Stress*. Rotterdam: A.A. Balkema, pp. 197-202.
17. Shkuratnik V.L., Lavrov A.V. (1997) *Memory effects in rocks: Physical features and theoretical models*. Moscow: Academy of Mining Sciences Press. 159 pp. (in Russian).
18. Lavrov A.V. (2001) "Features of the formation and manifestation of memory effects in rocks." D.Sc. dissertation. Moscow State Mining University. 582 pp.
19. Lavrov A., Vervoort A., Wevers M., Napier J.A.L. "Experimental and numerical study of the Kaiser effect in cyclic Brazilian tests with disk rotation." *International Journal of Rock Mechanics and Mining Sciences*, **39**(3): 287-302.
20. Lavrov A. (2001) "Kaiser effect observation in brittle rock cyclically loaded with different loading rates." *Mechanics of Materials*, **33**(11): 669-677.

LEAK DETECTION BY ACOUSTIC EMISSION USING SUBSPACE METHODS

AMANI RAAD^{1,3}, FAN ZHANG^{2,3} and MÉNAD SIDAHMED^{1,3}

¹ UTC, Laboratoire Heudiasyc, F60205 Compiègne, France

² CETIM, F60304 Senlis, France

³ LATIM (CNRS/UTC/CETIM)

Abstract

This paper deals with the leak detection by using AE signals. A method called subspace method is introduced and compared with the classical cross-correlation method. A brief review of the theory of both methods is presented. Application of these methods to industrial signals from a test bench of CETIM demonstrates the effectiveness of this subspace method for leak detection and shows the limitation of the cross-correlation method.

Keywords: leak detection, acoustic emission, subspace method, cross-correlation method.

1. Introduction

For a long time, the detection of leaks constitutes a crucial problem due to the diversity of applications. The consequences induced by the apparition of leaks are multiple and dangerous because they can generate a local dysfunction, which can lead to the ruin of all the system. It is imperative to detect them as soon as possible. Thus, the need for detecting the leaks in an early moment is related to safety constraints and environmental protection reliability. The need is also of a financial nature, because it is easier and less expensive to secure a small crack than to start an emergency procedure to stop a large leak. Losses are evaluated in terms of maintenance cost and non-production cost.

Several systems of detection have already been used but they make it possible only to detect big leaks [1 - 3]. With an aim of replacing these systems by more powerful digital systems, various approaches are being studied of which the method of acoustic emission (AE) constitutes one of the principal candidates because it showed during pressure tests a great sensitivity. Several studies were carried out, by various authors and especially in CETIM, to detect, localize and characterize leaks for nuclear or thermal power stations. Nevertheless, most of the techniques are based only on simple methods such as cross-correlation or interferometry. Some studies used time-frequency methods [4] or neural networks [5]. The principal objective in this paper is to research methods of detection and localization, based on signal processing. We propose in this study to use a method based on high-resolution techniques, which are developed and applied in the fields of sonar, radar, telecommunications, geophysics and biomedical signal processing.

This method is under certain conditions insensitive to the signal to noise ratio. This is of interest because the classical method based on cross-correlation function has this major drawback. The method is based on the SVD (Singular Value Decomposition) of the cross-spectral matrix issued from the AE sensors signals. The paper describes this method and compares it, on

the basis of simulated data and experiments conducted in CETIM, with the classical cross-correlation method. The paper is organized as follows: A review of the method of cross-correlation; The high-resolution or subspace method; Applications of these two methods, concerning simulated signals and industrial AE signals from a test bench of CETIM.

2. Correlation Method

The correlation method is a classical method, which was proposed to localize AE sources by using the delays observed on an array of sensors [6]. Otherwise, the autocorrelation function presents good performance in pure detection. In a matter of localization, the cross-correlation function was used to improve the AE techniques used for monitoring of the primary circuits in the nuclear power stations [1]. Despite the simplicity of the method, it encounters difficulties for the interpretation, and presents weak performances, which are due to the violation of the decorrelation assumptions and especially to the presence of parasites, which do not correspond to an effective delay. Moreover, these methods degraded completely in the presence of the noise.

We present a brief review of the method in the case of a linear localization, i.e. two sensors. The flow of the fluid through the leak generates a noise (fluctuations in pressure), which is propagated from its origin to both sides, $s(t)$. The AE signals in the two extremities of the pipe A and B have additive noise, $b_1(t)$ and $b_2(t)$, respectively. These noises, in general Gaussian, are uncorrelated between them, and with $s(t)$. The following equations can then be obtained

$$\begin{aligned} S_A(t) &= \alpha_A s\left(t - \frac{dA}{c}\right) + b_1(t) \\ S_B(t) &= \alpha_B s\left(t - \frac{dB}{c}\right) + b_2(t) \end{aligned} \quad (1)$$

α_A and α_B are the coefficients of diffusion between 0 and 1; dA and dB the distance from the leak to each sensor A and B and c is the propagation velocity.

The cross-correlation between S_A and S_B can be expressed as the following:

$$\begin{aligned} R_{AB}(\tau) &= \alpha_A \alpha_B R_{SS}(\tau - \tau_0) \\ \text{with } \tau_0 &= \frac{dA - dB}{c} \end{aligned} \quad (2)$$

$R_{AB}(\tau)$ is no more than the autocorrelation function of $S_B(t)$ with a delay of τ_0 and a multiplicative coefficient. The maximum of the cross-correlation can predict the leak position by the determination of the value of the delay.

3. Subspace Methods

3.1 Introduction

We introduce the high-resolution techniques called subspace methods. These methods constitute a significant tool used in various applications such as sonar, radar, telecommunications, geophysics, biomedical fields and the non-destructive testing [7]. These methods have been developed in array processing and especially in submarine acoustics. But they seem not to be applied to detect leaks. The advantage of these methods comes from their high resolution even in the presence of noise. Contrary to the traditional methods, its asymptotic performance are not limited by the signal-to-noise ratio (SNR). They use the decomposition of the observation space into a signal subspace (or source) and a noise subspace [8, 9].

3.2 Assumptions

The object of these methods is to characterize several sources received on an array of sensors. The model of propagation is linear and stationary. These sources must be perfectly coherent and statistically independent. In addition to the sources, all the noise sources are supposed to be known and uncorrelated between them. Moreover, the sources and the background noise must be statistically independent. Finally, it is necessary that the number of sources is lower than the number of sensors in order to be able to separate the sources.

3.3 Description of the method

First, a vectorial signal $x(t)$ is introduced where the k^{th} component corresponds to the signal received on the k^{th} sensor. $x(t)$ can be written as follows:

$$x(t) = b(t) + \sum_{i=1}^p S_i(t) \quad (3)$$

where $S_i(t)$ is the i -th source signal and $b(t)$ is the background noise.

Taking into account the mutual decorrelation between sources and noise, the correlation matrix is then equal to:

$$R(\tau) = E[b(t)b(t-\tau)] + \sum_{i=1}^p E[s_i(t)s_i^+(t-\tau)] \quad (4)$$

The FFT of the equation gives the following result:

$$\Gamma(f) = \Gamma_b(f) + \Gamma_s(f) \text{ avec } \Gamma_s(f) = \sum_{i=1}^p \Gamma_i(f) \quad (5)$$

where $\Gamma(f)$ presents the total cross-spectral matrix, $\Gamma_b(f)$ is the correlation matrix of noise. $\Gamma_s(f)$, the total cross-spectral matrix of sources can be decomposed into a sum of $\Gamma_i(f)$, the cross-spectral matrix of the source i .

The estimation of the source number is based on the decomposition of the cross-spectral matrix $\Gamma(f)$ into eigenvalues and eigenvectors. In practice, $\Gamma(f)$ is an estimated matrix and no eigenvalue is really zero. The number of higher eigenvalues corresponding to signal subspace determines the number of existing leaks.

The decomposition of the matrix $\Gamma(f)$ into eigenvalues and eigenvectors gives:

- **P eigenvectors** V_i are the eigenvectors of the source matrix $\Gamma_s(f)$, which correspond to the higher p eigenvalues of $\Gamma(f)$. These p eigenvectors constitute the signal subspace of dimension P .
- **K-P eigenvectors** where the eigenvalues correspond to the variance of the noise, and therefore are less than the other eigenvalues. These eigenvectors constitute the noise subspace.

4. Applications

4.1 Cross-correlation method

a) Simulated signals

Simulated signals consist of damped sinusoid with additive white Gaussian noise in order to approximate AE signals. In the case when there is no leak, the cross-correlation of the two sensors is a sequence of white noise. However, in the other case, the cross-correlation can make

it possible to determine the leak position. Figure 1 shows the presence of a peak appearing at 300 samples, corresponding to the delay between the first and second sensors. The assumption of decorrelation must be strictly respected; if not, the result of the cross-correlation could be distorted. The notion of SNR is a dominating factor for the final comparison of the performances of the two methods, and a comparison with a case of low SNR proved to be necessary. Figure 1(b) shows the result of the cross-correlation in the case of a simulated signal with low SNR. It appears that the peak that defines the leak position degrades in favor of the peak at zero. This confirms the degradation of the method performances due to the low SNR.

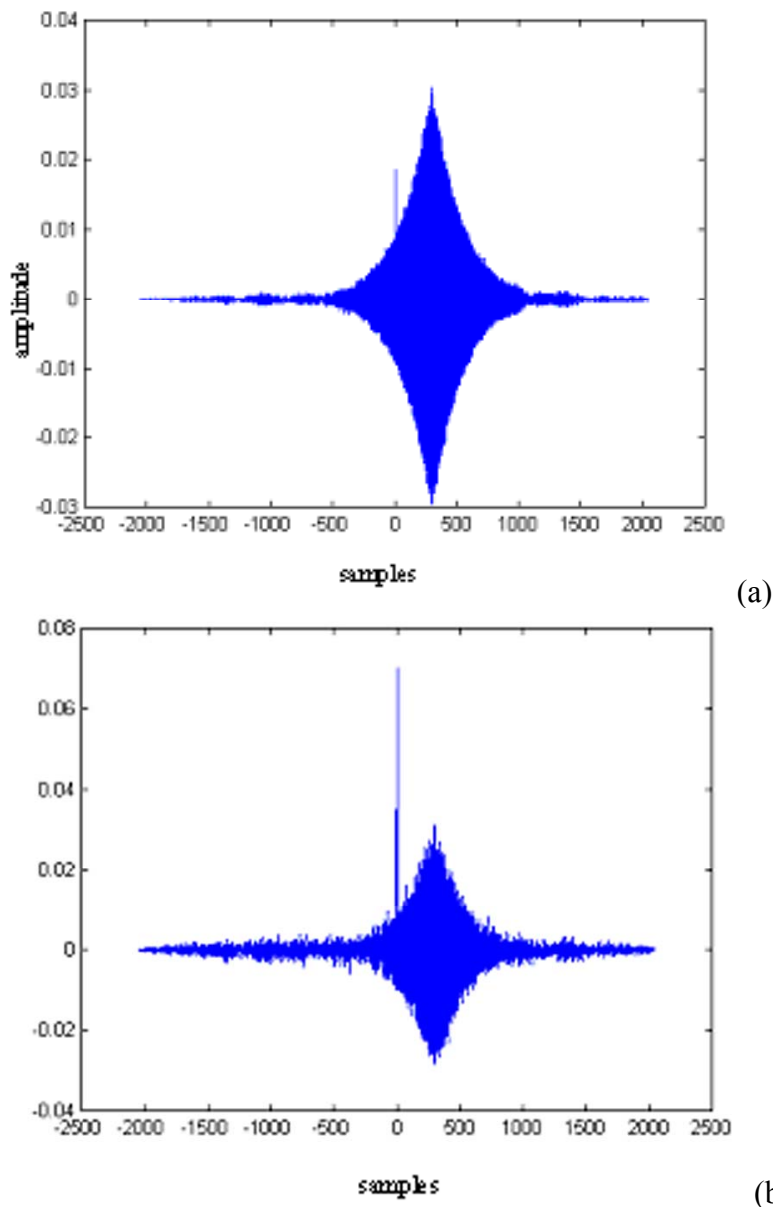


Fig. 1. Cross-correlation between two sensors in the case of leak (a) High SNR (b) Low SNR.

b) Real signals

Experiments have been conducted on an industrial test bench of CETIM. It consists of a compressed-air line of 2.5-cm diameter, in which it is possible to control the leak level. Two broadband AE sensors are used, the leak being generated between the two sensors. The sampling frequency is equal to 10 MHz. Figure 2 presents 10,000 samples of AE signals for various cases:

without leak, small and large leak. Figure 3 shows the result of cross-correlation of AE signals when there is no leak. It is normal to obtain the white noise sequence with a zero delay.

To complete the analysis, tests on AE signals coming from a small and large leak have been carried out. Figure 4 shows clearly the distinction between presence and absence of leak in the cross-correlation signals. The correlation tool proves to be a powerful tool for the leak detection. However, the limitations of the method in localization appear obviously. Indeed, there exist in the two cases several parasitic peaks distorting the exact value of delay. Moreover, there is no difference between small and large leaks.

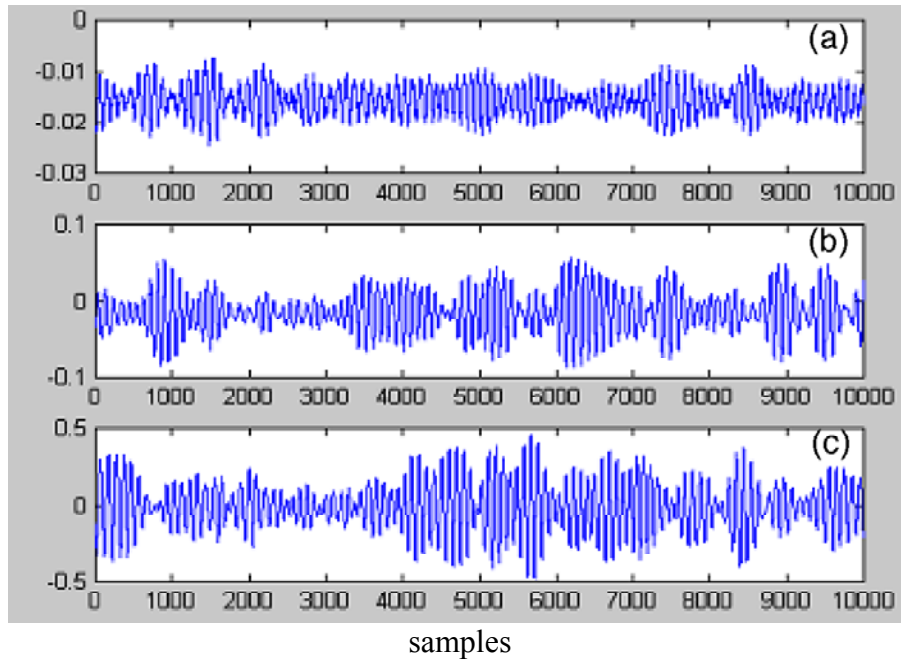


Fig. 2. Acoustic emission signals in three cases: (a) no leak, (b) small (c) large leak.

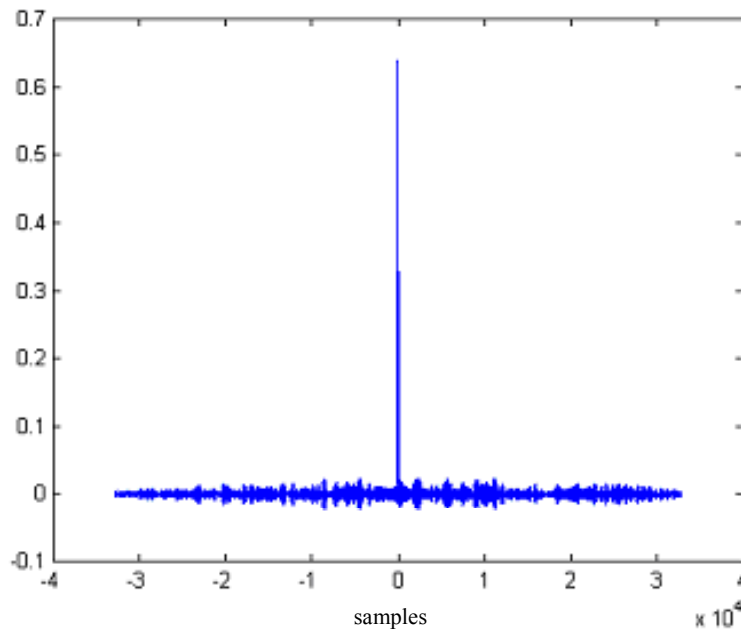


Fig. 3. Cross-correlation in the case of no leak.

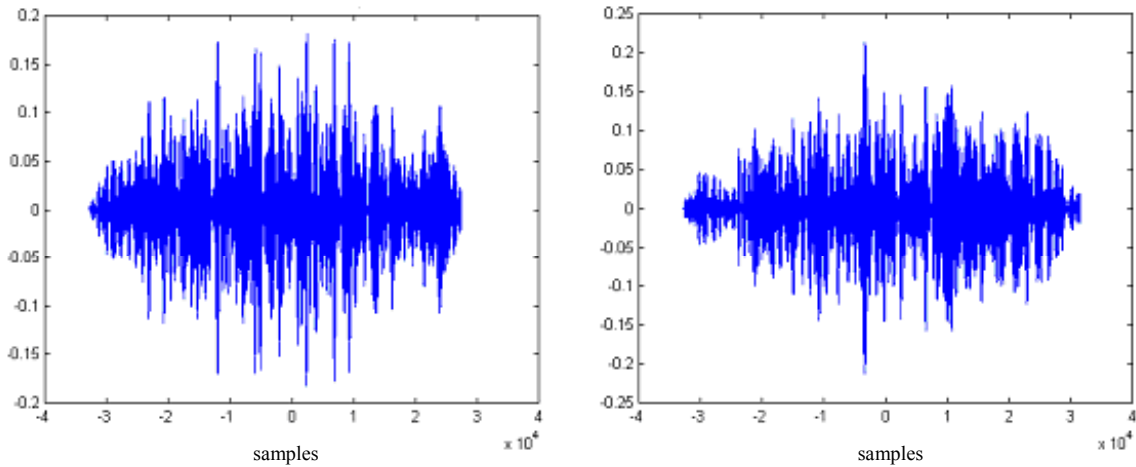


Fig. 4. Cross-correlation in the case of (a) small, (b) large leak.

4.2 Subspace method

a) Simulated signals

Simulated signals consist of one simulated sinusoidal source with 60-Hz frequency and 4 sensors with a respective delay of 0, 300, 600 and 900 samples. The subspace signal is one dimension and the subspace noise is three dimensions. The noise eigenvalues tend roughly towards zero. Figure 5(a) shows the evolution of the eigenvalue of the signal subspace with frequency. In this figure, the characteristic peak of the source frequency appears clearly. The eigenvalue evolution is thus an image of the sinusoidal signal in the frequency domain. To obtain the delay between sensors and source, the source eigenvector must be computed. It corresponds to eigenvalue at 60 Hz. Figure 6 presents the evolution of the magnitude and phase of the eigenvector components according to frequency. The delays obtained at frequency 60 Hz are [0, -0.3737, -0.7462, -1.1135]. The subspace method is very robust against the noise. Even if the SNR degrades considerably, the separation between sources and noise is easy to obtain. The degradation takes place only in the figure of the eigenvalue evolution. Figure 5(b) shows the presence of the parasitic peaks in the eigenvalue evolution.

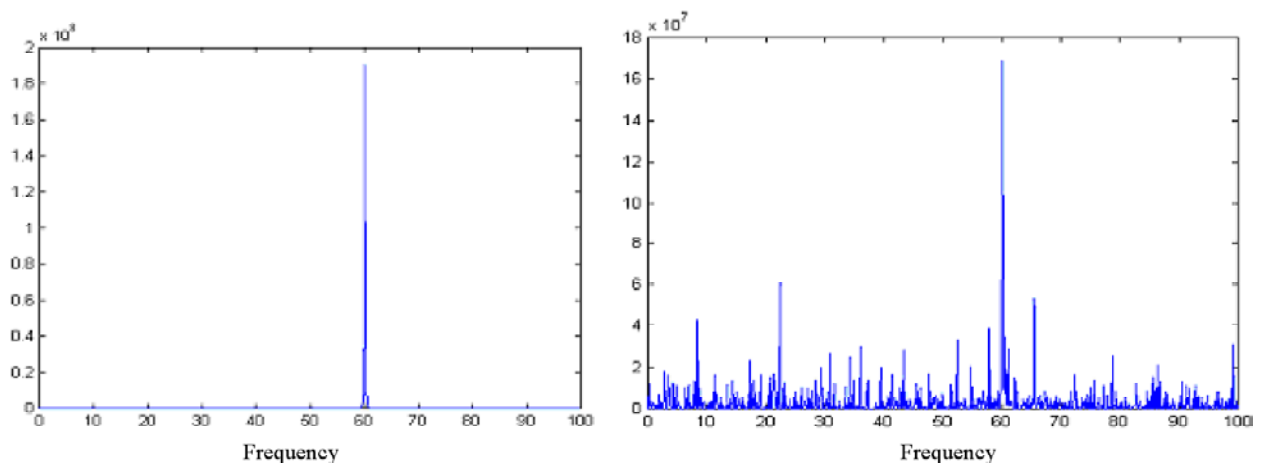


Fig. 5. Evolution of the eigenvalue of source with frequency (a) high SNR, (b) low SNR.

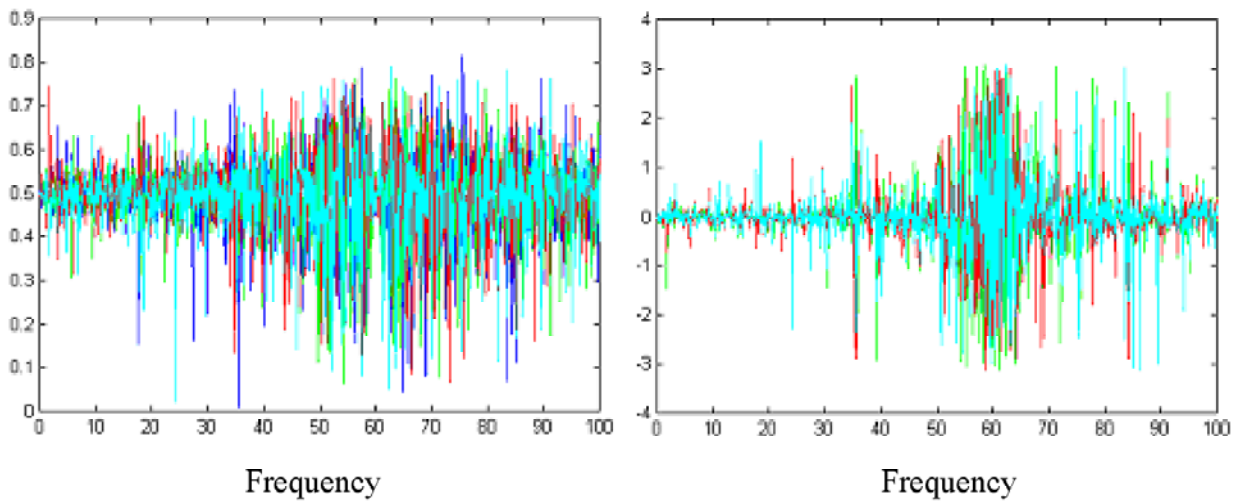


Fig. 6. Evolution of the magnitude and phase of the eigenvector components with frequency.

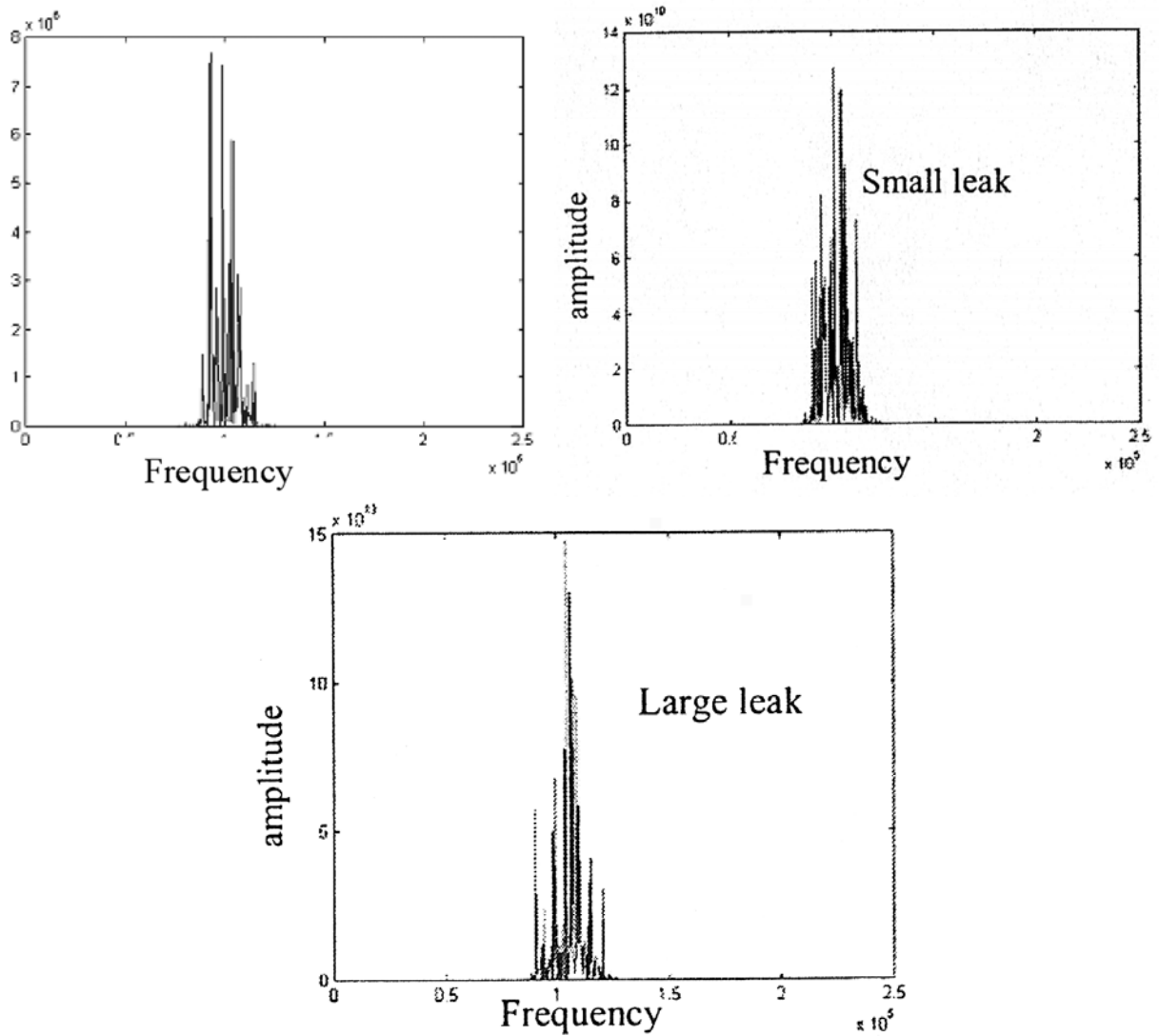


Fig. 7. Evolution of the eigenvalue with frequency for 3 cases: no leak, small and large leak.

b) Real signals

In this section, tests concern the same industrial signals from CETIM test bench. Filtering is a significant factor in this study. If the AE signals obtained from the sensors are not filtered, the subspace signal is equal to zero. Therefore, all tested signals are filtered broadband around 100 kHz. Figure 7 shows the eigenvalue evolution of the subspace signal for three cases: no leak, small and large leak. For example, in the case of small leak, the maximum eigenvalue does not correspond exactly to the sensor frequency. A broadband subspace method appears to be an excellent method for classification between small and large leaks.

5. Conclusion

This paper deals with a method for leak detection using acoustic emission. The subspace method is introduced and compared with the classical cross-correlation method. The subspace method proves to be a powerful tool for the detection and classification of leaks. Its power derives from the immunity against noise. Comparison of the two methods showed the limitations of the cross-correlation method due to the signal-to-noise ratio, the high capacity of the proposed method to detect the leaks, even 'small' leaks, and its insensitivity to signal to noise ratio.

We were only concerned with the leak detection and not the localization. This aspect is more difficult because it requires the knowledge of the propagation speed in the considered medium, at the specific frequencies. This is however under study.

Acknowledgements

The work is funded within the common laboratory LATIM (CETIM/UTC/CNRS).

References

- [1] Cécile Cornu, Study of a cross correlation technique for leak localisation on power primary circuits by acoustic emission, *Commissariat à l'énergie atomique*, France, 1993.
- [2] D.S. Kuppermann, T.N. Claytor, T. Mathieson, and D. Prine, Leak-detection technology for reactor primary systems, *Nuclear Safety*, **28**(2), April-June 1987, 191-198.
- [3] Pascal Boulanger, nouvelles méthodes de détection et de localisation de fuites Par émission acoustique, *Thèse de doctorat*, Université de Paris XI Orsay, 1993.
- [4] E. Serrano, M. Fabio, Detection of a transient signal by the wavelet transform, *International conference Sao Paolo*, Brasil, 1992, pp. 94-97.
- [5] M.C. Parpaglionne, Neural networks applied to fault detection using acoustic emission, *International conference Sao Paolo*, Brasil, 1992, pp. 71-75.
- [6] James Roger, Essais non destructifs, L'émission acoustique: Mise en œuvre et applications, AFNOR-CETIM, 1988.
- [7] Sylvie Marcos, Les méthodes à haute résolution: traitement d'antenne et analyse spectrale, Edition HERMES, Paris, 1998.
- [8] Georges Bienvenu, Influence de la cohérence spatiale du bruit de fond sur la résolution de sources ponctuelles, *Colloque national sur le traitement du signal et ses applications*, Nice, Avril 1977.
- [9] J.L. Lacoume, B. Bouthemy, F. Glageaud, C. Latombe, Use of spectral matrix for sources identification, Spectral Analysis and its use in underwater acoustics, *Proceedings of the Institute of Acoustics*, Imperial College, London, 29-30 April 1982.

EWGAE 2002

25th European Conference on Acoustic Emission Testing

EWGAE2002 was held 11 – 13 September 2002 at Prague, Czech Republic. It was sponsored by the Czech Society For Non-Destructive Testing in collaboration with Czech Technical University of Prague and Brno University of Technology. Proceedings in two volumes were edited by Dr. P. Mazal and were published by Brno University of Technology.

At the very successful 25th European working group on AE conference, 55 papers in 10 oral sections and about 15 papers in poster section were given. The Proceedings include 86 papers and abstracts. 107 participants from 20 countries attended the conference.

The Proceedings can be ordered from the Czech Society For Non-Destructive Testing. Contact:

Czech Society for Non-destructive Testing
Technická 2, CZ 616 69 Brno, Czech republic Or

Dr. Pavel Mazal
Brno University of Technology
Institute of Design
Technicka 2
616 69 Brno, Czech Republic

With the assistance of the editorial Board members who were present at the EWGAE2002, 22 papers were chosen and reviewed for the technical contents. These papers are included in this volume of Journal of Acoustic Emission with the permission of Brno University of Technology. Two papers were extensively revised and expanded by the authors, while 20 other papers were edited for clarity and/or received minor revisions by the authors.

Selected pages of the Proceedings are included here. EWGAE 2004 has been set to open at Berlin from September 15 to 17, 2004. See EWGAE2004.pdf enclosed for details. You can also access the conference information at

<http://www.EWGAE2004.de>

Editor

EWGAE 2002

25th European Conference on Acoustic Emission Testing

11 – 13 September 2002

Prague
Czech Republic

PROCEEDINGS

VOLUME I



CZECH SOCIETY FOR NON-DESTRUCTIVE TESTING

IN COLLABORATION WITH



CZECH
TECHNICAL
UNIVERSITY
IN PRAGUE



BRNO
UNIVERSITY OF
TECHNOLOGY
Faculty of Mech.
Engineering

Edited by:

P.Mazal

Copyright □ 2002
Brno University of Technology
all Rights Reserved

Editorial

These Proceedings contain contributions that were presented at the 25th conference of European Working Group on Acoustic Emission (EWGAE), which took place in Prague from 11th to 13th of September 2002.

The method of acoustic emission (AE) is one of fast developing methods used for non-destructive testing of constructions, for monitoring of technologic processes, for material properties evaluation etc. In some areas, it has become standard, fully certified testing method the utilization of which brings important economic savings. What is even more important, it improves safety and enables more precise estimate of service life of various technical constructions. AE methods provide researchers with new possibilities in the area of research of various materials.

EWGAE conference has become traditional possibility to meet prominent specialists who have been pursuing both development and practical applications of AE method. We can see permanent and agreeable tendency of growing number of students and young researchers who are going to develop this method in forthcoming years.

The problem of acoustic emission has been solved in the Czech Republic and its predecessor – Czechoslovakia – for over thirty years at several research and application workplaces. This tradition and very good reputation of Czech specialists were main reasons why Czech Society for NDT was entrusted with organizing of the 25th conference at previous conference EWGAE 2000 in Senlis, France.

These Proceedings include more than 70 contributions that prove the width of the problems that are currently being solved by this unique method. This publication provides a good overview not only about current application possibilities, but it shows a number of practical and theoretical problems the solution of which is necessary for further development of AE method.

Pavel Mazal

President of the CNDT

CONTENTS

- Volume I -

Contributions can be found in alphabetical order according to the surname of the first author.

Akematsu Y., Yoshida K., Sakamaki K., Horikawa K. Characteristics of AE waveform during gas leak from a pipe	I/15
Anastassopoulos A.A., Kouroussis D.A., Nikolaidis V.N., Proust A., Dutton A.G., Blanch M.J., Jones L.E., Vionis P., Lekou D.J., van Delft D.R.V, Joosse P.A., Philippidis T.P., Kossivas T., Fernando G. Structural integrity evaluation of wind turbine blades using pattern recognition analysis on acoustic emission data	I/21
Anastassopoulos A.A., Tsimogiannis A.N., Kouroussis D.A. Pressure vessel evaluation with pattern recognition acoustic emission data analysis	I/29
Bayray M., Rauscher F. Window Fourier Transform and Wavelet Transform in AE signal analysis	I/37
Belov V., Glushko A., Kozyrev O New AE source location method and its practical application	I/45
Benes P. Process analysis on heat transfer surface	I/51
Bláha J. Real source detection during continuous monitoring of pressure vessels	I/59
Blaháček M., Prevorovsky Z. Probabilistic definition of AE events	I/63
Boczar T. Comparison of the results of the frequency analysis of electric signals and AE generated by partial discharges	I/69
Boczar T. Determining identification possibilities of multisource partial discharges based on frequency analysis of their AE	I/77
Bordei M., Dragan V., Dragulin I., Goanta M.A., Constantinescu S. Researches regarding the role of the ultrasonic control at the fabrication of the guidance rolls curved thread at the continuous casting machines	I/85
Bradshaw T., Holford K., Cole P., Davies A. Ball bearing calibration of concrete structures using AE	I/91
Cerny L., Jirsík V. Signal source location by means of neural networks	I/99
Chlada M., Prevorovsky Z. Threshold counting in wavelet domain	I/107
Chmelík F., Máthis K., Lukác P., Langdon T.G. Investigating magnesium alloys and composites using the AE technique	I/117
Cole P.T., Gautrey S.N., Lenain J.C. On-stream monitoring of process plant by AE	I/125
Colombo S., Main I.G., Forde M.C., Halliday J. AE on bridges: experiments on concrete beams	I/127
Constantinescu S., Drugescu E., Dragan V., Radu T., Bordei M., Buburuzan L. Practical application of AE of the different grades of steel	I/135

Crha J. , Hahn J., Brom J. Leak monitoring by AE method	I/141
Derjagin B.V., Lipson A.G., Kluev V.A., Toporov Yu.P., Sodomka L. Mechanoemission of neutron from deuterated materials	I/149
Dragan V., Bordei M., Constantinescu S., Tudor B. Researches regarding the quantitative analysis of the heavy rolling plates of LRS-EH36 steel type, through ultrasonic control	I/155
Drummond G.R., Fraser K.F., Little J., Watson J.F., Campbell P. Assessing the structural integrity of crane booms using AE	I/161
Ennaceur C., Benmedakhene S., Laksimi A., Hervé C., Mediouni M., Cherfaoui M. Study of mechanical behaviour of 304L steel using AE technique and the method of potential difference	I/173
Ferrer F., Radigon E. Using AE in the objective to evidence corrosion rate evolutions during chemical process in service modifications	I/185
Fraser K., Drummond G., Little J., Fleisher S., Bailey J., Brown M. Investigation utilising AE into cracking of stainless steel aircraft tie down link plates	I/191
Gaillet L., Brevet P., Robert J.L., Tessier C. Acoustic monitoring of prestressed concrete bridge and other civil structures with cables	I/201
Golaski L., Gebiski P., Ono K. Diagnostics of reinforced concrete structures by AE	I/207
Goujon L., Baboux J.C., Zhang F. Reciprocity calibration of AE transducers	I/217
Hájek K., Sikula J., Tacano M., Hashiguchi S. Signal to noise ratio and preamplifier noise of AE measuring systems	I/223
Hatscher A., Chmelík F., Lukác P., Zenner H. Cyclic deformation of a magnesium based light alloy investigated by the AE technique ...	I/229
Holford K.M., Pullin R., Davies A.W. An investigation into location of damage in bridge details by AE	I/237
Horikawa K., Yoshida K., Sakamaki K. AE due to the intergranular fracture of Al-Mg-Si base alloys	I/239
Hünicke U.D., Schulz M., Budzier R., Eberlein J. Characterization of stress corrosion cracking of CuZn-alloys by AE testing	I/247
Kabanov B.S., Gomera V.P., Sokolov V.L., Okhotnikov A.A., Fedorov V.P. AE technology as a key element of the safe operation system at refinery	I/253
Korenská Ma., Pazdera L., Smutny J., Korenská Mo. Detection of defects in hourdis sandwich slabs by means of AE method	I/263
Krofta J., Prevorovsky Z., Raab M. AE during structure changes in semi-crystalline polymers	I/269
Kuravsky L.S., Baranov S.N. Condition monitoring of thin-walled structures suffered high-level acoustic excitation	I/277

Lackner G., Tscheliesnig P. AE testing on flat bottomed storage tanks: how to condense acquired data to a reliable statement regarding floor condition	I/279
Lamark T.T., Chmelík F., Estrin Y., Lukác P. Plastic deformation of a magnesium based light alloy investigated by the AE technique ..	I/287
Landa M., Novák V., Blaháček M., Sittner P. Investigation of transformation processes in shape memory alloys based on monitoring AE activity	I/293
Landa M., Wevers M. AE during constant loading or constant deformation tests of AISI 304 stainless steel in 5N H₂SO₄ + 0,1M NaCl	I/301
Lavrov A., Wevers M., Vervoort A. AE during monotonic and cyclic deformation of a brittle limestone	I/307
Little J., Drummond G.R., Fraser K.F., Bentley J.A., Jihan S., Siddiqui A.M. Lifespan prediction for composite cylinders using AE techniques	I/315

CONTENTS
- Volume II -

van de Loo P.J., Wolfert A., Schelling R., Schoorlemmer H.J., Kooistra T.M. Low alloy steel metal dusting: detailed analysis by means of AE	II/7
Loutas T.H., Koutsos A., Sotiriadis G., Pappas Y.Z., Kostopoulos V. On the identification of the damage mechanisms in Oxide/Oxide Composites using AE ...	II/15
March L. Application of AE transducers in advanced manufacturing and condition monitoring applications	II/25
Mazal P., Benes P., Pazdera L. AE laboratories at Brno University of Technology	II/27
Mizutani Y., Shimoda T., He J., Morino Y., Mizutani S. AE monitoring of cryogenic propellant tank	II/35
Mori Y., Obata Y. A method for reconstruction of dynamic fracture process occurred inside the material with the aid of AE	II/43
Nivesrangsana P., Cochrane C., Steel J.A., Reuben R.L. AE mapping of engines for spatially-located time series	II/51
de Oliveira R., Marques A.T., Berthelot J.M. Transverse matrix cracking monitoring in glass-fibre/polyester cross-ply laminates by AE	II/59
De Petris C., Agnello P., Lenzuni P., Rosatelli R. A basic approach to discriminate AE sources in composites	II/67
Poppeová V. Cutting tool condition monitoring	II/69
Prevorovsky D., Prevorovsky Z., Asserin J., Varchon D. AE characteristics of surface friction in bio-medical application	II/77

EWGAE 2002
25th European Conference on Acoustic Emission Testing
Prague, Czech Republic, 11 – 13 September 2002

Prevorovsky Z. Notes on wave and wave-guide concepts in AE	II/83
Proust A., Lenain J.C. AE monitoring of civil infrastructures	II/91
Pullin R., Holford K.M. Single sensor source location of AE from fatigue cracks	II/95
Raad A., Zhang F., Sidahmed M. Early detection of faults in gears using AE and vibration analysis	II/103
Raad A., Zhang F., Sidahmed M. Leak detection by AE using subspaces methods	II/111
Rauscher F., Bayray M. AE measurements on shell structures with directly attached piezo ceramic	II/119
Rogers L.M. Structural and engineering monitoring by AE methods - fundamentals and applications ..	II/125
Rowland C., Callaghan T., Coy J. Conditioning monitoring using AE on multiple roller bearings in Consignia's letter sorting machines	II/131
Sagar Remalli Vidya, Raghu Prasad B.K., Kumar Vijaya Fracture energy of high strength concrete beams using AE technique	II/133
Shinomiya T., Nakanishi Y, Morishima H., Shiotani T. Damage diagnosis technique for brick structures using AE	II/141
Shiotani T., Bisschop J., van Mier J.G.M. Evaluation of drying shrinkage microcracking in cementitious materials using AE	II/149
Shiraishi M., Koizumi T. Friction control of positioning system by AE detection	II/157
Sikula J., Pavelka J., Majzner J., Dobis P. Cracks characterisation by acoustic and electromagnetic emission	II/163
Sikula J., Strunc M., Majzner J., Koptavy P., Pavelka J., Hájek K. Electrical noise of piezoceramic sensors	II/171
Skalsky V., Andreykiv O., Serhiyenko O. AE modeling of microcracking in plastically deformed zones of crystalline solids	II/177
Sodomka L. Applications of the acoustical emission to textile fields	II/185
Sodomka L. To the history of acoustical emission	II/195
Spacková H. Tram track structure acoustic analysis	II/199
Svoboda V., Zemlicka F., Petrásek P., Proust A. Damage monitoring in high pressure vessels by means of AE	II/203
Theobald P.D., Esward T.J., Dowson S.P. Towards traceable calibration of AE transducers: a new development at the UK's NPL	II/211
Trapl K., Sajdl P., Kucera P., Novotny R. AE and electrochemical noise during stress corrosion cracking	II/219
Traxler H., Arnold W., Knabl W., Rödhammer P. Non-Destructive evaluation of brazed joints by means of AE	II/225

EWGAE 2002
25th European Conference on Acoustic Emission Testing
Prague, Czech Republic, 11 – 13 September 2002

Tscheliesnig P. Training and certification on the field of AE testing at according the European standardisation (EN 473)	II/233
Vales F., Lasová V., Las V., Adámek V. Interaction of elastic waves with plastic zone by the various types of loading	II/239
Vallen H., Forker J. A new AE-system approach with optimum speed and flexibility for use in field test and laboratory	II/247
Vallen H., Vallen J. Free-of-cost software tools generate dispersion curves, perform wavelet transform and help to correlate both kinds of information	II/255
Vougiouklakis Y. Hähner P., Kostopoulos V., Peteves S. Damage mode identification and analysis of coated gas turbine materials using a non-destructive evaluation technique	II/263
Winkelmans M., Wevers M. Non-Destructive testing for corrosion monitoring in chemical plants	II/271
Yan T., Jones B.E. In-situ AE transducer calibration using artificial AE energy sources	II/279
Yoshida K., Horikawa K., Sakamaki K. Characteristics of AE behaviour during tensile deformation of Ni-Al intermetallic compounds with boron additive	II/287
Zizka J., Prukner V., Ogawa D., Sumiya H., Shiraishi M. Neuronal network for tool wear monitoring on the AE signal basis	II/295
Zuev L.B., Semukhin B.S., Lunyev A.G. On the acoustic properties of metallic polycrystals under straining	II/303
Grad L., Polajnar I., Grum J. On line identification of gas metal arc welding (GMAW) process by detection of acoustic signals	II/305
Index of autors.....	II/313
Contact addresses of selected authors	II/315

Index of authors

Adámek V.	II/239	Esward T.J.	II/211	Landa M.	I/293, I/301
Agnello P.	II/67	Fedorov V.P.	I/253	Langdon T.G.	I/117
Akematsu Y.	I/15	Fernando G.	I/21	Las V.	II/239
Anastassopoulos A.A.	I/21, I/29	Ferrer F.	I/185	Lasová V.	II/239
Andreykiv O.	II/177	Fleisher S.	I/191	Lavrov A.	I/307
Arnold W.	II/225	Forde M.C.	I/127	Lekou D.J.	I/21
Asserin J.	II/77	Forker J.	II/247	Lenain J.C.	I/125, II/91
Baboux J.C.	I/217	Fraser K.F.	I/161, I/191, I/315	Lenzuni P.	II/67
Bailey J.	I/191	Gaillet L.	I/201	Lipson A.G.	I/149
Baranov S.N.	I/277	Gautrey S.N.	I/125	Little J.	I/161, I/191, I/315
Bayray M.	I/37, II/119	Gebski P.	I/207	van de Loo P.J.	II/7
Belov V.	I/45	Glushko A.	I/45	Loutas T.H.	II/15
Benes P.	I/51, II/27	Goanta M.A.	I/85	Lukác P.	I/117, I/229, I/287
Benmedakhene S.	I/173	Golaski L.	I/207	Lunyevev A.G.	II/303
Bentley J.A.	I/315	Gomera V.P.	I/253	Main I.G.	I/127
Berthelot J.M.	II/59	Goujon L.	I/217	Majzner J.	II/163, II/171
Bisschop J.	II/149	Grad L.	II/305	March L.	II/25
Bláha J.	I/59	Grum J.	II/305	Marques A.T.	II/59
Blaháček M.	I/63, I/293	Hahn J.	I/141	Mathis K.	I/117
Blanch M.J.	I/21	Hähner P.	II/263	Mazal P.	II/27
Boczar T.	I/69, I/77	Hájek K.	I/223, II/171	Mediouni M.	I/173
Bordei M.	I/85, I/135, I/155	Halliday J.	I/127	van Mier J.G.M.	II/149
Bradshaw T.	I/91	Hashigutchi S.	I/223	Mizutani S.	II/35
Brevet P.	I/201	Hatscher A.	I/229	Mizutani Y.	II/35
Brom J.	I/141	He J.	II/35	Mori Y.	II/43
Brown M.	I/191	Hervé C.	I/173	Morino	II/35
Buburuzan L.	I/135	Holford K.M.	I/91, I/237, II/95	Morishima H.	II/141
Budzier R.	I/247	Horikawa K.	I/15, I/239, II/287	Nakanishi Y.	II/141
Callaghan T.	II/131	Hünicke U.D.	I/247	Nikolaidis V.N.	I/21
Campbell P.	I/161	Jihan S.	I/315	Nivesrangsang P.	II/51
Cerny L.	I/99	Jirsík V.	I/99	Novák V.	I/293
Cherfaoui M.	I/173	Jones B.E.	II/279	Novotny P.	II/219
Chlada M.	I/107	Jones L.E.	I/21	Obata Y.	II/43
Chmelík F.	I/117, I/229, I/287	Joosse P.A.	I/21	Ogava D.	II/295
Cochrane C.	II/51	Kabanov B.S.	I/253	Okhotnikov A.A.	I/253
Cole P.T.	I/91, I/125	Kluev V.A.	I/149	de Oliveira R.	II/59
Colombo S.	I/127	Knabl W.	II/225	Ono K.	I/207
Constantinescu S.	I/85, I/135, I/155	Koizumi T.	II/157	Pappas Z.	II/15
Coy J.	II/131	Koktavy P.	II/171	Pavelka J.	II/163, II/171
Crha J.	I/141	Kontsos A.	II/15	Pazdera L.	I/263, II/27
Davies A.	I/91, I/237	Kooistra T.M.	II/7	Peteves S.	II/263
van Delft D.R.	I/21	Korenská M.	I/263	Petrásek P.	II/203
Derjagin D.V.	I/149	Kossivas T.	I/21	de Petris C.	II/67
Dobis P.	II/163	Kostopoulos V.	II/15, II/263	Philippidis T.P.	I/21
Dowson S.P.	II/211	Kouroussis D.A.	I/21, I/29	Polajnar I.	II/305
Dragan V.	I/85, I/135, I/155	Kozyrev O.	I/45	Poppeová V.	II/69
Dragulin I.	I/85	Krofta J.	I/269	Prevorovsky D.	II/77
Drugescu E.	I/135	Kucera P.	II/219	Prevorovsky Z.	I/63, I/107, I/269, II/77, II/83
Drummond G.R.	I/161, I/191, I/315	Kumar V. S.	II/133	Proust A.	I/21, II/91, II/203
Dutton A.G.	I/21	Kuravsky L.S.	I/277	Prukner V.	II/295
Eberlein J.	I/247	Lackner G.	I/279	Pullin R.	I/237, II/95
Ennaceur C.	I/173	Laksimi A.	I/173	Raab M.	I/269
Estrin Y.	I/287	Lamark T.T.	I/287		

Raad A.	II/103, II/111	Shiraishi M.	II/157, II/295	Tsimogiannis A.N.	I/29
Radigon E.	I/185	Sidahmed M.	II/103, II/111	Tudor B.	I/155
Radu T.	I/135	Siddiqui A.M.	I/317	Vales F.	II/239
Raghu Prasad B.K.	II/133	Sikula J.	I/223, II/163, II/171	Vallen H.	II/247, II/255
Rauscher F.	I/37, II/119	Sittner P.	I/293	Vallen J.	II/255
Reuben R.L.	II/51	Skalsky V.	II/177	Varchon D.	II/77
Robert J.L.	I/201	Smutny J.	I/263	Vervoort A.	I/307
Rödhammer P.	II/225	Sodomka L.	I/149, II/185, II/195	Vionis P.	I/21
Rogers L.M.	II/125	Sokolov V.L.	I/253	Vougiouklakis Y.	II/263
Rosatelli R.	II/67	Sotiriadis G.	II/15	Watson J.F.	I/161
Rowland C.	II/131	Spacková H.	II/199	Wevers M.	I/301, I/307, II/271
Sagar R.V.	II/133	Steel J.A.	II/51	Winkelmans M.	II/271
Sajdi P.	II/219	Strunc M.	II/171	Wolfert A.	II/7
Sakamaki K.	I/15, I/239, II/287	Sumiya H.	II/295	Yan T.	II/279
Schelling R.	II/7	Svoboda V.	II/203	Yoshida K.	I/15, I/239, II/287
Schoorlemmer H.J.	II/7	Tacano M.	I/223	Zenner H.	I/229
Schulz M.	I/247	Tessier C.	I/201	Zemlicka F.	II/203
Semukhin B.S.	II/303	Theobald P.D.	II/211	Zhang F.	I/217, II/103, II/111
Serhiyenko O.	II/177	Toporov Yu.P.	I/149	Zizka J.	II/295
Shimoda T.	II/35	Trapl K.	II/219	Zuev L.B.	II/303
Shinomiya T.	II/141	Traxler H.	II/225		
Shiotani T.	II/141, II/149	Tscheliesnig P.	I/279, II/233		

Modeling of AE Propagation in Anisotropic Composite Plates

W. H. Prosser*, Ajit Mal+, and Sauvik Banerjee+

*NASA Langley Research Center

+UCLA

Outline

I. Introduction

- A. Motivation
- B. Previous modeling review

II. SDPT and FE Modeling

- A. Very thin (1 mm) anisotropic (gr/ep) plate
- B. Simulated AE source
 1. Out-of-plane source motion
 2. Single cycle sine wave forcing function

III. Experimental Results

- A. Thicker (16 ply) anisotropic (gr/ep) plate
- B. Out-of-plane lead break source
- C. NIST sensor (not calibrated)

IV. Summary and Conclusions

Modeling of AE Signals

- Sensor/instrument calibration
- Optimization of sensor placement
- Scaling of coupon test results to practical structures
- Source inversion difficulties
- Train AI methods

Numerical Model (FE) Advantages

- Realistic source configurations
 - Subsurface location
 - Dipoles, etc.
- Realistic specimen geometries
 - Reflections
 - Thickness changes
 - Etc.
- Anisotropic materials

Anisotropic Composite Materials

- Increasing aerospace applications
 - Polymer matrix composites
 - Metal matrix composites
 - Ceramic matrix composites
- Need for improved NDE/SHM
 - X-33 tank failure
 - Airbus tail failure
- Complexities
 - Properties function of direction
 - Inhomogeneous
 - Laminated or layered
 - Woven or stitched
 - High attenuation



Composite X-33 LH2 Tank

Finite Element Modeling

- Gary and Hamstad (1994)
 - AE signals in thin plates (2D model)
 - Experimental verification
 - Examined source size, rise time, sensor aperture, FE cell size
- Hamstad, Gary, and O’Gallagher (1996)
 - AE signals in thick plates
 - Experimental verification
- Hamstad, Gary, and O’Gallagher (1998)
 - Scaling for different plate thicknesses and source rise times
 - Realistic source conditions
- Prosser, Hamstad, Gary, and O’Gallagher (1999)
 - Reflections in finite geometries
- Prosser, Hamstad, Gary, and O’Gallagher (1999)
 - Comparison with plate theory

Shear Deformation Plate Theory (SDPT)

- Mindlin (1951)
 - Effects of shear deformation and rotatory inertia in isotropic materials
- Yang et al. (1966)
 - Application to anisotropic materials
- Tang et al. (1987)
 - Dispersion predictions in anisotropic laminated composite plates
- Lih and Mal (1995 and 1996)
 - Waveform predictions in composite plates
 - Integral transform approach
 - Numerical solutions

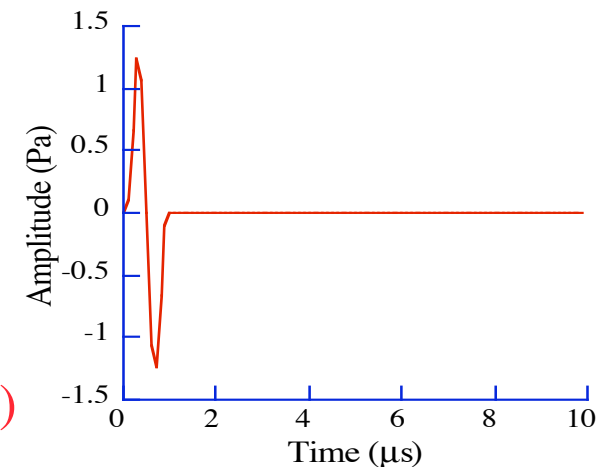
Parameters for Models

- Graphite/epoxy composite
 - Unidirectional “homogeneous” material
 - 1.0 mm thickness
 - 1580 kg/m³ density
 - Elastic properties (GPa)
 - $C_{11} = 160.7$ $C_{12} = 6.44$ $C_{22} = 13.9$
 - $C_{23} = 6.9$ $C_{66} = 7.1$
 - Sine source function applied normal to plate surface

- FE model

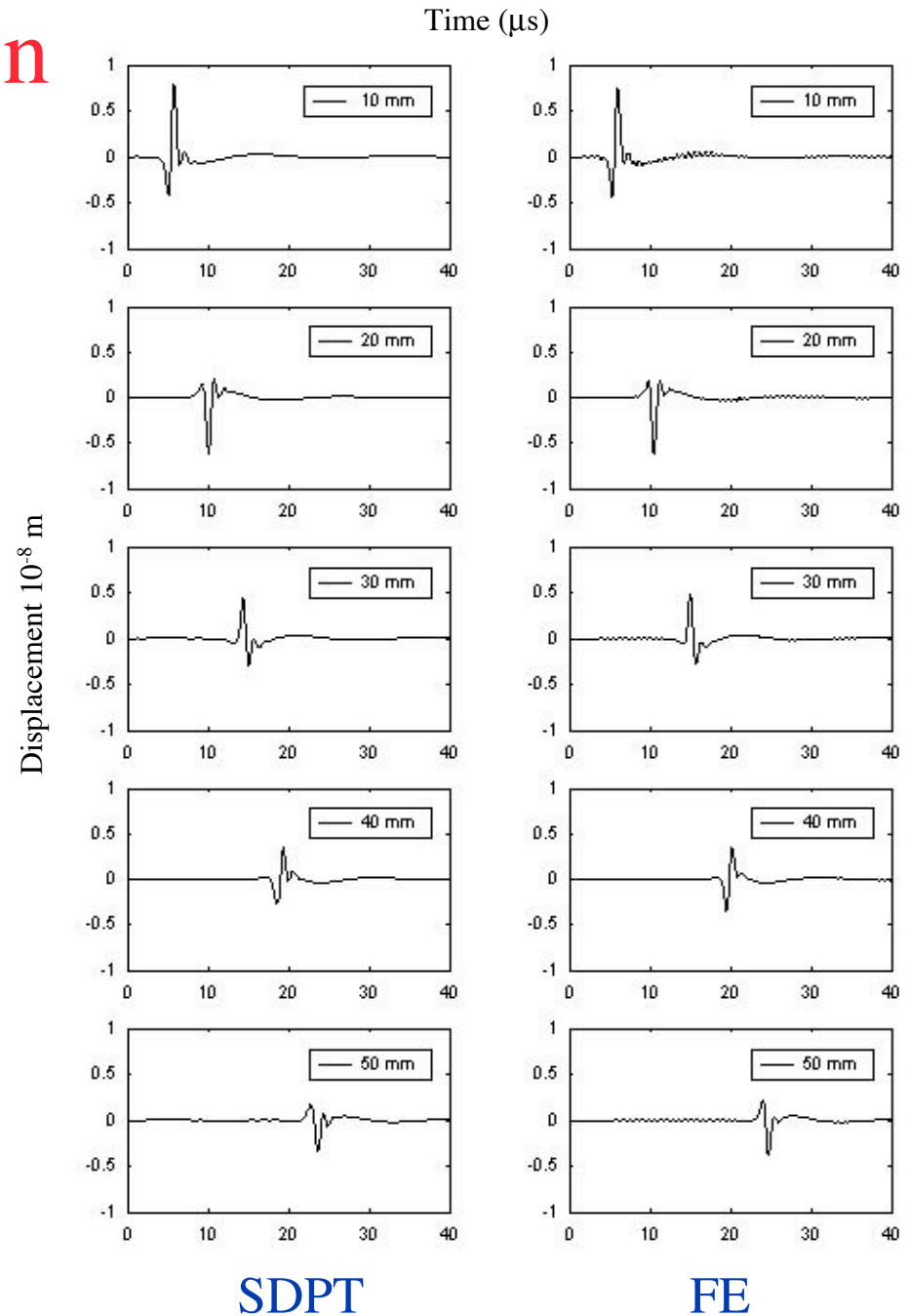
- 200 X 200 mm
- 10 cells through thickness
- Equi-axial cell size (0.1 mm)
- Stress free boundary conditions
- No attenuation effects
- Source diameter of four times cell size (0.4 mm)

$$f(t) = \sin\left(\frac{2\pi t}{\tau}\right) - 0.5 \sin\left(\frac{4\pi t}{\tau}\right), \quad 0 < t < \tau.$$



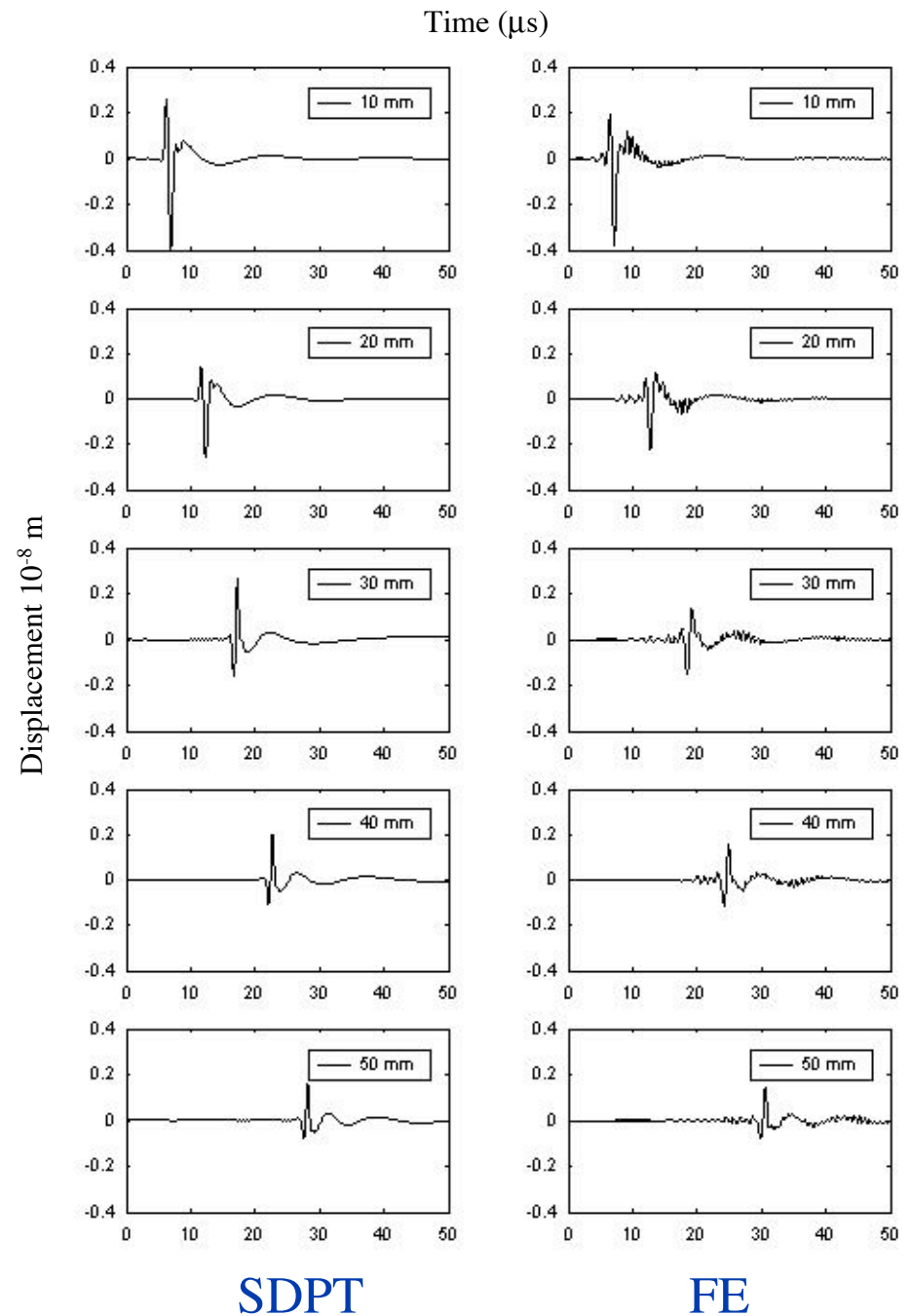
0 Degree Propagation

- All results bandpass filtered (50-650 kHz)
- Excellent agreement
 - SDPT does not predict very small extensional mode observed in FE
 - SDPT arrives slightly faster (higher velocities predicted)
 - Interesting “phase reversal” effect observed



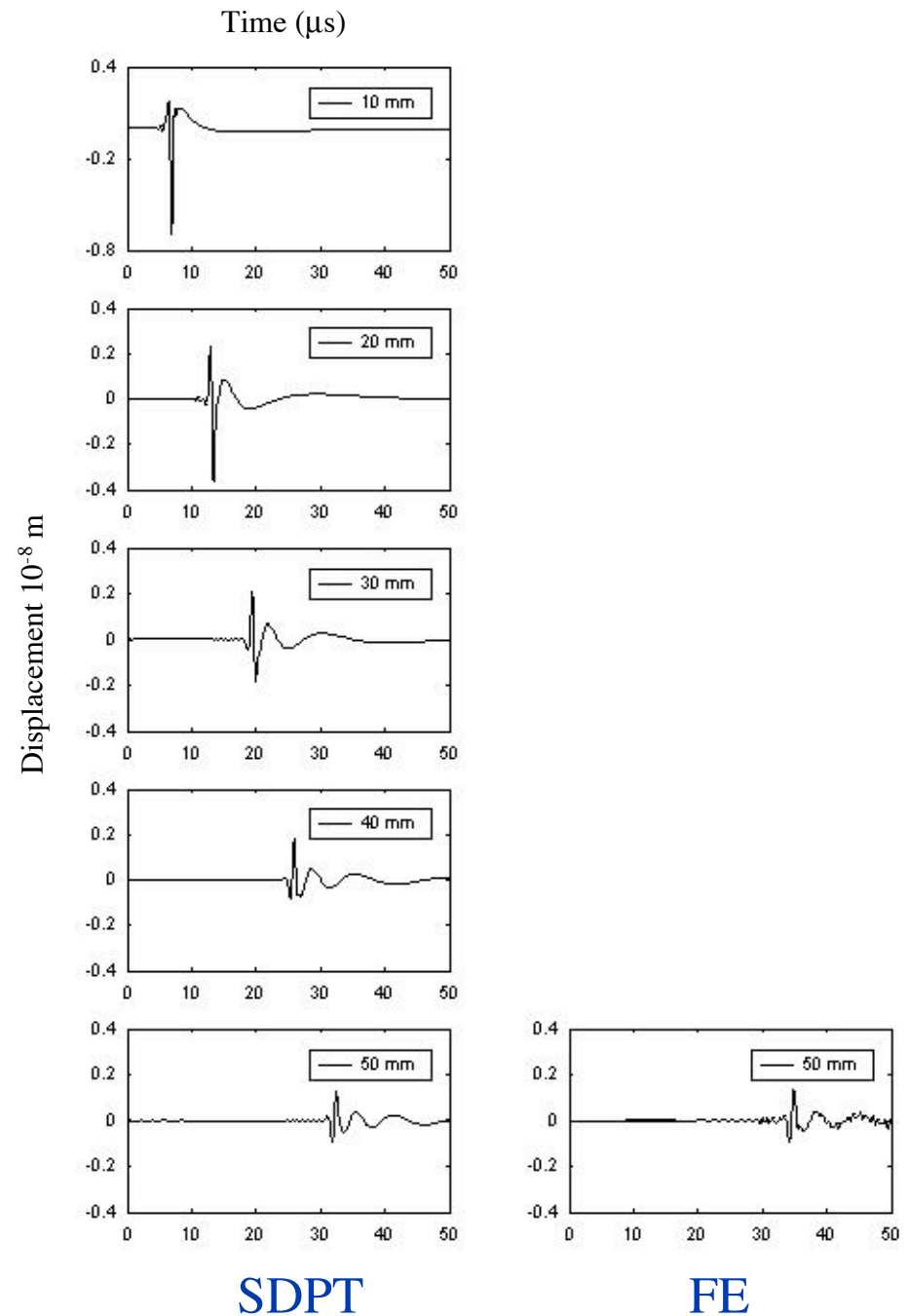
45 Degree Propagation

- Again excellent agreement
 - Larger extensional mode observed in FE
 - “Phase reversal” effect still observed but with different distance of propagation



90 Degree Propagation

- Again excellent agreement
 - Only one distance calculated with FE model
 - “Phase reversal” still present



Experimental Conditions

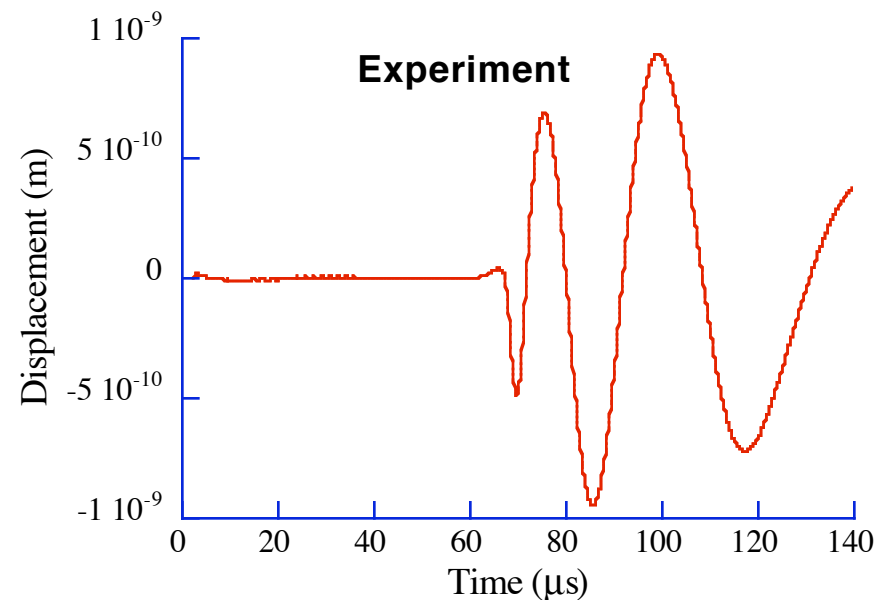
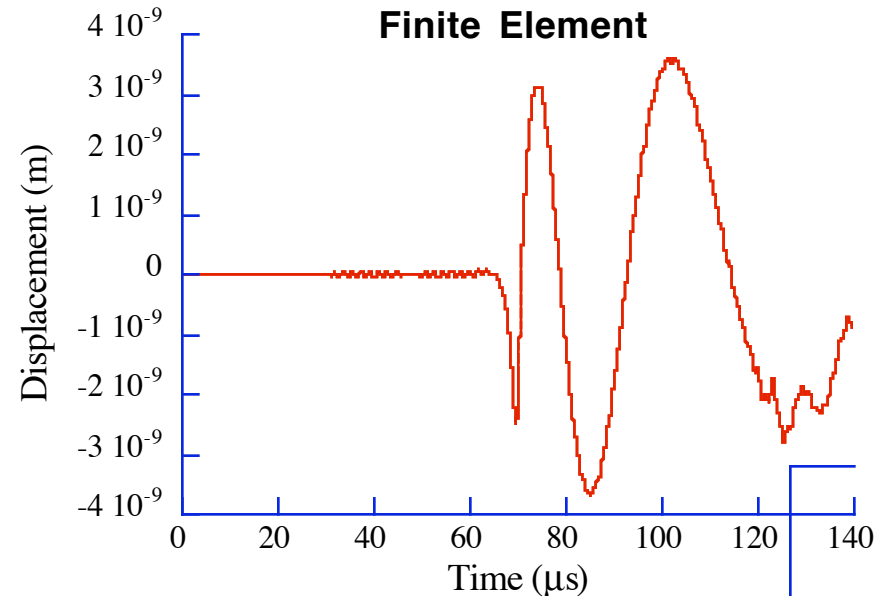
- Graphite/epoxy composite plate
 - Unidirectional 16 ply laminate (1.016 X 0.762 m)
 - 2.26 mm thickness
 - 13.34 cm propagation distance along 0, 45, and 90 degree directions
- 0.5 mm lead break source on center of plate
 - Sudden release of applied force
 - FE models sudden application of force
 - 180 degree shift of experimental waveform
- NIST wideband AE sensor
 - 20 kHz to 1 MHz
 - No calibration available for composite materials
 - Used metal plate calibration factor for comparison (5.6233×10^{-9} m/V)
 - Trigger sensor placed adjacent to lead break with further (2-3 μ s) timing refinement made based on first peak arrivals

FE Model Parameters

- Graphite/epoxy composite
 - Unidirectional material
 - Treated as “homogeneous” but anisotropic media
 - 2.26 mm thickness
 - 1550 kg/m³ density
 - Elastic properties (GPa)
 - $C_{11} = 147.1$ $C_{12} = 4.11$ $C_{22} = 10.59$
 - $C_{23} = 3.09$ $C_{66} = 5.97$
 - Lead break source function time response
- FE model
 - 282.5 X 282.5 mm
 - 12 cells through thickness
 - Equi-axial cell size (0.19 mm)
 - Stress free boundary conditions
 - Source diameter of four times cell size (0.75 mm)
 - No attenuation effects included

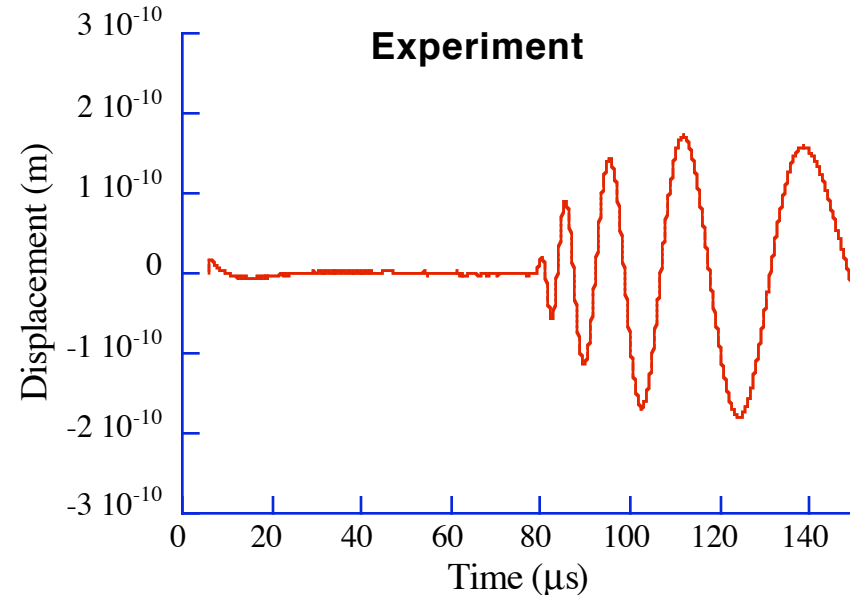
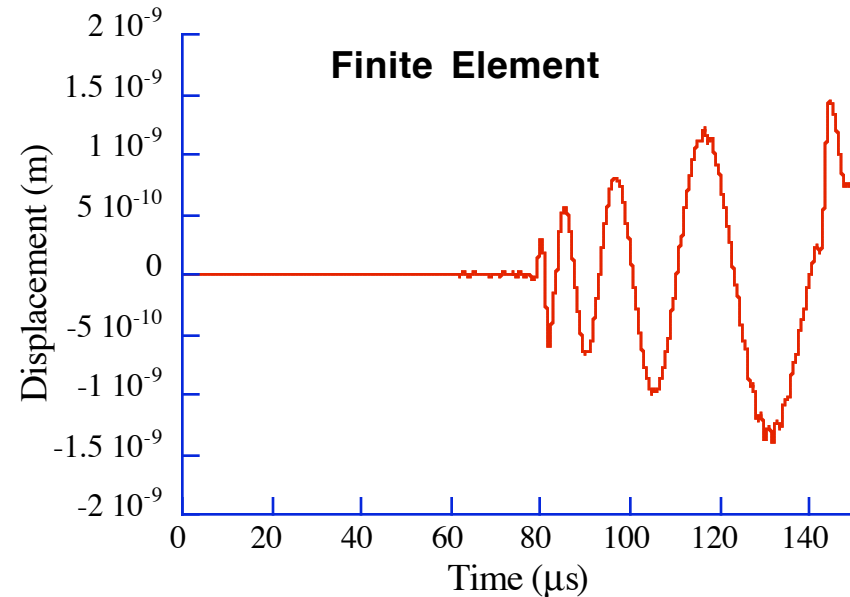
0 Degree Propagation

- 20-1500 kHz filtering
- Reasonable agreement for flexural mode
 - Large reflections in FE predictions beyond 140 μs
 - Uncertainty in actual properties
 - Smaller amplitude experimental results
 - Again, not calibrated
 - Also, FE does not include attenuation effects
- Extensional mode nearly in noise for experimental signal, but some correlation observed



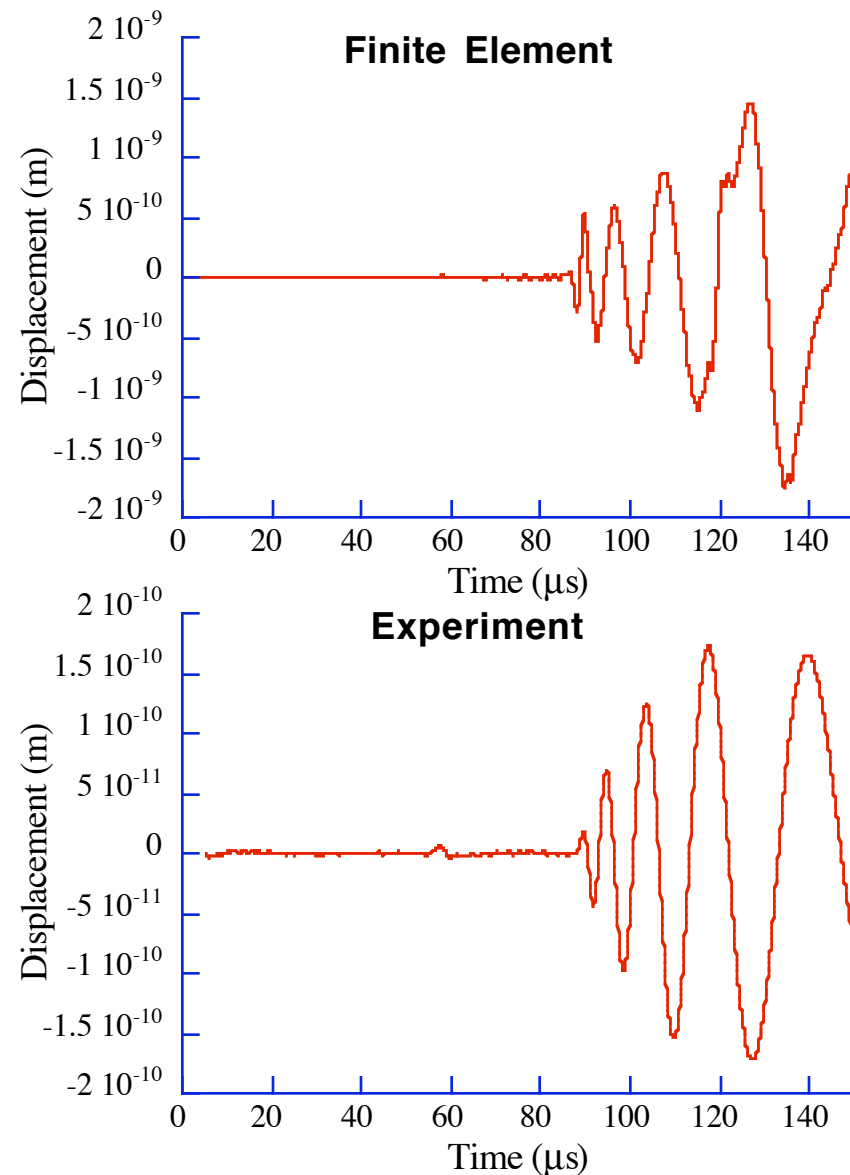
45 Degree Propagation

- Again reasonable agreement in shape of waves
 - Large reflections in FE predictions beyond 150 μs
 - Smaller relative amplitude of experimental results
 - Larger attenuation along 45 degree direction



90 Degree Propagation

- Not quite as good agreement in shape of waves
 - Large reflections in FE predictions beyond 150 μs
 - Smaller relative amplitude of experimental results
 - Largest attenuation along 90 degree direction
 - Again some correlation in extensional mode, but not shown



SUMMARY AND CONCLUSIONS

- Preliminary results on the applicability of the FE model for predicting AE signals in anisotropic composite plates
 - Good agreement with SDPT
 - Flexural plate mode only
 - Source normal to plate surface
 - Single cycle pulse shape
 - Interesting phase reversal effect seen as a function of propagation distance
 - Also interesting correlation with experimental signals
 - Lead break source normal to plate surface
 - 0, 45, and 90 degree directions
- Future work
 - Need calibrated transducer
 - Incorporation of attenuation effects
 - In-plane sources
 - Effects of laminates